ornl

ORNL-5640

OAK
RIDGE
NATIONAL
LABORATORY

UNION
CARBIDE

SOLID STATE DIVISION

PROGRESS REPORT
Period Ending February 29,1980

OPERATED BY
UNION CARBIDE CORPORATION
FOR THE UNITED STATES
DEPARTMENT OF ENERGY

ORNL-5640
Special Distribution

Contract No. W-7405-eng-26

SOLID STATE DIVISION PROGRESS REPORT For Period Ending February 29, 1980

M. K. Wilkinson, Director
F. W. Young, Jr., Associate Director
B. R. Appleton, Section Head
L. H. Jenkins, Section Head
R. M. Moon, Section Head
R. F. Wood, Section Head

Date Published: September 1980

OAK RIDGE NATIONAL LABORATORY
Oak Ridge, Tennessee 37830
operated by
UNION CARBIDE CORPORATION
for the
DEPARTMENT OF ENERGY

Reports previously issued in this series are as follows:

ORNL-1095	Period Ending April 30, 1951
ORNL-1128	Period Ending July 31, 1951
ORNL-1214	Period Ending October 31, 1951
ORNL-1261	Period Ending January 31, 1952
ORNL-1301	Period Ending May 10, 1952
ORNL-1359	Period Ending August 10, 1952
ORNL-1429	Period Ending November 10, 1952
ORNL-1506	Period Ending February 10, 1953
ORNL-1606	Period Ending August 10, 1953
ORNL-1677	Period Ending February 28, 1954
ORNL-1762	Period Ending August 31, 1954
ORNL-1851	Period Ending February 28, 1955
ORNL-1852	Period Ending February 28, 1955
ORNL-1944	Period Ending August 31, 1955
ORNL-1945	Period Ending August 31, 1955
ORNL-2051	Period Ending February 29, 1956
ORNL-2052	Period Ending February 29, 1956
ORNL-2188	Period Ending August 31, 1956
ORNL-2189	Period Ending August 31, 1956
ORNL-2413	Period Ending August 31, 1957
ORNL-2414	Period Ending August 31, 1957
ORNL-2614	Period Ending August 31, 1958
ORNL-2829	Period Ending August 31, 1959
ORNL-3017	Period Ending August 31, 1960
ORNL-3213	Period Ending August 31, 1961
ORNL-3364	Period Ending August 31, 1962
ORNL-3480	Period Ending May 31, 1963
ORNL-3676	Period Ending May 31, 1964
ORNL-3841	Period Ending May 31, 1965
ORNL-3935	Period Ending December 31, 1965
ORNL-4098	Period Ending December 31, 1966
ORNL-4250	Period Ending December 31, 1967
ORNL-4408	Period Ending December 31, 1968
ORNL-4526	Period Ending December 31, 1969
ORNL-4669	Period Ending December 31, 1970
ORNL-4779	Period Ending December 31, 1971
ORNL-4861	Period Ending December 31, 1972
ORNL-4952	Period Ending December 31, 1973
ORNL-5028	Period Ending December 31, 1974
ORNL-5135	Period Ending December 31, 1975
ORNL-5328	Period Ending April 30, 1977
ORNL-5486	Period Ending September 30, 1978

Special Dedication

This issue of the Solid State Division Progress Report is dedicated to the memory of a valuable Division member who died during the past year.

Thomas F. Connolly organized the Research Materials Information Center for the Division in 1962, and he served as its Director for 18 years. Through his leadership and personal efforts, the Center provided many services for Oak Ridge National Laboratory and the entire scientific community. His skills and his close association with Division members are greatly missed.

Contents

LASER ANNEALING

ELECTRONIC AND MAGNETIC PROPERTIES

2. SURFACE AND NEAR-SURFACE PROPERTIES OF SOLIDS

SURFACE PHYSICS

PLASMA MATERIALS INTERACTIONS

ION-SOLID INTERACTIONS

PULSED LASER ANNEALING

PHOTOVOLTAIC CONVERSION OF SOLAR ENERGY

3. DEFECTS IN SOLIDS

RADIATION EFFECTS

FRACTURE

DEFECTS AND IMPURITIES IN INSULATING CRYSTALS

4. TRANSPORT PROPERTIES OF SOLIDS

FAST-ION CONDUCTORS

SUPERCONDUCTIVITY

HIGH TEMPERATURE CONDUCTIVITY OF INSULATING MATERIALS

5. NEUTRON SCATTERING

SMALL-ANGLE NEUTRON SCATTERING

LATTICE DYNAMICS

MAGNETIC PROPERTIES

6. CRYSTAL GROWTH AND CHARACTERIZATION

7. ISOTOPE RESEARCH MATERIALS

Acronyms, Abbreviations, and Initialisms

aBR—anti-Beevers-Ross
ADAS—angular-dependent Auger spectroscopy
AERE—Atomic Energy Research Establishment
AES—Auger electron spectroscopy
ANL—Argonne National Laboratory
ASF—augmented space formalism
ATA—average *t*-matrix approximation
BCA—binary collision approximation
bcc—body-centered cubic
BCS—Bilby, Cottrell, Swinden
BNL—Brookhaven National Laboratory
BR—Beevers-Ross
BSF—back surface field
BSR—Bulk Shielding Reactor
CAF—*commensurate antiferromagnetic*
CB—coherent bremsstrahlung
CDW—charge-density wave
CENS—Centre d'Etudes Nucléaires Saclay
CL—crystal lattice
CLS—*characteristic loss spectroscopy*
CMA—cylindrical mirror analyzer
CNRS—Centre National de la Recherche Scientifique
CPA—coherent potential approximation
CSM—*critical-state model*
CVD—chemical vapor deposition
Cz—Czochralski
DGS—degenerate ground state
dHvA—de Haas-van Alphen
DLTS—deep-level transient spectroscopy
DOE—Department of Energy
DOS—density of states
dpa—displacements per atom
DPS—deuterated polystyrene
EBIC—electron-beam-induced current
EBFZ—electron-beam float zone
EBR—Experimental Breeder Reactor
ECD—Energy Conversion Devices
ELS—electron energy loss spectroscopy
ENDOR—electron nuclear double resonance
EPR—electron paramagnetic resonance
ER—electron resonance
EURATOM—European Atomic Energy Community
EXAFS—extended x-ray absorption fine structure
fcc—face-centered cubic
FFTF—Fast Flux Test Facility
FLL—flux-line lattice
FWHM—full width at half maximum
Fz—float zone
hcp—hexagonal close packed
HFIR—High Flux Isotope Reactor
HVEM—high-voltage electron microscopy
IAEA—International Atomic Energy Agency
IBM—ion beam mixing
IEEE—Institute of Electronic and Electrical Engineers
IFZ—induction float zone
IIT—Illinois Institute of Technology
ILL—Institut Laue-Langevin
IMS—intermediate mixed state
IR—infrared
IRML—Isotope Research Materials Laboratory
ISX—Impurity Study Experiment
JAERI—Japan Atomic Energy Research Institute
J-T—Jahn-Teller
KFA—Kernforschungsanlage
KKR—Korringa-Kohn-Rostoker
LASL—Los Alamos Scientific Laboratory
LBL—Lawrence Berkeley Laboratory
LCAO—linear combination of atomic orbitals
LDA—local density approximation
LCS—linear collision sequence
LEED—low-energy electron diffraction
LLL—Lawrence Livermore Laboratory
LSDW—longitudinal spin density wave
LSS—Lindhard, Scharff, Schiøtt
LTIF—Low-Temperature Irradiation Facility
MCD—*magnetic circular dichroism*
MCDL—minority carrier diffusion length
MCL—minority carrier lifetime
MHD—magnetohydrodynamics
MIT—Massachusetts Institute of Technology
mO—mid-oxygen
MOS FET—metal oxide semiconductor field-effect transistor
NASA—National Aeronautics and Space Administration

NBS—National Bureau of Standards
NBSR—National Bureau of Standards Reactor
NCSASR—National Center for Small-Angle Scattering Research
NEMA—National Electrical Manufacturers Association
NFS—Nuclear Fuel Services
NMR—nuclear magnetic resonance
NRC—National Research Council
NSF—National Science Foundation
NTD—neutron-transmutation-doped
OD—optical density
ODMR—optical detection of magnetic resonance
ORAU—Oak Ridge Associated Universities
ORIC—Oak Ridge Isochronous Cyclotron
ORNL—Oak Ridge National Laboratory
ORR—Oak Ridge Research Reactor
PCD—photoconductive decay
PICS—positive ion crystallography of surfaces
PKA—primary knock-on atom
PLD—periodic lattice distortion
PLM—pulsed laser mixing
PNL—Pacific Northwest Laboratories
PoCIS—poly(ortho-chlorostyrene)
Polysil—polycrystalline silicon
POR—planar oscillation radiation
PPO—polydimethyl phenylene oxide
PSH—hydrogenous polystyrene
RBS—Rutherford backscattering spectroscopy
RCA—Radio Corporation of America
REC—radiative electron capture
RID—radiation-induced displacement
RKKY—Ruderman, Kittel, Kasuya, Yosida
rms—root mean square
RPA—random phase approximation
RTNS—rotating target neutron source
SANS—small-angle neutron scattering
SAS—small-angle scattering
SAXS—small-angle x-ray scattering
SDI—Selective Dissemination of Information
SEM—scanning electron microscopy
SIMS—secondary ion mass spectroscopy
SLS—scanning laser spot
SRO—short-range order
SRP—Savannah River Plant
STO—Slater-type orbital
TEM—transmission electron microscopy
TPA—traveling pseudo-fermion approximation
TSDW—transverse spin density wave
UHV—ultra high vacuum
UNISOR—University Isotope Separator-Oak Ridge Facility
XES—x-ray energy spectroscopy
XFS—x-ray fluorescence spectroscopy
XPS—x-ray photoelectron spectroscopy

Introduction

The reporting period covered by this progress report of the Solid State Division includes the 17 months from October 1, 1978, through February 29, 1980. This period has seen a completion of the major transition in research emphasis that was initiated about five years ago, when the Atomic Energy Commission was replaced by the Energy Research and Development Administration (ERDA), and then was continued with the formation of the Department of Energy (DOE). The broad missions of ERDA and DOE in the development of new energy systems have required a very wide range of research investigations in the materials sciences; every advanced energy technology is faced with severe materials problems, and the solutions to those problems will depend strongly on information obtained through scientific research. During this five-year period, the Solid State Division has entered many new research areas, and over half of the Division's current programs are closely related to the nonnuclear energy technologies. Some increase in support has accompanied this change in emphasis, but much of the new research has resulted from a redirection of previously existing work. The transition has been accomplished smoothly, and the new programs are providing many interesting and productive investigations.

A major new change that is currently taking place in research activities of the Solid State Division concerns the diversity in users and sponsors of the facilities. When the Ames Laboratory Research Reactor was shutdown, three Ames Laboratory neutron scattering instruments were placed in operation at the ORR; this equipment and the ORNL instruments at the HFIR and ORR are available to scientists of both laboratories. A sophisticated 30-m small-angle neutron scattering facility, which was constructed at the HFIR through funds from the NSF, will soon be placed in routine operation. This facility is part of the National Center for Small-Angle Scattering Research that has been established at ORNL under a joint interagency agreement between NSF and DOE, and it will be utilized exclusively in the users' mode of operation. Through the efforts of DOE, preliminary negotiations have been made with the government of Japan to establish a United States-Japan Cooperative Program on Neutron Scattering. This program would involve the construction of one or two new instruments at the HFIR, which would be funded by the government of Japan in return for modest use of all HFIR neutron scattering facilities by Japanese scientists. Plans are also in progress to start a more formal users' program to make the neutron scattering facilities more accessible to university and industrial scientists within the United States. Although informal arrangements for users currently exist and have existed for many years, it is believed that a specific program will ensure the most effective utilization of these facilities. Although current plans for various users' programs involve the neutron scattering facilities, the Solid State Division also has other unique facilities, such as accelerators for ion implantation, channeling, and scattering, which are used informally by many scientists outside of ORNL. It is highly probable that more formal users' programs will be developed for these facilities in the future; such programs undoubtedly will strengthen interactions between members of the Solid State Division and a large number of scientists from other organizations.

The arrangement of this progress report has been chosen to emphasize the major areas of solid state science in which the Solid State Division conducted research during the reporting period. The areas are Theoretical Solid State Physics, Surface and Near-Surface Properties of Solids, Defects in Solids, Transport Properties of Solids, Neutron Scattering, Crystal Growth and Characterization, and Isotope Research Materials. Each constitutes a major section of the report, and additional subdivisions are included within the sections. A short introduction precedes each of the seven sections to indicate the scope and goals of the research and to give a few highlights of recent investigations. These introductions reflect many of the changes that have occurred in programs of the Division. It is also their intent to give a clearer picture of the manner in which the individual programs are interrelated and to indicate how the research activities of the Solid State Division contribute to various programs of ORNL and DOE.

There are very close interactions among various programs of the Division, so that many research summaries could have been placed very logically in two or more subsections. A particularly good example is the neutron scattering research on superconducting flux-line lattices; although these summaries are included in the subsection on superconductivity, they would have fit equally well under small-angle neutron scattering. The Division continues to have a major effort in the ion implantation and laser annealing of semiconductors, with particular emphasis on the development of better photovoltaic materials for solar energy conversion. Because the characterization and understanding of unique materials produced by these techniques have required the skills and experimental facilities of many Division members, the resulting research summaries could have been placed in several subsections. Moreover, there is a very close coupling of almost all of the experimental programs with ongoing theoretical research and with programs concerned with materials preparation and characterization. Consequently, a number of the research summaries have been placed somewhat arbitrarily in one of the appropriate subsections; it is hoped that the arrangement of the report minimizes difficulties for the reader in finding those summaries of interest.

I. Theoretical Solid State Physics

The research activities of the Theory Section cover a wide variety of disciplines and interests. This diversity results, to a certain extent, from close collaboration with the various experimental programs in the Division. This collaboration has led to state-of-the-art investigations, with relevant extensions of existing theories as well as the development of new concepts, theories, and procedures that are applicable to both current and future experimental programs. The development of efficient numerical procedures for obtaining realistic predictions from the complex theories of condensed matter and surfaces has led to important results that have been presented in invited papers at recent international scientific meetings and to considerable collaborative work with scientists from the United States and Europe. Examples of the use of some of these techniques are given below. For purposes of clarity, this section is divided into five subsections. Surfaces, Lattice Dynamics and Alloys, Particle Solid Interactions, Laser Annealing, and Electronic and Magnetic Properties.

Significant progress has been made in the area of surface structure analysis as the result of close cooperation between theoretical and experimental programs within the Division. For a number of years there has been disagreement concerning the accuracy of the surface structures that result from LEED analyses. A detailed analysis of Cu(100) and Ag(110) has revealed that LEED structural analysis for clean metallic surfaces can be sensitive to changes of the order of 2 pm in atomic arrangements, provided care is exercised both in data collection and in the corresponding dynamical calculations. Prior to this investigation it was generally thought that LEED was sensitive to changes in the range of 5 to 10 pm. An improved description of inelastic processes in electron spectroscopy has been made by taking into account the anisotropic terms in the optical potential. This work will have significant bearing on the analyses of future photoemission studies that are carried out at high-intensity synchrotron light sources. Calculations of localized phonon spectra at steps of the (332) surface of Pt have been carried out and compared with inelastic electron loss measurements. It has been shown that vibrational modes with frequencies above the maximum in the bulk can occur provided the largest force constants in a rotationally invariant first- and second-neighbor bond-angle model are increased by ~30 to 40% at the steps. With this adjustment the model calculations give excellent agreement with experiment.

First-principles calculations of the phonon spectra in transition metal superconductors have been continued. The results for Mo predict the anomalous minimum observed by neutron scattering experiments in the acoustic branches at the [100] zone boundary. As found in previous calculations for Nb, the phonon anomalies are not generated by resonant screening or Fermi surface effects but, instead, by

features of the band structure near the Fermi surface (about ±0.5 eV). Significant progress has also been made on the difficult problem of calculating the dynamical properties of random alloys. A new and completely general self-consistent theory for elementary excitations in random alloys has been developed. Approximate solutions using this theory have been shown to produce Green's functions, which are always analytic and have the proper translational symmetry. In addition, this theory has been shown to give better numerical agreement with exact results for model systems than has been obtained previously.

The recent observation of enhanced ion backscattering yields from disordered, amorphous, and polycrystalline targets has stimulated considerable theoretical interest in the general area of particle-solid interactions. This effect occurs in the near-surface region for angles very near 180° and has been shown to be a manifestation of the reversibility of ion trajectories in solids. It has also been found that this enhanced backscattering might occur under channeling conditions in single crystals. Another important area of research in particle-solid interactions is the study of damage produced by particles with high recoil energies characteristic of fusion neutron environments. To investigate fusion neutron damage production, models must be developed that are not only applicable at relatively high primary recoil energies but also at low recoil energies, which are characteristic of the motion of most of the particles in a displacement cascade. The binary collision approximation code MARLOWE has been used to study this problem. Results for Cu indicate that for a static lattice, the lengths of the ⟨110⟩ linear collision sequences are reproduced fairly accurately, while those along ⟨100⟩ and ⟨111⟩ are overestimated. Anomalies found in the mean number of distant Frenkel pairs calculated as a function of primary recoil energy have been attributed to the dynamics of ⟨111⟩ linear collision sequences. It has also been established that thermal energy plays a significant role in the development of displacement cascades in energy ranges below ~1 keV.

The Laboratory has continued to maintain an intense interest in the exploration of laser processing of semiconductor materials. Theoretical research to date is based on the concept that the near-surface region of a sample may melt and then regrow epitaxially as a consequence of irradiation with intense pulses of Q-switched ruby and Nd:YAG lasers. The one-dimensional dopant diffusion model used to describe this process includes the effects of melt-front motion on dopant profiles. Good agreement between calculated and measured profiles has been obtained for a series of dopants in Si. One of the most striking implications of the experimental and theoretical work is that there must be a very large difference between the equilibrium and nonequilibrium interface segregation coefficients. A phenomenological model based on the kinetic theory of melting has been developed which accounts for this effect. One interesting prediction of this model is that the nonequilibrium coefficient depends on the melt-front velocity in a rather simple manner. Because the theoretical calculations have shown that the melt-front velocity can be changed by substrate heating or cooling, a method is available for testing the theory and for studying other aspects of nonequilibrium segregation during ultrarapid resolidification.

Work on the theory of itinerant electron magnetism has continued in an effort to explain the unusual temperature behavior of spin-waves in transition metal

ferromagnets. Calculations of the inelastic neutron scattering cross section for Ni have revealed that at temperatures up to one-half of the Curie temperature essentially all of the spin-wave energy renormalization is due to the smearing out of the Fermi surface and not to spin-wave–spin-wave interactions. The results also indicate that the temperature dependence of spin-splitting of the ferromagnetic energy bands obtained from angular resolved photoemission experiments is not consistent with the spin-wave energy renormalization determined from the neutron scattering experiments.

SURFACES

HIGH-SENSITIVITY LEED ANALYSIS OF THE Cu(100) SURFACE

H. L. Davis J. R. Noonan

Since disagreement exists concerning the accuracy of the surface structures that result from LEED analyses, an investigation of Cu(100) was initiated to address general questions on the accuracy and sensitivity of LEED for the determination of surface crystallography. This investigation has been concerned with both the procedures used to collect the data and the techniques used to extract the desired surface structure information by a theoretical analysis of the data. Some of the results obtained from the experimental considerations are given elsewhere,[1] and the theoretical and calculational aspects are described here.

The data used in the theoretical analysis were collected at normal incidence for each of the individual beams in the symmetrically equivalent {10}, {11}, {20}, and {21} sets. To eliminate some errors in the raw data,[1] the data for the individual beams were then averaged over each symmetrical set to obtain four experimental I-V profiles that serve to represent the (10), (11), (20), and (21) beams. These four averaged profiles formed the input data base for the theoretical analysis.

Numerous sets of dynamical LEED calculations were performed in which the scattering potential, the complex optical potential, and the Debye temperature were all varied over reasonable limits. The only structural parameter varied in our calculations was the first interlayer spacing d_{12}, which was allowed to deviate −6 to +6% from its truncated bulk value. The experimental and calculated I-V profiles were compared by the use of three distinct reliability factors (R factors). These were R_{ZJ}, as defined by Zanazzi and Jona;[2] R_2, which is a measure of the mean square difference between the experimental and calculated profiles;[3] and R_5, which indicates the mean square difference between the slopes of the profiles.[3]

The above procedures have led to the striking agreement between experimental and calculated profiles shown in Fig. 1.1. The calculated profiles are based on a truncated-free-atom potential with full Slater exchange, a surface Debye temperature of 330 K (bulk value = 343 K), a value of 12.1 eV for the real component of the inner potential, and $0.85E^{1/3}$ eV for the imaginary component of the inner potential. The calculations were also for a deviation in the first interlayer spacing Δd_{12} of −0.6% from the bulk value, which implies that the first atomic layer of the Cu(100) surface is slightly contracted toward the second layer. The four-beam R_{ZJ} value for the comparison between experimental and calculated profiles of Fig. 1.1 is 0.046, which is the smallest multibeam R_{ZJ} value ever obtained in any LEED analysis. R_{ZJ} values below 0.20 have been considered

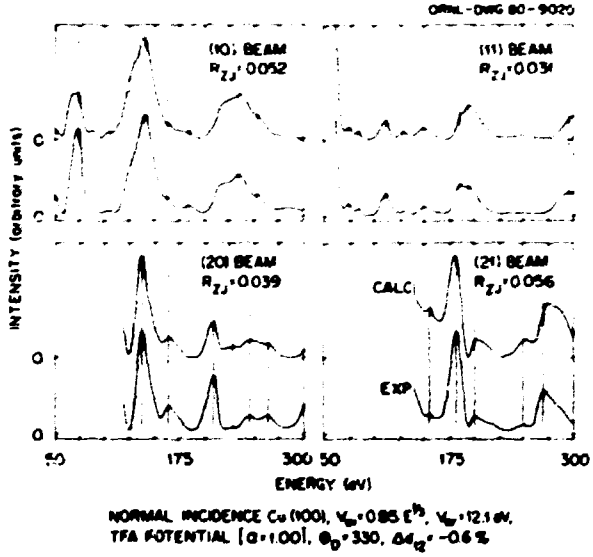

Fig. 1.1. Comparison of experimental and calculated I-V profiles for the clean Cu (100) surface. For each beam the top curve is the calculated profile and the bottom curve is the experimental data.

good for a LEED analysis, and very few LEED analyses have obtained values below 0.10.

One illustration of the sensitivity of the analysis to changes in Δd_{12} is provided by Fig. 1.2, which contains contour plots of the three R factors defined above. These plots are based on a complete set of LEED calculations in which Δd_{12} and the real component of the inner potential V_{or} were varied. The other parameters were fixed at the same values used for the data shown in Fig. 1.1. It should be noted from Fig. 1.2 that the three distinct R factors have their respective minima at values of Δd_{12} in the range -0.9 to -0.5%, which is one indication of the sensitivity of the LEED analysis in establishing the value of Δd_{12} for the clean Cu(100) surface. Another, and perhaps more important, indication of the sensitivity to the structural parameter Δd_{12} is the change in its optimal value as the nonstructural parameters used in the calculations are allowed to vary. The optimal value for a given set of nonstructural parameters is the one providing the minimum of, say, R_{ZJ}.

Sets of calculations have been performed using six different scattering potentials, several functional forms for the imaginary component of the inner potential, and a surface region Debye temperature variation from 250 to 350 K. Any one set of calculations for specific values of these nonstructural parameters could be used to produce plots such as those of Fig. 1.2, with the major differences being the magnitude of the R factors and the values of Δd_{12} and V_{or} giving the minima. For example, the minima of R_{ZJ} varied in the range 0.044 to 0.095, with the minima for Δd_{12} always occurring in the range -1.6 to 0.9%. However, for those sets with minima of $R_{ZJ} < 0.055$, the minima for Δd_{12} occurred in the range -1.0 to 0.5%. For this (and other) reason(s), we believe the analysis has established that $\Delta d_{12} = -0.3 \pm 0.8\%$ for the clean Cu(100) surface.

A variation of 0.8% in d_{12} for Cu(100) is equal to 1.44 pm. Therefore, the analysis for this surface has a sensitivity in the crystallography of approximately 2 pm. Thus, we infer that LEED structural analyses for clean metallic surfaces can be sensitive to changes of the order of 2 pm in atomic arrangements, provided care is exercised in both data collection and the corresponding dynamical calculations. Prior to our investigation of the Cu(100) surface, it was generally thought that LEED was sensitive only to changes in the range of 5 to 10 pm.

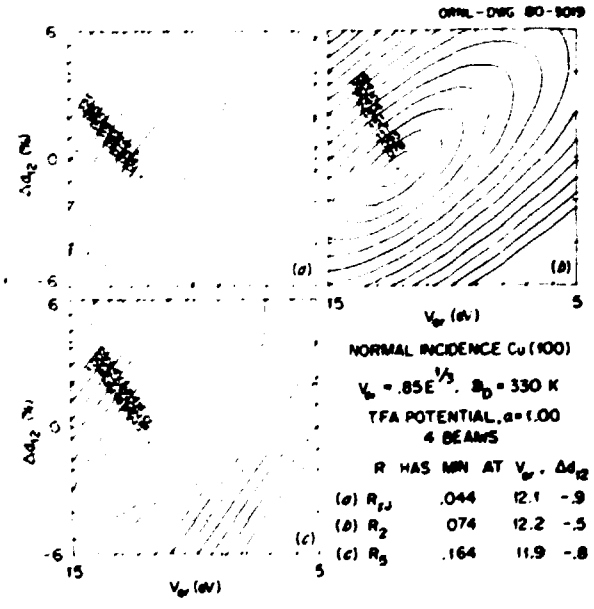

Fig. 1.2. Contour plots of three R factors for the clean Cu(100) surface.

1. J. R. Noonan and H. L. Davis, "Effects of Data Averaging on LEED Analyses: A Case Study of the Cu(100) Surface," this report.
2. E. Zanazzi and F. Jona, *Surf. Sci.* 62, 61 (1977).
3. M. A. Van Hove, S. Y. Tong, and M. H. Elconin, *Surf. Sci.* 64, 85 (1977).

STRUCTURE OF THE CLEAN Re(10$\bar{1}$0) SURFACE[1]

H. L. Davis D. M. Zehner

LEED has been shown to be a valuable tool for the investigation of surface crystallography. For example, past work has indicated that the distance between the first two atomic layers of a metal can range, depending on the surface, from an expansion of 2.5% to a contraction of 15% of the bulk value. However, this previous work has dealt overwhelmingly with the low-index surfaces of bcc and fcc crystals, and the limited work done on hcp metals has dealt only with the (0001) surface, where contractions of, at most, 5% have been found. Thus, it is interesting that the first attempt at a LEED analysis for the (10$\bar{1}$0) surface of an hcp metal, discussed here, produces the result that the first interlayer spacing is contracted by about 17%.

Data consisting of normal incidence I-V profiles for the (01), (10), and (11) beams from Re(10$\bar{1}$0) have existed for some time.[2] The predominant structure in the (01) profile exists below 40 eV, while structure exists in the (10) and (11) profiles up to the cutoff

energy of 200 eV. To avoid complications in the choices of some nonstructural parameters, it was decided to analyze only the data in the 50- to 200-eV energy range. Thus, the data base for the analysis consisted only of the (10) and (11) profiles.

As indicated by Fig. 1.3, the hcp structure could terminate in two different "ideal" $(10\bar{1}0)$ surfaces. By ideal we mean a perfectly planar surface with no steps. Of course, an actual "clean" surface from which data are collected could consist of either termination or some mixture of individual domains of both. Only a full theoretical LEED analysis of the experimental I-V profiles could determine which, or what combination, of the two terminations exists on the clean Re$(10\bar{1}0)$ surface. As outlined below, the results of our analysis indicate that the Re$(10\bar{1}0)$ surface, within the limits of the analysis, is composed totally of domains of the termination designated "A."

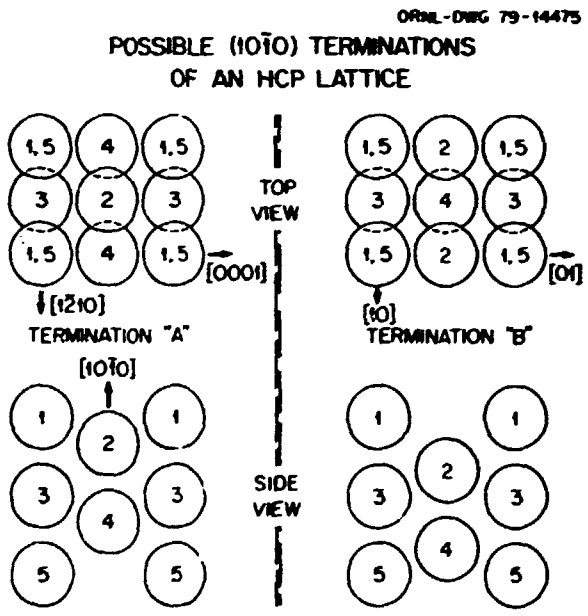

Fig. 1.3. The $(10\bar{1}0)$ terminations of an hcp crystal. The numbers indicate the layers for the respective terminations.

Dynamical LEED calculations were performed using both of the terminations illustrated in Fig. 1.3. Since some of the interlayer distances of either termination are quite short (1.5 a.u. = 80 pm), it was found convenient to treat both the intra- and interlayer multiple scattering by use of the angular momentum representation. Computer codes were written to utilize normal incidence, rotational symmetry, and mirror symmetry. The calculations used a Debye temperature of 320 K and eight phase shifts, which were obtained from a truncated-free-atom approximation using full Slater exchange. The imaginary component of the inner potential was 5 eV, and the real component was varied to obtain the best correspondence with the data. This variation produced a value of 14 eV.

The experimental (10) profile is compared with sets of calculated profiles for both terminations in Fig. 1.4, where distances between the first and second atomic layers d_{12} and the second and third layers d_{23} are specified in a.u. For the truncated bulk crystal (no interlayer relaxation), these have values of d_{12} (termination A) = d_{23} (termination B) = 1.51 and d_{23} (termination A) = d_{12} (termination B) = 3.01. Also indicated on Fig. 1.4 are single-beam reliability factors R (as defined by Zanazzi and Jona[3]) which resulted when the calculated profiles were compared with the data.

An examination of Fig. 1.4 indicates that the Re$(10\bar{1}0)$ surface is composed mainly of termination A, since all the R values for termination B are rather large compared to the minimum R for termination A. Decreases in the R values for termination B could only be achieved by increasing the value of d_{12} very significantly beyond the truncated bulk value. It is noted from Fig. 1.4 that the minimum R for termination A occurs when d_{12} is about 1.25 a.u. It is important that a minimum R occurs in the analysis of the (11) profile for termination A when d_{12} also is equal to about 1.25 a.u., since this provides a convincing consistency to our analysis. Thus, we conclude that within the limits of the analysis, termination B does not exist on the Re$(10\bar{1}0)$ surface. Although a d_{12} value of 1.25 a.u. for termination A means a 17% contraction in the interlayer spacing, this represents only a 1.3% decrease in bond length between nearest neighbors.

This is the first LEED analysis of a $(10\bar{1}0)$ surface of an hcp metal. Although we have employed a data base consisting of only two I-V profiles, the analysis has produced results that are consistent for both beams. Certainly a larger data base would have been useful, and it is hoped that our preliminary work on Re$(10\bar{1}0)$ will motivate future work on this surface and also on the $(10\bar{1}0)$ surfaces of other hcp metals. Such work could determine whether the single termination and large interlayer contraction indicated by our analysis for Re are common features for the $(10\bar{1}0)$ surfaces of hcp metals.

---

1. Summary of paper: *Journal of Vacuum Science and Technology* (in press).
2. D. M. Zehner and H. E. Farnsworth, *Surf. Sci.* **30**, 335 (1972).
3. E. Zanazzi and F. Jona, *Surf. Sci.* **62**, 61 (1977).

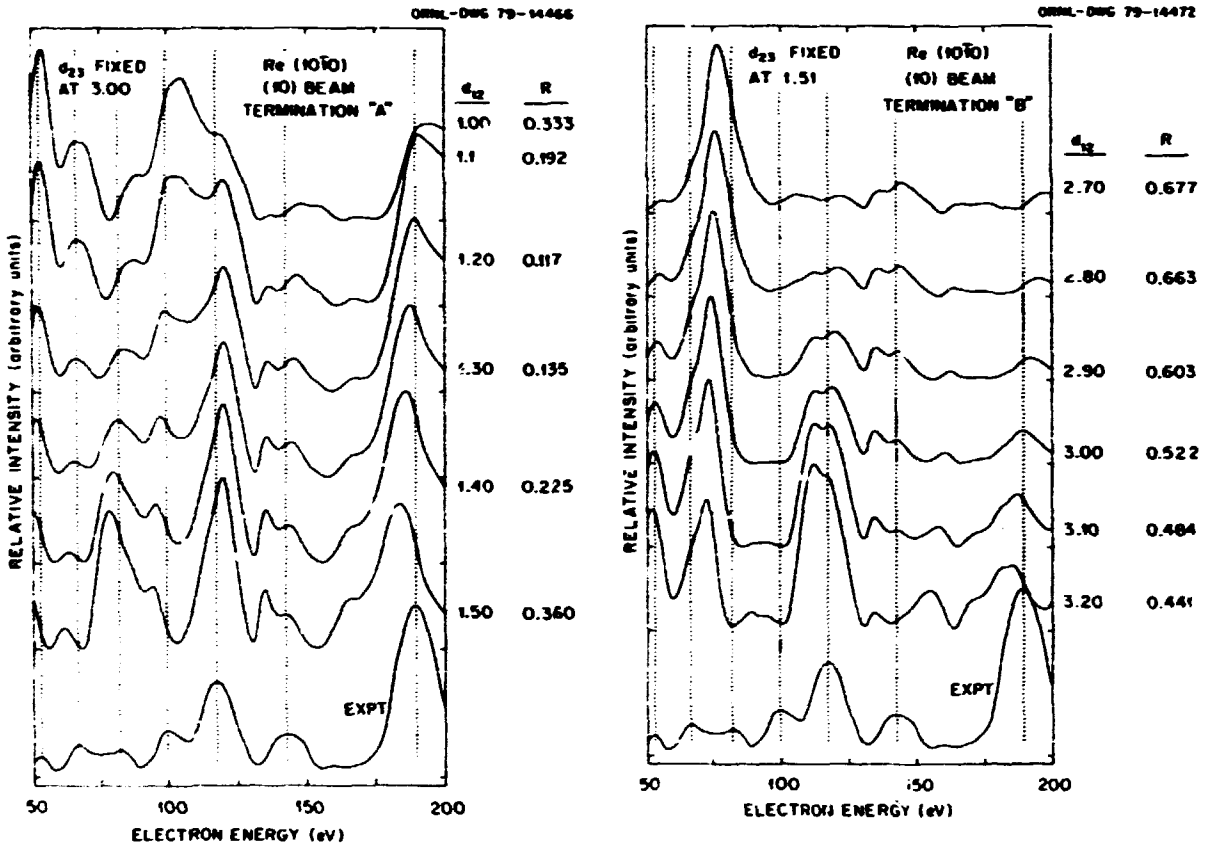

Fig. 1.4. Comparison of the experimental (10) profile with calculations for the two possible terminations.

LEED ANALYSIS OF Re(0001)

H. L. Davis D. M. Zehner

During the past few years a program has evolved at ORNL for the analysis of LEED data. This program has required the development of extensive computer codes to perform the necessary multiple scattering calculations. These codes have been thoroughly checked for accuracy and then used to analyze data collected at ORNL. Several applications of the codes have been made, and each new one has provided valuable experience and insight which prove useful as the LEED analysis program proceeds. To gain experience in treating the surfaces of hcp metals, it was decided to use the codes to analyze some existing data[1] for the (0001) and (10$\bar{1}$0) surfaces of Re. The investigation of the (0001) surface is summarized here, and the (10$\bar{1}$0) work is described elsewhere.[2]

The data base for this investigation consisted of experimental I-V profiles for the (01), (11), and (02) diffraction beams with an energy cutoff of 200 eV.[1] To determine the crystallography of the Re(0001) surface, these experimental profiles were compared with calculated profiles. Several sets of calculations were done in which the scattering potential, inner potential, and surface region Debye temperature were varied. The set that produced the best agreement with the data and whose results are presented here was performed using a truncated-free-atom potential with full Slater exchange, 5 eV for the imaginary component of the inner potential, 14 eV for the real component of the inner potential, and a Debye temperature of 350 K.

As has been discussed by others,[3] the hcp structure could terminate in two different ideal (0001) surfaces. By "ideal" we mean a perfectly planar surface with no steps. The two possible terminations are a consequence of the ... ABABAB ... stacking along the c axis (i.e., the crystal could terminate with either an A or a B layer). The LEED pattern observed for either of these two terminations would exhibit a threefold symmetry at all energies of the incident

beam, but the diffraction pattern actually observed from Re(0001) exhibited a sixfold symmetry. This implies that the experimentally investigated Re(0001) surface was probably composed of equal mixtures of domains of the individual terminations. A verification of this composition is provided by Fig. 1.5, where the experimental (01) profile is plotted and compared with calculations for the two possible terminations and their simple average. The calculated results were obtained from a model in which the first interlayer spacing of both terminations had a 6% contraction from the bulk value. (Results below verify that this is a reasonable choice.) Figure 1.5 clearly demonstrates that terminations A and B produce different I-V profiles and that reasonable agreement with experiment is obtained by the average of the profiles for A and B.

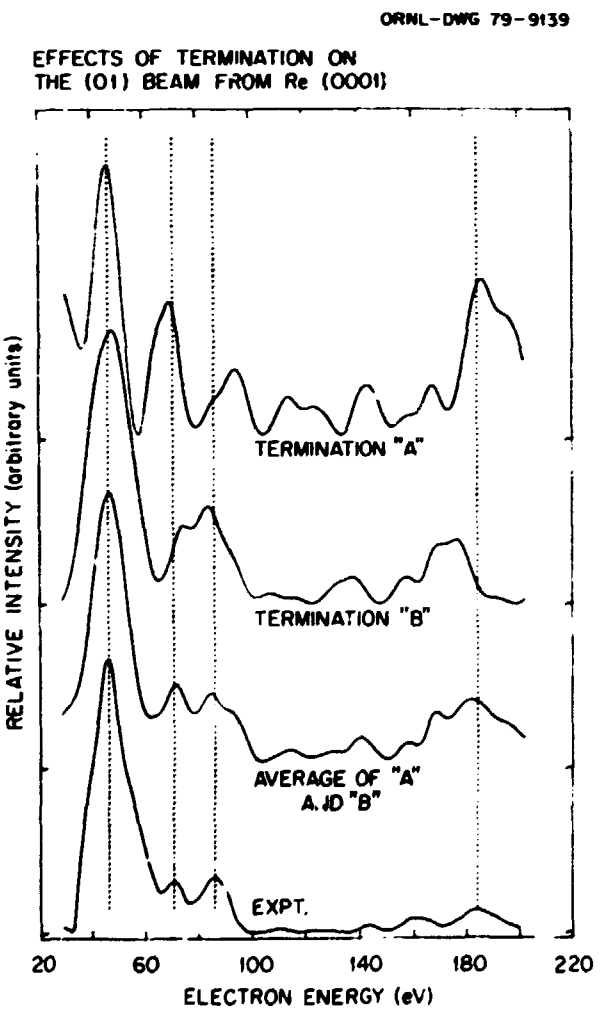

Fig. 1.5. Effects of termination on the (01) beam from Re (0001).

In order to determine any possible variation in the value of the first interlayer spacing Δd_{12} from the bulk value, calculations were performed in which this structural parameter was varied. Figure 1.6 compares the results of such calculations for the (01) beam with the experimental profile. The calculated profiles are the average of those for the two terminations, and both terminations assumed the same value of Δd_{12}. Also given with each calculated profile of Fig. 1.6 are values of the single-beam reliability factor R defined by Zanazzi and Jona.[4] These R values serve to compare numerically the calculated and experimental profiles, with the smallest R giving the best

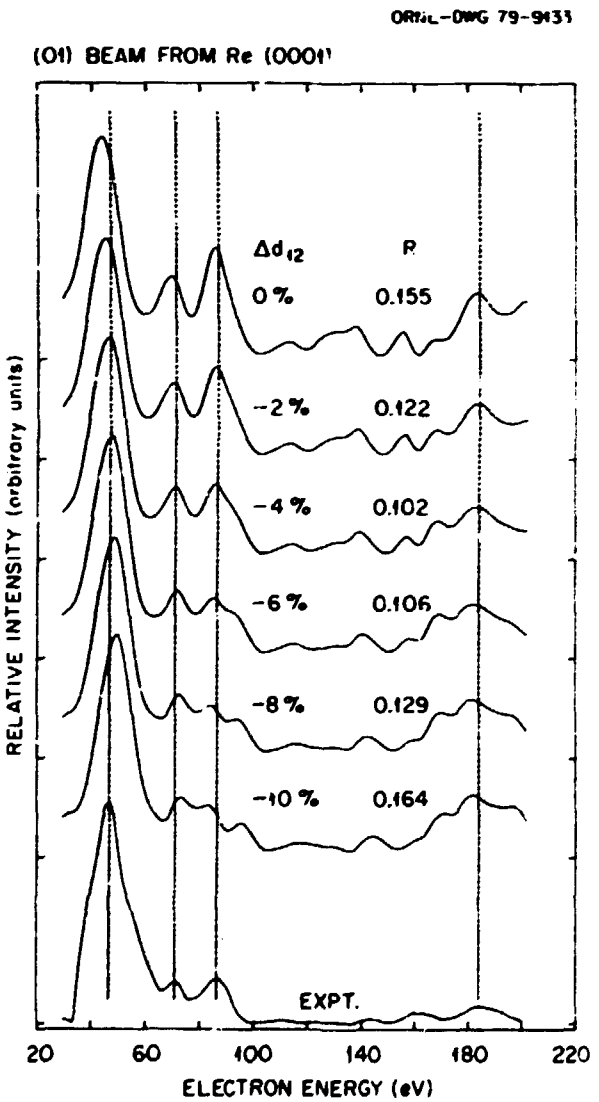

Fig. 1.6. Effects of variation of the first interlayer spacing on the calculational (01) profiles.

agreement. The R values obtained here have a minimum for $\Delta d_{12} \cong -5\%$.

The experimental profiles for the (11) and (02) beams have also been analyzed, and the results are consistent with those for the (01) beam. Therefore, we have concluded that the Re(0001) surface is composed of equal mixtures of domains of the two terminations, where both domains have about a $5 \pm 2\%$ contraction in their first interlayer spacing. The domains are probably connected by monatomic steps. In addition, the calculations would be expected to produce reasonable agreement with the experimental profiles only if the domain dimensions for both terminations were larger than the coherence length of the incident electrons. Therefore, our results for Re(0001) imply that the domain dimensions were at least of the order of 20 nm.

---

1. D. M. Zehner, Ph.D. thesis, Brown University, June 1972.
2. H. L. Davis and D. M. Zehner, "Structure of the Clean Re(10$\bar{1}$0) Surface," this report.
3. H. D. Shih et al., *J. Phys. C* **9**, 1405 (1976).
4. E. Zanazzi and F. Jona, *Surf. Sci.* **62**, 61 (1977).

HIGH-FREQUENCY VIBRATIONAL MODES AT STEPPED Pt(111) SURFACES[1]

Mark Mostoller Uzi Landman[2]

Ibach and Bruchmann[3] have recently reported inelastic electron-loss measurements of localized phonons at the (332) or 6(111) × (11$\bar{1}$) surface of Pt. The most interesting feature of their results is that the observed phonon-loss peak occurs at a frequency of 25.4 meV, slightly higher than the maximum frequency of 24.3 meV in bulk Pt and roughly 15% above the highest frequency peak at ~22 meV in the bulk density of states. This is somewhat unexpected, because phonon frequencies usually decrease at surfaces, thereby reflecting the missing bonds. To explain higher-frequency surface vibrational modes, the force constants in the surface region must increase over their bulk values by substantial amounts. Arguing by analogy to a linear chain with first-neighbor interactions, Ibach and Bruchmann estimated that the force constants for atoms at the steps must be increased by a factor of approximately 1.7 to explain their data.

Drawing conclusions for three dimensions from one-dimensional models is generally somewhat risky. On the other hand, high Miller index surfaces with regularly stepped structures are difficult to treat by conventional methods that rely on use of a two-dimensional Fourier transform with respect to surface wave vectors. An approach that does not vary in complexity with surface normal, that is, one that can be applied to (hkl) surfaces in the same way as to (100), (110), or (111), is the recursion method.[4] We have applied this method to large clusters of atoms to investigate vibrational modes at stepped fcc surfaces.

For the interatomic forces, we use a first- and second-neighbor ($1nn + 2nn$) bond-angle model like that described by Keating.[5] In the bulk, this is equivalent to a general $1nn + 2nn$ Born–von Kármán model, but unlike the latter, the bond-angle model is automatically rotationally invariant at surfaces. The first step in the calculations was to fit the five parameters of the force model to the neutron scattering data for bulk Pt.[5] Reasonably good agreement with the measured dispersion curves was obtained, although forces of longer range are needed to fit all details of the spectrum.

Figure 1.7 shows the regularly stepped fcc (332) surface. The atoms at (0, 0, 0), (0, −1, −1), and (0, −3, 3) are referred to here as edge, corner, and terrace atoms, respectively. Any atom that does not occupy a site on a surface step is called a bulk atom. For a surface as complex as that shown in Fig. 1.7, it is difficult to argue what relaxation will occur and how the force constants will change. We, therefore, adopted a pragmatic viewpoint and focused our attention on the step edges, allowing changes only in the first-neighbor bond-stretching force constants for edge and corner atoms.

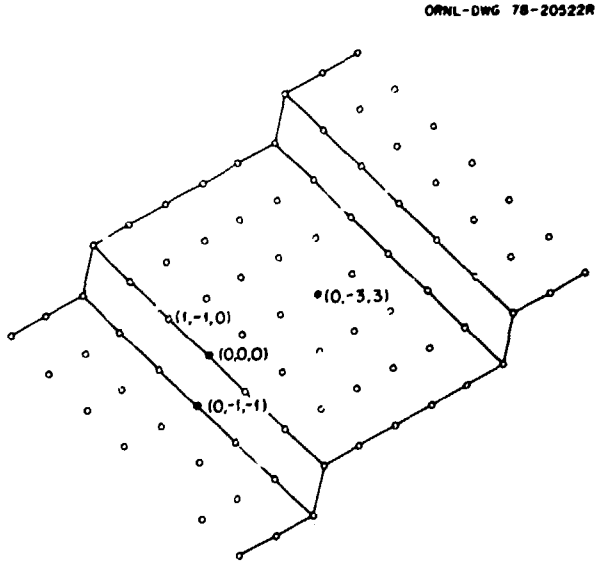

Fig. 1.7. The fcc (332) or 6(11$\bar{1}$) × (111) surface.

Figure 1.8 compares densities of states for edge, terrace, and corner atoms for vibrations along the [111] direction, the normal to the steps. To obtain these results, recursion was performed within clusters of 4099, 4313, and 4468 atoms, respectively. The dashed curves are those obtained with no changes in the forces at the surface except for the absence of interactions involving missing neighbors. The solid curves were calculated by assuming that all 1*nn* bond-stretching force constants for edge-corner, edge-bulk, and corner-bulk atom pairs were increased by about 35%.

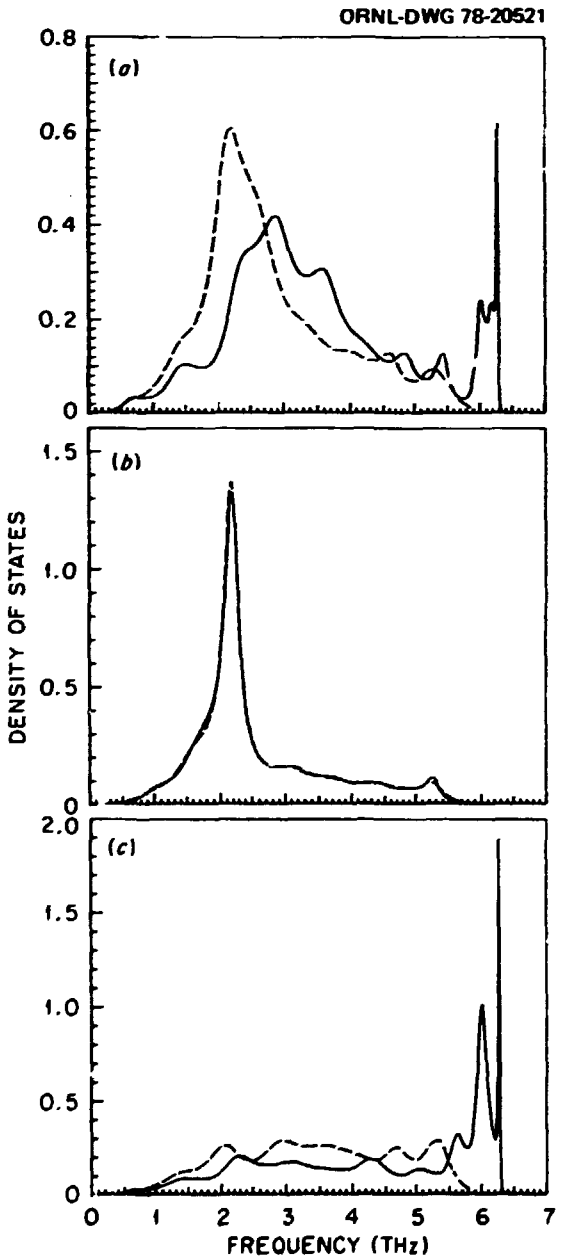

Fig. 1.8. Normalized densities of states for [111] vibrations at the Pt (332) surface for edge (*a*), terrace (*b*), and corner (*c*) atoms. Full lines are for 1*nn* bond-stretching force constant increases of 15,000 dynes/cm at the steps as described in the text, and dashed lines are for no force-constant changes.

Figure 1.8 shows that no high-frequency modes occur for edge, corner, or terrace atoms in the absence of force constant changes, although the [111] densities of states for the three atoms are quite different from one another and from the bulk results. With 1*nn* forces at the steps increased by ~35%, high-frequency peaks appear for both edge and corner atoms, while essentially no change is seen in the terrace atom density of states. The pronounced high-frequency structure for edge and corner atoms extends from about the top of the bulk spectrum at 24.4 meV to about 26.1 meV (5.9–6.3 THz; 1 THz = 4.135 meV), in excellent agreement with the electron-loss peak observed by Ibach and Bruchmann[3] at 25.4 meV (6.15 THz).

Other sets of force constant changes at the steps yield high-frequency modes for vibrations along the step-normal direction. These can be distinguished from one another by the structure they give for [111] vibrations and by their effects for other atoms and vibrational directions. All the sets that we have tested require substantial (30–40%) increases in the force model parameters at the steps but not of the magnitude (70%) inferred by Ibach and Bruchmann from one-dimensional arguments. We have also performed calculations for another stepped surface similar to the (332) or 6(111) × (11$\bar{1}$), namely the (755) or 6(111) × (100), and found similar results.

1. Summary of paper: *Phys. Rev. B* **20**, 1755 (1979).
2. Consultant from Georgia Institute of Technology, Atlanta.
3. H. Ibach and D. Bruchmann, *Phys. Rev. Lett.* **41**, 958 (1978).
4. R. Haydock, V. Heine, and M. J. Kelly, *J. Phys. C* **5**, 2845 (1972).
5. P. N. Keating, *Phys. Rev.* **145**, 637 (1966).

LATTICE RELAXATION AT METAL SURFACES: AN ELECTROSTATIC MODEL[1]

Uzi Landman[2] Ross N. Hill[3]
Mark Mostoller

The termination of a solid by a surface modifies both the atomic coordination and the conduction electron distribution. As a result, normal surface

relaxation (changes in interplanar spacings relative to their bulk values) and surface reconstruction (lateral structural modifications) may occur. Surface relaxation has been measured for a number of fcc, bcc, and hcp low-index clean metal surfaces and is the subject of the present investigation.

A first-principles determination of atomic positions at surfaces would require a very difficult, self-consistent energy minimization for the coupled system of ions and conduction electrons, and no such calculation has been done. On the other hand, approaches based on pair potentials have usually predicted outward relaxations for low-index faces, in contradiction with experimental evidence that contraction of the first interlayer spacing occurs in many, if not most, cases. The inadequacy of surface relaxation models based on pair potentials has been emphasized by Finnis and Heine,[4] who presented a heuristic model for sp-bonded metals. In their very simple picture, the electron density at the cleaved surface is smoothed to a perfectly flat, step-function distribution. As a result, the ions in the first layer experience an electrostatic force that produces an inward relaxation. Finnis and Heine found results for the low-index faces of Al that were in qualitative agreement with experiment, but their model is not material dependent; it depends only on the crystal structure and the surface normal.

It is clear that electrostatic forces make significant contributions to surface relaxation; these contributions cannot be neglected in comparison to those of short-range forces and broken bonds that generally (by themselves) predict outward relaxation. However, no systematic study of the effects of physically reasonable variations within an electrostatic model has heretofore been made. We have found that three such variations produce quantitatively significant effects: (1) multilayer relaxation; (2) charge density profiles; and (3) pseudopotential corrections.

The simple electrostatic model used here combines the contributions to the forces on ions in the surface layers due to the delocalized electron distribution with those arising from interactions with the other ionic charges in the planar nets. Three models for the electron density were studied: (1) a step-function density profile, (2) an exponential form,[5] and (3) a rigid self-consistent distribution derived from the jellium model.[6] For the exponential density profile, pseudopotential corrections were incorporated in a simple way. Under the influence of the forces acting on them, ions in an arbitrary number of surface planes were allowed to relax from their bulk positions, and the planar displacements were determined by a rapidly convergent iterative technique. Except for the step-function density, the method is material dependent, in contrast to the original Finnis and Heine method. It is easy to apply and it yields correct trends when compared with measured relaxation values for several simple metals.

To illustrate our results, Table I.1 shows the importance of multilayer relaxation mechanisms for exponential charge density profiles at Al and Na surfaces, with no pseudopotential corrections. The effect of allowing more than just the outermost layer to relax is significant for the surfaces that undergo large relaxations, which in Table I.1 are the fcc (110) and bcc (100) faces (these are the least densely packed faces). For these surfaces, allowing more layers to relax does not merely give nonzero values for the displacements of the deeper planes, but also modifies the displacements of previously considered layers. A tendency of the displacements to alternate in sign is noted, although for Na(111), for example, all layers relax outward. In general, after the first one or two layers, the magnitude of the relaxation decreases exponentially as one goes into the solid from the surface.

The possibility that several layers may participate in the relaxation is potentially significant for LEED analyses of clean metal surfaces, in most of which only the top layer of atoms has been allowed to relax. In a recent study of Cu(110) LEED intensity spectra, it was found that the structural model that fits the data best was about a 10% contraction of the spacing between the first and second layers accompanied by perhaps a slight contraction or expansion between the second and third layers.[7] Similarly, for the Re($10\bar{1}0$) surface, about a 17% contraction of the first-second layer distance and a modest expansion between the second and third layers appear to give the best agreement with experiment.[8] In light of these recent studies and our results, it is suggested that multilayer relaxation models be considered more routinely in LEED analyses and in the interpretation of ion scattering and channeling experiments.

---

1. Summary of paper: *Phys. Rev. B* 21, 448 (1980).
2. Consultant from Georgia Institute of Technology, Atlanta.
3. University of Virginia, Charlottesville.
4. M. W. Finnis and V. Heine, *J. Phys. F* 4, L37 (1974).
5. J. R. Smith, *Phys. Rev.* 181, 522 (1969).
6. N. D. Lang and W. Kohn, *Phys. Rev. B* 1, 4555 (1970).
7. H. L. Davis, J. R. Noonan, and L. H. Jenkins, *Surf. Sci.* 83, 559 (1979).
8. H. L. Davis and D. M. Zehner, *Journal of Vacuum Science and Technology* (to be published); "Structure of the Clean Re(1010) Surface," this report.

Table I.1. Relaxation of the spacing between the first and second layers, $\Delta_{12} = [\Delta(1) - \Delta(2)]/d$ (− denotes a contraction and + an expansion), and layer by layer displacements for the low-index faces of Al and Na using an exponential electron density taken from ref. 5; the integer L denotes the number of planes allowed to relax, and the numbers in the fourth column are the values obtained for $\Delta(n)/a$, where $n = 0, 1, \ldots$, is the layer index

Surface	L	Δ_{12} (%)	$\Delta(n)/a$
Al(100)	1	−1.1	−0.0054
	10	−1.2	−0.0054, 0.0006, −0.0001
Al(110)	1	−8.7	−0.0309
	2	−18.2	−0.0397, 0.0248
	5	−21.2	−0.0435, 0.0316, −0.0148, 0.0080, −0.0035
	10	−21.3	−0.0436, 0.0318, −0.0151, 0.0086, −0.0045
Al(111)	1	+0.6	+0.0036
	10	+0.6	+0.0036, 0.00001
Na(100)	1	−6.3	−0.0317
	2	−9.5	−0.0349, 0.0127
	5	−9.9	−0.0353, 0.0139, −0.0044, 0.0015, −0.0004
	10	−9.9	−0.0353, 0.0139, −0.0044, 0.0015, −0.0005
Na(110)	1	−0.6	−0.0043
	10	−0.7	−0.0043, 0.0003
Na(111)	1	+3.7	+0.0108
	2	+3.6	+0.0108, 0.0003
	10	+3.6	+0.0108, 0.0003, 0.0001

OPTICAL POTENTIAL IN ELECTRON SPECTROSCOPIES[1]

Mark Rasolt H. L. Davis

Until recently the major effort of solid state physics was concerned with the study of bulk properties. In the last decade, increasing attention has been given to both geometric and electronic structures at solid surfaces. Catalysis, corrosion, and high-energy atom-surface interactions are just a few examples of the need for detailed surface studies.

Because of the strong electron-surface interaction, electron spectroscopy has become a valuable tool in such studies. Photoemission, LEED, and AES are three examples of such commonly used electron spectroscopies in surface studies. They all share the same underlying principle, which is to inject a probing electron into the surface region and to measure the details of its outgoing intensity. By comparing these intensities with theoretical calculations, the surface geometry and electronic structure are then deduced.

If we confine our interest to the elastic part of the electron wave function $\phi(\mathbf{r},t)$, then the *full* theoretical description of the above experiments is given by the Dyson equation

$$\left[\frac{-\hbar^2}{2m}\nabla^2 + v(\mathbf{r})\right]\phi(\mathbf{r},t) + \int d\mathbf{r}'\,\Sigma(\mathbf{r},\mathbf{r}',\omega)\,\phi(\mathbf{r}',t) = i\hbar\frac{\partial}{\partial t}\phi(\mathbf{r},t)\,, \quad (1)$$

where $v(\mathbf{r})$ is the ionic potential screened by the electrostatic potential of the electrons, $\omega \equiv \epsilon_p \equiv \hbar^2 p^2/2m$ is the energy of the initial wave packet of the interacting electron, and Σ is the optical potential. The details that can be obtained about the surface region are primarily limited, on the theoretical side, by our knowledge of the extremely complex structure of Σ. The primary purpose of this study is to re-examine a commonly used model for Σ.

This model is known from the description of the interaction of electromagnetic waves with a dielectric

media interface in which the detailed interaction is replaced by a real and imaginary frequency-dependent dielectric constant, that is,

$$\Sigma(\mathbf{r}, \mathbf{r}', \omega) \approx \epsilon_r^1(\omega) + i\epsilon_i^1(\omega) . \quad (2)$$

However, since the electron wavelength and mean free path are comparable to the surface region dimensions, the nonlocal structure of $\Sigma(\mathbf{r}, \mathbf{r}', \omega)$ is likely to be much more important. This nonlocal structure of Σ can be shown to introduce additional dependence on the direction of the momentum p. Because of the broken symmetry along the direction normal to the surface, Σ *must* depend not only on the magnitude of $|\mathbf{p}|$ (or equivalently ω), but also on the direction relative to the surface normal. The optical potential should thus be generalized from that borrowed from optical studies, Eq. (2), to

$$\Sigma \approx \epsilon_r^1(z, \omega) + \epsilon_r^2(z, \omega)\cos^2\theta_p + \text{higher order in } \cos\theta_p + i\epsilon_i^1(z, \omega) + i\epsilon_i^2(z, \omega)\cos^2\theta_p + \text{higher order in } \cos\theta_p , \quad (3)$$

where θ_p is the angle of p relative to the surface normal.

The magnitudes of $\epsilon_r^1(z, \omega)$ and $\epsilon_i^1(z, \omega)$ have been previously estimated[2] and shown to be roughly -8 and -4 eV, respectively, in Al. We have carried out an equivalent calculation for $\epsilon_i^2(z, \omega)$ and have shown it to be given by

$$\epsilon_i^2(z, \omega) = +p^2 \,\mathrm{Im}\, \frac{\Lambda''[\mathbf{p}, \mathbf{p}, \omega, n(z)]}{\pi(0)} \frac{\partial^2 n(z)}{\partial z^2} , \quad (4)$$

where $n(z)$ is the electronic density and Λ'' and $\pi(0)$ are the well-known[3] vertex and polarization response functions, respectively, of the uniform electron gas. We have successfully carried out an estimate of Λ'' in the random phase approximation, and our results are presented in Fig. 1.9. We note that $\epsilon_i^2(z, \omega)$ is of the same order of magnitude as the isotropic $\epsilon_i^1(z, \omega)$ within the region $-0.5 < zk_F/2\pi < 0$. Even more important, since these anisotropic terms reflect the derivatives of the surface electronic density, Eq. (4), they are highly surface sensitive. In future studies of adsorbates or surface reconstructions, both of which

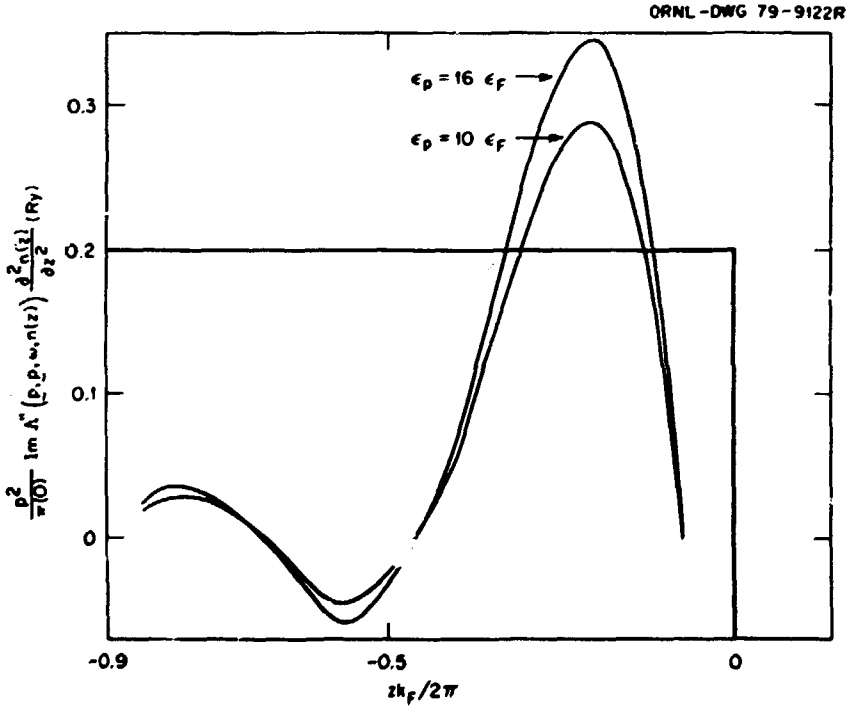

Fig. 1.9. The anisotropic contribution to the optical potential, Eq. (4), as a function of position z for two different energies of the scattering electron. The step jellium background is also shown. ϵ_F and k_F are the Fermi energy and momentum, respectively.

affect the electronic density $n(z)$, such terms could potentially contain a host of detailed surface information.

To measure the effect of these anisotropic terms on an electron intensity spectrum, we have carried out a model photoemission study[4] for the (100) surface of Al. For simplicity, in our initial calculation, we replaced the z dependence of $\epsilon_i^2(z, \omega)$ in the first layer by a constant equal to 2 eV. The effect on the photoemission intensity displayed in Fig. 1.10 clearly demonstrates the importance of such terms in detailed surface studies.

1. Summary of paper: *Phys. Rev. B* **20**, 5059 (1979).

2. J. B. Pendry, *Low Energy Electron Diffraction*, Academic Press, New York, 1979; J. E. Demuth, P. M. Marcus, and D. W. Jepsen, *Phys. Rev. B* **11**, 1460 (1975).

3. P. Nozieres, *Theory of Interacting Fermi Systems*, Benjamin, New York, 1964.

4. M. Rasolt and H. L. Davis, *Phys. Rev. B* **21**, 1445 (1980).

WAVE VECTOR ANALYSIS OF METALLIC SURFACE ENERGY[1]

Mark Rasolt G. Malmstrom[2]
D. J. W. Geldart[2]

One of the most challenging and difficult problems in a many-electron system is the treatment of the exchange and correlation contribution to its ground state energy. This is not just a formal problem but a problem of practical importance since the kinetic and electrostatic contributions are separately the largest

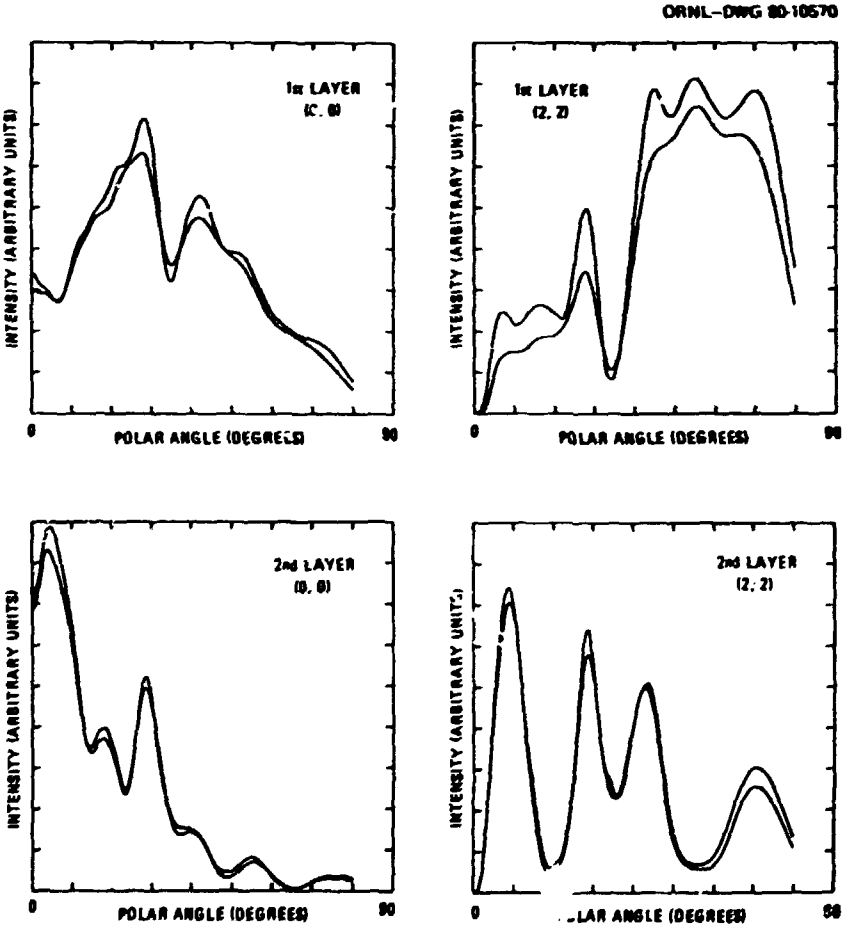

Fig. 1.10. Results from model photoemission calculations for an Al(100) surface. *The upper and lower curves in each subplot were obtained using, respectively, an isotropic and anisotropic imaginary part of the optical potential. The azimuthal angle for the calculations coincided with a (011) direction. In each subplot, the layer where the emission occurred and the angular momentum (l, m) of the emitted wave are indicated.*

contributions to the ground state energy. However, when combined, they tend to largely cancel one another and thus leave the exchange and correlation contribution to govern such practical aspects as the cohesion energy and surface energy of solids.

The exchange and correlation energy E_{xc} of such an arbitrary collection of N electrons in the presence of a nonuniform, external potential can be written as

$$E_{xc} \equiv N \int \frac{d^3q}{(2\pi)^3} E_{xc}(\mathbf{q}) = \frac{N}{2} \int \frac{d^3q}{(2\pi)^3} v(\mathbf{q}) \times \int_0^1 d\lambda [S_\lambda(\mathbf{q}, \mathbf{q}) - 1)] , \quad (1)$$

with

$$S_\lambda(\mathbf{q}, \mathbf{q}) \equiv \int d^3r \int d^3r' \, e^{-i\mathbf{q}\cdot\mathbf{r}} e^{i\mathbf{q}\cdot\mathbf{r}'} S_\lambda(\mathbf{r}, \mathbf{r}') , \quad (2)$$

where $v(\mathbf{q}) = 4\pi e^2/\mathbf{q}^2$ and λ is the usual coupling constant.

Equation (2) is *exact*, but its evaluation for an arbitrary nonuniform fermion system is presently a virtually impossible task. An approximation for Eq. (1) has been suggested by Hohenberg and Kohn[3] and is referred to as the LDA. In the LDA, Eq. (1) is approximated by

$$E_{xc} \approx E_{xc}^{LD} = \int d^3r n(\mathbf{r}) \epsilon_{xc}[n(\mathbf{r})] , \quad (3)$$

where $\epsilon_{xc}[n(\mathbf{r})]$ is the exchange-correlation energy per electron of a homogeneous electron gas of density $n(\mathbf{r})$. A connection between Eqs. (1) and (3) can be made if Eq. (3) is also decomposed in terms of its wave vector components. Then

$$E_{xc}^{LD} = \frac{1}{2} \int \frac{d^3q}{(2\pi)^3} \int d^3r \times \int_0^1 d\lambda v(\mathbf{q}) n(\mathbf{r}) \{S_\lambda^*[\mathbf{q}, n(\mathbf{r})] - 1\} , \quad (4)$$

where $S_\lambda^*[\mathbf{q}, n(\mathbf{r})]$ is the structure factor of the homogeneous electron gas with local density $n(\mathbf{r})$.

In the limit of large wave vector fluctuations, Eq. (4) can be shown to give an adequate description for Eq. (1).[4] We have begun to examine the accuracy of E_{xc}^{LD} [in Eq. (4)] for intermediate and small q regions. The nonuniform system which we are focusing on is that of a metal surface, and our motivation is to eventually gain a clearer appreciation for the importance of surface plasmons in metallic surface-energy calculations, which is a long-standing and controversial problem.[5]

We have completed a *full* treatment, via Eq. (1), for the exchange contribution *only* within the infinite barrier model of a metallic surface (see Fig. 1.11). A comparison with the equivalent local density form using Eq. (4) is given also in Fig. 1.11. The results clearly suggest that for intermediate and certainly small q, Eq. (4) is inadequate. We next examined higher-order corrections to E_{xc} via a gradient expansion:

$$E_{xc}^g \approx \int d^3r \, B_{xc}[n(\mathbf{r})] |\nabla n(\mathbf{r})|^2 . \quad (5)$$

The effect of including this contribution to the infinite barrier region is shown in Fig. 1.11. Clearly

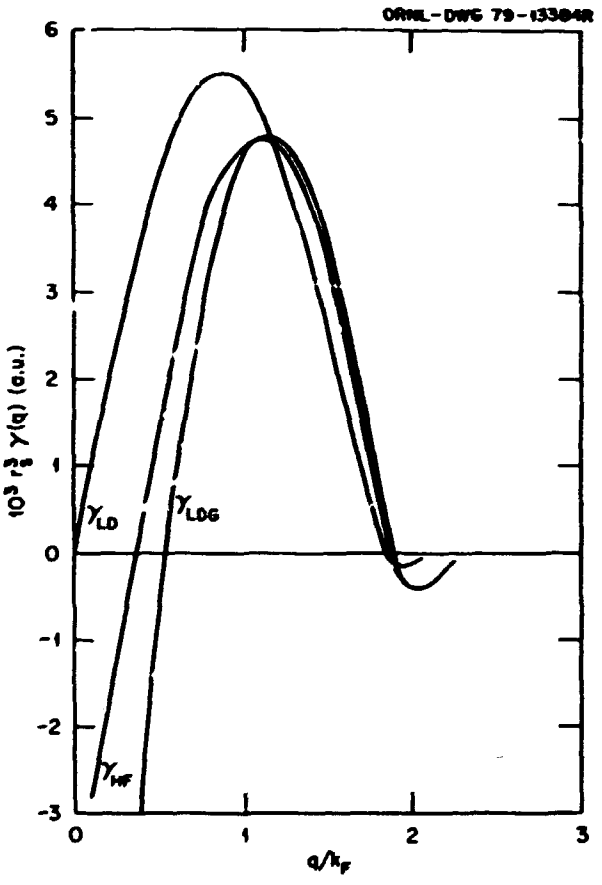

Fig. 1.11. Wave vector decomposition of the exchange contribution to the surface energy of the infinite barrier region with bare Coulomb interparticle interaction. The curve labeled γ_{LD} is the LDA, Eq. (4); the curve labeled γ_{LDG} is the LDA plus gradient, Eq. (5); and the curve labeled γ_{HF} is the full exchange results.

the intermediate and small q regions have improved significantly. In fact, we argue that for a realistic (and therefore more smoothly varying) density variation, the sum of Eqs. (4) and (5) should yield a very adequate description for the exchange contribution to a metallic surface energy for all regions of q. We are continuing our investigation of these points by including correlation in E_{xc}.

1. Summary of paper: *Phys. Rev. B* **20**, 3012 (1979).
2. Dalhousie University, Halifax, Nova Scotia, Canada.
3. P. Hohenberg and W. Kohn, *Phys. Rev.* **136**, B864 (1964).
4. D. C. Langreth and J. P. Perdew, *Phys. Rev. B* **15**, 2884 (1977).
5. J. Schmit and A. A. Lucas, *Solid State Commun.* **11**, 415 (1972); J. S. Phillips, *Comments Solid State Phys.* **6**, 91 (1975); W. Kohn and N. D. Lang, *Comments Solid State Phys.* **6**, 95 (1975).

MICROSCOPIC THEORY OF THERMAL DESORPTION AND DISSOCIATION PROCESSES CATALYZED BY A SOLID SURFACE[1]

Gopa Sarkar De[2] Uzi Landman[3]
Mark Rasolt

A microscopic model of thermal desorption and dissociation from metallic surfaces which exhibits explicit dependencies on characteristic parameters of the adsorption system has been developed. The evaluation of the rates of these processes involved a derivation of the thermal adatom-solid coupling, a stochastic incoherent multiphonon mechanism for bond rupture, and coupling to final-state reaction channels.

Figure 1.12 illustrates a model adsorption system of a positive ion placed at a distance z_i from the substrate. When the substrate is fixed (i.e., not allowed to exhibit thermal fluctuations), the adsorbed atom sits in a potential well that binds it to the substrate. In order for thermal desorption to take place, the substrate is allowed to emit phonons that are then coupled to the adsorbate. When enough phonons are absorbed, the ion climbs to the top of the potential well and then desorption can take place. We succeeded in calculating the coupling of the phonons to the adsorbate in a microscopic model. We then performed a numerical study of the stochastic

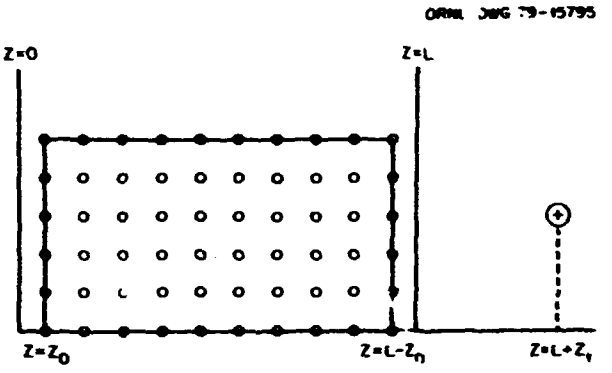

Fig. 1.12. The model adsorption system. The electron gas is bound in a slab of linear dimension L. The first plane of substrate ions is located at $z = L - z_n$ with $z_n = 0$. The adsorbed ion is located at $z = L + z_i$.

climbing of the levels as a function of the charge of the adsorbate, its distance from the substrate, and the temperature of the substrate. Transition probabilities and rates obtained by using both truncated-harmonic-potential and Morse-potential descriptions of the chemisorptive bond were calculated and compared with experimental data[4] for Xe and K desorption from a W substrate. Figure 1.13 presents the rate constant as a function of temperature for K adsorbed on W. The results show agreement with experiment and exhibit a linear relationship of the logarithm of the rate versus inverse temperature, thus justifying the use of absolute rate theory for these processes.

1. Summary of paper: *Physical Review B* (in press).
2. Georgia Institute of Technology, Atlanta.
3. Consultant from Georgia Institute of Technology, Atlanta.
4. L. Schmidt and R. Gomer, *J. Chem. Phys.* **42**, 3573 (1965).

LATTICE DYNAMICS AND ALLOYS

FIRST-PRINCIPLES CALCULATIONS OF THE PHONON SPECTRA OF Mo

J. F. Cooke

The lattice dynamics of transition metal superconductors is of interest because of the apparent correlation between anomalies in their phonon

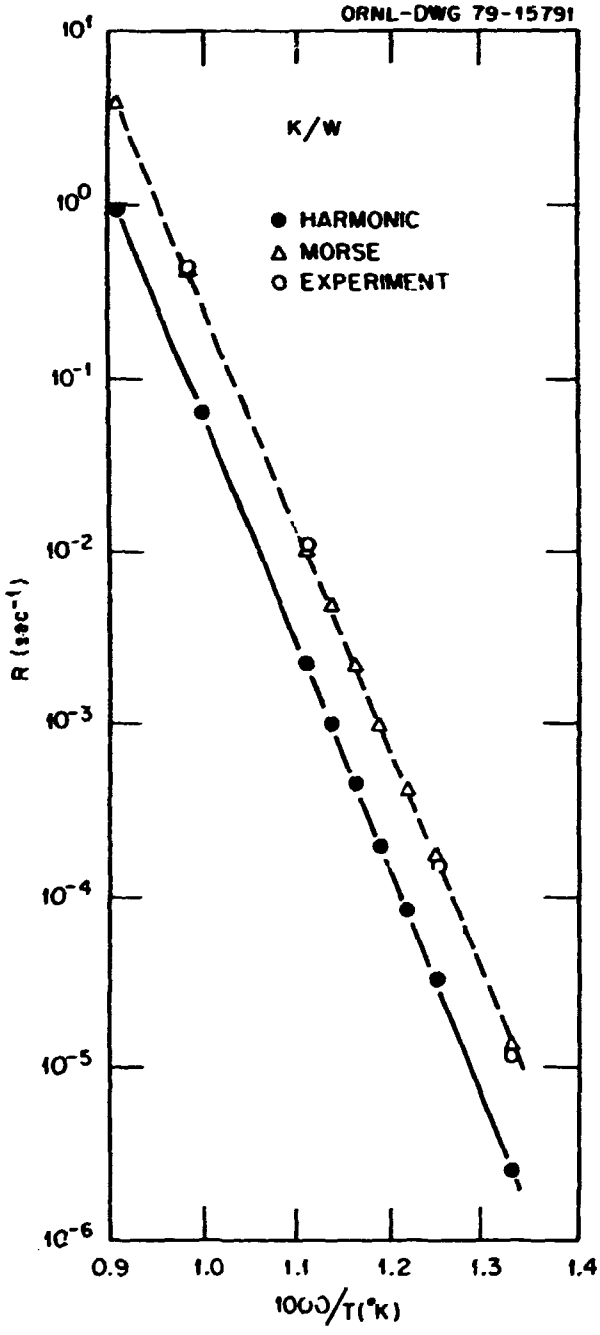

Fig. 1.13. Semilogarithmic plots of desorption rates versus inverse temperature for the system K adsorbed on W. The experimental points (open circles) were taken from ref. 4. Both the Morse potential (dashed) and truncated harmonic potential (solid) yield linear relationships in the plot of ln $R(T)$ vs inverse temperature, parallel to one another (same activation energy for desorption) but with different intercepts (frequency factors). The results based on the Morse potential description of the chemisorptive bond are in better agreement with the experimentally deduced results than those derived from a truncated harmonic potential.

spectra and the magnitude of the superconducting transition temperature. For example, anomalous dips observed in the phonon spectra of high T_c transition metal superconductors are not only unique to such materials, but also become more pronounced with increasing T_c.

In order to investigate the source of these anomalies and their relationship to superconductivity, first-principles calculations of the phonon spectra must be carried out. Such calculations are difficult to perform in metals because they depend on a detailed knowledge of the electronic band structure and certain many-body correlation functions. The method used here is based on the dielectric response formalism, which involves a calculation of the density-density correlation function, or equivalently, the dielectric screening matrix.

This formalism yields a result for the phonon energies which is exact to second order in lattice displacements; however, approximations to both the screening matrix and the band structure must be made in order to obtain numerical results. In particular, the RPA screening matrix is used, and explicit corrections to the electronic band structure which result from the electron-phonon interaction are ignored. Apart from these approximations, there are also strictly numerical problems associated with generating the band structure, relevant matrix elements, and Brillouin zone sums that must be solved.

In recent years, numerical techniques have improved to the point where the accurate calculations of the phonon spectra can be carried out within the RPA dielectric response formalism. In principle, only the nuclear charge is needed as input to the calculation. The electronic system is divided into core electrons, which move rigidly with the nucleus to form an effective ion, and the remaining (conduction) electrons, which contribute to an indirect coupling between the ions. The division considerably simplifies the calculation and can be shown to be correct provided the ionic potentials do not appreciably overlap from site to site. Direct numerical calculation has shown this to be the case for systems that have been considered thus far.

A numerical test of this theory was recently carried out for Nb.[1] The phonon spectra along [100] was calculated and found to be in good agreement with experiment. The anomalous dip in the longitudinal acoustic mode was found to result from the difference between two smooth functions of wave vector, one

generated by the direct (Coulomb) interaction between the vibrating ions and the other by the indirect interaction through the conduction electron system. It was shown that the anomaly could not result from resonant screening or from Fermi surface effects. Because of the complex nature of the calculation, it was not possible to determine the microscopic origin of the anomaly.

The calculations have now been extended to Mo in an effort to test further the theory and to investigate the differences in the calculation between high and low T_c materials. Two different calculations were carried out, one based on a rigid band calculation using the potential employed in the Nb calculation[1] and the other on a recently published potential based on the local density approximation to exchange and correlation.[2] The energy bands and wave functions were generated from a KKR band structure formalism.

The phonon spectra were calculated along the [100] direction. As in the Nb calculation, the square of the phonon energy naturally breaks up into two terms: $XC(q)$, which was generated by the direct Coulomb interaction, and $XE(q)$, which was generated by the indirect interaction referred to above. These two contributions are plotted in Fig. 1.14 for the case of the local density potential. Subscripts L and T refer to longitudinal and transverse modes, respectively. The results for the rigid band cases are similar in form. These results look very similar to those found for Nb except that the slope in the linear region of the $XE(q)$ curve is different. Notice that there is no unusual behavior near the zone boundary.

The square of the phonon frequency (in THz) for the local density case can be determined from Fig. 1.14 by using $\omega^2_{L,T}(q) = 1096.3\ [XC_{L,T}(q) + XE_{L,T}(q)]$. The theoretical and experimental spectra are compared in Fig. 1.15. In contrast to the local density case, calculations based on the rigid band approximation were found to yield very poor agreement with experiment. Both calculations, however, did reproduce the anomalous minimum at the [100] zone boundary. It was also shown by removing Fermi surface contributions from the calculation that this anomaly is associated with the Fermi surface.

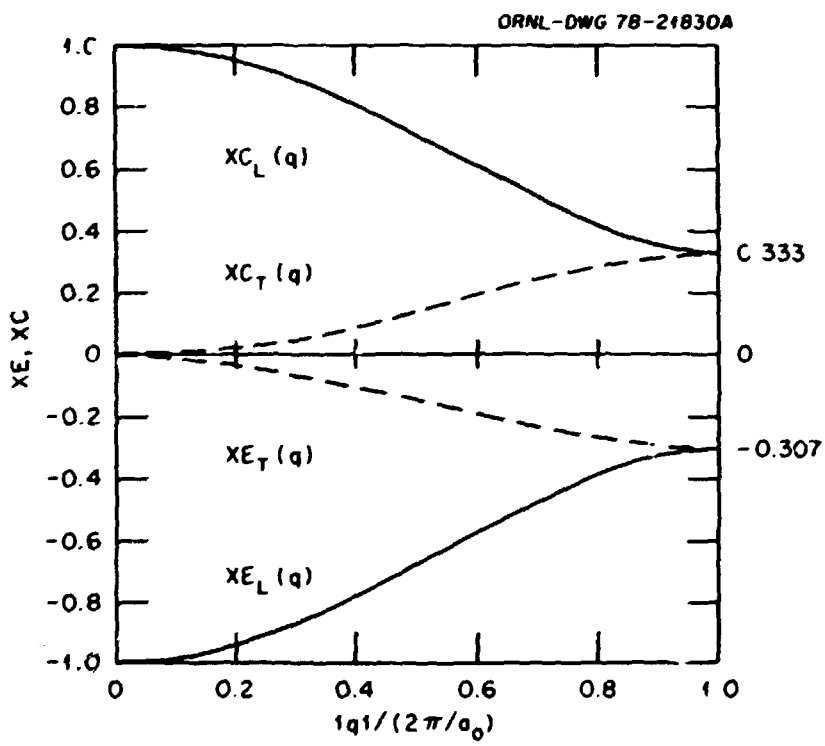

Fig. 1.14. Contributions to the phonon frequency for Mo along [100] from the direct (XC) and indirect (XE) interaction terms. Subscripts L and T refer to longitudinal and transverse modes, respectively.

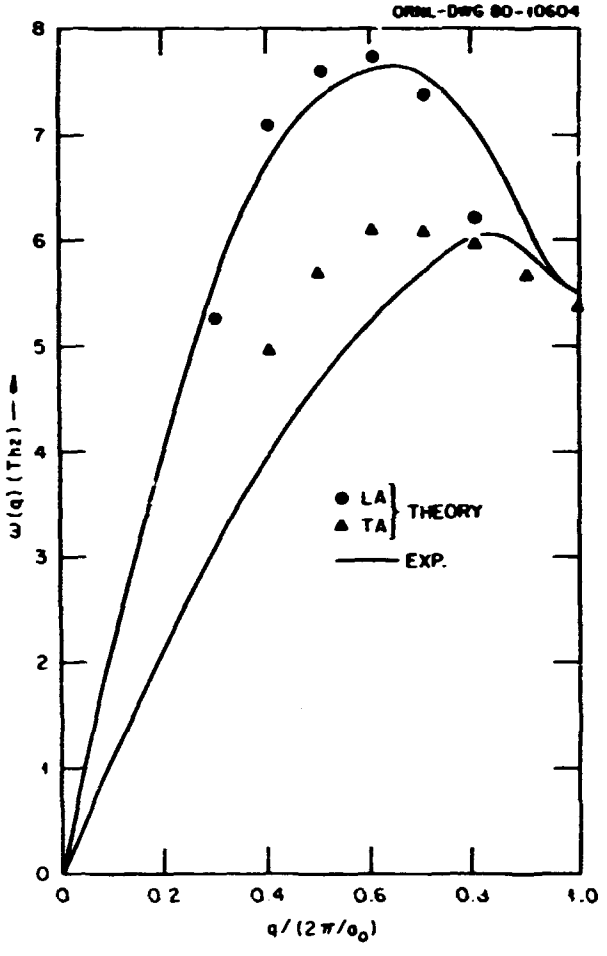

Fig. 1.15. Comparison between theory and experiment for longitudinal phonon modes along [100] for Mo.

These calculations have shown that the RPA dielectric response formalism can provide a good first-principles quantitative description of the phonon spectra in transition metal superconductors. The dramatic differences between the [100] phonon spectra in Nb and Mo can be accounted for simply on the basis of a relatively small change in slope of the linear part of the indirect interaction contribution $XE(q)$. Since the anomalies in both of these materials are not associated with the Fermi surface, it appears that T_c and the anomalies are not directly related but instead depend independently on some special feature of the band structure that exists within an electron volt or so of the Fermi energy. Further analysis of the results obtained thus far is needed to identify uniquely the relevant behavior.

1. J. F. Cooke, *Solid State Div. Prog. Rep. Sept. 30, 1978*, ORNL-5486, p. 13.

2. *Calculated Electronic Properties of Metals*, ed. by V. L. Moruzzi, J. F. Janak, and A. R. Williams, Pergamon, New York, 1978.

SELF-CONSISTENT CLUSTER THEORY FOR RANDOM ALLOYS[1]

Theodore Kaplan L. J. Gray[3]
P. L. Leath[2] H. W. Diehl[4]

The treatment of disordered solids poses a difficult problem in solid state physics since, unlike the perfect crystal problem, there is no translational symmetry. As a result, a proper theory for this class of materials has developed quite slowly. The best known approximation for random alloys, the coherent potential approximation (CPA),[5,6] was introduced in 1967. This is a self-consistent theory that includes only the scattering from a single site and is applicable to Hamiltonians which are a sum of terms that depends on, at most, the type of atom at one site (diagonal disorder), that is,

$$H = H^0 + \sum_i H^1(s_i) . \qquad (1)$$

H^0 is the contribution that is independent of the disorder and s_i is the site occupation variable that denotes the type of atom at site i. (For example, in an alloy composed of A and B atoms, $s_i = A$ or B.) Such simplified Hamiltonians neglect the effects of the neighboring sites (environmental disorder). The expression for a general Hamiltonian would have the form

$$H = H^0 + \sum_i H^1(s_i) + \sum_{ij} H^2(s_i, s_j) + \sum_{ijk} H^3(s_i, s_j, s_k) + \ldots . \qquad (2)$$

Environmental effects represented by all additional terms in the Hamiltonian can be very important. For example, in a tight-binding representation, the hopping elements must depend on the type of atoms at the two sites connected (off-diagonal disorder), so

that it is necessary to include terms of the form H^2 in the Hamiltonian.

Attempts to extend the CPA to more general Hamiltonians and to include cluster scattering as well met with limited success until quite recently. In 1978, Mills and Ratanavararaksa[7] developed a self-consistent theory that properly included cluster scattering but still was restricted to diagonally disordered Hamiltonians.

We have developed a completely general self-consistent theory for elementary excitations in random alloys. It includes cluster scattering and is applicable to general Hamiltonians. It is based on the augmented space formalism,[8,9] which is an operator technique for treating functions of random variables, and on the self-consistent approximation of Mills and Ratanavararaksa.[7]

Although this theory is valid in all dimensions, we have chosen to present one-dimensional model calculations because exact results are available for comparison. We have calculated the electronic density of states of a one-dimensional, tight-binding alloy composed of A and B atoms. The Hamiltonian of this system is

$$H_{ij} = e(s_i)\delta_{ij} + W_{ij}(s_i, s_j) , \qquad (3)$$

where i and j label the sites, $s_i = A$ or B, and W_{ij} is nonzero only for i and j nearest neighbors. Note that both the diagonal and off-diagonal elements are functions of the atoms occupying the sites that they connect (i.e., there is diagonal and off-diagonal disorder).

Figure 1.16 compares the densities of states calculated by use of our self-consistent approximation with exact results for linear chains with $e(A) = -e(B) = -2.5$, $W(A, A) = 1.0$, $W(A, B) = W(B, A) = W(B, B) = 0.5$, and a concentration of B atoms $c_B = 0.3$. We have plotted the result for the self-consistent approximation with single-site scattering in Fig. 1.16*a* and the results for pair scattering in Fig. 1.16*b*.

The single-site approximation produces a smooth distribution that predicts the edges of the host band centered at -2.5 quite accurately. For the defect band, the approximation results in a distribution that underestimates the band width but is centered properly about the major defect band peaks.

As expected, the change from a single-site to a pair approximation produces a significant improvement in the density of states generated by the self-consistent approximation. We find that not only does the self-consistent theory give excellent estimates of the band widths in both host and defect bands, but a distinctive three-peaked structure has appeared in the

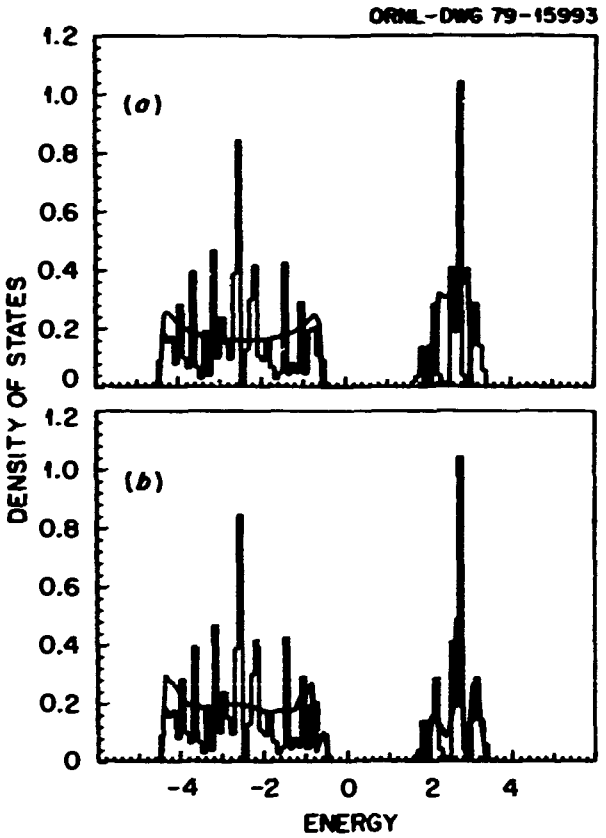

Fig. 1.16. Density of states for electrons in a linear chain with $e(A) = +e(B) = +2.5$, $W(A, A) = 1.0$, $W(A, B) = W(B, B) = 0.5$, and $c_B = 0.3$. Comparison of the exact results (histogram) with the self-consistent (*a*) single-site and (*b*) nearest-neighbor pair approximations (This is a model system and the units are arbitrary.)

defect band which closely matches the major peaks in the exact results. The central peak in the defect band corresponds primarily to states localized on isolated B atoms, and the two satellite peaks correspond primarily to bonding and antibonding states localized on B-B pairs. Furthermore, there is some smaller structure that appears in the host band due to A-A and A-B pairs.

In order to reproduce more of the detailed structure in the one-dimensional density of states, we would need to do self-consistent calculations that include scattering from larger clusters.

---

1. Summary of paper: *Physical Review B* (in press).
2. Rutgers University, New Brunswick, N.J.
3. Computer Sciences Division, UCC-ND.
4. University of Munich, Munich, West Germany.
5. P. Soven, *Phys. Rev.* **156**, 809 (1967).
6. D. W. Taylor, *Phys. Rev.* **156**, 1017 (1967).
7. R. Mills and P. Ratanavararaksa, *Phys. Rev. B* **18**, 5291 (1978).
8. A. Mookerjee, *J. Phys. C* **6**, L205 (1973).
9. Theodore Kaplan and L. J. Gray, *Phys. Rev. B* **14**, 3462 (1976).

DIFFUSION IN THE PRESENCE OF RANDOM DEFECTS

Theodore Kaplan L. J. Gray[1]

A study of the effects of a random distribution of defects on diffusion at surfaces and in the bulk has been initiated. We use a stochastic theory of transport, wherein the evolution of the system proceeds via transitions between elementary kinetic steps.[2] These steps can be mapped onto a lattice, and the stochastic time development can be treated as a continuous time random walk. The presence of the defects in the systems is accounted for by modified transition rates in the neighborhood of a defect. All experimentally observable quantities can be determined from the particle propagator. Using the self-consistent approximation of Kaplan et al.,[3] we have developed an effective-medium approximation for the particle propagator. Preliminary calculations for one-dimensional lattices have been carried out.

1. Computer Sciences Division, UCC-ND.
2. Uzi Landman and M. F. Shlesinger, *Phys. Rev. B* 19, 6207 (1979).
3. Theodore Kaplan et al., *Physical Review B* (in press); "Self-Consistent Cluster Theory for Random Alloys," this report.

GAUGE FIELDS AND CHARACTER OF ORDER IN SOLIDS

Martin Ülehla

Although the study of ordered and amorphous states in solids has a long and distinguished tradition, a satisfactory understanding and description of a glasseous state are still lacking. In this work, we exploit some geometric concepts and reconsider the notion of order in solids. The dynamical variables (as given by the Hamiltonian) are treated as a field in a fiber over point x of the base manifold M (which we take as a one-, two-, three-dimensional Euclidean space) and globally form a section through a fiber bundle. The fiber over a base point x is generated by a (local) group of transformations G_0. We are led to introduce gauge fields as connections, allowing us to determine the variation in the dynamical variables due to variation of $x \in M$. The structure group G associated with the gauge fields need not, in general, be the same as G_0. This leads to the idea of broken (or hidden) symmetry, whereby the structure group can be used to classify the states of order in a solid. An example leading to the dislocation mediated theory of melting in two dimensions[1] has been treated in some detail.

1. D. R. Nelson and B. I. Halperin, *Phys. Rev. B* 19, 2457 (1979).

PARTICLE-SOLID INTERACTIONS

ROLE OF REVERSIBILITY IN ENHANCED ION BACKSCATTERING NEAR 180° SCATTERING ANGLE[1]

J. H. Barrett B. R. Appleton
O. W. Holland[2]

Enhanced ion backscattering yields from the near-surface region for scattering angles very near 180° have been reported recently by Pronko et al.[3] The effect occurs in its simplest form for disordered, amorphous, or polycrystalline targets, although it may also occur under channeling conditions in single crystals. We have used computer simulation to show that this enhancement is a manifestation of the reversibility of ion trajectories in solids and to explore the dependence of the angular and depth variations of this phenomenon on ion charge and energy and on target atom charge and mass.

In addition to the usual features of computer simulation, we have included certain extra features. The key one is the storage of atomic positions near the ingoing part of an ion trajectory for use in calculating the outcoming part. Without this feature, the reversibility property is lost and the effect completely disappears in the simulation. A second feature we have included is the effect on the atomic positions and ion energy due to collision-induced recoils; this results in a noticeable reduction of the effect. A third feature, the inclusion of the depth resolution of the detector, gives a broadening of the depth range showing enhancement and noticeable reduction in the maximum enhancement.

Figure 1.17 shows experimental measurements[3] of the peak enhancement made for Pt at a series of angles together with calculated values. The angle ψ is the amount by which the scattering angle deviates from 180°. The yields are normalized to the Rutherford scattering cross section. The error bars shown for the calculated points are estimated standard deviations for the statistical uncertainties of the simulation method. The horizontal bars associated with the experimental points are the ±0.04°

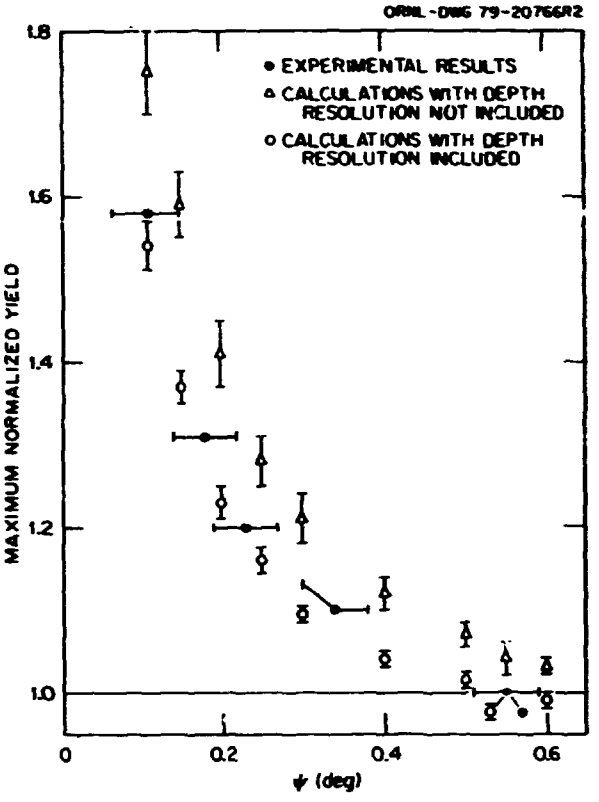

Fig. 1.17. Maximum normalized yields at various angles for 1-MeV He ions backscattered from disordered Pt.

angular range that the planar detector subtends at a point on the target. The calculated values in Fig. 1.17 illustrate the importance of including the depth resolution. The yield calculated at $\psi = 0.55°$, including depth resolution, was 1.00 ± 0.01, confirming the normalization of the data made in ref. 3. No further normalization is required in making the comparison of experimental and calculated values.

We have also done calculations for Al to explore the charge dependence and the influence of nuclear recoil effects. Figure 1.18 shows the results for the depth range that gave the largest enhancement. The comparison in Fig. 1.18*a* shows that the effect of nuclear recoil is quite large. One feature to be noted is the existence of a region of yield deficit of 1–2% at angles beyond about 0.25°. To test whether this deficit region provides compensation for the enhancement region as one might expect, Fig. 1.18*b* shows a plot of the yield enhancement (or deficit) without nuclear recoil multiplied by $\sin \psi$, the appropriate weighting factor for solid angle. The negative area corresponding to the deficit cannot be estimated accurately, but it appears very plausible that the region of yield deficit above 0.25° provides compensation for the region of yield enhancement below 0.25°. The area of the enhancement region may be taken as a measure of the strength of the enhancement. For Al, the area of the enhancement region, with nuclear recoil taken into account, is 40 to 50% less than the area shown in Fig. 1.18*b*. The corresponding reduction for 1-MeV He on Pt is 10 to 20%.

For the annular detector used in the experiments,[3] which covered the range 0.05 to 0.20°, the maximum enhancement factor for 1-MeV He on Pt is 1.64 ± 0.04, while that for 0.5-MeV He on Al is 1.20 ± 0.02. The difference for these two cases is due about equally to the greater influence of nuclear recoil on the Al results and to a shrinkage of the angular range of the effect for Al relative to Pt. The different enhancements seen in the Pt and Al calculations are in reasonable agreement with the limited experimental results[3] available for dependence on target atomic number.

Other simulations have been done to assess the strength of this enhancement under channeling conditions, in particular for the double alignment

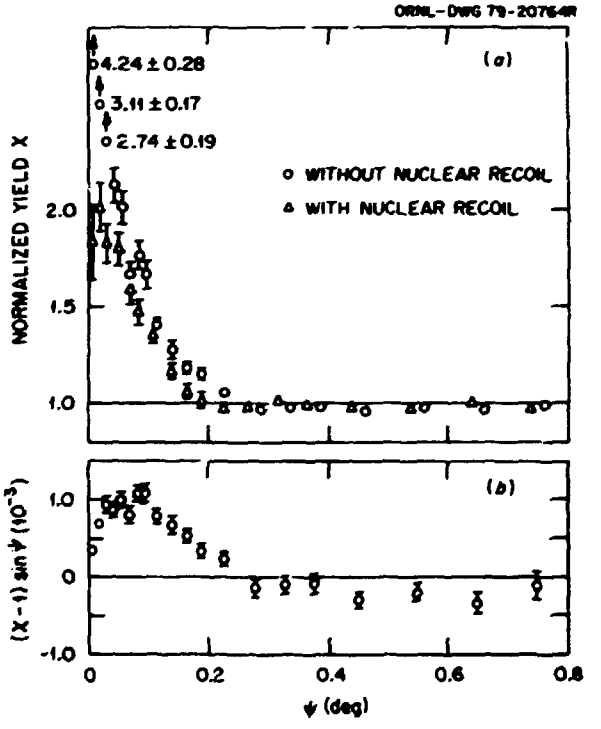

Fig. 1.18. Calculated angular dependence of the anomalous backscattering of 0.5-MeV He ions from depths of 8 to 12 nm in disordered Al: (*a*) normalized yield and (*b*) yield weighted by $\sin \psi$ to assess angular compensation.

surface yield. Results were obtained for 1-MeV He ions incident on Au at room temperature along [110]. We computed the single alignment surface yield to be 2.176 ± 0.003 atoms per row. The uniaxial double alignment yield was found to be 3.15 ± 0.10 for $\psi \lesssim 0.02°$ and 2.79 ± 0.02 for an annular detector covering the range 0.05 to 0.20°. The enhanced surface yield in uniaxial double alignment is due to increased scattering by atom layers just below the surface layer and hence by atoms that are sensitive to any atomic rearrangements in the surface region.

These computer simulations have shown that the enhanced scattering yield near 180° is a manifestation of the reversibility of ion trajectories in solids. We have found that the calculated results show important dependencies on the inclusion of nuclear recoil effects, experimental depth resolution, ion energy, and ion and target atomic numbers. Our calculations have been able to reproduce accurately the observed angular and depth dependencies and the variation with target atomic number. They also show that the effect will be seen under channeling conditions and may provide additional information about surface structure.

1. Summary of paper to be published.
2. ORAU graduate laboratory participant from North Texas State University, Denton.
3. P. P. Pronko et al., *Phys. Rev. Lett.* 43, 779 (1979); B. R. Appleton et al., "Enhanced Yield Effect for Ions Scattered near 180°," this report.

POTENTIAL AND STOPPING POWER INFORMATION FROM PLANAR CHANNELING OSCILLATIONS[1]

J. H. Barrett

When a beam of high-energy ions is directed parallel or nearly parallel to rows or planes of atoms in a crystalline solid, the ions are steered by a collective action of the rows away from the rows or planes into the regions between them, a behavior called channeling. For alignment of the beam with a set of planes, the ions oscillate back and forth between the planes as shown in Fig. 1.19. Inasmuch as the ions can only be scattered to large angles when they are close to the planes, their oscillatory motion causes the scattering to occur selectively at certain depths. At each successive scattering region, the stopping power acts along both a longer ingoing and a longer outcoming path so that the intensity as a function of energy observed in the detector presents a series of peaks. The relation between the separation

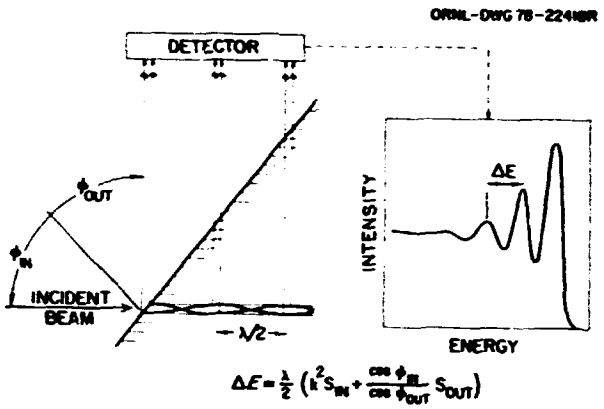

Fig. 1.19. Schematic illustration of oscillations of ions when a beam is incident parallel to a planar channel in a crystal and of the experimental manifestation of these oscillations.

of the energy peaks, the half wavelength of the oscillation, and the stopping powers is given by

$$\Delta E = \frac{\lambda}{2}\left(k^2 S_{in} + \frac{\cos\phi_{in}}{\cos\phi_{out}} S_{out}\right), \qquad (1)$$

where λ is the wavelength, the S's are stopping powers, the ϕ's are as defined in Fig. 1.19, the subscripts "in" and "out" refer to the ingoing and outcoming paths, and k^2 is the standard kinematic factor, determined by the scattering angle and the ion and atomic masses. The quantities ΔE, k^2, ϕ_{in}, and ϕ_{out} are all determined by the experiment, and S_{out} may be assumed to be the random stopping power S_{ran} obtainable from standard tables. This leaves S_{in} and $\lambda/2$ as unknown quantities in Eq. (1).

One of the striking features of planar channeling is the series of strong peaks, illustrated schematically in Fig. 1.19, that occurs for exact alignment of the ion beam with the planar channels. A second feature is a very strong peak in the scattering that occurs at an angle near the critical angle for channeling between the planes and at a depth of $\sim\lambda/4$. Both of these features have been calculated by computer simulation, and the second one is illustrated by the set of backscattering yield contours shown in Fig. 1.20. The angular coordinate of the maximum will be called ψ_M. It may be combined with the half wavelength and the planar spacing d_p to give a parameter

$$q = (\lambda/2)\,\psi_M/d_p\,. \qquad (2)$$

Several calculations were done to see how these quantities might depend on certain aspects of the

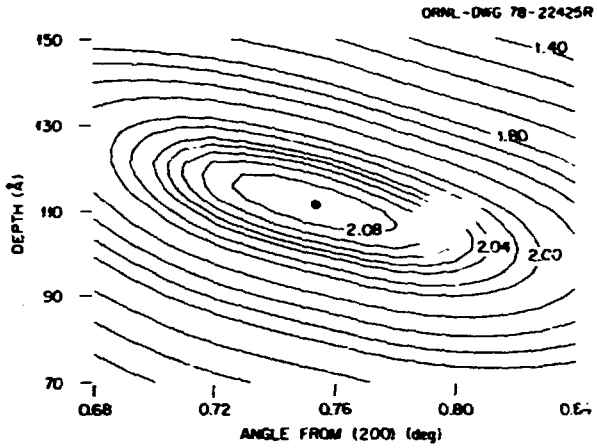

Fig. 1.20. Contours of backscattering for 1-MeV He incident near the (200) planes of Au at room temperature. The yield is normalized to the scattering for random incidence, and a depth resolution of 7-nm FWHM has been included. The contours between the labeled ones are spaced at equal intervals, and the dot gives the estimated position of the maximum yield.

simulations. All were found to be very insensitive to the depth resolution function. For three different potentials, $\lambda/2$ and ψ_M were found to vary by 8 to 10%, but q was found to be 1.46 and independent of the potential to within the estimated accuracy of 1.4%. Calculations were also done for various potentials and depth resolutions for 1.9-MeV He in Be(0002) and with a single potential and depth resolution each for 0.25-MeV H in Si(022) and 1.9-MeV He in Fe(011). All of these ion-target combinations were chosen to correspond to existing experiments. In these additional cases, all quantities were again insensitive to the depth resolution, and q was insensitive to the potential. For Be, Si, and Fe, q was 1.38 to within the estimated accuracy of 1.4%. The reason why q for Au differs from that for the other materials is unclear; it may be due to much stronger multiple scattering for this material when the ions are close to the planes.

There appear to be two possible applications of these results. The first concerns the use of ψ_M as a measure of the strength of the potential. This quantity can be calculated to an accuracy of 1% but was found to vary by 8% for Au and 11% for Be for the different potentials tried. Hence, experimental values of ψ_M can be used to determine which of several possible potentials is best for a material. The measured value of ψ_M can also be used together with Eq. (2) and the calculated value of q to obtain a value of $\lambda/2$. This value of $\lambda/2$ can then be used with Eq. (1) and the measured value of ΔE to obtain a value of S_{in}. Past attempts to obtain S_{in} by other methods have led to conflicting results, and it is hoped that the method proposed here may provide greater accuracy and help resolve the conflicts. The value of S_{in} is of interest because of the relatively larger fraction of the time that trajectories spend near the atoms in comparison to a random trajectory; it would be expected that S_{in} would be somewhat larger than S_{ran}. This proposed method of analysis has been applied to some of the past measurements, but the estimated errors are quite large. It is hoped that future experiments can be made that provide greater accuracy.

1. Summary of paper: *Phys. Rev. B* **20**, 3535 (1979).

ROLE OF CORRELATIONS OF LATTICE VIBRATIONS IN CHANNELING[1]

J. H. Barrett D. P. Jackson[2]

Ion backscattering under channeling conditions has been used to infer information about various properties of crystalline solids, with much recent interest in studying surface structure. In interpreting almost all such experiments, thermal vibrations of the lattice atoms play a significant role, but past work has not included the effects of correlations between the vibrations of neighboring atoms. This work reports the first systematic calculations taking such effects into account.

For studying surface structure, the ion beam will be directed nearly parallel to a set of rows in the crystals. In these circumstances, a single atomic row adequately represents the geometry of the backscattering since this portion of the backscattered ion spectrum arises from the uppermost few layers. Hence, the surface yield may be expressed as an effective number of atoms per row contributing to the backscattering. The calculations employed a standard computer simulation program for channeling[3] with the addition of a previously developed statistical continuation procedure[4] to incorporate the effects of correlations. All atoms in the row were mutually correlated, and the length of the row was varied to ensure that no numerical artifacts were present in the calculations.

Figure 1.21 shows a calculation of the surface yield L over a range of temperatures. The contribution from the first two atoms in a row was compared with the analytic expression of Oen,[5] which is exact for two atoms; the comparison serves as a check on the computer simulations. The major result of the

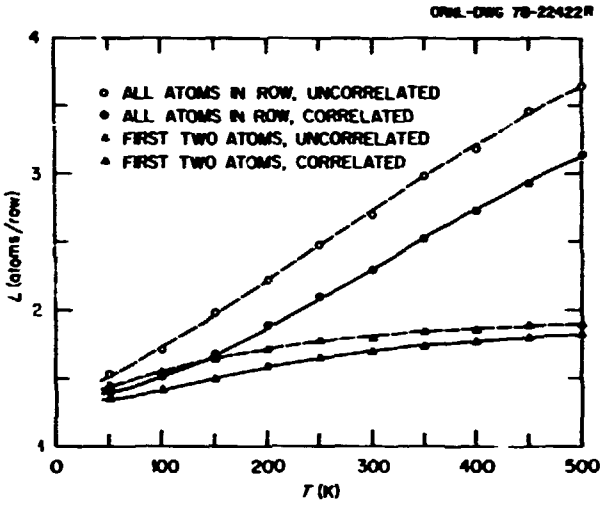

Fig. 1.21. Surface yield as a function of temperature of 2-MeV He directed along Mo (111).

calculations in this case is that correlations reduce the surface yield by about 15% over the range of parameters studied; this is noted in the first two columns of the first line of Table 1.2. There is a clear indication that correlations need to be taken into account whenever comparisons of the magnitudes of measured and calculated yields are used to infer information about surfaces. The present calculations have used bulk thermal vibrations and correlations and neglected any enhancement of vibrations at the surface over those in the bulk. Enhanced surface vibrations will probably produce an increase in the surface yield of comparable magnitude to the decrease produced by correlations. Consequently, the only truly satisfactory procedure will be one which takes account of correlations and surface vibrations together.

Table 1.2. Changes in various quantities calculated for 2-MeV He in Mo (111)

Quantity	Change produced by correlations (%)	Equivalent change in vibration amplitude (%)
Surface peak at $\psi = 0°$	−15	−13
Surface peak at $\psi = 0.6°$	−14	−12
Half angles ($\psi \sim 1.0°$)	+3	−8
Minimum yield	−11	−6

An additional calculation was done to explore the dependence of the surface yield on the angle of the beam direction from a row direction. The result is summarized in the first two lines of Table 1.2. The change produced by correlations is seen to be small over the limited angular range for which the surface yield can be separated from the bulk yield.

A second quantity we calculated was the half angle $\psi_{1/2}$, the angle at which the backscattering yield is halfway between its minimum value (attained when the ion beam is directed along an axis) and the value when it is far from any axis in a random direction. The change for this case is shown in the third line of Table 1.2.

The third quantity we calculated was χ_{min}, the minimum value of the backscattering yield occurring when the beam is directed along an axis. Calculations between 50 and 500 K indicate that correlations produce a rather uniform reduction in χ_{min} at all temperatures.

The qualitative nature of the change due to correlations noted in column 2 of Table 1.2 is the same as would be produced by a reduction in vibration amplitude. Hence, it is of interest to explore what reduction in amplitude would be required to produce the same change as calculated in each case. Estimates of these reductions are given in column 3, using previous results[3] for dependencies on vibration amplitude.

The first three lines in Table 1.2 show an obvious trend; the effect of correlations, as measured by the change in equivalent vibration amplitude, decreases as the angle of inclination to the row of the relevant trajectories increases. Although in a less obvious way, the minimum yield also fits into this trend, since many of the trajectories contributing to it have been scattered to relatively large angles as they impinged on the surface of the solid. So, for all the quantities calculated, the effect of correlations is largest for a quantity that is most sensitive to trajectories aligned with a channeling direction and smallest for a quantity that is least sensitive to aligned trajectories.

1. Summary of papers: *Phys. Lett.* **71A**, 359 (1979); *Nuclear Instruments and Methods* (in press).
2. Chalk River Nuclear Laboratories, Atomic Energy of Canada Limited, Chalk River, Ontario, Canada.
3. J. H. Barrett, *Phys. Rev. B* **5**, 1527 (1971).
4. D. P. Jackson and J. H. Barrett, *Comput. Phys. Commun.* **13**, 157 (1977).
5. O. S. Oen, *Phys. Lett.* **19**, 358 (1965).

RADIATION FROM CHANNELED LEPTONS[1]

M. J. Alguard[2] S. Datz[3]
R. L. Swent[2] J. H. Barrett
R. H. Pantell[2] B. L. Berman[4]
S. D. Bloom[4]

This report presents some of the principal results obtained from a classical calculation of positron channeling by computer simulation.[5] The simulations were adapted to include a Fast Fourier Transform of the motion of the particle through the three-dimensional crystal resulting in a classical calculation of the low-energy (i.e., $\hbar\omega \ll \gamma mc^2$) emission spectrum. The effects of thermal vibrations and beam divergence were included in the calculation, and the contributions of ordinary and coherent bremsstrahlung were obtained in a natural way within the context of the classical approximation. For 56-MeV positrons, the simulations successfully predicted the energies of the main spectral peaks observed for channeling in {100}, {110}, and {111} planes of Si; these peaks had already been predicted by quantum and by classical continuum calculations. However, the simulations showed, in addition, that a second broad feature observed in the 60- to 90-keV range for the {111} channel results from channeling in the set of narrow {111} channels. The major peak at 35 keV in this case arises from channeling in the set of wide {111} channels.

At angles close to a ⟨110⟩ direction (which we call the z axis), coherent bremsstrahlung (CB) features identifiable with the frequency of crossing planes parallel to that axis also appear in the low-energy spectrum. Fig. 1.22*a* shows the projection in the x-y plane of a typical {110} trajectory. In Figs. 1.22*b* and 1.22*c* the direction cosines (β_x/β and β_y/β, respectively) of the positron motion also are plotted as a function of x along the channeling plane.

The planar oscillation frequency is seen clearly in Fig. 1.22*a* and gives rise to planar oscillation radiation (POR) at 48 keV. The planar crossing

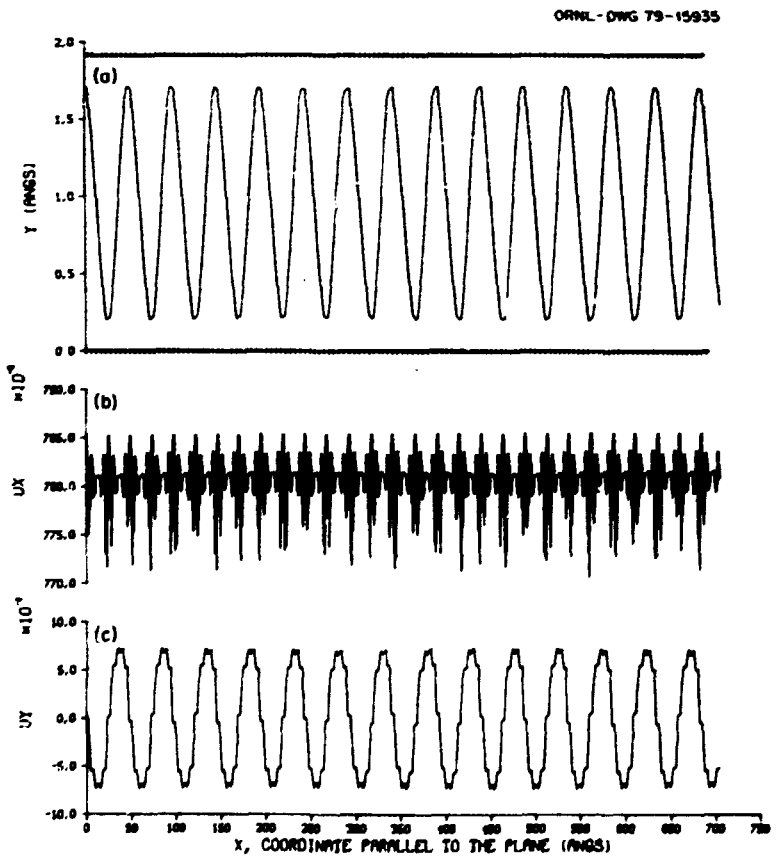

Fig. 1.22. Calculated trajectory and direction cosines of a 56-MeV positron in a {110} channel in Si for an angle $\theta = 0.45°$ from a ⟨110⟩ axis and entrance point 0.75 Å from the midplane.

frequency, seen as the high-frequency component in Fig. 1.22*c*, gives CB at 432 keV. Figure 1.22*b* contains frequency components showing strong coupling of the POR and CB radiations; these give major spectral peaks at 480 and 384 keV corresponding to $\hbar\omega_{CB} \pm \hbar\omega_{POR}$. The strength of the coupling between POR and CB depends, principally, on the planar channel and on the amplitude of the channeling oscillation; in some cases, the sideband intensity exceeds the intensity of the CB.

The POR frequency does not depend on the angle θ relative to the crystal axis, but ω_{CB} is proportional to $\sin\theta$, and hence the angular divergence of the beam strongly affects the width of the spectral peak. For 56-MeV e^+, the CB energy is calculated (at small θ) to be 1.45, 0.966, and 1.57 MeV per degree of θ for {100}, {110}, and {111}, respectively. Thus, for example, a beam divergence of $\lesssim$0.4 mrad is required to resolve the CB and CB $\pm$ POR peaks in the {111} plane.

The experimental (110) e^+ channeling-radiation spectrum contains indirect evidence for these phenomena. A computer simulation of the experiment, including beam divergence, yielded a similar spectrum. It showed that $\cong$40% of the trajectories were actually planar channeled at small angles with respect to the axis. The axially channeled component gave the feature observed at $\cong$50 keV (a combination of POR for all intersecting planes) and an additional broad feature in the 100-keV region similar to that seen experimentally; this feature probably arises from CB for paths 1–2 mrad from the axis.

1. Summary of paper: *Nuclear Instruments and Methods* (in press).
2. Stanford University, Stanford Calif.
3. Chemistry Division, ORNL.
4. Lawrence Livermore Laboratory, University of California, Livermore.
5. M. J. Alguard et al., *IEEE Trans. Nucl. Sci.* **NS26**, 3865 (1979); R. L. Swent et al., *Phys. Rev. Lett.* **43**, 1723 (1979).

REDEFINED SCATTERING CROSS SECTION IN MONATOMIC SOLIDS[1]

O. S. Oen

The redefined binary elastic scattering cross section between like atoms is derived directly from the conventional classical elastic cross section by defining the primary to be that atom emerging with the greater energy following a two-atom collision. The new perspective provided by this redefined primary concept is useful in studying radiation damage and ion penetration phenomena in monatomic solids. Stopping powers and range quantities of this redefined primary were calculated for a structureless solid using inverse power potentials (r^{-s}) and the Molière potential. For power law scattering, the redefined stopping power is $s(2^{1/s}-1)$ times the conventional nuclear stopping. By applying these results to the case of self-ion irradiation, one obtains improved simple estimates of the mean damage depth, the spatial density of nascent defects, and the primary recoil spectrum produced by the bombarding ion. Furthermore, although the redefined scattering expression was developed for classical collisions between identical atoms, it can also be used for unlike atoms whose masses are fairly similar, such as the atoms of FeNi alloys.

1. Summary of paper: *Nuclear Instruments and Methods* (in press).

THE TWO-ATOM SCATTERING MODEL IN ION REVERSIBILITY STUDIES

O. S. Oen

The recent discovery[1] of enhanced backscattering yields from the near-surface regions of amorphous solids for scattering angles near 180° has been interpreted by Barrett[2] through computer simulations as originating from the reversibility property of ion trajectories. This interpretation suggests that the two-atom scattering (blocking) model[3] might shed some insight into this phenomenon. Preliminary studies show that the model reproduces some of the typical features of this enhancement effect. The model consists of the following elements (see Fig. 1.23).

Let the atom responsible for the near-180° backscattering be located at O, a distance D below the surface. Consider a second atom at a distance l from O, such that the pair of atoms is inclined at a small angle θ with respect to the surface normal. The condition that a normally incident ion is focused to O (and therefore backscattered(by the second atom is $\theta = s/l + \phi(s)$, where s is the impact parameter and $\phi(s)$ is the scattering angle (small-angle approximation) determined by the ion-atom scattering potential. Because $\phi(s)$ generally increases with decreasing s, θ has an extreme value θ_c for $s = s_c$. Because of this extremum, backscattered ions require

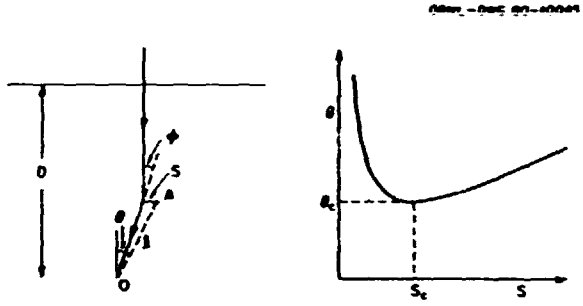

Fig. 1.23. Incident ion focused to atom O by atom A (left) and schematic drawing of ion deflection angle θ vs impact parameter (right).

their trajectories to lie only in the neighborhood of the critical impact parameter s_c in order to emerge at angles close to the surface normal. This is believed to be the basic reason for the enhancement of the backscattering yield. For the two atoms discussed above, the differential scattering cross section for a normally incident beam to be focused to O is

$$\frac{1}{l^2}\frac{s}{\theta}\left|\frac{ds}{d\theta}\right| .$$

The two-atom scattering model should be a good approximation in a solid of N atoms per unit volume provided there is only one significant scattering before the ion strikes the backscattering atom. Taking the probability for a single scattering with an impact parameter s to be $e^{-\pi NDs^2}$, the fraction of incident intensity focused to O from a layer of random atoms at distance l and of thickness τ is proportional to

$$\iint e^{-\pi NDs^2}\,\tau N\frac{s}{l^2\theta}\left|\frac{ds}{d\theta}\right| l^2\theta\,d\theta\,d\phi = \int_0^\infty e^{-\pi NDs^2}\,2\pi N\tau s\,ds . \quad (1)$$

The total focused intensity is found by summing Eq. (1) over all atomic layers between the surface and O. Knowing the critical impact parameter s_c, Eq. (1) can be used to calculate the fraction of ions focused to O with impact parameters near s_c. This fraction will maximize for some depth D which is expected to correspond to the maximum in the strength of the backscattering enhancement. For 1-MeV He ions, the calculated values of D are 60 and 120 Å for Pt and Al, respectively, which agree quite well with Barrett's simulation results.

The backscattering intensity at an exit angle ψ from O and from a layer of scattering atoms of thickness τ may be found by convoluting the incoming and backscattered fluxes to give

$$\iint e^{-\pi NDs^2}\,\tau N'\frac{s}{l^2\theta}\left|\frac{ds}{d\theta}\right|\frac{s'}{l^2\beta}\left|\frac{ds'}{d\beta}\right| l^2\theta\,d\theta\,d\phi , \quad (2)$$

where

$$\beta^2 = \psi^2 + \theta^2 - 2\psi\theta\cos\phi,\ \beta = \frac{s'}{l} + \phi(s') .$$

The total backscattering yield is found by summing over l for all contributing atomic layers. An exact evaluation of the above integral is difficult because of the singularities in the integrand arising at the critical angle in the differential scattering function

$$\frac{s'}{\beta}\left|\frac{ds'}{d\beta}\right| .$$

To date, the integral has been evaluated by approximating the scattering function as a delta function plus a step function at the critical angle ψ_c. The results give a backscattering enhancement as a function of exit angle ψ and for small to moderate depths D that are in fair agreement with the computer simulations of Barrett.[2] For large depths, the enhancement predicted by Eq. (2) does not vanish, which is believed to be a consequence of the breakdown of the two-particle scattering picture. The results show that the enhancement region is compensated by a deficit region at larger backscattering angles. Studies to evaluate Eq. (2) more precisely are continuing.

---

1. P. P. Pronko et al., *Phys. Rev. Lett.* 43, 779 (1979); B. R. Appleton et al., "Enhanced Yield Effect for Ions Scattered near 180°," this report.
2. J. H. Barrett, B. R. Appleton, and O. W. Holland, "Role of Reversibility in Enhanced Ion Backscattering near 180° Scattering Angle," this report.
3. O. S. Oen, *Phys. Lett.* 19, 358 (1965).

STUDIES OF LOW-ENERGY DISPLACEMENT CASCADES IN THE BINARY COLLISION APPROXIMATION

M. T. Robinson

The production of radiation damage in solids has been studied by computer simulation models of varying degrees of exactness.[1-6] Only the simplest

models are computationally efficient enough to be applied at the relatively high primary recoil energies characteristic of fusion neutron environments. However, simple models such as the BCA are of limited applicability at the low recoil energies which characterize the motion of most of the particles in a displacement cascade. An important aspect of modeling fusion neutron damage production is thus an understanding of the low-energy behavior of the computer simulation codes which have been developed for high-energy damage studies. This report summarizes some recent work in this area with the BCA code MARLOWE.[6-8]

A detailed study has been made of collision cascades generated in Cu by primary recoils of initial kinetic energies E_0 ranging from 10 to 500 eV. At each energy, a set of 1000 isotropically distributed primary particles was used. The quasielastic scattering of particles in a cascade was governed by the Molière approximation to the Thomas-Fermi interatomic potential with the screening length $a_{12} = 7.38$ pm. All collisions with impact parameters less than p_m were considered, with $p_m/a = 0.62$, where $a = 0.3615$ nm is the lattice constant of Cu. Target atoms were added to the cascade if they received kinetic energy in a collision exceeding $E_m = 5.0$ eV. All displaced atoms were required to surmount a binding energy $E_b = 0.2$ eV and were followed until their energies fell below $E_c = 4.8$ eV. The value of E_b was chosen by comparing six LCSs evaluated with MARLOWE with the same events evaluated with the classical dynamical code COMENT.[3] With the parameters chosen, MARLOWE represents the length of ⟨110⟩ LCSs fairly accurately but overestimates the length of ⟨100⟩ and ⟨111⟩ LCSs. Inelastic energy losses were included in the calculations using a model described previously.[6] When thermal displacements of the lattice atoms were wanted, the Debye temperature $\theta_D = 314$ K was used. MARLOWE organizes Frenkel defect pairs into classes based mainly on the separation between the paired interstitial and vacancy.[7] Pairs remaining after removing all interstitials located in an 18-site instability region about each vacancy are termed "distant." These, in turn, are organized according to whether or not their separation exceeds a vacancy capture radius r_v.

Figure 1.24 shows the energy dependence of $\langle \nu \rangle$, the mean number of distant Frenkel pairs, for several cases. It is convenient to discuss first the results for the static lattice with $r_v = 0$. In this case, the curve shows three inflections, indicated in the figure by the letters a(~50 eV), b(~125 eV), and c(~310 eV). Below a, the curve shows well-marked threshold

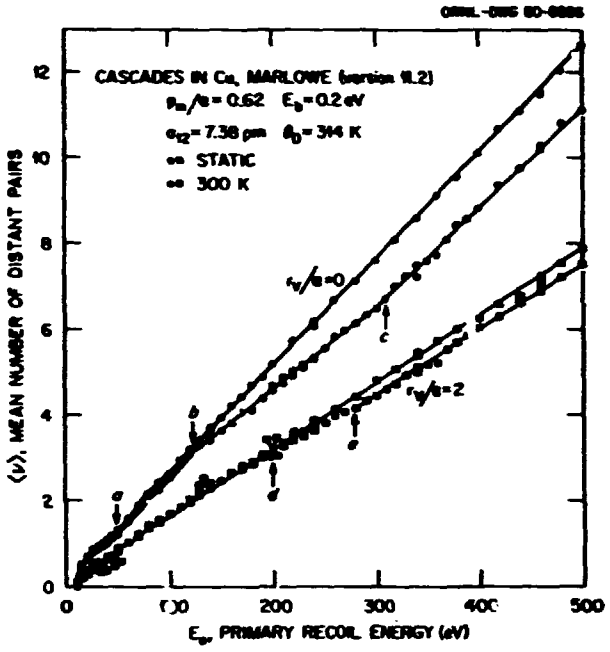

Fig. 1.24. Mean number of distant Frenkel pairs produced by Cu atoms recoiling in Cu.

behavior, similar to that expected from a Kinchin-Pease model[9] with a threshold energy of about 20 eV. Near a, defect multiplication begins to be important and the curve rises approximately linearly to point b, again consistently with the Kinchin-Pease model. From b to c, however, although the curve is still plausibly linear, its slope is significantly less. Above c, finally, the slope increases again to something like its original value. When the value $r_v/a = 2$ is used to remove the Frenkel pairs of smallest separation, the energy dependence of $\langle \nu \rangle$ is similar, but the threshold is less well marked and the inflections are moved to different values, marked d and e in the figure. The introduction of thermal displacements corresponding to room temperature completely eliminates the inflections b, c, d, and e, without altering much the threshold region.

Leibfried[10] found that for the Kinchin-Pease model, the variance of the number of distant pairs was a linear function of the energy, that is,

$$\sigma^2/m \equiv [\langle \nu^2 \rangle - \langle \nu \rangle^2]/\langle \nu \rangle = 4 \ln 4/3 - 1 = 0.1507 \ldots \quad E > 4E_d .$$

This quantity, the scaled variance, is plotted in Fig. 1.25 for the MARLOWE cascades with $r_v = 0$. The hard-core result is shown for an assumed E_d value.

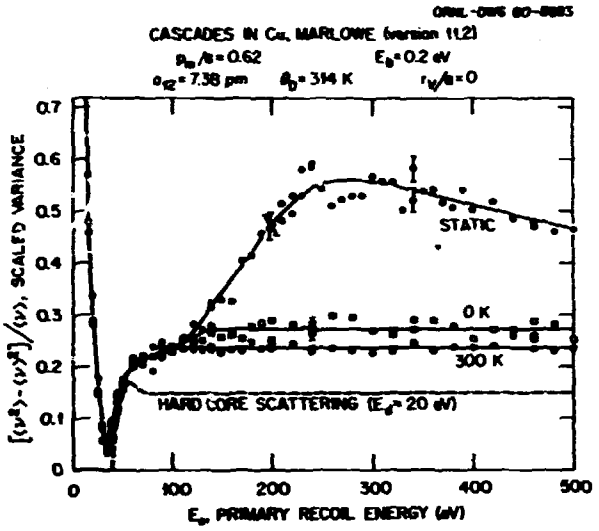

Fig. 1.25. Scaled variance of the number of distant Frenkel pairs produced by Cu atoms recoiling in Cu.

Below about 80 eV, the computer simulations are all much alike and differ from the hard-core result only because there is no sharp threshold in the calculation. The simulations including thermal displacements show σ^2/m to be constant above about 80 eV at 300 K or about 140 eV at 0 K. In sharp contrast to this behavior, however, is that of the static lattice simulations. Here, σ^2/m continues to rise until a maximum is reached near 260 eV and then decreases. The behavior above 500 eV has not yet been examined.

Detailed examination of the simulations shows that the anomalies in both figures can be associated with primary recoils starting near the ⟨111⟩ directions. Multiple defects are substantially prevented from being formed as long as E_0 is less than the ⟨111⟩ focusing energy, about 250 eV for the potential used in the calculations.[3,11] At higher energies, multiple defects are formed by ⟨111⟩ primaries, but, up to 500 eV, not as copiously as for primaries starting in other directions. Approximately 5 percent of the primary particles can be assigned to the ⟨111⟩ region, that is, to a cone about a ⟨111⟩ direction with a half angle of about 9 degrees.

The static crystal results may be interpreted in terms of a simple modification of the Kinchin-Pease model originally proposed to describe the effects of channeling.[12] In this model, in addition to the usual assumptions, it is imagined that each particle in the developing collision cascade has an energy-independent probability p of slowing down to rest without producing further displacements. This feature, though originally assigned a different physical origin, can clearly be assigned equally well to ⟨111⟩ LCS production. In this model,[12]

$$\langle\nu\rangle \sim [E/2E_d]^{1-2p}$$

and the scaled variance can be written as[13]

$$\sigma^2/m \sim \langle\nu\rangle .$$

The latter dependence accounts for the results in Fig. 1.25. Furthermore, if the data from Fig. 1.24 are replotted bilogarithmically, the static crystal results are fit very well over the energy range up to about 350 eV by the value $p = 0.05$, in complete agreement with the size of the ⟨111⟩ region. The 300 K results, in contrast, require $p = 0$.

Thus, a consistent picture emerges in which all of the anomalies shown in Figs. 1.24 and 1.25 for the static lattice simulations can be attributed to the dynamics of ⟨111⟩ LCSs. The introduction of thermal displacements into the model removes the anomalies by interfering with the propagation of these sequences. It seems probable, therefore, that thermal energy plays a significant role in the development of displacement cascades in the energy range below ~1 keV and must be included in computer simulation models to obtain correct results.

1. J. B. Gibson et al., *Phys. Rev.* **120**, 1229 (1960).
2. A. Scholz and C. Lehmann, *Phys. Rev. B* **6**, 813 (1972).
3. J. O. Schiffgens et al., *Radiat. Eff.* **39**, 221 (1978).
4. H. L. Heinisch, J. O. Schiffgens, and D. M. Schwartz, *J. Nucl. Mater.* **85/86**, 607 (1979).
5. J. R. Beeler, Jr., *Phys. Rev.* **150**, 470 (1966).
6. M. T. Robinson and I. M. Torrens, *Phys. Rev. B* **9**, 5008 (1974).
7. M. T. Robinson, *Solid State Div. Annu. Prog. Rep., April 30, 1977*, ORNL-5328, p. 12.
8. M. T. Robinson, *Damage Analysis and Fundamental Studies Quart. Prog. Rep., October–December 1978*, DOE ET-0065/4, p. 73.
9. G. H. Kinchin and R. S. Pease, *Rep. Prog. Phys.* **18**, 1 (1955).
10. G. Leibfried, *Nukleonik* **1**, 57 (1958).
11. D. K. Holmes and M. T. Robinson, *Solid State Div. Annu. Prog. Rep., Dec. 31, 1975*, ORNL-5135, p. 16.
12. O. S. Oen and M. T. Robinson, *Appl. Phys. Lett.* **2**, 83 (1963).
13. M. T. Robinson, *Philos. Mag.* **12**, 741 (1965).

LASER ANNEALING

DOPANT PROFILE CHANGES INDUCED BY LASER IRRADIATION OF Si: COMPARISON OF THEORY AND EXPERIMENT[1]

J. C. Wang B. R. Appleton
R. F. Wood P. P. Pronko[2]
C. W. White S. R. Wilson[3]
W. H. Christie[4]

The dopant profile changes induced by pulsed-laser annealing of B-, P-, As-, Fe-, or Cu-implanted Si, as measured by secondary ion mass spectrometry and Rutherford ion backscattering, have been analyzed with thermal- and mass-diffusion calculations. The results show that these profile changes are consistent with near-surface melting and liquid-phase recrystallization. Values of diffusion coefficients for B, P, and As in liquid Si obtained by fitting the dopant profiles agree quite well with those reported in the literature.

To calculate the change of profiles, we first assumed that a near-surface layer much thicker than the doped region is melted instantaneously at $t = 0$ and then frozen instantaneously at a later time $t = \tau$. The one-dimensional Green's function solution of the diffusion equation was used to calculate the final profile. A good fit for a sample doped with B was obtained when $D\tau \approx (668\ \text{Å})^2$, where D is the diffusion coefficient in liquid Si. The result is shown by the dashed line in Fig. 1.26. The discrepancy near the 3000-Å region was thought to be due to the neglect of the melt-front motion. To include this effect in the calculation, we first solved the problem in which the dopants were limited to diffusion in a slab of thickness x, where $0 \leq x \leq l$, from $t = 0$ to $t = \Delta t$. The melt-front was then moved in small steps, and at each step the dopants were allowed to diffuse only in the slab between the surface (at $x = 0$) and the melt-front (at $x = l$) for a short time Δt. The l and Δt values were determined from the location of the melt-front as a function of t, for which we used the melt-front movement reported previously[5] but scaled it with a factor F. For the B redistribution, a good fit with this method was obtained when $F = 0.764$ and $D = 3.09\ \text{cm}^2/\text{s}$. The fitted dopant distribution shown by the solid line in Fig. 1.26 is an improvement over that shown by the dashed line. The fitted values of B, P, and As diffusion coefficients in liquid Si are compared to experimental values in Table 1.3.

The segregation of implanted Fe and Cu to the surface during laser annealing was explained by a model that assumes an accumulation of impurities in the liquid in the immediate vicinity of the advancing melt-front and the incorporation of impurities into the solid phase when the accumulation in the liquid is sufficiently high.

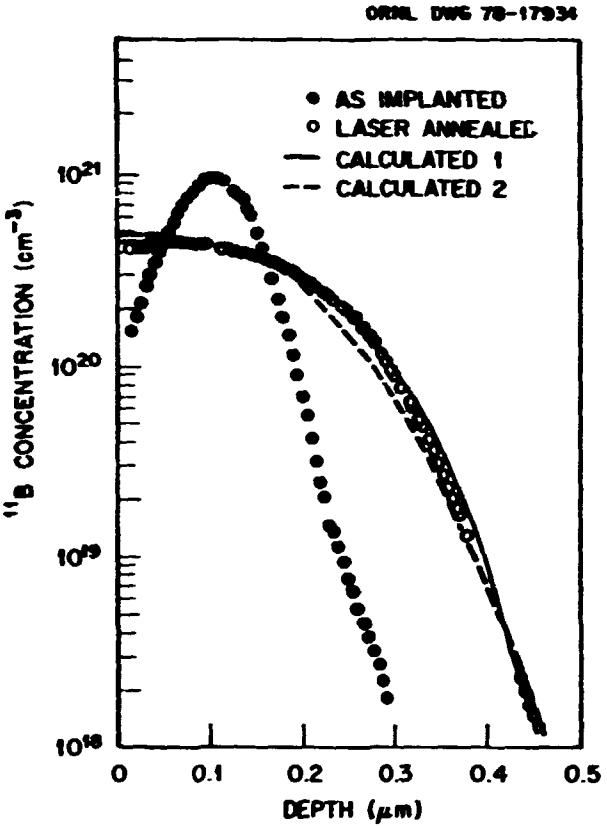

Fig. 1.26. Comparison of experimental and theoretical B profiles in Si. The solid (dashed) line was calculated with (without) the effect of melt-front movement included.

Table 1.3. Fitted values of melt-front penetration and diffusion coefficients

Dopant	Melt-front penetration (Å)	D_{cal} (10^{-4} cm^2/s)	D_{exp} (10^{-4} cm^2/s)	
B	7120	3.09	2.4[a]	3.3[b]
P	4460	5.36	5.1[a]	2.7[b]
As	7920	2.97	3.3[a]	

[a]See ref. 6.
[b]See ref. 7.

1. Summary of paper: *AIP Conf. Proc.* **50**, 123 (1978).
2. Guest scientist from Argonne National Laboratory, Argonne, Ill.

3. ORAU graduate laboratory participant from North Texas State University, Denton; present address, Motorola, Inc., Phoenix, Ariz.

4. Analytical Chemistry Division, ORNL.

5. J. C. Wang, R. F. Wood, and P. P. Pronko, *Appl. Phys. Lett.* 33, 455 (1978).

6. H. Kodera, *Jpn. J. Appl. Phys.* 2, 212 (1965).

7. Yu. M. Shashkov and V. M. Gurevich, *Russ. J. Phys. Chem.* 42, 1082 (1968).

EFFECTS OF THERMAL PROPERTIES OF AMORPHOUS LAYERS ON PULSED-LASER ANNEALING

R. F. Wood G. E. Giles[1]

The lattice damage created by ion implantation of semiconductors depends on the dopant, the implantation energy, and the dose. In many cases (e.g., 100 keV implantation of As into Si), the near-surface region is made almost completely amorphous. The optical absorption coefficient of amorphous Si is approximately one order of magnitude greater than that of crystalline Si ($\sim 5\times 10^4$ cm^{-1} compared to $\sim 3\times 10^3$ cm^{-1}) at the fundamental wavelength of a ruby laser (0.693 μm). This enhanced coupling of the laser radiation to the sample is the most obvious effect of the amorphous layer on pulsed-laser annealing and is accounted for in most theoretical calculations. However, the effects of the thermal, as well as the optical, properties of the amorphous layer have not been carefully studied, and it has been suggested that they would be large enough to invalidate the melting model of laser annealing. We show here that these effects play a minor role in determining the melt-front penetration and velocity during laser annealing.

The calculations were carried out with the computer program HEATING5, which has been described elsewhere.[2] The thermal conductivity K, melting temperature T_M, and latent heat of fusion L_a in the amorphous layer were substantially altered from their crystalline values; accurate values of these quantities in amorphous Si are not known. The general result of the calculations was that the gross features of the laser annealing were changed very little by varing the thermal properties, although there were differences in detail. An illustration is given in Fig. 1.27 which shows melt-front position as a function of time for laser pulses of energy $E_l = 1.4$ J/cm^2 and pulse duration $\tau_l = 15$ ns and for $E_l = 1.5$ J/cm^2, $\tau_l = 60$ ns. The amorphous layer was 0.15 μm thick, and the ratios of amorphous to crystalline latent heats L_a/L_c were chosen as indicated on Fig. 1.27. The melting temperature and thermal conductivity

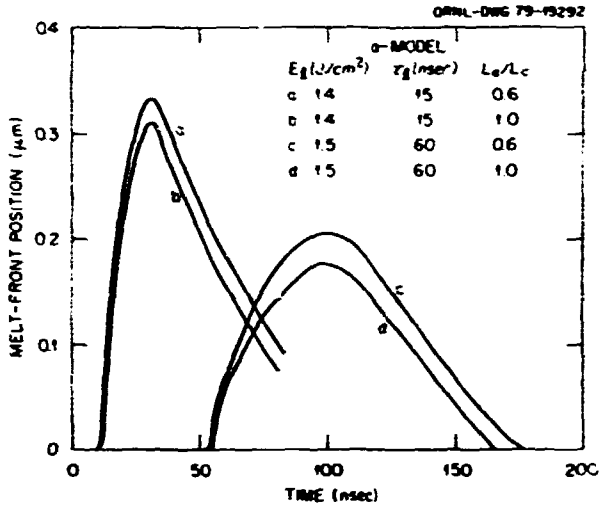

Fig. 1.27. Melt-front position as a function of time with and without reduction of the latent heat in the amorphous layer.

were not changed from their crystalline values. It can be seen that a 40% reduction of the latent heat in the amorphous region increases the penetration by only $\sim$0.02 μm. Similarly, small changes in annealing behavior were obtained when T_M was decreased from 1410 to 1000°C and K was modified to have the low-temperature behavior of an amorphous material.

Evidently, substantial reductions in K, T_M, and L do not cause large changes in the melt-front histories, as has been suggested. The reasons for this somewhat surprising result are quite simple, as some of the subsidiary output data of the computer calculations showed. When K, T_M, and L are reduced, it takes less time and energy to melt the surface, as expected. However, because the reflectivity switches from 0.35 (solid) to 0.60 (liquid) earlier in the laser pulse, the total energy absorbed may not be greatly different. For a quite similar reason, reducing T_M and K also have relatively minor effects.

1. Computer Sciences Division, UCC-ND.

2. W. D. Turner, D. C. Elrod, and I. I. Siman-Tov, *HEATING5 – An IBM 360 Heat Conduction Program*, ORNL CSD TM-15 (March 1977).

DOPANT PROFILES IN LASER-RECRYSTALLIZED DEPOSITED LAYERS

R. F. Wood R. T. Young

Doped layers of amorphous Si deposited on single-crystal substrates can be epitaxially recrystallized by

pulses from a Q-switched ruby or Nd:YAG laser. A uniformly doped amorphous layer might be expected to lead to abrupt p-n junctions such as those typically obtained by conventional epitaxial techniques. However, since the molten layer produced by the laser irradiation must contact the single-crystal substrate before good epitaxial regrowth can occur, questions arise concerning the extent of dopant profile spreading into the substrate region. Theoretical studies of profile spreading in laser-recrystallized deposited Si layers have been carried out in conjunction with experimental studies[1] in the photovoltaic program.

The experimental profiles after laser treatment were determined by Hall effect measurements in combination with anodic oxidation and stripping. This method is unable to determine the initial dopant distribution because the dopant atoms are not electrically active in amorphous silicon. Figure 1.28 shows results for the cases of 1000 and 2000 Å As-doped layers, epitaxially regrown with 15-ns pulses of 1.55 and 1.78 J/cm^2, respectively. The dopants have spread deeper into the substrate in a manner very similar to dopant redistributions in As-implanted, laser-annealed samples. The complete absence of concentration spikes at the surface should be noted. The solid lines in the figure are profiles calculated by techniques described elsewhere.[2,3] The liquid-phase diffusion of As was calculated from ideal (completely uniform As concentration) as-deposited profiles (dotted lines) without considering the possible complications due to interfacial oxygen films between the substrate and the deposited layers. The as-deposited profiles were adjusted to give the same total dopant content as that measured after the laser-induced diffusion. This implies that no dopant escaped from the front surface, which is consistent with measurements on ion-implanted, laser-annealed samples. Because there is no evidence in the experimental profiles of an abrupt buildup in the concentration very near the surface due to terminal transients, the interface segregation coefficient k_i was taken to be 1.0. The equilibrium segregation coefficient k_i^0 for As in Si is reported in the literature to be 0.3, but the experimental data could not be fitted with this value, primarily because of the concentration spike it produces at the surface.[4] The fact that k_i must be made larger than k_i^0 clearly establishes that segregation effects during laser annealing depart substantially from those exhibited under near-equilibrium conditions of solidification. This is not surprising when the high crystal regrowth rates (3 to 4 m/s) involved in laser annealing are considered. The

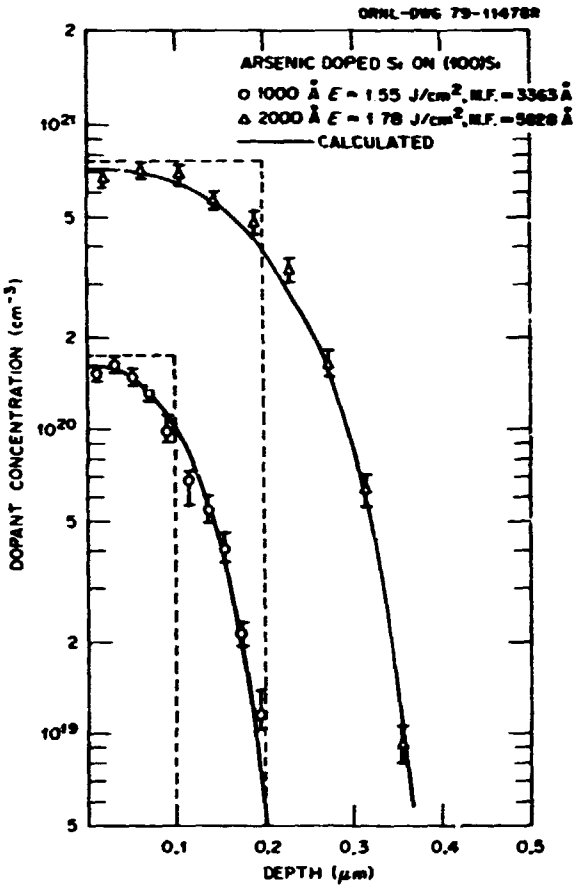

Fig. 1.28. Comparison of experimental and calculated dopant profiles after laser irradiation of 1000- and 2000-Å deposited layers. The dashed curves are the assumed, ideal starting profiles normalized to the concentration measured after the irradiation.

agreement between the experimental and calculated profiles is very good. Calculations[2,3] of the liquid-solid interface motion under the conditions used in these experiments show that the near-surface region of the sample melted to depths of approximately 3360 and 5830 Å, respectively. The melted region then recrystallized epitaxially from the underlying substrate in a defect-free layer, as expected from previous experience with laser-annealed samples.

It can be seen from Fig. 1.28 that the dopant profiles, after the laser irradiation, penetrate into the substrate region and are rounded as compared to the assumed starting profile (dotted line). The melt-front penetrations for both the 1000- and 2000-Å layers, as determined by the calculations, are substantially greater than those needed to epitaxially regrow the deposited layers. The laser energies used in the experiments were made rather high because of concern about the oxide interface layer between the

deposited film and the substrate. With improved experimental conditions, it should be possible to reduce the melt-front penetration to the point where the spreading of the dopant into the substrate region is virtually eliminated.

---

1. R. T. Young et al., "Electrical and Structural Characteristics of Laser-Induced Epitaxial Layers in Si," this report; *Appl. Phys. Lett.* 35, 447 (1979).
2. J. C. Wang, R. F. Wood, and P. Pronko, *Appl. Phys. Lett.* 33, 455 (1978).
3. R. F. Wood et al., p. 37 in *Laser and Electron Beam Processing of Materials*, ed. by C. W. White, Academic Press, New York, 1980.
4. V. G. Smith, W. A. Tiller, and J. W. Rutter, *Can. J. Phys.* 33, 723 (1955).

CARRIER DIFFUSION DURING PULSED-LASER ANNEALING

R. F. Wood

Recent calculations by Yoffa[1] would seem to imply that the diffusion of the hot, dense gas of electrons and holes generated during laser annealing of Si plays a dominant role in determining the temperature rise of the lattice. The idea is that at the high excitation rates used in pulsed laser annealing, the laser energy is given to the lattice within a characteristic depth determined primarily by carrier diffusion rather than by the absorption coefficient of the sample. Here it is shown that such carrier diffusion does not alter the picture of melting and liquid epitaxial regrowth that is used to interpret most of the laser annealing experiments at ORNL.

The following expression for the electron density in the near-surface region of a laser-irradiated sample, derived in ref. 1, is

$$N_{e,ss}(x) = \frac{g\hbar\omega_L\tau_e}{\hbar\omega}\,\frac{\delta/\alpha}{1-(\delta/\alpha)^2} \times (e^{-x/\alpha} - (\delta/\alpha)\,e^{-x/\delta}) , \quad (1)$$

where g is the carrier generation rate, δ is the absorption length for laser radiation of frequency ω_L, τ_e is the phonon emission rate due to collisions of the photoexcited electrons with the lattice, and $\hbar\omega$ is the energy of the emitted phonons. The parameter α, the characteristic diffusion length of the carriers, is discussed at length by Yoffa.

Equation (1) has a form analogous to the familiar expression for the spatial falloff in intensity $I(x)$ of radiation incident on an absorbing medium,

$$I(x) = (1-r)I_0 k e^{-kx} , \quad (2)$$

where r is the reflectivity, $k = \delta^{-1}$ is the absorption coefficient, and I_0 is the intensity of the incident laser beam. Equation (2) is generally the form chosen for the source function in calculations of heat generation and conduction during laser annealing.[2] In Eq. (1), $gh\omega_L$ is the rate at which the incident radiation is absorbed in the sample by electronic excitations and is therefore equivalent to $(1-r)I_0k$ in Eq. (2). The quantity $N_{e,ss}(x)(\hbar\omega/\tau_e)$ from Eq. (1) can be interpreted as the rate at which the absorbed energy is given up to the lattice through electron-lattice interactions and is equivalent to $I(x)$ in Eq. (2). Equation (1) can thus be rewritten as

$$I(x) = (1-r)I_0(\alpha-\delta)^{-1}(\alpha+\delta)^{-1}(\alpha e^{-x/\alpha} - \delta e^{-x/\delta}) . \quad (3)$$

If carrier diffusion is negligible, $\alpha = 0$ and Eq. (3) reduces to Eq. (2) as it should.

In her illustrative calculation, Yoffa chose $\hbar\omega_L = 2.3$ eV, $\delta = 10^{-5}$ cm, $r = 0.5$, and a typical annealing pulse of 10^8 W/cm^2. This choice corresponds approximately to a 1.5-J/cm, 15-ns square pulse of a frequency doubled Nd:YAG laser and leads to an estimate for α of 2.5×10^{-5} cm. Figure 1.29 shows the ratio $F_{abs} \equiv I(x)/[(1-r)I_0]$ as a function of x for four different sets of values for α and δ. The very high value of $k = 1/\delta = 10^5$ cm^{-1} assumed by Yoffa does indeed make the effects of carrier diffusion *appear* to be significant (compare • with ▲). However, from Fig. 1.29, it is seen that this situation can be approximated very well by using an effective absorption coefficient of $k = (1.0+2.5)^{-1}\times10^5\,\text{cm}^{-1} = 2.86\times10^4\,\text{cm}^{-1}$ in the simple exponential form of Eq. (2).

The results of calculations of melt-front penetration as a function of absorption coefficient for two

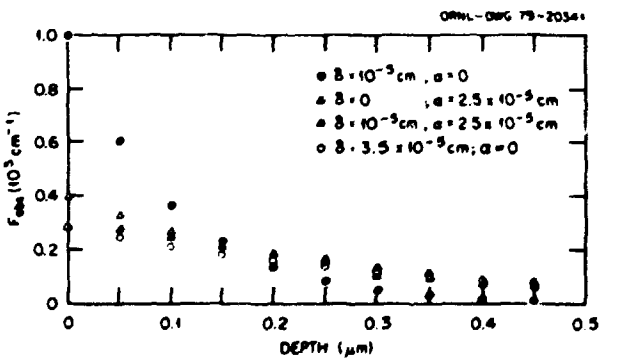

Fig. 1.29. The ratio $F_{abs} = [I(x)/(1-r)I_0]$ as a function of distance from the front surface of the sample.

different models are shown in Fig. 1.30. The *c*-model assumes that there is no distinct amorphous layer present and that, as a consequence, the absorption coefficient has some average constant value throughout the sample. The *a*-model, on the other hand, assumes that there is a 0.15-μm-thick amorphous layer at the surface of the sample. Within this layer, the value of k ($\equiv k_a$) was varied over the range shown, while keeping k in the crystalline region beyond the amorphous layer fixed at its perfect crystal value. The

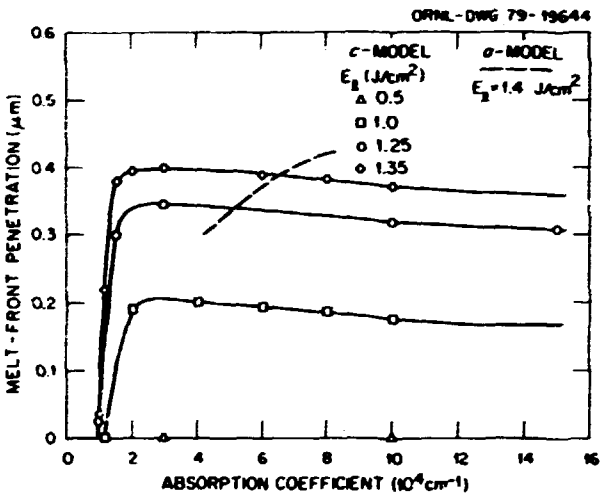

Fig. 1.30. Melt-front penetration as a function of absorption coefficient for the two different models described in the text.

latter value of k is that appropriate for single-crystal Si at the wavelength ($\lambda = 0.693$ μm) of the fundamental mode of a ruby laser. It can be seen that the maximum penetration depth of the melt-front in the *c*-model is essentially constant for wide ranges of the effective absorption coefficient. Hence, within certain limits, it does not really matter with this model whether or not carrier diffusion of the magnitude estimated by Yoffa is present. The results for the *a*-model are more sensitive to values of k_a for an obvious reason. With an amorphous layer only 0.15 μm thick, much of the absorption of the laser radiation may occur in the crystalline region, where k is assumed to be only 5×10^3 cm^{-1}. As k_a increases, the percentage of the radiation absorbed in the 0.15-μm layer increases rapidly also, leading to the dashed curve on Fig. 1.30. Nevertheless, even for this model, much larger values of α than those estimated by Yoffa would be required to reduce the effective absorption coefficient to the extent that the predictions of the melting model of pulsed-laser annealing would be made invalid.

1. E. J. Yoffa, *Applied Physics Letters* (in press).
2. J. C. Wang, R. F. Wood, and P. P. Pronko, *Appl. Phys. Lett.* 33, 455 (1978).

MODEL FOR NONEQUILIBRIUM SEGREGATION DURING PULSED-LASER ANNEALING

R. F. Wood

Values of the equilibrium interface segregation coefficient k_i^0 for B, P, and As in Si[1] are 0.80, 0.35, and 0.3, respectively. Standard theories of crystallization under equilibrium conditions,[2] applied to the laser annealing process, show that in As- and P-implanted Si these values of k_i^0 should produce large concentration spikes at the surface. These surface spikes are not observed in , As-, and P-implanted, laser-annealed Si[3] or in As-doped amorphous Si layers recrystallized by a laser.[4] Moreover, satisfactory fits to the dopant profiles in these cases can only be obtained with values of k_i nearly equal to unity.[4,5] Recently White et al.[6] used Rutherford backscattering techniques to measure the profiles of As, Sb, Ga, In, and Bi in ion-implanted, laser-annealed Si. From fits of the measured profiles, values of k_i were extracted. The results in refs. 3–6 provide data on the segregation behavior of B, P, As, Sb, Ga, In, and Bi in Si during laser annealing. Values of k_i^0 and k_i are shown in Table 1.4. The most striking feature of these data is the very large differences between k_i^0 and k_i when k_i^0 is small.

A phenomenological model based on the kinetic theory of melting has been developed to explain these nonequilibrium segregation effects. The model takes into account the idea that for a recrystallization velocity $v \gg 0$, new layers may be added to the solid so quickly that dopant atoms in the interface region have a reduced probability of escape from the solid being formed.

Rate equations for the incorporation of host h and dopant d atoms into the solid are written as

$$R_j^S = K_j^f C_j^L - K_j^r C_j^S \qquad j = h, d \,, \tag{1}$$

where C_j^L and C_j^S are the concentrations of j-type atoms in the liquid and solid, respectively, and K_j^f and K_j^r are the forward (liquid $\rightarrow$ solid) and reverse rate constants in m/s. The rate constants are assumed to be of the standard activated form, for example,

Table 1.4. Results of calculation of k_i and comparison to experiment

Dopant	k_i^0	k_i (exp)	k_i (v_0 = constant)	k_i ($v_0 = D_l/x_0$)	ΔU_d^m (eV)	C_d^S/C_d^{So}
B	0.8	1.00	0.98	0.99	−0.032	
P	0.35	1.00	0.90	0.95	−0.152	1.5
As	0.3	1.00	0.86	0.97	−0.175	1.4
Sb	0.023	0.7	0.68	0.88	−0.547	26
Ga	0.008	0.2	0.61	0.31	−0.700	14
In	0.0004	0.15	0.45	0.15	−1.134	400
Bi	0.0007	0.4	0.48	0.39	−1.053	1000
Al	0.0020		0.53	0.52	−0.901	55

$$K_d^l = A_d^l \exp\left(-U_d^l / RT\right), \tag{2}$$

where U_d^l is the barrier height; similar forms hold for K_i^l, K_d^l, and K_k^l. To account for dopant trapping, U_d^l is written as

$$U_d^l(v) = U_d^m + \Delta U_d^l(v), \tag{3}$$

where U_d^m is the equilibrium value. The term $\Delta U_d^l(v)$ may be a complicated function of v, but is must go to zero as $v \to 0$ and to a constant value as v becomes large. After some simplifying assumptions and a moderate amount of algebra, one obtains

$$k_i = k_i^0 \exp[\Delta U_d^l(v)/RT], \tag{4}$$

where

$$k_i^0 \equiv \left(C_d^S/C_d^L\right)_{v=0} \text{ and } k_i \equiv \left(C_d^S/C_d^L\right)$$

are the equilibrium and nonequilibrium segregation coefficients, respectively.

Several simple forms for $U_d^l(v)$ have been used in the calculations to date; one of these is

$$U_d^l(v) = U_d^{l0} + \Delta U_d^m[1 - \exp(-v/v_0)]. \tag{5}$$

With this form and the requirement that $k_i \to 1$ as $v \to \infty$, Eq. (4) becomes

$$k_i = k_i^0 \exp\{(-RT \ln k_i^0)[1 - \exp(-v/v_0)]/RT\}. \tag{6}$$

Column 4 of Table 1.4 shows the results obtained from Eq. (6) when a single value of v_0, independent of dopant species, is used. Clearly, the model can account for the extraordinarily large differences between k_i^0 and k_i(exp). This is a major success of the model and shows that it is not necessary to abandon the melting hypothesis of laser annealing, as some have contended. The velocity v_0 can be related to an average diffusion coefficient D_i in the interface region by $D_i = v_0 x_0$. Of course, D_i is not known, but if it is assumed that it is proportional to D_l, the dopant diffusion coefficient in the liquid, then $v_0 = D_l/x_0$, and with $x_0 = 225$ Å, the results in column 5 are obtained. Values of D_l were taken from the literature and varied within the stated error ranges to fit k_i(exp). Only for Sb and Ga are there appreciable differences between columns 4 and 5. Approximately 10 and 40%, respectively, of these dopants were lost during annealing, and this made a fit to the experimental profiles difficult. Figure 1.31 shows the results for k_i as a function of v using Eq. (6).

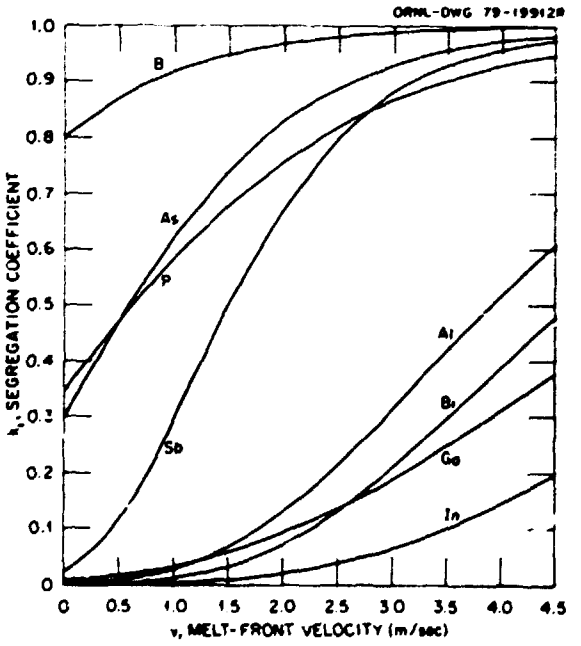

Fig. 1.31. Dependence of k_i in Si on melt-front velocity using Eq. (6).

Column 6 in Table 1.4 gives values for ΔU_d^a. When these "trapping energies" are compared to values of U_d^s, the activation energy for dopant diffusion in the solid, it is found that ΔU_d^a is a rather small fraction of U_d^s. Thus, for the dopants listed in Table 1.4, the bonding between the dopant and host atoms is adequate to account for the trapping.

From the expression for C_k^L in an ideal dilute solution, one can obtain

$$C_d^S = k_i[1 - \exp(-v\ K_k')] \ . \qquad (7)$$

With the values of k_i in column 5 of Table 1.4, v = 4 m s, and K_k' = 100 m s, C_d^S was calculated. The ratios of C_d^S to the maximum equilibrium solubility C_d^{Se} are given in the last column. These ratios are in satisfactory agreement with the experimental estimates in ref. 5.

1. F. A. Trumbore, *Bell System Tech. J.* **39**, 205 (1960).
2. V. G. Smith, W. A. Tiller, and J. W. Rutter, *Can. J. Phys.* **33**, 723 (1955).
3. C. W. White, J. Narayan, and R. T. Young, *Science* **204**, 461 (1979).
4. R. T. Young, J. Narayan, and R. F. Wood, *Appl. Phys. Lett.* **35**, 447 (1979).
5. J. C. Wang, R. F. Wood, and P. P. Pronko, *Appl. Phys. Lett.* **33**, 455 (1978).
6. C. W. White, S. R. Wilson, and B. R. Appleton, *J. Appl. Phys.* **51**, 738 (1980).

SUBSTRATE HEATING DURING LASER ANNEALING

R. F. Wood G. E. Giles[1]

For a number of reasons it may be desirable to heat or cool semiconductor samples during pulsed-laser annealing. If, for example, an available laser cannot supply the energy required to melt the near-surface region to a particular depth, sample heating may extend the melting range to that depth. Even with a laser of sufficient power, it may be advantageous to heat the substrate so that the lowest possible energy density for annealing can be used. In this way, the effects of the spatial inhomogeneities in the laser beam can be better controlled. The most interesting use of substrate heating and cooling at this time may be to control the melt-front velocity v during resolidification of the melted near-surface region. In a model developed by one of us,[2] the interface segregation coefficient k_i for an impurity in the semiconductor is directly related to v and to the equilibrium interface segregation coefficient k_i^0. If the melt-front velocity can be changed by substrate heating, a relatively simple method for testing the model and for studying other aspects of nonequilibrium segregation during ultrarapid resolidification is available.

Figure 1.32 shows a series of calculated melt-front histories for a Si sample held at various steady-state temperatures before and after irradiation with a single 15-ns, 0.82-J/cm^2 pulse from a ruby laser.

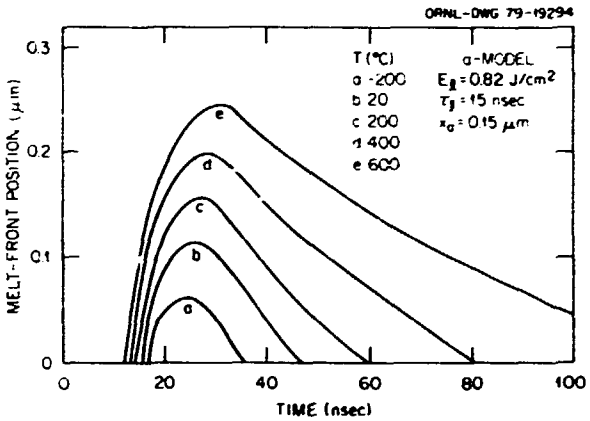

Fig. 1.32. Calculated melt-front histories for a Si sample cooled or heated to the temperatures indicated.

These calculations model the laser annealing of a single-crystal sample of Si implanted with ^{75}As (100 keV, 1.4×10^{16} cm^{-2}). The As implantation was assumed to make the near-surface region nearly amorphous to a depth of 0.15 μm. The absorption coefficient of the laser radiation was taken to be 5×10^4 cm^{-1} in this region and 3×10^3 cm^{-1} at greater depths. The reflectivities in the solid and liquid states were 0.35 and 0.60, respectively. From a series of results such as those in Fig. 1.32, the melt-front penetration as a function of substrate temperature can be obtained; this is shown in Fig. 1.33 for three different pulse energy densities.

Values of the melt-front velocity can be found from curves such as those shown in Fig. 1.32 by taking the derivative at any time. The recrystallization velocity is clearly not constant, but an average velocity is all that is needed at the present stage of the development of laser annealing. Figure 1.32 shows that variations of factors of 2 to 3 in the average melt-front velocity during recrystallization can be produced by substrate heating in easily accessible temperature ranges. Although larger variations of v are desirable, it is apparent that substrate heating can be used to study

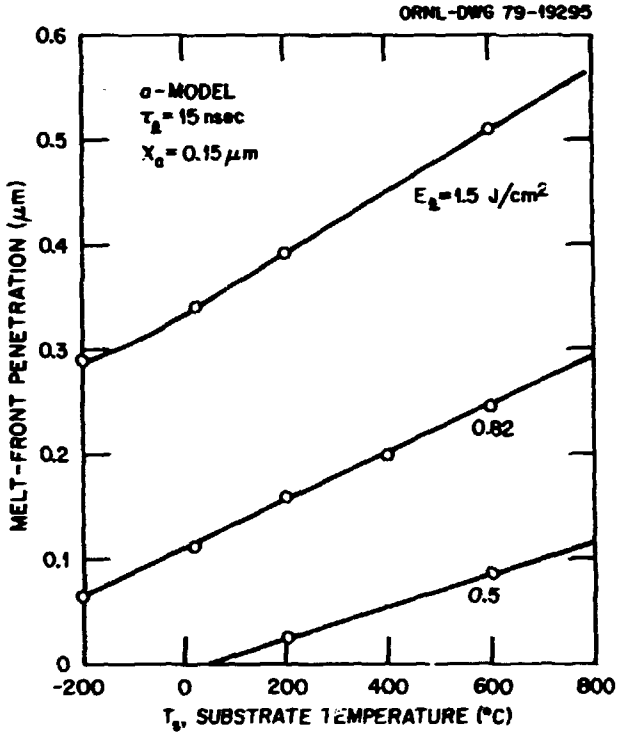

Fig. 1.33. Maximum melt-front penetration as a function of substrate heating for three different laser energies.

the effects of melt-front velocity on dopant segregation during laser annealing. Experiments by White et al.[3] confirm the utility of the technique.

1. Computer Sciences Division, UCC-ND.
2. R. F. Wood, "Model for Nonequilibrium Segregation During Pulsed Laser Annealing," this report.
3. C. W. White et al., "Kinetic Effects in Laser Annealing of Ion-Implanted Si," this report.

ELECTRONIC AND MAGNETIC PROPERTIES

FINITE-TEMPERATURE CALCULATIONS FOR ITINERANT ELECTRON FERROMAGNETS

J. F. Cooke

Inelastic neutron scattering experiments performed at ORNL have revealed a variety of interesting and unusual phenomena associated with the spin dynamics of the 3-*d* transition metal ferromagnets Ni and Fe. In contrast to local moment, or Heisenberg, systems, spin waves were found to exist only at wave vectors below a certain cutoff value that is characteristic of both the material and the temperature. The cutoff energy, on the other hand, was observed to be independent of temperature. In addition, the spin-wave energy was found to renormalize with temperature but not to vanish at the Curie temperature. Instead, spin waves were observed at temperatures well above the transition temperature with no additional renormalization taking place.

The observed disappearance of spin waves above a cutoff energy is strong evidence in support of the view that both Ni and Fe are itinerant ferromagnets. In the itinerant model, strong correlations between electrons of opposite spin generate a splitting of the paramagnetic energy bands and impart a corresponding spin dependence to the electronic energies and wave functions. The disappearance phenomenon can be understood quite simply in terms of the spin wave, which is a bound electron-hole pair, entering a region of high density of states for single-particle, spin-flip excitations across the Fermi energy (Stoner excitations) and decaying.

An extensive series of calculations based on the zero-temperature itinerant electron theory has shown that this theory provides an excellent quantitative, as well as qualitative, model for the magnetic behavior of Ni and Fe.[1] The ferromagnetic band structure derived from these calculations implies a band- and wave-vector-dependent spin-splitting of the paramagnetic bands that is in excellent agreement with recent photoemission results. Calculations of the neutron scattering cross section yielded spin-wave dispersion curves that are also in excellent agreement with experiment[2] and predicted an "optical" mode in Ni that was recently observed.[3]

The extension of the itinerant theory to high temperatures is very difficult, and while considerable progress has been made recently, realistic numerical calculations are not yet possible. An alternate approach is simply to extrapolate the successful low-temperature theory to higher temperatures. The traditional method for doing this has been to require that the spin-splitting decrease with temperature in some prescribed manner and vanish at the Curie temperature T_c. Unfortunately, this approach cannot be entirely correct, because it leads to a rather strong temperature dependence of the spin-wave cutoff energy, which is inconsistent with the neutron scattering results. Recent angular resolved photoemission experiments have suggested that the splitting for Ni does not drop to zero at T_c but only to one-half its zero-temperature value.[2] Relatively crude

calculations, however, indicate that this result may also be inconsistent with the neutron results.

In order to investigate this point and also the origin of the spin-wave renormalization, an extensive series of calculations of the inelastic neutron scattering cross section has been undertaken for Ni. These calculations are based on three different extrapolations of the low-temperature theory. The first approach incorporates the temperature dependence of the Fermi factors, which account for the only explicit temperature dependence in the low-temperature theory. This simple extrapolation of the theory gives a Curie temperature T_c^* which is 1.7 T_c, where T_c is the measured Curie temperature. One interesting aspect of this result is that the magnetization calculated as a function of $X = T/T_c^*$ is in excellent agreement with experiment. The calculated spin-wave dispersion curves are shown in Fig. 1.34 for $T = 0$ and $T = 0.5T_c$. The agreement with experiment indicates that the entire renormalization for $T < T_c/2$ can be attributed to the temperature dependence of the Fermi factors. Very little change in the dispersion curve was found for $T_c/2 \leq T \leq T_c$, which indicates that some additional temperature dependence must be included in this temperature range.

The second method of extrapolation attempted to introduce some additional temperature dependence by requiring that the spin splitting be adjusted at each temperature to give the correct moment. Spin-wave dispersion curves calculated for $T = 0$ and $T = 0.86T_c$ are shown in Fig. 1.35. The latter temperature was chosen because it corresponds to a splitting that is about one-half its zero temperature value. The poor agreement with experiment indicates that this extrapolation is too severe.

The final extrapolation method is based on the concept that, as in the local-moment theory, there

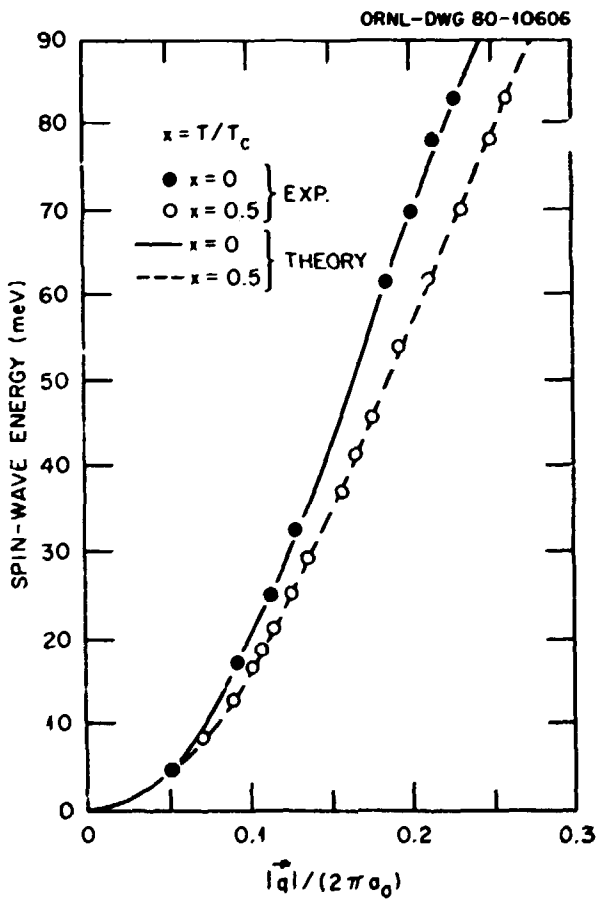

Fig. 1.34. Comparison of theoretical and experimental spin-wave dispersion curves for ferromagnetic Ni at $T = 0$ and $T = T_c/2$. Temperature extrapolation is based on Fermi factors only. The lattice parameter is a_0.

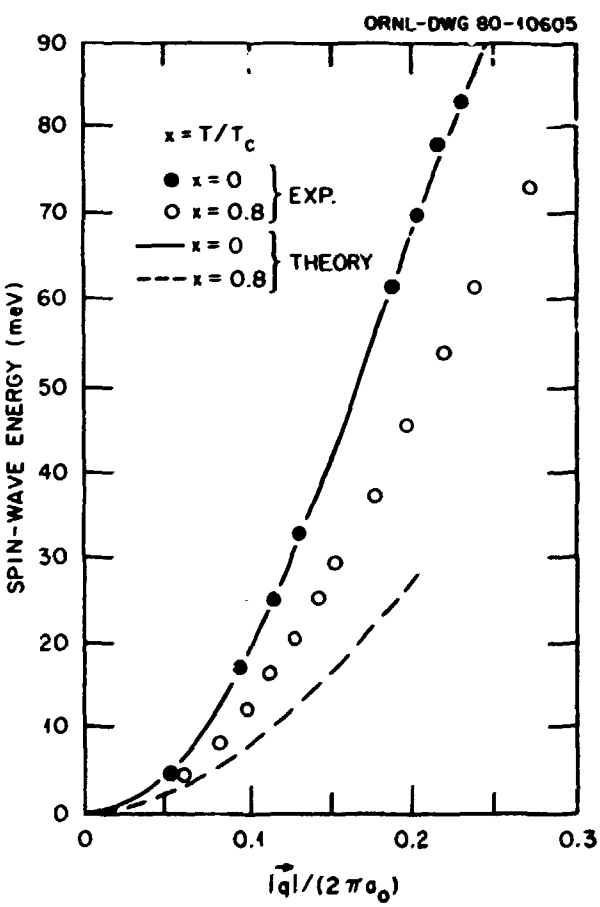

Fig. 1.35. Comparison of theoretical and experimental spin-wave dispersion curves for ferromagnetic Ni at $T = 0$ and $T = 0.86T_c$. Spin-splitting at $0.86T_c$ is equal to one-half its zero temperature value. The lattice parameter is a_0.

will be a spin-wave contribution to the magnetization and, therefore, the spin splitting does not have to vanish at $T = T_c$. Unfortunately, the spin-wave contribution cannot be accurately calculated at present, and thus the magnetization curve cannot be used as a way to determine the relevant splitting as a function of temperature. Alternatively, it was determined that a splitting of about eight-tenths of its zero temperature value gave the correct renormalization at $T = 0.86T_c$ and that this relatively small reduction produced no change in the spin-wave cutoff energy.

These calculations taken together imply that the entire renormalization of the spin-wave dispersion curve can be attributed to the Fermi factors for $T < T_c/2$ and that an additional, relatively small, reduction in the spin-splitting can account for the renormalization for temperatures up to $0.86T_c$. In addition, the cutoff energy is not affected by this reduction of the splitting. A splitting of one-half the zero temperature value generates too large a renormalization and a substantial change in the cutoff energy, which implies that there is a real discrepancy between the neutron and photoemission experimental results regarding the temperature dependence of the spin-splitting of the electronic energy bands.

1. J. F. Cooke and H. L. Davis, *AIP Conf. Proc.* **10**, 1218 (1973); J. F. Cooke, J. W. Lynn, and H. L. Davis, *Solid State Commun.* **20**, 799 (1976).

2. D. Eastman, F. J. Himpsel, and J. A. Knapp, *Phys. Rev. Lett.* **40**, 1514 (1978); F. J. Himpsel, J. A. Knapp, and D. E. Eastman, *Phys. Rev. B* **19**, 2919 (1979).

3. H. A. Mook and D. Tocchetti, *Phys. Rev. Lett.* **43**, 2029 (1979).

HEAT OF SOLUTION OF H IN Al[1]

L. M. Kahn[2] F. Perrot[3] Mark Rasolt

The interaction of H with its metallic host has been given wide attention in many recent publications. Primarily two different regions, with distinct theoretical emphasis, have been examined. The region of high concentration of H has generally been treated via a band structure approach[4] and applied to nonsimple metals like Pd which can dissolve large quantities of H. The region of low concentration has been largely treated from a proton jellium interaction and applied to simple metals like Al,[5] which can dissolve only small quantities of H. It is the second region that we have treated. The small amount of H dissolved in most metals does not make this problem without practical interest. As an illustration, the formation of H gas bubbles upon solidification is just one example of the need for a microscopic treatment of H metal interaction. From a theoretical point of view, the simplicity of a proton embedded in an almost uniform electron gas makes it potentially useful for studying electron impurity interactions.

The heat of solution ΔH of an impurity of nuclear charge $Z_1 e$ (at point $\mathbf{r}_1$) with its equal number of Z_1 electrons is defined as the difference between the energy of this configuration and the one where the neutral impurity is removed to infinity. This energy can be readily[1] written as

$$\Delta H = \Delta H_0 + \Delta H_1 + \Delta H_2 + \Delta H_3 + \Delta H_4 + \Delta H_5 + \Delta H_6 , \quad (1)$$

with

$$\Delta H_1 = \sum_{i=1}^{ZN} \left\{ \epsilon_i^1 - \epsilon_i^0 \right\} , \quad (1a)$$

$$\Delta H_2 = Z_1 \epsilon_N^0 , \quad (1b)$$

$$\Delta H_3 = \sum_{c=1}^{Z_c} \epsilon_c , \quad (1c)$$

$$\Delta H_4 = -\frac{e^2}{2} \int d^3r \int d^3r' \Big\{ [n_1(\mathbf{r}') - n_0(\mathbf{r}')][n_1(\mathbf{r}) - n_0(\mathbf{r})] + [n_1(\mathbf{r}') - n_0(\mathbf{r}')][n_0(\mathbf{r}) - n_0] \Big\} / |\mathbf{r} - \mathbf{r}'| , \quad (1d)$$

$$\Delta H_5 = E_{xc}[n_1(\mathbf{r})] - E_{xc}[n_0(\mathbf{r})] - \int d^3r \Big\{ v_{xc}[n_1(\mathbf{r})]\, n_1(\mathbf{r}) - v_{xc}[n_0(\mathbf{r})]\, n_0(\mathbf{r}) \Big\} , \quad (1e)$$

$$\Delta H_6 = Z_1 Z e^2 \sum_{i=1}^{ZN} \frac{1}{|\mathbf{r}_1 - \mathbf{R}_i|} - Z_1 e^2 \int \frac{d^3r\, n_0}{|\mathbf{r}_1 - \mathbf{r}|} . \quad (1f)$$

In Eqs. (1a–1f), $E_{xc}[n(\mathbf{r})]$ is the exchange and correlation functional, v_{xc} is the functional derivative $\delta E_{xc}/\delta n$, ϵ_c is the binding energy of the Z_c bound states (if any), n_0 is the uniform density of the ZN

electrons in volume Ω_0, and $n_1(\mathbf{r})$ is the electron density of the $ZN + Z_1$ electrons in the presence of the impurity and N ions.

If we assume an adequate knowledge of E_{xc}, the difficulty lies entirely in solving the self-consistent equations of Hohenberg, Kohn, and Sham[6] for the densities $n_0(\mathbf{r})$ and $n_1(\mathbf{r})$ and eigenvalues ϵ_i^0 and ϵ_i^1. The strong proton-electron interaction makes any low-order treatment of ΔH inadequate.[5]

We achieved our solution in two stages. We first centered our coordinates at the proton site $\mathbf{r}_1$ and approximated the ionic potential around the proton by only its spherical component. This was done for four positions of the proton in an fcc Al lattice: three interstitial positions at the octahedral site ($\mathbf{r}_1 = a\ 2, a\ 2, a\ 2$), the tetrahedral site ($\mathbf{r}_1 = a\ 4, a\ 4, a\ 4$), and the midpoint between them ($\mathbf{r}_1 = 3a\ 8, 3a\ 8, 3a\ 8$), and one substitutional position ($\mathbf{r}_1 = 0, 0, 0$). These positions are specified in terms of the length a of the fcc cube edge. The results are given in Table 1.5, from which we note (1) a preference for an interstitial site ($a\ 2, a\ 2, a\ 2$) of 0.061 eV over a substitutional one, (2) an activation energy for diffusion of roughly 0.5 eV (the difference of lines 3 and 4 of Table 1.5) in good agreement with most recent experimental values,[7] and (3) a heat of solution of 0.59 eV compared with the experimental value of 0.66 eV.

We next treated the nonspherical components $V_0^{n.s.}(\mathbf{r})$ of $V_0(\mathbf{r})$ as a linear order correction to the above spherical solution. From the Feynman-Hellman theorem, the correction to ΔH is given by

$$\Delta H^{n.s.} = \frac{1}{2}\int d^3r V_0^{n.s.}(\mathbf{r})[n_1^{n.s.}(\mathbf{r}) - n_0^{n.s.}(\mathbf{r})] . \quad (2)$$

We succeeded in carrying out a first estimate of these nonspherical corrections by solving for $n^{n.s.}(\mathbf{r})$ within a statistical approximation for the nonuniform many-electron system.

Our results are listed in Table 1.5, and, surprisingly, these contributions to the heat of solution of H in Al are very small. In addition, we can conclude with some confidence that these corrections are likely to be small in other metal hydrides such as Mg and Na. For theoretical studies of impurities in simple metals at low concentration, these are important and useful conclusions. They imply that further refinements can be achieved without overdue concern for these very hard to treat nonspherical terms. For example, the replacement of the crystal pseudopotential by the full ionic potential and the treatment of lattice relaxation, all within the spherical solid, are presently being investigated.

---

1. Summary of paper: *Physical Review* (in press).
2. University of Virginia, Charlottesville.
3. Commissariat a l'Energie Atomique, Saint Georges, France.
4. D. E. Eastman, J. K. Cashion, and A. C. Switendick, *Phys. Rev. Lett.* 1, 35 (1971).
5. C. O. Almbladh et al., *Phys. Rev. B* 14, 2250 (1976).
6. P. Hohenberg and W. Kohn, *Phys. Rev.* 136, 3864 (1964); W. Kohn and L. J. Sham, *Phys. Rev.* 140, A1133 (1965).
7. Von W. Eichenauer and A. Pebler, *Z. Metallkd.* 48, 373 (1957); S. Matsuo and T. Hirata, *Trans. Natl. Res. Inst. Met.* (Jpn) 11, 22 (1969).

ON THE CHARGE COMPENSATION PROBLEM IN β-ALUMINA

J. C. Wang

Possible charge compensation models for the excess conducting Na^+ ions in Na β-alumina have been investigated with potential energy calculations. The cases studied include an artificial transfer of charge from Al^{3+} ions in the spinel block to Na^+ ions in the conducting plane, the replacement of an Al^{3+} ion with three Na^+ ions, the replacement of an Al^{3+} ion with an Mg^{2+} and an Na^+ ion, and the defect model proposed by Roth et al.[1] In the last model, an interstitial O^{2-} ion in the conducting plane is assumed to displace two nearby Al^{3+} ions toward it from the adjacent spinel blocks to form two Frenkel pairs. The calculations show that this formation of the

Table 1.5. The different contributions to the heat of solution of a proton in Al host

For a proton at ($3a$ 8, $3a$ 8, $3a$ 8), the nonspherical contributions were neglected and the heat of solution ΔH is that of the spherical solid model only; all energies are in electron volts

Position (r)	ΔH_1	ΔH_2	ΔH_3	ΔH_4	ΔH_5	ΔH_6	$\Delta H^{n.s.}$	ΔH
(0, 0, 0)	−3.991	7.526	0.000	27.780	2.495	−48.999	−0.017	0.654
(a 4, a 4, a 4)	−11.927	7.526	−0.134	−5.265	3.361	−8.570	0.024	0.875
($3a$ 8, $3a$ 8, $3a$ 8)	−10.716	7.526	−0.004	−6.024	3.361	−8.912		1.091
(a 2, a 2, a 2)	−9.507	7.526	0.000	−4.812	3.156	−11.646	0.016	0.593

V_{Al}-Al^{3+}-O^{2-}-Al^{3+}-V_{Al} defect, where V_{Al} stands for an Al^{3+} vacancy, is the most likely model of charge compensation.

The Coulombic potential in the conducting plane as a function of distance r from the O^{2-} ion in the V_{Al}-Al^{3+}-O^{2-}-Al^{3+}-V_{Al} model was calculated and found be quite flat for 2 Å $\leq r \leq$ 4 Å. This may explain why the two excess Na^+ ions associated with the defect are not tightly bound to the O^{2-} ion and can contribute to the high conductivity. When the O^{2-} ion and the two Na^+ ions are removed from the crystal, the two interstitial Al^{3+} ions will combine with the vacancies.

The replacement of an Al^{3+} ion with an Mg^{2+} and an Na^+ ion was also found to be energetically possible. However, such a replacement may have a higher activation energy and therefore occur only under special crystal growth conditions.

1. W. L. Roth, F. Reidinger, and S. LaPlaca, p. 223 in *Superionic Conductors*, ed. by G. D. Mahan and W. L. Roth, Plenum, New York, 1976.

LOCAL FIELDS NEAR A POINT-CHARGE DEFECT IN CUBIC IONIC CRYSTALS[1]

J. C. Wang

Local fields (E_{loc}) at ions near a point-charge defect in some cubic crystals have been accurately calculated with a polarizable-rigid-ion model. As an example, the result for a Na^+ vacancy in the NaCl crystal is shown in Fig. 1.36. If the ionic polarizabilities of Cl^- and Na^+ ions were zero, the local field at an ion located at distance r away from the Na^+ vacancy would have a magnitude of $E_0 = D = e/r^2$. But because of the nonzero polarizabilities and the mutual interactions among the induced dipoles, the actual magnitude E_{loc} is different from E_0. The upper part of Fig. 1.36 shows the calculated ratio $C = E_{loc}/D$ as a function of r for ions around the vacancy. The ionic polarizabilities[2] used are 2.974 and 0.255 Å^3, respectively, for the Cl^- and Na^+ ions, and the lattice constant[3] is taken to be 5.6387 Å.

Far away from the vacancy, the value of C approaches the constant $C_0 = 0.624$, shown by the horizontal dashed line in Fig. 1.36. This constant can

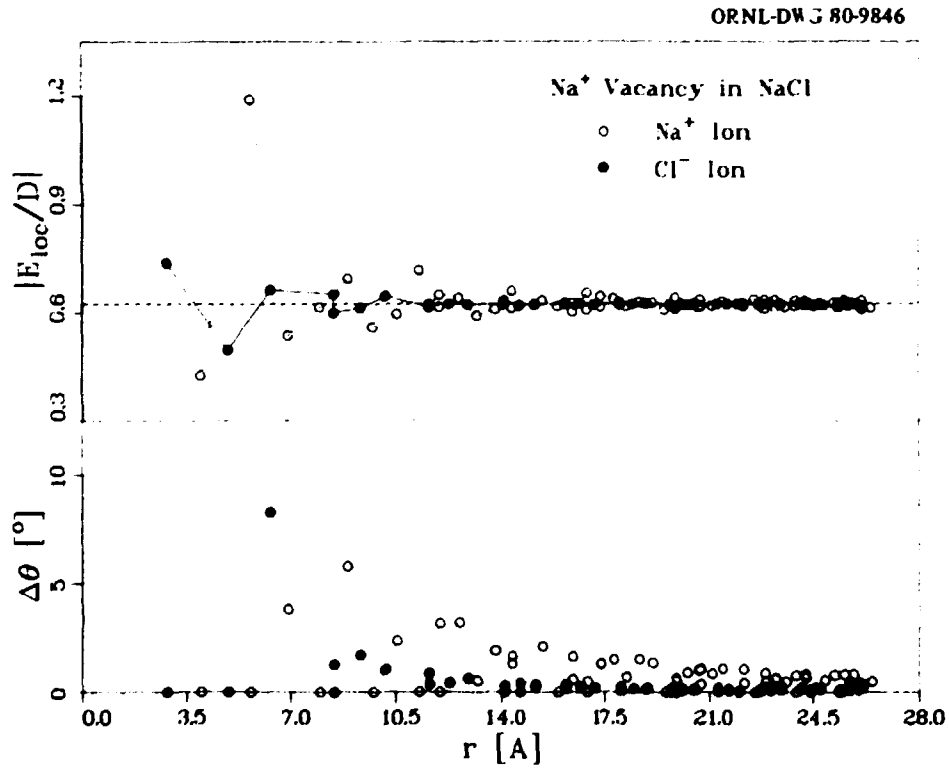

Fig. 1.36. Calculated magnitudes of the local fields (upper) and the angular deviations from the radial directions (lower) at ions near an Na^+ vacancy in the NaCl crystal. The vacancy is located at $r = 0$. The horizontal dashed line represents $|E_{loc}/D| = (\epsilon - 2)/3\epsilon$ derived from the Clausius-Mossotti relation for large r.

be determined as follows. The dielectric constant ϵ of the medium contributed by the undisplaced ions (in our polarizable-rigid-ion model) is first evaluated from the ionic polarizabilities and the Clausius-Mossotti relation. Then C_0 can be calculated from $C_0 = (\epsilon + 2)/3\epsilon$.

Close to the vacancy, the value of C oscillates rapidly about C_0. These oscillations near a point-charge defect are quite general for ionic crystals and originate from the discrete nature of the ionic arrangements. It is interesting to note that the local fields at most ions in this region are not precisely along the radial directions (lines connecting the defect and the ions). The lower part of Fig. 1.36 shows these angular deviations ($\Delta\theta$).

In most defect formation and diffusion energy calculations, it is not possible to allow *all* ions in a system to move and to find the local fields at *all* ions. Some approximations must be made. Usually the system is divided into two regions[4] and only the inner-region ions are allowed to move. The local fields at these ions are calculated self-consistently. The present results (oscillations and angular fluctuations) demonstrate that ions within a sphere of radius of about 20 Å may have to be considered in this self-consistent calculation, which means that about two to three thousand ions are involved.

---

1. Summary of paper to be published.
2. J. R. Tessman, A. H. Kahn, and W. Shockley, *Phys. Rev.* **92**, 890 (1953).
3. R.W.G. Wyckoff, *Crystal Structures*, vol. 1, Wiley, New York, 1965.
4. N. F. Mott and M. J. Littleton, *Trans. Faraday Soc.* **34**, 485 (1938).

2. Surface and Near-Surface Properties of Solids

Almost all energy technologies encounter materials problems that are affected by the surface and near-surface properties of solids. Within the Division, research in these areas is focused primarily on investigations relevant to photovoltaic conversion of solar energy, magnetic fusion energy, superconductivity, catalysis, and corrosion. Continuing a trend established during the previous reporting period, the techniques of ion implantation and/or laser processing to alter the properties of solid surfaces in a desired manner are frequently employed. Research supportive of the ORNL Magnetic Fusion Energy Program continues at a high level, and cooperative efforts with other ORNL divisions, as well as with other laboratories (both industrial and academic), are increasing. Much of the experimental work summarized in this section of the report relies strongly on theoretical support. Therefore, to obtain a more complete view of research concerning surface and near-surface properties, the reader is referred to the first section of this report, which is devoted to theoretical solid state physics.

Studies in the Surface Physics Program have continued to emphasize examination of the geometry of relaxed and reordered surfaces by the use of the combined techniques of LEED, ion scattering, and theoretical modeling studies. A new method of LEED data averaging to produce better agreement between theory and experiment was developed. Pulsed laser annealing in UHV was used to demonstrate that clean, well-ordered surfaces of either Si or Ge could be produced by this method. Moreover, in certain instances laser annealing produced surface geometric ordering that cannot be obtained by conventional methods of sputtering and thermal annealing. High-resolution electron energy loss studies concentrated on the effects of coadsorption on the surface of different species in order to gain insight into the initial stages of processes occurring in heterogeneous catalysis.

Members of the Plasma-Materials Interactions Program have used deposition probes to study plasma-wall interactions in the ISX-B tokamak. Probes placed at various distances from the wall to the limiter edge were used to examine surface erosion and impurity transport in the plasma edge, as well as the flux and energy of deuterium in the boundary region. Initial results were interpreted to suggest that (1) sputtering was the dominant erosion mechanism at the limiter edge with negligible erosion at the wall, (2) metallic impurity deposition was linear to 12 tokamak discharges while O on the probes saturated in one to four discharges, and (3) the energy of deuterium in the plasma edge decreased with radial distance from the plasma and was estimated to be ~150 eV at 2 cm behind the limiter edge Reported also is the development of a Doppler-shifted laser fluorescence spectrometer system and an application of the

technique to a determination of the density and velocity distribution of neutral Fe atoms in the plasma edge of ISX-B.

A new and unusual ion-scattering effect was detected during ion-solid interaction studies. An enhanced yield, observable only under stringent alignment and beam collimation conditions, for 180° (±0.5°) scattering was measured. The effect, associated with the reversibility of the trajectories of ions scattered near 180°, should result in enhanced sensitivity of PICS for surface analysis. Two new techniques, ion beam mixing and pulsed laser mixing, for inducing materials interactions to form metastable near-surface alloys were examined, and initial results are reported here. Ion-induced damage and laser-induced damage in several compound superconductors were studied and found to be complex problems. A tentative explanation of the results is that ion damage disrupts the short-range order, which probably could be restored by laser annealing, but the latter process initiates long-range lattice disorder. Studies of the effects of laser annealing on both pure and ion-implanted Si were continued, and the results of research on alloy formation, defect structures, and kinetic effects in rapid epitaxial regrowth are reported here.

Pulsed laser annealing studies conducted during the reporting period focused primarily on the annealing behavior of Si implanted with a variety of materials. A large number of samples implanted with other than Group III and V materials exhibited segregation or zone refining to the surface. However, the behavior of similarly treated Group III and V dopants has been demonstrated to be quite different; concentrations of these dopants in substitutional lattice sites can far exceed equilibrium solubility limits. Furthermore, for these dopants it was shown that subsequent thermal annealing, combined with measurements of the maximum substitutional dopant concentrations, permitted an accurate determination of the dopant solubility limit at the thermal annealing temperature. Studies of the effects of oxide layers on the annealing of arsenic-implanted Si were conducted, and the surface structure and composition of the Si/As system, pulse-annealed in UHV, were determined.

Research on the photovoltaic conversion of solar energy has been expanded substantially during the period covered by this report. Progress on developing high-efficiency, single-crystal Si solar cells by the ion-implantation, laser-annealing process has continued, and efficiencies of 15 to 16% are now routinely obtained. Improvements in fabrication techniques are expected soon to increase efficiencies to levels of about 18%. Solar cells made by the laser-induced diffusion technique had measured efficiencies of about 14%, but improved fabrication techniques should also lead to substantially higher efficiencies for such cells. Perhaps the most exciting developments occurred in the area of polycrystalline solar cells. The ORNL studies have established that the rapid diffusion of impurities along grain boundaries and the segregation of dopants at grain boundaries can be controlled by laser techniques. These and other studies are being used to obtain insight into fundamental ionic and electronic processes at grain boundaries.

SURFACE PHYSICS

EFFECTS OF DATA AVERAGING ON LEED ANALYSES: A CASE STUDY OF THE Cu(100) SURFACE

J. R. Noonan H. L. Davis

In order to obtain information concerning the crystallography of surfaces, LEED *I-V* profiles have been collected and analyzed at ORNL for the past few years. Insight gained during this undertaking has led to the realization that several experimental limitations exist in a standard LEED apparatus, and these problems could affect significantly the accuracy and sensitivity of the crystallographic information obtained via a theoretical analysis. Limitations that need to be considered are beam incoherence and divergence, surface topography, alignment of the sample, and the inability to null completely residual electromagnetic fields. To investigate whether any, or all, of these limitations could be overcome, it was decided to initiate a case study of the clean Cu(100) surface. During this study a technique of data averaging was examined to determine whether errors caused by the above limitations could be reduced, and this relatively simple technique has appeared to be quite successful. Indeed, when such averaged data are used as a base for a theoretical analysis, a most striking agreement is obtained between experimental and calculated *I-V* profiles.[1] Some aspects of our data collection and averaging for Cu(100) will be described here, while details of the resulting theoretical analysis are presented elsewhere.[1]

The data for Cu(100) were collected using somewhat standard procedures.[2] Briefly, a Cu single crystal was cut, lapped, and electropolished to expose the (100) face. The sample was then mounted in a UHV chamber for preparation and analysis. It was cleaned by sputtering with 500-eV Ar^+ ions followed by a 700 K anneal to reduce damage disorder. The sample was considered clean and ordered when no Auger signals (monitored by a CMA) from contaminants were detectable, and a sharp, well-focused, LEED diffraction pattern was observed. This (100) surface was then aligned perpendicular to the incident beam by equalizing intensities of prominent peaks in the *I-V* profiles of beams which are symmetrically equivalent. In addition, diffraction scattering angles were monitored to ensure that surface grating diffraction conditions were satisfied. It is believed that these techniques produced normal alignment of the sample to better than 0.1°.

Use of the above procedures enabled *I-V* profile data to be collected that were reproducible such that prominent features in sets of equivalent diffraction beams agreed within 1 eV and had, at most, a 12% variation in intensity. An illustration of the quality of the data obtained from Cu(100) is provided by Fig. 2.1, which shows plots of the four, symmetry-related, {10} beams. The four top curves of Fig. 2.1 are quite similar; however, there are differences that undoubtedly are caused by the experimental limitations discussed above. For example, the shoulder on the peak near 140 eV has some variation from profile to profile. These {10} profiles also can be compared numerically by using a reliability factor, R_Z, defined by Zanazzi and Jona.[3] R_{ZJ} has been defined so that

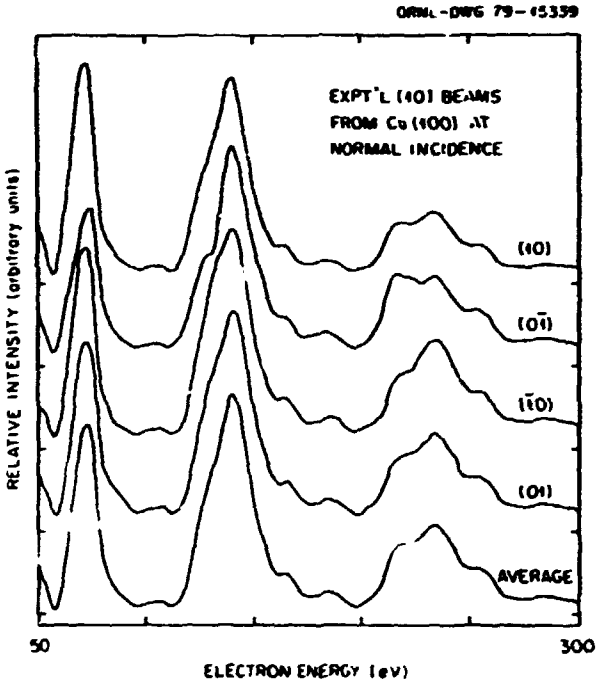

Fig. 2.1. A comparison of the measured {10} profiles and an average of the top four profiles.

perfect agreement between two curves would produce a value of zero, and unity would be obtained as the average value of comparing curves with no correlation. Comparison of the (10) profile of Fig. 2.1 with that of the (0$\bar{1}$) produced an R_{ZJ} value of 0.061, (10) with ($\bar{1}$0) gave 0.027, and (10) with (01) produced 0.044. In our study of Cu(100), data were collected for each of the individual profiles in the symmetrically equivalent {10}, {11}, {20}, and {21} sets. When the

individual profiles in each of these $\{ij\}$ sets were compared with each other, R_{ZJ} values in the range of 0.027 to 0.090 were obtained.

Although the R_{ZJ} values found when symmetrically related profiles were compared might be considered small, the differences between the profiles can influence the accuracy and sensitivity of the crystallographic information obtained from a theoretical analysis. That is, if only one of the profiles in a given $\{ij\}$ set is used in the analysis, some bias would be introduced. Also, some scatter would exist in results obtained using different profiles from the same $\{ij\}$ set. This point is illustrated by Fig. 2.2, which contains contour plots of R_{ZJ} values obtained when experimental profiles are compared with calculated profiles. The LEED calculations were done using eight phase shifts from the Chodorow potential, a Debye temperature of 250 K, and 0.85 $E^{1/3}$ eV for the imaginary component of the inner potential. Each subplot of Fig. 2.2 represents R_{ZJ} as a function of the change in the first interlayer spacing from its truncated bulk value, Δd_{12}, and the real component of the inner potential, V_{or}. The optimal values of Δd_{12} and V_{or} for each subplot are those giving the smallest R_{ZJ}.

As seen, some scatter is present in the optimal values of Δd_{12} and V_{or} when the individual (10), $(0\bar{1})$, and $(\bar{1}0)$ profiles of Fig. 2.1 are compared with the calculated profiles. But it is noted that consistently lower R_{ZJ} values are obtained when the average {10} profile is compared with calculations than when any of the individual profiles are compared. This means

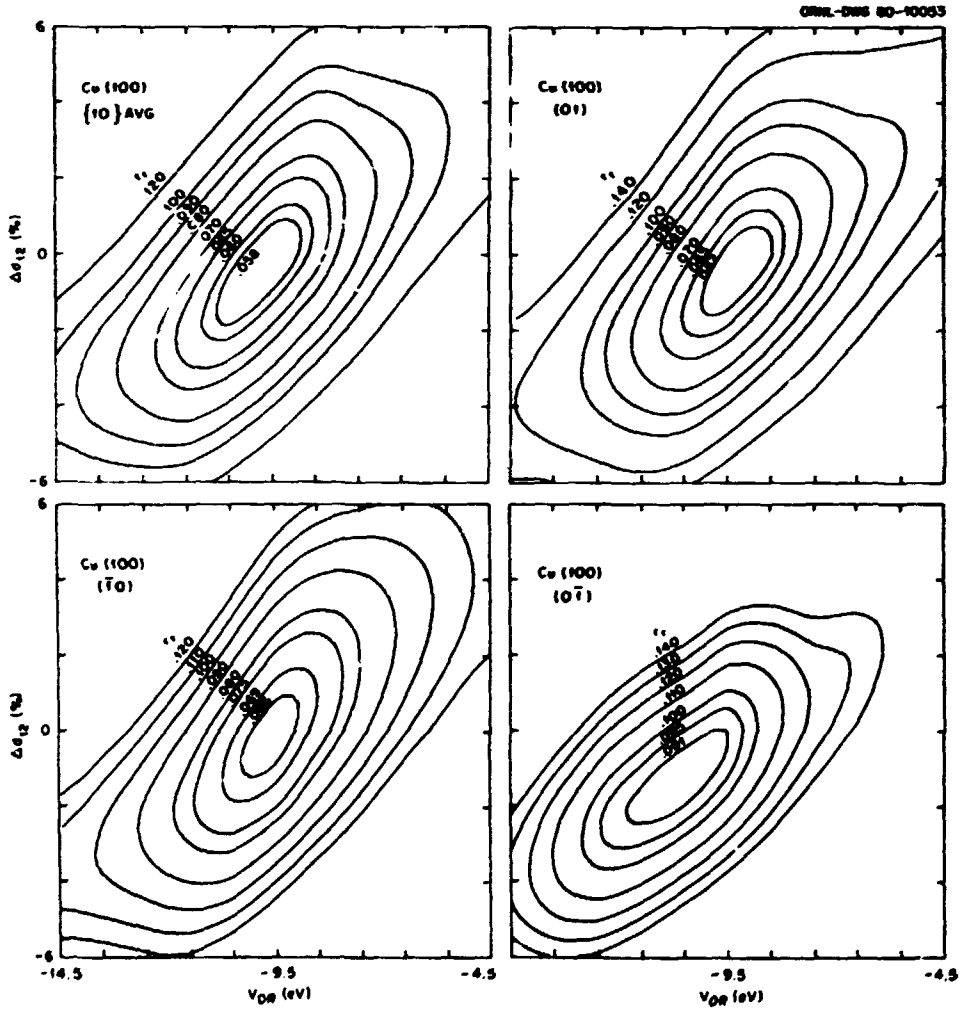

Fig. 2.2. Plots of the reliability factor R_{ZJ} when some of the profiles of Fig. 2.1 are compared with calculated profiles described in the text.

that the averaging process has served to cancel errors in the data due to experimental limitations. Thus, the Δd_{12} and V_{or} values obtained using the averaged profile should be more accurate than those obtained from any one of the individual profiles. Also, use of the averaged profile provides more sensitivity, since the relative changes in R_{ZJ} with variations in Δd_{12} and V_{or} are larger for the averaged profile than for the individual profiles.

From the results obtained in this case study of Cu(100) and in our other LEED investigations, we are able to formulate definite experimental procedures to use in future LEED analyses. When employed, these procedures should improve the accuracy and sensitivity of the analysis for the determination of a given surface crystallography. First, data should be collected with the incident electron beam normal to the investigated surface, since this angle of incidence can be obtained with more accuracy than any other when using presently available LEED goniometers. Then all the individual *I-V* profiles in a given symmetrically related set should be measured and their average employed in the subsequent theoretical analysis. Although these simple procedures have been formulated using experience gained from the investigation of clean surfaces of noble metals, we believe that they should be generally applicable to most LEED investigations.

---

1. H. L. Davis and J. R. Noonan, "High Sensitivity LEED Analysis of the Cu(100) Surface," this report.
2. H. L. Davis, J. R. Noonan, and L. H. Jenkins, *Surf. Sci.* 83, 559 (1979).
3. E. Zanazzi and F. Jona, *Surf. Sci.* 62, 61 (1977).

ANALYSIS OF THE LEED SPECULAR REFLECTION FROM A CLEAN Cu(110) SURFACE

J. R. Noonan H. L. Davis

We have previously reported a LEED analysis for the Cu(110) surface, which was based on data for six nonspecular beams collected with the incident beam normal to the surface.[1] It was inferred from this previous work that the first interlayer spacing of Cu(110) was 0.115 ± 0.003 nm, which represents a 10.0 ± 2.5% contraction from the truncated bulk value. In order to test this result and also to study its possible sensitivity due to sample alignment, we initiated an investigation of the specular reflection from this surface. (Such a study, by experimental necessity, means the incident beam is not normal to the sample.) The specular beam data were analyzed by comparison with the results of dynamical LEED calculations, where the same nonstructural parameters were employed as used for the nonspecular data. Although the analysis of the specular data confirms our earlier work, during its course some problems related to the accuracy of sample alignment and structural sensitivity became apparent.

An oriented and polished Cu(110) crystal was mounted in a UHV chamber, cleaned in situ by using standard Ar ion sputtering techniques, and then annealed in vacuum. These procedures produced a sample from which no Auger signals from trace contaminants were seen, and a sharp, well-defined LEED diffraction pattern characteristic of Cu(110) was observed. The sample was aligned at the desired angles by positioning it until the scattering angles for the specular, and several nonspecular, beams satisfied surface diffraction grating conditions. It is believed that these alignment procedures are accurate to within ±0.5°. Once the sample was aligned, data were collected in the 20- to 220-eV energy range.

Computer codes developed at ORNL[1] were used to perform LEED calculations, the results of which were then compared with the specular beam data. These calculations were based on the same nonstructural parameters employed in the analysis of nonspecular data,[1] which were eight phase shifts from the Chodorow potential, a Debye temperature of 250 K, a value of 8.5 eV for the real component of the inner potential, and 0.85 $E^{1/3}$ eV for the imaginary component of the inner potential.

Calculated and experimental *I-V* profiles for three specular reflections are illustrated in Fig. 2.3. Each frame of Fig. 2.3 specifies the alignment used in obtaining the data, with θ measured from the surface normal and ϕ measured from a ⟨110⟩ surface direction. The estimated alignment error in ϕ is the same as that specified for θ. The calculations used to prepare Fig. 2.3 were performed at the experimentally designated angles [i.e., those of frame (*c*) were done exactly for $\theta = 8.5°$ and $\phi = 91°$]. The bottom curve of each frame represents the experimental profile, while the upper curves are for calculations with the denoted variations [see frame (*a*)] in the first interlayer spacing Δd_{12} from the bulk value. Also, with each calculated curve are given values of r_r, which are single beam reliability factors as defined by Zanazzi and Jona.[2] It is noted that r_r for data shown in frames (*a*) and (*b*) has its minimum for Δd_{12} between −6 and −8% and between −8 and −10% for frame (*c*). Thus, from Fig. 2.3 it would be inferred

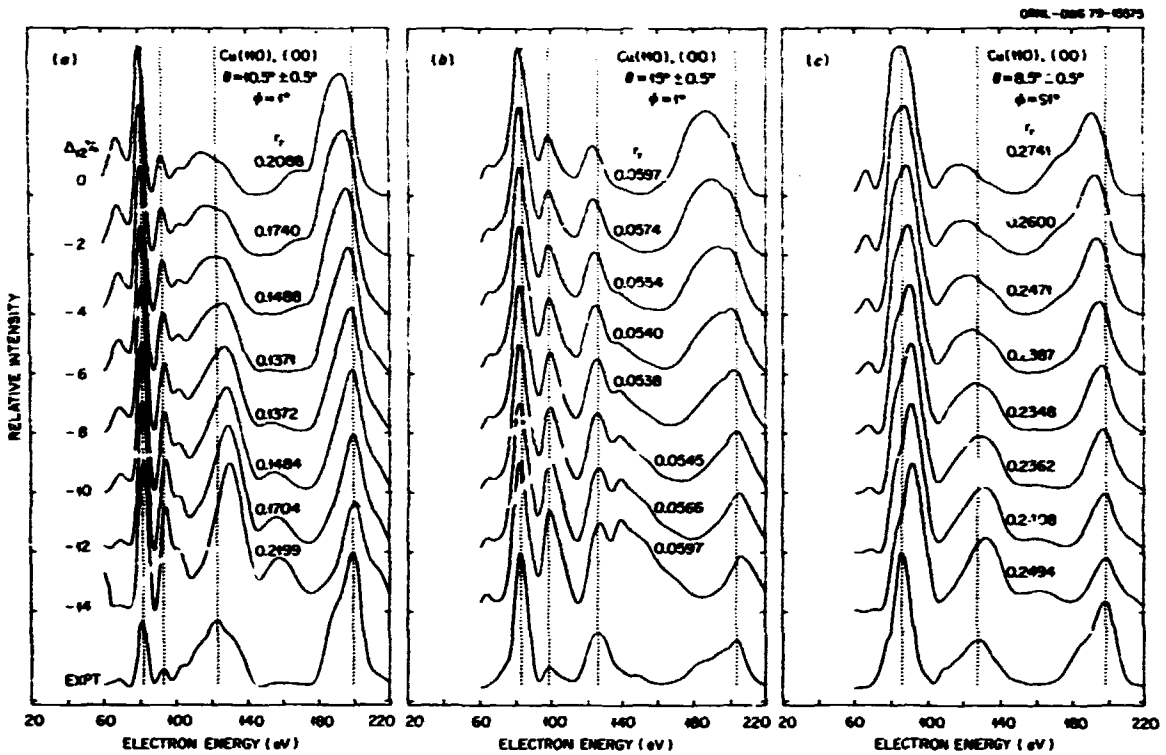

Fig. 2.3. Comparison of calculated and experimental specular reflections for the Cu(110) surface.

that the Cu(110) surface has about an $8 \pm 3\%$ contraction in its first interlayer spacing. This result is reasonably consistent with that obtained from our previous analysis of nonspecular data.

Although the present study has provided some confirmation of our previous work, perhaps its most interesting aspects are the general questions it has raised concerning possible limitations in the analysis of specular data. First, it is noted that the r_r values of both frames (*b*) and (*c*) show relatively minor changes as Δd_{12} is varied; that is, the analysis is quite insensitive in the determination of the desired structural parameter. Thus, only after the analysis has it been found that two-thirds of the calculated data show little sensitivity to variation assumed for Δd_{12}. It is desirable to determine, in future work, whether this unsatisfactory aspect will be found generally in the analysis of specular data. Another question is more serious. As stated before, errors of the order of $\pm 0.5°$ can exist in the experimental specification of the polar angle θ; these errors result principally from misalignment of the center of rotation of the Faraday cup with respect to the axis of the incident electron beam. Such errors are unsatisfactory, since both experimental and calculated *I-V* profiles can vary significantly over 0.5°. For example, if the empirical curve of frame (*c*) of Fig. 2.3 is compared with calculations performed for $\theta = 9°$ and $\Delta d_{12} = -8\%$, an r_r value of 0.15 is obtained. Thus, such variance with θ suggests that greater weight should be given to analyzing LEED data obtained at normal incidence, where techniques can be used to align the sample perpendicular to the incident beam to within 0.1°.[3]

1. H. L. Davis, J. R. Noonan, and L. H. Jenkins, *Surf. Sci.* **83**, 559 (1979).
2. E. Zanazzi and F. Jona, *Surf. Sci.* **62**, 61 (1977).
3. J. R. Noonan and H. L. Davis, "Effects of Data Averaging on LEED Analyses: A Case Study of the Cu(100) Surface," this report.

ANALYSIS OF NONSPECULAR LEED FROM A CLEAN Ag(110) SURFACE

J. R. Noonan H. L. Davis

In some recent work we have been concerned with a LEED analysis of the reconstructed Au(110)-(1×2)

surface[1] and have been unable to determine satisfactorily its atomic structure. We now believe that some of the difficulties with this analysis are due to the behavior of the electron's inelastic mean-free-path, since work has been reported[2] which indicates that this mean-free-path increases quite dramatically as the energy is decreased below 80 eV. A similar behavior was also reported[2] for Ag at energies below 60 eV. Thus, the Ag(110) surface could eventually provide a means to study the influence of this parameter on a LEED analysis, without the additional complication of surface reconstruction. At the same time, an investigation of Ag(110) would provide another test for the data-averaging techniques being developed at ORNL.[3,4] Also, since an independent analysis of Ag(110) has been performed,[5] an additional study of this surface would test the reproducibility of LEED analyses between laboratories as deemed desirable by a recent DOE panel report.[6] For the above reasons we have initiated work on Ag(110) and report some preliminary results here.

A (110)-oriented Ag crystal was cut from a rod, lapped, and electropolished. After this initial preparation, the sample was mounted in a UHV chamber and cyclically sputtered with 500-eV Ar^+ ions and annealed at 700 K until no Auger signals other than those of Ag were detectable by a CMA. A well-ordered LEED pattern with low background intensity was then obtained from the sample. The sample was aligned perpendicular to the incident beam by equalizing the intensities of prominent peaks in the *I-V* profiles for beams of symmetrical equivalence. Data were collected using a movable Faraday cup with a retarding field analyzer. The *I-V* profile data were collected for all symmetrically equivalent beams in the {01}, {10}, {11}, {02}, {20}, {12}, and {21} sets. Then the equivalent beams in these sets were averaged to obtain experimental profiles to serve as the data base for the theoretical analysis.

An extensive series of dynamical LEED calculations was performed, where the effects of both structural and nonstructural parameters on the results were examined. The experimental and calculated *I-V* profiles were compared in the 60- to 280-eV range by using three distinct reliability factors (*R* factors), which are defined elsewhere.[4] The comparison for the energy range below 60 eV has been postponed for future investigation. It is in this lower energy range where we hope to obtain information that would be useful in understanding the effects of energy-dependent changes in the inelastic mean-free-path.

The set of calculations that has given the best agreement, to date, with the experimental profiles employed a Ag band structure potential,[7] a Debye temperature of 190 K, and an imaginary component of the inner potential that corresponded to the electron having a constant amplitude attenuation, λ_{ee}, of 0.75 nm. Within this set, variations were considered in both the real component of the inner potential, V_{or}, and the deviation of the first interlayer spacing from the bulk value, Δd_{12}. Comparison of the results of this set of calculations with the experimental profiles has led to the contour plots of the three *R* factors given in Fig. 2.4. For example, frame (*a*) indicates that the optimal agreement (smallest R_{ZJ}) is obtained when $\Delta d_{12} = -5.5\%$ and $V_{or} = 10.1$ eV. The ranges in the values of Δd_{12} and V_{or}, which produce the minima of the *R* factors (Fig. 2.4), can be considered as one indication of the sensitivity of the analysis to these quantities. Thus, the analysis indicates that the first layer in the clean Ag(110) surface is contracted toward the second by about $6.6 \pm 1.5\%$.

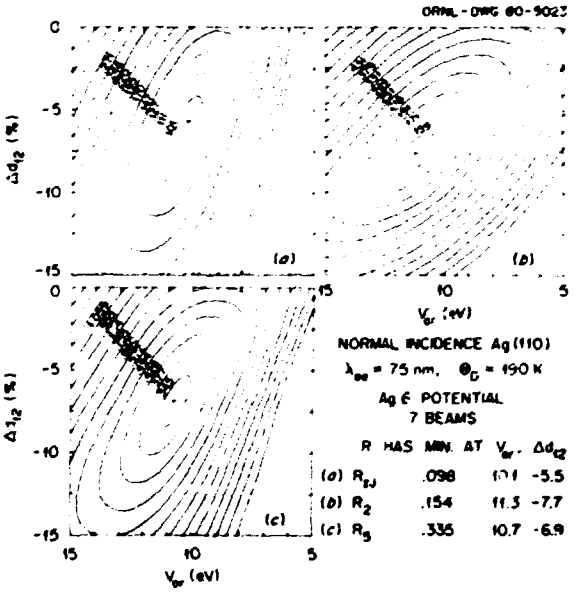

Fig. 2.4. Contour plots of *R* factors for the normal incidence LEED from Ag(110).

An illustration is provided in Fig. 2.5 of the agreement between the experimental and calculated *I-V* profiles obtained in our analysis. Only four of the seven profiles considered are plotted in Fig. 2.5 and are based on the calculated parameters giving the

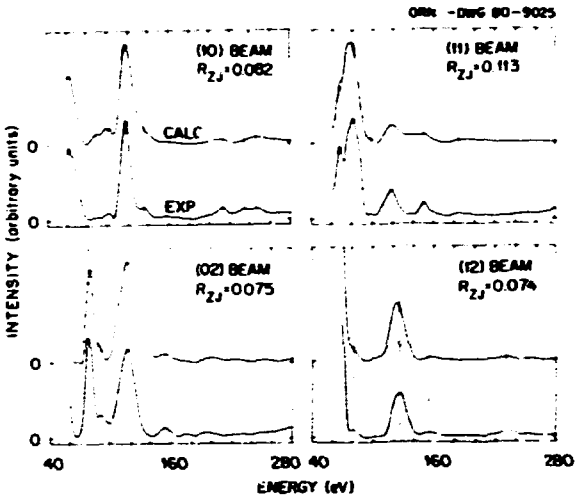

Fig. 2.5. Comparison of experimental and calculated *I-V* profiles for normal incidence LEED from Au(110).

minimum R_{ZJ} of Fig. 2.4. It is noted that the major features of the experimental profiles, as well as most of the weaker structure, are well reproduced by the calculations. However, some of the lower energy peaks are not as well resolved in the calculations as in the empirical profiles [e.g., the structure near 60 eV in the (10) and (11) profiles]. We hope to investigate these differences (as well as the energy range below 60 eV) in future work, since it is anticipated that information concerning the electron's inelastic mean-free-path behavior as a function of energy is contained therein.

The result for Δd_{12} obtained in this investigation needs to be compared with that obtained by Maglietta et al. (hereafter denoted MZJJM).[5] MZJJM obtained a contraction of 10% (no error quoted), while we obtained 6.6 ± 1.5%. Although both investigations deduced a contraction, the difference in the results can be important for considerations concerning the sensitivity and accuracy of LEED analyses. MZJJM analyzed a total of 15 specular and nonspecular profiles, with 12 of these being measured with a nonnormal incident beam. Also, to our knowledge, no data averaging was used. Thus, errors due to minor sample misalignment and other possible causes might have influenced their analysis. Although our analysis was based on 7 experimental profiles, these were obtained by the averaging of symmetrically equivalent profiles from a total of 20 measured at normal incidence. Such an averaging technique is believed to reduce errors caused by minor misalignment of the sample and other experimental limitations.[3] That experimental errors are reduced in our analyzed profiles appears to be indicated by the fact that we have obtained a multibeam R_{ZJ} value of 0.098 (see Fig. 2.4), while MZJJM obtained a value of about 0.20. Of course, only future work by LEED (or other methods) can determine which value of Δd_{12}, if either, is accurate for the clean Ag(110) surface. However, at present, we feel that the available evidence adds credibility to the application of data-averaging techniques to LEED analyses.

1. J. R. Noonan and H. L. Davis, *J. Vac. Sci. Technol.* **16**, 587 (1979).

2. D. Norman and D. P. Woodruff, *Surf. Sci.* **75**, 179 (1978).

3. J. R. Noonan and H. L. Davis, "Effects of Data Averaging on LEED Analyses: A Case Study of the Cu(100) Surface," this report.

4. H. L. Davis and J. R. Noonan, "High-Sensitivity LEED Analysis of the Cu(100) Surface," this report.

5. M. Maglietta et al., *J. Phys. C* **10**, 3287 (1977).

6. *Panel Report on the Theory of Surfaces*, Council on Materials Science, Division of Materials Sciences, U.S. DOE, January 1979.

7. H. L. Davis, p. 123 in *Proceedings of the International Conference on the High Pressure Properties of Solids*, ed. by D. Bloch, Grenoble, France, 1969.

LOW-ENERGY ION SCATTERING FROM THE REORDERED Au(110) SURFACE

D. M. Zehner S. Datz[1]
S. H. Overbury[1] W. Heiland[2]

The clean Au(110) surface that is known to exhibit a reconstructed (2 × 1) geometric arrangement at room temperature has been the subject of both LEED[3] and high-energy ion scattering[4] investigations. Although the results of these investigations have provided information which permits the elimination of some structural models, to date it has not been possible to construct a model in which the predictions of model calculations are in agreement with experimental results. Because it is well known in surface studies that it is frequently necessary to apply several differing spectroscopic techniques in the investigation of a surface property, this past year a collaborative effort with members of the Chemistry Division has been initiated in which the technique of low-energy ion scattering has been used to examine the Au(110) surface.

A K^+ ion beam and a rotatable spherical detector have been used to obtain angularly resolved low-energy ion scattering spectra from the (110) Au sample subsequent to standard cleaning treatments (sputter-anneal). Spectra were obtained for an incidence angle of $\psi = 30°$, with azimuthal orientations ranging from the [110] to [100] directions, $\phi = 0$ to 90°, respectively. Several different total laboratory scattering angles have been used. In addition to the sharp "quasi-single" peak (QS) near the kinematical single scattering energy E_K, the energy spectrum exhibits strong plural scattering structures at energies greater than E_K. The intensity of all spectral features is dependent upon ϕ. At $T = 300$ K, there is a plural scattering peak (PS) with intensity about 2.5 times greater than the QS intensity at $\phi = 27°$, although it is nearly absent at $\phi = 0°$ and 60°. The ratio PS/QS exhibits marked temperature dependence, although these variations are smooth, in agreement with previous LEED observations. Extensive data have been obtained at $T = 800$ K also, where LEED observations indicate the surface to have the normal (1 × 1) arrangement. These results will be compared with predictions of Monte Carlo calculations and should aid in the determination of the correct structural model for this surface.

1. Chemistry Division, ORNL.
2. Max-Planck-Institut für Plasmaphysik, Garching, Germany.
3. J. R. Noonan and H.L. Davis, *J. Vac. Sci. Technol.* 16, 587 (1979).
4. B. R. Appleton et al., *Solid State Div. Prog. Rep., Sept. 30, 1978*, ORNL-5486, p. 38.

PREPARATION OF ATOMICALLY CLEAN SEMICONDUCTOR SURFACES BY PULSED LASER IRRADIATION[1]

D. M. Zehner C. W. White G. W. Ownby

The production of atomically clean surfaces in UHV is a basic requirement in many areas of technological importance. Basic studies of surface chemistry and physics require clean surfaces where the level of unwanted contaminants in the first few monolayers is ≤1 at. %. For many applications in device technology, surface contaminants will contribute greatly to degradation of device performance. As device dimensions become increasingly smaller, the near-surface region will become even more important, and it will be necessary to pay ever increasing attention to the production of atomically clean surfaces during device processing.

Recently, widespread interest has been generated in the possibility of using a new technique known as laser annealing to process semiconductor materials.[2] In order to determine the effects of this process on the surface region of these materials and to assess the possibility of using this technique to remove impurities from this region, a series of experimental investigations has been performed. The experimental arrangement involved irradiating samples in a UHV environment with the output of a pulsed ruby laser (15×10^{-9} s pulse) whose energy density could be varied between ~0.2 and 4.0 J/cm^2. The experimental facility contained equipment which could be used in a variety of surface-sensitive spectroscopic techniques.

Several polished single-crystal samples of Si and Ge were cut from Czochralski-grown material and oriented to have low Miller index surfaces. The as-prepared crystals were mounted on the manipulator and received no cleaning treatment prior to insertion into the UHV chamber.

The Auger electron spectrum obtained from an air-exposed Si sample after insertion into the UHV system and following bakeout is shown at the top of Fig. 2.6. Oxygen [O (510 eV)/Si (91 eV) = 2.3×10^{-1}] and C [C (272 eV)/Si (91 eV) = 3.8×10^{-2}] are readily detected. Occasionally, a small signal from S was also detected. The shape of the spectrum in the region of the Si $L_{2,3}VV$ transition (70–100 eV) is that expected for an oxide-covered surface. Examination of the as-inserted samples with LEED showed that diffraction spots could be observed only at relatively high energies (>250 eV), accompanied by an intense background resulting from diffuse scattering. Irradiation with one laser pulse (~2.0 J/cm^2) caused a substantial reduction in the levels of O (O/Si = 4.3×10^{-2}) and C (C/Si = 7.9×10^{-3}) present in the surface region as shown in Fig. 2.6. Moreover, observations with LEED indicated a well-ordered surface layer, although some diffuse scattering producing a weak background was still present. After exposing the same spot to five laser pulses, the Auger electron spectrum (Fig. 2.6) indicated that for the same detection conditions the O and C signals were now within the noise level. The LEED patterns exhibiting sharp diffraction spots and very low background intensity were observed at this stage. The Auger electron spectrum obtained from the same spot after irradiation with 15 laser pulses is shown at the bottom of Fig. 2.6. Although the O and C signals are not observable in this trace, by increasing the effective sensitivity of the electron detection system, O and C intensity ratios were determined as O/Si ≤ 5.5×10^{-4}

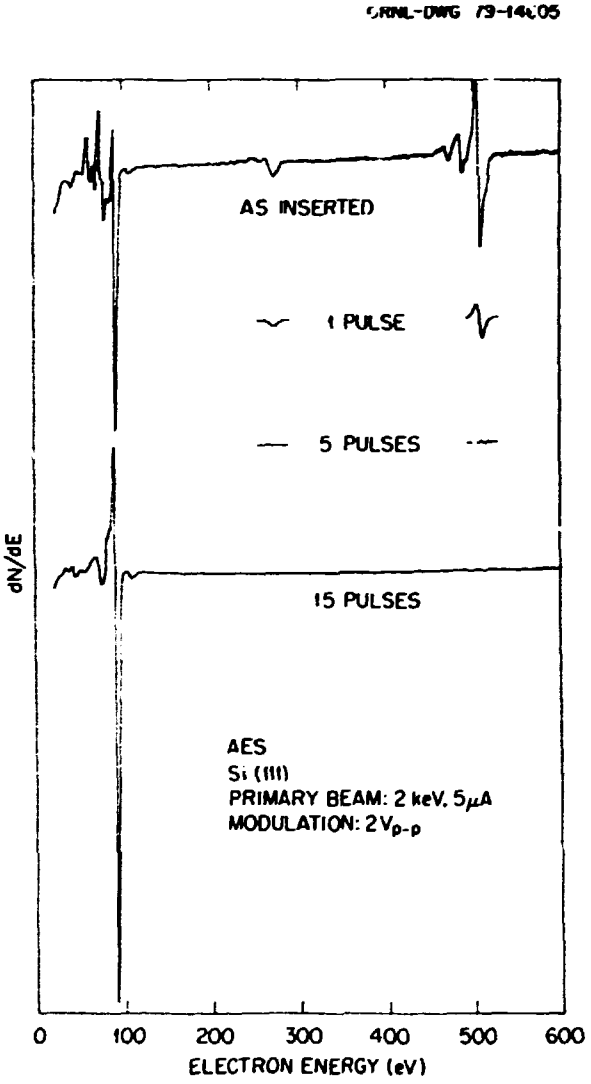

Fig. 2.6. Auger electron spectra obtained from an uncleaned Si surface and after pulsed laser annealing at ~2.0 J/cm².

and C/Si $\leq 7.6 \times 10^{-4}$, indicative of surface concentrations of $\leq 0.1\%$ of a monolayer. In addition, the Si $L_{2,3}VV$ transition is that expected from a clean Si surface.

Consequently, by exposing the crystal to several (~5) laser pulses, the O and C contamination has been reduced by factors of 500 and 50, respectively, accompanied by the development of well-defined LEED patterns. These reduced contaminant levels, obtained in a processing time of ≤ 1 s, are slightly better than those obtained by repeated sputtering and conventional thermal annealing over a time period of several days. It should be noted that the residual O and C contamination on this surface may arise due to adsorption and cracking from the gas phase during the time required to make the Auger measurements.

Results similar to these have been obtained with Ge samples also. However, a large number of pulses (at a lower energy density) were required to obtain the same degree of surface cleanliness. In general, the results obtained were found to be independent of the crystal orientation for both Si and Ge.

Removal of surface contaminants by laser irradiation was accompanied by an increase in background pressure as measured with a nude ionization gauge. Using laser pulses of ~2.0 J/cm² and starting with a background pressure of 2.5×10^{-8} Pa, the first laser pulse on an as-inserted or freshly sputtered Si sample caused a transient pressure rise into the 6.5×10^{-6} to 4×10^{-5} Pa range. Subsequent pulses on the same area were accompanied with pressure rises into the 10^{-7} Pa range, and these continued to drop until the pressure stayed in the 10^{-8} Pa range by about the tenth pulse. Because of the position of the ionization gauge relative to the sample location, these observations did not provide an accurate measure of the pressure increase in front of the sample, which was probably much higher than measured.

Previous experiments have shown that pulsed laser irradiation at these energy densities causes the surface region of the crystal to be melted to a depth of several thousand angstroms. The melted layer then regrows from the underlying substrate by means of liquid phase epitaxial regrowth, and the regrown region has the same crystalline perfection as the substrate. The present results show that the crystalline order extends to the first monolayer, since well-defined LEED patterns are observed after laser irradiation. There are two possibilities as to the ultimate fate of the original O and C surface contaminants. The fact that a pronounced pressure rise is observed during the first laser pulse suggests that the contaminants are desorbed from the surface during irradiation. Alternatively, since pulsed laser annealing causes a melted region to be formed to a depth of several thousand angstroms, impurities can undergo substantial redistribution by means of liquid phase diffusion during the time the surface region is molten.

Redistribution deeper into the sample occurs predominantly for those impurities which have a relatively high segregation coefficient from the melt. Impurities which have a low segregation coefficient from the melt have been shown to segregate to the surface during annealing. For C and O, the equilibrium segregation coefficients[3] in Si are 0.07 and 0.5, respectively, and considering the high solubility and diffusivity of impurities in liquid Si, these impurities

may be redistributed over a depth interval equivalent to the melt depth (~5000 Å for laser energy densities of ~2.0 J/cm^2). Complete redistribution over this depth interval would give rise to a surface concentration of ~0.3% for O and 0.1% for C, both of which are near the detection limits for Auger electron spectroscopy; these values are consistent with our measurements. Whether these impurities are desorbed from the surface or redistributed in depth or both can be determined by experiments designed to measure the total C and O contamination in the near-surface region. Such experiments are in progress.

---

1. Summary of paper: *Appl. Phys. Lett.* 36, 56 (1980); (in press).

2. C. W. White, J. Narayan, and R. T. Young, *Science* 204, 461 (1979).

3. K. J. Bachmann, *Current Topics of Material Science*, vol. 3, North Holland, New York (in press).

Si SURFACE STRUCTURES AFTER PULSED LASER ANNEALING[1]

D. M. Zehner C. W. White G. W. Ownby

The ability to prepare clean, well-ordered surface structures on single crystals is a principal requirement for many basic investigations concerned with the processes occurring at the surface of a solid. Conventional methods of producing such surfaces include sputtering followed by thermal annealing, in situ cleavage, and in situ evaporation. These conventional methods are frequently time consuming and in some cases restricted to a relatively small surface area.

A new technique known as pulsed laser annealing has been applied recently to the processing of semiconductor materials.[2] In order to evaluate the application of this technique to the investigation of basic surface properties, we have determined the surface structures on single-crystal Si samples following pulsed laser irradiation in UHV. Some of these results are reported here and compared with the surface structures obtained by conventional sputtering and thermal annealing.

The light from a pulsed ruby laser was coupled through a glass window into a UHV system in which were mounted a four-grid LEED optics and a single-pass CMA used for AES to monitor surface impurities. Samples were irradiated (beam diameter ~3.5 mm) using the single mode (TEM_{00}) output of the laser at energy densities that could be varied between 0.2 and 4.0 J/cm^2. A constant pulse duration time of 15×10^{-9} s was used throughout the experiment. Reported energy densities have been corrected for the reflectivity (~10%) of the glass window. Silicon samples cut from wafers supplied by the Monsanto Company received no cleaning treatment prior to insertion into the UHV chamber.

The diffraction patterns obtained from several Si samples subsequent to laser annealing with 5 to 15 pulses of 1.0 to 2.0 J/cm^2 are shown in Figs. 2.7 and 2.8. Figure 2.7*a* and *c* show LEED patterns obtained from (100) and (110) Si samples subsequent to laser annealing. These diffraction patterns are indicative of reconstructed surface layers exhibiting unit cells commonly indexed (2 × 1) and (1 × 2), respectively. Comparison of these LEED patterns with those obtained after using conventional sputter-annealing techniques, as shown in Figs. 2.7*b* and *d*, indicate that the same reconstructed surface structure is present following both types of annealing treatments.

The LEED pattern obtained from a Si(111) crystal subsequent to laser annealing is shown in Fig. 2.8*a*. This (1 × 1) pattern is indicative of a filled outermost (111) surface layer and is to be contrasted with the pattern shown in Fig. 2.8*b* obtained from a (111) sample following a conventional sputter-annealing treatment; the observed (7 × 7) pattern indicates a reconstructed surface layer. A similar pattern was obtained from the laser-annealed surface (Fig. 2.8*a*) after subsequent thermal heating to ~700 K.

Similar observations were made on a (111) crystal whose surface was cut at 4.3° from a (111) plane toward the [$\bar{1}\bar{1}$2] direction. After laser annealing, the pattern observed and shown in Fig. 2.8*c* indicates the existence of a surface that can be indexed [14(111) × ($\bar{1}\bar{1}$2)]. This surface consists of monatomic steps with average height of one double layer (3.14 Å) with terraces containing (1 × 1) domains.[3] Thermal annealing of a crystal in this state resulted in a surface from which the diffraction pattern shown in Fig. 2.8*d* was obtained; all indications of the steps are gone, and the (7 × 7) pattern was observed over the entire area irradiated.

The results obtained from the (100) and (110) surfaces indicate that the atoms in the outermost layers have sufficient energy under these annealing conditions to reorganize into the reordered arrangements from which the (2 × 1) and (1 × 2) LEED patterns are obtained. This is consistent with the small displacements required in the variations of the dimer model employed in recent theoretical LEED analyses of the (100) surface.[4] Although quarter-order LEED beams

SSDN-2376

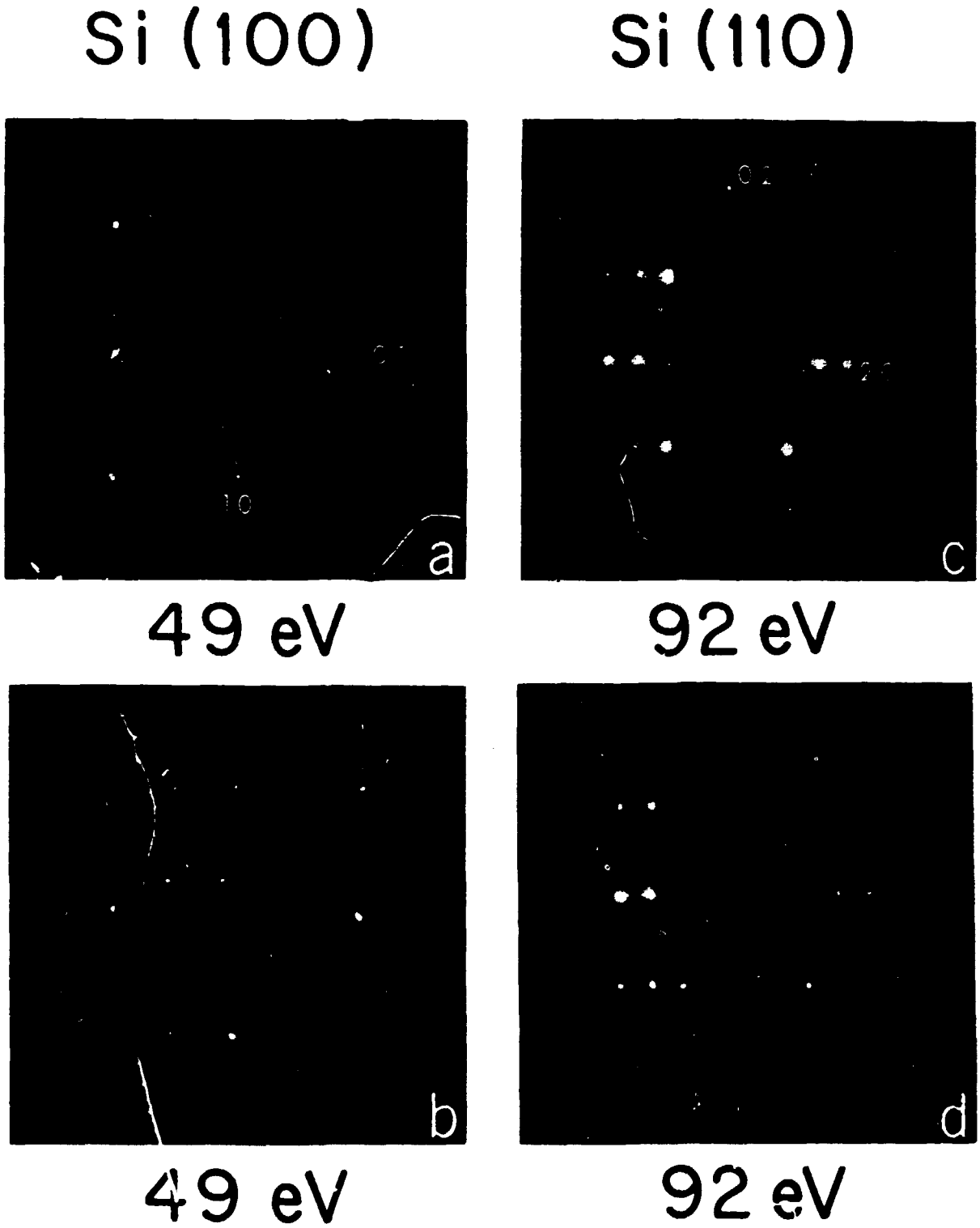

Fig. 2.7. LEED patterns from clean (100) and (110) Si surfaces at primary beam energies of (*a*, *b*) 49 eV and (*c*, *d*) 92 eV; (*a*, *c*) laser annealed; (*b*, *d*) thermally annealed.

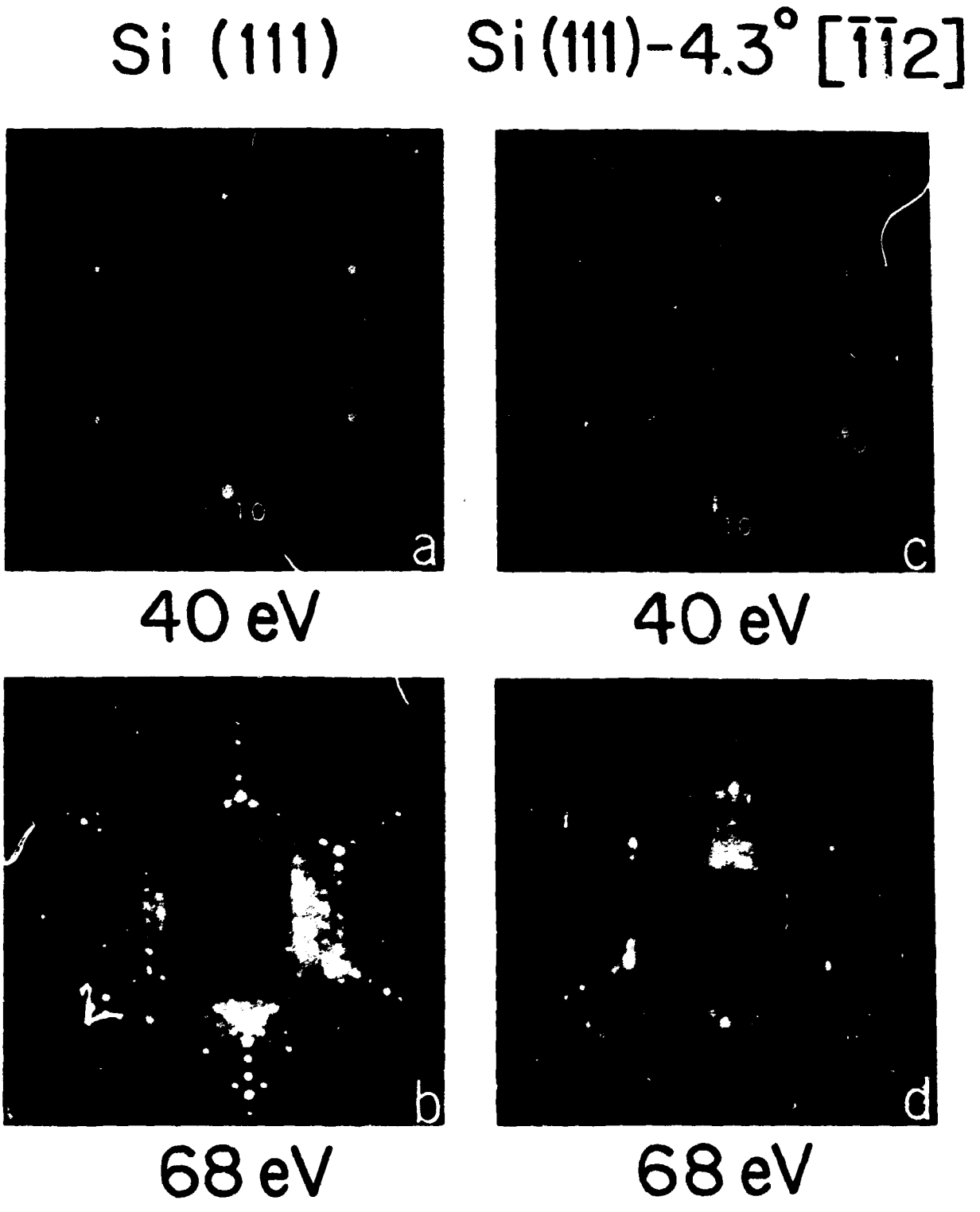

Fig. 2.8. LEED patterns from clean (111) and stepped (111) Si surfaces at primary beam energies of (*a*, *c*) 40 eV and (*b*, *d*) 68 eV; (*a*, *c*) laser annealed; (*b*, *d*) thermally annealed.

SSDN-2376

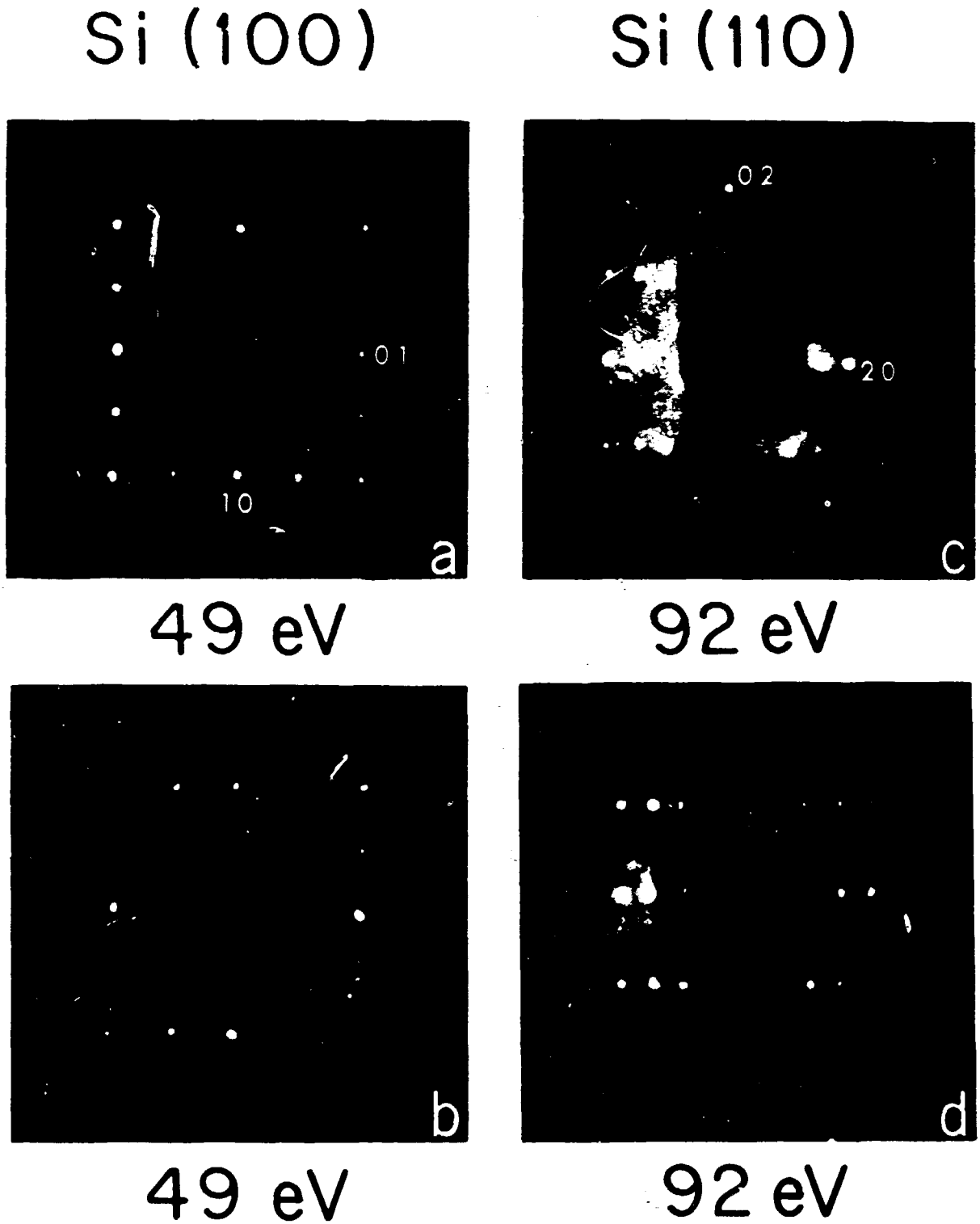

Fig. 2.7. LEED patterns from clean (100) and (110) Si surfaces at primary beam energies of (*a, b*) 49 eV and (*c, d*) 92 eV. (*a, c*) laser annealed, (*b, d*) thermally annealed

SSDN-2381

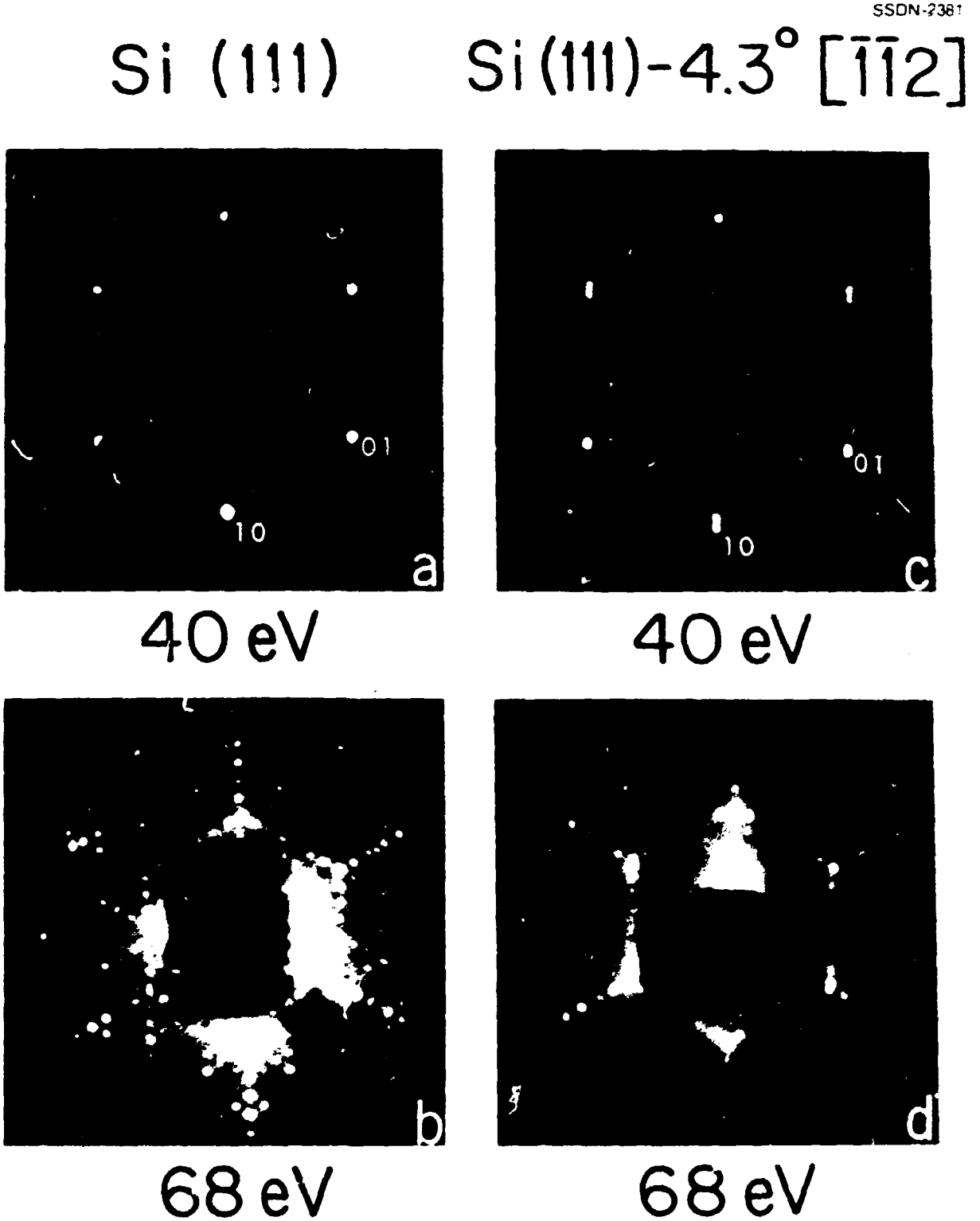

Fig. 2.8. LEED patterns from clean (111) and stepped (111) Si surfaces at primary beam energies of (*a*, *c*) 40 eV and (*b*, *d*) 68 eV, (*a*, *c*) laser annealed; (*b*, *d*), thermally annealed.

indicative of a (4 × 2) structure have been observed occasionally in previous examinations of the (100) surface, they were not observed in this investigation subsequent to either laser annealing or thermal treatments. In contrast, the results obtained from the oriented (111) surface indicate that the surface terminates with a metastable ideal bulklike structure and does not exhibit any lateral rearrangement. Moreover, the results obtained for the vicinal (111) surface indicate that a stepped surface, consistent with the physical orientation of the crystal, is present after laser annealing and that the diffraction pattern from the terraces is that expected for unreconstructed (111) planes. It has been suggested that the reconstructed surface exhibiting the (2 × 1) LEED pattern is one that contains a large number (~25%) of vacancies that may be combined with some form of ripple distortion. The results presented here indicate a completely filled outermost monolayer on both oriented and misoriented (111) crystals after laser annealing, suggesting that the atomic migration necessary to form the reconstructed surface cannot occur in the extremely short (~10 μs) time during which the sample cools.

These observations show that pulsed laser annealing can be used to provide well-ordered surface structures on Si single crystals in very short processing times (seconds) which are also after vacuum clean. The ability to prepare unreconstructed surfaces on the (111) oriented samples provides an opportunity to study the surface properties of a semiconductor surface without having to deal with the problem of large atomic rearrangements.

[1] [illegible] *Appl. Phys. Lett.* **36**, 56 (1980); "Preparation of Atomically Clean Semiconductor Surfaces by Pulsed Laser Irradiation," this report.

[2] C. W. White, J. Narayan, and R. T. Young, *Science* **204**, 461 (1979).

[3] M. Hanzer, *Surf. Sci.* **19**, 159 (1970); **22**, 12 (1970).

[4] F. [illegible] *J. Phys. C* **12**, 1455 (1979).

[5] W. Monch, *Surf. Sci.* **86**, 672 (1979).

[6] D. M. Zehner, C. W. White, and G. W. Ownby, *Appl. Phys. Lett.* **36**, 56 (1980); "Preparation of Atomically Clean Semiconductor Surfaces by Pulsed Laser Irradiation," this report.

Ge SURFACE STRUCTURES AFTER PULSED LASER ANNEALING

D. M. Zehner, C. W. White, G. W. Ownby

Previous investigations of the surface structures of clean single crystals of Ge have produced results which indicate that the atomic arrangements of low index orientations are reconstructed with respect to the terminations of an ideal bulk crystal. Although reconstruction has been observed for all crystal orientations, the observed structure in some cases depends on whether the surface is prepared by cleaving in situ or by sputtering followed by thermal annealing. It has been demonstrated recently that, subsequent to pulsed laser annealing, well-ordered surface structures exist on Si single crystals.[1] Moreover, in the case of a Si (111) orientation, it was observed that a metastable unreconstructed surface structure could be prepared by use of this annealing process. As a consequence of these observations, it was decided to investigate the application of the pulsed laser annealing technique to single crystals of Ge in order to determine its effect on surface structure.

The experimental arrangement, similar to that described previously, permitted irradiation of the Ge samples with the output of a pulsed ruby laser (15 × 10^{-9} s pulse, ~0.2 to 4.0 J cm^{-2}) in a UHV environment. Observations of the surface structure and cleanliness were made using LEED and AES techniques, respectively. The Ge samples were cut from Czochralski-grown material and prepared using standard polishing techniques.

After insertion into the UHV system and prior to any cleaning treatment, diffraction patterns could not be obtained from the samples due to the presence of a native oxide at the surface. Following irradiation with five pulses of ~1.0 J cm^{-2}, a well-defined (2 × 1) LEED pattern was obtained from a (100) oriented sample. Additional pulses improved the quality of the pattern, and after a total of 15 pulses, the pattern shown in Fig. 2.9*a* was obtained. Auger measurements indicated this surface to be atomically clean.[2] A comparison of this pattern with that shown in Fig. 2.9*b*, which was obtained from a (100) oriented sample subsequent to a standard sputter thermal anneal treatment, shows that the same surface structure was present after either type of annealing treatment.

The LEED pattern obtained from a (111) oriented sample following a laser annealing treatment similar to that specified previously is shown in Fig. 2.9*c*. This well-defined (1 × 1) LEED pattern with low background intensity indicates that, as a result of the laser annealing, the normal surface structure (truncation of the bulk) is obtained and there is no evidence of any lateral reconstruction. The sample temperature range over which the (1 × 1) LEED pattern was observed subsequent to laser irradiation was determined to be between ~100 and ~1000 K. In contrast,

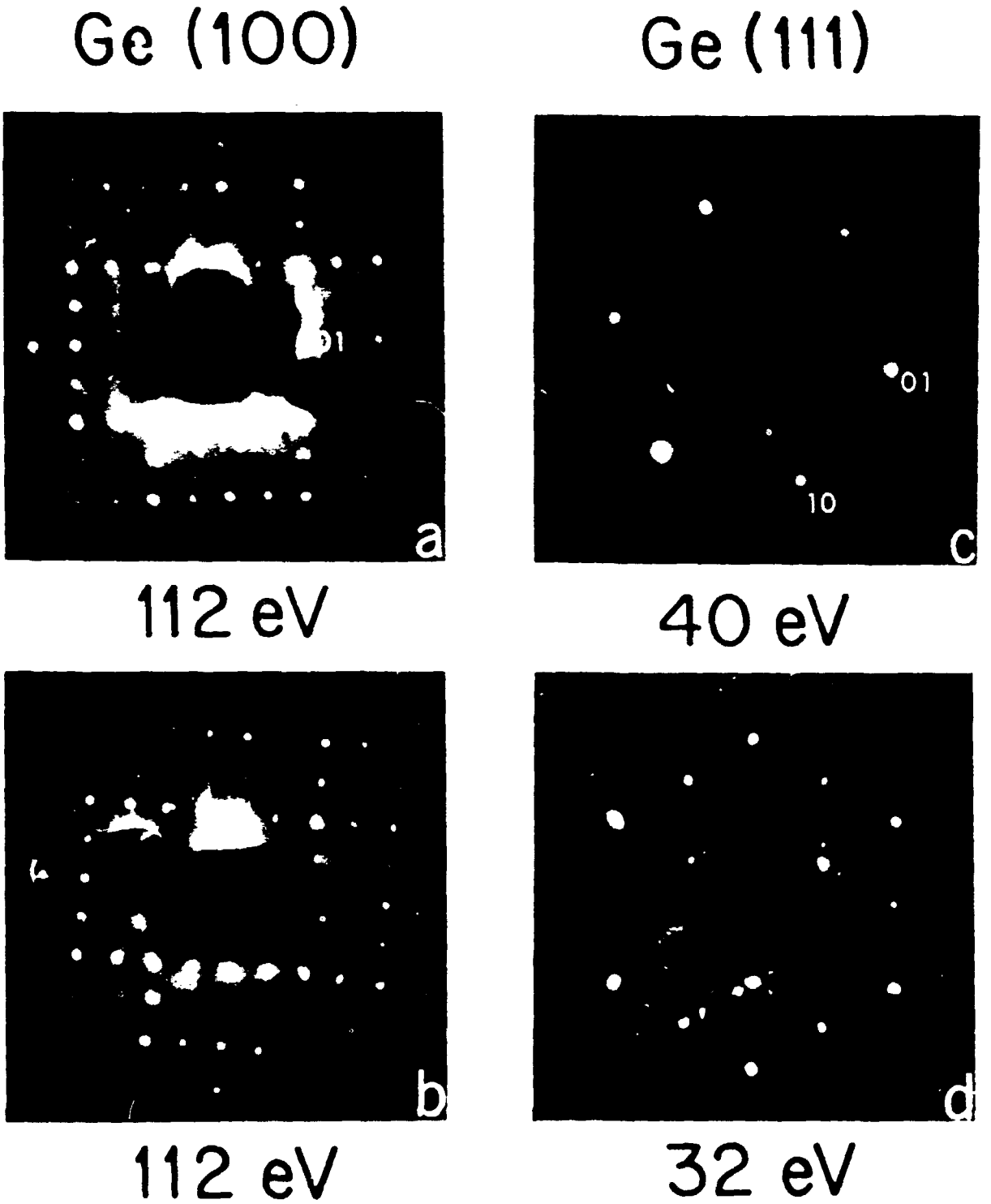

Fig. 2.9. LEED patterns from clean (100) and (111) Ge surfaces at primary beam energies of (*a, b*) 112 eV, (*c*) 40 eV, and (*d*) 32 eV; (*a, c*) laser annealed, (*b, d*) thermally annealed

the (2 × 8) LEED pattern shown in Fig. 2.9*d*, indicative of a reconstructed surface, was obtained from a (111) sample after sputtering with the sample held at ~900 K.

Since the initial observations that the (100) and (111) surfaces of Ge are reconstructed subsequent to a sputter-anneal treatment, much effort has been expended in determining geometric models appropriate for these atomic structures and in obtaining a variety of experimental data to support these models. Although the exact details of the correct atomic arrangement for either reconstructed surface are still lacking, there is a large body of evidence which suggests that the top layer on the (100) surface has the correct monolayer density in which adjacent atoms in the (110) directions are displaced to form dimers.[5] In contrast, the reconstructed (111) surface layer is believed to contain a large concentration of vacancies (16.7%) which form an ordered array.[6]

The conclusions to be drawn from the results presented above are similar to those obtained in investigations of Si surface structures. Specifically, the results obtained on the Ge (100) surface support the dimer model in which only small displacements of atoms in a complete monolayer are required to form the reconstructed surface. Apparently these small motions can take place after the laser annealing process is complete. The (1 × 1) LEED patterns obtained from the laser-annealed (111) surface of Ge also indicate a completely filled top monolayer and thus suggest that the diffusion of atoms which would be required to provide the large concentration of surface vacancies cannot occur after the rapid epitaxial regrowth process is complete.

These results on surface structure, along with the observations concerned with surface cleaning,[3] indicate that the laser annealing process is suitable for preparing atomically clean, well-ordered surfaces on Ge in very rapid processing times (seconds).

1. D. M. Zehner, C. W. White, and G. W. Ownby, p. 201 in *Laser and Electron Beam Processing of Materials*, ed. by C. W. White and P. S. Peercy, Academic, New York, 1980; *Surf. Sci. Lett.* **92**, L67 (1980).
2. D. M. Zehner, C. W. White, and G. W. Ownby, "Si Surface Structures After Pulsed Laser Annealing," this report.
3. D. M. Zehner, C. W. White, and G. W. Ownby, "Preparation of Atomically Clean Semiconductor Surfaces by Pulsed Laser Irradiation," this report.
4. D. M. Zehner, C. W. White, and G. W. Ownby, *Appl. Phys. Lett.* **36**, 56 (1980).
5. F. Jona et al., *J. Phys. C* **12**, L455 (1979).
6. J. C. Phillips, *Surf. Sci.* **40**, 459 (1979).

ELECTRON SPECTROSCOPIC INVESTIGATIONS OF THE OXIDATION OF Be

D. M. Zehner H. H. Madden[1]

AES, CLS, and XPS measurements have been made on clean and oxidized Be surfaces. These spectroscopies allow investigation of the changes in electronic structure of a Be surface on oxidation. Core-valence-valence AES lines give information on the valence band structure, while the CLS spectra give information on the conduction band DOS. The Be *KVV*-Auger line and the K-CLS (K core level) spectra were measured for both clean and oxidized Be surfaces. The oxygen *KVV*-Auger and K-CLS spectra were also measured for the oxidized surface. Because both of these spectroscopies involve the production of core-hole states, they are site specific and hence sample the electronic DOS in the vicinity of the core-hole site. As the valence-electron distribution is directly related to the chemistry of the system, AES measurements probe the chemical environment about a specific site (e.g., about the Be ion or about the O ion for the oxidized Be surface). CLS measurements give complementary specific-site information about the empty DOS distribution. XPS measurements serve as an aid in interpreting the AES and CLS data and provide information about the core level binding energies and the chemical shifts associated with oxidation.

The background-corrected, loss-deconvoluted, integral $N(E)$ Auger spectrum from clean Be and its interpretation have been reported previously.[2] Briefly, this signal may be thought of as being made up of three components which depend on the symmetries (s and/or p) of the valence electrons that take part in the *KVV* Auger decay. Using a theoretical total DOS from Loucks and Cutler,[3] together with the K soft x-ray emission spectrum of Aita and Sagawa[4] to simulate the p-partial DOS, the experimental *KVV* lineshape (dashed line, Fig. 2.10) could be synthesized by *ss*-to-*pp* and *sp*-to-*pp* ratios of 1.82 and 0.55, respectively. Theoretical interpretations of these results[2] indicate that the values of these ratios for elemental Be are determined not only by the Auger-transition matrix elements and the number densities of s- and p-valence electrons but also by an initial-state screening of the core hole that is largely s-like.

Exposure of a clean Be surface to 10,000 L of O_2 with the sample held at ~900 K resulted in a heavily oxidized surface layer. Both the Be- and O-*KVV* [loss-corrected, $N(E)$] Auger spectra from the

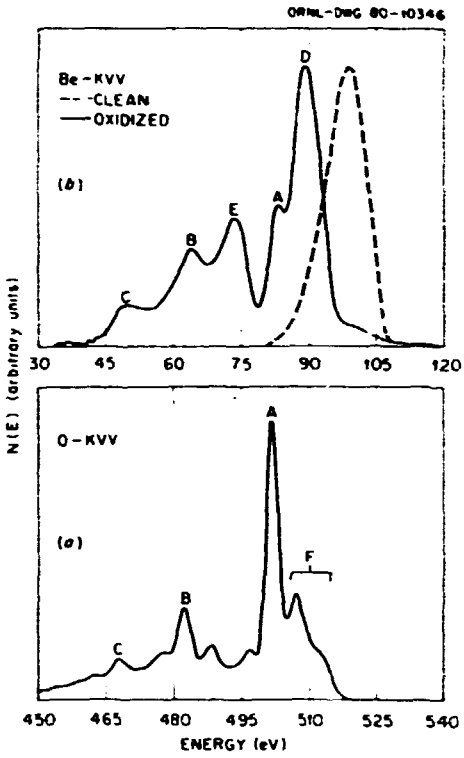

Fig. 2.10. Auger spectra from clean and oxidized Be. (*a*) Be *KVV*; (*b*) O *KVV*.

oxidized Be surface are shown in Fig. 2.10. The spectrum from oxidized Be is more complex in shape than is the corresponding signal from clean Be (Fig. 2.10), and its major peak occurs some 10 eV lower in energy. (A small high-energy shoulder on this peak is probably due to a remnant of elemental Be in the sample surface.) Tentative interpretation of these two *KVV* spectra assumes significant ionic bonding in BeO leading to interatomic Auger transitions for the Be-*KVV* signal (i.e., the valence electrons in this compound are localized on the O site). The *A*, *B*, and *C* peaks in both of these spectra are thought to arise from *pp*, *sp*, and *ss* valence-electron transitions, respectively, with both valence electrons that take part in the Auger decay coming from the same O site. Peaks *D* and *E* in the BeO spectrum are due to nonlocalized interatomic transitions, with the two valence electrons involved coming from different O sites. The difference in energy in these features with respect to the localized-site spectra are due to the smaller hole-hole repulsion energy for the nonlocalized transitions. The peak/shoulder structure (*F*) on the high-energy side of the O-*KVV* spectrum is also thought to be due to nonlocalized transitions.

The CLS data for clean and oxidized surfaces are shown in raw form in Fig. 2.11. After loss correction,

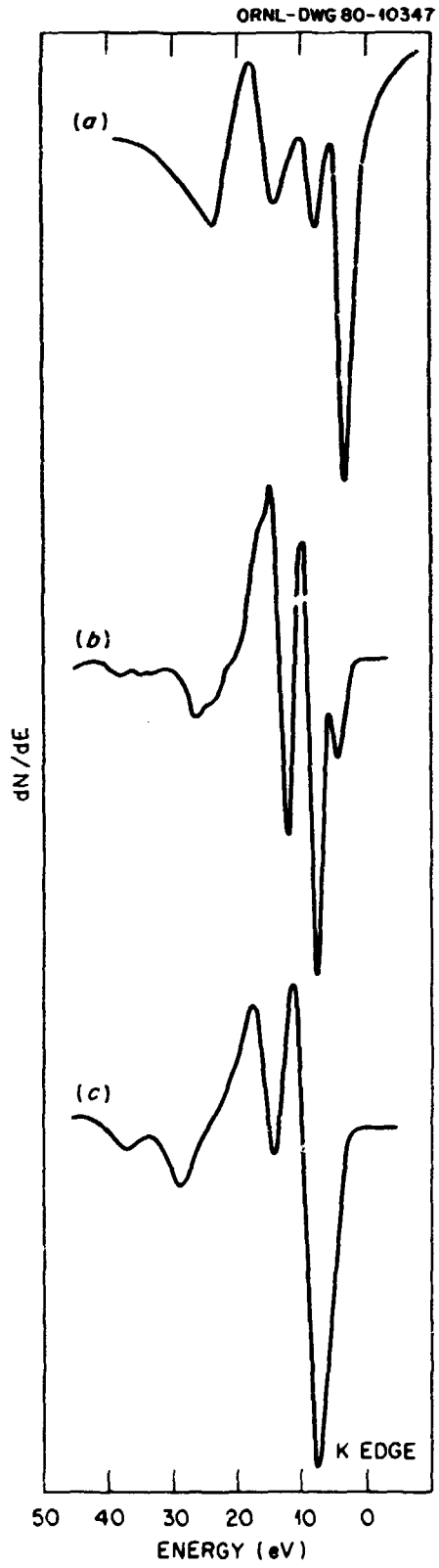

Fig. 2.11. CLS spectra from clean and oxidized Be. (*a*,*b*) Be K edge; (*c*) O K edge.

the $N(E)$ spectrum for the clean surface has been found to be in reasonably good agreement with theoretical (conduction-band) DOS calculations and with the results of other experimental probes of the empty DOS of elemental Be. Comparing the raw data, one sees that the empty DOS at the Fermi level changes, upon oxidation, from a steplike function to a more peaklike distribution. The energy difference between the highest energy minimum, probably due to a remnant of elemental Be in the sample surface, and the most intense minimum is in good agreement with the XPS measurement of the chemical shift of the Be K-core level due to oxidation. One also finds that the Be K-CLS spectrum from oxidized Be is closer in shape to the O K-CLS spectrum than it is to K-CLS spectrum from clean Be. These results may be consistent with the ionic-bonding picture of Be, although it is not clear as to why the empty DOS distribution (near the Fermi level) should be the same at the O site unless, perhaps, the empty Be states lie well above the Fermi level and the CLS measurements are sampling only those empty states due to the O. The data reduction of the CLS spectra from the oxidized surface has still to be completed.

---

1. Sandia Laboratories, Albuquerque, N.M.

2. D. R. Jennison, H. H. Madden, and D. M. Zehner, *Phys. Rev. B* 21, 430 (1980).

3. T. L. Loucks and P. H. Cutler, *Phys. Rev.* 133, A819 (1964).

4. O. Atta and T. Sagawa, *J. Phys. Soc. Jpn* 27, 164 (1969).

ADSORPTION OF O ON Cu(110) STUDIED WITH ELS AND LEED[1]

J. F. Wendelken Martin Ulehla

In the study of adsorbate site locations and adsorbate reactions on surfaces, surface vibrational spectroscopies have become increasingly important. Currently, the most popular of these vibrational spectroscopies is ELS. We report here the use of this technique in conjunction with LEED to investigate the adsorption of O on the Cu(110) surface. This adsorption system is of interest because of the role of O in a variety of catalytic reactions on this surface. For example, the dissociative chemisorption of ethanol on Cu(110) and Ag(110) is strongly promoted by preadsorption of oxygen.[2]

The measurements were made using a high-resolution electron spectrometer under UHV conditions.[3] The spectrometer operates with 20 meV energy resolution and 1° angular resolution. A movable, rear-viewing LEED display screen is mounted in the same system so that all measurements are made without moving the target.[4]

The LEED observations are summarized in Fig. 2.12. When a clean Cu(110) surface (Fig. 2.12*a*) at a temperature of 80 K was exposed to 20 L of O_2, only the relative intensities of the LEED beams were observed to change. No additional beams were observed and only a small increase in diffuse scattering was seen. However, when the crystal was subsequently heated above 160 K, additional one-third order beams from a (3×1) pattern appeared, and finally a $c(6 \times 2)$ pattern was observed after a temperature of 400 K was reached. Above this temperature the pattern eventually changed completely to a (2×1) pattern as shown in Fig. 2.12*c*. Figures 2.12*b*, *d* show a $c(6 \times 2)$ pattern in which a (2×1) pattern has begun to develop. When O exposures were made at room temperature, only the (2×1) pattern (Fig. 2.12*c*) developed for the exposures reported here.

The ELS measurements were made as a function of O exposure and the various LEED patterns. After a series of O_2 exposures at room temperature followed by annealing at 500 K to produce a sharp (2×1) LEED pattern, an energy loss at 49 meV was observed. This energy loss was observed to increase in intensity relative to the elastic scattering intensity up to an exposure of 6 to 8 L. At the specular scattering angle of 80° from the surface normal, which was used for these measurements, the elastic intensity was seen to increase also with O exposure by nearly a factor of 3 when saturation was reached at 8 L. Most interesting was the fact that no energy shift was observed as a function of exposure up to 50 L.

A direct comparison of the ELS results with the LEED results is shown in Fig. 2.13. In each case the O dose was 20 L with a crystal temperature of 80 K. Again, the same vibrational loss energy was observed in all three cases. Only changes in total and relative intensities were observed. Upon heating the crystal to obtain the $c(6 \times 2)$ pattern, the elastic intensity nearly doubled while the intensity of the loss peak diminished relative to the elastic peak as shown in Fig. 2.13*b*. Further heating to obtain the (2×1) structure again nearly doubled the intensity of the elastic peak, and the loss peak was now increased relative to the elastic peak as shown in Fig. 2.13*c*.

As a check on these results, ELS data were also obtained by using $^{18}O_2$ instead of $^{16}O_2$. If the vibrational energy varies as the inverse square root of the mass, then a shift from 49 to 46.2 meV is expected. The measured value for $^{18}O_2$ was 46 + 0.5 meV. The

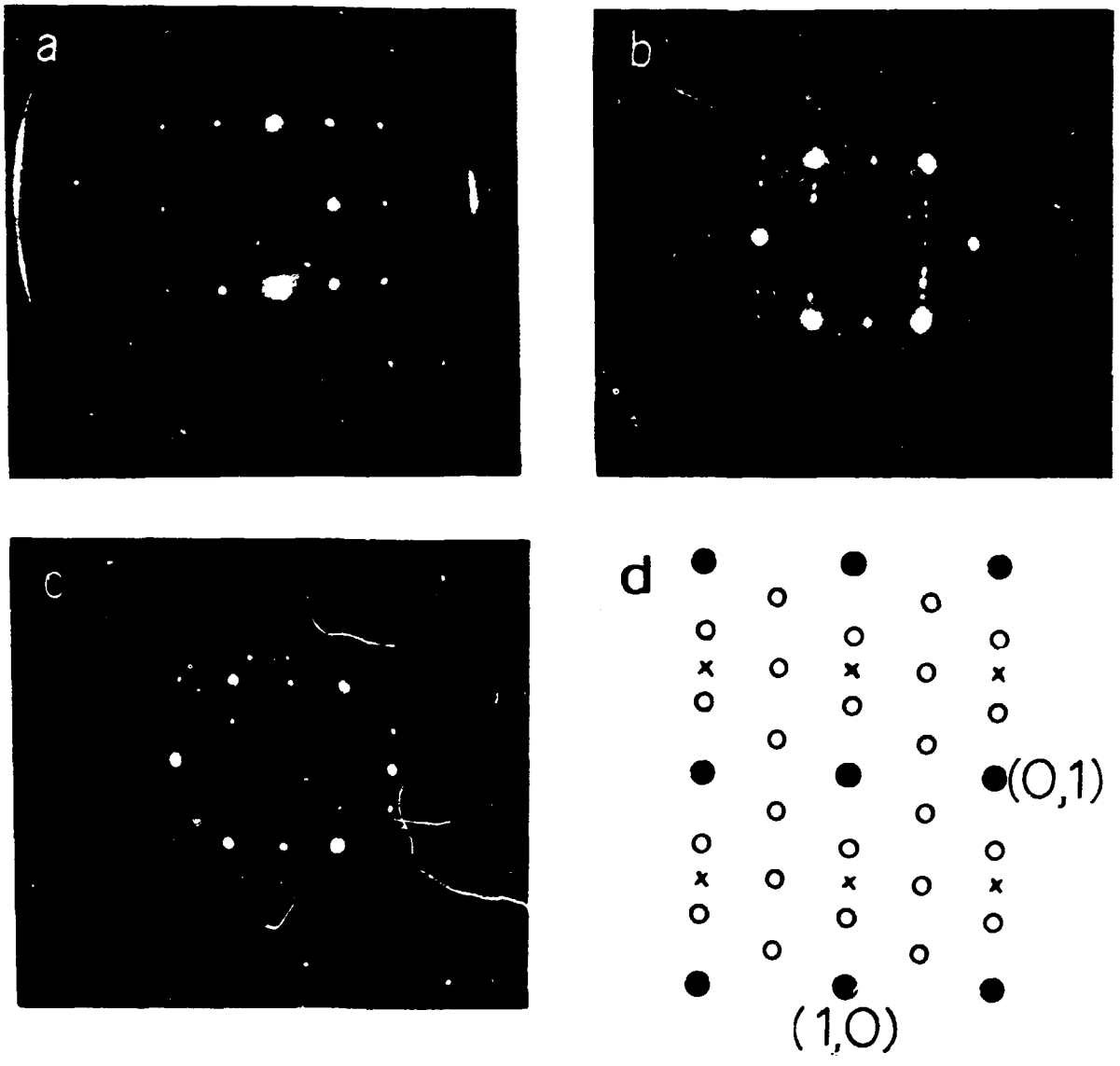

Fig. 2.12. LEED patterns with E_p = 200 eV. (*a*) The clean Cu(110) surface at T = 160 K, (*b*) after exposure to 20 L O_2 at T = 80 K followed by heating to 400 K for 10 min and recooling to 100 K, and (*c*) the same O exposure as in (*b*) but after heating to 500 K for 10 min and recooling to 100 K. In (*d*) the integral order beams are indicated by solid circles, the one-sixth order beams of the $c(6 \times 2)$ pattern are indicated by open circles, and the half-order beams of the (2×1) pattern are indicated by crosses.

observed angular distribution of the scattered electrons with the characteristic energy loss of 49 meV ($^{16}O_2$) showed that the inelastic scattering was peaked in the elastic beam direction with an angular spread of 0.8° more than the elastic beam. This is characteristic of dipole scattering[4] in which the inelastic intensities are proportional to the elastic intensities as a result of a two-step scattering process. At any rate, we may be confident that the measured vibrational energy is associated with O.

Unfortunately, the site location of O on Cu(110) cannot be determined from the observation of a single vibration. However, restrictions may be placed on the site. The observed vibrational energy indicates that the O does dissociate since the molecular vibrational energy is 193 meV.[5] Further, the energy value

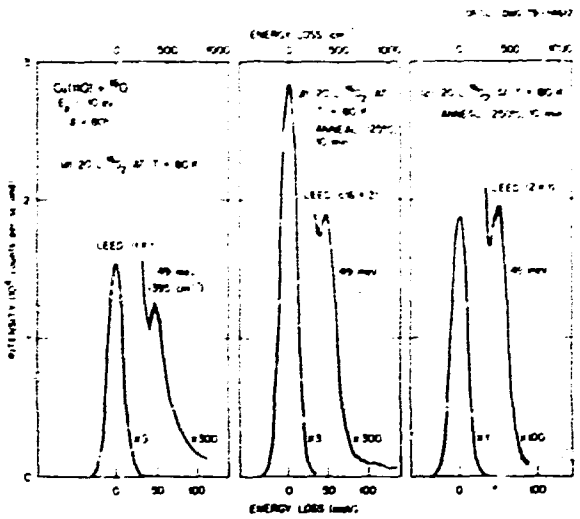

Fig. 2.13. Energy loss profiles for an initial O exposure of 20 L at 80 K but after different temperature cycles to produce the (1 × 1), $c(6 \times 2)$, and (2 × 1) LEED patterns.

indicates that the O atoms are coordinated to more than one Cu atom since the Cu-O stretching mode energy is 76 meV.[6] In general, a decrease in the vibrational energy can be associated with an increase in the bond number.[5] The fact that the vibrational energy does not depend on O coverage argues for a site in which the O atoms do not interact strongly with each other. It is known that the vibrational energy of O on Cu(100) does vary as a function of coverage,[7] and there is some evidence that the O may sit above the surface with fourfold coordination.[8] Hence, a reasonable site on Cu(110) could be in or beneath the surface, and a simple consideration of space indicates that the long bridge position may be preferable. This suggestion is in agreement with ion scattering results[9] which indicate that under dynamic exposure conditions, the oxygen is located at the long bridge position, 0.6 Å beneath the surface. Thus, the effect of this work, in part, is to extend the ion scattering results to lower O coverage levels and to different surface structures, and to explore differences between dynamic and static systems.

It could be assumed that the different LEED patterns in Fig. 2.12 are associated with different densities of O, but with the O always in the same site. The ELS intensities are confusing on this point since the inelastic intensity relative to the elastic intensity (I_L/I_E) decreases upon formation of the $c(6 \times 2)$ structure and increases upon formation of the (2 × 1) structure. The initial loss of intensity is probably associated with O incorporation into the bulk as has been indicated for O on Cu.[10] The $c(6 \times 2)$ pattern may be associated with a one-sixth monolayer surface coverage or with a high-coverage coincidence structure, as suggested in a recent study of adsorption above room temperature.[10] In the first case, formation of the (2 × 1) structure requires either a threefold increase in surface O or the formation of (2 × 1) islands. If the (2 × 1) structure that is formed by heating the $c(6 \times 2)$ structure is then viewed as a surface that is two-thirds clean and one-third covered by (2 × 1) islands and if the scattering from the islands is weighted to reflect the increased elastic scattering from the (2 × 1) surface, an increase in (I_L/I_E) by a factor of 1.8 is expected. The observed increase is a factor of 1.6, a value which could be affected by further O incorporation. If the surface were completely covered by a (2 × 1) structure, the increase in (I_L/I_E) should be a factor of 3. Such a large increase was not observed for exposures up to 50 L at room temperature and above, which suggests that a completely saturated (2 × 1) structure may be difficult to form, possibly as the result of further O incorporation. In the case of the $c(6 \times 2)$ coincidence model, a reduction in (I_L/I_E) should have been observed for the (2 × 1) structure.

Finally, it is noted from a comparison with published ELS[7] and angle-resolved SIMS[8] results for O on Cu(100) that, despite a very different bonding configuration compared to Cu(110), the Cu-O force constant is nearly the same in both cases. If it is assumed that the force constant calculated in the Cu(100) case is a reasonable value for the Cu(110), the best agreement is found for the long bridge site with a predicted vibrational energy of 49.9 meV.

---

1. Summary of paper to be published.
2. J. E. Wachs and R. J. Madix, *Appl. Surf. Sci.* **1**, 303 (1978).
3. J. F. Wendelken and F. M. Propst, *Rev. Sci. Instrum.* **47**, 1069 (1976).
4. J. F. Wendelken, S. P. Withrow, and P. S. Herrell, *Rev. Sci. Instrum.* **51**, 255 (1980).
5. H. Froitzheim, *Electron Spectroscopy for Surface Analysis*, ed. by H. Ibach, Springer-Verlag, New York, 1977.
6. G. Herzberg, *Spectra of Diatomic Molecules*, Van Nostrand Reinhold, New York, 1950.
7. B. A. Sexton, *Surf. Sci.* **88**, 299 (1979).
8. S. P. Holland, B. J. Garrison, and N. Winograd, *Phys. Rev. Lett.* **43**, 220 (1979).
9. A. G. J. DeWitt, R. P. N. Bronckers, and J. M. Fluit, *Surf. Sci.* **82**, 177 (1979).
10. F. H. P. M. Habraken et al., *Surf. Sci.* **86**, 285 (1979).

NO AND NO_2 ADSORPTION AND DISSOCIATION ON Cu(110) STUDIED WITH ELS AND LEED

J. F. Wendelken

The study of NO and other oxide forms of N on metal surfaces is of interest for the wide variety of catalytic reactions that are known to occur with such systems. NO is also of interest because of its structural similarity to CO. However, as is reported here, the behavior of NO on Cu(110) is totally different from that of CO.

The LEED patterns following NO exposure were observed and found to have similarities to the patterns that have been observed following O exposures.[1] An exposure of 20 L of NO at a crystal temperature of 80 K resulted in no additional diffraction beams, but the relative intensities of the integral order beams were altered. Subsequent heating of the crystal to 400 K resulted in a $c(6 \times 2)$ pattern. With further heating, the pattern began to change to a (2×1) structure, but the change was never complete as was the case with O. Exposure of the clean crystal to 20 L of NO at 500 K produced no change in the LEED pattern, whereas a similar exposure to O would produce a sharp (2×1) structure.

Electron energy loss vibrational spectra were obtained for both adsorbed ^{14}NO and ^{15}NO. Results from several exposures of ^{14}NO at a crystal temperature of 80 K are shown in Fig. 2.14. Two energy loss peaks that are associated with NO can be seen. For an exposure of 0.5 L, the losses are at 106 and 195 meV. At 1.2 L, the losses shift slightly to 104 and 194 meV. Nearly identical results were obtained for adsorption of ^{15}NO. In this case, the first loss peak was shifted downward by 2 meV and the second loss peak by 4 meV for all exposures. A third loss peak that appears in the spectra is the result of adsorption of CO that is present in the vacuum chamber. Based on an earlier study of CO on Cu(110),[2] it is estimated that this represents less than 0.05 monolayer of CO coverage. Although greater amounts of CO have been observed to shift energies and intensities in the NO vibrational spectrum,[3] this is not considered a serious problem in this study. An upward shift in the CO vibrational energy from the 260 meV observed for CO alone[2] is in fact useful to this study as discussed below.

The behavior of the relative intensities of the loss peaks as a function of coverage is of particular interest. The low-energy peak develops first at low coverage. Its maximum intensity occurs at about 0.5 L, and then its intensity decreases. The higher

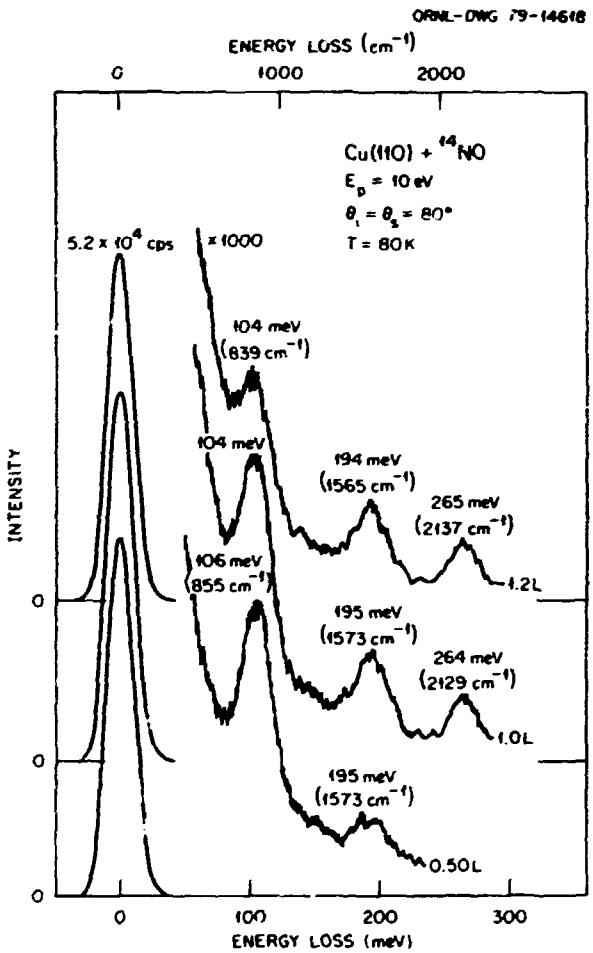

Fig. 2.14 Electron energy loss profiles obtained after several exposures of a Cu(110) surface to ^{14}NO. The loss peak at 264 to 265 meV is the CO stretching vibration which results from background contamination.

energy NO peak develops more slowly, and a maximum intensity is reached at 1.2 L. For greater exposures, both loss peaks vanish. However, the CO loss peak does not concurrently vanish or shift down in energy, so it must be concluded that the NO does not simply vanish from the surface. With an exposure of 20 L a shoulder in the loss profile is observed at about 50 meV. Heating to 500 K to produce the mixed $c(6 \times 2)$ and (2×1) LEED pattern results in a distinct loss peak at 49 meV, which is the energy observed for adsorbed atomic O.[1]

By observing the loss profiles as a function of temperature after an initial exposure of NO of less than 1.0 L, it was found that the NO loss peaks diminished as the temperature was increased and vanished above a temperature of 113 K. However, the residual CO loss peak was again unaffected by this

disappearance of the NO peaks. Thus, the NO must dissociate without desorption when either heated above 113 K or at exposures greater than 1.2 L.

A possible explanation for the behavior of the Cu(110)-NO system was given by results of a recent XPS study of NO on Cu(100) in which it was concluded that N_2O is formed and desorbs at 110 K, leaving behind only O. However, in the present work this possibility may be ruled out for three reasons. First, the gas phase NO stretching energy[4] of 159 meV would require an increase in energy upon adsorption. Second, the energy shifts in the gas phase stretching and bending modes between ^{14}NO and ^{15}NO are 2.5 and 2.1 meV, respectively, and we observed shifts of 4 and 2 meV. Third, the inability of the LEED pattern to shift completely to the (2 × 1) structure indicates the presence of something other than O alone after heating.

Another possible reaction product is NO_2. This possibility was checked by adsorption of NO_2 under the same conditions as for the NO studies. The same loss energies were observed; however, intensities were generally weaker. From this it is concluded that NO_2 reacts to form the same species that result from NO adsorption but with less efficiency.

The explanation of the vibrational spectra which appears most likely is that the NO is adsorbed in a bent configuration. In an IR study concerning nitrosylplatinum complexes,[5] it was found that the NO stretching and bending modes at 212 and 64 meV shifted down in energy by 3.75 and 1.3 meV, respectively, when the isotope was changed from ^{14}N to ^{15}N. This corresponds closely to the presently observed shifts of 4 and 2 meV. In the above study, an NO-Pt vibration was observed at 36 meV. A loss in this energy range might not be resolved with the spectrometer employed in this experiment. If the vibrational mode reported here at 194 meV is assumed to be the NO linear stretching mode and the mode at 106 to 104 meV is assumed to be the bending mode, the observed energies and relative intensities at the two losses can be understood if the molecule is strongly bent (i.e., almost parallel to the surface). Since the energy loss process involves dipole scattering in this case, the dipole selection rule states that only vibrational components perpendicular to the surface should be observed with ELS.[6] Hence, the stretching mode of a strongly bent NO molecule would appear weak and the bending mode would be strong in the energy loss spectrum. The low energy of the stretching mode compared to the gas phase value of 233 meV is an indication of either a multiply coordinated site, severe distortion of the molecule by strong bonding forces, or of both. Distortion is certainly responsible for the observed dissociation at very low temperatures, and site coordination effects are considered likely. The relative intensities of the two vibrational modes as a function of coverage indicate that, with increasing coverage, the molecules stand more upright. At high exposures, the presence of O and perhaps N from dissociation of NO possibly prevents the adsorption of NO in molecular form. Such an occurrence would explain the disappearance of the NO loss peaks, for preadsorption of O alone has been shown to prevent molecular NO adsorption.

---

1. J. F. Wendelken and M.V.K. Ülehla, "Adsorption of O on Cu(110) Studied with ELS and LEED," this report.
2. J. F. Wendelken and M V.K. Ülehla, *J. Vac. Sci. Technol.* **16**, 441 (1979).
3. J. F. Wendelken, "Effect of Co-Adsorption of CO with O and NO on Cu(110) on Observed Vibrational Spectra," this report.
4. D. W. Johnson, M. H. Matloob, and M. W. Roberts, *J. Chem. Soc. D* **40**, 2 11. (1978).
5. B. Miki et al., *Bull. Chem. Soc. Jpn* **47**, 656 (1974).
6. H. Frotzheim, *Electron Spectroscopy for Surface Analysis*, ed. by H. Ibach, Springer-Verlag, New York, 1977.

EFFECT OF CO-ADSORPTION OF CO WITH O AND NO ON Cu(110) ON OBSERVED VIBRATIONAL SPECTRA

J. F. Wendelken

Carbon monoxide is a principal component of the background gas in UHV systems. Since CO is readily adsorbed on many surfaces, it is a frequent contaminant in surface studies. The adsorption of CO on Cu(110) has been studied previously by means of electron energy loss vibrational spectroscopy.[1] Here the effect of CO co-adsorption with O and NO on vibrational spectra is examined.

In the case of co-adsorption with O, it has been reported that at high temperatures ($T > 500$ K) and high CO exposures (10^3 L) preadsorbed O may be removed from Cu(110) by oxidation of the CO and subsequent desorption.[1] The present measurements involve adsorption at 80 K, where atomic adsorption of O and molecular adsorption of CO have been observed.[2,3] Oxygen was adsorbed first (20 L at a temperature of 80 K). The presence of atomic O was indicated by a weak vibrational loss at 49 meV.[2] Then, an exposure of 20 L of CO was made. The CO stretching mode vibration appeared at 264 meV, which is 4 meV higher than that observed for CO alone on Cu(110).[3] This is quite interesting in view of the previous observations[3] that the CO vibration

displayed a shift of only 2 meV from 258 meV at low coverage to 260 meV at high coverage. Hence, CO is more strongly affected by O than by neighboring CO molecules. In a second experiment, the Cu(110) surface was first exposed to 20 L of O_2 at $T = 270$ K and then annealed at 500 K to produce a sharp (2×1) LEED pattern. The target was then cooled to 80 K and exposed to 20 L of CO. Again, the CO stretching mode was observed at 264 meV. The Cu-O vibrational mode, which is better resolved with the (2×1) surface structure, appears to be shifted upward by 1 to 50 meV, although this shift is too small to be measured reliably with present instrumentation. No shift in vibrational energy has been observed as a function of O coverage alone.[2] In both cases, the intensity of the O loss peak is little affected by the CO adsorption, whereas the CO adsorption is seen to be inhibited by the O preadsorption. Hence, a much smaller background exposure of CO does not appear to present difficulties with studies of O on the surface.

The interaction of CO with NO on the Cu(110) surface produced somewhat stronger effects. For this experiment, the Cu(110) surface at 80 K was first exposed to 0.5 L of CO. This results in approximately a 0.25 monolayer coverage.[3] Then 0.5 and 1.0 L exposures of NO were made, also at $T = 80$ K. The CO stretching vibration loss intensity was reduced by 20% for the first exposure of NO and by 30% for the second. The energy of this loss was shifted upward again to 263 meV, almost the same value as for O coadsorption. The NO stretching and bending modes which are observed with NO adsorption alone[4] at 195 and 106 meV, respectively, were shifted to 190 and less than 100 meV for the 0.5 L NO exposure. The intensity of the NO bending mode is also seen to be suppressed by the presence of CO. At an exposure of 1.0 L of NO, the intensity of the bending mode without pre-exposure of CO is almost twice that of the stretching mode. With the CO exposure, the bending mode almost vanishes from the spectrum, indicating that the NO molecule is more perpendicular to the surface.[4] Thus in studies of molecular NO adsorption, it is important to reduce CO contamination as much as possible.

1. F.H.P.M. Habraken et al., *Surf. Sci.* **88**, 285 (1979).
2. J. F. Wendelken and M.V.K. Ulehla, "Adsorption of O on Cu(110) Studied with ELS and LEED," this report.
3. J. F. Wendelken and M.V.K. Ulehla, *J. Vac. Sci. Technol.* **16**, 441 (1979).
4. J. F. Wendelken, "NO and NO_2 Adsorption and Dissociation on Cu(110) Studied with ELS and LEED," this report.

EFFECT OF ORDERED O OVERLAYERS ON SPIN-POLARIZED LEED FROM W(001)

J. F. Wendelken[1] J. Kirschner[2]

In the study of both clean and adsorbate covered single-crystal surfaces, LEED has become an accepted and useful tool. However, additional information may be gained by examining the spin dependence of the scattered electrons in such experiments,[3] particularly for large-Z materials where spin-orbit coupling leads to strong polarization effects. Such a spectroscopy as spin-polarized LEED (SPLEED) was recently made more practical by the development of a double-scattering LEED spin detection apparatus.[4] We report here the application of this apparatus to a study of the effect of the chemisorption of ordered overlayers of O on W(001) on the observed polarization intensities.

The adsorption of O on W(001) is known to produce a large variety of surface structures[5] as a function of coverage and thermal treatment. These structures have been attributed to a reconstruction process at the surface in which the W atoms undergo large displacements.[6] Since spin-orbit coupling is strongest for large-Z atoms, measurements of the spin polarization of electrons scattered from surfaces with relatively light adsorbates should be preferentially sensitive to the structure of the substrate surface atoms.

In this study, we have observed the polarization dependence of electrons diffracted from W(001) with $p(4 \times 1)$ and $p(2 \times 1)$ O overlayers as well as for the clean surface. The measurements of both intensities (I) and polarization (P) consist of specular beam rotation diagrams [$I(\phi)$ and $P(\phi)$ for V = constant] and energy profiles [$I(V)$ and $P(V)$ at ϕ = constant].

The W surface was cleaned by standard procedures that involve first heating the crystal to a temperature of ~1500 K in a 5×10^{-6} Pa O atmosphere to remove C. Subsequently, the crystal is flashed several times to 2700 K in high vacuum to remove O. During the measurements, the surface is then maintained clean by flashing every 15 to 30 min to a temperature of 2100 K to remove CO. The $p(4 \times 1)$ surface structure was formed by an exposure of 0.7 L of O with the crystal at room temperature. The $p(2 \times 1)$ structure was then formed by heating the crystal to about 1100 K. Both structures exist in two domains rotated by 90° from each other.

The measurements reported here were all made with the polar angle θ of $14 \pm 0.5°$ from the surface normal. This angle was chosen because of the exis-

tence of a strong polarization feature that is not highly sensitive to the polar angle for the clean surface at 77 eV for $\phi = 0°$. In Fig. 2.15, both $P(V)$ and $I(V)$ profiles are shown for $\phi = 0$ and 45°. In the case of $\phi = 0°$ (Fig. 2.15*a*) the strong negative polarization feature of the clean surface at 77.2 eV is greatly reduced when the $p(2 \times 1)$ O structure is formed. At the same time a new positive polarization feature develops in the 70- to 75-eV range. Corresponding changes are also observed in the intensity profiles. In particular, the loss of the distinct minimum near 77.2 eV is noted because strong polarization features are often, though not always, associated with minima in the intensity profiles.[7] In the case of $\phi = 45°$ (Fig. 2.15*b*) strong differences are seen in the polarization profiles for the clean surface and the surfaces with $p(4 \times 1)$ and $p(2 \times 1)$ O structures. The intensity profiles also show large changes, but these are primarily a shift in relative intensities rather than a complete alteration of structure. For the $p(4 \times 1)$ and $p(2 \times 1)$ surface structures, totally new polarization features are displayed near 102 and 67 eV, respectively.

Intensity rotation diagrams have recently been successfully applied to the clean W(001) surface[8] and are seen to have several advantages. Data obtained at constant energy of primary electrons simplifies the theoretical considerations because the inner potential is constant. Also, it is helpful that experimental results are obtained under conditions such that instrumental efficiency is constant. Since these same advantages will apply in the case of SPLEED measurements, polarization rotation diagrams were incorporated in this study. Figure 2.16 shows several sets of such $P(\phi)$ and $I(\phi)$ profiles. In Fig. 2.16*a* profiles for the clean and $p(2 \times 1)$ surfaces are compared at an energy of $E_p = 55$ eV. Note that while there is qualitatively little change in the intensity profiles, there is a total loss of clean surface polarization feature at $\phi = 45°$. Figure 2.16*b* shows rotation diagrams for energies at which new polarization features are created by the $p(2 \times 1)$ structure. Note that for the two energies chosen, $E_p = 66.1$ and 67.2 eV, which represent the positive and negative extremes in polarization, the intensity profiles show very little difference. For the clean surface, the profiles are nearly the same at both energies, so only the profile for 67.2 eV is shown. The asymmetries that appear in the rotation diagrams may result from small instrument misalignments or may be a result of a two-domain structure.

Measurements were also made at O exposures beneath and above the required for the $p(2 \times 1)$. After

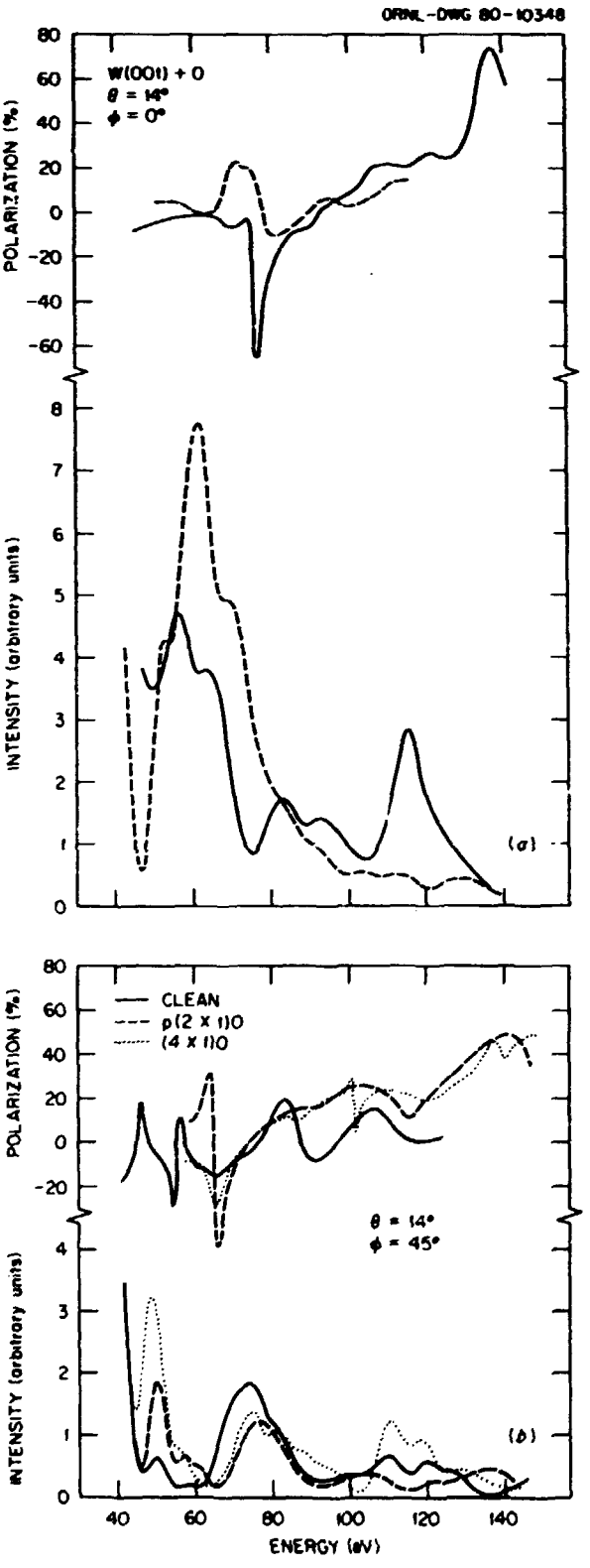

Fig. 2.15. Polarization and intensity as a function of energy for clean, $p(4 \times 1)$ O and $p(2 \times 1)$ O surface structures.

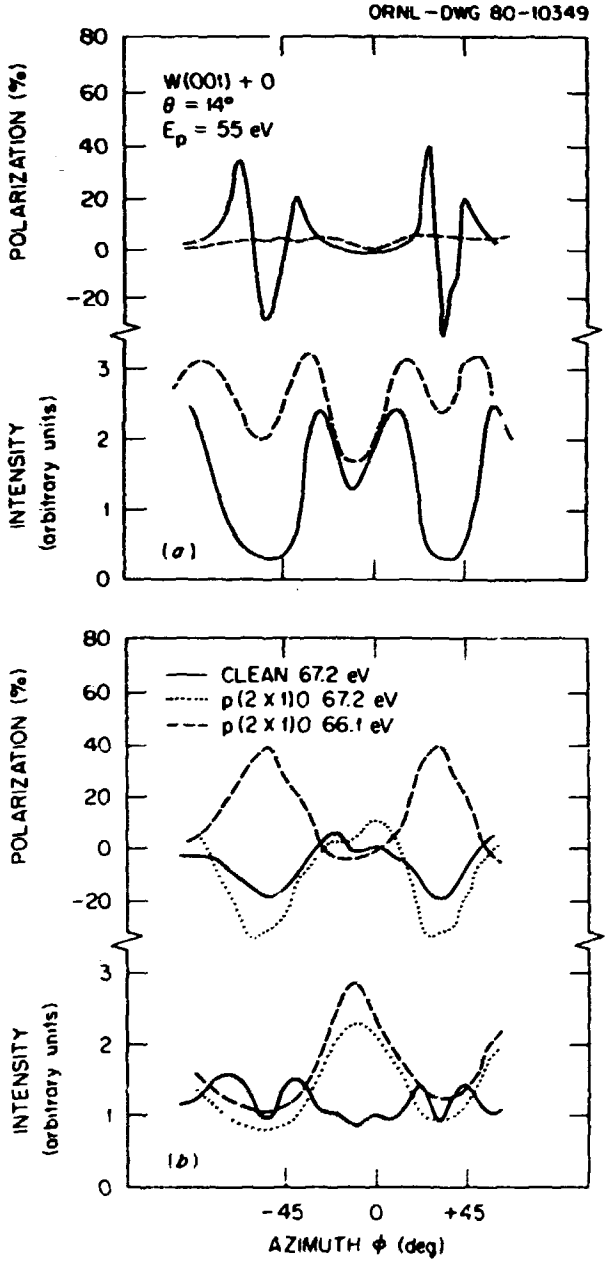

Fig. 2.16. Polarization and intensity rotation diagrams for clean and $p(2 \times 1)$ O surface structures.

an exposure of 2 L followed by annealing at 1300 K, the negative polarization maximum at $E_p = 67.2$ eV and $\phi = 45°$ was reversed to become the positive maximum of polarization with no negative polarization remaining in this feature. At very low exposures, such as 0.1 L, an increase in positive polarization is observed at 72 eV and a negative feature develops at 67 eV for $\phi = 0°$. These features are greatly diminished when the exposure is sufficient for the development of the $p(2 \times 1)$. Although the LEED patterns also change as a function of exposure, the changes are again primarily a change in relative intensities. The sensitivity of the polarization profiles as a function of exposure provides hope that they will be a very sensitive probe of the reconstruction process.

It is of interest to compare these results with the only other published polarization study on adsorbate systems by Riddle et al.[9] In this study they examined the effect of disordered layers of O and CO and ordered layers of CO on $P(V)$ profiles at $\theta = 13°, \phi = 0°$ for W(001). We also looked at the effect of a disordered layer of O and found good agreement with the published results. The surprise comes with the comparison of our data for ordered overlayers of O to the published data for ordered overlayers of CO. While the results look quite different in the case of the saturated $p(2 \times 1)$ oxygen and $c(2 \times 2)$ CO structures, the results obtained for a very low exposure (0.1 L) of O followed by annealing at 1300 K look very similar to the CO results that required a 20-L exposure followed by annealing at 1150 K. Perhaps a small percentage of the CO is dissociated, and a similar reconstruction is caused in both cases by the O.

It is not possible at this time to make a definitive statement as to whether polarization measurements are more sensitive to reconstructive adsorption than intensity measurements. However, in the data obtained the changes in the polarization features are often more distinct and sensitive than the changes in the intensity features. Certainly, the polarization measurements are complementary to the intensity measurements, and a combined analysis of data of both types should increase the reliability of surface structure determinations.

---

1. This research conducted while on foreign assignment at the Institut für Grenzflachenforschung und Vakuumphysik, Kernforschungsanlage, Jülich, Germany.
2. Institut für Grenzflachenforschung und Vakuumphysik, Kernforschungsanlage, Jülich, Germany.
3. R. Feder, *Surf. Sci.* **63**, 283 (1977).
4. J. Kirschner and R. Feder, *Phys. Rev. Lett.* **42**, 1008 (1979).
5. E. Bauer, H. Poppa, and Y. Viswanath, *Surf. Sci.* **58**, 517 (1976).
6. P. J. Estrup and J. Anderson, *Proceedings of the 27th Physical Electronics Conference*, 1967.
7. J. Kessler, *Polarized Electrons*, Springer, Berlin, 1976.
8. J. Kirschner and R. Feder, *Surf. Sci.* **79**, 176 (1979).
9. T. W. Riddle et al., *Surf. Sci.* **82**, 511 and 517 (1979).

DEVELOPMENT OF RETRACTABLE, REAR-VIEWING LEED/AES SYSTEMS[1]

J. F. Wendelken S. P. Withrow
P. S. Herrell[2]

Display-type LEED systems with AES capabilities have been added recently to two different UHV experimental chambers. In both cases, the intrinsic design of existing equipment prevented the use of conventional, commercially available LEED systems. In one chamber that houses a high-resolution electron spectrometer, the target is mounted in a fixed position on a large mechanical base that blocks the view of the front side of a LEED screen. The second experimental apparatus is a positive ion scattering system in which the target manipulator is necessarily large and presents the same viewing problem. In both systems a normally located LEED screen was also found to interfere with other measurements.

These problems were solved by constructing two LEED/AES systems that use phosphor coatings on glass for display screens, thus making it possible to view the screens from behind (opposite side of the glass from the phosphor). In addition, the systems are mounted on large bellows-sealed drive mechanisms that allow them to be retracted when not in use. The design of the LEED system used with the high-resolution electron spectrometer is shown in Fig. 2.17. The retracting mechanism is driven by a large threaded nut and has a total travel of 20 cm. Atmospheric pressure, which makes turning the nut difficult, is counterbalanced by two air pistons. The second LEED system, shown in Fig. 2.18, is driven by air pistons alone and has a travel of 15 cm. The two LEED systems are nearly identical otherwise. Both use commercially available electron guns to which shields for blocking light from the cathode have been added. The glass screens are cut from flasks. They were coated first with tin oxide to make them conducting, and then thin, nearly transparent layers of phosphor were added by settling from solution. The phosphors appear as bright from the back side as from the front side, and due to the absence of light-

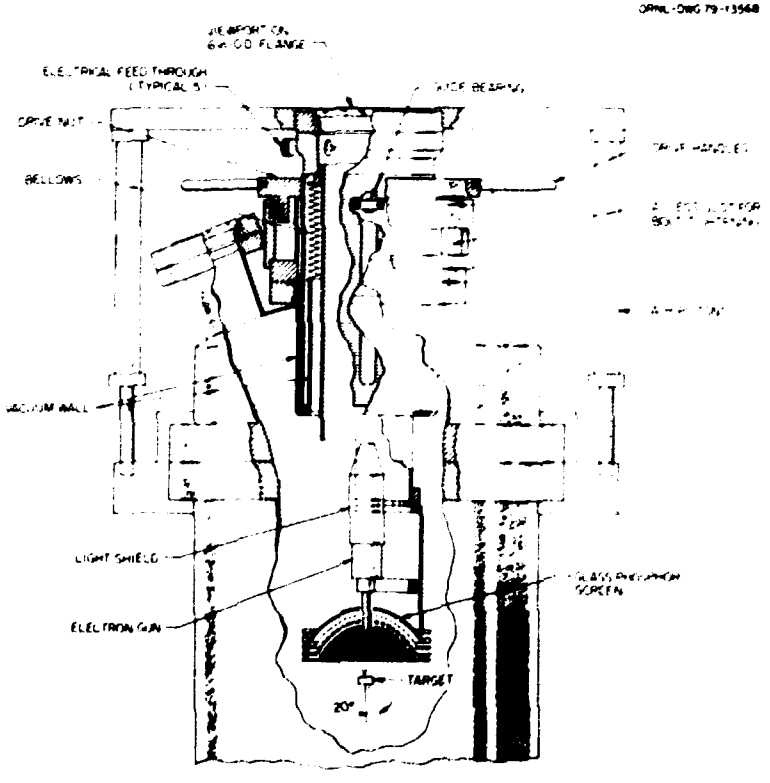

Fig. 2.17. Rear-viewing LEED system as mounted on high-resolution electron spectrometer system. The retracting mechanism is driven with a double threaded screw and assisted by pneumatic pistons.

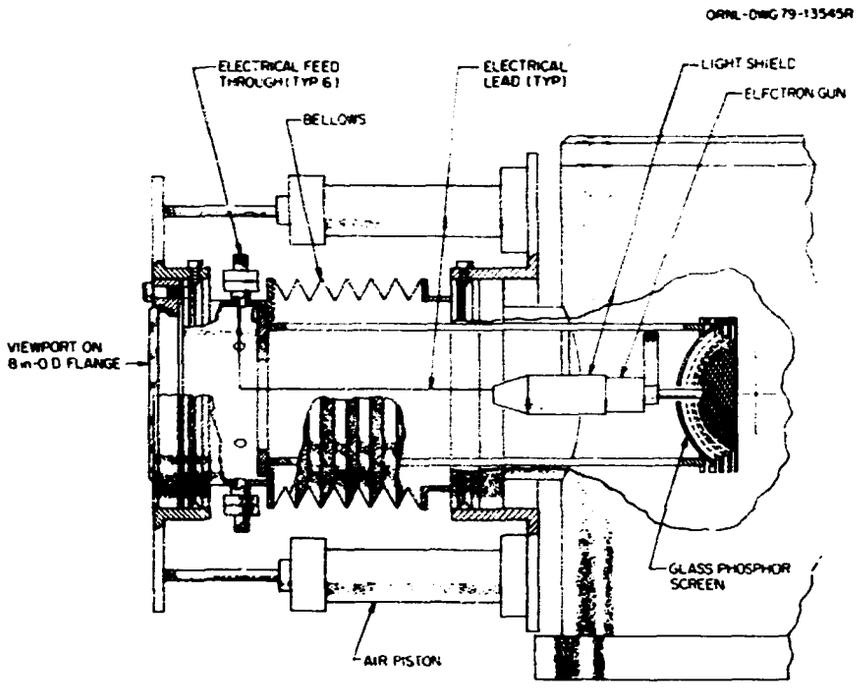

Fig. 2.18. Rear-viewing LEED systems as mounted on positive ion scattering apparatus. The retracting mechanism is driven totally by pneumatic pistons.

blocking grids when viewed from the back side, the LEED patterns actually appear brighter. The four grids in front of the screens were obtained commercially and permit use of the LEED systems for AES.

---

1. Summary of paper: *Rev. Sci. Instrum.* 51, 255 (1980).
2. Plant and Equipment Division, ORNL.

PLASMA MATERIALS INTERACTIONS

UHV SAMPLE TRANSFER SYSTEM

R. A. Zuhr J. B. Roberto

The plasma-wall interaction in tokamaks has been studied on ISX using accelerator-based techniques such as Rutherford backscattering and nuclear reaction analysis.[1-3] These techniques rely on the exposure of deposition probe samples in the plasma edge to accumulate both plasma and impurity fluxes that can later be quantified in the laboratory. To make such exposures, a mechanical system is required that can insert the probe into the vacuum vessel, position it accurately during the discharge, and then remove it from the vessel without compromising the vacuum integrity of the machine. Additional features, such as the ability to make electrical connections or to rotate the probe for multiple sample exposures and time-resolved experiments, are also desirable. In certain cases, it may be necessary to transport the exposed probe from the tokamak to the analysis chamber under UHV conditions without exposure to the atmosphere. Such a system has been designed and built and is currently in use on ISX-B.

The design of the system was based on the use of two concentric tubes, the outer one to hold a sample shield and the inner one to carry the rotating samples. The tubes slide together into and out of the plasma, with the rotating drive motor mounted directly on the outer end of the tubes to minimize the rotational inertia presented to it and to eliminate backlash in the drive train. The major components of the transfer system are a modified 60 L/s ion pump that is mounted coaxially around the sample support tubes and can be operated from either ac power or batteries, a long welded bellows that allows samples to be moved more than 75 cm from the transfer system into the tokamak, and a stepping motor that can be programmed to rotate the samples a specified amount either during a discharge or between discharges. In accordance with the operation criteria for ISX, the system is automated so that the probe

will be withdrawn and the isolating valve will be closed in the event of a vacuum failure in the tokamak. There are no sliding seals in the system. The linear motion is sealed by the long bellows, and the rotary motion is transmitted through a bellows-type UHV rotary feedthrough. Viton sealed gate valves are used to close off both the system and the tokamak when the unit is not in position. Base pressure of the transfer system is 10^{-7} to 10^{-8} torr without baking.

This transfer system gives the capability of exposing samples up to 8 cm in diameter at any position between the vacuum wall and the limiter radius. The samples may be cleaned prior to insertion, exposed in the tokamak, removed, and analyzed at a remote facility under continuous high vacuum conditions without exposure to the air. Provisions are also included for multiple sample operation, time-resolved deposition measurements, and electrical measurements. The system has been used successfully for measuring the saturation behavior of impurity depositions[4] and D trapping[5] and is now being used for time-resolved measurements of both impurity and D fluxes in the plasma edge.

1. R. A. Zuhr et al., *J. Nucl. Mater.* **85/86**, 979 (1979).
2. S. P. Withrow et al., *Solid State Div. Prog. Rep., Sept. 30, 1978*, ORNL-5486, p. 50.
3. B. R. Appleton et al., *Solid State Div. Prog. Rep., Sept. 30, 1978*, ORNL-5486, p. 51.
4. R. A. Zuhr, S. P. Withrow, and J. B. Roberto, "Impurity Transport in the Plasma Edge of ISX-B," this report.
5. S. P. Withrow, R. A. Zuhr, and J. B. Roberto, "D Profiling in the Plasma Edge of ISX-B," this report.

IMPURITY TRANSPORT IN THE PLASMA EDGE OF ISX-B[1]

R. A. Zuhr S. P. Withrow
J. B. Roberto

The performance of magnetic fusion devices depends critically on the impurity content of the plasma. Even small concentrations of heavy elements (<0.1% for W) can preclude the achievement of break-even conditions in tokamaks. The impurities are introduced as a result of interactions of the plasma with the wall and the limiter. In this work, we have used deposition probe measurements of retained impurities as a means of studying impurity transport in the limiter shadow of ISX-B. Measurements have been made of the species and quantities of impurities present, their radial distributions behind the limiter, and their behavior as saturation levels are approached. Simultaneous measurements of retained D made under the same conditions are discussed elsewhere in this report.[2]

Single-crystal Si samples were exposed to varying numbers of tokamak discharges in the plasma edge of ISX-B by use of a compact sample insertion system.[3] The impurities retained on the samples were determined quantitatively at the Solid State Division accelerator facility using Rutherford ion backscattering of 2.5-MeV ^{4}H ions. The channeling phenomenon was used to reduce background from the Si substrate. The principal impurities deposited on the probes were the components of stainless steel, O, and C. In addition, lesser amounts of S (associated with arcing) and Pb (from soft solder joints) were detected. The amounts retained per discharge of these and other impurities at 2 cm behind the limiter for a typical ohmically heated D plasma are given in Table 2.1.

Measurements of deposition rates were made as functions of radius behind the limiter (impurity profiles) and the number of discharges to which the samples were exposed (saturation measurements). Combined saturation and radial profile results for O are shown in Fig. 2.19. Results for ohmically and beam heated (350 kW) D discharges are given. It is clear from Fig. 2.19 that the accumulation of O on the probe is saturating after a few discharges. After four discharges, 90% of the final O concentration has been reached for both injected and noninjected plasmas. This is in marked contrast to the behavior of Cr and Fe, which is illustrated in Fig. 2.20. Here the Fe concentration, with and without injection at 2.5 cm behind the limiter, is plotted against the number of discharges. For both Cr and Fe the deposition increases linearly with exposure throughout the range investigated, indicating that erosion is not an important factor for these metals at this radius. Oxygen, on the other hand, is being removed at a rate

Table 2.1. Impurity concentrations per discharge, cm^{-2}

C	3.0×10^{14}
N	8.2×10^{13}
O	4.3×10^{15}
S	2.0×10^{13}
Cr	1.1×10^{14}
Fe	3.0×10^{14}
Ni	2.3×10^{13}
Pb	2.1×10^{11}

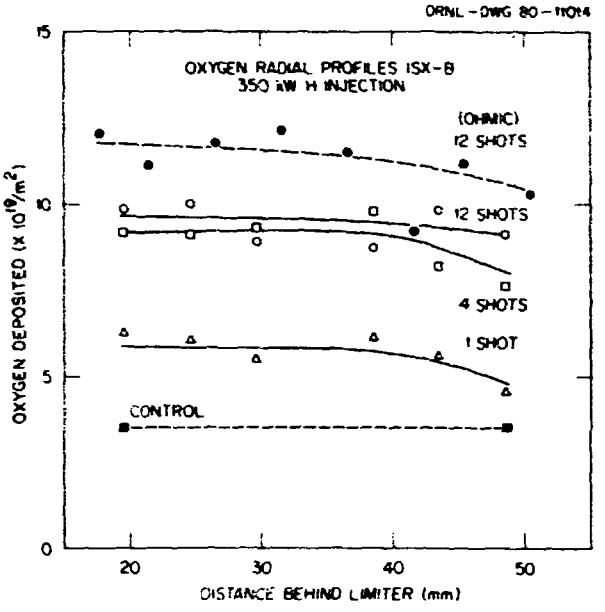

Fig. 2.19. Retained O as a function of position and number of discharges for Si probes exposed in ISX-B with and without 350 kW H neutral beam injection.

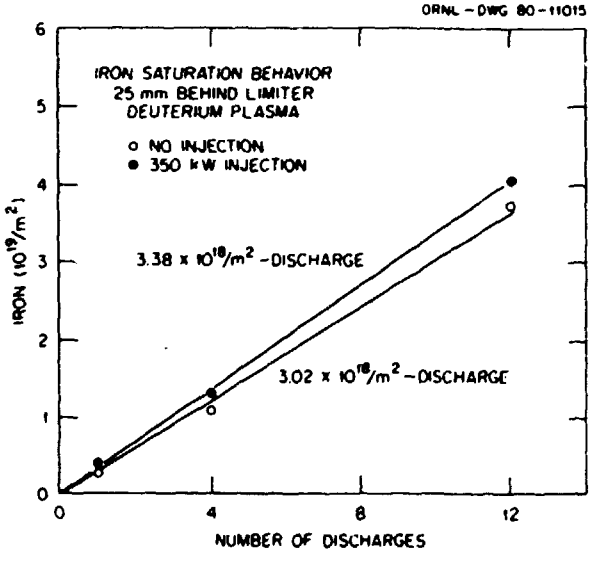

Fig. 2.20. Retained Fe as a function of number of discharges for Si probes exposed in ISX-B with and without neutral beam injection.

of ~4 × 10^{15}/cm^2-discharge after several shots, indicating that a different mechanism is operating. In particular, chemical sputtering of the O by atomic H may be taking place. An alternative explanation is that at high O concentrations (~1 × 10^{16}/cm^2), there are no longer any sites available at which incident O can be trapped.

If an initial sticking coefficient of unity is assumed, incident fluxes of Fe and O can be determined from these data. In turn, if an assumption of ion temperature is made, densities of these materials in the plasma edge can be estimated. Results for 25-eV ion temperatures are given in Table 2.2 for injected and ohmically heated discharges. The modest changes in Fe and O densities for ohmically and beam heated plasmas indicate that neutral injection is not appreciably altering plasma edge conditions or carrying large amounts of heavy impurities into the plasma.

Table 2.2. Fe and O fluxes and densities

		Ohmic	Neutral beam injected
Flux	Fe	3.0 × 10^{14}	3.4 × 10^{14} cm^2-discharge
	O	4.3 × 10^{15}	2.4 × 10^{15} cm^2-discharge
Density	Fe	5.7 × 10^9	6.5 × 10^9 cm^3
	O	4.4 × 10^{10}	2.5 × 10^{10} cm^3

The estimated impurity densities can also be compared with results from optical profiles within the plasma. For Fe, optical measurements give values of ~6 × 10^8/cm^3 without injection and ~1.8 × 10^9/cm^3 with injection inside the limiter radius. The estimated density of O for an ohmically heated discharge is ~1 × 10^{11}/cm^3. These rates are substantially lower than our deposition probe results and indicate that most of the Fe and O in the limiter shadow is not reaching the plasma interior.

Measurements have been made of impurity densities, profiles, and saturation behavior in the plasma edge of ISX-B for both ohmically heated and neutral beam injected discharges. From these measurements, we can infer conclusions about erosion processes, the effects of neutral beam injection, and the coupling of impurities between the plasma and the edge region. Time-resolved measurements currently in progress should clarify further the conditions prevailing in the limiter shadow.

1. Summary of paper to be published.
2. R. A. Zuhr and J. B. Roberto, "UHV Sample Transfer System," this report.
3. S. P. Withrow, R. A. Zuhr, and J. B. Roberto, "L_α Profiling in the Plasma Edge of ISX-B," this report.

D PROFILING OF SAMPLES EXPOSED IN THE PLASMA EDGE OF ISX-B

S. P. Withrow R. A. Zuhr
J. B. Roberto

Plasma particles that strike the limiter and first wall of a tokamak can have significant effects on plasma performance due to interactions that result in particle recycling and impurity introduction. In order to assess the potential impact of these phenomena, it is necessary to know the density and velocity distributions of plasma particles in the boundary region. This report gives results obtained on the ISX-B tokamak from experiments utilizing a deposition probe diagnostic for D. This work represents a continuation of similar measurements on ISX-A.[1]

Amorphous and single-crystal Si samples were exposed to 1, 4, and 12 tokamak discharges at locations varying between 10 and 50 mm behind the limiter radius facing the electron drift direction. The exposed samples were then transferred to the Solid State Division accelerator facility for analysis. Total D retention in the amorphous Si was determined using the $D(^3He,p)^4He$ nuclear reaction by detecting the emitted protons in a surface barrier detector. Depth profiles of D were also determined from the energy spectrum of ^4He produced in the same nuclear reaction. Estimates of the incident D energy were made by comparisons of the D concentrations and depth profiles with theoretical predictions. In addition, Rutherford backscattering of ^4He was used to monitor the damage to single-crystal Si as a result of D bombardment. The depth distribution of the damage provides another measure of incident D energy.

Figure 2.21 shows D radial profiles for samples exposed to 1, 4, and 12 discharges. The maximum absolute concentration retained after 12 shots is $2.3 \times 10^{20}/m^2$ at 20 mm from the limiter. The concentration of D retained is seen to be approximately two-thirds saturated after one discharge. The amount retained, however, decreases with distance from the plasma. Since maximum concentrations obtainable for D retention in Si depend on incident energy, this decrease in saturation concentration suggests a decrease in D energy away from the limiter. For discharges with 350-kW neutral beam injection, qualitatively similar results were obtained with slightly greater saturation levels obtained 20 mm behind the limiter and approximately twice the saturation values at 50 mm.

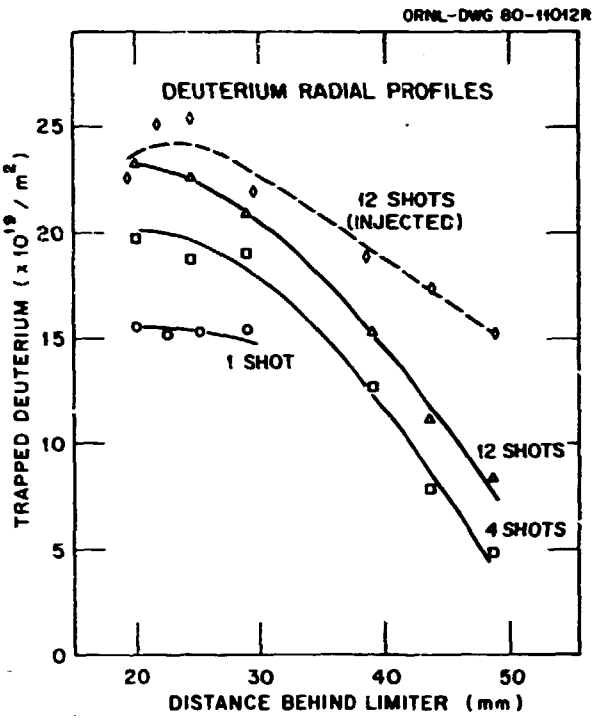

Fig. 2.21. D radial profiles for 1, 4, and 12 discharges

The D edge temperature was estimated using three methods—comparison of D depth profiles with theoretical profiles generated using the MARLOWE binary collision code,[2] comparison of the damage in single-crystal Si to the mean D range predicted by the MARLOWE code, and comparison of retained D concentrations as a function of exposure to trapping curves.[3] Table 2.3 shows the FWHM of the measured D profiles and the damage depth in the single-crystal Si. Data are presented for both 1 and 12 shots. The damage apparently results from D bombardment, as can be seen by the agreement in damage and D depths.[4] The experimental widths increase with exposure, reflecting dose-dependent straggling and saturation. Theoretical data for the FWHM, mean depth, and mean maximum range obtained using MARLOWE for 50-, 150-, and 300-eV D incident on Si are given for comparison.

The D and damage depths (Table 2.3) are consistent with incident D energies on the Si samples of 150 to 300 eV. From concentration vs exposure data, energies between 50 and 150 eV are predicted assuming normal incidence of monoenergetic D, whereas for an incident cosine angular distribution with a Maxwellian velocity distribution, plasma temperatures below 50 eV are obtained. The presence

Table 2.3. Comparison of D and damage depth profiles to MARLOWE code predictions

	Experiment		Theory			
	D profile FWHM (Å)	Damage depth (Å)	Energy (ev)	FWHM (Å)	Range (Å)	Mean depth (Å)
1 Shot	92	95	50	15	23	18
12 Shots	134	130	150	35	60	49
			300	135	115	95

of a sheath potential is consistent with the normal incidence monoenergetic case, which also gives the best agreement with the D energies derived from damage and depth profiles. For plasmas heated with neutral beam injection (increasing central electron temperatures from 1050 to 1450 eV), results similar to those without injection are found; this fact indicates that the energy of D in the boundary layer does not reflect very strongly the increase in central plasma temperatures.

1. S. P. Withrow et al., *Solid State Div. Prog. Rep., Sept. 30, 1978*, ORNL-5486, p. 50.
2. M. T. Robinson and I. M. Torrens, *Phys. Rev. B* 9, 5008 (1974).
3. S. A. Cohen and G. M. McCracken, *A Model for Hydrogen Isotope Backscattering, Trapping, and Depth Profile in C and a-Si*, PPL-1529, Princeton (1979).
4. R. A. Zuhr et al., *Solid State Div. Prog. Rep., Sept. 30, 1978*, ORNL-5486, p. 53.

Al TRANSPORT IN THE T-12 POLOIDAL DIVERTOR

S. P. Withrow N. N. Brevnov[1]

The removal of impurities (and ashes) from a tokamak reactor can be achieved by applying a suitable magnetic field arrangement, called a divertor, which guides the outermost layers of the plasma out of the main reaction region to where the impurities can be collected. Some initial measurements have been made on the transport of particles in the poloidal divertors on the T-12 tokamak at Kurchatov Institute, Moscow, USSR.

Aluminum was injected into the edge of the plasma during the stable portion of a plasma discharge and subsequently collected on Si deposition probes positioned at suitable locations in the divertors. Quantitative measurements of Al and other elements collected on the probes were made at the positive ion accelerator facility in the Solid State Division using Rutherford backscattering spectroscopy.

The results show a direct dependence of the retained Al on the divertor configuration. Aluminum output into the upper and lower divertors is nearly symmetric with a symmetric magnetic field arrangement. A substantial fraction of the Al can be output predictably into either divertor by a suitable change in the fields. The concentration of Al shows a strong positional dependence. Additional work is necessary to relate this result to tokamak parameters. Because of difficulties in quantifying the Al input, the absolute levels of Al cannot be related to divertor efficiency or directly compared as a function of field configuration.

In addition to Al, significant amounts of O (of the order ten times the Al collected) and Fe were detected on the deposition probes. These impurities tended to show the same spatial distributions as the Al, although in some cases concentrations relative to the Al concentration differed substantially.

1. Kurchatov Institute, Moscow, USSR.

MEASUREMENT OF THE DENSITY AND VELOCITY DISTRIBUTION OF NEUTRAL Fe IN THE PLASMA EDGE OF ISX-B BY LASER FLUORESCENCE SPECTROSCOPY[1]

H.-B. Schweer[2] W. R. Husinsky[3]
J. B. Roberto

The presence of low concentrations of impurity atoms in the hot plasma of controlled fusion devices is detrimental to the energy balance of the plasma. In tokamaks, the processes responsible for the introduction of impurities may include evaporation, sputtering, and arcing from both the limiter and the wall. An understanding of the origin, time, and spatial development of impurity atoms under various

plasma conditions and for various wall and limiter materials is essential for the operation of present day tokamaks and for the planning of future devices.

Laser fluorescence spectroscopy has been proposed[4] as a method for in situ measurement of the particle density and velocity distribution of impurities in the plasma edge of tokamaks with high sensitivity and excellent space and time resolution. In the present work, we report some of the first laser fluorescence measurements of impurities in a tokamak. The density and velocity distribution of neutral Fe in the plasma edge of ISX-B was determined as a function of discharge time for various distances from the wall. The population density of the a^5D levels of the ground state of Fe was also measured and interpreted in terms of a temperature for thermal neutral Fe.

The laser system consisted of a flashlamp-pumped dye laser which produced 700 W of frequency-doubled output at 300 nm in a 0.5-ns pulse. The laser beam entered the tokamak along a major radius 30 cm above the midplane and about 45° toroidally from the limiter. The fluorescence radiation was detected off-resonance through a 10-cm viewing port on top of the vacuum vessel using an interference filter and photomultiplier. The laser could be operated broadband (~10 pm) to excite all particles for density measurements and narrowband (~0.6 pm) for measurements of Doppler broadening with a sensitivity of 6×10^4 cm/s.

Results of density measurements for neutral Fe at 5.5 and 10.5 cm from the wall as a function of time during the discharge are shown in Fig. 2.22. Also shown in the figure is the temporal behavior of the plasma current (which was ramped down beginning at 160 ms), magnetic field, and optical background to the detection system. Two distinct peaks in the Fe density at 5.5 cm are observed, a smaller peak at the beginning of the discharge and a large peak at the end about 30 ms beyond the initialization of current rampdown. This latter peak does not correlate with the optical background peak at 160 ms, which presumably signals the collapse of the plasma outward through the observation volume. Laser fluorescence measurements 10.5 cm from the wall lead to similar Fe densities at the end of the discharge, but no corresponding peak is observed at the beginning. These results suggest that the initial peak is associated with proximity to the wall and that the accumulation of Fe in the edge may be dominated by transient effects.

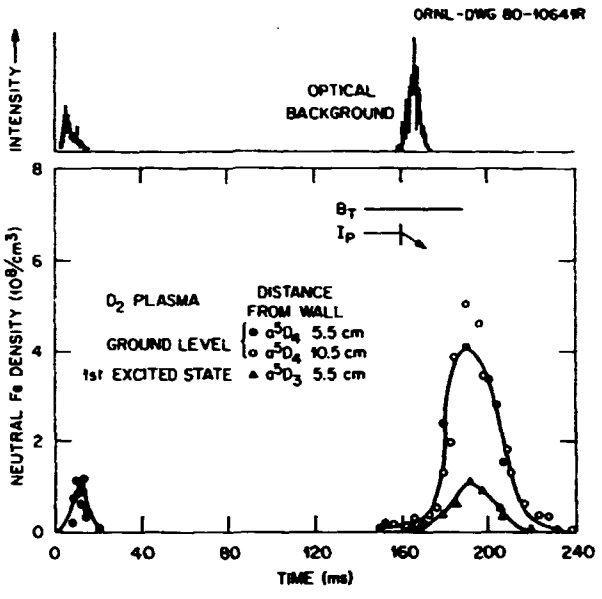

Fig. 2.22. Neutral Fe density in ISX-B at 5.5 and 10.5 cm from the wall as a function of discharge time. The temporal behavior of the optical background, toroidal field, and plasma current is also shown.

Estimates of the temperature of neutral Fe at 5.5 cm from the wall were made from Doppler broadening measurements and from the ratio of Fe in the first excited state to Fe in the ground state (Fig. 2.22). Both determinations suggest thermal velocities (~500 K) for Fe in the plasma edge of ISX-B. A substantial sputtering component from the wall would be characterized by Fe energies of 1 to 2 eV and can be ruled out for the peak at the end of the discharge.

Overall, the results demonstrate the application of laser fluorescence spectroscopy for measurements of impurity atom densities and velocities in tokamaks with sensitivities of 10^6 atoms/cm^3 and 0.1 eV for Fe. The technique has excellent space and time resolution and is independent of the plasma. Further measurements using a high-resolution cw dye laser are under way.[5]

---

1. Summary of paper to be published.
2. Guest scientist from Institut für Festkorperförschung, Kernforschungsanlage, Jülich, Germany.
3. Guest scientist from Technische Universität Wien, Vienna, Austria.
4. A. Elbern, D. Rusbüldt, and E. Hintz, p. 475 in *Plasma-Wall Interaction*, Pergamon, New York, 1977.
5. W. R. Husinsky and J. B. Roberto, "Development of a CW Laser Fluorescence System," this report.

SURFACE EROSION IN THE PLASMA EDGE OF ISX-B[1]

J. B. Roberto R. A. Zuhr
S. P. Withrow

An understanding of erosion processes in tokamaks is essential for developing criteria for the selection of wall and limiter materials. In this work, erosion yields have been determined for Au thin films exposed to tokamak discharges in the plasma edge of ISX-B. This represents the first systematic study of erosion in a tokamak and presents interesting possibilities for determining erosion characteristics and mechanisms.

Samples consisting of ~3 nm Au deposited on Si substrates were exposed to 20 and 46 D discharges at various locations in the limiter shadow of ISX-B. Erosion of the Au films, as well as accumulation of D, O, Fe, and damage on the samples, was measured using ion scattering, channeling, and nuclear reaction techniques.[2,3] Erosion rates of ~0.05 to 0.1 nm per discharge were observed for samples facing the plasma and the torodial field lines at ~2 cm behind the limiter. The total erosion increased with the number of discharges and decreased to zero as the wall was approached. Scanning electron microscopy revealed no evidence of arcing on the exposed samples.

The radial dependence of the erosion, as well as the retained D, O, and Fe for samples facing the field lines, is shown in Fig. 2.23. The erosion correlates well with the retained D but not with O or Fe. Because the D on the samples saturates in a few discharges, the D radial dependence reflects a decreasing incident energy as the wall is approached.[2] Sputter yields of 5×10^{-3} are consistent with the observed erosion at 2 cm from the limiter for D fluences of 10^{17} cm^{-2} per discharge. These yields would require average incident D energies (including sheath acceleration) of ~250 eV. This fluence-energy combination is slightly higher than recent estimates of D fluences and energies in ISX-B based on saturation measurements.[2]

The overall interpretation of the results is consistent with a dominant role for D sputtering for erosion near the limiter radius with negligible erosion at the wall. We cannot, however, rule out the possible contribution of heavy impurity sputtering (particularly O) to the erosion yields. We are currently repeating the erosion experiment in an H plasma where the increased sputtering threshold (H vs D) should lead to results that establish more clearly the dominant erosion mechanism.

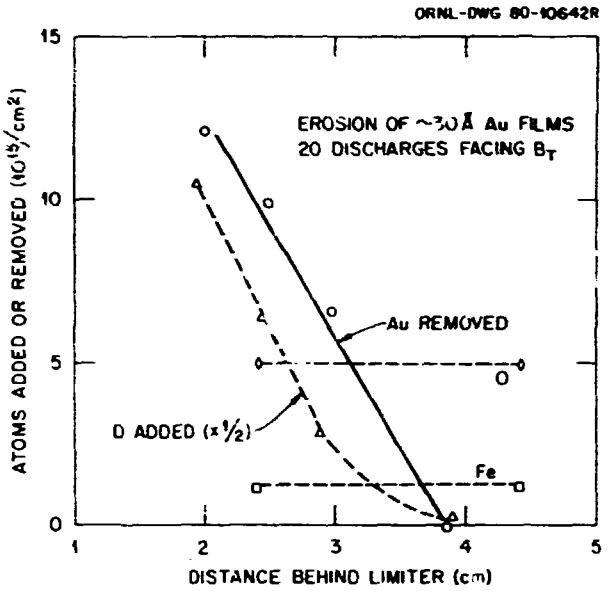

Fig. 2.23. Radial dependence of Au erosion and D, O, and Fe accumulation for samples facing the toroidal field lines for 20 D discharges.

1. Summary of paper to be published.
2. S. P. Withrow, R. A. Zuhr, and J. B. Roberto, "D Profiling in the Plasma Edge of ISX-B," this report.
3. R. A. Zuhr, S. P. Withrow, and J. B. Roberto, "Impurity Transport in the Plasma Edge of ISX-B," this report.

REVIEW OF LIGHT-ION SPUTTERING[1]

J. B. Roberto

The status of light-ion sputtering in relation to plasma-surface interactions is reviewed. The emphasis is on total physical sputtering yields for H isotopes and He and on those parameters that affect total yields, such as angle of incidence, dose, and temperature. Two energy regions are distinguished: a low-energy near-threshold region characteristic of plasma ion temperatures and a higher energy region characteristic of neutral beams and energetic alphas. In each case, the existing experimental data are reviewed and compared with theoretical predictions for total yields and angular, dose, and temperature effects.

In summary, the available experimental data and empirical relationships for low-energy light-ion sputtering are adequate for factor-of-2 estimates of total yields in all materials and compounds where the sputtering is dominated by collisional effects. For higher energy light ions ($E > 10$ keV), existing

theories predict the correct energy dependence of the sputtering but overestimate the yields by factors of as much as 10 in some cases. Overall, physical sputtering yields by light ions are understood adequately for the present needs of the fusion community, with the exception of additional experimental measurements for specific materials at low doses and in the high-energy region.

1. Summary of paper: *Proceedings of the Workshop on Sputtering Caused by Plasma (Neutral Beam)-Surface Interaction*, DOE report (in press).

LOW-ENERGY H^+ SPUTTERING OF METALS[1]

J. B. Roberto J. L. Moore
R. A. Zuhr J. Bohdansky[2]

The sputtering of limiter and wall materials by low-energy light ions which escape the plasma may contribute significantly to erosion and impurity introduction in fusion devices. Recently, extensive measurements[3] of light-ion sputtering yields using the weight-loss method have led to an improved understanding of low-energy sputtering processes at high ion doses ($\geq 10^{20}/cm^2$ for H^+). In the present work, a more sensitive Rutherford backscattering technique has been used to determine normal incidence sputtering yields for 0.2 to 2.0 keV H^+ on Au, Ni, and type 304 stainless steel at doses as low as $10^{18}/cm^2$. The results of the backscattering measurements have been compared with the weight-loss technique in a sample exchange with Max-Planck-Institut, Garching, and have been correlated with theoretical predictions based on binary collision models.[4,5]

The sputtering beam was extracted from the Solid State Division's ion implantation accelerator at 35 keV and decelerated to its final energy using an electrostatic lens system.[6] The loss of sputtered material on the thin film target was monitored by changes in the backscattering yield of a 2.5-MeV He^+ beam from a Van de Graaff accelerator. The sputtering yields for the present experiment are compared with results from the weight-loss method and with recent theoretical calculations in Table 2.4. The present results are generally in agreement with the higher dose weight-loss data, as well as with predictions of the binary collision calculations. Overall, the results indicate similar sputtering behavior for thin films and bulk material and an improved theoretical understanding of physical sputtering for low-energy light ions. Additional weight-loss measurements at Garching using ORNL-prepared Au and Ni thin film samples resulted in essentially the same yields as shown in Table 2.4, indicating the reliability of the backscattering and weight-loss techniques.

1. Summary of paper: *J. Nucl. Mater.* 85/86, 1073 (1979).
2. Max-Planck-Institut für Plasmaphysik, Garching bei München, Germany.
3. J. Roth, J. Bohdansky, and W. Ottenberger, Max-Planck-Institut für Plasmaphysik Report IPP 9/26, Garching (1979).

Table 2.4. Normal incidence H^+ sputtering yields for Au, Ni, and type 304 stainless steel

Target	Energy (ev)	Sputtering yield (atoms/ion)		
		Backscattering	Weight loss[3]	Theory[4,5]
Au	400	0.9×10^{-3}	0.8×10^{-3}	1.4×10^{-3}
	750	4.1×10^{-3}	3.5×10^{-3}	5.2×10^{-3}
	1000	7.0×10^{-3}	5.8×10^{-3}	7.2×10^{-3}
	1500	1.1×10^{-2}	0.9×10^{-2}	0.9×10^{-2}
	2000	1.3×10^{-2}	1.1×10^{-2}	1.1×10^{-2}
Ni	200	3.0×10^{-3}	4.0×10^{-3}	4.0×10^{-3}
	400	7.7×10^{-3}	9.2×10^{-3}	1.0×10^{-2}
	750	1.2×10^{-2}	1.3×10^{-2}	1.4×10^{-2}
	1000	1.1×10^{-2}	1.4×10^{-2}	1.6×10^{-2}
	1500	1.0×10^{-2}	1.4×10^{-2}	1.6×10^{-2}
304 SS	400	0.7×10^{-2}	0.6×10^{-2}	0.8×10^{-2}
	750	0.7×10^{-2}	0.8×10^{-2}	1.0×10^{-2}
	1000	0.9×10^{-2}	1.0×10^{-2}	1.2×10^{-2}

4. R. Behrisch et al., *Appl. Phys.* **18**, 391 (1979).
5. L. G. Haggmark and W. D. Wilson, *J. Nucl. Mater.* 76/77, 149 (1978).
6. G. D. Alton et al., "Design Features and Focal Properties of a Simple Lens System for Decelerating Intense Ion Beams to Very Low Energies," this report.

Table 2.5. Selected lens data

a_1	2.54 mm	a_2	15.24 mm	a_3	15.24 mm
t_1	12.70 mm	t_2	6.35 mm	t_3	6.35 mm
d_1	9.53 mm	d_2	10.05 mm	x	Variable
ϕ_1	0.3 keV	ϕ_2	−1.0 keV		(34.8–33.0 keV)

DESIGN FEATURES AND FOCAL PROPERTIES OF A SIMPLE LENS SYSTEM FOR DECELERATING INTENSE ION BEAMS TO VERY LOW ENERGIES[1]

G. D. Alton[2] C. W. White
J. B. Roberto R. A. Zuhr

A simple electrostatic lens system has been designed and constructed for decelerating ion beams to very low energies. Such a system is useful for a variety of atomic and solid state physics applications, including ion beam deposition techniques. The present development was motivated by the need for low-energy, high-density H^+ ion beams for use in determining the sputtering rates of fusion reactor components.[3]

The design characteristics of the system were determined numerically by computing the electrostatic field distributions and particle trajectories for various electrode configurations. The influence of space charge, angular distribution, and aperture size on focal properties was also determined numerically. A schematic of the selected lens geometry is shown in Fig. 2.24. The associated lens apertures a, electrode potentials ϕ, electrode spacings d, and thicknesses t are given in Table 2.5.

The lens of Fig. 2.24 was used to decelerate and focus a 35-keV H^+ beam to final energies of 200 to 2000 eV and current densities >1 mA/cm^2. The focal properties of the lens, resulting in increases of beam density by more than a factor of 10, were essential for producing the necessary intensities for low-energy sputtering experiments. The measured focal position x of the lens as a function of final beam energy was in good agreement with the calculated foci. The results demonstrate that computer-assisted design and analysis methods provide an accurate and inexpensive means for determining properties of electrostatic systems.

1. Summary of paper to be published.
2. Physics Division, ORNL.
3. J. B. Roberto, R. A. Zuhr, and J. L. Moore, "Low Energy H$^+$ Sputtering of Metals," this report.

DEVELOPMENT OF A CW LASER FLUORESCENCE SYSTEM

W. R. Husinsky[1] J. B. Roberto

The method of Doppler-shifted resonance fluorescence of neutral atoms excited by intense laser

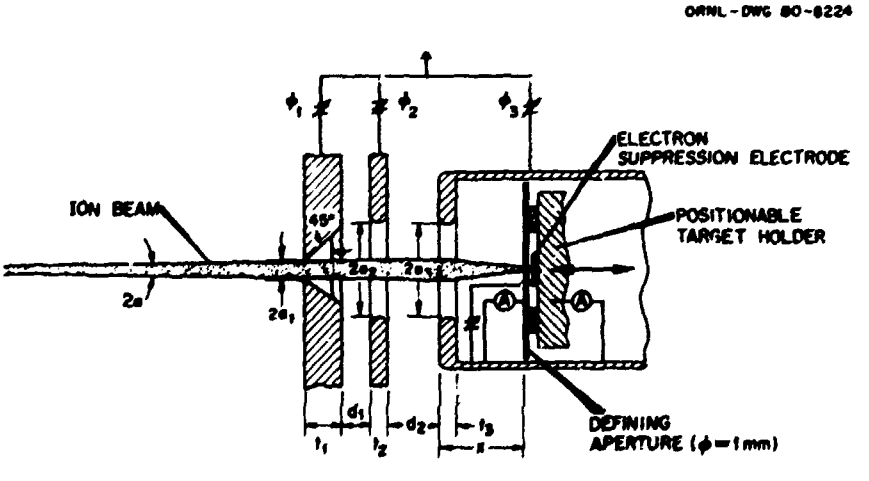

Fig. 2.24. Schematic of the lens system.

radiation has proven to be an excellent tool for the measurement of the density and velocity distribution of sputtered particles[2-3] and impurities in fusion devices.[4] Most particle-solid interactions (such as sputtering, desorption, and reflection) are dominated by the emission of neutral species, and the laser fluorescence technique allows the detection of neutral particles with great sensitivity.

We have recently set up a laser fluorescence system in the Solid State Division based on a tunable, actively stabilized cw ring dye laser pumped by an argon ion laser. The system produces single-frequency laser radiation with an effective linewidth of about 1 MHz and can also be operated broadband (2–20 GHz). Continuous single-frequency outputs of more than 2 W can be achieved at 560 to 620 nm using R6G laser dye and 50 to 200 mW at 410 to 450 nm using Stilbene dyes. The high spectral intensity and narrow bandwidth of the system allow measurement of $\sim 10^2$ atoms/cm^3 with thermal velocity resolution.

At the present time, most of the preparations have been completed for installing the system on the Solid State Division's ion implantation accelerator for sputtering experiments. A thermal atomic beam reference source has been constructed using a single crucible e-gun evaporator, and preliminary fluorescence experiments have been performed on Cr beams using the resonance transitions at 425.43, 427.48, and 428.97 nm. The optical arrangement of the experiment will allow measurements of the velocity and angular distributions of particles sputtered from various targets for various angles of ion beam incidence. Preparations are also nearly complete for use of the system on the ELMO Bumpy Torus fusion device, where measurements of impurity and excited atomic hydrogen fluxes are planned.

1. Guest scientist from Technische Universität Wien, Vienna, Austria.

2. W. Husinsky et al., *J. Appl. Phys.* 48, 11 (1977).

3. A. Elbern, E. Hintz, and B. Schweer, *J. Nucl. Mater.* 76/77, 143 (1978).

4. H.-B. Schweer, W. R. Husinsky, and J. B. Roberto, "Measurement of the Density and Velocity Distribution of Neutral Fe in the Plasma Edge of ISX-B by Laser Fluorescence Spectroscopy," this report.

ION-SOLID INTERACTIONS

ENHANCED YIELD EFFECT FOR IONS SCATTERED NEAR 180°[1]

B. R. Appleton S. R. Wilson[3]
P. P. Pronko[2] O. W. Holland[4]

A new and unusual ion scattering effect has been observed for energetic ions backscattered from solids at $180 \pm 0.5°$. Although the effect was discovered in the course of experiments utilizing a uniaxial double-alignment channeling geometry that requires stringent collimation near 180° scattering angle,[5] it is not an ion channeling effect. The effect has been observed on a wide range of amorphous and polycrystalline materials and for H^+ and He^+ beams with energies from 0.2 to 2.5 MeV. It is not seen under small-acceptance-angle collimation at 90° scattering or in wide-acceptance-angle geometry for 180° scattering events. These results lead to the conclusion that the effect is uniquely associated with small impact-parameter scattering within ±0.5° of the 180° direction.

Helium and proton beams from the Solid State Division's Van de Graaff accelerator were collimated to a half-angle beam divergence of 0.008° with a spot size ~1 mm in diameter and were directed onto a variety of targets. Two in-line annular detectors (cooled to −22°C) could be positioned such that the one farthest from the target had an acceptance half-angle $\theta_{1/2} = 0.1°$ and the closest one had $\theta_{1/2} = 4.5°$. Both detectors recorded scattering about the 180° direction. Measurements were also made using small, movable planar detectors with small acceptance angles ($\lesssim 0.1°$). These were scanned from ~0.10 to 1.0° of the 180° direction to determine the angular dependence of the effect.

The depth dependence of this enhanced scattering yield is illustrated in Fig. 2.25, which contrasts the yields of 0.8-MeV He^+ ions backscattered to 180° from fine-grained polycrystalline Cu as measured in the wide- and narrow-acceptance-angle annular detectors. These spectra have been converted to depth in the usual fashion and properly normalized. The wide-acceptance-angle data show a typical thick-target Rutherford backscattering yield distribution. The spectrum from the narrow-acceptance-angle detector contains a substantial and distinctive

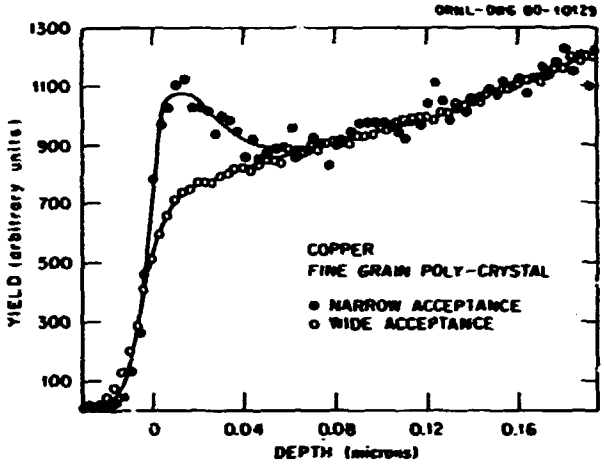

Fig. 2.25. Comparison of 180° scattering yields vs depth in annular detectors with narrow- and wide-acceptance-angle geometries for 800-keV He^+ on Cu.

enhancement in yield observable as a broad peak in the near-surface region.

The angular dependence of this effect was determined by stepping the small-acceptance-angle planar detector over a range of angles near the 180° scattering direction. The rapid decline of the effect for scattering angles deviating from 180° and its depth dependence can be seen from the series of analyzed spectra in Fig. 2.26 for 1.0-MeV He^+ scattered from polycrystalline Pt. These results show the percent enhancement in scattering yield over that observed in a normal Rutherford scattering distribution. The results were obtained by normalizing and subtracting the spectra at each angle shown from a spectrum taken at large angles (~1.0°), where the enhancement does not occur. The effect is most pronounced (~140% over Rutherford) at the angle nearest 180° ($\psi = 0.08°$) and decreases rapidly with increasing angle. Furthermore, at increased angles the maximum enhancement occurs closer to the surface.

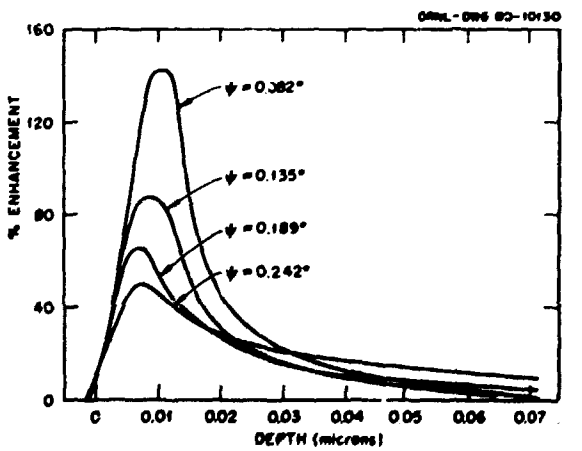

Fig. 2.26. Depth dependence of the percent yield enhancement for 1.0-MeV He ions in Pt at different angles ψ. Between successive curves $\Delta\psi = 0.054°$; the curve with the largest enhancement corresponds to the smallest angle $\psi = 0.082 \pm 0.01°$.

The angular and depth dependencies of this effect have been studied for H^+, $^3He^+$, and $^4He^+$ beams with energies from 0.2 to 2.5 MeV, on amorphous and polycrystalline targets ranging from $82 \leq Z_2 \leq 13$, and on single crystalline targets of Au and Ge. We have deduced from comparison of our results with computer simulation calculations[6] that the effect originates from the reversibility of the incoming and outgoing trajectories of ions scattered sufficiently close to 180°. The dependence of this phenomenon on ion charge and energy and on target atom charge and mass is discussed in a separate paper,[6] as is the utilization of this effect for surface studies of single crystals.[7]

---

1. Summary of papers: P. P. Pronko et al., *Phys. Rev. Lett.* 43, 779 (1979); *Nuclear Instruments and Methods* (in press).
2. Guest scientist from ANL, Argonne, Ill.
3. ORAU graduate laboratory participant from North Texas State University, Denton; present address: Motorola, Inc., Phoenix, Ariz.
4. ORAU graduate laboratory participant from North Texas State University, Denton.
5. B. R. Appleton and L. C. Feldman, p. 417, *Atomic Collisions Phenomena in Solids*, ed. by D. W. Palmer, M. W. Thompson, and P. D. Townsend, North-Holland, Amsterdam, 1970.
6. J. H. Barrett, B. R. Appleton, and O. W. Holland, "Role of Reversibility in Enhanced Ion Backscattering near 180° Scattering Angle," this report.
7. B. R. Appleton et al., "Enhanced Sensitivity for PICS Analysis of Surfaces," this report.

ENHANCED SENSITIVITY FOR PICS ANALYSIS OF SURFACES

B. R. Appleton O. E. Schow III
O. W. Holland[1] J. H. Barrett

The combined techniques of ion scattering and ion channeling have been utilized previously to investigate the atomic structure of single-crystal surfaces (so-called PICS technique).[2] These experiments are usually performed with a single alignment wide-acceptance-angle (only the channeling effect is utilized) detector geometry.[2] It is possible, however,

to utilize a uniaxial double-alignment (both channeling and blocking are utilized)[3] or a narrow-acceptance-angle detector geometry such as that described previously.[4] When this is done, however, as the previous paper shows, the enhanced ion scattering effect will alter the results significantly. This report describes work in progress to assess the effects of the enhanced ion scattering yield on surface peak studies performed in a uniaxial double-alignment detector geometry.

The surface sensitivity in the PICS technique, when the single-crystal axes are aligned parallel to the incident ion beam, originates from the shadowing effect by the surface atoms of the aligned atoms beneath the surface. Thus, the surface peak yield in a PICS analysis results from the number of atoms per row that scatter ions from the aligned ion beam. In the case of 1.0-MeV He^+ ions incident parallel to the (110) axial direction perpendicular to a Au(110) surface, the surface peak yield is expected to be 2.17 atoms per row for a normal unreconstructed Au(110) surface. This value of 2.17 atoms per row is the yield calculated from computer simulations which include thermal vibrations[5] and also, within experimental error, is the value measured (2.2 atoms per row) in a wide-acceptance-angle detector geometry. A perfect surface with no thermal vibrations would have a yield of one atom per row (i.e., from the surface atoms only), and the additional yield that is observed (1.17 atoms per row) comes from atoms in layers beyond the surface that are exposed to the incident ion beam because of thermal vibrations. In the uniaxial double-alignment geometry, the enhanced ion scattering effect that was discussed in the previous paper[4] will cause an increase in the surface peak yield for angles near 180°. This increase is due to increased scattering from the atoms immediately below the surface atoms. Thus, this phenomenon can be utilized in PICS investigations of surfaces to achieve increased sensitivities to any atomic rearrangement of the surface.

A comparison of the initial measurements and calculations of the surface peak enhancement that occurs for 1-MeV He^+ ions incident on Au[110] at room temperature is shown in Fig. 2.27. The data were obtained using an array of small-acceptance-angle (~1.0°) detectors which could be scanned near the 180° direction to measure the scattered energy spectra as a function of angle. The circles plotted in Fig. 2.27 represent the enhanced surface peak yields computed for 1.0-MeV He scattered from Au[110] in the uniaxial double-alignment geometry. These calculations are normalized so that 0% enhancement corresponds to the calculated surface peak yield for Au [110] (2.17 atoms per row) at large ψ, where no enhancement occurs. Measurements analogous to the calculated yields are plotted as triangles, and these are also normalized to 0% enhancement at large $\psi \gtrsim 0.8°$. These preliminary results show a marked enhancement over the calculated values. It is not clear at present whether this difference is due to the reconstructed nature of the Au (011) surface, which is the subject of an ongoing investigation by the combined techniques of PICS and LEED and is not included in the model calculations, or to subtleties of the effect not yet determined. Nevertheless, this observed enhancement will surely provide enhanced sensitivity for application of the PICS technique to surface studies.

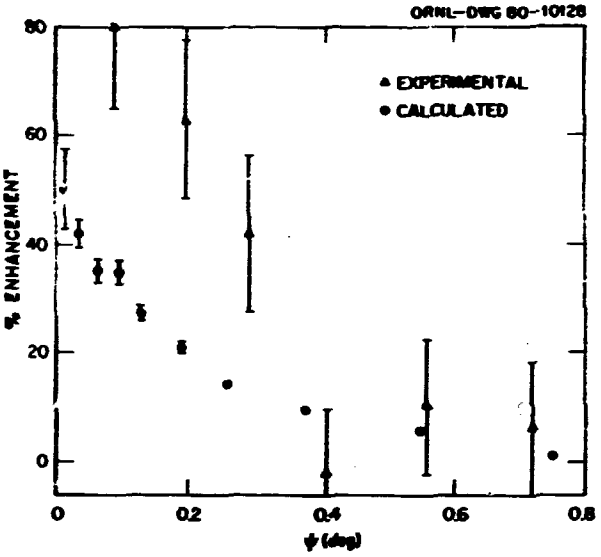

Fig. 2.27. Comparison of calculated and measured enhancements in the surface peak yields which occur for 1.0-MeV He scattered from Au[110] to angles (ψ) near the 180° backscattering direction.

---

1. ORAU graduate laboratory participant from North Texas State University, Denton.

2. B. R. Appleton et al., p. 607 in *Ion Beam Surface Layer Analysis*, vol. 2, ed. by O. Meyer, G. Linker, and F. Käppeler, Plenum Press, New York, 1976.

3. B. R. Appleton and L. C. Feldman, p. 417 in *Atomic Collisions Phenomena in Solids*, ed. by D. W. Palmer, M. W. Thompson, and P. D. Townsend, North-Holland, Amsterdam 1970.

4. B. R. Appleton et al., "Enhanced Yield Effect for Ions Scattered near 180°," this report.

5. J. H. Barrett, *Phys. Rev. B* 3, 1527 (1971).

DEPENDENCE OF SURFACE PEAK YIELD IN Au ON INCIDENT ION BEAM DOSE

S. P. Withrow D. M. Zehner

The backscattered energy distribution of a beam of ions incident along an axial channeling direction of a single crystal has a pronounced peak at the high-energy end of the spectrum. This peak, referred to as the surface peak, results from the interaction of the incident beam with the atoms in the top several layers of the solid. The surface peak yield can be explained using classical backscattering and channeling theory and can be compared to calculations using models of the crystal surface, thus providing a useful technique for studying surface crystallography.

It has been observed recently, for measurements on Pt, that the surface peak yield exhibits a significant increase with beam dose as a result of radiation damage in the surface region.[1] This increase was observed for doses up to ~30 $\mu C/mm^2$. Because of the interest within the Solid State Division in using the backscattering/channeling technique to study surface crystallography, experiments have been made to test for beam dose effects. Data were obtained for 1-MeV ^4He incident along the [110] axes of an Au(110) crystal.

For normal incidence, the percent change in surface yield, normalized to the yield at a 2.5 μC dose, is 0.05% $\mu C/mm^2$. This value represents the slope of a line drawn through the data for doses up to 50 $\mu C/mm^2$.[2] Typically, measurements on Au involve doses of 0.5 $\mu C/mm^2$ per data point and total accumulated doses of $\leq$20 $\mu C/mm^2$, which translate into surface peak yield changes of $\leq$1%. This result is less than the statistical error for a 1-$\mu C/mm^2$ dose in the experiment, ~1.5%, and compares favorably with uncertainties introduced by background subtraction, stopping powers (needed to convert yields into atoms per row), etc. Under these conditions damage in the surface region is not a problem. For incidence along the [110] axis at 60° to the normal, the limited data obtained suggest that the surface peak yield increases with dose at a rate somewhat greater than that for normal incidence. Changes in the surface peak yield under other incident angle or beam energy conditions or at lower temperatures could be more severe.

1. J. A. Davies et al., *Surf. Sci.* 78, 274 (1978).

ION BEAM ANALYSIS TECHNIQUES AS A SUPPLEMENT TO COAL CATALYSIS

B. R. Appleton C. W. White E. L Fuller, Jr.[1]

With the increasing interest in various catalytic methods for processing coal, it is important to develop techniques to evaluate the coal samples and thereby assess the effectiveness of the processes. These are difficult tasks due to the great variability among coals and the complexity of the material. Experiments have been started to determine the usefulness of ion beam analysis techniques for characterization of coals. We report here preliminary results using ion scattering to determine the elemental compositions vs depth of several coal samples and ion-induced nuclear resonance techniques to determine the H concentrations vs depth in the same samples.

The results shown in Fig. 2.28 were obtained by measuring yields of 2.5-MeV He ions scattered from a Texas lignite coal and a bituminous Illinois coal. Because the energy of the scattering ions depends on the mass of the scattering atom, it is possible to identify the scattering species present in the coal. The elemental labels above the steps in the yield distribution in Fig. 2.28 are the calculated energies for scattering from these elements located on the surface. Because ion scattering is quantitative, the heights of these yield steps are proportional to the concentrations of the scattering atoms. The peaks at a step in Fig. 2.28 signal an

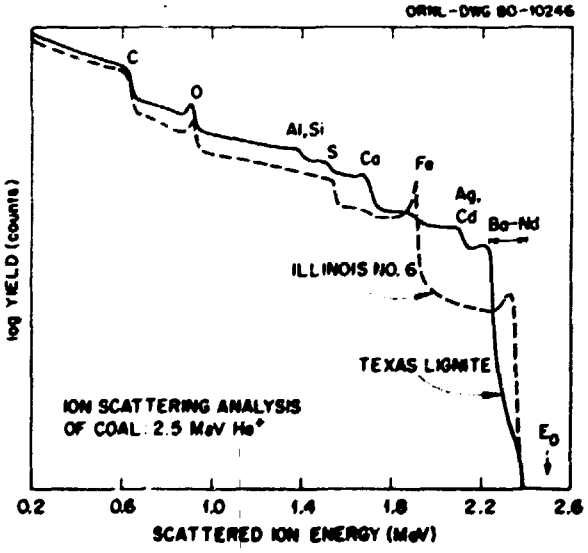

Fig. 2.28. 2.5-MeV He ion scattering analysis of coal.

excess of that element at the surface compared to its concentration in the bulk. If the density of the coal is known, the scattered energy can be converted to depth. Thus, it is possible from such measurements to make quantitative determinations of the elemental compositions as a function of depth.

Measurements of the H concentrations as a function of depth in the Texas lignite coal before and after an 800°C char treatment are shown in Fig. 2.29. These results were obtained using the $^{1}H(^{19}F,\alpha\gamma)^{16}O$ resonant nuclear reaction. The measurement method is described in the following paper.[2] The H profiles are shown near the surface and at a depth of ~2 μm beneath the solid.

Quantitative comparisons of these data cannot be made at this stage for several reasons. Some of the results observed are due to sample preparation and/or handling; for example, all measurements were made in vacuums ~1×10^{-7} torr, and the Illinois No. 6 sample was cut and polished. The purpose of these preliminary results is to illustrate the capabilities of the ion beam techniques as supplemental analysis tools for evaluation of coal catalysis methods. One possible example is the use of such measurements to determine H/C ratios. Because this is an important parameter for many gasification or liquification processes, such results could be used to identify the most efficient process for a given coal. Quantitative, elemental characterization of coal samples used in laboratory experiments is another possible use. On the more practical side, ion-induced nuclear reactions, x rays, and gamma rays could be utilized for bulk coal analysis in a processing line once the techniques were calibrated in the laboratory.

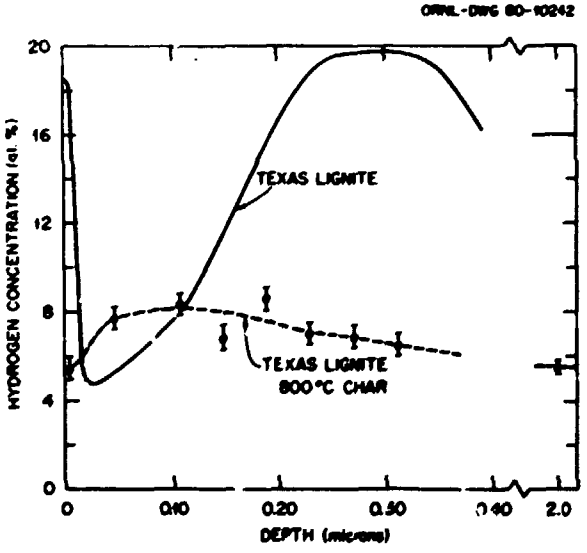

Fig. 2.29. Quantitative H depth profiles of coal.

1. Chemistry Division, ORNL.
2. C. W. White et al., "Quantitative H Depth Profiling in Fluorinated Amorphous Si," this report.

QUANTITATIVE H DEPTH PROFILING IN FLUORINATED AMORPHOUS Si (aSi:F:H)

C. W. White R. Tsu[1]
B. R. Appleton D. D. Allred[2]

The ability to determine quantitatively the H content and concentration profiles in solids is becoming increasingly important in materials science. One area where this is of paramount importance is amorphous Si, a material that has shown great promise for the production of large-area, low-cost photovoltaic devices. Conventional amorphous Si is prepared by the decomposition of SiH_4, and our previous measurements[3,4] have shown this material to contain very high concentrations of H (>10 at. %). Recently, researchers at ECD have shown that the addition of F to amorphous Si leads to amorphous Si (aSi:F:H) with superior characteristics compared to conventional hydrogenated amorphous Si (aSi:H) in at least four important areas: (1) the electronic density of states in the gap is reduced by 10 to 20%, (2) the density of states at the Fermi level is reduced by a factor of ~2, (3) the electrical conductivity is better for all doping levels, and (4) the aSi:F:H exhibits much better mechanical stability than does aSi:H. Each of these characteristics suggests that fluorinated amorphous Si will be superior to hydrogenated amorphous Si for the fabrication of low-cost, large-area photovoltaic devices. Due to the potential importance of fluorinated amorphous Si to photovoltaic devices, it is necessary to determine the complete physical and chemical characteristics of this material. We report here quantitative measurements of the H profiles in this material.

A fluorinated amorphous Si film (approximately 5400 Å thick) on a Si single-crystal substrate was prepared by ECD. The amorphous Si film was deposited using a typical rf glow discharge process to decompose SiF_4 gas with a gas mixture of SiF_4 to H_2 ratio of 9:1. The pressure during deposition was ~0.5

torr. The substrate temperature was ~300 K. In the glow discharge deposition process, As doping can be accomplished by simultaneous introduction of AsH_3. For the present measurements, however, the films were As free.

The H profile was determined quantitatively by use of the $^1H(^{19}F,\alpha\gamma)^{16}O$ nuclear reaction, which exhibits a strong resonance at a ^{19}F energy of 16.44 MeV in the laboratory system. To determine the H concentration as a function of depth, one measures the gamma-ray yield as a function of ^{19}F beam energy as the resonance is stepped through the sample.[3] Conversion of energy to depth is accomplished using standard stopping power tables.[5] Conversion of gamma-ray yield to H concentration is accomplished using suitable calibration standards. Details of the deconvolution of the gamma-ray yield data are included in our previous publications.[3,4] Calibration standards used in this work include three Si crystals implanted with H at ORNL (11.7 keV, doses of 10^{15}, 10^{16}, and $10^{17}/cm^2$) as well as one crystal implanted with H by RCA (40 keV, $1 \times 10^{16}/cm^2$). The calibration constants determined from these four standards differed by less than 10%. Measurements were performed using a $^{19}F^{4+}$ beam from the ORNL Tandem Van de Graaff Accelerator.

Figure 2.30 shows the gamma-ray yield data and the H concentration vs depth in the aSi:F:H film. The gamma-ray yield data are normalized to a $^{19}F^{4+}$ dose of 1.56×10^{13} particles with the beam spot size being $\sim 4 \times 10^{-2}$ cm^2. In determining the H concentration profile, the gamma-ray yield data have been corrected for the effects of a nonzero off resonance cross section and for the effects of lower energy resonances.[3,6] Beam energy was converted to depth in the sample using information in ref. 5. In Fig. 2.30, the H peak at the surface is believed to be due to surface contamination (water vapor or hydrocarbons). The absolute H concentration in the film is $\sim 7.5 \times 10^{21}/cm^3$ (~15 at. %), and the profile suggests a deficiency of H in the near-surface region of the film. The film thickness is too great to allow a clear determination of the amorphous-to-crystalline interface, but subsequent Rutherford backscattering measurements with 2.5-MeV He^+ ions show the film thickness to be ~5400 Å.

The H concentration and profile in this film are not radically different from those in conventional aSi:H films. At present, measurements are being carried out to determine the F profile in this film and the As concentration and profile of films that are doped with ^{75}As and to determine the Si density in these films.

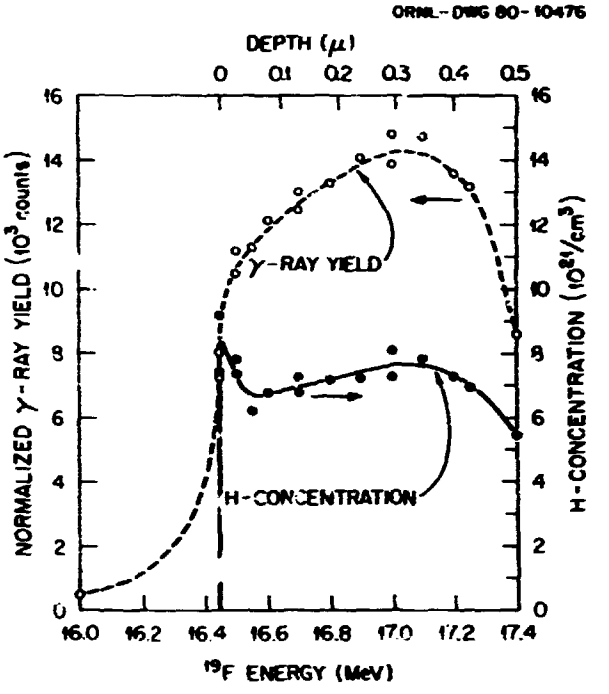

Fig. 2.30. Hydrogen profiles and gamma-ray yields from amorphous Si (aSi:F:H). The gamma-ray yield and H concentration are plotted independently as a function of beam energy (or depth). Absolute concentrations are determined from H^+-implanted calibration standards.

Measurements of the stoichiometry of these films and changes in stoichiometry with deposition parameters, combined with electrical measurements, should provide insight into the mechanisms responsible for the superior properties of these films. Such measurements are in progress.

1. ECD, Troy, Mich.
2. University of Arizona, Tucson.
3. G. J. Clark et al., *Nucl. Instrum. Methods* **149**, 9 (1978).
4. G. J. Clark et al., *Appl. Phys. Lett.* **31**, 582 (1977).
5. L. C. Northcliffe and R. F. Schilling, *Nucl. Data Tables, USAEC* **A7**, 233 (1970).
6. G. J. Clark et al., *Phys. Chem. Mater.* **3**, 199 (1978).

THERMAL ANNEALING OF ^{75}As-IMPLANTED (111) Si

S. R. Wilson[1] C. W. White B. R. Appleton

Solid phase regrowth of (111) Si implanted to high doses with ^{75}As is used in the fabrication of bipolar

transistors. Others have studied the solid phase regrowth process of (100) and (111) Si crystals rendered amorphous by Si^+ ion beams,[2-4] and small concentrations of impurities are known to affect the regrowth rate for (100) crystals.[5] However, no data are available on solid phase regrowth of (111) crystals implanted with ^{75}As under the implant conditions used by industry in the fabrication of bipolar transistors. Consequently, we have begun systematic investigations of the solid phase regrowth process under conditions of direct importance to device fabrication.

Rutherford backscattering and ion channeling techniques were used to investigate the effects of implant dose and substrate temperature during implantation on the regrowth of amorphous layers on (111) Si. Crystals were implanted with ^{75}As at 60 keV to doses ranging from $1 \times 10^{14}/cm^2$ to $1.5 \times 10^{16}/cm^2$. These implant conditions create an amorphous layer extending to a depth of ~1100 Å. Samples were implanted at room temperature and with the substrate cooled to LN_2 temperatures and were then annealed at 550°C for 18 h. These annealing conditions are sufficient to regrow ~3500 Å using reported values of regrowth rates of impurity-free (111) Si.[4]

Figure 2.31 shows the high-resolution channeling spectra obtained with the beam aligned along a (110) axis for crystals implanted to different doses at room temperature. The As-implanted spectrum shows that the crystal has been made amorphous to a depth of ~1100 Å. For doses of $1.5 \times 10^{15}/cm^2$ and below, the 18-h, 550°C annealing caused the entire amorphous region to be regrown by solid phase epitaxial regrowth, but residual defects remained in the regrown layer. Channeling measurements showed As to be ~80% substitutional in the regrown layer, with no spreading of the profile. At the dose of $7 \times 10^{15}/cm^2$, the amorphous layer regrows only to a depth of ~450 Å as measured from the surface, and significant disorder remains in the vicinity of the original amorphous-crystalline interface (~1100 Å). In this crystal, As is 70–80% substitutional in the regrown layer and randomly placed in the amorphous region. At a dose of $1.5 \times 10^{16}/cm^2$, the amorphous region after annealing extends to a depth of ~600 Å as measured from the surface, and considerably more disorder remains at the original amorphous-to-crystalline interface. These results demonstrate that solid phase regrowth rates in (111) Si will be considerably reduced by ^{75}As, because the time and temperature used for annealing are sufficient to regrow ~3500 Å of impurity-free amorphous Si.[4] Wafers implanted at LN_2 temperatures showed a similar phenomenon, but the residual disorder at the original amorphous-crystalline interface is greatly reduced in comparison to room-temperature implants, suggesting that room-temperature implantation or the early stages of thermal annealing create stable defects at the interface which will be difficult to anneal by solid phase regrowth.

Experiments are in progress to determine solid phase regrowth rates as a function of ^{75}As concentration and to determine the nature of the defects remaining in the regrown layers.

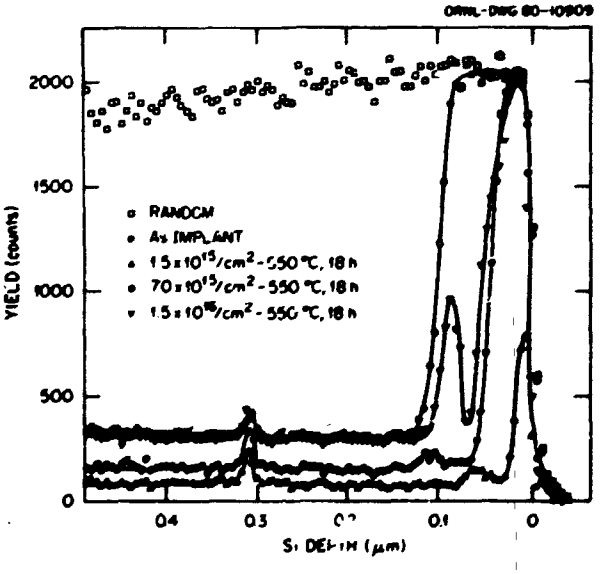

Fig. 2.31. The (110) aligned channeling spectra for (111) Si crystals implanted by 60-keV ^{75}As to doses of 1.5×10^{15}, 7×10^{15}, and $1.5 \times 10^{16}/cm^2$ and annealed for 18 h at 550°C.

1. Motorola, Inc., Phoenix, Ariz.
2. S. S. Lau, J. W. Mayer, and W. Tseng, *AIP Conf. Proc.* **50**, 84 (1979).
3. L. Csepregi, J. W. Mayer, and T. W. Sigmon, *Appl. Phys. Lett.* **29**, 92 (1976).
4. L. Csepregi et al., *J. Appl. Phys.* **48**, 4234 (1977).
5. E. F. Kennedy et al., *J. Appl. Phys.* **48**, 4241 (1977).

ION BEAM MIXING AND PULSED LASER MIXING

B. R. Appleton[1] S. S. Lau[2]
B. Stritzker[1] C. W. White

Two new processing techniques have emerged that are proving quite useful for forming near-surface alloys with metastable properties and for studying

the materials interactions leading to these properties. The techniques are illustrated by the ion scattering analyses shown in Figs. 2.32 and 2.33. Figure 2.32 (IBM) typifies the materials interactions that can be initiated in evaporated thin films of Au (400 Å) on Ge (3000 Å) on sapphire by bombardment with only 5×10^{15} 450-keV Xe ions/cm^2. The initial thin film composite (solid curve) is uniformly transformed into an amorphous mixture of $Au_{0.55}Ge_{0.45}$ over a depth of several hundred angstroms. Moderate

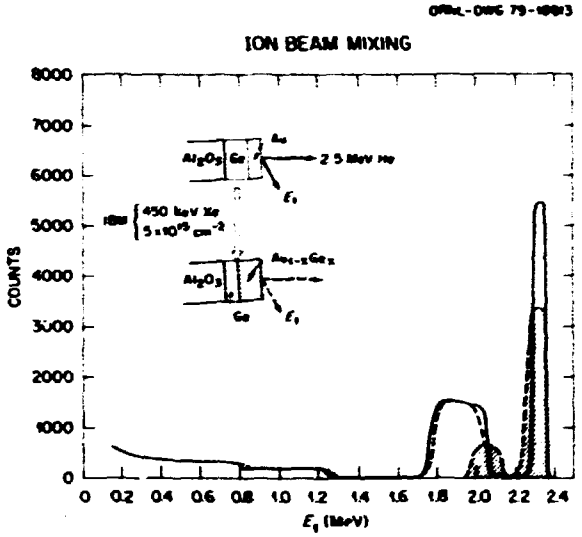

Fig. 2.32. 2.5-MeV He backscattering analysis of evaporated Au/Ge/Al_2O_3 before (solid curve) and after (dashed curve) IBM to yield $Au_{0.55}Ge_{0.45}$.

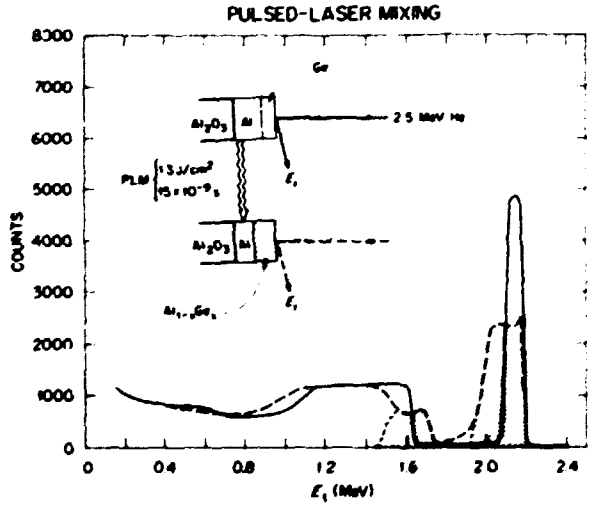

Fig. 2.33. 2.5-MeV He backscattering analysis of evaporated Ge/Al/Al_2O_3 before (solid curve) and after (dashed curve) PLM to achieve $Al_{0.70}Ge_{0.30}$.

temperature (~100°C) thermal processing of this metastable amorphous mixture leads to the formation of new metastable Au-Ge phases. If the IBM technique is applied to the Al/Ge system, which has a binary phase diagram nearly identical to that of Au/Ge, negligible mixing occurs even when the films are bombarded with ion doses an order of magnitude greater. The second technique, PLM, is illustrated in Fig. 2.33. When the Al/Ge system (solid curve) is annealed with a single laser pulse, the near-surface region melts and forms a metastable amorphous mixture similar in character to the IBM Au/Ge system just discussed but at the eutectic composition ($Al_{0.70}Ge_{0.30}$).

These two techniques have been utilized to study a variety of binary systems with systematic variations of the bombarding ion species, energy and dose, laser energy density, and substrate temperature (4 to 400 K). In many cases the mechanisms for the induced materials interactions are not yet known. Both cascade mixing and radiation-enhanced diffusion appear to be important factors in understanding the IBM results, and rapid quenching and phase growth from amorphous mixtures are probably important elements of both IBM and PLM. Results from some of the systems investigated are summarized below.

1. *Au/Si, Au/Ge, Al/Ge, and Ag/Si.* The PLM of all these systems tends toward metastable amorphous mixtures of the eutectic composition. The materials interactions that dictate this particular composition in these rapidly quenched systems are not understood. The IBM is quite successful in the Au/Si and Au/Ge systems, leading to uniformly mixed layers of well-defined compositions ($Au_{0.71}Si_{0.29}$ and $Au_{0.55}Ge_{0.45}$). In contrast, IBM is much less efficient in the Al/Ge and Ag/Si systems, and uniform compositions do not result. Low- and high-temperature measurements indicated that the ease of mixing is probably related to the higher diffusivities of Au in Si and Ge compared to those of Al and Ag.

2. *Low-temperature IBM.* The Au/Ge system has been studied at 4, 150, and 300 K. The results discussed above are applicable to the room-temperature measurements. At low temperatures, two distinct differences were observed. First, larger ion doses were required to induce mixing of any kind. Second, once mixing occurred, the elements did not mix uniformly but showed continuously varying compositions throughout the mixed region. In some cases these composition profiles are consistent with those expected from extrapolations of equilibrium phase diagrams under rapid quenching conditions.

3. *V/Si.* Both IBM and PLM of evaporated V/Si/sapphire samples lead to amorphous V_3Si mixtures that are not superconducting. Thermal annealing of the IBM mixtures leads to *A*15 phase V_3Si with superconducting transition temperatures $T_c \sim 16$ K. Thermal annealing to 500°C of V_3Si mixed with a single laser pulse leads to a $T_c \sim 10$ K, and PLM with ~10 laser pulses of a V/Si thin film composite leads to V_3Si with $T_c \sim 9$ K. This system is quite complicated, and one must include considerations of ion- and laser-induced defects on the superconducting properties of the *A*15 structure[3-5] as well as IBM and PLM effects in deducing the interaction mechanisms involved.

These techniques show great promise for materials fabrication and as fundamental research tools, particularly when used in conjunction with ion implantation and laser annealing. In particular, near-surface alloys such as Pt_2Si, which could not be made by ion implanting Pt into Si because of the limitations imposed by sputtering, can be easily made by IBM of evaporated films. Also, the fact that these two techniques often lead to new metastable materials properties when phase growth starts from an amorphous mixture makes them particularly valuable for fundamental materials studies.

1. Guest scientist from Institut für Festkorperforschung, Kernforschungsanlage, Jülich, Germany.
2. California Institute of Technology, Pasadena.
3. B. R. Appleton et al., "Laser- and Ion-Induced Damage in Superconducting Single Crystals," this report.
4. B. R. Appleton, O. Meyer, and Y. K. Chang, "Ion Channeling Analysis of Defect Structures in *A*15 Superconducting Single Crystals," this report.
5. J. R. Thompson et al., "Recovery of Superconductivity by Laser Annealing of Ion-Damaged V_3Si," this report.

ION CHANNELING ANALYSIS OF DEFECT STRUCTURES IN *A*15 SUPERCONDUCTING SINGLE CRYSTALS

B. R. Appleton B. Stritzker[2]
O. Meyer[1] Y. K. Chang

Superconducting compounds that have the *A*15 crystal structure have exhibited the highest superconducting transition temperature, T_c, measured in any material. The origin of the high T_c is believed to be related to the linear chains of transition metal atoms in the *A*15 structure. It has been found that defects produced by ion irradiation of the *A*15 crystals decrease T_c drastically,[3,4] and ion channeling studies have shown that in V_3Si these defects take the form of small displacements (0.05–0.1 Å) of the V atoms from their linear chain structure.[5-7] The nature of this defect was determined for measurements of the detailed angular scans of He^+ ions scattered from V atoms in the V_3Si single-crystal lattice. The channeling critical angle, $\psi_{1/2}$, showed a pronounced narrowing which, when compared to model calculations or computer simulations, specified the defect as a small displacement of the V atoms.

In the present work, a similar study was performed to determine the nature of the defect structures of the nontransition metal constituents in the *A*15 structure. This study was done by using 2.0-MeV He^+ ion scattering combined with channeling to make detailed angular scans of the (110) and (100) critical angles of Nb_3Ir and V_3Ge single crystals. In these crystals, because Ir and Ge atoms are the constituents that are easily detected by Rutherford backscattering, it was possible to determine their behavior under ion damage. In both cases it was found the He^+ ion damage caused a narrowing of the critical angles for Ir and Ge in a manner analogous to that observed for V in V_3Si. These results suggest that ion damage to the *A*15 structure causes slight displacements (~0.05–0.1 Å) of both elements from their equilibrium positions. This "kinking" of the linear chain structure is probably the cause of the decrease in T_c. The relationship of this damage to antisite defects is not clear. In future studies ion channeling results will be correlated with TEM and x-ray scattering investigations to clarify these defects.

1. Guest scientist from Nuclear Research Center, Karlsruhe, Germany.
2. Guest scientist from Institut für Festkorperforschung, Kernforschungsanlage, Jülich, Germany.
3. O. Meyer, H. Mann, and E. Phrilingos, p. 15 in *Applications of Ion Beams to Metals*, ed. by S. T. Picraux, E. P. EerNisse, and F. L. Vook, Plenum Press, New York, 1974.
4. J. M. Poate et al., *Phys. Rev. Lett.* **37**, 1308 (1976).
5. O. Meyer and B. Seeber, *Solid State Commun.* **22**, 603 (1977).
6. L. R. Testardi et al., *Phys. Rev. Lett.* **39**, 716 (1977).
7. R. Kaufmann and O. Meyer, *Radiat. Eff.* **40**, 161 (1979).

LASER- AND ION-INDUCED DAMAGE IN SUPERCONDUCTING SINGLE CRYSTALS

B. R. Appleton B. Stritzker[1]
C. W. White O. Meyer[2]
Y. K. Chang

Because of the important role of defects in understanding the behavior of superconducting

materials,[3,4] we have initiated a program to investigate ion- and laser-induced defect structures in Nb_3Ir, V_3Si, V_3Ge, and NbN single crystals.[3,6] Ion channeling techniques have been used to measure lattice disorder, and superconductivity measurements made on thin film samples subjected to the same ion (laser) processing have been used to gain some insight as to how this disorder correlates with the superconducting properties of the materials. To detect surface damage SEM was used, and TEM will be used at a later stage of the research to determine defect structures.

In general, ion bombardment of the superconducting materials being investigated here induces short-range disorder in the form of defect clusters, and an overall decrease in T_c is observed. Similarly, thermal annealing can be used to restore order and increase T_c. Contrary to expectations, pulsed laser annealing was found to induce disorder in the undamaged crystals studied and to have little beneficial annealing effects on previously ion-damaged samples. The first of these effects is exemplified by the results shown in Fig. 2.34. Figure 2.34*a* shows energy spectra for 2.5-MeV He^+ backscattered from a random orientation and the (111) axial direction of a NbN single crystal before (curve labeled (111)) and after laser annealing with single, 15×10^{-9} s pulses at energy densities ranging from 0.7 to 1.0 J/cm^2. As the laser energy density increased, the backscattering yields for the (111) channeling spectra approached that of the random value, signifying an increasing amount of lattice disorder. At 1.5 J/cm^2 the surface became heavily damaged, as can be seen from the SEM pictures in Fig. 2.35*b* of the laser-annealed spot. This laser energy density where visible damage occurred was a factor of 5 less than that used to anneal the NbN and Nb-N-C films discussed in the previous sections. Furthermore, laser annealing of these films resulted in either little change in T_c in initially high T_c films or an increase in T_c for initially low T_c films.[5,6]

Results from ion channeling studies of Nb_3Ir single crystals that were subjected to ion damage prior to laser annealing are shown in Fig. 2.35. After bombardment with 6×10^{15} Kr ions/cm^2 at 300 keV, channeling analysis showed pronounced damage distributions at the range of the Kr ions. (Although the channeling spectrum for undamaged Nb_3Ir is not shown, it would appear as a curve with much lower yield than any of the spectra in Fig. 2.35.) Laser annealing at 1.0 J/cm^2 caused only slight recovery of this disorder, and annealing to higher energy densities showed an increasing amount of disorder similar to that seen for NbN. At ~2.0 J/cm^2 the Nb_3Ir single-crystal surface showed disruption in the form of irregular flakes. A similar experiment was performed on a (100) V_3Si single crystal, and the results were correlated with superconducting measurements of V_3Si films. The single crystal was predamaged with 4×10^{16} He^+ cm^2 at 300 keV, resulting in a measurable damage distribution which was detected by ion channeling. Pulsed laser annealing did not repair this damage but instead increased the disorder until at 1.5 J cm^2 surface flaking occurred. The energy dependence of the dechanneling in the laser-annealed V_3Si was found to behave similar to that for edge dislocations in Si. Correlated measurements[7] on predamaged V_3Si films showed that the ion predamage decreased T_c and laser annealing caused T_c to increase, but never to its original value (~16 K).

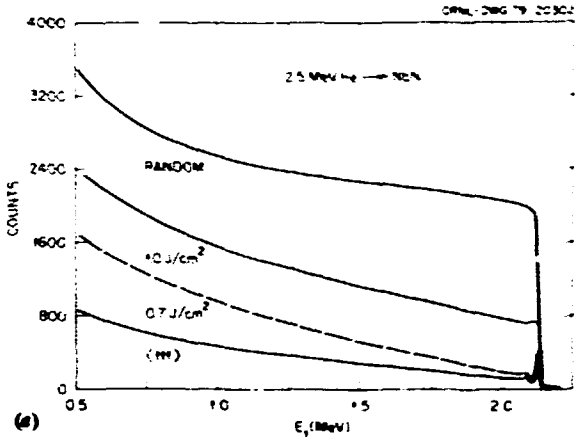

SSDN-2434

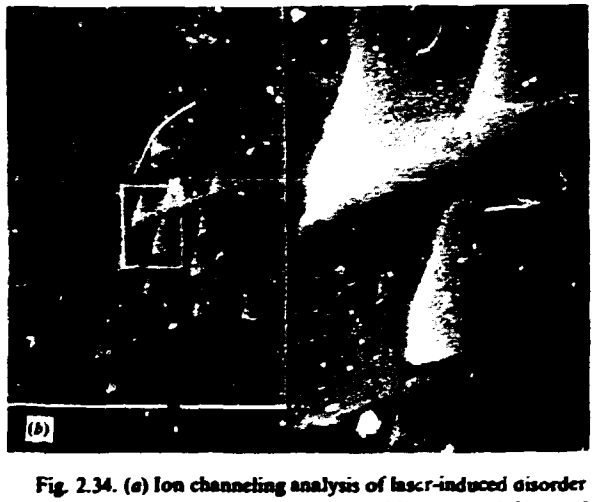

Fig. 2.34. (*a*) Ion channeling analysis of laser-induced disorder in NbN single crystal; (*b*) SEM analysis (2500× and 12,500×) of NbN single crystal after single 1.5-J/cm^2 laser pulse.

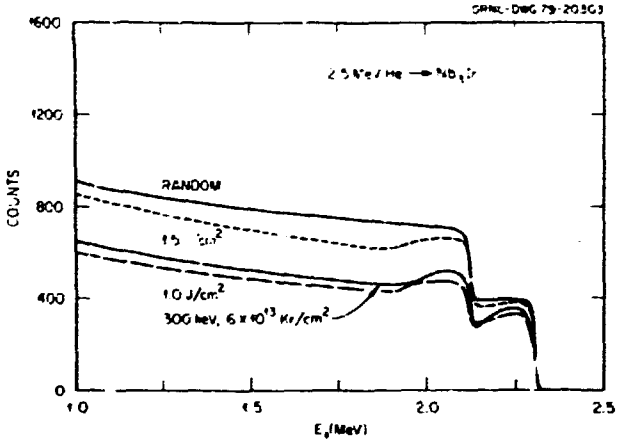

Fig. 2.35. Ion channeling analysis of ion-bombarded and laser-annealed Nb_3Ir single crystals.

The exact nature of these ion- and laser-induced defects must await further analysis, but the combined results do suggest some explanations. Ion damage could disrupt the short-range order (and T_c), and laser annealing could restore the short-range order (and T_c) but introduce defects that disrupt the long-range order of the lattice. This would explain both the channeling results and thin film measurements. The nature of the laser-induced disorder and eventual surface disruption probably results from strains caused by the extreme temperature gradients in the near-surface region. Although not conclusive, these preliminary results suggest several experiments that could be used to identify the defects involved and to understand their effects on T_c. Furthermore, the surface strain phenomenon may occur for a wide range of metals and may complicate laser annealing studies of metals.

1. Guest scientist from Institut für Festkorperforschung, Kernforschungsanlage, Jülich, Germany.

2. Guest scientist from Nuclear Research Center, Karlsruhe, Germany.

3. J. M. Poate et al., *Phys. Rev. Lett.* **35**, 1290 (1975).

4. O. Meyer and B. Seeber, *Solid State Commun.* **22**, 603 (1977); O. Meyer, *J. Nucl. Mater.* **72**, 182 (1978).

5. B. R. Appleton et al., p. 714 in *Laser and Electron Beam Processing of Materials*, ed. by C. W. White and P. S. Peercy, Academic Press, New York, 1980.

6. B. R. Appleton, O. Meyer, and Y. K. Chang, "Ion Channeling Analysis of Defect Structures in A15 Superconducting Single Crystals," this report.

7. J. R. Thompson et al., "Recovery of Superconductivity by Laser Annealing of Ion-Damaged V_3Si," this report.

SUPERSATURATED ALLOYS IN Si FORMED BY ION IMPLANTATION AND PULSED LASER ANNEALING[1]

C. W. White B. R. Appleton
S. R. Wilson[2] J. Narayan
F. W. Young, Jr.

The formation of supersaturated substitutional alloys by ion implantation and pulsed laser annealing have been studied systematically for a wide range of group III and V dopants in Si.[3,4] The laser-annealing-induced, liquid-phase epitaxial regrowth process has been found to take place under highly nonequilibrium conditions, and values have been determined for the (nonequilibrium) interfacial distribution coefficients during regrowth.[3,5] These are the first determinations of interfacial distribution coefficients under nonequilibrium growth conditions for any system. In addition, maximum substitutional solubilities (C_s^{max}) for group III and V dopants in Si have been measured for present laser annealing conditions.[3,4] The maximum substitutional solubilities exceed equilibrium solubility limits by factors of up to 500 (in the case of Bi). The achieved substitutional solubilities are approaching the absolute maximum substitutional solubilities predicted from thermodynamic considerations.[6] When the total dopant concentration greatly exceeds C_s^{max}, a cell structure develops in the near-surface region due to interfacial stability and constitutional supercooling at the interface during solidification.[3]

Silicon single crystals, (001) orientation, were implanted by group III and V dopants (Ga, In, As, Sb, and Bi) to doses in the range 10^{15} to 10^{17}/cm^2 at energies in the range 100 to 250 keV. Annealing was carried out using single pulses from a Q-switched ruby laser (~1.5 J/cm^2, 15 $\times$ 10^{-9} s pulse duration time). Crystals were examined before and after annealing using 2.5-MeV He^+ Rutherford backscattering and ion channeling techniques to determine the dopant concentration profiles and the substitutional concentration as a function of depth. Selected crystals were also examined by TEM. Dopant profiles after laser annealing were compared to model calculations using a model that incorporates both dopant diffusion in the liquid during regrowth and an interfacial distribution coefficient k' from the melt. (k' is defined as the ratio of dopant concentrations in solution in the solid and liquid phases at the interface.) Comparing calculations to experimental results allows k' values to be determined for these very rapid regrowth conditions (velocity ~4.5 m/s).

Details of these calculations have been published elsewhere.[3]

Figure 2.36 shows results obtained for the case of ^{209}Bi (1.2×10^{15}/cm^2, 250 keV) in Si. Laser annealing causes ~12% of the implanted Bi to be segregated to the surface. The Bi that is trapped in the lattice after annealing is highly substitutional (~96%) even though the concentration exceeds the equilibrium solubility limit by almost two orders of magnitude. The solid line in Fig. 2.36 is a profile calculated assuming $k' = 0.4$. The dotted line is a profile calculated assuming k' is the equilibrium value, k_0. Clearly, if regrowth occurred under conditions of *local equilibrium at the interface*, very *little Bi would* have remained in the solid. A reasonable fit to the experimental results requires that $k' \gg k_0$.

Table 2.6 summarizes values for k' determined for each of the dopants we have studied and compares them to corresponding equilibrium values. In each case $k' \gg k_0$, and this provides a measure of the departure from local equilibrium at the interface. This departure is brought about by the rapid regrowth velocity (~4.5 m/s).

Table 2.6. Distribution coefficients in Si for equilibrium (k_0)[a] and laser annealing (k') growth conditions

Dopant	k_0	k'	k'/k_0
As	0.3	1.0	3.3
Sb	0.023	0.7	30
Bi	0.0007	0.4	571
Ga	0.008	0.2	25
In	0.0004	0.15	375

[a] $k_0 = \left.\frac{C_s}{C_L}\right|_{\text{equilibrium}}$; $k' = \left.\frac{C_s}{C_L}\right|_{\text{interface}}$.

As the implanted dose is increased, ultimately a limiting concentration (C_s^{max}) is reached above which dopants do not occupy substitutional lattice sites. The limiting substitutional solubility is determined by using Rutherford backscattering and ion channeling techniques to compare the total dopant concentration with the substitutional dopant concentration as a function of depth. Figure 2.37 shows results for a

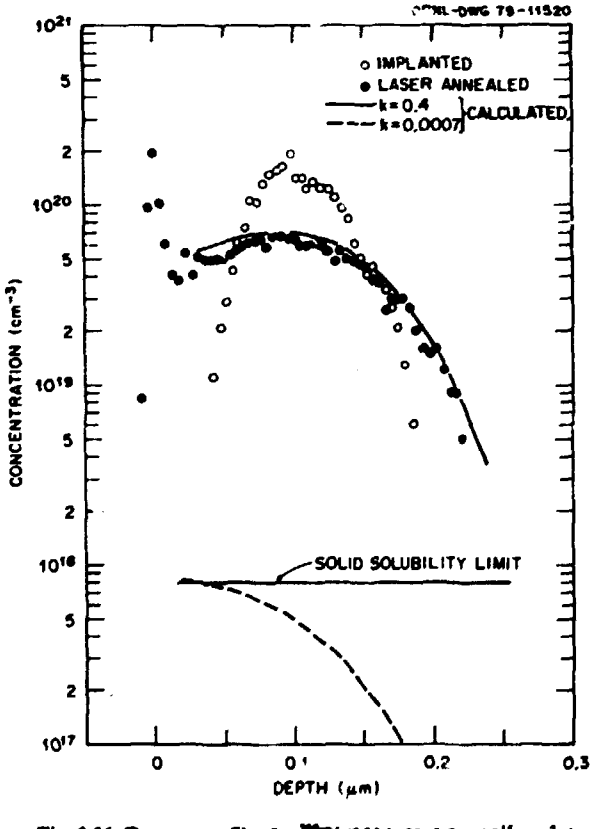

Fig. 2.36. Dopant profiles for ^{209}Bi (250 keV, 1.2×10^{15}/cm^2) in Si compared to calculations.

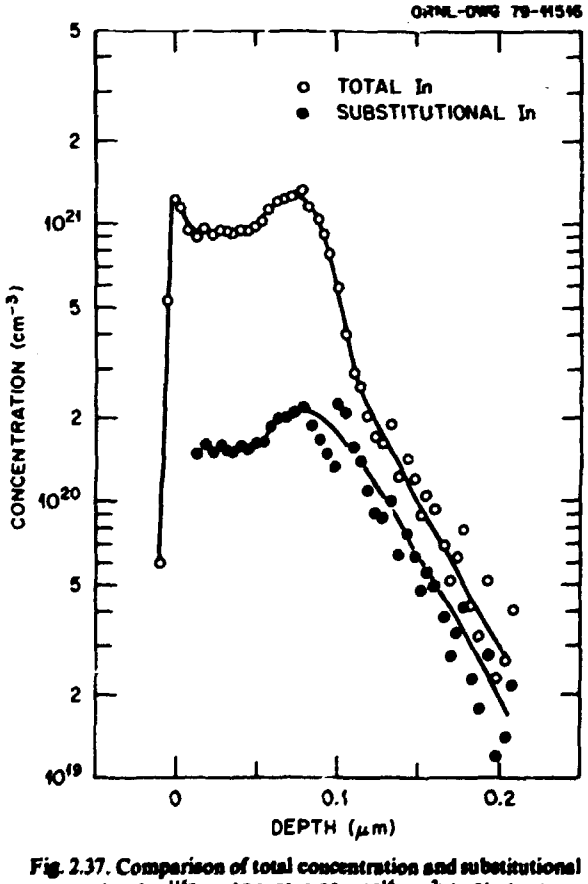

Fig. 2.37. Comparison of total concentration and substitutional concentration for ^{115}In (125 keV, 1.25×10^{16}/cm^2) in Si after laser annealing.

high dose implant of ^{115}In in Si. In Fig. 2.37, the total and substitutional dopant concentrations are very nearly the same up to a limiting value of $\sim 1.5 \times 10^{20}/cm^3$, whereas, in the near-surface region, the total dopant concentration considerably exceeds this value.

Table 2.7 summarizes results for C_i^{max} for each of the dopants and compares them to equilibrium solubility limits (C_i^0). As shown, by using ion implantation and laser annealing, we have exceeded C_i^0 in each case (by factors that range from 4 to 500). Each of these dopants exhibit retrograde solubility in Si, and, as others have shown,[7] for retrograde alloys the equilibrium solubility limit can be exceeded only by a nonequilibrium solidification process. Our results, therefore, conclusively demonstrate the nonequilibrium nature of the laser-annealing-induced, liquid-phase epitaxial regrowth. Dopant incorporation under nonequilibrium conditions presumably takes place by solute trapping at the interface.[7,8]

Table 2.7. Comparison of equilibrium solubility limit (C_i^0), laser annealing solubility (C_i^{max}), and predicted thermodynamic solubility limit

Dopant	C_i^0 (cm^{-3})	C_i^{max} (cm^{-3})	Thermodynamic[a] limit (cm^{-3})
As	1.5×10^{21}	6×10^{21}	5×10^{21}
Sb	7×10^{19}	1.3×10^{21}	3×10^{21}
Bi	8×10^{17}	4×10^{20}	1×10^{21}
Ga	4.5×10^{19}	4.5×10^{20}	6×10^{21}
In	8×10^{17}	1×10^{20}	2×10^{21}

[a]Ref. 6.

Table 2.7 also compares our observed values for C_i^{max} with the absolute maximum solubilities (absolute limits to solute trapping at infinite growth velocity) predicted by theoretical thermodynamics.[6] One can expect to approach these limits as $k' \rightarrow 1.0$. In only two cases (Ga and In) do our results differ significantly from the predicted absolute maximums. These two dopants have the lowest values for k' under present laser annealing conditions. The trapping probability during regrowth is expected to be a strong function of velocity,[8] and experiments are in progress to increase the growth velocity and to trap higher concentrations of Ga and In into the lattice.[9]

When the total dopant concentration considerably exceeds C_i^{max}, the nonsubstitutional dopant is found to be highly concentrated in the walls of a cell structure that develops in the near-surface region during laser annealing.[5] The interior of each cell is an epitaxial column of Si extending to the surface, but the cell walls contain very high concentrations of segregated dopant. The cell structure is believed to result from lateral segregation of rejected dopant due to an interfacial instability developed during regrowth (i.e., constitutional supercooling at the interface). The condition for the onset of constitutional supercooling can be qualitatively expressed as

$$G \leqslant \frac{\Delta T_f}{D/v}, \qquad (1)$$

where G is the thermal gradient in the liquid at the interface, ΔT_f is the interfacial undercooling due to the rejected dopant, D is the liquid-phase diffusivity, and v is growth velocity. Estimates of ΔT_f can be made using the liquidus line of the equilibrium phase diagram and our derived values of k'. With these estimates and using Eq. (1) to predict the presence or absence of a cell structure, we can determine bounds for the thermal gradient in the liquid at the interface. The result[5] is $4 \times 10^6 < G \leqslant 2 \times 10^7$ °C/cm. This result is in good agreement with detailed predictions of the thermal model of laser annealing.[8] For high dose implants, in order to avoid constitutional supercooling, the thermal gradient in the liquid must be increased. This, in turn, implies that a higher regrowth velocity must be achieved, which should be accompanied by an increased trapping probability.

1. Summary of papers: C. W. White et al., *J. Appl. Phys.* **51**, 738 (1980); p. 111 and p. 124 in *Laser and Electron Beam Processing of Materials*, ed. by C. W. White and P. S. Peercy, Academic Press, New York, 1980.

2. ORAU graduate laboratory participant from North Texas State University, Denton; present address: Motorola, Inc., Phoenix, Ariz.

3. C. W. White et al., *J. Appl. Phys.* **51**, 738 1980.

4. C. W. White et al., p. 111 in *Laser and Electron Beam Processing of Materials*, ed. by C. W. White and P. S. Peercy, Academic Press, New York, 1980.

5. C. W. White et al., p. 124 in *Laser and Electron Beam Processing of Materials*, ed. by C. W. White and P. S. Peercy, Academic Press, New York, 1980.

6. J. W. Cahn, S. R. Coriell, and W. J. Boettinger, p. 89 in *Laser and Electron Beam Processing of Materials*, ed. by C. W. White and P. S. Peercy, Academic Press, New York, 1980.

7. J. C. Baker and J. W. Cahn, *Acta Metall.* **17**, 575 (1969).

8. R. F. Wood et al., p. 37 in *Laser and Electron Beam Processing of Materials*, ed. by C. W. White and P. S. Peercy, Academic Press, New York, 1980.

9. J. Narayan et al., "Cell Formation in Ion-Implanted, Laser-Annealed Si," this report.

ION IMPLANTATION DOPING AND PULSED LASER PROCESSING OF HIGH T_c SUPERCONDUCTING MATERIALS[1]

B. R. Appleton O. Meyer[3]
C. W. White J. R. Gavaler[4]
B. Stritzker[2] A. I. Braginski[4]
M. Ashkin[4]

Most superconducting materials that exhibit high T_c behavior are fabricated by evaporation, sputter deposition, or CVD. Much of the success of these techniques has been attributed to their ability to (1) form metastable phases by rapid quenching, (2) form phases at low temperatures, or (3) introduce stabilizing impurities during growth. It is well established that ion implantation doping and pulsed laser annealing are capable of (1) extremely rapid heating and cooling rates, (2) introducing impurities in a controlled manner, (3) forming low temperature phases, (4) forming amorphous mixtures, and (5) creating new materials properties. The rationale for the present work was to utilize these combined processing techniques to test some of the materials preparation concepts associated with high T_c behavior. The materials investigated consisted of thin films of Nb-Ge, V-Si, Nb-N, Nb-C-N, and Nb-Ir prepared by evaporation, sputtering, or CVD onto substrates of alumina, sapphire, or polycrystalline Hastelloy B. Laser annealing was performed in air using a Q-switched (15×10^{-9} s duration) ruby laser with energy densities ranging from 0.1 to 10 J/cm^2. Single, sometimes overlapping, pulses were used. The texture, microstructure, and phase composition of the films were examined by x-ray diffraction. Ion scattering and nuclear reaction analysis were used to determine stoichiometries vs depth in the films. Near-surface melting was monitored from ion scattering measurements of the depth profiles of an ion-implanted marker species before and after laser annealing. Surface topography was monitored with optical microscopy and SEM. These various analyses were correlated to measurements of superconducting transition temperatures, T_c, before and after laser annealing. The T_c measurements were made by a standard four-point resistive technique. Some typical results follow.

Nb_3Ge. Surface melting occurred in the Nb-Ge films for laser pulse energy densities >1.5 J/cm^2. Evidence to support this is illustrated in Fig. 2.38, which shows the depth (scattered ion energy) distribution of 400-keV Bi implanted into a Nb_3Ge film before and after laser annealing. The Bi distribution following laser annealing is typical of

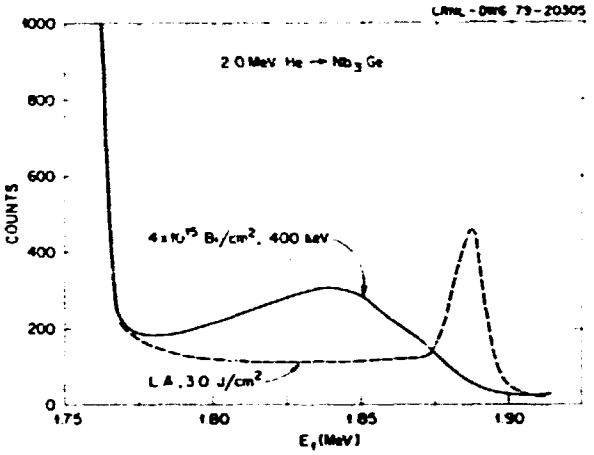

Fig. 2.38. Ion scattering analysis of the redistribution of Bi implanted in Nb_3Ge as a result of laser annealing.

that expected from diffusion in the liquid upon surface melting and segregation to the surface as the melt front advances toward the surface. In general, the combined analyses suggest that the sample surfaces melted and resolidified into a finer-grained microstructure with a deterioration of the $A15$ phase in favor of the more stable tetragonal or hexagonal phases. This interpretation is consistent with Nb-Ge phase diagrams, which show that the high T_c stoichiometric $A15$ phase is not stable. The observed decreases in T_c may be related to heating to greater depths in the samples than just the melted surface. It has been shown that when annealed above 1000°C, the metastable stoichiometric phase, prepared by thin film methods, decomposes into the Nb-rich $A15$ phase and the tetragonal Nb_3Ge phase. In contrast to the above results, laser annealing of a low-T_c sample, one-Nb_3Ge-rich (30 vol %) irradiated to 3 J/cm^2, had the opposite effect: the $A15$ (200) texture was significantly enhanced and the concentration of Nb_3Ge decreased. No change in T_c occurred.

NbN and Nb-C-N. These films were annealed with laser pulses from 0.5 to 7.5 J/cm^2, and little or no surface melting occurred even at the highest laser powers. Nevertheless, ion scattering analysis with H and He ions showed significant redistribution of the near-surface stoichiometry and indicated that the light elements in the films (C, O, N) were also redistributed or possibly lost.

The films with the highest critical temperatures (T_c ~ 15 to 17 K) and the smallest transition widths (ΔT_c ~ 1 K) showed the smallest changes in T_c after annealing. X-ray analysis of annealed and unannealed films showed that in each case they were of

single-phase B1 structure with lattice parameters of ~4.40 Å. The second group of samples consisted of NbN films that initially had T_c of ~11 K and ΔT_c of ~3 K. After annealing the critical temperature increased to between 15 and 16 K; ΔT_c remained approximately the same. X-ray analysis of these films again showed no significant differences between the annealed and unannealed films. In both cases the films were found to be multiphase; and although enhancement of the B1 phase could not be shown from the x-ray data, the increase in T_c to >15 K strongly suggests that such an enhancement had occurred. One possible explanation for the enhancements of T_c is that some O was incorporated into, or redistributed in, the films during the laser annealing process. Since O is known to stabilize the B1 phase, some growth of the cubic phase could occur near the surface of the films. The slight decrease in T_c that was observed in a few of the high-T_c films after laser annealing is not understood.

Phase growth from amorphous films. Increasing evidence from several recent results reveals that new metastable phases can be produced from thermal and laser annealing of amorphous mixtures or from annealing of alloys made amorphous by ion bombardment mixing. We investigated this possibility by laser annealing amorphous Nb-C-N films prepared by sputtering at low substrate temperatures (<300°C). These films were all nonsuperconducting prior to annealing. After pulsed laser annealing, several of these amorphous films became superconducting with $T_c \simeq 12$ K. The ΔT_c values were very broad (i.e., ~7 to 8 K). As with the previous results, so little of the film was altered that x-ray data from the annealed and unannealed films were similar. These results can be understood if it is assumed that laser-induced heating leads to some δ phase, because it has been shown recently that heating amorphous Nb-C-N deposits to temperatures as low as 600°C can form the superconducting δ phase with T_c in excess of 16 K. Both these results are significant because they show that the δ phase can be achieved quite easily when starting from amorphous films. These results do not directly indicate whether the superconducting phase in this case is metastable or impurity stabilized, but they do suggest that phase formation from amorphous structures, utilizing ion implantation and ion beam mixing as well as laser processing, is a promising approach for future study.

1. Summary of paper: B. R. Appleton et al., p. 714 in *Laser and Electron Beam Processing of Materials*, ed. by C. W. White and P. S. Peercy, Academic Press, New York, 1980.

2. Guest scientist from Institut für Festkörperforschung, Kernforschungsanlage, Jülich, Germany.

3. Guest scientist from Nuclear Research Center, Karlsruhe, Germany.

4. Westinghouse Research and Development, Pittsburgh, Pa.

LATTICE STRAIN DISTRIBUTION IN IMPLANTED, LASER-ANNEALED Si[1]

B. C. Larson J. F. Barhorst

Substitutional B atoms in Si contract the Si lattice as a result of the smaller relative size of the B atoms. In B-implanted, laser-annealed Si, this lattice strain has been shown[2] to be one-dimensional along the surface normal, using Bragg reflection profiles and ion channeling. The present study extends the Bragg profile analysis to a quantitative determination of the depth distribution of the strain through the use of Taupin's dynamical diffraction theory for deformed crystals.

According to Taupin's theory,[3] the scattering amplitude

$$X = X_1 + iX_2 \tag{1}$$

as a function of the reduced spatial (depth) parameter $A(t)$ is given in terms of the differential equation

$$i\frac{dX}{dA} = \pi^2(1 + ik)$$

$$- 2X(y + ig) + (1 + ik)\,, \tag{2}$$

where $y(\Delta\theta, \epsilon)$ is a reduced quantity specifying the crystal orientation $\Delta\theta$ with respect to the uncontracted substrate lattice, the local strain is introduced through $\epsilon(t)\tan\theta_B$, where θ_B is the uncontracted Bragg angle, and g and k are constants related to the ratio of the imaginary and real parts of the scattering factors. After specifying $\epsilon(t)$ and applying boundary conditions, Eq. (2) can be evaluated numerically to obtain the reflectivity $R(\Delta\theta)$ of the crystal as

$$R = |X(0)|^2\,. \tag{3}$$

An incident x-ray beam power of I_0 then leads to a measured scattering power of

$$I(\Delta\theta) = I_0 R(\Delta\theta)\,. \tag{4}$$

Through the use of a trial $\epsilon(t)$ and a cyclic procedure of calculations using Eqs. (2, 3, 4) and appropriate adjustments of $\epsilon(t)$, a simulation of the measured

reflection profiles can be achieved in which the resulting $\epsilon(t)$ represents the strain distribution in the crystal.

For the case of a (100) Si crystal implanted with 1×10^{16} B/cm^2 and pulse laser annealed with 1.6 J/cm^2 from a Q-switched ruby laser, the measured 400 Bragg reflection profile using Cu Kα x rays is shown in Fig. 2.39*a*. The solid line shows a calculated reflection profile using the above procedure. All the features in the measured data are represented in the calculated profile, and the overall correspondence is quite good. The strain distribution associated with Fig. 2.39*a* is shown in Fig. 2.40. The strain has a maximum value near the surface of -5.8×10^{-3} and falls off rapidly with increasing depth. It can also be seen that the strain distribution is quite similar to published[4] SIMS measured profiles of B in similarly processed Si.

Making use of lattice parameter change measurements[5] in homogeneously B-doped Si and taking the one-dimensionality of the strain in the present case into account, the relationship

$$C(t) = 1.13 \times 10^{23}\ \text{B/cm}^3\ \epsilon(t) \qquad (5)$$

gives the B concentration $C(t)$ as a function of $\epsilon(t)$. Using Eq. (5), the B concentration corresponding to the x-ray measurement in Fig. 2.40 corresponds to 1.5×10^{16} B/cm^2 compared to the implant dosimetry value of 1×10^{16} B/cm^2. The SIMS B concentration profile in Fig. 2.40 (when multiplied by this factor of ~1.5) corresponds rather well with the x-ray-determined profile. As shown in Fig. 2.39*b*, though, the small differences in the B profile shapes do lead to appreciable scattering profile changes, indicating the sensitivity of the scattering method

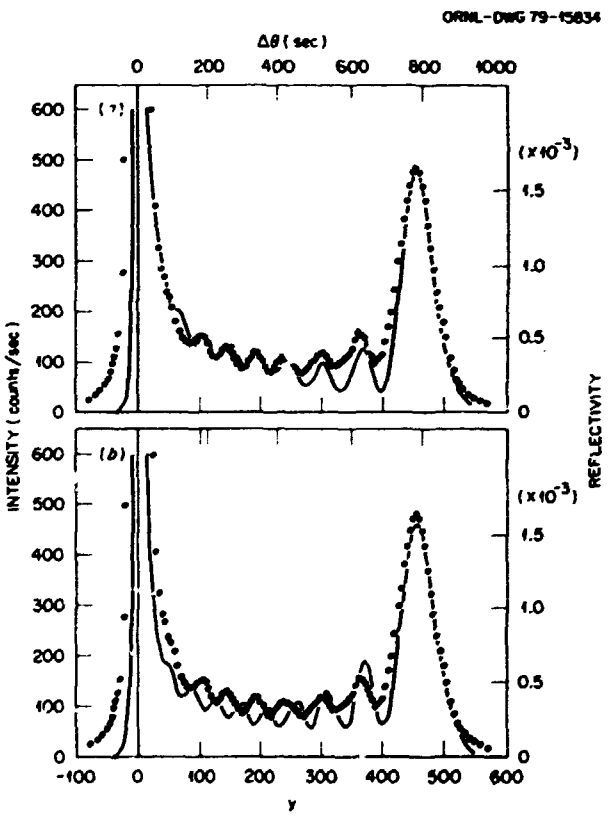

Fig. 2.39. (*a*) Measured (points) and calculated (solid line) x-ray scattering intensity for B-implanted, laser-annealed Si. The angular scale is given in seconds and as a function of y. (*b*) Measured x-ray scattering [as in *a*] and calculations (solid line) using a B profile of 1.58 × SIMS profile to match the large peak position.

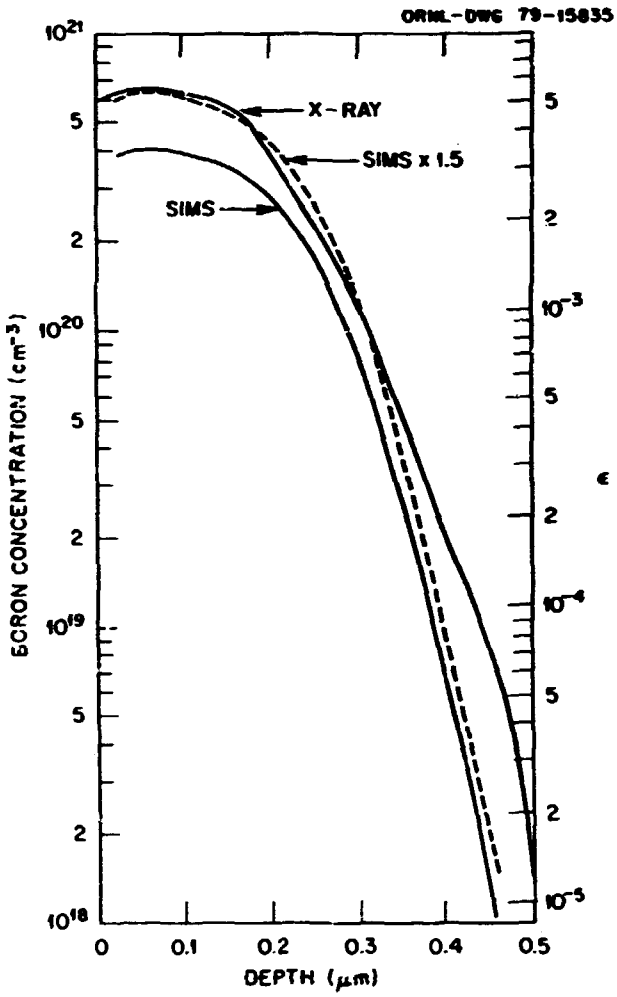

Fig. 2.40. Boron concentration and strain profile (ϵ) as a function of depth in B-implanted, laser-annealed Si as determined by the fitting in Fig. 2.39*a* (solid line) and by the SIMS method.

Although the factor of 1.5 has not been explained, it should be pointed out that the proportionality factor relating the B concentration to the strain in Eq. (5) is based on the use of electrical resistivity measurements to determine the B concentration in the crystals. This may be important in view of the fact that electrical measurements[6] on B-implanted, laser-annealed specimens similar to those studied here also indicate ≈1.5 times more electrically active carriers per square centimeter than specified by the implant dosimetry. No evidence has been found for lattice defects in the B-implanted region (after laser annealing) that might have spuriously enhanced the lattice strain measured by the x-ray technique. A reconsideration of the parameter in Eq. (5) specifying the lattice strain, an examination of the B-implant dosimetry, and a review of the correspondence of the electrical properties of doped Si with dopant concentration would all seem to be useful in resolving this apparent discrepancy.

---

1. Summary of paper: *Journal of Applied Physics* (in press).
2. B. C. Larson, C. W. White, and B. R. Appleton, *Appl. Phys. Lett.* 32, 801 (1978).
3. B. Klar and F. Rustichelli, *Il Nuovo Cimento* 13B, 249 (1973).
4. C. W. White et al., *Appl. Phys. Lett.* 33, 662 (1968).
5. A. Fukuhara and Y. Takano, *Acta Crystallogr. Sect A* 33, 137(1977).
6. R. T. Young et al., *Appl. Phys. Lett.* 32, 139 (1978).

GROWTH OF DISLOCATIONS DURING LASER MELTING AND SOLIDIFICATION[1]

J. Narayan F. W. Young, Jr.

Since Frank[2] proposed the concept of screw dislocations providing perpetual steps for crystal growth, the role of dislocations in crystal growth has been of great interest. The observation of growth spirals in many cases of growth from solution and from vapor provide evidence for the Frank mechanism. However, during crystal growth from the melt, interfacial thermal stresses and high concentrations of defects generally lead to glide and climb of dislocations. As a result, the observed directions of dislocations in crystal growth from the melt do not usually represent the true crystal growth directions, thus obscuring the determination of the role of dislocations in crystal growth. During laser irradiation, a typical ruby laser pulse (energy density $E = 1.5$ J/cm^2, $\tau = 50$ ns) melts the Si surface after 10 to 20 ns of the laser pulse, and then the melt front penetrates to about 300 nm. The melt front then sweeps back to the surface with crystal growth rates of a few meters per second, compared to the 10^{-5} m/s that is typical of normal melt growth. The time intervals involved in laser melting and solidifications are of the order of 100 ns, during which calculated climb distances are less than 0.1 nm; therefore, it is believed that the observed directions of dislocations after laser melting and solidification represent the true crystal growth directions.

The growth of perfect $^a/_2\langle 110\rangle$ and partial $^a/_3\langle 111\rangle$ dislocations was investigated in B-doped (100) Si specimens. These dislocations, shown in Fig. 2.41*a* were generated by thermal annealing (at 1100°C for 30 min) the B-implanted (35-keV, $^{11}B^+$, 3.0×10^{15} cm^{-2}) specimens. The Burgers vectors of dislocations lying in [110] and [1$\bar{1}$0] directions were determined to be $^a/_2[1\bar{1}0]$ and $^a/_2[110]$, respectively. Dislocations along the [1$\bar{1}$0] directions with $^a/_2[110]$ Burgers vector are shown in contrast in Fig. 2.41*a*. The dislocations are pure edge type with extra half-planes between the dislocations lines and the free surface; the deviations from these directions are the measure of the screw component. Faulted dislocations (containing fringes) were of extrinsic type with $^a/_3\langle 111\rangle$ Burgers vectors.

One laser pulse melted the top approximately 0.4-μm-thick layer, and the growth of perfect and partial dislocations is shown in Fig. 2.41*b*. One end of the $^a/_2[110]$ dislocation [labeled 1 in Fig. 2.41*a*] grew along $25 \pm 2°$ from the surface normal (approximately in [113] direction), while the other end split according to the following dislocation reaction:

$$^a/_2[110] - {}^a/_2[101] + {}^a/_2[01\bar{1}]. \qquad (1)$$

These $^a/_2[101]$ and $^a/_2[01\bar{1}]$ dislocations were of near screw type (29° from the pure screw orientation). These growth directions are described in a stereogram shown in Fig. 2.42. The splitting of a partial $^a/_3[11\bar{1}]$ dislocation associated with the fault (shown at 2 in Fig. 2.41*b*) occurs as follows:

$$^a/_3[11\bar{1}] - {}^a/_2[01\bar{1}] + {}^a/_6[2\bar{1}1]. \qquad (2)$$

The growth of the $^a/_2[01\bar{1}]$ dislocation at 2 was similar to that of the $^a/_2[01\bar{1}]$ dislocation at 1, which resulted from splitting according to Eq. (1). It was found that dislocations of a given Burgers vector always grew in the same direction regardless of their origin. These growth directions were also found to be unaffected by impurity content of the crystals. On increasing the pulse energy density, the thickness of

SSDN-2397

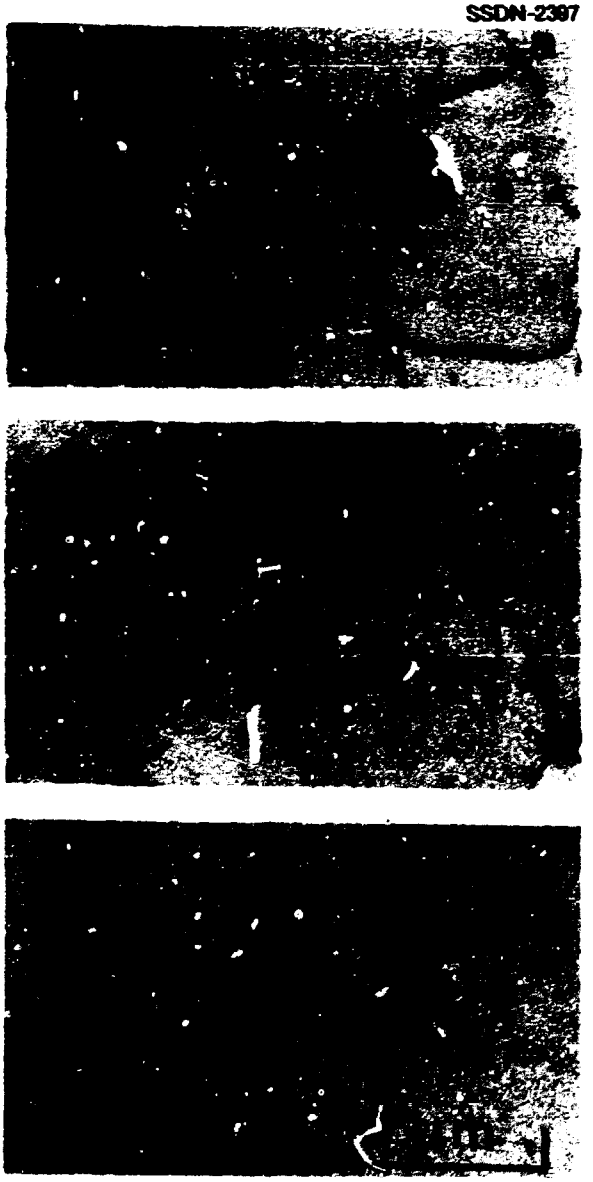

Fig. 2.41. Growth of dislocations in B-doped silicon. (*a*) Perfect $^a/_2$(110) and faulted $^a/_3$(111) dislocations in a B-implanted, thermally annealed Si. (*b*) The growth of a perfect $^a/_2$[110] dislocation at the point labeled 1, and the splitting of perfect $^a/_2$[110] and partial $^a/_6$[11$\bar{1}$] dislocations at 1 and 2, respectively. (*c*) A complete removal on increasing the pulse energy density.

the melted regions increased; and whenever the melt front penetrated beyond the outer boundaries of the dislocations, a complete removal of the dislocations occurred, as shown in Fig. 2.41*c*.

1. Summary of paper: *Appl. Phys. Lett.* 35, 330 (1979).
2. W.K. Burton, N. Cabrera, and F.C. Frank, *Philos. Trans. R. Soc. London* A243, 299 (1951).

SSDN-2193

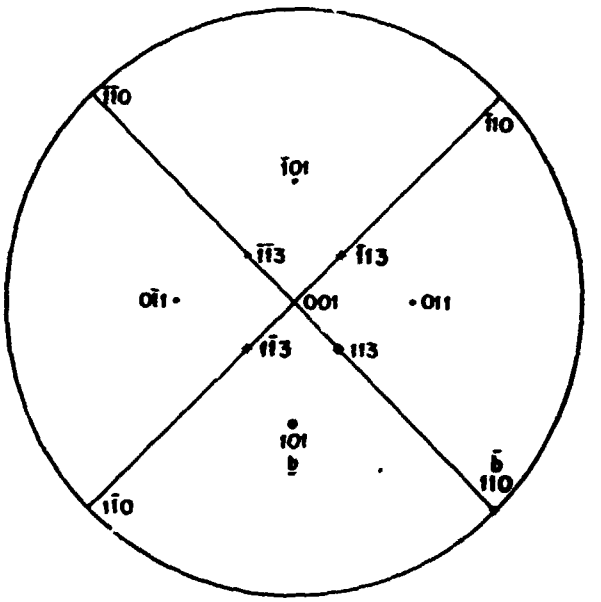

Fig. 2.42. Stereogram showing the growth directions of perfect $^a/_2$[110] and $^a/_2$[1$\bar{1}$0] edges, and $^a/_2$[101] and $^a/_2$[011] near screw dislocations.

CELL FORMATION IN ION-IMPLANTED, LASER-ANNEALED Si

J. Narayan C. W. White B. R Appleton

When Ga-, In-, Fe-, and Sb-implanted Si specimens are laser annealed, pronounced solute segregation is observed near the surface. This segregation is related to the small distribution coefficients (k_0) of these impurities in Si, where $k_0 = C_S/C_L$ and C_S and C_L are the equilibrium impurity concentrations in the solid and liquid phase, respectively, as determined from phase diagrams. It was determined from ion-channeling measurements that, in each of these retrograde systems, the solute concentration in substitutional lattice sites exceeded the equilibrium limit of solid solubility. There appeared to be a maximum solute concentration that could be incorporated into substitutional lattice sites, and these limiting concentrations exceeded the equilibrium (retrograde maximum) solubility limits by factors as high as 500. These observations provided evidence for solute trapping and metastable alloying. At still higher solute concentrations, TEM analysis revealed a cell structure arising from the instability of the planar liquid-solid interface during regrowth.

Mullins and Sekerka[1] have shown that during constant-velocity, undirectional solidification of a

dilute binary alloy, a planar solid-liquid interface is unstable when

$$-\frac{1}{2\bar{K}}(G_S K_S + G_L K_L) + mG_C > h\,. \qquad (1)$$

where K_S and K_L are thermal conductivities of the solid and liquid, G_S and G_L are average temperature gradients in the solid and liquid, respectively, $\bar{K} = (K_S + K_L)/2$, and m is the slope of the liquidus line on the phase diagram. The term G_C corresponds to the average solute gradient in the liquid and is equal to

$$G_C = VC_\infty (k - 1)/Dk\,, \qquad (2)$$

where V is the average velocity of solidification, D is the diffusion coefficient in the liquid, k is the distribution coefficient, and C_∞ is the average concentration in the solid. The value of h in Eq. (1) is given by

$$h = |\max f(\omega)|\,, \qquad (3)$$

where

$$f(\omega) = -T_M \Gamma \omega^2 - \frac{2\,kmG_c}{[1 + (2\omega D/V)^2]^{1/2} + 2k - 1}\,. \qquad (4)$$

The term T_M is the melting point of pure solute, Γ is the capillarity constant defined as the ratio of the solid-liquid surface energy to the latent heat of fusion, and $\omega = 2\pi/\lambda$, with λ being the wavelength of interface instability.

Equations (3) and (4) were solved numerically to find the value of h. The wavelength corresponding to the value of h gives the cell size. Once h is known, one can test the absolute stability criterion given by Eq. (1). In the calculation, the following values for the constants were used:

$$V = 3\ \text{m/s}\,, \quad D = 1.0 \times 10^{-8}\ \text{m}^2/\text{s}\,,$$

$$T_M \Gamma = 1.3 \times 10^{-7}\ \text{K/m}\,,$$

$$K_S = 22\ \text{J m}^{-1}\,\text{s}^{-1}\,\text{K}^{-1}\,,$$

$$K_L = 70\ \text{J m}^{-1}\,\text{s}^{-1}\,\text{K}^{-1}\,,$$

$$G_S \sim 2 \times 10^9\ \text{K/m}\,, \quad G_L \sim 10^9\ \text{K/m}\,.$$

For a particular case of In in Si, $k = 1.0 \times 10^{-4}$, $m = 300$ K (atom fraction)$^{-1}$, and C_∞ was determined to be 3×10^{-3} (atom fraction).

Using these values in Eq. (4) and the maximization in Eq. (3) led to $h = 3.813 \times 10^9$ K/m and the corresponding value of $\omega_m = 1.2 \times 10^8\ \text{m}^{-1}$. From this, the value of λ_m, the cell size, was calculated to be 52 nm. The values of λ_m were calculated as a function of V and k, and the results, plotted in Fig. 2.43, indicate that the cell size is relatively insensitive to k.

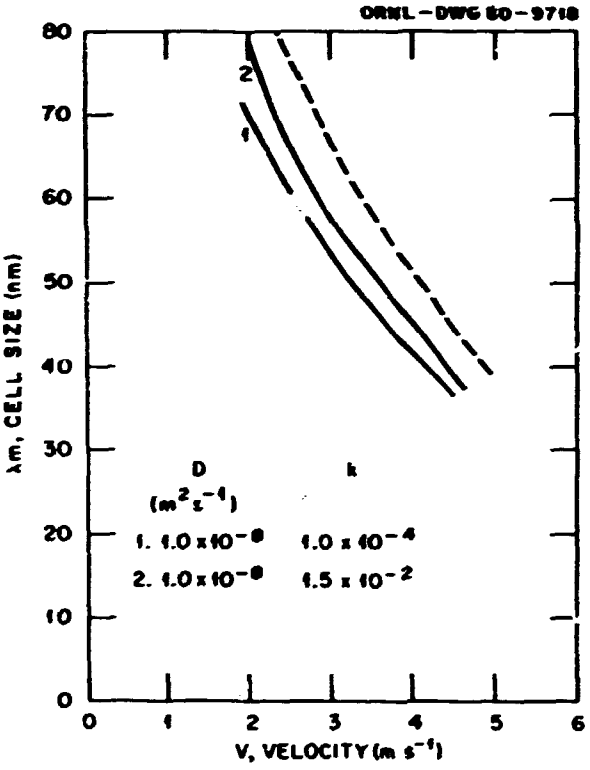

Fig. 2.43. Cell size as function of solidification velocity for different values of k. The dotted curve is for a still higher value of k.

The electron micrographs in Fig. 2.44 show a cell structure in In-implanted (dose = 1.0×10^{16} cm^{-2}), laser-annealed Si. The average cell size was determined to be 50 nm, which is in good agreement with the calculated value of 52 nm. However, the agreement between the experimental and calculated cell sizes should be considered tentative because of the uncertainties in the values of D, k, and V. The interior of each cell in Fig. 2.44*a* is a defect-free column of epitaxial Si where the In concentration trapped in substitutional sites was determined to be 3×10^{-3} atom fraction, which is about 200 times the

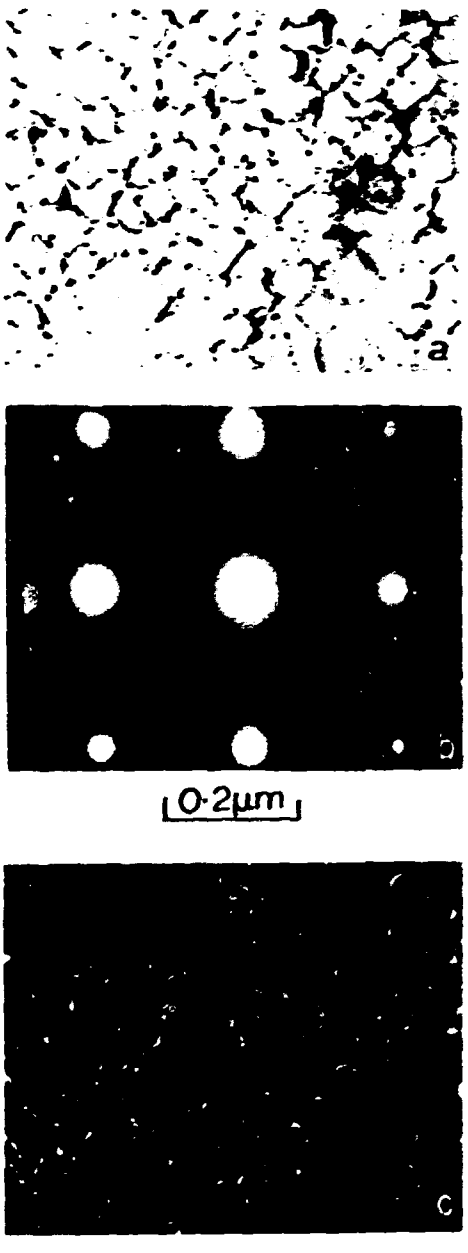

Fig. 2.44. Bright-field electron micrographs showing cells in In-implanted Si. (*a*) cell with average size 52 nm, (*b*) selected area diffraction pattern, and (*c*) dark-field micrograph using In diffraction spots.

maximum equilibrium retrograde solubility. The cell walls (width = 5 nm) contain massive concentrations of segregated In and extend down to a depth of 100 nm. The diffraction pattern in Fig. 2.44*b* shows In diffraction spots near the position where the forbidden 200 Si diffraction spots would have appeared. A dark-field micrograph, obtained using In diffraction spots, clearly delineates the cell walls.

---

[1]. W. W. Mullins and R. F. Sekerka, *J. Appl. Phys.* 35, 444 (1964).

KINETIC EFFECTS IN LASER ANNEALING OF ION-IMPLANTED Si

C. W. White D. M. Zehner
B. R. Appleton B. Stritzker[1]
S. R. Wilson[2]

Systematic studies of kinetic effects in laser annealing of ion-implanted Si have been initiated. Our previous results[3] showed that implanted group III and V dopants in Si can be incorporated very effectively into substitutional lattice sites by the laser-annealing-induced liquid-phase epitaxial regrowth process. At the growth velocities which can be achieved by pulsed laser annealing in the nanosecond time regime (several m/s), dopant incorporation into substitutional lattice sites occurs by solute trapping,[4-6] and the trapping probability and interfacial distribution coefficient k' are predicted to depend strongly on velocity.[6] Measurements of the kinetic effects of dopant incorporation, consequently, should provide information that is essential to model the trapping process.

Two methods exist to change systematically the growth velocity during liquid phase epitaxial regrowth. In one method, the temperature of the substrate during annealing is maintained above or below room temperature. Increasing the substrate temperature leads to a slower growth velocity, while higher growth velocities can be achieved by holding the substrate at liquid nitrogen or liquid helium temperatures. The other method for achieving faster growth velocity involves using faster pulses. In the present experiments, the former method was used because of the lack of ready access to a mode-locked laser.

To study kinetic effects, Si single crystals, (001) orientation, were implanted by ^{209}Bi (250 keV, 1.1×10^{15} cm^{-2}). Annealing was accomplished using single pulses of radiation from a *Q*-switched ruby laser (15×10^{-9} s pulse duration time). Annealing was carried out while maintaining the substrate at temperatures of 650, 300, and 100 K and using energy densities of 1.2, 1.4, and 1.7 J cm^{-2}, respectively. A different energy density was used at each temperature in an effort to maintain the same melt depth (380 nm). Estimates of regrowth velocity achieved at the three substrate temperatures are 2.6, 4.5, and 6.0 m/s.

Crystals were examined before and after annealing by using 2.5-MeV He^+ Rutherford backscattering and ion channeling techniques to determine the damage distribution, dopant profile distribution, and substitutional dopant concentration as a function of depth.

Figure 2.45 shows experimental Bi concentration profile results obtained after annealing at the three different substrate temperatures. At each temperature, Bi is segregated to the surface, but ion channeling measurements show that in each case the Bi in the lattice is highly substitutional ($\geq 96\%$) even though the concentration significantly exceeds the equilibrium solubility limit ($\sim 8 \times 10^{17}/cm^3$). Figure 2.45 demonstrates significant kinetic effects on the shape of the dopant profile and the interfacial distribution coefficient (k') during regrowth. At low substrate temperature (i.e., high growth velocity), the profile does not redistribute as much and a relatively small amount of Bi is segregated to the surface. At high substrate temperature (i.e., slow growth velocity), the profile spreads deeper into the crystal and substantially more segregation to the surface occurs. The fraction of Bi segregated to the surface is 54.9, 11.2, and 4.6% for annealing temperatures of 650, 300, and 100 K. This striking difference in the fraction segregated is due to the change in the interfacial distribution coefficient caused by the velocity dependence of the trapping probability. Model calculations will be used to extract values for k' from the dopant profile measurements, but it is clear that we have been able to change the distribution coefficient by almost an order of magnitude. These results are in qualitative agreement with calculations,[5] and a detailed comparison with theoretical predictions[6] will be possible when values for k' are determined. This comparison should provide information necessary to model the solute trapping process.

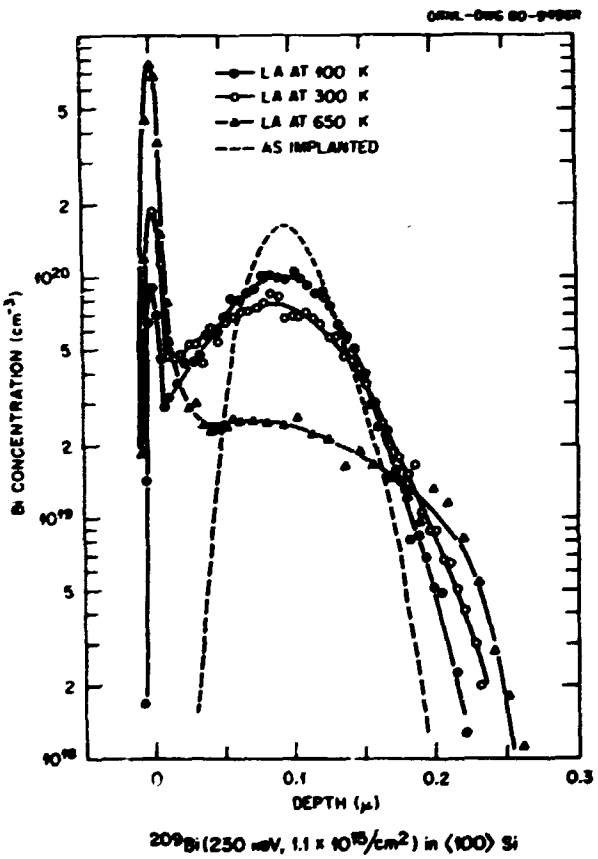

^{209}Bi(250 keV, $1.1 \times 10^{15}/cm^2$) in ⟨100⟩ Si

Fig. 2.45. Kinetic effect on the segregation of Bi to the surface during laser annealing. Temperatures indicate the substrate temperature during annealing. Growth velocities are estimated to be ~2.6, 4.5, and 6.0 m s for temperatures of 650, 300, and 100 K, respectively.

It will be necessary to use picosecond pulses from a mode-locked laser as well as nanosecond pulses from a Q-switched laser at higher substrate temperatures in order to determine the velocity dependence of k' over a wider velocity range. Such experiments are in progress. Experiments are also in progress to determine the velocity dependence of the interfacial distribution coefficients for the other dopants and to determine the velocity dependence of the limiting substitutional solubilities (C_s^{max}).

1. Guest scientist from Institut für Festkorperforschung, Kernforschungsanlage, Jülich, Germany.
2. ORAU graduate laboratory participant from North Texas State University, Denton; present address: Motorola, Inc., Phoenix, Ariz.
3. C. W. White et al., *J. Appl. Phys.* 51, 738 (1980).
4. J. C. Baker and J. W. Cahn, *Acta Metall.* 17, 575 (1969).
5. K. A. Jackson, G. H. Gilmer, and H. J. Leamy, p. 104 in *Laser and Electron Beam Processing of Materials*, ed. by C. W. White and P. S. Peercy, Academic Press, New York, 1980.
6. R. F. Wood et al., p. 37 in *Laser and Electron Beam Processing of Materials*, ed. by C. W. White and P. S. Peercy, Academic Press, New York, 1980.

PULSED LASER ANNEALING

HIGH-SPEED ZONE REFINING IN PULSED LASER ANNEALING OF ION-IMPLANTED Si[1]

C. W. White B. R. Appleton
S. R. Wilson[2] J. Narayan

Systematic studies have been initiated to study the effects of pulsed laser annealing on Si crystals that have been implanted with a wide range of nongroup III and V impurities.[3] Implanted impurities that have been investigated include Cu, Fe, Zn, Mn, W, and Mg. These species were implanted into single-crystal Si, (001) and (111) orientations, at doses in the range 10^{14} to 5×10^{16}/cm^2 and at energies in the range 100 to 250 keV. Annealing was carried out using single pulses from a *Q*-switched ruby laser (~1.5 J/cm^2, 15×10^{-9} s pulse duration). Crystals were examined before and after annealing using 2.5-MeV He^+ *Rutherford backscattering and ion channeling* techniques to determine the damage distribution, dopant profile distribution, and the substitutionality of the dopant. Transmission electron microscopy was used to study the microstructure in the near-surface region after laser annealing.

The impurities listed above exhibit segregation or zone refining to the surface which is a function of the implantation dose and number of pulses used for annealing. Results for the case of Fe in Si are summarized in Fig. 2.46. At low doses (1.1×10^{15}/cm^2), one pulse of laser radiation is sufficient to cause complete zone refining of the impurity to the surface. At intermediate doses (5.5×10^{15}/cm^2), a substantial segregation toward the surface occurs during the first pulse, but two pulses are required to cause complete surface segregation. At high doses (1.8×10^{16}/cm^2), significant quantities of Fe are left in the bulk of the crystal, even after ten pulses. Channeling studies show that the Fe left in the bulk of the crystal does not occupy a regular lattice site and, therefore, has not been incorporated into solution by solute trapping during liquid-phase epitaxial regrowth. Qualitatively similar results have been obtained for the other impurities listed above.

The TEM studies show that at high doses a cell structure develops in the near-surface region during laser annealing.[1] The interior of each cell is an epitaxial column of Si extending to the surface, but the cell walls contain very high concentrations of segregated impurity. In the high-dose Fe case of Fig. 2.46, the Fe that appears to be distributed in the bulk of the crystal is highly concentrated in the cell walls, which extend to a depth of ~1000 Å in the crystal. By contrast, for low doses, a well-defined cell structure does not develop, and the Fe is localized to the first few monolayers of the crystal.

The development of a well-defined cell structure in crystals implanted to high doses is believed to be related to lateral segregation of rejected dopant caused by an interfacial instability that develops during regrowth (i.e., constitutional supercooling at

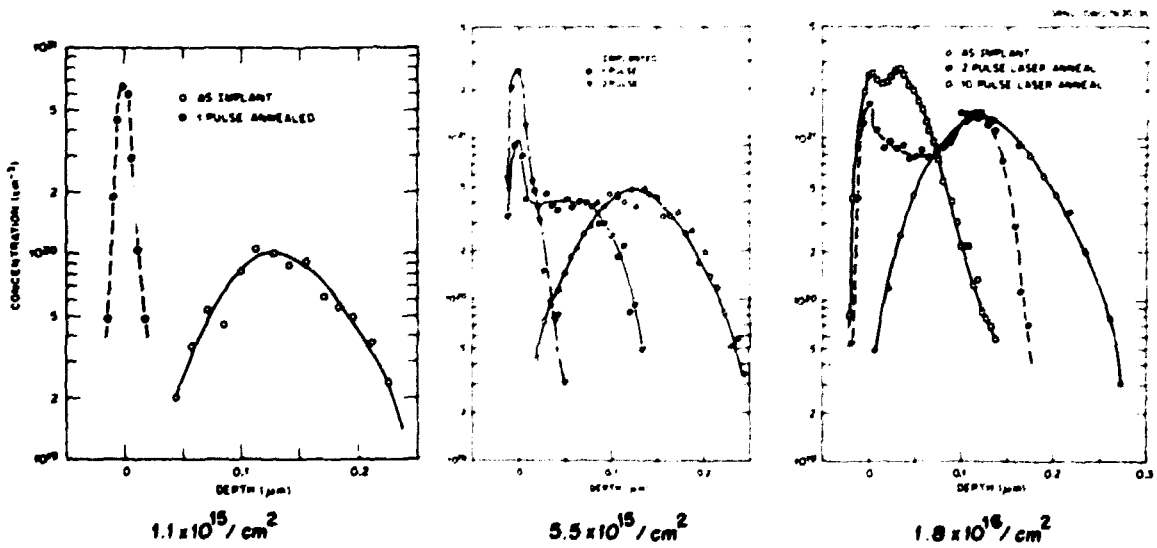

Fig. 2.46. Profiles of ^{56}Fe in Si.

the interface). For low doses, the interface is stable during regrowth, and a regular cell structure does not develop.

These results show that the trapping probability at the interface for the impurities listed above is significantly less than that for group III and V impurities, which are trapped with high probability into substitutional lattice sites during the laser-annealing-induced liquid-phase epitaxial regrowth Each of the impurities in this investigation is an interstitial diffuser in the solid, and presumably the bonding properties of these impurities in the solid are such that the required trapping energies cannot be supplied.[3] Efficient trapping of these impurities may be possible, however, at significantly higher growth velocities. Experiments to test these ideas are in progress. These results also demonstrate that very effective high-speed zone refining of undesirable impurities in Si can be accomplished by using a series of high-powered laser pulses.

1. Summary of paper: p. 124 in *Laser and Electron Beam Processing of Materials*, ed. by C. W. White and P. S. Peercy. Academic Press, New York, 1980.

2. ORAU graduate laboratory participant from North Texas State University, Denton; present address: Motorola, Inc., Phoenix, Ariz.

3. R. F. Wood et al., p. 37 in *Laser and Electron Beam Processing of Materials*, ed. by C. W. White and P. S. Peercy Academic Press, New York, 1980.

MEASUREMENTS OF EQUILIBRIUM SOLUBILITY LIMITS FOR GROUP III AND V DOPANTS IN Si

C. W. White B. R. Appleton
S. R. Wilson[1]

Previous determinations of equilibrium solubilities for group III and V dopants in Si employed electrical measurements or radiotracer techniques. These results are summarized in ref. 2. Recently, it has been demonstrated that supersaturated alloys of group III and V dopants in Si can be fabricated using ion implantation doping and pulsed-laser-annealing techniques.[3,4] These alloys can have dopant concentrations in substitutional lattice sites that are far above the reported equilibrium solubility limit. However, upon subsequent thermal annealing, the dopant concentration in excess of the equilibrium solubility limit at the annealing temperature will form precipitates, and a measurement of the maximum substitutional dopant concentration as a function of depth after thermal annealing then allows the equilibrium solubility limit at the annealing temperature to be determined.[5] We report here measurements of the equilibrium solubility limit for As and Sb in Si at a temperature of 1100°C, a temperature close to that corresponding to the retrograde maximum solubility.

Silicon single crystals, (001) orientation, were implanted with ^{75}As (100 keV, $6 \times 10^{16}/cm^2$) and ^{121}Sb (100 keV, $2 \times 10^{15}/cm^2$). After implantation, the crystals were laser annealed using single pulses of radiation from a *Q*-switched ruby laser (~1.5 J/cm², 15×10^{-9} s pulse duration). The crystals were then examined using 2.5-MeV He^+ Rutherford backscattering and ion channeling techniques to determine the dopant concentration and substitutionality as a function of depth. After laser annealing, these measurements showed that the dopants were >96% substitutional in the lattice even though the dopant concentration in the near-surface region was ~$6 \times 10^{21}/cm^3$ for As and ~$1.8 \times 10^{20}/cm^3$ for Sb. These concentrations significantly exceed previously reported[2] equilibrium solubility limits for As ($1.5 \times 10^{21}/cm^3$) and Sb ($7 \times 10^{19}/cm^3$). The crystals were then thermally annealed at 1100°C in an N_2 atmosphere (8 min for the As-implanted crystal and 30 min for the Sb-implanted sample). Rutherford backscattering and ion channeling measurements were used to compare the total dopant concentration with the substitutional dopant concentration as a function of depth.

Figures 2.47 and 2.48 show the experimental results for ^{75}As and ^{121}Sb in Si after thermal

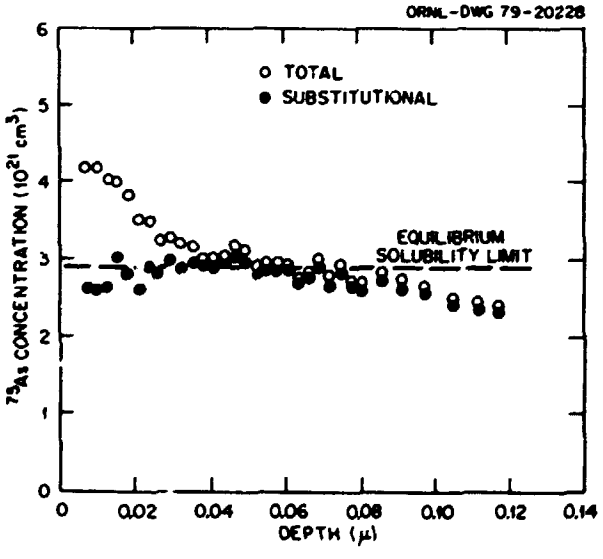

Fig. 2.47. Comparison of total and substitutional As concentrations in Si after thermal annealing (1100°C) of a supersaturated, solid solution.

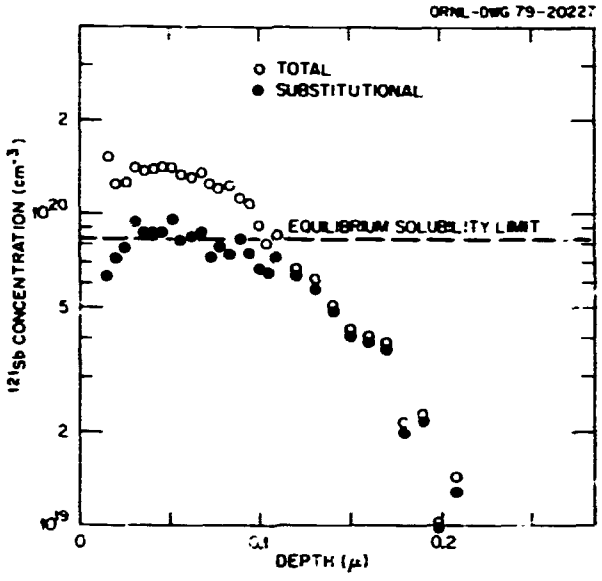

Fig. 2.48. Comparison of total and substitutional ^{121}Sb concentrations in Si after thermal annealing (1100°C) of a supersaturated, solid solution.

annealing at 1100°C. For ^{75}As, the maximum substitutional concentration after thermal annealing is 2.9×10^{21}/cm^3, whereas the total dopant concentration reaches as high as 4.2×10^{21}/cm^3. Therefore, the equilibrium solubility limit for ^{75}As in Si is 2.9×10^{21}/cm^3 at a temperature of 1100°C. This value is almost a factor of 2 higher than that reported in ref. 2 ($\sim 1.5 \times 10^{21}$/cm^3). In Fig. 2.48, the maximum substitutional concentration after thermal annealing is 8.2×10^{19}/cm^3, which is, therefore, the equilibrium solubility limit for Sb in Si at 1100°C, in good agreement with the value of 7×10^{19} cm^3 reported in ref. 2. This technique provides an accurate and versatile experimental method for determining equilibrium and metastable phase relationships. Such measurements could, in principle, be extended to determine the solidus line on the equilibrium phase diagram[4] over a much wider temperature range than that covered by previous measurements.

1. ORAU graduate laboratory participant from North Texas State University, Denton; present address: Motorola, Inc., Phoenix, Ariz.
2. F. Trumbore, *Bell System Tech. J.* **39**, 205 (1960).
3. C. W. White et al., *J. Appl. Phys.* **51**, 738 (1980).
4. C. W. White et al., *J. Appl. Phys.* **50**, 3261 (1979).
5. C. W. White et al., p. 111 in *Laser and Electron Beam Processing of Materials*, ed. by C. W. White and P. S. Peercy, Academic Press, New York, 1980.

INFRARED REFLECTIVITY AND TRANSMISSIVITY OF B-IMPLANTED, LASER-ANNEALED Si[1]

Herbert Engstrom

The development of laser annealing of ion-implanted semiconductors has allowed the fabrication of surface layers of heavier doping than has heretofore been possible.[2] Because this technique has been applied successfully to produce solar cells of increased efficiency,[3] it is of interest to examine the optical properties of these ion-implanted materials. In the present work the midinfrared reflectance and transmittance spectra of B-implanted, laser-annealed samples have been measured and analyzed on the basis of the Drude theory to obtain approximate values of the relaxation time for hole scattering.

Reflectance and transmittance spectra in the wavelength range of 2.5 to 20 μm were measured using a Digilab model FTS-20 Fourier transform spectrometer. All measurements were made for approximately normal incidence. The measured reflectance and transmittance are shown in Fig. 2.49. The dip visible at approximately 15 μm is from second-order absorption in the underlying pure Si bulk due to the Si optic mode. The nearby structure is due to other Si phonons. (First-order lattice absorption is forbidden in Si.)

The presence of the B ions substituting for Si leaves holes in the valence bands. In the Drude theory[4] of electrical conductivity, these holes give rise to a complex dielectric constant of the form

$$\hat{\epsilon} = \epsilon_\infty - \frac{4\pi N e^2}{m^*} \frac{\tau^2}{(1+\omega^2\tau^2)} + i \frac{4\pi N e^2}{m^*} \frac{\tau}{(1+\omega^2\tau^2)} , \quad (1)$$

where ϵ_∞ = dielectric constant due to the core electrons, N = hole concentration, m^* = effective hole mass, e = electronic charge, ω = angular frequency of light, and τ = relaxation time.

The complex refractive index is

$$\hat{n} = n + i\kappa = \hat{\epsilon}^{1/2} , \quad (2)$$

and from Maxwell's equations, the propagation of light in the dielectric medium is given by

$$E = E_0 \exp i(\hat{n}\kappa r - \omega t) . \quad (3)$$

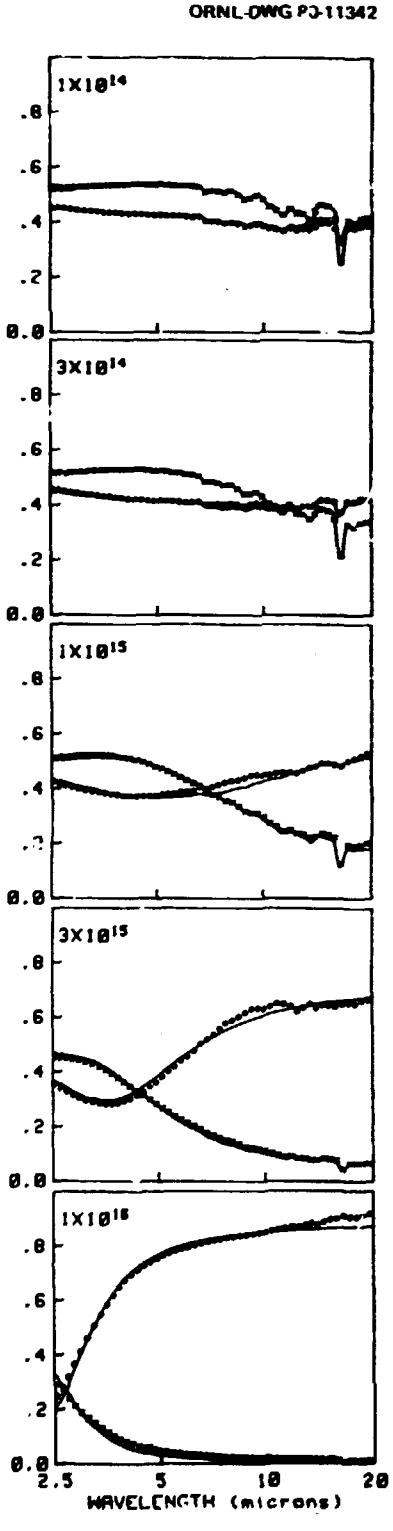

Fig. 2.49. Experimental values of reflectance (circles) and transmittance (x's) and theoretical fit (solid lines). Implant doses (ions/cm²) are shown at upper left corner of each graph. For clarity, only every third experimental point is shown.

Given the refractive index, the reflection and transmission coefficients may be calculated according to well-known procedures for thin films.[5]

In B-implanted Si, the boron concentration in the implanted layer is not constant with depth. To apply the expressions for thin films, the implanted layer was approximated by a series of 10 laminas, each 0.05 μm thick. The B concentration in each lamina was estimated from SIMS measurements on a similarly prepared sample. Using τ and N_0/ρ^* as adjustable parameters, where N_0 is the B concentration at the sample surface and ρ^* is the ratio of the effective hole mass to electron mass, it was possible to fit the measured reflectance and transmittance for all implant doses over the entire spectral range. The calculated values are shown as solid lines in Fig. 2.49.

The parameters so determined are shown in Fig. 2.50; the scale on the left shows the relaxation time τ, and that on the right shows the peak concentration to effective hole mass ratio N_0/ρ^*. As is seen, the relaxation time is essentially independent of implant dose, and the straight line is the best-fit graph to N_0/ρ^* vs implant dose. The slope of the line was found to be 0.981 $\pm$ 0.023. That the slope is very nearly unity indicates that essentially all of the implanted B contributes to the optical properties, even at very high doping levels.

These results indicate that the Drude theory provides a good accounting for the changes in the optical properties of Si with doping level. Thus, the

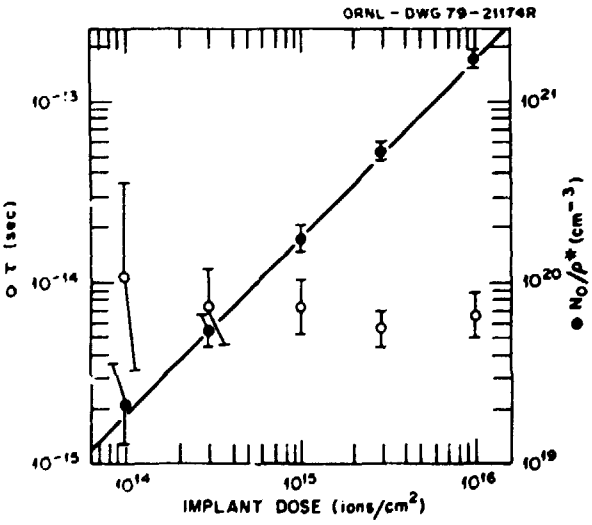

Fig. 2.50. Relaxation time τ (left-hand scale) and peak concentration/effective mass ratio N_0/ρ^* (right-hand scale) vs B implant dose. The solid line is the best straight line through the values of N_0/ρ^*.

simple theory may be used with reasonable success to describe the optical interactions, even in very heavily implanted samples.

1. Summary of paper to be published.
2. R. T. Young et al., *Appl. Phys. Lett.* 32, 139 (1978).
3. C. W. White, J. Narayan, and R. T. Young, *Science* 204, 461 (1979).
4. See, for example, F. Wooten, p. 52 in *Optical Properties of Solids*, Academic Press, New York, 1972.
5. A. Vasicek, p. 90 in *Optics of Thin Films*, North-Holland, Amsterdam, 1960.

SURFACE STRUCTURE OF ION-IMPLANTED, LASER-ANNEALED Si

C. W. White G. W. Ownby
D. M. Zehner W. H. Christie[1]

The basic surface properties have been determined for the first time for ion-implanted Si crystals laser annealed in a UHV environment. Previously, we reported the surface properties (structure and impurities) of unimplanted Si crystals subsequent to laser annealing in UHV,[2-5] but for many applications, Si must be implanted with group III or V dopants in order to form a junction. The surface structure and impurities after annealing play a major role in determining the surface electronic properties, and such determinations have not been made, to our knowledge, using ion-implanted Si.

Silicon single crystals, (001) orientation, were implanted with either ^{75}As (100 keV, 8×10^{14} cm^2) or ^{11}B (35 keV, 1×10^{16}/cm^2). The implanted crystals were then inserted into a UHV system (pressure $\sim 10^{-10}$ torr) which contained a four-grid LEED system and a single-pass CMA used for AES to monitor surface impurities. The light from a pulsed ruby laser was coupled through a glass window into the UHV system. Samples were irradiated by using the single mode output (TEM_{00}) of the pulsed ruby laser at an energy density of ~ 2.0 J/cm^2. A constant pulse duration time of $\sim 15 \times 10^{-9}$ s was used throughout the experiments. Previous work[2,3] has shown that atomically clean, well-ordered surfaces can be produced on unimplanted crystals by using these laser conditions. After removing these crystals from the UHV environment, the dopant profiles were determined using 2.5-MeV He$^+$ Rutherford backscattering and SIMS techniques.

Figure 2.51 shows the LEED patterns obtained from the crystal implanted with ^{75}As after 2, 5, and 10 pulses. No discernible LEED pattern could be observed after one pulse, indicating considerable disorder in the first few monolayers of the crystal. After 2 or 5 laser shots, a basic 1×1 LEED pattern is observed with weak half-order spots. The quality of the LEED pattern continues to improve until a well-defined 2×1 pattern is observed after 10 shots. There is little, if any, change in the quality of the LEED pattern after 10 shots (up to a total of 15 shots).

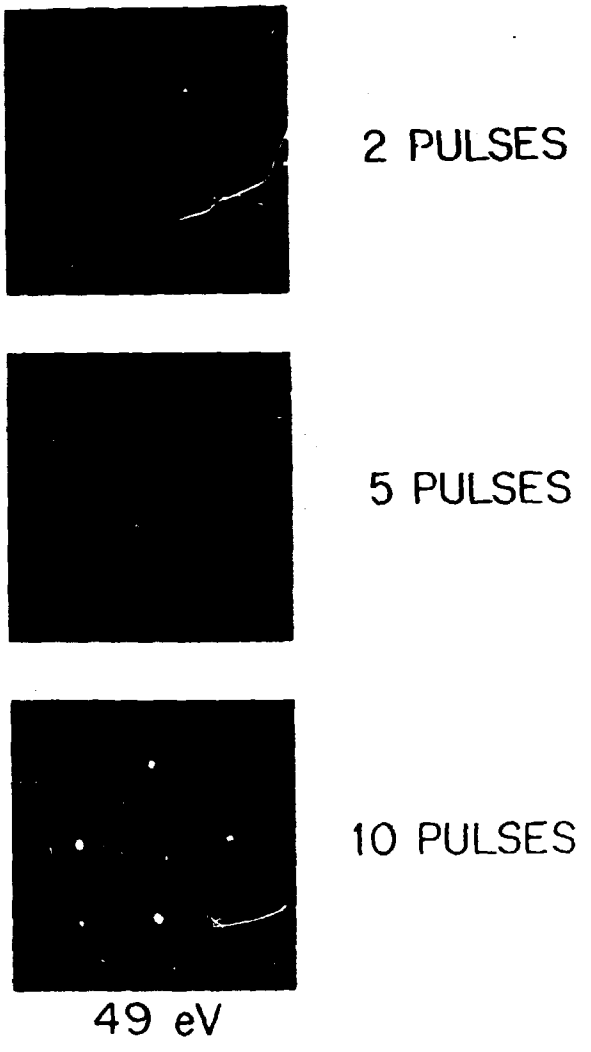

Fig. 2.51. LEED patterns subsequent to laser annealing ^{75}As (100 keV, 8.3×10^{14}/cm^2) implanted (100) Si.

AES measurements show that after one shot, only trace amounts of C and O contaminants remain. These contaminants are reduced to the detection limit after ~ 5 shots, in agreement with previous results.[3] Substantial quantities of As are detected by

AES after laser irradiation. The signal strength of the As Auger transition was found to decrease monotonically as a function of the number of pulses.

Figure 2.52 shows the As dopant profiles measured by RBS after removing the crystal from the UHV environment. Extrapolation of these profiles to the surface suggests that the As concentration at the surface after the first pulse is $\sim 5.3 \times 10^{21}/cm^3$. Subsequent pulses give rise to additional redistribution and, consequently, a lower concentration at the surface. These results are in qualitative agreement with the AES measurements.

The gradual improvement of the clarity of the LEED pattern with additional pulses and the reduction in the As concentration at the surface from the RBS and AES measurements suggest that very large concentrations of As at the surface will stabilize the 1×1 LEED pattern. As the concentration at the surface is reduced by repeated pulses, a well-defined (2×1) LEED pattern develops when the dopant concentration at the surface is reduced to $\sim 1.5 \times 10^{21}/cm^3$. Qualitatively similar results were obtained for the case of ^{11}B-implanted Si.

The development of well-defined LEED patterns after only a few pulses indicates that the annealing resulting from the rapid liquid-phase epitaxial regrowth process extends to the outermost monolayers of the crystal. At very high dopant concentrations, however, residual disorder remains in the first few monolayers. As the dopant concentration is reduced, the dopants stabilize the 1×1 pattern, and a further reduction in the concentration leads to the development of a well-defined 2×1 LEED pattern. These experiments are being extended to other crystal surfaces and to other implanted impurities, particularly those that are strongly zone refined at these fast growth rates.

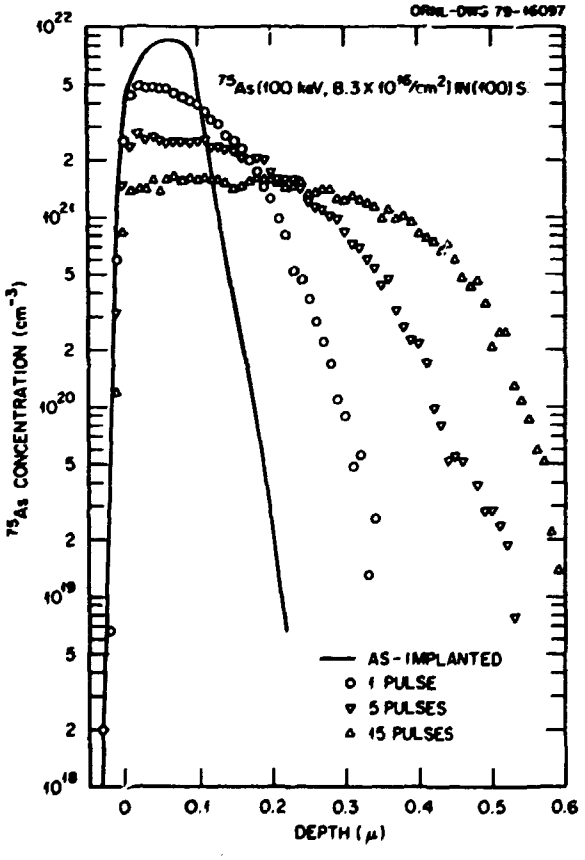

Fig. 2.52. ^{75}As profiles in (100) Si after pulsed-laser annealing.

1. Analytical Chemistry Division, ORNL.

2. D. M. Zehner et al., p. 201 in *Laser and Electron Beam Processing of Materials*, ed. by C. W. White and P. S. Peercy, Academic Press, New York, 1980.

3. D. M. Zehner, C. W. White, and G. W. Ownby, *Appl. Phys. Lett.* 36, 56 (1980).

4. D. M. Zehner, C. W. White, and G. W. Ownby, *Surf. Sci. Lett.* 92, L67 (1980).

5. D. M. Zehner, C. W. White, and G. W. Ownby, *Applied Physics Letters* (to be published).

LASER ANNEALING UNDER OXIDE LAYERS IN Si[1]

J. Narayan

High-power laser pulses have been successfully used to remove displacement damage and other defects in bare Si.[2] However, for device manufacturers, laser annealing of Si with SiO_2 layers on the surface is of particular interest. The feasibility of this process and electrical characteristics of laser-annealed specimens have been demonstrated.[3] The purpose of this investigation was to provide clear evidence of melting under oxide layers. The melting can be used to remove/anneal defects present in the Si substrate.

Arsenic-doped (1.0×10^{16} cm^{-2} implanted and thermally annealed at 1100°C for 30 min) Si crystals with thermally grown SiO_2, 25 nm thick, were used in this investigation. These specimens were treated with ruby laser pulses (wavelength $\lambda = 0.694$ μm, pulse duration $\tau = 20 \times 10^{-9}$ s, energy density $E = 1$–2 J/cm^2). The effect of ~25-nm-thick SiO_2 on the transmissivity (T) of laser energy is negligible.[4]

An electron microscope investigation of the (111) oxide-coated specimens, which had been ion implanted and thermally annealed, showed that beneath the oxide layer, the dislocations lay approximately in ⟨112⟩ directions with ½⟨110⟩ Burgers vectors that are parallel to the specimen surface. These dislocations were pure edge dislocations, the amount of deviation from ⟨112⟩ directions being a measure of the screw character. The dislocations were in the form of arcs extending from the surface to a depth of about 0.6 μm. The dislocation segments near the surface lay approximately in the [111] direction (i.e., normal to the specimen surface). Fig. 2.53*a* is an optical micrograph of the specimen after one laser pulse ($E = 1.3$ J/cm^2) showing a ripple pattern on the surface. The wavelength of the ripple pattern was determined to be ~1.6 μm. An electron microscope examination of this specimen (Fig. 2.54*a*) showed that the dislocations reoriented in a 0.25-μm-thick Si layer beneath the oxide. These segments remained in edge orientation with unchanged Burgers vectors but lay at 21 ± 2° from the [111] surface normal. Because the reoriented segments of dislocations lie precisely in the same crystallographic direction, these observations are consistent with melting and subsequent recrystallization, with the underlying dislocations providing nuclei for grown-in dislocations. It should be mentioned that reorientation of dislocations in the solid state would require climb distances of ~0.2 μm in order to be consistent with the observations, whereas calculated climb distances, even close to the melting point of Si, are only the order of 1 Å. It has been proposed[3] that the ripple pattern observed in Fig. 2.53 is due to thermal expansion of the oxide layer during laser melting of the underlying Si and to subsequent stress relief, which results in a buckling of the thin oxide layer.

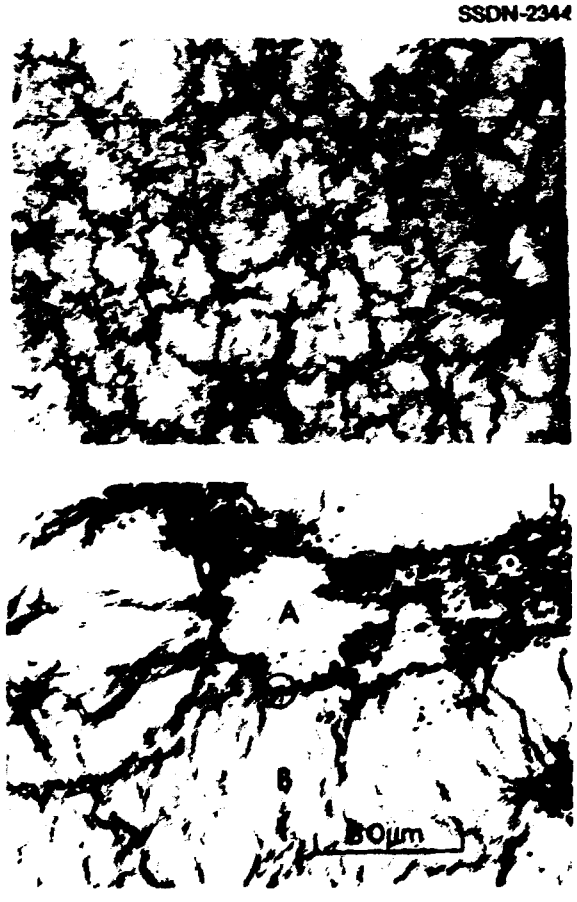

Fig. 2.53. Optical micrographs of a (111) Si specimen with an ~25-nm-thick SiO_2 layer after laser annealing: (*a*) ripple pattern appearing after a laser pulse of energy $E = 1.3$ J/cm^2, $\tau = 15$ to 20 ns; (*b*) companion specimen after a laser pulse of energy $E = 2.0$ J/cm^2. The oxide melted in the area indicated by A, and the lines of the ripple pattern are normal to the melted boundary. The area encircled was thinned for electron microscopy [see (*b*)].

When the pulse energy was increased to 2.0 J/cm^2, a complete removal of the dislocations occurred, which indicated that the depth of melting had exceeded the boundaries of the dislocations at 0.6 μm. Some specimens were irradiated with spatially nonuniform laser pulses such that some area of the specimens received more energy than 2.0 J/cm^2 and probably caused melting of the oxide layer. An optical micrograph from such a specimen is shown in Fig. 2.53*b*, which shows an area without an oxide layer (A) and an area containing a rippled oxide layer (B). A part of this specimen (encircled in Fig. 2.53*b*), which contained both areas A and B, was thinned for electron microscopy; and the results are shown in Figs. 2.54*b–d*. Area B in Fig. 2.54*b* is free of the dislocation network but has an oxide layer intact on the surface, as indicated by the selected area diffraction pattern in Fig. 2.54*d*. The removal of the dislocation network in Fig. 2.54*b* shows that the melt front penetrated to at least 0.6 μm so that the underlying defect-free substrate could act as a seed for crystal growth. Area A in Fig. 2.54*b* indicates the absence of an oxide layer on the top, as indicated by the selected area diffraction pattern in Fig. 2.54*c*. However, a careful examination of electron micrographs showed the presence of stacking fault tetrahedra in area A, whereas no defects were observed in area B. These faults were found to exist throughout the melted layer.

The formation of stacking faults in area A (Fig. 2.53) is presumably related to the presence of SiO_2 in

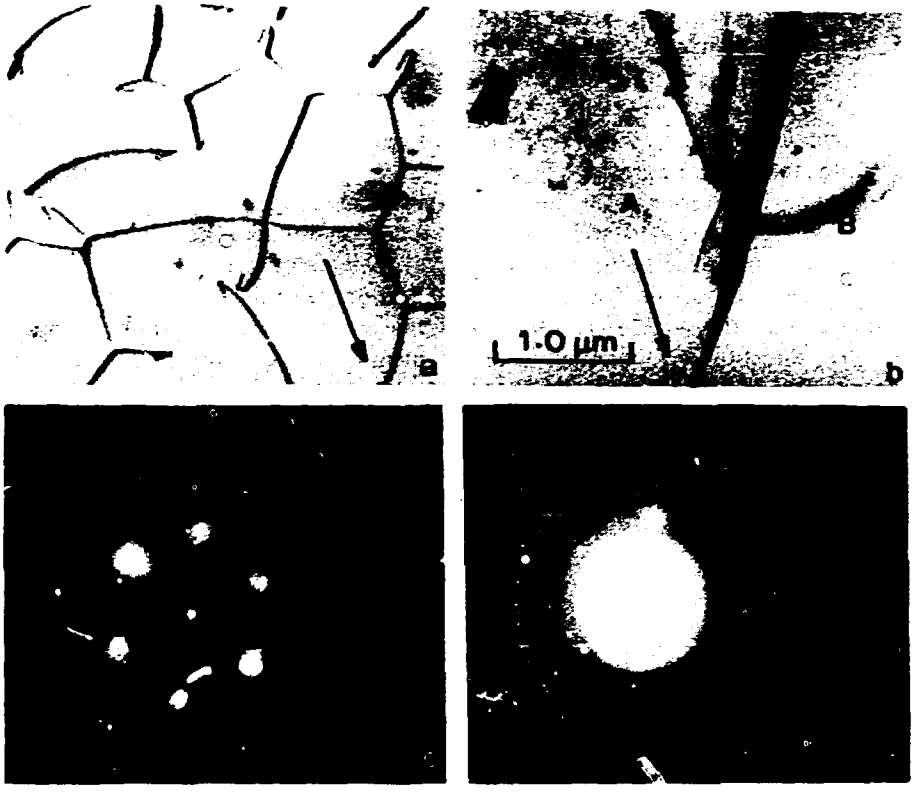

Fig. 2.54. Electron micrographs from the specimen shown in Fig. 2.53: (*a*) micrograph from the specimen of Fig. 2.53*a*, where the depth of melting was determined to be 0.25 μm; (*b*) micrograph from the specimen of Fig. 2.53*b* showing the oxide melted area A and the oxide containing area B; (*c*) selected area diffraction corresponding to area A; and (*d*) selected area diffraction corresponding to area B.

the regrown layers. A "dektak" trace of the specimen in Fig. 2.53*b* showed that the average elevations of areas A and B were equal, within experimental error (~5 nm), indicating that most of the oxide in area A had melted and mixed with the Si. These results suggest that the energy density of the laser pulse in area A is sufficiently high that the surface temperature of the crystal exceeds the melting point of SiO_2. The melting point of pure Si is 1410°C; that of SiO_2 is ~1720°C and depends slightly on the stoichiometry of the oxide layer. It is speculated that the oxide mixes with Si and disturbs the stacking of atoms during the crystal growth, which leads to the formation of the faults. Since O is almost always present as a contaminant in Si while faults are not usually observed, it seems reasonable that clusters of SiO_2 rather than single O atoms are involved in the nucleation of faults. We have proposed a model in which, if Si is forced to grow around an oxide inclusion, stacking faults would be introduced to accommodate misfit strains. The oxide inclusions produce steps equal to the Burgers vector of the fault. The faults nucleate at the edge of the oxide layer and grow in the [111] planes.

1. Summary of paper: *Applied Physics Letters* (in press).
2. J. Narayan, R. T. Young, and C. W. White, *J. Appl. Phys.* **49**, 3912 (1978).
3. C. Hill, *J. Electrochem. Soc.* **80** (1), 1315 (1980).
4. H. Tamura, M. Miyao, and T. Tokuyama, *J. Appl. Phys.* **50**, 3783 (1979).

EFFECT OF THERMAL ANNEALING ON B-IMPLANTED, LASER-ANNEALED Si

J. Narayan B. C. Larson
J. F. Barhorst

Transmission electron microscopy studies have shown that no detectable damage (dislocations, stacking fault loops, or precipitates down to a resolution of 1.0 nm) remained in B-implanted Si after ~1.5 J/cm^2 pulsed laser annealing,[1] and x-ray

studies showed this treatment to produce a one-dimensional contraction of the ion doped layer.[3] With implanted ion doses ranging from 3×10^{15} to 2.5×10^{16} B/cm^2 and distributed in depth to about 0.3 μm, B-doped layers with concentrations extending from below to well above the solubility limits in Si were produced with large one-dimensional strains. Whereas these nonequilibrium conditions were observed to be stable at room temperature, the question of the stability of the supersaturated B concentration and the unrelaxed interfacial strains at elevated temperatures is of particular interest.

In this work (100) Si crystals were implanted (35 keV) with 0.3, 1.0, and 2.5×10^{16} B/cm^2 and subsequently laser annealed (ruby laser, 50 ns, 1.5 J/cm^2). These samples were then isochronally annealed in the temperature range of 600 to 1000°C under a flowing Ar atmosphere. For the 3×10^{15} B/cm^2 implanted Si, which had doping concentrations below the equilibrium solid solubility limit, isochronal annealing up to 900°C for 30 min showed no observable clustering of defects, and electrical measurements on parallel samples indicated no decrease in the carrier concentration. Furthermore, the absence of dislocations at the interface, as determined by electron microscopy and x-ray topography, showed that the strains at the interface were not relaxed during the heat treatment. On the other hand, for the 2.5×10^{16} cm^{-2} sample, where the B concentration was ~3 times the equilibrium solubility limit, it was found that B precipitation started at 600°C and continued through 900°C. Concomitant decreases in the carrier concentrations were measured; these correspond approximately to the number of B atoms observed in the precipitates, assuming the precipitates are spherical.

A very small amount of precipitation was observed in electron microscope observations of the 1×10^{16} B/cm^2 implanted Si after annealing to 1000°C. This amount is consistent with the fact that the B doping level for this implant was close to the solubility limit at these temperatures. Although x-ray Bragg profile measurements on this sample showed the strain decreased by more than a factor of 2 following a 1000°C anneal, the measurements also showed the strain remained essentially one dimensional. Both electron microscope and x-ray topography observations indicated the presence of some interfacial dislocations in this sample as shown in Fig. 2.55. The microscope study of these dislocations was done on samples thinned before the thermal annealing, while the x-ray observations were made on bulk crystals. The density of these dislocations, as indicated by the

SSDN-2279

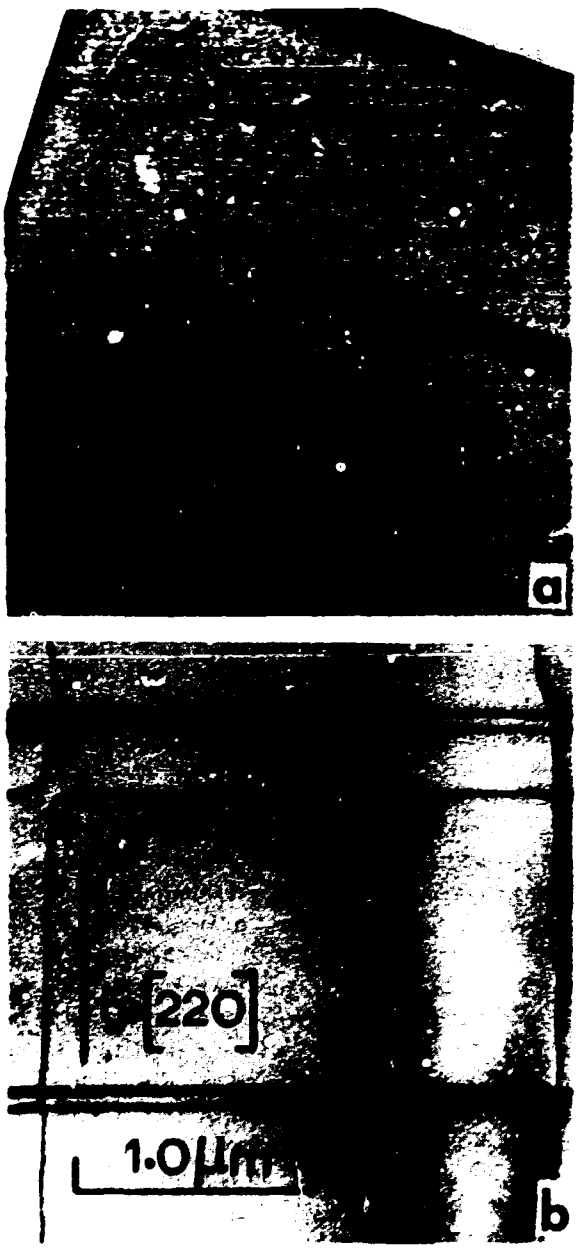

Fig. 2.55 (*a*) Bright-field electron micrograph showing dislocations after 1000°C thermal annealing of B implanted (1×10^{16} cm^{-2}) laser-annealed Si; (*b*) x-ray transmission topograph of a similarly treated crystal.

electron micrograph in Fig. 2.55, is relatively low and could account for, at most, only ~5% of the unrelaxed strain. The density of dislocations indicated by the x-ray topograph is even lower; therefore, the presence of these dislocations is not inconsistent with the retention of the one dimensionality of the

lattice contraction. X-ray studies of the depth profiles of the strain and SIMS measurements[3] of the B concentration profiles in these specimens have indicated the formation of bimodal depth distributions as a result of the thermal annealing. These effects are presently under investigation.

1. J. Narayan, R. T. Young, and C. W. White, *J. Appl. Phys.* **49**, 3912 (1978).
2. B. C. Larson, C. W. White, and B. R. Appleton, *Appl. Phys. Lett.* **32**, 801 (1978).
3. W. H. Christie, private communication.

IMPROVEMENT IN CORROSION RESISTANCE OF INCOLOY 800 ACHIEVED BY PULSED-LASER ANNEALING

C. W. White[1] H. F. Bittner[1]
B. R. Appleton J. T. Bell[2]
W. H. Christie[3]

Incoloy 800 is a corrosion-resistant alloy that, due to its strength and heat resistant qualities, is well suited for application to heat exchangers. Although this alloy is considered to be corrosion resistant, it requires pretreatment to affect the formation of a corrosion-resistant surface oxide layer. Currently employed pretreatments include electropolishing and various types of abrasion that result in the formation of predominantly Fe_2O_3 surface layers. These oxides have poor mechanical integrity, tend to spall off, and offer little resistance to subsequent oxidation. An oxide layer rich in Cr (Cr_2O_3) has been found to be more effective in preventing further oxidation. Using laser annealing, we have found that the corrosion resistance of Incoloy 800 can be significantly improved. Laser irradiation at ~3.0 J/cm^2, 15×10^{-9} s pulse duration gives rise to a thin surface layer enriched in all components except Ni and Fe that has favorable corrosion-resistant properties under harsh steam exposure conditions.

Tab samples, approximately 2 × 1 cm, were cut from an Incoloy 800 sheet and subsequently lapped, buffed, and electropolished using a procedure standardized for 300 series stainless steel. These samples were then irradiated in air with *Q*-switched ruby laser ($\lambda = 0.694$ μm) pulses of energy density 3 J/cm^2 and pulse duration times of approximately 15×10^{-9} s. A region approximately 0.5 cm^2 was irradiated, which allowed direct comparison of the annealed region with unannealed regions on the same sample. Samples were then oxidized at 660°C in 0.94 atm steam carried by an Ar-H mixture that yielded an H to H_2O ratio of 2.2×10^{-5}. Oxidation was carried out for 48, 144, and 528 h. These samples and a sample that had been laser annealed but not oxidized were analyzed by optical microscopy and a SIMS depth profiling technique with a resolution of about 0.05 μm. The SIMS analysis showed a slight enrichment of all components except Fe and Ni in the near-surface region, presumably as a result of zone refining during regrowth of the melted region.

For all three exposure times employed, optical microscopy in the unannealed regions showed the presence of thick, scaly oxides after steam oxidation. Optical microscopy and SIMS analysis showed that the oxides formed in the annealed region after steam exposure were significantly thinner and richer in chromium than those formed in the unannealed region. Presumably, the surface enrichment of chromium gives rise to the formation of Cr_2O_3, which protects the surface against Fe oxidation.

The technique employed in this development may be useful for a variety of alloys. Because it affects only the surface of the alloy and not the bulk properties, pretreatments (such as cold working) that produce desirable structural properties in the bulk material but undesirable surface corrosion properties could be followed by laser annealing. This development could find application for heat exchangers in energy systems such as fossil fuel, fission, and fusion. Laser annealing could also be used as a surface pretreatment where an oxide coating is needed for a gaseous permeation barrier such as for hydrogen isotope containment.

Further improvements in corrosion resistance of a variety of alloys may be achieved by using the combined techniques of ion implantation and pulsed laser annealing. Using ion implantation, selected impurities can be introduced into the near-surface region. Laser annealing can then be used to zone refine these impurities to the first few monolayers to form thin protective barriers on the surface. Experiments to test these ideas are in progress.

1. Chemistry Division, ORNL; present address: Aerospace Corporation, El Segundo, Calif.
2. Chemistry Division, ORNL.
3. Analytical Chemistry Division, ORNL.

FORMATION OF OHMIC CONTACTS IN SEMICONDUCTING OXIDES[1]

J. Narayan V. N. Shukla[2]

For wide-band-gap oxide semiconductors, conventional electrode contacts such as evaporated Au or Ag, fired-on Au, Ag, Pt or Pd paste, and coated graphite have high resistance and are nonohmic. In these electrode systems, contact materials cover the semiconductor surfaces without disrupting the space charge layer that leads to high resistance.[3] The high contact resistance on *n*-type oxide semiconductors has been attributed to the presence of absorbed O acceptor states at the oxide surface and results in a depletion layer at the metal-oxide interface, thereby creating a current barrier.[4,5] In the present investigation, Ni or Al was evaporated on donor-doped $BaTiO_3$, and these specimens were irradiated with *Q*-switched ruby laser pulses. By a proper choice of the laser pulse energy density and pulse duration, it was found that the deposited layer could be melted, thereby removing the space charge layer and forming good ohmic contacts.

Polycrystalline, Y-doped $BaTiO_3$ disks (*n* type, 35 Ω-cm) 1.5 cm diameter and 0.1 cm thick were used in this investigation. These specimens were mechanically polished using alumina powder of up to 0.1 μm particle size, followed by chemical etching in a 5% HF + 10% HNO_3 + 85% H_2O solution. The specimens were rinsed with deionized water and oven-dried at 200°C for 30 min. Then, In-Sn solder contacts were applied ultrasonically to determine the apparent resistivity of the disk specimens. Heretofore, the ultrasonic soldering technique produced the lowest resistance contacts.[3] The ultrasonic contacts were removed by mechanical grinding, and the sample was again subjected to the above polishing and cleaning procedures. Thin films of Al or Ni were then deposited on both sides of these specimens by using electron-beam evaporation in a vacuum of $<10^{-6}$ torr. These specimens were treated with single pulses of *Q*-switched ruby laser light ($\lambda = 0.694$ μm) with a pulse duration τ between 15 and 25×10^{-9} s. The energy density of the laser pulse (in the range of 1.0 to 1.2 J/cm^2) was controlled such that melting of the whole deposited layer occurred without evaporation.

The apparent resistivity as a function of electric field for various Ni-deposited and In-Sn ultrasonically soldered contacts is plotted in Fig. 2.56. The apparent resistivity in as-deposited specimens was considerably higher and exhibited a nonohmic behavior that indicated the presence of a space charge

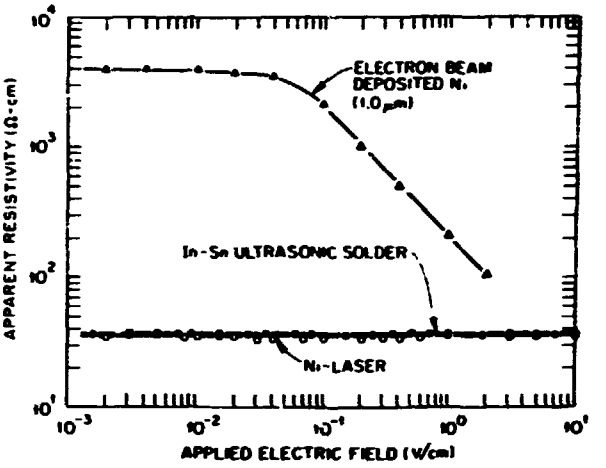

Fig. 2.56. Apparent electrical resistivity as a function of applied electric field on various Ni-deposited and In-Sn ultrasonically soldered $BaTiO_3$ samples. The thickness of the Ni film was 1.0 μm.

region between the metal and semiconductor layers. After treating the as-deposited layers with one laser pulse (E = 1.2 J/cm^2, τ = 20 ns), the resistivity dropped considerably, as shown in Fig. 2.56. The resistivity remained constant with applied electric field, indicating completely ohmic behavior. These resistivity values were slightly lower than those obtained by the In-Sn soldering technique which is known[3] to produce contacts with resistances of about 0.1 Ω cm^{-2}. Therefore, contacts produced by the laser treatment are as good as or better than those produced by the In-Sn ultrasonic soldering technique. The effect of aging on contact resistance at room temperature and at high temperatures up to 700°C was studied. Contact resistances were found to be unchanged after heating to 450°C for 20 min. After heating to 700°C for 30 min, the contact resistance increased, but contacts exhibited ohmic behavior. In the perovskite class of transition metal oxides, such as $BaTiO_3$, it has been shown[4] that absorbed O at the surface provides acceptor states and acts as a barrier for contact formation. The increased *n*-type conductivity at the interface is derived primarily from O vacancies. Therefore, those electrode materials that have a strong affinity for O should lead to low-resistance ohmic contacts in *n*-type material.

It is believed that laser melting of Ni and Al layers on $BaTiO_3$ leads to reaction between metal and O atoms, which either completely disrupts the high-resistance space charge layer or creates a high concentration of vacancies in the $BaTiO_3$ substrate

just beneath the deposited layers. The enhanced O-vacancy concentration or *n*-type conductivity leads to a reduced current-barrier-thickness and hence provides low-resistance ohmic contacts.

1. Summary of paper: *Journal of Applied Physics* (in press).
2. Texas Instruments Inc., Attleboro, Mass.
3. J. W. Fleming, Jr., and H. M. O'Bryan, Jr., *Am. Ceram. Soc. Bull.* 55, 715 (1976).
4. M. Aven and R. K. Swank, p. 69 in *Ohmic Contacts to Semiconductors*, ed. by B. Schwartz, The Electrochemical Society, New York, 1969.
5. S. H. Wemple, p. 128 in *Ohmic Contacts to Semiconductors*, ed. by B. Schwartz, The Electrochemical Society, New York, 1969.

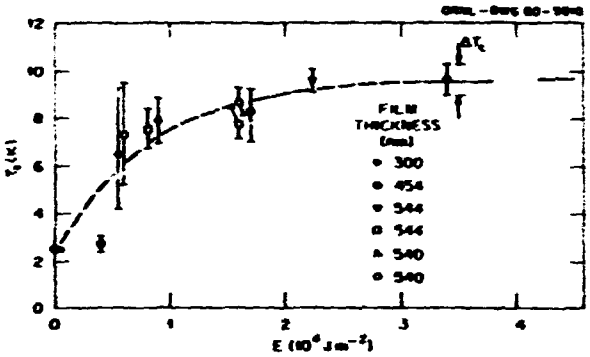

Fig. 2.57. Superconducting transition temperature T_c of damaged V_3Si vs E, the cumulative laser energy density.

RECOVERY OF SUPERCONDUCTIVITY IN ION-DAMAGED V_3Si BY LASER ANNEALING

J. R. Thompson[1] B. R. Appleton
O. Meyer[2] S. T. Sekula
C. W. White

A study of the effect of pulsed laser annealing of superconductors has been initiated. The materials investigated in this work were single-crystal thin films of V_3Si of thickness 300 to 610 nm prepared by sputtering epitaxially onto sapphire substrates.[3] The virgin films had transition temperatures T_c in the range 14.5 to 15.5 K, where T_c is defined to be the midpoint of the transition (i.e., where the electrical resistance of the film is one-half of the low-temperature, normal-state value). Irradiation of these films with 300-keV B ions ($0.25–1.0 \times 10^{20}$ ions/m^2) depressed T_c to ~2.4 K by radiation damage with minimal implantation of B in the sample. This procedure ensured that the films had the optimal V-Si stoichiometry and were capable of displaying high T_c that might result through pulsed laser annealing.

The damaged films were then irradiated by a Q-switched ruby laser ($\lambda = 694$ nm, $\tau = 15$ ns) at energy densities in the range 0.4 to 1.1×10^6 J/m^2. Using a continuous-flow, variable-temperature He cryostat, T_c and the superconducting transition width ΔT_c of the irradiated films were measured by standard four-wire dc methods. A calibrated Si diode was used for thermometry. Some films were subjected to additional laser pulses to observe further changes in T_c. This is shown in Fig. 2.57, where T_c is plotted vs the cumulative deposition of laser energy density, E, for several V_3Si samples of varying thickness. A recovery of T_c from low initial values of ~2.5 K is observed but only up to 10 K. The data can be fit to a saturating function $T_c = A - B\exp(-CE)$, where $C^{-1} = 1.2 \times 10^4$ J/m^2, with an rms deviation in T_c of 1 K. Qualitatively, there also appears to be a reduction in ΔT_c, shown in Fig. 2.57 by the vertical bars at larger energy depositions. This reduction suggests that the annealing pulses promote metallurgical uniformity as well as removal of radiation defects.

It is not yet understood why the limit of the recovery of T_c is only 10 K. However, it is observed that, at the higher energy depositions, the single-crystal thin-film samples exhibit cracking and peeling from the sapphire substrates perhaps because of differential thermal stresses within the film and at the substrate interface. Further study of the role of the substrate on the recovery of T_c appears to be necessary.

1. Adjunct research and development participant from the University of Tennessee, Knoxville.
2. Guest scientist from Nuclear Research Center, Karlsruhe, Germany.
3. O. Meyer and R. Smithey, Kernforschungszentrum Report KFK 2670, p. 94 (1978).

PHOTOVOLTAIC CONVERSION OF SOLAR ENERGY

LASER PROCESSING FOR HIGH-EFFICIENCY SOLAR CELLS

R. T. Young R. F. Wood
P. H. Fleming

Ion implantation and thin-film deposition, followed by pulsed laser irradiation of the samples, have been demonstrated to be excellent techniques for junction formation in Si solar cells.[1,2] During the past year, our efforts to fabricate higher efficiency solar

cells by laser processing have been concentrated in the areas of laser beam homogenization, optimization of implantation, thin-film deposition, and laser annealing parameters, and in the improvement of our metallization techniques for shallow junction cells. By using shallow ^{75}As implantation (5 keV), laser annealing with the spatially homogenized output of a Q-switched ruby laser, and 15 Ω-cm polished Cz Si wafers with areas of 2 to 4 cm^2, solar cells with AM1 conversion efficiencies of 14 to 15% can be readily obtained.

Figure 2.58 shows the current-voltage characteristics of a cell approximately 2 cm^2 in area with 64 nm of Ta_2O_5 for an antireflection coating and with no BSF. Using thinner cells, with the thickness less than the MCDL, the open-circuit voltage V_{oc} and the fill factor FF can be improved to 585 mV and 78 to 79%, respectively, by creating a BSF by laser-induced diffusion of B or Al into the back surface of the cell. As a result, the back surface recombination is greatly reduced and the dark current lowered; these, in turn, combine to raise the V_{oc} and improve the FF. The best cell parameters obtained thus far by laser techniques are generally comparable with or superior to those of cells fabricated by the most advanced conventional techniques. However, quantum response curves for the laser-annealed cells often decrease more strongly at short wavelengths than one might expect they should. This behavior indicates that the laser-induced surface melting may cause rather high values of the surface recombination velocity. The flat-topped dopant profiles in the near-surface region, which are characteristic of ion-implanted, laser-annealed samples,[3] may make surface recombination even more significant. Surface passivation studies now under way should help to clarify the role played by surface recombination in laser-annealed samples.

ORNL-PHOTO 2008-80

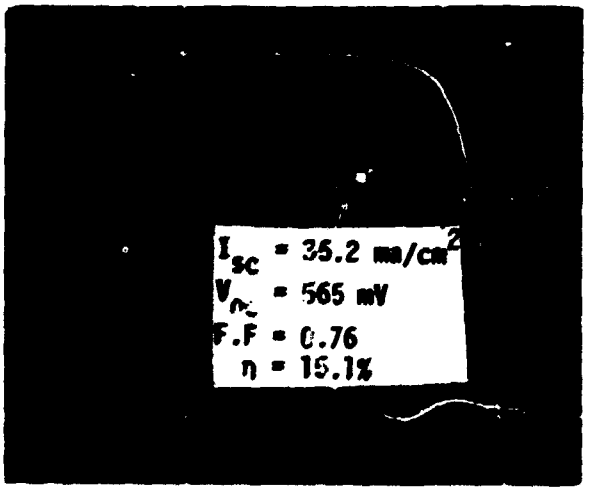

Fig. 2.58. Current-voltage relationship for a solar cell made from As-implanted (5 keV, 2×10^{15} cm^{-2}) Si annealed with one pulse of a Q-switched ruby laser.

1. R. T. Young et al., p. 717 in *Thirteenth IEEE Photovoltaic Specialists Conference—1978*, IEEE, New York, 1978.
2. J. Narayan, R. T. Young, and R. F. Wood, *Appl. Phys. Lett.* 33, 338 (1978).
3. See, for example, J. S. Wang, R. F. Wood, and P. P. Pronko, *Appl. Phys. Lett.* 33, 455 (1978).

ELECTRICAL AND STRUCTURAL CHARACTERISTICS OF LASER-INDUCED EPITAXIAL LAYERS IN Si[1]

R. T. Young J. Narayan
R. F. Wood

For many Si devices, especially microwave diodes, transistors, and photovoltaic cells, the growth of thin, uniform epitaxial layers with abrupt doping profiles is desired. It was demonstrated recently[2,3] that epitaxial regrowth of undoped amorphous Si on (100) Si substrates can be achieved with conventional vacuum deposition techniques followed by short pulses of laser radiation. However, the effects of dopants on the laser-induced crystallization of the amorphous layer and on the electrical properties of the resulting material have not been reported until now.

In our experiments, 10 Ω-cm p-type (100) and (111) single-crystal polished Si wafers were used as substrates. The evaporant source material was Si doped with As to a concentration of $\sim 5 \times 10^{19}$ cm^{-3}. The Si substrates, whose surfaces were first made completely hydrophobic, were quickly loaded into an e-beam evaporator, and amorphous Si layers of 50 to 300 nm were deposited. After exposure to 15-ns ruby laser pulses of various energy densities, the films were examined by TEM, their electrical properties were determined by Hall effect measurements, and anodic stripping techniques were used to determine the carrier concentration profile in the crystallized layer. Junction characteristics were studied by I-V and C-V measurements on mesa diode structures.

Figure 2.59a is a bright-field micrograph of a 100-nm amorphous film on a (100) substrate after laser annealing with one pulse of 1.5 J/cm^2. No defects in any form were observed in the crystallized layer down

ORNL-PHOTO 1686-79

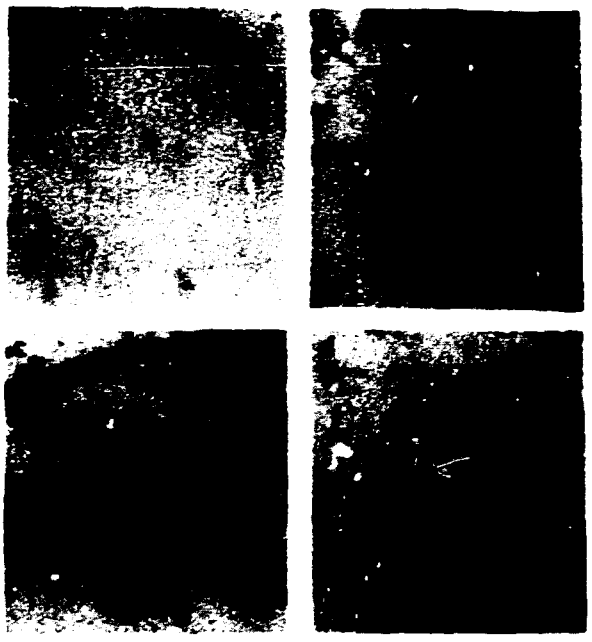

Fig. 2.59. TEM micrographs of laser-annealed, As-doped amorphous films deposited on Si. The micrographs are explained in the text.

to the microscope resolution of 1 nm. A micrograph of a 300-nm film on the same substrate with the same laser annealing parameters is shown in Fig. 2.59*b*. These specimens contained mostly defect-free regions, but some regions contained polycrystalline structures, twins, and dislocations. We believe these defective regions are due to the inhomogeneity of the laser beam, which resulted in the energy density in those regions being insufficient to provide melt-front penetration through the native oxide and/or other contaminants near the original amorphous/crystalline interface, thus preventing epitaxial regrowth. As shown in Fig. 2.59*c*, a 100-nm amorphous film on a (111) substrate after the same laser treatment contained a high density of stacking faults. However, the regrown layer had the same orientation as the (111) substrate. We speculate that the formation of stacking faults and microtwins results from a single mistake in stacking of atoms during crystal growth, which could be caused by even a very small amount of impurities. For a (111) orientation, a single mistake in stacking would lead to the formation of a twin or a stacking fault. For the (111) sample, a second laser pulse of 2.0 J/cm^2 greatly reduced the density of stacking faults (Fig. 2.59*d*).

The *I-V* plot of a typical mesa diode is illustrated in Fig. 2.60*a*. The forward current showed satisfactory characteristics over a reasonable voltage range. At higher currents, the diodes were series-resistance limited. The leakage current in the diode was low, as indicated from the low reverse-bias current. The measurements of barrier capacitance on reverse-bias voltage with the same mesa diode is shown in Fig. 2.60*b*. The straight line indicates that the capacitance varied with voltage as $(V + V_{pct})^{-0.56}$, which shows that the dopant distribution changed abruptly in going from the *n* to the *p* region. The measured junction potential (V_{pct}) was 0.82 V, which agrees very well with the expected junction potential at a doping level of $\sim 1 \times 10^{15}$ cm^{-3} and suggests that a defect-free junction was obtained. The resulting dopant profiles of the regrown layers are presented elsewhere in this report.[4]

In conclusion, we have demonstrated that doped epitaxial layers of controlled thicknesses and with

ORNL-DWG 79-11900

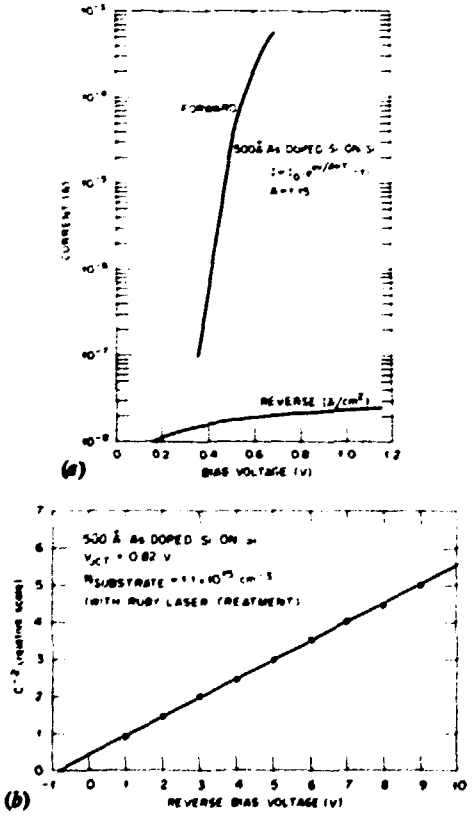

Fig. 2.60. Junction characteristics of a typical As-doped, laser-induced mesa diode: (a) forward and reverse *I-V* measurement and (b) reverse-bias *C-V* measurement.

good electrical characteristics can be grown on Si (100) and (111) substrates by pulsed laser radiation. With an appropriate deposition technique (chemical vapor deposition, a dual-crucible electron beam coevaporation system, or an ion beam coating system) for precise control of the alloy composition in the deposited layer, this technique can potentially be competitive with or replace ion implantation for many semiconductor device applications.

1. Summary of paper: *Appl. Phys. Lett.* 34, 447 (1979).
2. D. Hoonhout, C. B. Kerkdijk, and F. W. Saris, *Phys. Lett.* 66 A, 145 (1978).
3. S. S. Lau et al., *Appl. Phys. Lett.* 33, 130 (1978).
4. R. F. Wood and R. T. Young, "Dopant Profiles in Laser Recrystallized Deposited Layers," this report.

SOLAR CELLS FROM CAST POLYCRYSTALLINE Si[1]

R. T. Young R. F. Wood
R. D. Westbrook P. H. Fleming

Solar cells have been fabricated from cast polycrystalline Si by ion implantation followed by pulsed laser annealing and by conventional thermal diffusion. The most significant characteristics of the Wacker cast polycrystalline Si used in these studies are its relatively large grain size (mm) and its columnar grain structure. The material is doped with B to a concentration of 3×10^{15} cm^{-3}. Examination by TEM of the defect microstructures in the as-received material indicated that dislocations, stacking faults, and twins are normally present inside the grains. The individual grains are rather randomly oriented as revealed by x-ray Laue spot examination. Junctions were formed by implanting As at 5 keV to a dose of 2×10^{15} cm^{-2} and by diffusing P at 900°C for 60 min. Parameters of cells made from different ion-implanted samples annealed by laser pulses of energy densities from 1.2 to 1.6 J cm^{-2} are given in Table 2.8. For comparison, data on a diffused cell (D1) and a single-crystal As-implanted control cell (S1) annealed with a laser energy density of 1.2 J cm^{-2} are also included. The open circuit voltage V_{oc} and the fill factor FF decreased slightly with increasing laser energy density. The best cell efficiency was obtained by laser annealing at 1.2 J cm^{-2}. The values of V_{oc} and FF in cells A1 and A2 are comparable to the corresponding values in the single-crystal cell S1. In comparison to the cell fabricated by conventional diffusion techniques (D1), the laser-annealed cells give better V_{oc} and short-circuit current I_{sc}. The laser-induced reduction of defects in the emitter and space charge regions and the preservation of the MCDL are believed to be the reasons for the good values of V_{oc} and I_{sc}.

The quantum efficiencies as a function of wavelength of cells A1 and S1 are shown in Fig. 2.61. The almost identical efficiencies of the two cells in the short-wavelength region (0.4 to 0.6 μm) indicate that emitter regions of comparable quality to single-crystal cells can be obtained in large-grained polycrystalline cells by ion implantation and laser annealing. The loss of long-wavelength response of sample A1 compared to that of sample D1 is most likely a consequence of the difference in the MCDL in these two samples. Values of the MCDL in various samples obtained by surface photovoltage measurements are also given in Table 2.8. Postannealing of the laser-annealed cells at 450°C from 1 to 17 h in H_2 gas did not improve the short-wavelength response

Table 2.8. Solar cell parameters[a] of As-implanted (5 keV, 2×10^{15} cm^{-2}), laser-annealed cast polycrystalline Si

Cell number	Laser energy density (J cm^{-2})	MCDL (μm)	V_{oc} (mV)	J_{sc} (mA cm^{-2})	FF	η (%)
A1	1.2	73	566	28.6	0.75	12.14
A2	1.2	75	561	28.2	0.76	12.02
B1	1.4	71	557	27.7	0.76	11.73
B2	1.4	75	562	28.7	0.72	11.61
C1	1.6	76	539	28.6	0.72	11.10
C2	1.6	50	536	27.4	0.71	10.43
D1	Diffused	43	540	25.2	0.76	10.30
S1	1.2	250	560	33.7	0.76	14.40

[a]Under AM1 illumination and at 22°C.

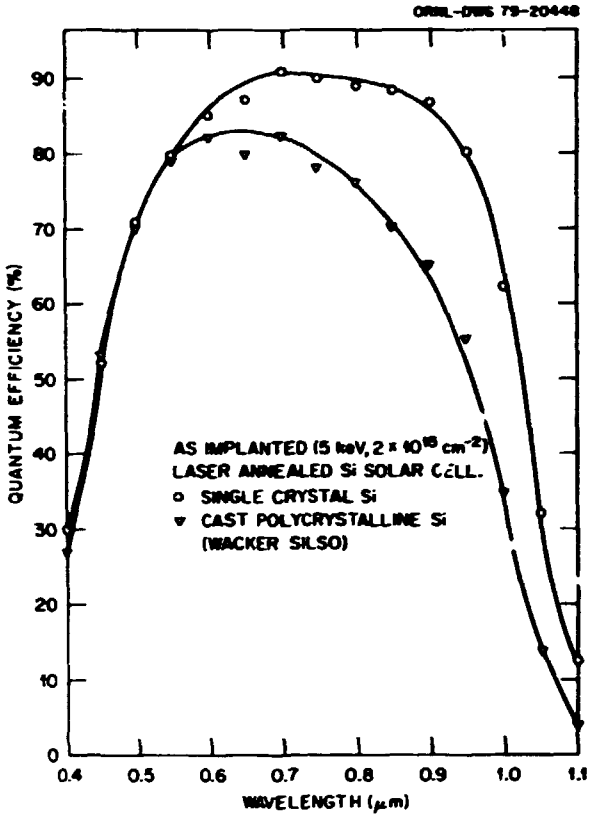

Fig. 2.61. Comparison of quantum efficiency spectra of ion-implanted, laser-annealed single and polycrystalline Si solar cells.

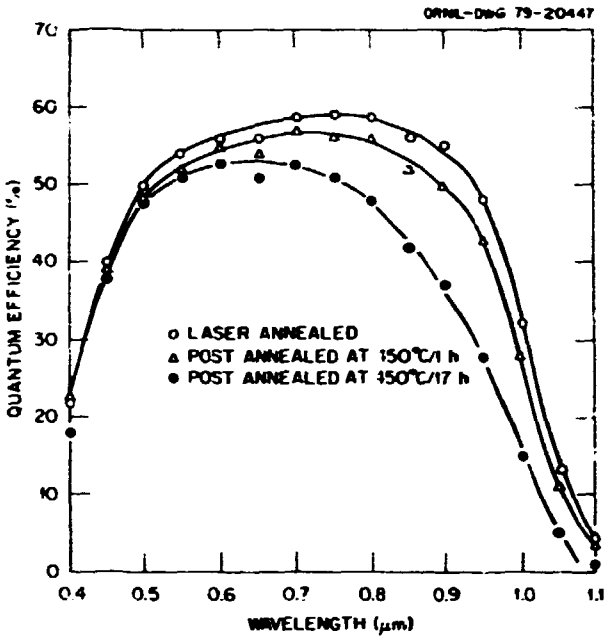

Fig. 2.62. Effects on the quantum efficiency (without antireflection coating) of heating laser-annealed cast polycrystalline solar cells in an H_2 atmosphere.

out decreased the long-wavelength response, as can be seen in Fig. 2.62. These results indicate that annealing in H_2 gas cannot serve as a means either to anneal the residual defects or to compensate grain-boundary effects. Because of the grain boundaries, contamination effects that degrade the MCDL in the substrate may occur, even with low-temperature annealing, and lower the long-wavelength response.

The good fill factors and high open-circuit voltages shown in Table 2.8 result, for the most part, from the nearly ideal *I-V* characteristics of the laser-annealed *p-n* junctions. In the diffusion-dominated portion of the *I-V* characteristics (>0.4 V), the diode factor of cell A1 was found to be 1.28 and the saturation current density was 1.0×10^{-9} A/cm^2, which indicate that a good junction was formed.

In conclusion, we have demonstrated that 12% efficient, large-grained polycrystalline Si solar cells with nearly ideal *I-V* characteristics, high open-circuit voltages, and good fill factors can be obtained by ion implantation and laser annealing. To our knowledge, these are the highest efficiencies reported to date for cells made from the Wacker material.

1. Summary of paper: p 214 in *Fourteenth IEEE Photovoltaic Specialists Conference*, IEEE, New York, 1980.

STUDY AND CONTROL OF GRAIN-BOUNDARY EFFECTS BY LASER TECHNIQUES[1]

R. F. Wood W. H. Christie[2]
R. T. Young J. Narayan
C. W. White

One of the major problems in the use of small-grained polycrystalline Si for solar cells arises from the difficulty in control of dopant diffusion along grain boundaries. This problem can now be circumvented during *p-n* junction formation by the recently developed technique of pulsed laser annealing.[3] We demonstrate here that, in addition to the control of grain-boundary diffusion, the use of short pulses of laser radiation in processing polycrystalline materials can provide other advantages such as elimination of sample contamination by undesired impurities, grain growth in fine-grained polycrystalline material, and

removal of inherent defects (dislocations, stacking faults, and twins, etc.) in the junction depletion region of large-grained polycrystalline Si cells.

In this work, three kinds of polycrystalline material were used: CVD thin-film Si grown on SiO_2 layers (grain size ~0.02 μm), Texas Instruments (TI) bulk Si (grain size of 25 μm), and Monsanto (MS) single-pass float-zoned material (grain size of millimeters).

Figure 2.63 shows the dopant profiles of B diffused (890°C/15 min) into the various samples; the profiles were obtained by SIMS. The effects of enhanced grain-boundary diffusion are clearly seen in the profiles of the CVD and TI samples, where two components of diffusion are obvious. The effects in the large-grained MS material are much less obvious, as expected. In solar cell applications, this long-range diffusion, which can significantly affect the shunt resistance of the cell, must be prevented. Figure 2.64 shows SIMS profiles for B-implanted CVD thin-film samples after thermal annealing and after laser annealing at two different energy densities. The data from the thermally annealed (10 min at 900°C)

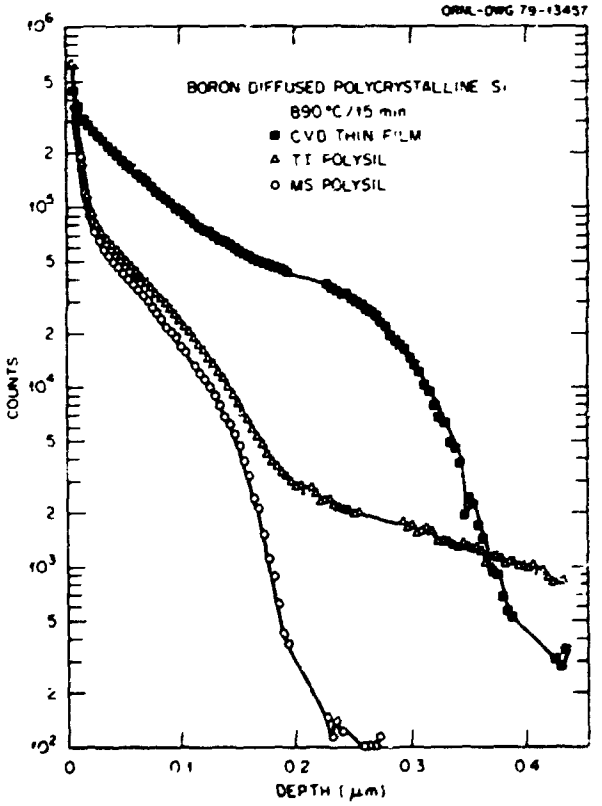

Fig. 2.63. Comparison of dopant profiles of thermally diffused polycrystalline Si of different grain size.

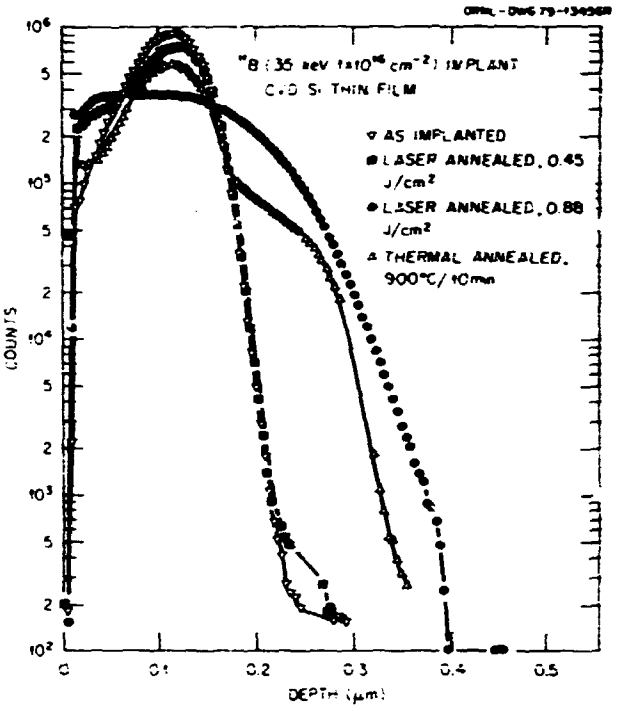

Fig. 2.64. Comparison of dopant profiles of thermally and laser-annealed CVD polycrystalline Si.

samples can be fit reasonably well by a simple model we have developed. In this model, it is assumed that two components of dopant diffusion are present, one appropriate to grain-boundary diffusion and one appropriate to diffusion in the bulk of the grains. The diffusion coefficient for the former component is of the order of 10^{-13} cm^2 s at 900°C, and for the latter it is of the order of 10^{-15} cm^2 s.

The profiles for the laser-annealed samples are in strong contrast to that for the thermally annealed sample. In the laser-annealed material, diffusion characteristic of two species with widely different diffusion coefficients is never seen. Instead, the profile spreading, when laser pulses of 0.88 J cm^{-2} energy density are used, is completely consistent with the laser-induced melting and diffusion in the liquid state associated with laser annealing of single-crystal Si. This observation is strong confirmation of our hypothesis that grain boundaries simply do not exist in the near-surface region that is melted during laser annealing. The samples annealed with 0.45 J cm^{-2} pulses showed some diffusion on the edge of the implanted profile nearest the surface but none at greater depths. Calculations of the melt-front penetration, modified to take into account the SiO_2 layer, indicated that the melt front penetrated to a

depth of approximately 120 nm for 0.45 J/cm^2 pulses. However, the electrical measurements indicated that there was almost full recovery of electrical activity of the sample annealed with 0.45 J/cm^2. This suggests that complete melting may not be necessary for the electrical activation of the implanted dopants in the fine-grained material. Higher laser energy is required for complete electrical activation of the implanted dopants in the larger grained T. material, indicating that the annealing threshold is a function of a number of materials parameters, such as grain size, substrate, and film thickness. The TEM studies on these samples show that substantial grain growth occurs in the fine-grained CVD polysil during the laser annealing process. The average grain size increased from 0.02 to 0.5 μm in the top 0.2- to 0.3-μm thick layer when the film was irradiated with a laser pulse of 0.45 J/cm^2. When the laser energy density was increased to 0.88 J/cm^2, the average grain size increased to 1.5 μm. These large grains were relatively defect-free, containing only a small density of stacking faults or twins. Surface damage and/or peeling were observed with laser energy densities greater than 1 J/cm^2. The mechanism for the recrystallization phenomena in these samples, which were annealed with energy densities apparently too low to melt the entire implanted region, requires further study.

1. Summary of papers: *Solar Cell.* (in press); *IEEE Trans. Electron Devices* (in press).
2. Analytical Chemistry Division, ORNL.
3. R. T. Young et al., *Appl. Phys. Lett.* 32, 139 (1978).

STUDIES OF POLYCRYSTALLINE Si SOLAR CELLS BY EBIC

R. T. Young R. D. Westbrook
R. D. Taylor

The understanding of the basic mechanisms that affect carrier transport at or near grain boundaries is the most critical problem in the development of solar cells made from small-grained polycrystalline material. A variety of measurement techniques that can be used for studying grain-boundary effects are needed. In the past year, the photovoltaic group has implemented two recently developed experimental techniques that have proved useful in grain-boundary studies. One of these is discussed here, and the other is discussed in the following contribution.[1]

SEM techniques, especially those utilizing the EBIC mode of operation, have been used for studies of grain-boundary effects in polycrystalline Si solar cells. In the EBIC mode, carriers generated in the vicinity of an electrical junction by the electron beam of an SEM induce a current in an external circuit. This current, which can be fed into the video system of the microscope, shows directly the efficiency with which electrical carriers are collected in various parts of the cell. In contrast to the image from secondary electron emission, which gives information about surface features, the EBIC image gives information about the electrical activity of imperfections and defects lying in the near-surface region. Furthermore, by varying the energy of the electron beam, depth resolution can be obtained. Figures 2.65*a* and *b*

ORNL-PHOTO 2009-80

Fig. 2.65. (*a*) Image of a portion of a laser-annealed polycrystalline solar cell taken with an electron microscope operating in the standard (secondary electron emission) operating mode, (*b*) image of the same area on the sample taken with the microscope operating in the EBIC mode, and (*c*) high-resolution EBIC image of a crater produced by laser annealing.

provide a comparison of images from the secondary electron emission and EBIC modes of an electron microscope on a laser-annealed polycrystalline Si solar cell. The dark regions in Fig. 2.65*b* represent a reduction in current and, hence, in the efficiency with which carriers are collected. Some of the features shown in Fig. 2.65*a* are much less pronounced in Fig. 2.65*b* and show that not all grain boundaries and twins are equally important in degrading the carrier collection efficiency. A high-resolution EBIC image of a surface crater produced by laser annealing is shown in Fig. 2.65*c*. The current response during a line scan across the center portion of the crater is shown in Fig. 2.65*c*. The dark ring around the crater suggests that the crystal structure in this area was poor, and TEM measurements showed that this was indeed the case.

Figures 2.66*a–c* demonstrate the type of depth resolution that can be obtained with EBIC measurements. Figure 2.66*a* shows that when the electron beam had an energy of 30 keV (maximum penetration depth of ≃6.5 μm), certain grain boundaries were clearly visible. It can be seen from Fig. 2.66*b* that, when the electron energy was reduced to 15 keV (maximum penetration depth≃2 μm), there was little or no change in the grain-boundary features. When the electron energy was further reduced to 10 keV (maximum penetration ≃1 μm), Fig. 2.66*c* shows that the grain boundaries were no longer visible and, hence, not electrically active. It is believed that the lack of electrical activity of the grain boundaries within 1 μm of the surface is caused by the heavy doping in this region (the emitter region), which results in an effective passivation of the grain boundaries.

ORNL-PHOTO 2010-80

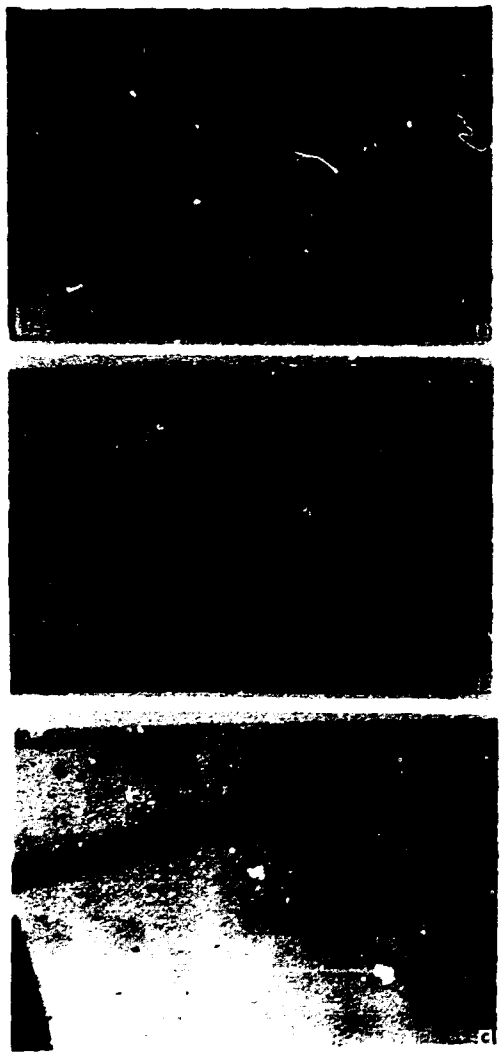

Fig. 2.66. (*a*) Results when the *e*-beam has an energy of 30 keV (penetration ≃ 6.5 μm); grain boundaries are clearly visible. (*b*) Results with an *e*-beam energy of 15 keV (penetration ≃ 2 μm); grain boundaries are still visible. (*c*) Results with an *e*-beam energy of 10 keV (penetration ≃ 1 μm); grain boundaries have virtually disappeared.

STUDIES OF POLYCRYSTALLINE Si SOLAR CELLS BY THE SLS TECHNIQUE

R. D. Westbrook R. T. Young

A technique that complements the EBIC type of measurements described in the previous contribution[1] is the SLS method. In this method, a laser beam instead of an electron beam is used to create the electron-hole pairs; otherwise, the techniques are very similar. Because of relative beam diameters, EBIC has better resolution than the SLS method, but it is not yet clear how significant the differences are. The SLS technique is very simple, requires no vacuum, and can be used for a preliminary screening of samples to be examined by EBIC. With this technique, the wavelength of the exciting light can be chosen to achieve absorption at a suitable depth. An He-Ne laser (λ = 0.633 μm) that gives an absorption depth of 2.8 μm in Si is currently used in our system. The spot size can be varied from ≃10 to 100 μm by using different lenses. The scan is accomplished by

1. R. D. Westbrook and R. T. Young, "Studies of Polycrystalline Si Solar Cells by the SLS Technique," this report.

deflecting the beam with rotating galvanometer mirrors. During the scan, the signal can be modulated in intensity and/or amplitude. Single line scans or quasi-three-dimensional scan maps can be obtained on the oscilloscope screen. As with EBIC, the signal may be influenced by many factors, such as grain boundaries, crystal imperfections, and any other variations in resistivity, diffusion length, or surface recombination effects.

Figure 2.67*a* shows examples of single line scans of a solar cell made from ribbon Si. The large dips in the curve spaced 2 mm apart are due to the light spot passing over the metal fingers on the top surface of the cell. All the other dips occur where either grain boundaries or regions of poor response caused by other factors are crossed. Figure 2.67*b* shows the SLS map of the region between two fingers obtained by using both intensity and amplitude modulation. To obtain a map such as this, compromises must be made between the amplitudes of the low-response dips, the resolution of the dips, and the time required to obtain the map. Therefore, the maps do not give the accuracy that can be obtained with a single optimized line scan; nevertheless, they are sufficient to show areas of low response that can subsequently be studied by individual line scans.

Both EBIC and SLS techniques can provide valuable information about grain-boundary effects, crystal imperfections, and other variations in the solar cell that may influence cell efficiency. However, complete interpretation of the data requires correlations with the results of other measurement techniques and a quantitative analysis of the photocurrent response.

ORNL-PHOTO 2011-80

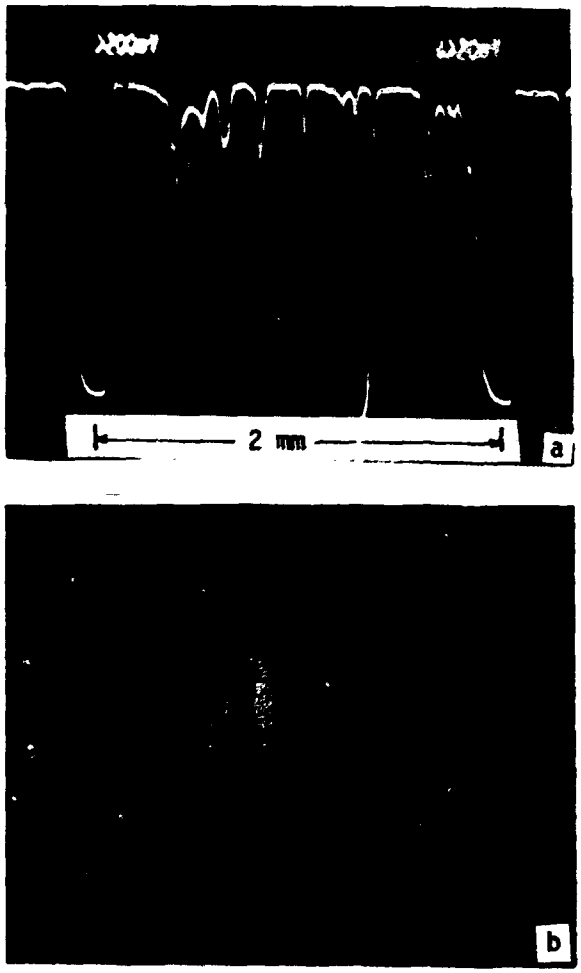

Fig. 2.67. (*a*) **Single laser-scan photoresponse curve of a solar cell from ribbon Si.** The large dips in the curve spaced 2 mm apart are due to metal fingers. (*b*) Laser scan map between the two metal fingers.

---

1. R. T. Young, R. D. Westbrook, and R. D. Taylor, "Studies of Polycrystalline Si Solar Cells by EBIC," this report.

GASEOUS DISCHARGE ION IMPLANTATION

R. D. Westbrook R. T. Young

It has been shown[1,2] that shallow layers of doping elements can be introduced into Si by bombarding an Si cathode with dopant atoms in a gaseous discharge chamber. The amount of dopant implanted is proportional to the coulombic transfer and, therefore, depends on the current and the time. Satisfactory deposition conditions for solar cell applications are obtained with the voltage between 3 and 10 keV, the current between 1 and 5 mA/cm^2, and discharge times from 5 to 15 min. These conditions result in sheet resistivities from 150 Ω/□ to 30 Ω/□. Because the apparatus is simple and more economical than standard ion implantation equipment, great potential exists for the technique as a method for low-cost solar cell fabrication.

As with any ion-implantation process, damage is created in the near-surface region. In the case of gaseous discharge of BF_3, not only B^+ but also multiply ionized gaseous species, such as BF_3^+, B^{2+}, and B^{3+}, are generated, and these impinge on the surface, producing a thin, heavily damaged surface layer. Appropriate annealing is needed to remove the damage and electrically activate the implanted ions. Our initial results obtained with *n*-type base material,

BF_3 as the B source, and laser annealing for damage removal have shown that satisfactory sheet resistances can be obtained. The MCDL in the base region remains high, as is expected with ion-implantation laser-annealing processing. Solar cells have not yet been made by this method.

---

1. R. Wichner, p. 243 in *Eleventh IEEE Photovoltaic Specialists Conference—1975*, IEEE, New York, 1975.
2. J. P. Ponpon and P. Stiffert, p. 342 in *Eleventh IEEE Photovoltaic Specialists Conference—1975*, IEEE, New York, 1975.

DLTS STUDIES OF ELECTRON-IRRADIATED P- AND O-DOPED Si

G. E. Jellison, Jr. J. W. Cleland

Deep level transient spectroscopy is an extremely sensitive technique for the detection and study of deep-lying defect states or carrier traps in semiconductors.[1] From DLTS measurements, it is possible to measure the activation energy ΔE, the trap concentration profile in the depletion region, and the majority and minority carrier capture cross sections. Measurements of the minority carrier capture cross sections require detailed characterization of the diodes, and such measurements were not made in this work.

DLTS studies of deep levels, introduced by 1.5-MeV electron irradiation of float-zone-refined (Fz), P-doped, and Czochralski-grown (Cz) O-cluster doped (O_c) Si, indicate the presence of six electron (majority carrier) traps and three hole (minority carrier) traps. Typical DLTS spectra are shown in Fig. 2.68, and Table 2.9 summarizes the parameters and lists possible trap identifications. A blank in Table 2.9 means that the designated trap was not observed in the indicated sample; it does not mean that the trap was absent (for example, E-5 was probably present in P-doped samples but not observed because of E-6).

Trap E-1 was observed only in the O-doped samples and was found to be present in the same concentrations in both unirradiated and irradiated samples. Therefore, it is reasonable to assign this trap to an O_c donor state. The trap E-2 was found only in P-doped samples and only when trap E-3 was in a zero charge state; therefore, this trap must be related to E-3. Traps E-3, E-4, E-5, and E-6 have all been observed previously by Kimerling.[2] Trap E-3 is the O-vacancy trap, E-4 and E-5 are different charge states of the divacancy, and E-6 is the P-vacancy pair. The

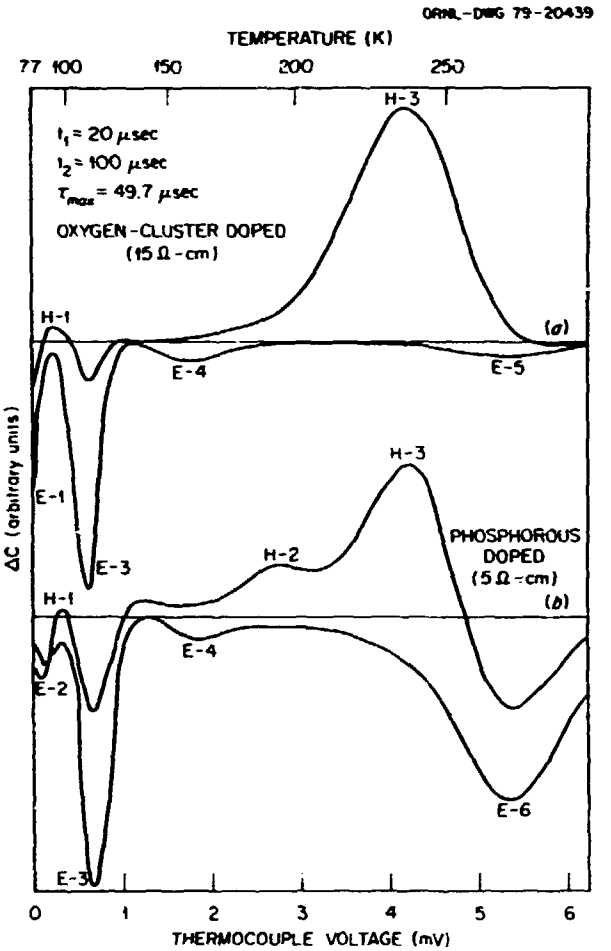

Fig. 2.68. The DLTS spectra of P- and O-doped Si irradiated with 4.6×10^{14} electrons/cm² at 1.5 MeV. Peak identification and characterization are given in Table 2.9; $\Delta C = C(t_2) - C(t_1)$, where $C(t)$ is the capacitance measured at time t after the pulse.

presence of trap E-3 indicates that O has diffused into the depletion region of the Fz P-doped diodes during fabrication.

The hole traps H-1, H-2, and H-3 are not as well characterized as the electron traps, because they are minority carrier traps. Trap H-1 had a nonexponential decay, which indicates that it is really produced by a distribution of traps; trap H-2 occurred only in the 5 Ω-cm P-doped sample, which means it cannot be solely O related. The work of Kimerling[2] and Mooney et al.[3] indicates that there is a hole trap related to C at this energy. Trap H-3 occurred in large concentrations in three of the samples, but in a small concentration in the 15 Ω-cm P-doped sample. Therefore, this trap cannot be associated with the O-vacancy pair, as was previously stated by Kimerling;[2] however, it could be C related

Table 2.9. Trap parameters obtained from DLTS measurements after irradiation with 4.5×10^{14} electrons/cm^2 at 1.5 MeV (see Fig. 2.68)

ΔE is the activation energy, σ_n is the electron capture cross section, and N_T is the trap concentration

Trap	ΔE (eV)	σ_n (10^{14} cm^2)	n_t ($\times 10^{12}$ cm^{-3})				Identification
			O-doped		P-doped		
			5 Ω-cm	15 Ω-cm	5 Ω-cm	15 Ω-cm	
E-1	<0.10	1.0	40[a]	23[a]			O donor
E-2	0.10	1.0			10[a]	9[a]	Related to O-V
E-3	0.17	1.0	10.2[a]	10.8[a]	10.6	8.8	O-vacancy[b]
E-4	0.23	0.016	0.6	0.6	0.8	0.5	Divacancy[b]
E-5	0.42	0.4	0.5	0.5			Divacancy[b]
E-6	0.44	0.015			9.7	2.9	P-vacancy[b]
H-1	0.09		0.6	0.7	0.7	0.3	?
H-2	0.26				4.1		C related (?)
H-3	0.42		9.4	10.5	10.0	0.5	C related (?)

[a]Maximum value; decreases closer to the junction.
[b]See ref. 2.

The results of these DLTS studies can be correlated with the observation that solar cells fabricated from O_i-doped material are more tolerant to radiation than cells fabricated from Fz P-doped material.[4] The major difference between the two types of materials is that the P-doped material contains a large concentration of trap E-6, while the O_i-doped material does not have a large concentration of any deep-lying majority carrier trap. The creation of the E-6 traps in P-doped material lowers the Fermi level and, hence, the open circuit voltage. The E-6 traps also act as recombination centers deep in the gap and thus decrease the minority carrier diffusion length and the short-circuit current. All these effects will result, after electron irradiation, in lower efficiencies of cells fabricated from P-doped material than cells fabricated from O-doped material.

1. D. V. Lang, *J. Appl. Phys.* **45**, 3023 (1974).
2. L. L. Kimerling, p. 221 in *Radiation Effects in Semiconductors, 1976*, ed. by N. B. Urli and J. W. Corbett, Institute of Physics, London and Bristol, 1977.
3. P. Mooney et al., *Phys. Rev. B* **15**, 3836 (1977).
4. G. E. Jellison, Jr., J. W. Cleland, and N. Fukuoka, "A Radiation-Resistant Substrate for a p^+-n-n^+ Solar Cell," this report.

A RADIATION-RESISTANT SUBSTRATE FOR A p^+-n-n^+ SOLAR CELL[1]

G. E. Jellison, Jr., J. W. Cleland
N. Fukuoka[2]

It is well known that the annealing of Cz Si that contains 5×10^{17} to 5×10^{18} interstitial O cm^{-3} at 350 to 500°C increases the donor concentration. The number of donors created is a complex function of the O content and duration of the heat treatment. The results of this report show that solar cells made from Si doped with O donors are more tolerant of radiation damage due to 1.5-MeV electrons than are cells made from conventionally doped Fz n-type Si.

Solar cells were fabricated from both 15- and 5-Ω-cm Si containing donors introduced by P- (Fz material) or O- (Cz material) doping. The cells were then irradiated at 300 K with 1.5-MeV electrons at several different fluences up to 8×10^{15} e$^-$ cm^{-2}. The resulting solar cell parameters determined for AM1 conditions are shown in Fig. 2.69 as a function of total electron fluence. It is clear that the O-doped cells are less susceptible to radiation damage than the P-doped cells.

Differences between the solar cell parameters for the O- and P-doped cells have been correlated with electrical van der Pauw (vdP) and DLTS measurements. The vdP results show that there is a dramatic decrease in majority carrier concentration with

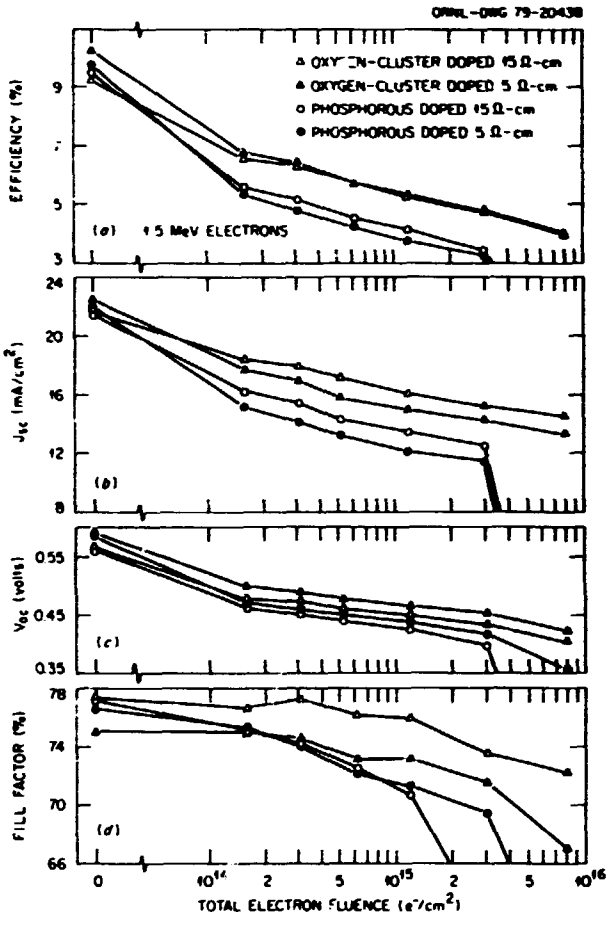

Fig. 2.69. Comparison of O- and P-doped solar cells (AM1 conditions) showing (*a*) efficiency, (*b*) short-circuit current, (*c*) open circuit voltage, and (*d*) fill factor vs the total electron fluence for 1.5-MeV electrons.

increased electron fluence for the P-doped samples, while the O-doped samples show very little decrease. DLTS results in P-doped Si after electron irradiation show a large concentration of an electron trap 0.44 eV below the conduction band (this trap is associated with the P-vacancy defect), while O-doped Si does not show a large concentration of any deep-lying majority carrier trap after irradiation. Creation of the P-vacancy defect in the P-doped Si results in the destruction of P as an effective donor, lowers the Fermi level, and creates recombination centers. This makes the efficiency, open circuit voltage, and the short-circuit current of the P-doped cells lower than the corresponding quantities of the O-doped cells after electron irradiation.

1. Summary of paper: *Proceedings of the Fourteenth IEEE Photovoltaics Specialists Conference*, IEEE, New York, in press.
2. Guest scientist from Osaka University, Osaka, Japan.

ANNEALING STUDIES OF Cz-GROWN, NTD Si

J. W. Cleland N. Fukuoka[1]

It is well known that the initial *n*- or *p*-type carrier concentration in Cz-grown Si is altered if electrically active donors are formed by O, clustered O, or O-vacancy (OV) type defects. Commercially available Cz Si ingots are usually annealed after growth for 1 to 3 h at 650 to 750°C and cooled under natural or forced convection to minimize any O-related donor concentration. However, Capper et al.[2] have stated that additional annealing of ingot slices is required for close tolerance specifications.

We have now determined the initial rates of O-related donor formation and the maximum donor concentrations as functions of isochronal and isothermal annealing conditions in pure and conventionally doped Cz Si samples of different O concentrations. Figure 2.70 shows the carrier concentrations vs time of annealing at five different temperatures for representative samples of Cz Si. Note that the maximum O-related donor concentration decreased with annealing temperature but that some donors are formed by extended annealing at 750°C.

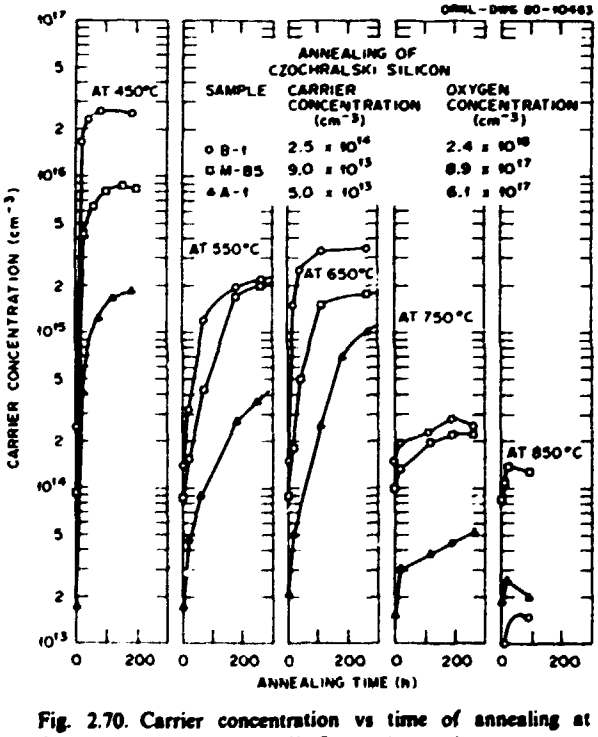

Fig. 2.70. Carrier concentration vs time of annealing at different temperatures for Cz Si (O-doped) samples.

In order to explore the reversibility of O-related donor formation, samples similar to those shown in Fig. 2.70 were first annealed for 200 h at 450°C to introduce a large initial O-donor concentration and were then reannealed at 550, 650, 750, or 850°. The donor concentration decreased to almost the initial value in every sample in less than 1 h on reannealing, but then increased, in every sample at each temperature, in a manner almost identical to that shown in Fig. 2.70. These data indicate that one can use short-term (≤1 h) annealing at 550°C or higher to remove most of the O-related donors initially formed at lower temperatures but that other O-related donors are then formed by extended annealing at higher temperatures.

To explore the possible connection between lattice damage and O-related defect formation, other samples of Cz Si and of Fz-refined Si of low O content were neutron irradiated at a series of doses, and the concentration of P and of fast-neutron-induced lattice defects (D_f) was estimated as previously described.[3] Some of the NTD Cz Si samples were then annealed for ≥100 h at 450°C. For those irradiated samples that contained up to 10^{16} D_f cm^{-3}, the initial rate of O-donor formation and the final concentration were found to be almost identical to the values obtained with unirradiated samples. Both the initial rate of donor formation and the final donor concentration after extended annealing at 450°C were reduced in the more heavily irradiated samples, but a considerable (≥10^{15} cm^{-3}) concentration of O-related donors was still formed in NTD Cz Si samples that contained up to 10^{18} D_f cm^{-3}.

These results suggest that O-related donor formation in NTD Cz Si at temperatures below 750°C may serve to mask any isothermal or isochronal annealing study of removal of D_f. We have determined that annealing for 30 min at 750°C is sufficient to observe the anticipated concentration of P in NTD Fz Si, up to a total concentration of >10^{18} cm^{-3}, and that an equivalent annealing is probably sufficient for NTD Cz Si when the separate effect of O-donor formation is taken into account.

1. Guest scientist from Osaka University, Osaka, Japan.
2. P. Capper et al., *Appl. Phys. Lett.* 32, [illegible] (1978); *J. Appl. Phys.* 48, 1846 (1977).
3. J. W. Cleland et al., *Solid State Div. Prog. Rep., Sept. 30, 1978*, ORNL-5486, p. 83.

SUBSTITUTION OF IMPURITY ATOMS BY SELF-INTERSTITIALS IN THERMAL-NEUTRON-IRRADIATED Ge[1]

N. Fukuoka[2] H. Saito[3]
J. W. Cleland

We have used the recoil energy associated with gamma-ray emission following thermal-neutron absorption to introduce a predetermined concentration of activated ^{71}Ge self-interstitial atoms in selected samples of Ge. The samples were supplied by ORNL and irradiated in the Kyoto University Research Reactor in Japan.

Initial carrier concentrations and conductivities were determined by conventional Hall coefficient and resistivity measurements at 77 K before irradiation. Following an initial radioactive decay period of about 50 h at 300 K, the samples were then kept at 77 K both during and between all subsequent measurements.

A small fraction of the activated ^{71}Ge may have recombined with vacant lattice sites during irradiation or initial storage at 300 K. However, it was established that most of the ^{71}Ge atoms were mobile and able to replace substitutional *n*- or *p*-type dopant atoms, making the dopant atoms interstitial, so long as a sufficient concentration of dopant atoms was available. This model of replacement is consistent with that proposed by others for experiments that involved low-temperature irradiation of Si and Ge. Irradiation in another reactor locale, with a much lower thermal to fast neutron ratio, was found to introduce complex lattice defect structures. These are believed to be due to fast-neutron collisions with Ge atoms, which result in trapping a significant fraction of the ^{71}Ge atoms in interstitial positions.

1. Summary of paper: *Jap. J. Appl. Phys.* 19, 11 (1980).
2. Guest scientist from Osaka University, Osaka, Japan.
3. Osaka University, Osaka, Japan.

OPTICAL STUDIES OF RADIATION DAMAGE IN NTD Si[1]

N. Fukuoka[2] J. W. Cleland

A study with IR spectroscopy techniques was made of the near-edge absorption and distinct absorption bands introduced by intersitital oxygen (O_i) in two different types of single-crystal Si. The

samples used were high-purity Fz Si containing $<10^{16}/cm^3$ O_i and high-purity Cz Si containing $2.4 \times 10^{18}/cm^3$ O_i. Absorption spectra were taken in the 1- to 50-μm wavelength region following reactor neutron irradiation at temperatures not exceeding 100°C and during 20-min isochronal annealing at 50°C steps from 150 to 900°C.

The relationship between absorption due to near-edge, divacancy, single-phonon, and higher-order band formation was investigated as a function of O_i content and fast-neutron fluence. Six distinct new absorption bands were observed in the 9.9- to 12.1-μm region after irradiation and partial annealing of the Cz Si samples. These bands may correspond to various vacancy–O defect structures that were previously identified by EPR techniques,[3] but further study is needed to establish the correspondences.

Almost complete removal of all IR-active defect centers was observed in all Fz and Cz Si samples after annealing for 20 min at 750°C; electrical property measurements on companion samples indicated the anticipated carrier concentration and mobility for the ^{31}P introduced by transmutation.

---

1. Summary of paper: *Radiation Effects* (in press).
2. Guest scientist from Osaka University, Osaka, Japan.
3. J. W. Corbett et al., p. 1 in *Radiation Effects in Semiconductors, 1976*, ed. by N. B. Urli and J. W. Corbett, Institute of Physics, London and Bristol, 1977.

3. Defects in Solids

A mechanistic understanding of defects and defect interactions in solids is important and sometimes crucial to the development of special-purpose materials utilized in the various energy technologies. It has been recognized for many years that a thorough understanding of radiation effects on materials that are used in the nuclear energy technologies is essential. Superconducting materials important to a broad range of technologies can have their properties altered or even dictated by defects. Similarly, in semiconductor devices and solar cells, defect and defect interactions are the dominant effects. In recent years, as this report illustrates, research in the Division has expanded into several new areas where defects continue to play an important role. This is not only reflected by the work reported in this section but by much of the work reported in Sect. 2 on Surface and Near-Surface Properties of Solids and in Sect. 4 on Transport Properties of Solids.

The research efforts for nuclear-related energy technologies are reflected both in the introduction of a new program on the behavior of gases in metals and in continued work on radiation effects in materials of interest for magnetic fusion energy development. The scope of electron microscopy and x-ray diffraction research on crystal defects and defect structures has been increasingly directed toward a broader range of research programs within the laser-annealing, ion-implantation, ion-solid interactions, photovoltaic, and superionic conductivity programs within the Division.

Basic studies of radiation damage in metals have focused on accurate determinations of defect production rates in pure fission neutron irradiations. These measurements have application in connection with the program on normalization of ion-irradiation-damage and fast-neutron-irradiation-damage production rates, which has now addressed itself to the study of damage production in alloys. A significant advancement has been made in the study of radiation-induced vacancy and interstitial loops by x-ray diffuse scattering, where an analysis procedure has made it possible to obtain separate size distributions for the vacancy and interstitial loop components. This capability will complement the tedious electron microscopy procedure for obtaining such information and should prove to be especially useful for the smaller size loops. The role of detailed analyses in obtaining these results underscores the need for ongoing support of defect measurements through the determination of accurate defect models and accurate scattering cross sections for both x-ray and electron microscopy investigations.

Direct observation of crack propagation and the dislocation behavior at the crack tip during in situ tensile deformation in the electron microscope has been extended to

various materials including Ni and amorphous niobium oxide. The results show that the physical processes occurring at the crack tip are sensitive to materials properties such as slip geometry, stacking fault energy, and lattice friction stress. These experiments probe the fundamental aspects of fracture phenomena and provide the first experimental verification of the well-known Bilby, Cottrell, Swinden theory of fracture. Theoretically, the energy release rate associated with crack propagation has been shown to be equivalent to the total force on the dislocations in the plastic zone. This result serves as a direct link between the microscopic dislocation theory of fracture and the macroscopic fracture mechanics.

The stringent demands placed on insulating materials in many energy technologies, such as the requirement to function at extreme temperatures in hostile environments, have underscored the need to understand the roles of defects and impurities in insulating crystals. Basic studies have focused on impurity-defect interactions, thermally generated defect complexes, aggregation of impurities, and the effect on mechanically deformed and strained insulators.

RADIATION EFFECTS

RATES OF DEFECT PRODUCTION BY FISSION NEUTRONS IN METALS AT 4.7 K[1]

R. R. Coltman, Jr. C. E. Klabunde
J. M. Williams

As part of an interlaboratory program, we have measured the resistivity-damage rates at 4.7 K for the dilute alloys V–300 ppm Zr, Nb–300 ppm Zr, and Mo–300 ppm Zr irradiated by virtually unmoderated fission neutrons.[2] In addition, Al, Ni, Cu, and stainless steel have also been measured to provide a broader data base for comparison with other experimental work and with defect-production theory.

Figure 3.1 shows the results for Cu as an example of the data obtained in the present fission-neutron damage-rate studies. Analysis of this type of data has been made in terms of the electrical size effect or deviations from Matthiessen's Rule as needed to determine the best initial damage rate. The values for the initial damage rates are listed in Table 3.1. By dividing the Frenkel-pair resistivity values[3,4] listed in Table 3.1 into the damage-rate values, we obtain the initial defect production rates $(dc/d\Phi)_0$, where c is the atomic fraction of Frenkel pairs and Φ is the fission-neutron fluence in neutrons/m^2.

Corresponding theoretical values listed in Table 3.1 are obtained from the commonly used "modified Kinchen-Pease relation,"

$$\left(\frac{dc}{d\Phi}\right)_0 = \frac{0.8(\sigma T)}{2E_d} ,$$

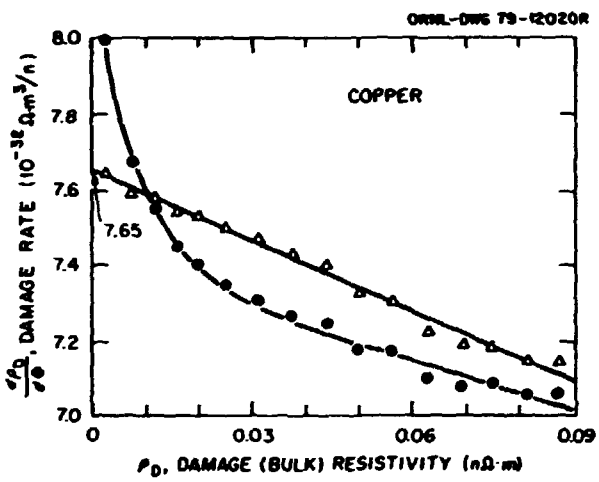

Fig. 3.1. Fission-neutron damage rate in Cu: • = observed resistivity damage rates; Δ = size-effect-corrected rates. Both are plotted against size-corrected (bulk) damage resistivity. Line is linear-least-squares fit to corrected rates. Curve is the line-transformed back to uncorrected rates. A small contribution due to thermal neutrons has not been deducted from the rates.

where E_d is the displacement threshold energy[3,5] and (σT) are the damage-energy cross sections taken from computer-code calculations by Kirk and Greenwood[6] for the fission-neutron spectrum. Damage efficiencies, which are the ratios of experimental to theoretical initial defect production rates, are shown in column 3 of Table 3.2. In addition, Table 3.2 also shows for various other neutron-energy-spectra damage-efficiency values calculated by Kirk and Greenwood, who used the same computer code, and the experimental data obtained by other investigators.

Table 3.1. Comparison of experiment and theory

	Experiment			Theory		
	Initial damage rate, corrected (10^{-} Ω·m^{-} neutron)	Frenkel-pair resistivity, ρ_F (10^{-} Ω·m at fr)[a]	Frenkel-defect production rate, $\left(\frac{dc}{d\Phi}\right)_0$ (10^{-} m^{-} at fr neutron)	Threshold displacement energy, E_d (eV)	Damage energy cross section[b] (σT) (keV b)	Frenkel-defect production rate, $\left(\frac{dc}{d\Phi}\right)_0$ (10^{-} m^{-} at fr neutron)
Al	2.19	3.9	5.6	27	94.4	14.0
Ni	1.71	6.0	2.9	34	77.8	9.2
Cu	0.723	2.0	3.6	29	77.3	10.7
V	1.17	18	4.0	26	107[c]	16.5
Nb	3.43	16	2.1	79	74.9	3.8
Mo	3.38	13	2.6	77	80.0	4.2
SS	6.37					

[a]at. fr = atomic fraction.
[b]Ref. 7.
[c]Ref. 4.

Table 3.2. Damage efficiencies for various neutron spectra

	Moderated fission		Fission, ORNL	Be(d,n), ORNL	T(d,n), LLL
	ANL	LLL			
Al	0.34		0.40		
Ni	0.27		0.31		
Cu	0.27		0.34	0.27	
V		0.64[a]	0.53		0.57[a]
Nb	0.49	0.69	0.56	0.50	0.54
Mo	0.45	0.66	0.62		0.57
Pt	0.32			0.30	

[a]Ref. 4.

A broad view of the results shown in Table 3.2 suggests that present theory overestimates initial defect production rates for various fast-neutron spectra by a factor of about 2 to 4 compared with the experimental results. While uncertainties in ρ_F and E_d values are large for some elements and may contribute to the variations in the damage efficiencies, the uncertainties are not the basic cause for the efficiencies being less than unity. A test of the response of the theory to target mass for a fixed spectrum (see vertical comparisons in Table 3.2) is limited by the uncertainties in the ρ_F and E_d values. On the other hand, the response of the theory to variations in a neutron-energy spectrum for a given element (horizontal comparisons in Table 3.2) does not depend on ρ_F or E_d. In this latter case, the theory performs quite well, giving variations in efficiency values of only 7-30% for neutron-energy spectra peaked from 1 to 15 MeV.

As a continuation of the work described above, the displacement production rates for unmoderated fission neutrons on Mg, Ti, Zr, Pd, Ta, W, and Pt have recently been measured at 4.8 K, and similar measurements are being made on Fe and Co. Analysis of the results for damage efficiency is under way using the code RECOIL to calculate damage energies.[7] The results for all metals will be analyzed in terms of systematic correlations of damage efficiency with respect to crystal structure and atomic weight.

1. Summary of paper to be published.
2. C. E. Klabunde, J. M. Williams, and R. R. Coltman, Jr. (to be published).
3. P. Lucasson, p. 42 in *Fundamental Aspects of Radiation Damage in Metals*, vol. 1, ed. by M. T. Robinson and F. W. Young, Jr., ERDA CONF-751006-P1, Oak Ridge, Tenn., 1976.
4. M. W. Guinan and C. E. Violet, private communication. To make a consistent comparison between the present ORNL result for V and the LLL experimental data, we use their value for ρ_F and the RECOIL code (see ref. 7) to obtain these damage-efficiency values.
5. M. G. Miller and R. L. Chaplin, *Radiat. Eff.* 22, 107 (1974).
6. M. A. Kirk and L. R. Greenwood, *Journal of Nuclear Materials* (to be published).
7. The damage-energy cross section for V was calculated using the code RECOIL by T. A. Gabriel, J. D. Amburgey, and N. M. Greene, *Radiation-Damage Calculations, Primary RECOIL Spectra Displacement Rates, and Gas-Production Rates*, ORNL/TM-5160 (1976).

THE EFFECTS OF IRRADIATION ON THE NORMAL METAL OF A COMPOSITE SUPERCONDUCTOR: A COMPARISON OF Cu AND Al[1]

C. E. Klabunde R. R. Coltman, Jr.
J. M. Williams

The most economical design of a composite superconducting magnet for a fusion reactor will depend sensitively on the irradiation-induced changes in the magnetoresistance of the normal metal. In an earlier report[2] we calculated the effects to be expected for Cu normal metal in service on the composite superconducting toroidal field coils of a tokamak fusion reactor.[3] The calculation was accomplished by first establishing from available data and theory[4,5] the production of damage resistivity in zero field:

$$\rho_D(0) = s[1 - \exp(-iD/s)] + \rho_0(0) , \qquad (1)$$

where D is the neutron dose in dpa, s is the saturation value of the damage resistivity, and i is the initial rate of resistivity increase vs D. The values for Cu were $s \cong 4.0$ nΩ·m and $i = 649$ nΩ·m/dpa. A large body of data on the magnetoresistivity of irradiated Cu was shown to lie within a suitably broad envelope of Kohler plot curves expected to encompass the present application. The envelope was described by two lines of the form

$$\rho_D(H) = \rho_D(0) + 10^{\alpha} H^{\beta} \rho_D(0)^{1-\beta} , \qquad (2)$$

where α and β are intercepts and slopes of the two straight lines on the Kohler plot, with H, the field in tesla, and ρ, the resistivity in nΩ·m. The values were as follows: $\alpha_1 = -1.25$ and $\beta_1 = 0.95$; $\alpha_2 = -1.77$ and $\beta_2 = 1.23$.

Substituting the zero-field resistivity given by Eq. (1) into Eq. (2) gives a family of curves of total resistivity vs dose, initial resistivity, and magnetic field.

The same data sources on damage production were used for Al as for Cu. For the saturation resistivity, we used a value $s \cong 9.0$ nΩ·m; and for the initial damage rate, we used $i = 1520$ nΩ·m/dpa.

For the magnetoresistivity of damaged Al, we used data of Böning et al.[6] As with Cu, we took an empirical approach to describe the range of magnetoresistivity values to be found in the damaged material. The values were contained within two curves, A and B, of the form

$$\rho_D(H) = \rho_D(0) + \rho_D(0) \cdot 10^{a}[1 - 1/(1 + z)]^{b} , \qquad (3)$$

$$z = 10^{c}[H/\rho_D(0)]^{d} ,$$

with the following parameter values:

	a	b	c	d
A	0.17	1.73	1.1	−0.7
B	0.34	1.77	1.1	−0.9

By combining Eqs. (1) and (2) for Cu and Eqs. (1) and (3) for Al, we generated the families of curves seen in Fig. 3.2. Instead of dpa, we use neutron fluence in order to compare directly Cu and Al for the same service time in a given neutron flux. For this example, fission-spectrum neutrons were used.[7] We see that, because of the larger initial magnetoresistivity in Cu, Al is, in fact, better up to a fluence of about 1×10^{21} neutrons/m^2, provided Al has an initial resistivity less than ~0.1 nΩ·m. This fluence translates to dpa values of 1.2 and 1.5×10^{-4} for Cu and Al, respectively.

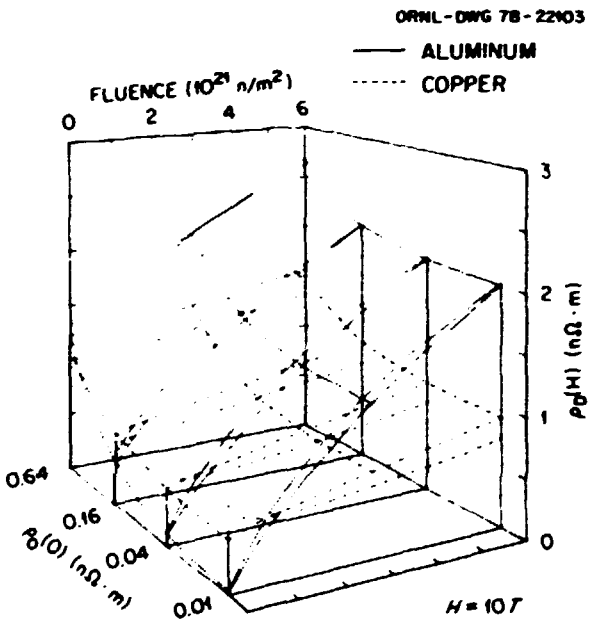

Fig. 3.2. Three-dimensional plot of magnetoresistance for Cu and Al as a function of magnetic field, neutron fluence, and initial resistivity.

These dpa values are found to occur in one year about halfway through the toroidal field coils, according to ref. 3. However, in considering positions other than the innermost winding, we must also take into account the decrease in magnetic field (approximately linearly) with radial position. ($H \to 0$ at some point near the outer winding.) As a result, we find that nowhere is Al better than Cu in this design. Only

at much lower doses than those projected in the high-field region would there be any location where Al would be better, assuming, that is, that the use of such high-purity material is feasible.

Santoro et al.[3] have calculated the annual fluence at certain magnet locations for a reference tokamak design having a neutron wall loading of 1.0 MW m^{-2}. When our analysis is applied to one of their highest fluence values found adjacent to a penetration into the first wall, we find that the field-on (10 T) resistivity for Cu increases about 600% in one year. This result indicates the need for additional shielding at some locations.

From the foregoing analysis it appears that Cu is the stabilizer material of choice, and because of its high initial magnetoresistivity, ultra-high purity is not important. Nevertheless, as our earlier report cites,[2] Cu is not so superior as to preclude the need for design compromises that take radiation damage to the stabilizer into account. Such compromises may entail trade-offs between additional shielding and additional stabilizer material, especially in hot-spot regions that result from penetrations.

1. Summary of paper: *J. Nucl. Mater.* **85/86**, 385 (1979).
2. J. M. Williams et al., *IEEE Trans. Magn.* **MAG-15**, 731 (1979).
3. R. T. Santoro et al., *Nucl. Technol.* **37**, 65 (1978).
4. M. Nakagawa et al., *Phys. Rev. B* **16**, 5285 (1977).
5. C. E. Klabunde et al. (to be published).
6. K. Böning et al., *Phys. Status Solidi* **34**, 395 (1969).
7. With fission-spectrum neutrons, D fluence for Cu is 1.176×10^{-25} dpa·m^2 neutron and for Al is 1.465×10^{-24}.

EFFECTS OF RADIATION AT 5 K ON ORGANIC INSULATORS FOR SUPERCONDUCTING MAGNETS[1]

R. R. Coltman, Jr. R. H. Kernohan
C. E. Klabunde C. J. Long[2]

A program in progress at ORNL aims to understand the effects of irradiation at liquid-He temperature on insulator materials that may be used in the construction of large superconducting coils that provide magnetic containment for the plasma in a fusion reactor. In our previous studies, the principal damaging radiation was an energetic spectrum of gamma rays arising largely from thermal-neutron capture in a Cd shield surrounding the specimens. In the tokamak application, however, in addition to gamma rays, neutrons with a variety of energies will be present at many insulator locations. Few studies exist on the irradiation of insulators near 4 K by fast neutrons. To examine their possible influence, the ratio of fast-neutron flux to the gamma-ray dose rate in the present experiment was increased by a factor of 17 over that in previous irradiations. Also, the gamma-ray dose was extended from 2×10^9 to 1×10^{10} rads.

The following materials chosen for study were those presently in use for magnet construction and already known to have good radiation resistance at room temperature:

1. Stycast 2850 FT (Blue): Epoxy, with 7% 24-LV hardener; an inorganically filled epoxy: Emerson and Cuming, Inc.
2. EPON 828: Epoxy, with 20-pph-Z curing agent, 0.5% Z6020 Silane couplant; filled with 40 wt % 400-mesh SiO_2; Shell Chemical Company.
3. G-10 CR: National Electrical Manufacturers Association, a heat-activated amine-catalyzed bisphenol solid-type epoxy resin laminate reinforced with continuous filament E Glass fabric, silane finished; designated for cryogenic use; Spaulding Fibre Company.
4. G-10 CR (BF): Same as No. 3, except made with boron-free E Glass.
5. G-11 CR: Same as No. 3, except that an aromatic amine-hardened bisphenol liquid-type epoxy resin is used in its fabrication.
6. Nomex 410: Paper, type 410; aromatic polyamide (aramid) sheet; E. I. du Pont de Nemours & Company.
7. Kapton H: Polyimide film; E. I. du Pont de Nemours & Company.
8. Aluminized Kapton: Type NRC-2; used for multilayer superinsulation; King-Seeley Thermos Company.

Irradiations were made in the Low-Temperature Irradiation Facility located at the ORNL Bulk Shielding Reactor.[3] The specifications for two irradiations made on identical sets of specimens are given in Table 3.3.

The postirradiation testing of electrical properties was done at room temperature, and mechanical properties at liquid nitrogen temperature. The electrical results are given in Table 3.4, and results for flexure and compressive strength are given in Figs. 3.3 and 3.4.

Pieces of aluminized Kapton 37.5 × 25 mm were each folded in a Z shape, heavily creased, and then wrapped in Al foil to give a flat packet ~13 × 25 mm.

Table 3.3. Specifications of irradiations at 4.98 K

	Gamma-ray dose (rads)	Fast-neutron fluence (neutrons m^{-2} > 0.1 MeV)	Irradiation time (h)
Low	2.4×10^{9}	2.2×10^{20}	48
High	1.0×10^{10}	8.7×10^{20}	193

Table 3.4. Electrical measurements at room temperature after irradiation at 5.0 K

Each result the average of three measurements

Dose (10^{10} rads)	Resistivity (10^{11} Ω·m)					
	Stycast 2850 FT	EPON 828	G-10 CR	G-11 CR	Nomex 410	Kapton H
Control	0.24	20.0	8.2	4.4	3.3	20
0.24	0.25	5.5	8.5	2.8	2.2	29
1.0	0.27	8.1	0.64	0.14	2.0	22
	Electrical breakdown (kV/mm)					
Control	28	33	23	24	36	66
0.24	31	34	23	23	38	66
1.0	8	31	8	10	36	68

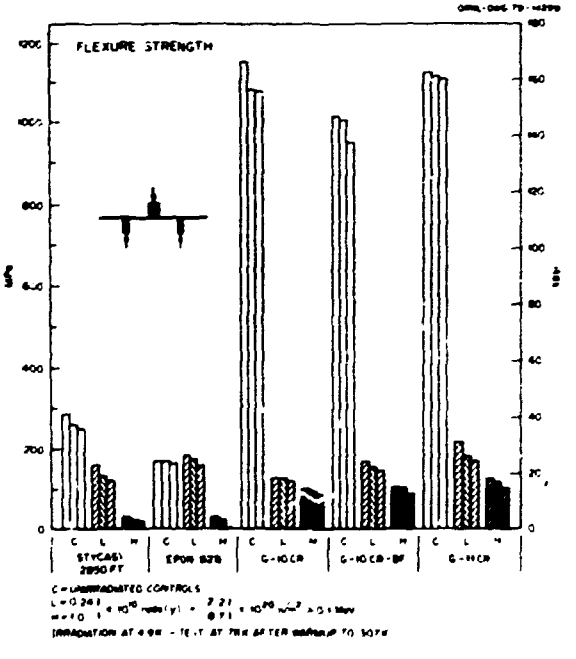

Fig. 3.3. Flexure strength as a function of irradiation.

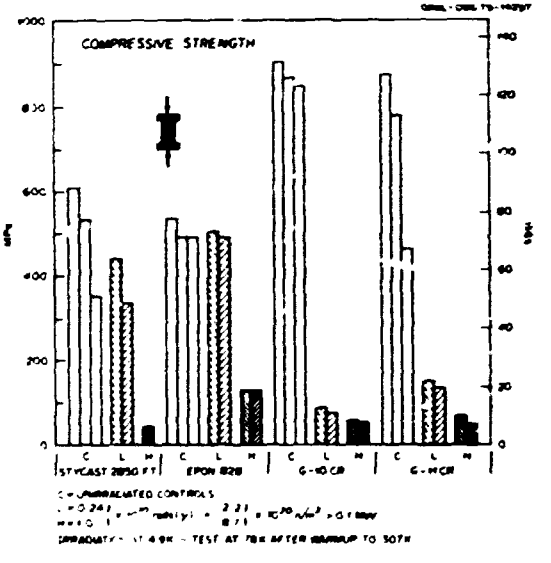

Fig. 3.4. Compressive strength as a function of irradiation.

After irradiation, no failure of any type was observed in any of the specimens after repeated flexing of the creases. This lack of failure is in sharp contrast to aluminized Mylar, which broke apart upon handling after a dose of 2.0×10^{9} rads.[4] It appears that the Kapton could serve as superinsulation for cryogenic systems exposed at least up to a dose of 1×10^{10} rads.

Although the resistivity decreased substantially at the high dose, it probably still remained in a usable

range for all materials tested. The loss in voltage-breakdown strength was minimal, except for Stycast 2850 FT and the glass-cloth-filled epoxies, which might require design adjustments for use at 1×10^{10} rads.

In the case of mechanical properties, the dependence of strength upon dose was different for flexure and compression strengths. The results suggest that the choice of a material may depend upon the stress conditions in service. In the case of flexure, while the strength of glass-cloth-filled epoxies was greatly reduced at 2.4×10^{9} rads over initial values, these epoxies remain competitive with the particle-filled epoxies for that dose. At 1×10^{10} rads, the flexure strength of the particle-filled epoxies is at end of life, while the glass-cloth-filled epoxies retain usable strength. In compression, however, at 1×10^{10} rads, the strength of all materials is reduced to barely useful levels; however, EPON 828 retains the greatest strength.

A comparison of the present results with previous ones suggests that an increase by a factor of 17 in the fast-neutron dose rate had little, if any, effect upon the results at the doses studied. While ratios of neutron flux to gamma-ray dose rates, n/γ, comparable to that in our work are found in many magnet locations, others have higher ratios. We believe that studies to check the influence of fast neutrons should be carried out using sources having higher n/γ values than for the work reported here.

Design calculations of Santoro et al.[5] show that various magnet locations encompass a wide range of gamma-ray dose rates, the highest being adjacent to penetrations through the shield and blanket to the first wall. From their results, we calculate that for some magnet locations our high dose of 1×10^{10} rads, at which some materials reached end of life, corresponds to a service time of only 0.2 years for a first-wall loading of only 1.0 MW/m^2. Thus, it is clear that in those locations additional shielding will be necessary if some of these materials are to be used.

1. Summary of papers: ORNL/TM-7077 (November 1979); *IEEE-Nuclear and Plasma Sciences Society* (to be published).

2. Metals and Ceramics Division, ORNL.

3. R. R. Coltman Jr., et al., *Radiation Effects on Organic Insulators for Superconducting Magnets*, ORNL/TM-7077 (November 1979).

4. R. R. Coltman, Jr., et al., *IEEE-Nuclear and Plasma Sciences Society* (to be published).

5. R. T. Santoro et al., *Nucl. Technol.* 37, 65 (1978).

He DIFFUSION IN Ni AT HIGH TEMPERATURES[1]

J. M. Williams[2] V. Philipps[3] K. Sonnenberg[3]

The developing nuclear technologies present a need to understand better the mechanisms and parameters of long-range migration of He in metals. The extremely low solubility of He in metals has made experimentation difficult. Experiments designed to overcome the solubility problem by implanting He and studying its release upon raising the temperature[4] have yielded information about the dissociation of He from radiation-produced defects but little information about the mechanisms of diffusion. To study diffusion we made use of deep implantations at high temperatures and studied the simultaneous release of He. The depth of implantation guaranteed that the released He had traveled a large distance, and the high temperature ensured that involvement with radiation-produced defects was minimal.

One procedure was to implant He to depths of up to 85 μm in 10-mm-thick samples of Ni at temperatures betweem 900° and 1250°C. The samples were heated from the back side by means of an electron gun. At the start of an implantation, the He diffused immediately, some diffusing to internal sinks (bubbles) and some to the surface, where it was detected by a mass spectrometer as emitted gas. A steady-state gradient was soon established between the implantation zone and the surface, at which time the emission rate was constant. The diffusivity was determined by analyzing the transient to this steady state.

The diffusivity results can be summarized in an equation of the usual Arrhenius form,

$$D = (2.7 \pm 1) \times 10^{-3} \exp\left(\frac{-0.81 \pm 0.05\ \text{eV}}{kT}\right) \frac{\text{cm}^2}{\text{sec}} .$$

In our polycrystalline material (of approximately 1-mm grain diameter), some of the He was apportioned to a coarse distribution of bubbles that grew internally because of preexisting nuclei that probably had their origin in the metallurgical history of the material. In single crystals all of the He was released.

In seeking a mechanistic interpretation of the activation energy, 0.8 eV, we ruled out simple interstitial diffusion because, at these temperatures, interstitial He will encounter many thermal vacancies on its way to the surface and because it is generally accepted that He has a high binding energy with

vacancies. Two other models, the substitutional impurity (SI) model and the hindered-diffusion model, were considered. In the SI model, the He in its first vacancy is joined by a second vacancy that renders the complex mobile. The complex migrates until the second vacancy is thermally dissociated, leaving the He again immobilized as a substitutional atom. In the hindered diffusion model, the He diffuses interstitially until it falls into a vacancy where it resides as a substitutional atom. Later it thermally dissociates and again wanders interstitially until it encounters another vacancy. The effective activation energy related to each of these models can be derived in terms of the activation energies for the component processes, but some of the component activation energies are not well known. Perhaps the most crucial of these is the binding energy of the second vacancy in the SI model. A theoretical value of 0.47 eV has been derived for this energy;[5] if the true value is no more than 1.2 eV, the SI model can be ruled out. The effective activation energy for the hindered-diffusion model is approximately

$$E_D^{EFF} = E_{He,v}^{DISS} - E_v^F ,$$

where $E_{He,v}^{DISS}$ is the energy for dissociation of the He + 1V complex (substitutional He) and E_v^F is the vacancy-formation energy. Existing experimental values of the quantities on the right-hand side are 2.1 eV for the dissociation energy[4] and 1.4 to 1.6 eV for the vacancy-formation energy; thus the difference ranges from 0.5 to 0.7 eV, which is to be compared with the experimental value of 0.8 eV. Considering the approximations involved and the uncertainties in the experimental data, the hindered-diffusion model is a probable mechanism, though it is not established with accuracy.

1. Summary of paper: *Proceedings of Consultant Symposium on Rare Gases in Metals and Ionic Solids*, Harwell, England, Sept. 10-14, 1979 (to be published).

2. This author carried out this research while on foreign assignment at the Institut für Festkorperforschung, Kernforschungsanlage, Jülich, Germany.

3. Institut für Festkorperforschung, Kernforschungsanlage, Jülich, Germany.

4. E. V. Kornelsen and D. E. Edwards, Jr., p. 521 in *Application of Ion Beams to Metals*, ed. by S. T. Picraux, E. P. EerNisse, and F. L. Vook, Plenum Press, New York, 1974.

5. W. D. Wilson and C. F. Melius, *Proceedings of Consultant Symposium on Rare Gases in Metals and Ionic Solids*, Harwell, England, Sept 10-14, 1979 (to be published).

He-RELEASE EXPERIMENTS IN NEUTRON-IRRADIATED Ni

D. B. Poker J. M. Williams

Another approach to determining the diffusivity of He in Ni involves degassing of reactor-irradiated bulk samples. The samples were open-ended cylinders of commercial "A" Ni 100 mm in length, 19 mm in diameter, and 1.5 mm in wall thickness, with an average grain diameter approximately equal to the wall thickness. Neutron doses were chosen such that He concentrations of approximately 1 ppb were produced by the series reactions,

$$^{58}Ni(n,\gamma)^{59}Ni , \qquad ^{59}Ni(n,\alpha)^{56}Fe .$$

Two methods of heating, a hot-wall furnace and induction heating, have been used in the release studies. In the furnace technique, the sample was contained in a degassed Ni tube, which was, in turn, contained in a vacuum-pumped annulus to shield it from the atmosphere. The released He was detected by a Veeco MS-12 leak detector.

Preliminary indications are that all of the He was released at temperatures above 900°C, with activation energies of 0.6 to 1.5 eV, but accurate values and error limits cannot yet be quoted. It is not clear that the release occurs with a single activation energy. Grain boundaries or clustering may be playing a role. The experiments are being extended to single crystals, wire samples with a bamboo type of grain structure, and stainless steels.

Ni-ION DAMAGE PRODUCTION RATES IN Fe-17% Cr

T. S. Noggle D. B. Poker B. R. Appleton

The study of damage production rates in Al[1] and Ni[2] has indicated generally excellent agreement between the damage rates measured as a function of ion penetration depth and the damage energy calculated by the computer code E-DEP-1.[3] Extension of these studies to alloys has been made on Fe-17% Cr alloy thin film specimens prepared by vacuum evaporation. The damage rate measurements on the alloy were made for the same conditions previously employed for the Ni damage-rate studies, that is, 17.4-MeV Ni ions and Ni absorber foils.[2]

Figure 3.5 shows the comparison of the experimentally measured damage rates of 17.4-MeV Ni ions in Fe-17% Cr with the damage energy calculated by

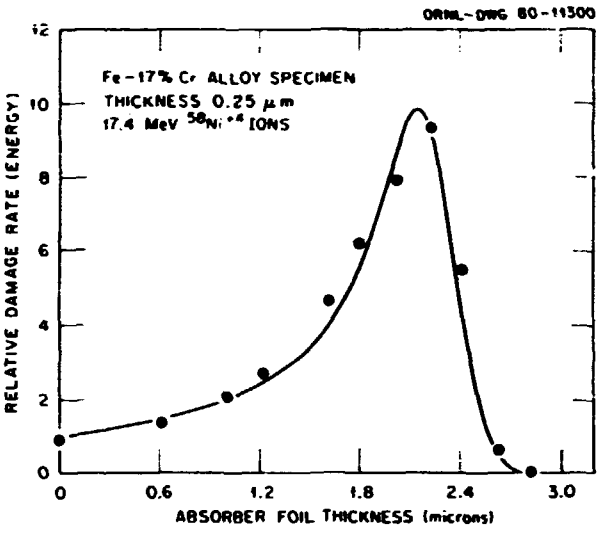

Fig. 3.5. Relative damage rates of 17.4-MeV Ni ions in an Fe–17% Cr alloy vs Ni absorber foil thickness. The smooth curve was calculated using E-DEP-1 computer code (ref. 3).

the E-DEP-1 code. The excellent agreement to be noted here in part represents adjustment of both the calculations and experimental measurements. The E-DEP code does not provide for the case where the absorber foil and specimen are different materials as employed in the experiment. However, by suitable adjustment of the electronic stopping parameter used in the calculations, the program will calculate damage energies in a uniform alloy medium for which the ion energies incident on the alloy specimen are approximately the same (within 1–2%) as the ion energies emerging from Ni foils of the same thickness. This procedure was employed to obtain the calculated curve in Fig. 3.5. The damage rates measured for the open beam condition (no absorber foil) decreased rapidly with the accumulated damage, while the damage-rate measurements with absorber foils did not show this strong dependence on the accumulated damage. This type of behavior is essentially the same as previously reported for Ni;[2] it has subsequently been studied further in Ni without identifying the physical basis of this phenomenon. This behavior raises questions as to the proper value for the open beam that should be employed for normalizing the data for comparison with the calculations. In the present case, the normalizing value was chosen to give the best fit of the experimental points to the leading edge of the calculated curve. The value used is about 10% larger than, but within the uncertainty limit of, the open beam value extrapolated to zero dose.

These results have demonstrated that, for the case of an alloy, the E-DEP-1 code does a good job of scaling the damaging production rate as a function of ion penetration depth. These results further indicate that the experimental procedures developed for pure metals extend readily to alloy systems; thus they will be employed in the measurements of damage rates in Fe-Ni-Cr ternary alloys that approximate the composition of commercial grades of stainless steel.

---

1. T. S. Noggle et al., *Solid State Div. Prog. Rep., Sept. 30, 1978*, ORNL-5486, p. 98.
2. T. S. Noggle et al., *Solid State Div. Annu. Prog. Rep. Apr. 30, 1977*, ORNL-5328, p. 103.
3. I. Manning and G. P. Mueller, *Comput. Phys. Commun.* 7, 85 (1974); *Nucl. Engr. Design* 33, 78 (1975).

LOW-TEMPERATURE ION DAMAGE IN METALS

B. C. Larson J. F. Barhorst T. S. Noggle

X-ray diffuse scattering studies have been initiated on the fundamental aspects of high-energy displacement cascades and lattice defect evolution in metals at low temperatures. Copper and Ni single crystals have been irradiated at 4 K with 17.4-MeV Ni ions with the use of the ORNL Tandem Van de Graaff. A technique developed[1] for the program on the Normalization of Ion and Neutron Damage, involving the use of absorber foils, was used to produce a 2.4-μm irradiated layer that was homogeneously damaged from the standpoint of damage-energy deposition.

Diffuse scattering measurements have been made on Cu and Ni single crystals after irradiation with 2×10^{12} ions/cm^2 at 4 K using a linear position-sensitive detector and a 12-kW rotating anode x-ray generator. Similar to results found for 300-K ion-irradiated Ni and Cu, a significantly larger number of lattice defects were found to be retained in Cu after warming from 4 K to 300 K than were found in Ni. Size distributions of vacancy and interstitial loops in the Cu sample have been determined after 30-min thermal anneals to 548 and 573 K as well as at 300 K. These results indicate a considerable coarsening of the interstitial loop size distribution over this temperature range, while smaller size increases were observed in the vacancy loop component. An overall decrease of ~60% in the total number of point defects contained in the loop distributions was found for the anneal from 300 to 573 K; however, at each tempera-

ture, the relative numbers of vacancies and interstitials were found to be equal within the measuring uncertainties (~±7%).

---

1. T. S. Noggle et al., p. 225 in *Proceedings, Fourth Conference on the Scientific and Industrial Applications of Small Accelerators*, ed. by J. L. Duggan and I. L. Morgan, IEEE 76CH1175-9, NTS, Piscataway, N.J., 1976.

VACANCY AND INTERSTITIAL LOOPS IN IRRADIATED Cu

B. C. Larson J. F. Barhorst

The extent of vacancy clustering following high-energy displacement cascades in irradiated metals is of considerable importance as a parameter in the development of void structures during prolonged irradiation. Although electron microscopy has the capability of investigating the aggregation of vacancies into loops, because of the small size of vacancy loops in irradiated metals and the tedious nature of the measurements, detailed results on vacancy clustering under these conditions have been inconclusive. In this study, an x-ray diffuse scattering method for determining the size distribution of both vacancy and interstitial loops has been developed and applied to the case of high-energy Ni-ion-irradiated Cu.

Diffuse x-ray scattering calculations for dislocation loops have shown that the diffuse intensity in the asymptotic scattering region ($1 < qR < 6$, where R is the loop radius and q is the distance from a reciprocal lattice point) falls off as $\sim 1/q^4$. However, calculations along the ±[111] direction near the 222 reflection have shown this intensity to be modulated by Bragg-like scattering from the compressed (interstitial) or expanded (vacancy) region in the immediate vicinity of dislocation loops. Because the sense of the strain is opposite for the two kinds of loops, interstitial loops scatter more heavily for q along the [111] direction while the vacancy loop scattering is more concentrated along the $[\bar{1}\bar{1}\bar{1}]$ direction near the 222 reciprocal lattice point. In plots of intensity × q^4, these calculations indicate a maximum at $q \approx \pm 3/R$ for interstitial (+) and vacancy (−) loops, respectively.

X-ray diffuse scattering measurements made along the ±[111] directions near the 222 reflection of Cu that had been irradiated with 60-MeV Ni ions (1.2×10^{13} cm^{-2} at 300 K) are shown in Fig. 3.6. The measured intensity (multiplied by q^4) is shown as the

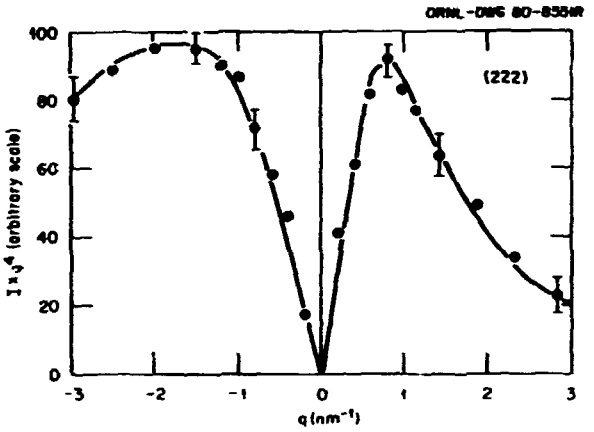

Fig. 3.6. Measured diffuse scattering from Ni-ion-irradiated Cu at the 222 reflection.

solid points (Fig. 3.6), and it can be inferred from the sizable scattering on both the plus and minus sides that both vacancy and interstitial loops are present. The fact that the maximum on the plus side occurs at a q value that is lower than that on the minus side is qualitative evidence that the average size of the interstitial loops is larger than the average size of vacancy loops. The solid lines in Fig. 3.6 represent a least squares fit of calculated diffuse scattering data for 1.0-, 2.0-, 3.0-, 4.0-, and 6.0-nm loops of vacancy and interstitial nature to the measured scattering, with the concentration of each of the sizes of both vacancy and interstitial loops as fitting parameters.

The results of the fitting in Fig. 3.6 are shown in Fig. 3.7, where the results are scaled to represent the concentrations for the peak damage region.[1] The concentrations of each of the sizes are represented by histograms 1.0 nm wide and reduced to units of loops cm^{-3} nm^{-1} so that the total area under the graph is a measure of the total loop density. The 6.0-nm concentration is represented by a 3.0-nm histogram. As suggested above, the vacancy loops are found to be smaller than the interstitial loops, and it can be seen that there are fewer interstitial loops present than vacancy loops. Calculating the total number of point defects in each kind of loop, we find 53.6% of the point defects in loops to be vacancies and 46.4% to be interstitials. These values can be taken as evidence that equal numbers of vacancies and interstitials are present in clusters (considering an estimated uncertainty of ±7%) and that all of the vacancies are clustered into loops. The equal numbers of vacancies and interstitials found here are to be compared with reported values ranging from a factor of twice as many vacancies as interstitials to

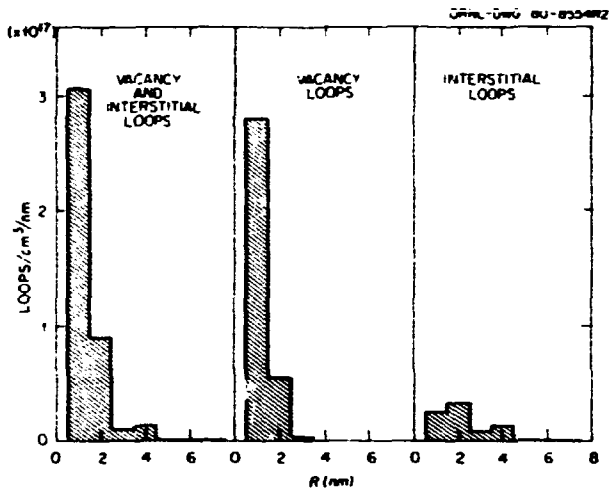

Fig. 3.7. Size distribution for vacancy and interstitial loops in Ni-ion-irradiated Cu as obtained from x-ray diffuse scattering.

less than half as many vacancies as interstitials in loops in microscopy investigations[2,3] of irradiated Cu. The possible role of undetected vacancy stacking fault tetrahedra in both the x-ray and microscopy results is being considered.

1. J. B. Roberto and J. Narayan, p. 120 in *Fundamental Aspects of Radiation Damage in Metals*, ed. by M. T. Robinson and F. W. Young, Jr., ERDA CONF-75-1006-P1, Oak Ridge, Tenn., 1976.
2. M. Ruhle, F. Häuserman, and M. Rapp, *Phys. Status Solidi* **39**, 609 (1970).
3. J. Narayan and S. M. Ohr, *J. Nucl. Mater.* **85/86**, 515 (1979).

CALCULATION OF DIFFUSE SCATTERING FROM DISLOCATION LOOPS[1]

P. Ehrhart[2] B. C. Larson H. Trinkaus[2]

Numerical calculations of the diffuse scattering from perfect and faulted dislocation loops in an isotropic fcc lattice have been carried out for q values out to the zone boundaries. Previously available continuum calculations,[3] which were restricted to q's near Bragg reflections, were extended to take the atomistic nature of the crystal lattice into account so that stacking faults and the lattice symmetry would be properly represented at all scattering vectors. The lattice sums were made tractable by the use of structure factors for "super-cells" varying from 12 to 6144 atoms and by the use of damping functions to limit integration volumes.

Diffuse scattering calculations made in this study for the region near Bragg reflections, for both faulted and perfect loops of 2.0-nm radius on {111} planes, reproduced the characteristic features that had been found previously using continuum calculations. However, for larger q values the atomistic calculations were important, where the stacking fault scattering from faulted interstitial (extrinsic) loops was found to contain nodal points at characteristic reciprocal lattice positions, but the scattering streaks from faulted vacancy (intrinsic) loops contained no nodal points. This stacking-fault scattering was found along all (111) directions except those radial from the origin in reciprocal space; and, as expected, perfect (unfaulted) loops produced no such streaking in the calculated diffuse scattering. Analytical schemes for predicting the general features of the diffuse scattering received special attention as a means for providing a physical interpretation of the scattering and as an aid in detecting spurious effects. The analytic methods predicted the fine structure in the extrinsic stacking fault scattering, and the use of caustics and the method of stationary phase were found to be useful in interpreting the scattering nearer to the reciprocal lattice points.

1. Summary of paper to be published.
2. Institut für Festkorperforschung, Kernforschungsanlage, Jülich, Germany.
3. B. C. Larson and W. Schmatz, *Physica Status Solidi* (in press).

BLACK-WHITE CONTRAST OF DISLOCATION LOOPS IN ANISOTROPIC CUBIC CRYSTALS[1]

S. M. Ohr

A computer program to generate simulated electron micrographs has been used to calculate the image contrast of dislocation loops in cubic crystals by taking into account the effect of elastic anisotropy. The displacement field was numerically calculated for a circular dislocation loop of finite size from the Fourier transform of the elastic Green's function. The image contrast was calculated under two-beam dynamical diffraction conditions using the Howie-Whelan equations. In an isotropic medium, the black-white contrast direction of a Frank loop imaged under the exact (002) Bragg reflection makes an angle of approximately 15° from the direction of the Burgers vector. In Cu and Ni, the anisotropic calculations show that the black-white contrast is

parallel to and is elongated considerably along the direction of the Burgers vector. In Nb, the black-white contrast direction of a perfect loop of $a/2[111]$ type lies about halfway betwe n the directions of the Burgers vector and the diffraction vector. It is concluded that the image contrast of dislocation loops in cubic crystals is highly sensitive to the elastic anisotropy, and it is necessary to take the effect of anisotropy into account in order to perform an accurate analysis of the loop image.

1. Summary of paper: *Phys. Status Solidi A* 56, 527 (1979).

CALCULATION OF DIFFUSE SCATTERING FROM SPHERICAL PRECIPITATES

B. C. Larson J. F. Barhorst

X-ray studies of the structure and evolution of energetic particle-induced displacement cascades in materials require the interpretation of scattering from three-dimensional def ct clusters as well as from planar loop structures. Whereas numerical diffuse scattering calculations have been made for dislocation loops,[1] detailed scattering calculations for three-dimensional clusters are not yet availab.e As part of a study directed toward the calculation of diffuse scattering from three-dimensional aggregates in anisotropic materials, we report on some characteristic features of the scattering from spherical inclusions in an isotropic material.

Analytic scattering models are available[2] for the calculation of diffuse scattering from strain centers with large distortion fields, but these models do not consider strain centers with finite sizes such as required to simulate properly the scattering from solute precipitate particles in alloys. Quite analogous to the case for scattering from dislocation loops, if we consider a scattering vector given by $K = h + q$, where h is a reciprocal lattice vector and q the scattering vector relative to h, the region $qR_c < 1$ defines the Huang scattering domain; and the region for $qR_c > 2$ can be defined as the asymptotic region. Here, R_c is loosely referred to as the defect radius but is more precisely defined by $K \cdot S(R_c) \approx 1$ where $S(r)$ specifies the lattice distortion surrounding the strain center. The scattering for $qR_c < 1$ tends toward a q^{-2} falloff because of the well-known Huang scattering; however, for the asymptotic region, the scattering is characterized in the analytic model by local Bragg reflections from the highly strained material within a radius of R_c. According to the model, an oscillating q^{-4} fallout is predicted for the asymptotic scattering region as a result of interference effects; and for the particular direction of $q \| h$ in the case of negative lattice strain surrounding the defect site ($-q \| h$ for positive lattice strain), a smooth $q^{-10/3}$ falloff is expected.

For a coherent solute precipitate in an alloy lattice, the diffuse scattering is complicated by the finite size of the precipitate. A negative (compressive) lattice strain is generated in the region surrounding a precipitate with a positive misfit strain relative to the host lattice. This aspect of the defect character is not incorporated in the above analytical predictions; however, through numerical calculations this property was found to lead to an important feature in the asymptotic scattering profile. The scattering at small q for a precipitate with negative misfit strain followed the usual Huang q^{-2} form, and for the case of $q < 0$ the oscillating q^{-4} behavior was present as expected from the analytic model. On the other hand, the $q^{-10/3}$ form expected for $q > 0$ was interrupted by a shoulder at the position corresponding to Bragg scattering from the inclusion. This aspect of diffuse scattering profiles from precipitates can, therefore, be used to determine independently the misfit strain inside precipitate particles. This work is being extended to include elastically anisotropic lattices as well.

1. B. C. Larson and W. Schmatz, *Physica Status Solidi* (in press).
2. H. Trinkaus, *Z. Angew. Phys.* 31, 229 (1971).

FRACTURE

IN SITU ELECTRON MICROSCOPE FRACTURE STUDIES IN Ni

S. Kobayashi S. M. Ohr

We have shown that in situ electron microscope fracture experiments can provide useful information regarding the structure of the plastic zone ahead of a crack tip. In stainless steel, the plastic zone was in the form of an inverse pileup of screw dislocations, and the dislocations were split into partials with stacking faults between the partials. Because the detailed structure of the plastic zone was expected to be sensitive to the stacking fault energy of the material, the studies were extended to Ni, which has a relatively high stacking fault energy. Contrary to our expectation, the structure of the plastic zone in Ni, as shown in Fig. 3.8, was very similar to that found in stainless steel. However, further studies showed that the

Fig. 3.8. Electron micrograph showing the distribution of dislocations in the plastic zone of a crack observed in Ni. The tensile axis is close to the (111) orientation, and the dislocations are split and are in the form of an inverse pileup.

structure of the plastic zone depended on the orientation of the tensile axis. The pileup structure of the type shown in Fig. 3.8 was formed only for the tensile axes near the ⟨111⟩ orientation. The plastic zone for the tensile axes near the ⟨100⟩ orientation has a quite different structure (Fig. 3.9); that is, the dislocations observed were perfect and many of them cross-slipped from the original pileup plane to form a broad plastic zone. This broad plastic zone is very similar to that found in bcc metals, which are known to be the metals of high stacking fault energy. Detailed analyses indicated that the planar fault shown in Fig. 3.8 consisted of overlapping stacking faults on parallel planes and, hence, may have represented thin twin lamellae. Similar studies in Cu confirmed this conclusion. Because the twin formation is easier for the tensile axis near the ⟨111⟩ orientation compared to the ⟨100⟩ orientation, the effect of tensile axis orientation on the structure of the plastic zone can be directly related to the orientation dependence of twin formation. Because Ni has a high stacking fault energy, twinning is not a common mode of deformation at room temperature. The possible causes for this anomaly are (1) the high stress concentration at the crack tip and (2) a reduction of the stacking fault energy because of H absorption during electropolishing.

STUDIES OF CRACK PROPAGATION IN AMORPHOUS NIOBIUM OXIDE

S. Kobayashi S. M. Ohr

The propagation of cracks and the structure of plastic zones ahead of crack tips in amorphous Nb_2O_5 have been studied using the technique of in situ TEM. When the specimen was deformed in tension, the crack was initiated at the edge of a polishing hole and gradually propagated into the specimen. The plastic zone was in the form of a shear band, which appeared as a narrow ribbon of white contrast (Fig. 3.10). The detailed shape of the plastic zone depended on the specimen thickness. In a thin area, the plastic zone was in the form of a straight ribbon. As the specimen thickness was increased, the plastic zone started to show a periodic pattern of the type shown in Fig. 3.10. The contrast of the plastic zone could be interpreted in terms of the thickness change caused by the shear deformation of thin foils. The plane of the shear was determined from the change in the width of the plastic zone during tilting experiments and was found to deviate from the plane of maximum

Fig. 3.9. Electron micrograph showing a crack and its plastic zone observed in Ni. For this specimen, the tensile axis is close to the (100) orientation. The plastic zone is broadened by the cross-slipping of perfect dislocations from their original slip plane.

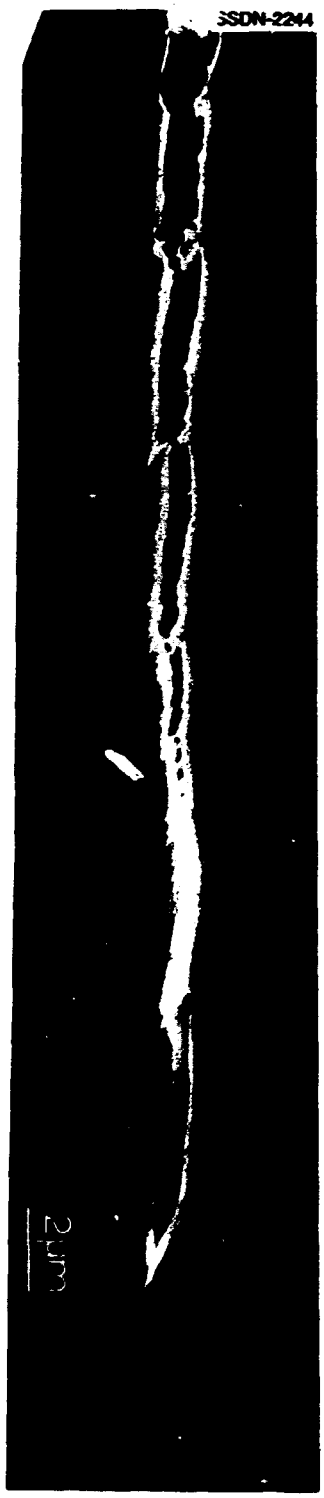

Fig. 3.10. Electron micrograph showing a shear crack and its plastic zone in amorphous Nb_2O_5. The white contrast, arising from the change in specimen thickness, represents the zone of shear deformation.

shear stress, which makes an angle of 45° with the tensile axis. Slip-on planes other than the plane of maximum shear stress have been reported previously in bulk specimens of amorphous metals and polymers. The observed relationship between the plastic zone size and the crack tip displacement was analyzed in terms of the Dugdale model of fracture.[1] The results showed that the value of E/σ_y was approximately equal to 60, where E is Young's modulus and σ_y is the yield stress. Although the value of E/σ_y for amorphous Nb_2O_5 is not available in the literature, the reported values for amorphous metals range from 50 to 80. This range is taken as evidence that our experimental results in amorphous Nb_2O_5 are in good agreement with the Dugdale model.

1. D. S. Dugdale, *J. Mech. Phys. Solids* **8**, 100 (1960).

ELECTRON MICROSCOPE OBSERVATION OF SHEAR CRACKS IN STAINLESS STEEL SINGLE CRYSTALS[1]

S. M. Ohr J. Narayan

Direct observations by TEM have been made of the propagation of shear cracks and the distribution of dislocations in the plastic zone of stainless steel single crystals during in situ tensile deformation. In thin foil specimens under plane stress conditions, the plastic zone was coplanar with the crack, and it represented the slip system of maximum resolved shear stress. The dislocations in the plastic zone were in the form of an inverse pileup. Contrast analysis has shown that these dislocations were of pure-screw type. The plastic zone, therefore, represented pure-shear deformation, and the crack was an antiplane strain shear crack of Mode III type. The crack opening displacement was measured directly by counting the number of dislocations in the plastic zone, and it was found to be approximately equal to the foil thickness. These observations are in good agreement with the model of shear cracks proposed by Bilby, Cottrell, and Swinden[2] and represent the first experimental confirmation of the theory.

1. Summary of paper: *Philos. Mag. A* **41**, 81 (1980).
2. B. A. Bilby, A. H. Cottrell, and K. H. Swinden, *Proc. R. Soc. London* **A272**, 304 (1963).

THICKNESS DEPENDENCE OF THE PLASTIC ZONE SIZE IN THE BCS THEORY OF FRACTURE

S.-J. Chang[1] S. M. Ohr

In the fracture theory of BCS,[2] the plastic zone was represented by a distribution of dislocations in an infinitely thick specimen. In a specimen of finite thickness, Eshelby and Stroh[3] have shown that the interaction force between two screw dislocations can be expressed in terms of a modified Bessel function, which decays much faster than the inverse first power law. By assuming a continuous distribution of dislocations, an integral equation is formulated based on the Eshelby-Stroh interaction force to examine the effect of specimen thickness on the size of the plastic zone as well as the distribution function for the dislocations.

Figure 3.11 shows the numerical results for the distribution function plotted as a function of distance along the crack for various ratios of the crack length and the specimen thickness. It is found

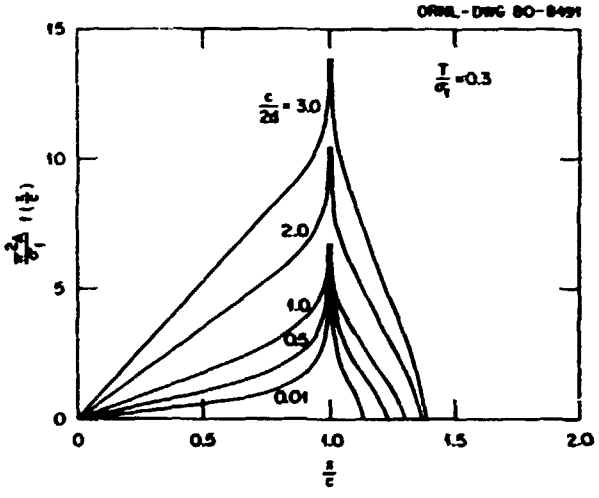

Fig. 3.11. Distribution function for dislocations along a crack of length c for various specimen thickness, d.

that, for a fixed value of crack opening displacement, the length of the plastic zone *decreases with decreasing specimen thickness. This* result is in agreement with the size of the plastic zone observed in thin foil specimens by electron microscopy.

1. Computer Sciences Division, UCC-ND.

2. B. A. Bilby, A. H. Cottrell, and K. H. Swinden, *Proc. R. Soc. London* **A272**, 304 (1963).

3. J. D. Eshelby and A. N. Stroh, *Philos. Mag.* **42**, 1401 (1951).

A MODEL OF BCS CRACKS WITH A DISLOCATION-FREE ZONE

S.-J. Chang[1] S. M. Ohr

In their dislocation theory of fracture, BCS[2] considered a plastic zone consisting of an inverse pileup of dislocations that was coplanar with the crack. The crack opening displacement was defined by the sum of the Burgers vectors of the dislocations that were introduced into the plastic zone at the crack tip. The theory has since been elaborated in various ways and has been widely applied to various aspects of fracture. Recently, direct observations have been made of the distribution of dislocations in the plastic zone of cracks during in situ deformation in the electron microscope.[3,4] The plastic zone was coplanar with the crack, the dislocations were in the form of an inverse pileup, and the number of dislocations observed in the plastic zone was consistent with the crack opening displacement required to propagate the crack. These observations were generally in good agreement with the predictions of the BCS theory. The only exception was that in many instances there was a zone near the crack tip which was devoid of dislocations.

We have, therefore, examined the equilibrium between the crack and the linear array of dislocations in the presence of a dislocation-free zone near the crack tip. A governing singular integral equation was formulated to describe the regions of the crack, the dislocation-free zone, and the plastic zone. The integral equation was inverted by the method of Muskhelishvili to obtain the distribution function for the dislocations. This distribution function was expressed in a closed form in terms of complete and incomplete elliptic integrals of the first and third kinds. The condition of compatibility between the sizes of the crack, the dislocation-free zone, and the plastic zone was obtained as a function of the applied stress, similar to the relationship derived in the BCS theory. As the size of the dislocation-free zone approached zero, our results approached those of the BCS theory. If the dislocation-free zone exists, the dislocation density in the plastic zone is required to vanish at the beginning and the end of this zone. This is shown in Fig. 3.12, where the distribution function is shown as a function of the distance along the crack for a small dislocation-free zone. Because the crack

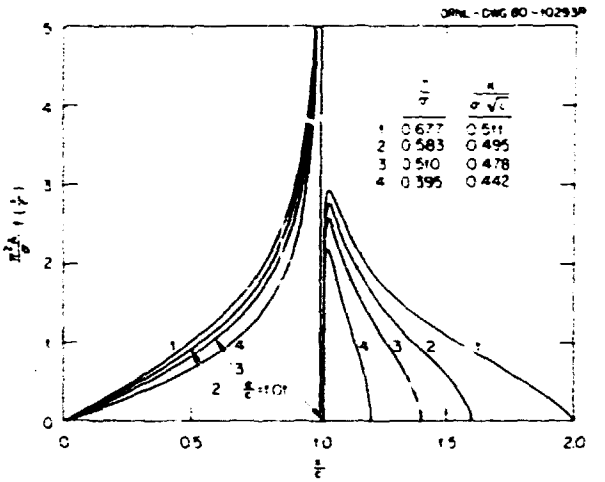

Fig. 3.12. Distribution function for dislocations along a BCS crack of length c with a dislocation-free zone. The curves are for different levels of applied stress.

itself is modeled in terms of a dislocation array, this dislocation density diverges at the crack tip, leading to a finite stress intensity factor at the crack tip. Within the dislocation-free zone, a stress gradient exists which would tend to force freshly generated dislocations to move away from the crack tip toward the plastic zone. The energy release rate associated with the crack has been calculated by applying the result of a recently developed theory[5] relating the complex J-integral to the total force on the dislocations in the plastic zone given by the Peach-Koehler formula.[6] These results indicate that, in the presence of the dislocation-free zone, an additional term appears in the expression for the energy release rate due to the finite stress intensity factor.

1. Computer Sciences Division, UCC-ND.

2. B. A. Bilby, A. H. Cottrell, and K. H. Swinden, *Proc. R. Soc. London* **A272**, 304 (1963).

3. S. M. Ohr and J. Narayan, *Philos. Mag.* **A41**, 81 (1980).

4. S. Kobayashi and S. M. Ohr, *Philosophical Magazine* (to be published).

5. S.-J. Chang, *International Journal of Fracture* (to be published).

6. S.-J. Chang, "Complex J-Integral and Peach-Koehler Equation," this report.

COMPLEX J-INTEGRAL AND PEACH-KOEHLER EQUATION[1]

S.-J. Chang[2]

Budiansky and Rice[3] derived an expression for the J-integral in terms of complex stress functions.

The expression is useful in calculating the force on an elastic singularity or the energy release rate for a crack if the corresponding elasticity problems can be solved by the method of complex variables. In the present study, it is shown that the complex J-integral can be reduced to the Peach-Koehler equation[4] for the force acting on a dislocation. Both edge and screw dislocations are treated. The method is then applied to a linear array of dislocations in the plastic zone of a shear crack treated in the elastoplastic model of fracture by BCS.[5] It is shown that, for the linear array of dislocations, the J-integral is equal to the total force on the dislocations in the plastic zone. Physically the present interpretation of the J-integral as applied to the BCS model is that the crack will propagate if the force acting on each dislocation in the plastic zone surpasses the lattice friction and if the total force exceeds a critical value dictated by the rate of surface energy release.

1. Summary of paper: *International Journal of Fracture* (to be published).
2. Computer Sciences Division, UCC-ND.
3. B. Budiansky and J. R. Rice, *J. Appl. Mech.* **40**, 201 (1973).
4. M. O. Peach and J. S. Koehler, *Phys. Rev.* **80**, 436 (1950).
5. B. A. Bilby, A. H. Cottrell, and K. H. Swinden, *Proc. R. Soc. London* **A272**, 304 (1963).

DEFECTS AND IMPURITIES IN INSULATING CRYSTALS

INFRARED SPECTRA OF H ISOTOPES IN α-Al_2O_3[1]

Herbert Engstrom J. C. Wang
J. B. Bates M. M. Abraham

Possible technological applications of refractory oxides in the development of new energy sources have led to much interest in and research on these materials. Because of its strength and high melting temperature, aluminum oxide is particularly interesting as a potential wall material in thermonuclear reactors and for H containment applications. In regard to the latter, the characterization of hydrogenic species in α-Al_2O_3 is important in order to determine the solubility and diffusivity of H. We report here our observations of the absorption of infrared light due to H, D, and T in α-Al_2O_3.

Measurements of the intensity of the OH^- band as a function of polarization of the light were made using a Perkin-Elmer 621 double beam spectrophotometer. All other infrared measurements were made on a Digilab FTS-20 Fourier transform spectrometer. The resolution of this instrument was about 3 cm^{-1}. In these experiments, between 500 and 1000 spectral scans were made and averaged. Figure 3.13 shows the spectra of OH^-, OD^-, and OT^- ions. The

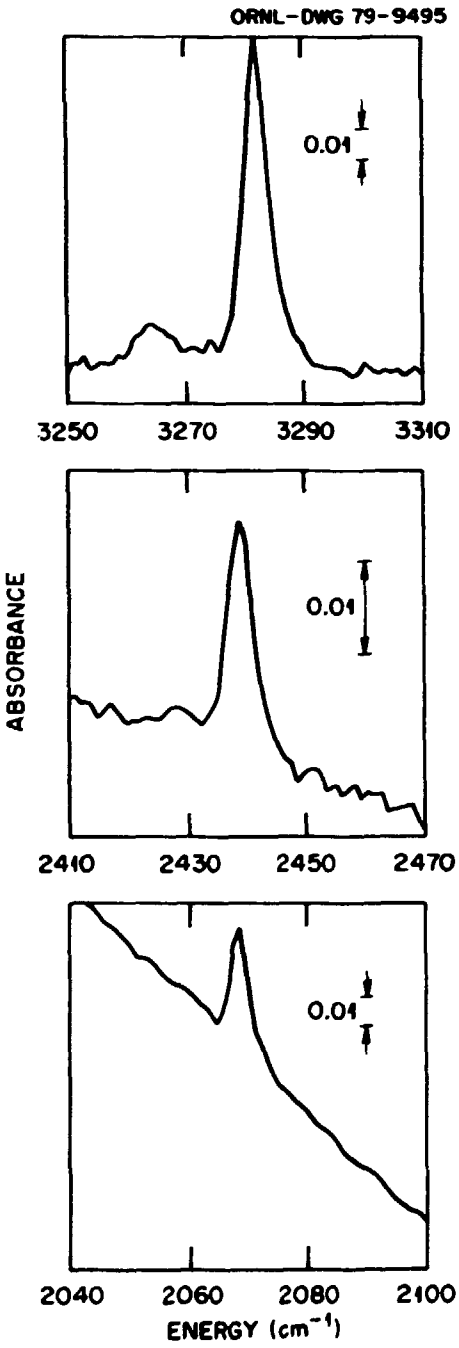

Fig. 3.13. The OH^- (top), OD^- (center) and OT^- (bottom) infrared absorption bands in α-Al_2O_3 at 77 K.

respective values of each peak wave number and its uncertainty as determined by fitting a Gaussian function to the absorption band are given in the column headed ν_{exp} in Table 3.5.

As in the case of rutile,[2] the model of an anharmonic diatomic oscillator, which consists of the H isotope bound to an O ion, yielded a very good fit of the isotopic frequencies. Herzberg[3] gives the energy levels for such an oscillator as

$$E_n = (n + {}^1/_2)\rho_i\omega_e - (n + {}^1/_2)^2\rho_i^2\omega_e x_e + \ldots , \quad (1)$$

where E_n is the energy of a level of vibrational quantum number n, where ω_e and x_e are constants, and when ρ_i is given by

$$\rho_i = (\mu_1/\mu_i)^{1/2} , \quad (2)$$

where μ_i is the reduced mass, $m_i m_o/(m_i + m_o)$, of the oscillator of the H isotope i of atomic mass m_i (where m_o is the atomic mass of O). Using the atomic masses of H, D, T, and O (1.007825, 2.0140, 3.01605, and 15.99491 amu, respectively), we find $\rho_1 = 1.0000$, $\rho_2 = 0.7280$, and $\rho_3 = 0.6112$. Using only the first- and second-order terms of Eq. (1), we find that the wave number for the ground to the first excited state transition is given by

$$\nu_i = \rho_i\omega_e - 2\rho_i^2\omega_e x_e . \quad (3)$$

We made a least squares fit of this equation to the observed wave numbers and determined the values of $\rho_i\omega_e$ and $\rho_i^2\omega_e x_e$ shown in Table 3.5. The wave numbers calculated from these best fit parameters are given in the column labeled ν_{fit}. As noted in most cases, these calculated wave numbers are within 1 cm^{-1} of those observed experimentally.

The quantity $D_e = (\rho_i\omega_e - \rho_i^2\omega_e x_e)^2/4\rho_i^2\omega_e x_e$, also shown in Table 3.5, represents the dissociation energy of the ion.[3,4] The slight variations in D_e with isotopic mass are due to differences in the zero-point energies of OH^-, OD^-, and OT^-.

To learn something about the orientation of the OH^- ion within the crystal, we measured the polarization of the absorbed light. For these measurements the crystal was mounted with its c axis perpendicular to the beam direction. The OH^- band shape was recorded for 10° increments of the angle, θ, between the polarization of the light and the c axis. The intensity of the transmitted light was found to be zero for light polarized along the c axis. Because the dipole moment of the ion lies along the OH^- band, we conclude that the OH^- ion lies in the basal plane.

We have made an approximate calculation of the potential of the OH^- ion in the crystal by using a procedure similar to that described by Bates et al.[5] Three possible orientations of the OH^- were found by the calculation. In the aluminum oxide molecular unit, the three O atoms form an equilateral triangle, the plane of which is the crystal basal plane, with the two Al atoms directly above and below the center of the triangle.[6] One orientation of the OH^- ion, labeled $H^+(1)$ in Fig. 3.14, has the proton lying in the basal plane in a direction directly away from the center of the O triangle. The other two orientations, labeled $H^+(2)$ and $H^+(3)$, are such that the O-H bonds make angles of +13° and −13°, respectively, to the basal plane. The projections of the bonds onto the basal plane are at 30° from the nearby O-O bonds.

The parameters used in the above calculation are not well enough known to be able to trust the calculated values of the minimum potential energy. However, if the OH^- ions lie in the ±13° orientations, it would be possible to observe the OH^- band for any

Table 3.5. Wave numbers (ν), bandwidths (δ), and spectroscopic constants for OH^-, OD^-, and OT^- bands in a α-Al_2O_3[a]

	T(K°)	ν_{exp} (cm^{-1})	δ_{exp} (cm^{-1})	$\rho_i\omega_e$ (cm^{-1})	$\rho_i^2\omega_e x_e$ (cm^{-1})	ν_{fit} (cm^{-1})	D_e (eV)
OH	300	3279.1 ± 0.4	9.3 ± 0.6	3535.7 ± 3.9	128.3 ± 2.0	3279.1	2.80 ± .05
	77	3282.4 ± 0.3	5.6 ± 0.4	3542.2 ± 2.3	129.9 ± 1.2	3282.4	2.78 ± .03
OD	300	2436.9 ± 1.4	6.8 ± 2.8	2574.0 ± 2.9	68.0 ± 1.1	2438.0	2.86 ± .05
	77	2438.9 ± 0.9	5.3 ± 1.6	2578.7 ± 1.7	68.9 ± 0.6	2441.0	2.83 ± .03
OT	300	2065.7 ± 1.1	5.6 ± 2.4	2161.0 ± 2.4	47.9 ± 0.8	2065.2	2.89 ± .05
	77	2068.7 ± 0.6	4.0 ± 1.0	2165.0 ± 1.4	48.5 ± 0.4	2067.9	2.86 ± .02

[a] δ_{exp} is the full width at half-band maximum. The band energy calculated from the best fit parameters $\rho_i\omega_e$ and $\rho_i^2\omega_e x_e$ is ν_{fit}.

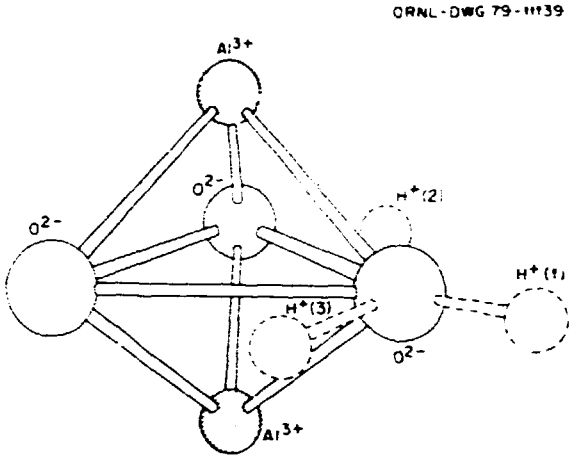

Fig. 3.14. The aluminum oxide molecular unit. The dashed circles show possible orientations of the proton of the OH^- ion based on calculations of the potential energy.

polarization. Because the curve of the intensity-vs-polarization angle clearly passed through zero, we are led to conclude that the OH^- ion lies in the basal plane according to orientation (1).

---

1. Summary of paper: *Phys. Rev. B* **21**, 1520 (1980).
2. J. B. Bates and R. A. Perkins, *Phys. Rev. B* **16**, 3713 (1977).
3. G. Herzberg, Chap. 3 in *Molecular Spectra and Molecular Structure: I. Spectra of Diatomic Molecules*, Van Nostrand, New York, 1950.
4. G. W. King, Chap. 5 in *Spectroscopy and Molecular Structure*, Holt, Rinehart, and Winston, New York, 1964.
5. J. B. Bates, J. C. Wang, and R. A. Perkins, *Phys. Rev. B* **19**, 4130 (1979).
6. R.W.G. Wyckoff, p. 6 in *Crystal Structures*, vol. 2, Wiley Interscience, New York, 1964.

AGGREGATION OF Fe^{3+} IN MgO

E. Sonder J. Gastineau[1] R. A. Weeks

In a number of studies of equilibrium valence states and solubilities of Fe in MgO, it was assumed that the high-temperature equilibrium state of the Fe would be retained upon rapid cooling to room temperature. We have used quantitative electron-resonance (ER) measurements to investigate the distribution of Fe^{3+} in dissolved and aggregated states in MgO:Fe samples cooled from high temperatures. The experiments have been performed with the samples treated in ambient air (O_2 partial pressure of 0.2 atm), for which condition 80% of the Fe is in the trivalent state and 20% is in the divalent state. When samples containing different amounts of Fe from 100 to 8000 ppm are examined after cooling to room temperature, evidently at the lowest concentrations (~100 ppm) essentially all the Fe^{3+} remains dissolved upon cooling and substitutes for Mg^{2+} on octahedral sites. However, in MgO containing higher concentrations of Fe, a maximum of 300 ppm Fe^{3+} in octahedral sites is observed in MgO crystals cooled as rapidly as is possible in air. The remainder of the Fe^{3+} is in the form of aggregates and, at the highest concentrations, of precipitates large enough to exhibit ferromagnetic characteristics.

In order to ascertain whether the aggregates exist at high temperatures or are produced during the cooling process, the distribution of Fe^{3+} was measured as a function of heating temperature before cooling and as a function of the cooling rate. We found that for a series of samples, all containing 1000 ppm Fe, the distribution measured at room temperature was not a function of the heat-treatment temperature but did depend on the quench rate. Figure 3.15 shows that quenching a sample from 1200°C into liquid N_2 produces much faster cooling than quenching the sample in ambient air. A water quench is even faster but causes fracturing of samples. Our results show that a significantly larger fraction of Fe^{3+} ions remained in solution, substituting for Mg^{2+} ions, in samples quenched in liquid N_2 than in those cooled in air. This difference was similar for a number of

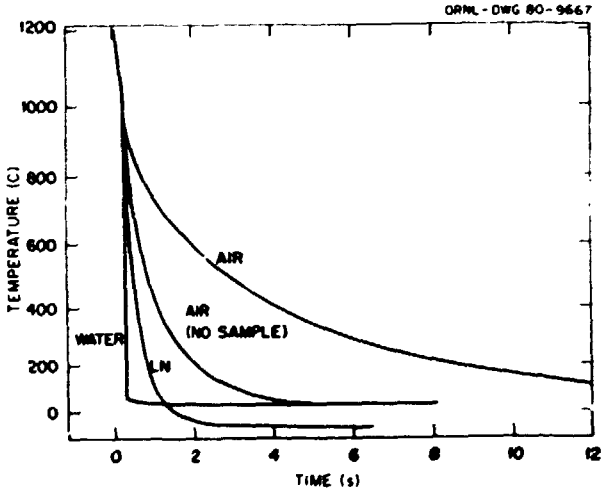

Fig. 3.15. Cooling curves for MgO:Fe samples removed from a furnace at 1200°C and quenched in different media. The curve labeled "Air (no sample)" was obtained with a bare thermocouple, whereas the other curves were obtained with a thermocouple in contact with a sample of approximate dimensions 2 × 3 × 4 mm.

treatment temperatures between 800 and 1600°C. A water quench from 1200°C produced an even larger fraction of dissolved Fe^{3+}.

Isochronal anneals performed with a sample quenched in liquid nitrogen indicated that Fe^{3+} is mobile at temperatures below 400°C. Figure 3.16 depicts room-temperature spectral intensities of EPR components, measured after annealing 1 h at the indicated temperatures. The octahedral spectrum is due to substitutional Fe^{3+}, and the orthorhombic spectrum is presumed to be due to substitutional Fe^{3+} ions that are perturbed by cation vacancies in nearest-neighbor ⟨110⟩ lattice sites. When all the Fe^{3+} ions aggregate, these two spectra are not observed. It is noteworthy that the decrease in intensity of these Fe^{3+} spectra is not accompanied by observation of any new spectral components that might be attributed to Fe pairs, triplets, and so forth. The spectra that appear above 650°C are of an intensity and exhibit a temperature dependence (of intensity) that indicate that they are due to ferromagnetic particles that must be made up of 1000 or more Fe^{3+} ions. Such ferromagnetic particles have been observed previously[2] by other techniques in highly doped (>1%) MgO:Fe that had been annealed for lengthy periods at 800°C.

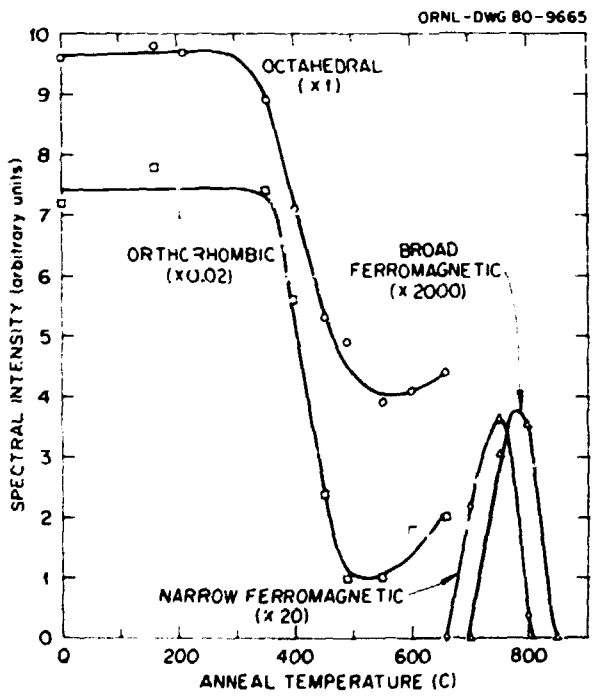

Fig. 3.16. Intensity of different electron-resonance components in MgO:Fe samples after 1 h of heating at successively higher temperatures. The multiplication factors indicated next to the curves should be applied to the ordinate scale.

An attempt has been made to account for the observed aggregation by extrapolating diffusion coefficients[3] measured at high temperature to temperatures relevant to these studies. However, the reported diffusion activation energy of 3.2 eV would allow only one jump in approximately 1000 h at the temperatures at which aggregation takes place. Therefore, a mechanism for decreasing the barrier for Fe^{3+} motion at these temperatures must exist.

---

1. Great Lakes College Association Science Semester student from Lawrence College, Appleton, Wis.

2. G. W. Groves and M. E. Fine, *J. Appl. Phys.* **35**, 3587 (1964); G. P. Wirtz and M. E. Fine, *J. Appl. Phys.* **38**, 3729 (1967) and *J. Am. Ceram. Soc.* **51**, 401 (1968); K. N. Woods and M. E. Fine, *J. Am. Ceram. Soc.* **52**, 186 (1969).

3. S. L. Blank and J. A. Pask, *J. Am. Ceram. Soc.* **52**, 669 (1969).

CHARACTERIZATION OF DEFECTS IN Ni-DOPED MgO CRYSTALS[1]

J. Narayan Y. Chen

A recent demonstration that Ni-doped magnesium oxide (MgO:Ni) crystals can be used as versatile and commercially viable laser materials for infrared tuning[2] has provided the impetus for characterizing these crystals. These lasers can operate continuously or can be pulsed with either excitation by a lamp or a 1.06-μm Nd laser and are capable of being tuned in the 1.3–1.5-μm wavelength region. During pulsed operation at very high power levels, imperfections such as dislocations, grain boundaries, impurity precipitates, voids, and cracks in the laser host crystals can lead to local enhancement of the electric field strength, which in turn often causes a reduction in the damage-breakdown threshold. The present investigation was undertaken to characterize Ni-doped crystals in terms of the above imperfections using TEM and optical microscopy. Also, yield stress measurements were made to determine how the Ni impurities affect the mechanical properties of the crystals.

Crystals of MgO:Ni were grown by an arc-fusion technique that utilizes MgO powder from the Kanto Chemical Company mixed with NiO powder to about 5% in weight. The resulting single crystals were found by spectrographic analysis to contain about 0.4 at. % Ni impurity, representing an unusually high level of impurity concentration. Because of the low oscillator strength of the Ni^{2+} ions, a high doping level was necessary to maximize the absorption of the exciting photons.

Figure 3.17 shows a typical optical micrograph revealing etch pits corresponding to dislocations and subgrain boundaries. The average subgrain size was determined to be 0.1 cm. From the number of etch pits inside the grains, the average dislocation density in these regions was estimated to be approximately 10^5 cm^{-2}. Figure 3.18a is a transmission electron micrograph from the area inside the subgrains, showing dislocations which run from one surface to the other in a thin TEM specimen. The number density of dislocations was found to be in reasonable agreement with that found from the etch-pit technique. No precipitates were observed inside the subgrains down to the microscope resolution limit of about 10 Å.

Figure 3.18b shows typical dislocation structure and impurity precipitates associated with a tilt subboundary. These subboundaries consist of parallel edge dislocations, which have $^a/_2[101]$ Burgers vector, lie in $(10\bar{1})$ planes, and have axes of rotation $[10\bar{1}]$. The tilt subboundaries were often decorated with impurity precipitates (seen as dark spots in the micrograph) with an average size of about 500 Å and number density of 3×10^8 cm^{-2} of the boundary area. From these results, we deduced that only a very small fraction of the Ni impurity was in precipitate form. The impurity precipitates were not found near twist subboundaries (Fig. 3.18c), which consist of sets of $^a/_2[101]$ and $^a/_2[01\bar{1}]$ screw dislocations, and at the intersection (denoted as *I*) these dislocations react to produce a $^a/_2[110]$ dislocation. Neither optical nor electron-microscopy studies revealed the presence of voids or cracks in this material.

Yield stress measurements were made to assess how the large Ni concentration affected the mechanical properties of the crystals. The average yield stress values, τ_c, were 5.0 kg-mm^{-2} for MgO:Ni and 1.8 kg-mm^{-2} for the undoped MgO. The differential $\Delta\tau_0 =$ 3.2 kg-mm^{-2} between the doped and undoped crystals is attributed to the influence of the ~0.4 at. % Ni dopant.

The role of absorbing inclusions, cracks, and pores in laser materials has been discussed by Bloembergen,[3] who concluded that these imperfections, with characteristic dimensions less than 100 Å, would not appreciably affect the breakdown threshold, whereas absorbing imperfections with dimensions exceeding 10^3 Å can be expected to have adverse effects in high-power pulsed laser operations. For doping levels of nearly 1%, the imperfections in these crystals were moderate in dimension and concentration. It would appear that this material could very well withstand very high-power beams without appreciable degradation.

1. Summary of paper: *Journal of Applied Physics* (in press).
2. P. Moulton et al., to be published.
3. N. Ploembergen, *Appl. Opt.* 12, 661 (1973).

Fig. 3.17. Optical micrograph showing dislocations in the form of etch pits at the subboundaries (B) and in the regions enclosed by subboundaries. Magnification: ~125×.

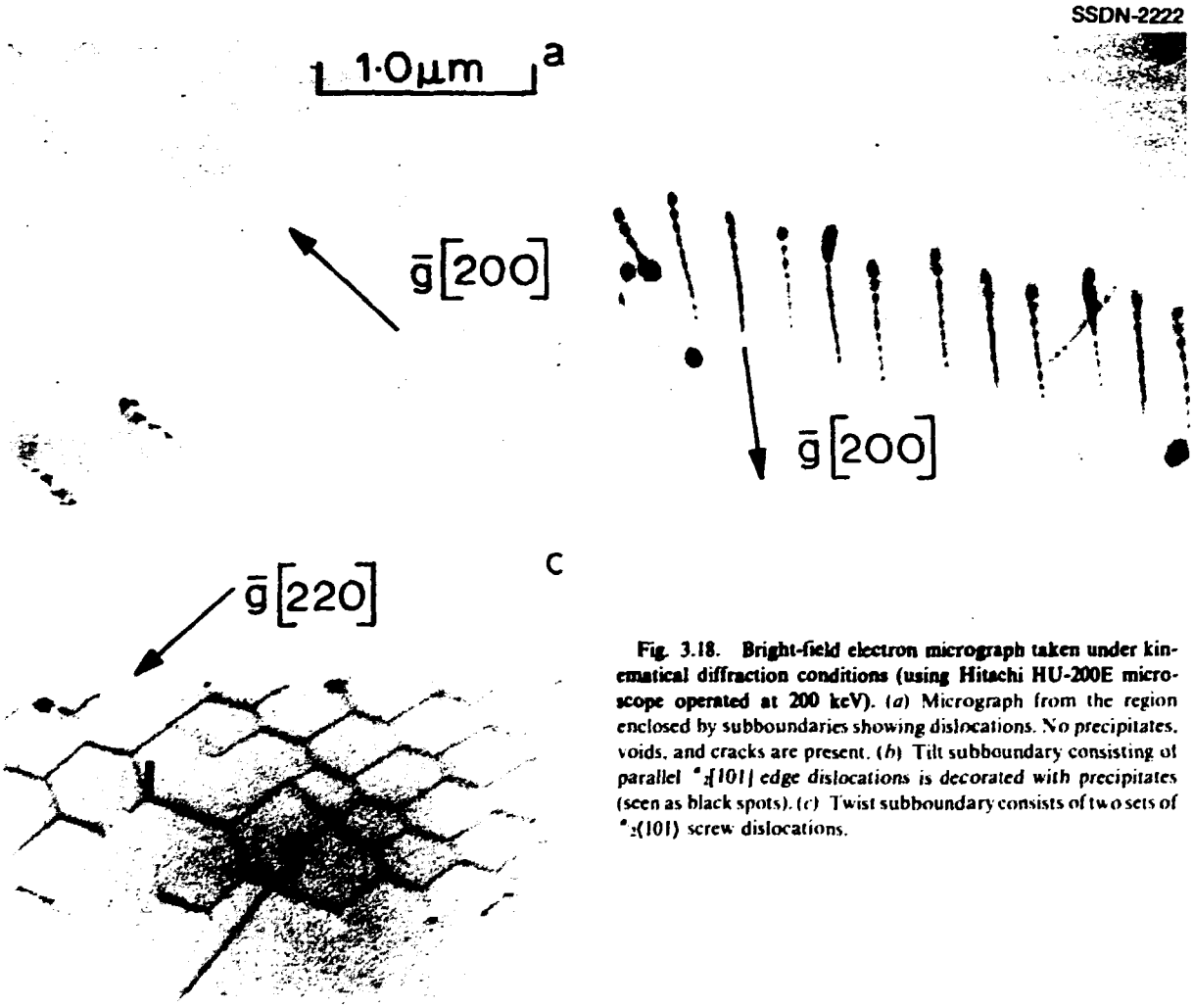

Fig. 3.18. Bright-field electron micrograph taken under kinematical diffraction conditions (using Hitachi HU-200E microscope operated at 200 keV). (*a*) Micrograph from the region enclosed by subboundaries showing dislocations. No precipitates, voids, and cracks are present. (*b*) Tilt subboundary consisting of parallel $\frac{a}{2}[101]$ edge dislocations is decorated with precipitates (seen as black spots). (*c*) Twist subboundary consists of two sets of $\frac{a}{2}(101)$ screw dislocations.

VALENCE COMPENSATION OF THERMALLY GENERATED $[Li]^0$ DEFECTS IN MgO[1]

J. L. Boldú[2] M. M. Abraham Y. Chen

The creation of thermally generated $[Li]^0$ defects (configuration: O^{2-}-Li^+-O^-) and other Li-associated centers in MgO is attended by valence changes of transition-metal impurities, such as Fe and Cr. The EPR technique was used to monitor the concentration of these impurities and the $[Li]^0$ defects as a function of the treatment temperature in static air.

Figure 3.19 shows a plot of the absolute concentrations, as determined by EPR, of all the dominant paramagnetic impurities vs the treatment temperature. It can be seen that no drastic concentration change occurs below $T \sim 1200$ K. This value approximated the threshold temperature for the thermal generation of stable $[Li]^0$ defects in static air, as previously determined by optical-absorption measurements.[3] A sizable concentration of $[Li]^0$ defects (2×10^{17} cm^{-3}) was generated at 1300 K and continued to increase at least up to $T \sim 1600$ K. With the emergence of the $[Li]^0$ signal, an isotropic signal ($g = 2.014 \pm 0.001$) appeared and also grew in intensity with increasing temperature. Because this signal has been observed in Li-doped crystals, it is attributed to a Li-associated defect. The trivalent impurities Fe^{3+} and Cr^{3+}, on the other hand, diminished in intensity with increasing temperature, suggesting that they contribute to the charge compensation of the $[Li]^0$ and the isotropic defects. Both the axial and cubic Mn^{4+} concentrations do not appear to be strongly affected by the $[Li]^0$ formation.

Because Fe and Li represent the most abundant impurities identified in the crystal, we can compare the increase of the $[Li]^0$ concentration to the decrease of Fe^{3+}. A plot of the concentration ratio of the thermally generated $[Li]^0$ to the loss of Fe^{3+} vs temperature is shown in Fig. 3.20. In effect, this figure describes the fractional contribution of holes from the Fe^{3+} to the $[Li]^0$ defects. The ratio increased with temperature and was >60 at $T \sim 1600$ K. This increase indicates that impurities are not sufficient for charge compensation of the thermally generated $[Li]^0$ defects, especially at very high temperatures.

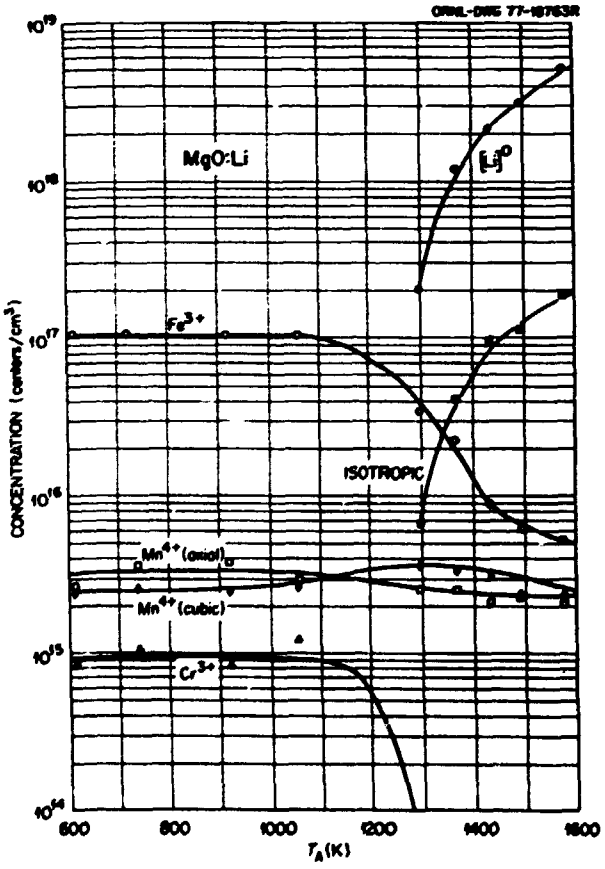

Fig. 3.19. Absolute concentrations of paramagnetic impurities in MgO:Li as a function of the quenching temperature.

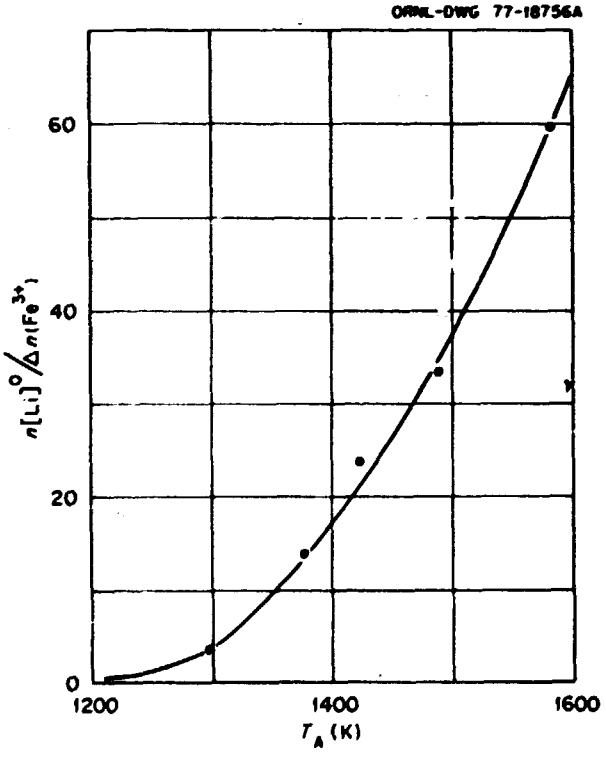

Fig. 3.20. Concentration ratio of $[Li]^0$ to Fe^{3+} as a function of quenching temperature.

Therefore, the total amount of all the paramagnetic impurities cannot be equated with the number of stable $[Li]^0$ defects formed. The predominant paramagnetic impurity in our crystals is Fe^{3+} (Fig. 3.19). Figure 3.20 shows that, at 1300 K, the Fe can contribute a significant fraction of the holes for the valence compensation of stable $[Li]^0$ defects. However, at 1600 K, Fe^{3+} is clearly inadequate because it can supply only 1–2% of the holes required.

Our present understanding is that, at elevated temperatures, the monovalent Li ions abandon the Li_2O precipitates and occupy Mg sites around the precipitates, provided the sample is immersed in an atmosphere containing O_2. Each of these substitutional Li^+ ions serves to capture a hole and can be identified as a neutral $[Li]^0$ defect. The dissociation of O_2 at the surface into O ions provides the required source of positive holes. The process is represented by

$$O_2 \rightarrow 2O^{2-} + 4 \text{ holes}. \qquad (1)$$

The presence of O_2 also serves to satisfy ionic requirements for the formation of $[Li]^0$ defects. The net reaction is $2Li_2O + O_2 \rightarrow 4(Li^+O^-)$.

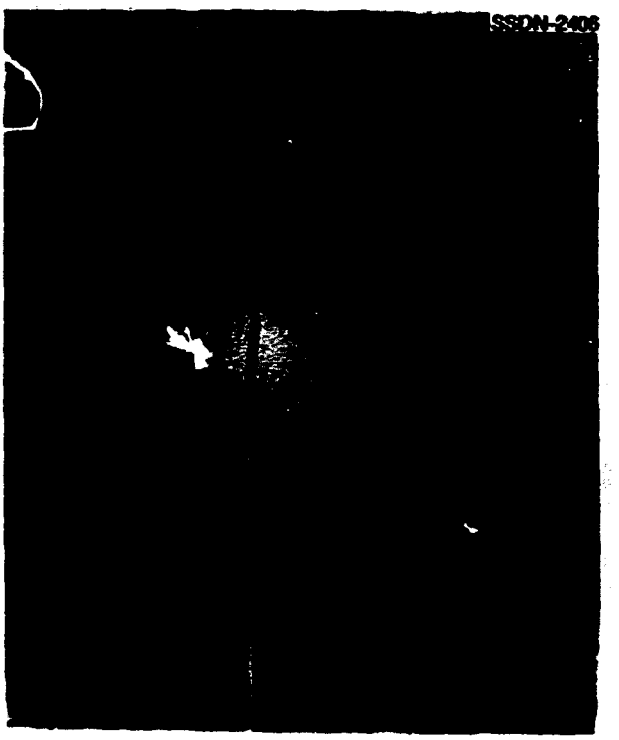

Fig. 3.21. Transmission photograph of a Li-doped MgO crystal, which was deformed 3% and heated at 1275 K in O_2 for 5 min. The clear streak parallel to the crystal edge is due to a crack propagated during the heat treatment.

1. Summary of paper: *Phys. Rev. B* **19**, 4421 (1979).
2. Guest scientist from Instituto de Física, U.N.A.M., Mexico, D.F.
3. Y. Chen et al., *Phys. Rev. B* **16**, 5535 (1977).

NEGATIVE IMPRINTING OF SLIP BANDS IN MECHANICALLY DEFORMED MgO CRYSTALS USING Li IMPURITIES[1]

V. M. Orera[2] Y. Chen M. M. Abraham

Lithium impurities in MgO can be used to imprint slip bands produced by plastic deformation. The principal defect involved is the $[Li]^0$ defect, a ⟨100⟩ substitutional Li^+-O^- complex that absorbs light at 680 nm (1.8 eV). Slip bands are observed as decolored regions against the background of dark blue coloration due to these defects; the imprinting, in the photographic sense, is negative. The decoloration can be achieved by two different processes: either by oxidation at 1275 K of a deformed crystal or by deformation of a previously oxidized crystal.

Figure 3.21 is a photograph of a crystal that was deformed 3% and subsequently heated at 1275 K in O_2 for 5 min. Two broad dislocation bands parallel to the $[0\bar{1}1]$ and $[01\bar{1}]$ directions crisscross at the center of the crystal. The optical-absorption spectrum following the deformation is illustrated by curve (*a*) in Fig. 3.22 and that following the heat treatment by curve (*b*). The thermal treatment destroyed the 5.7-eV band produced by the deformation. Instead, two bands emerged at 1.8 and 5.3 eV. The 1.8-eV $[Li]^0$ band was expected to result from oxidation at $T > 1100$ K. The appearance of the 5.3-eV band was unexpected because it could only be obtained in nondeformed crystals at $T > 1400$ K. For comparison, the spectrum of an undeformed sample, after the same thermal treatment, is shown in curve (*c*) where the 5.3-eV band is conspicuously absent and the $[Li]^0$ concentration is measurably larger. If a deformed crystal was heated at 1275 K in an inert atmosphere to destroy the 5.7-eV band, the 5.3-eV band did not appear. Clearly the interaction between the defects causing the 5.7-eV band and the $[Li]^0$ defects results in the emergence of the 5.3-eV band and the loss of $[Li]^0$ coloration.

Deformation of a crystal containing $[Li]^0$ defects produced by heating at 1275 K for 5 min in O_2 also results in loss of $[Li]^0$ coloration along slip planes.

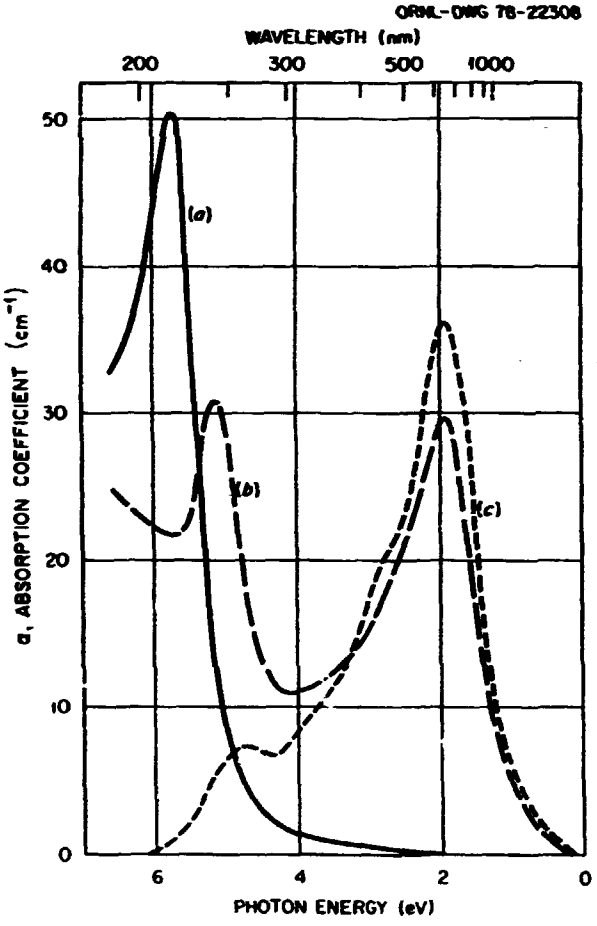

Fig. 3.22. Optical-absorption spectra of the crystal shown in Fig. 3.21. (*a*) After the deformation; (*b*) following the heat treatment; (*c*) the spectrum of an undeformed crystal after a similar heat treatment.

The decoloration is explained in terms of loss of holes from $[Li]^0$ defects. These holes are loosely bound at $[Li]^0$ sites, which are concentrated along dislocations in the crystals, and hop from site to site. If new defects, which have a stronger affinity for the holes than do the substitutional Li^+ ions, are introduced by the deformation, correspondingly fewer holes will be shared among the Li^+ ions, the result being a loss of $[Li]^0$ coloration.

SUBTHRESHOLD $[Li]^0$ COLORATION AND DECORATION OF STRAINED REGIONS IN CRYSTALLINE MgO

Y. Chen J. Narayan
N. J. Dudney[1] V. M. Orera[2]

The effect of surface and bulk deformation on $[Li]^0$ coloration in Li-doped MgO crystals is being investigated. This study focuses on the observation that below the observed threshold temperature for $[Li]^0$ formation in etched specimens a temperature range exists (referred to as the subthreshold) in which $[Li]^0$ defects can also be formed if the sample surfaces were previously deformed. Such strained surfaces are found to induce propagation of dislocations into the specimen at elevated temperatures.

Figure 3.23 illustrates the absorption coefficient of the $[Li]^0$ band produced by heat treatments in O_2 at different temperatures. The lower curve corresponds to samples etched in hot phosphoric acid to remove a thin layer of the sample surfaces. The threshold temperature was determined to be ~1160 K. The upper curve represents crystals whose surfaces were deformed by abrasion with SiC-240 paper prior to heat treatment in O_2. The temperature for $[Li]^0$ formation for these samples extended down to $T \sim$ 1050 K. We refer to the temperatures between 1050 and 1160 K as the subthreshold range.

Strained surfaces in abraded, cut, and cleaved crystals were found to induce propagation of dislocations into the specimens at elevated temperatures. A slab of crystal, initially etched, was abraded

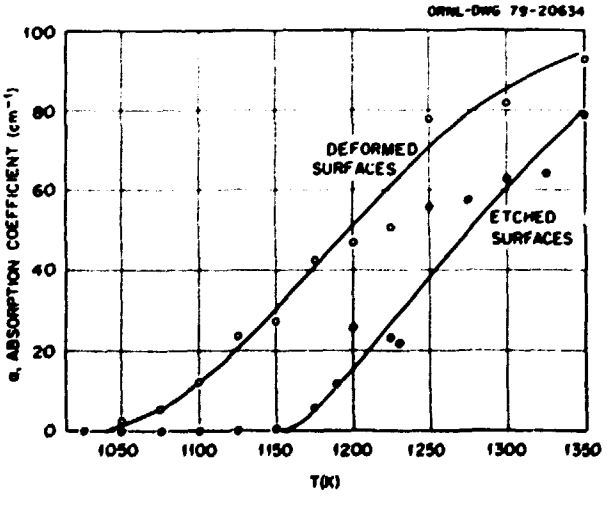

Fig. 3.23. Optical absorption coefficient of the $[Li]^0$ band produced at different temperatures for etched and mechanically deformed specimens.

1. Summary of paper: *Philosophical Magazine* (in press).
2. Guest scientist from University of Zaragoza, Zaragoza, Spain.

on SiC-240 paper on one end. Following heating at 1150 K for 5 min in O_2, the ground end conspicuously exhibited $[Li]^0$ coloration (Fig. 3.24*a*). The depth of coloration appeared to be ≈1 mm. Figure 3.24*b* is an optical micrograph of the specimen etched with a solution (5:1:1 proportions of NH_4Cl, H_2SO_4, and H_2O). Deformation bands revealed by etch pits were observed to start from the abraded end and extend into the interior of the specimen. The propagation at high temperatures presumably occurs by multiplication of dislocations from stress concentrators associated with the surface microcracks. Figure 3.24*c*, a bright-field transmission electron micrograph from the deformed region (Fig. 3.24*b*), shows the dislocation network associated with the deformation bands.

It is not uncommon for high-temperature measurements such as diffusion and conductivity to be made on specimens that were either cleaved, mechanically polished, or abraded. The present investigation provides evidence that sample preparation without a final chemical etch involves possible risk of having undesirable dislocations at high temperature.

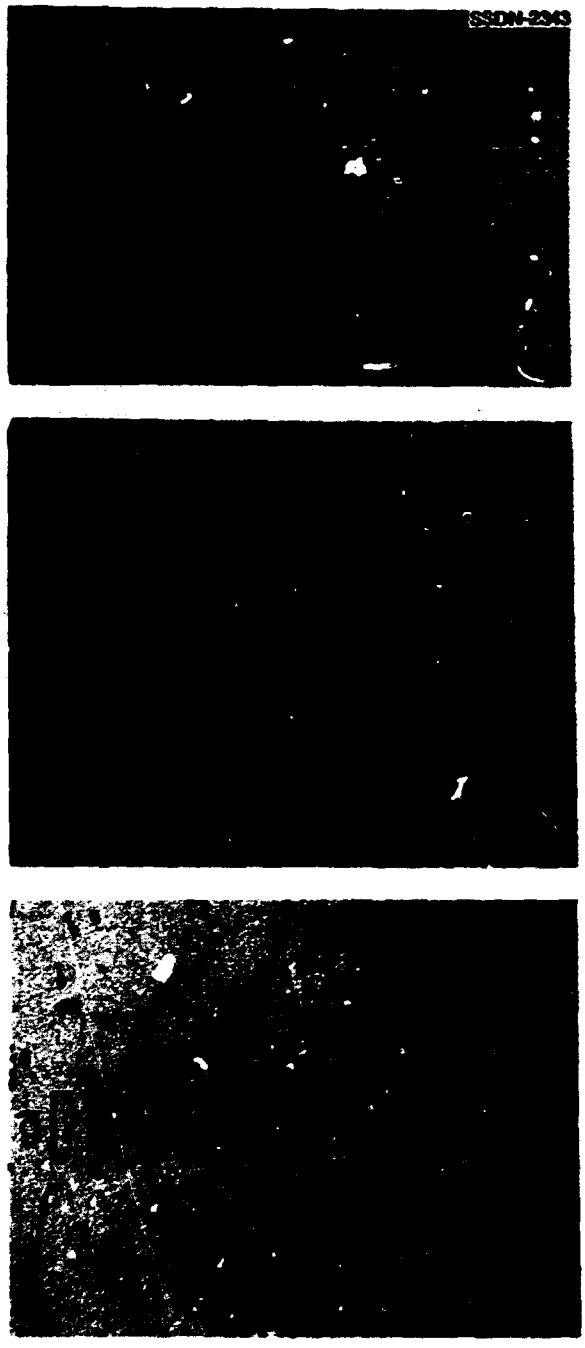

Fig. 3.24. Photographs of a crystal that was etched, abraded at one end, and heat treated in O_2 at 1150 K for 5 min. (*a*) The optical photograph of a crystal showing the optically colored region at one end. The crystal underwent the following treatment: it was etched, abraded at one end, and heat treated in O_2 at 1150 K for 5 min. The abraded end is on the left side of the figure. (*b*) The optical micrograph of the abraded end of the crystal showing slip bands and microcracks. The length of the micrograph corresponds to 1.0 mm. The abraded end is on the left side of the figure. (*c*) The electron micrograph (bright field) revealing dislocations, their debris, and Li_2O precipitates. The length of the arrow is 0.5 μm.

1. Eugene P. Wigner Fellow.
2. Guest scientist from the University of Zaragoza, Zaragoza, Spain.

CORRELATION OF THE DIELECTRIC PROPERTIES WITH $[Li]^0$ FORMATION IN MgO

N. J. Dudney[1] E. Sonder R. A. Weeks

Centers of $[Li]^0$, which absorb light at 1.8 eV, are rapidly formed in single crystals of Li-doped MgO by a 10-min preparatory heat treatment in O_2 at temperatures above ~1200 K followed by a quench to room temperature. At lower temperatures, these $[Li]^0$ centers disappear by a thermally activated process.[2] An enhanced electrical conductivity in MgO at temperatures below 450 K has been associated with the presence of the $[Li]^0$ defects.[3,4]

AC-impedance (100 Hz to 10 kHz) and optical-absorption (2500 to 190 nm) measurements were made to study the changes brought on by preparatory and by annealing heat treatments. Preparatory heat treatments were performed at 1475 K for extended times, and the changes were measured under conditions where the defect structure was allowed to approach equilibrium. This required periodic interruptions of the heat treatments and rapid cooling of

the sample to make the measurements. Annealing heat treatments at 1000 K were performed to determine the rate of disappearance of the $[Li]^0$ centers and accompanying changes in impedance. Because the annealing of the $[Li]^0$ centers was very slow below 625 K, electrical measurements could be made as a function of temperature as well as frequency. The electrical properties were found to be characteristic of thermally activated polarization and conduction processes with activation energies of 0.86 and 2.9 eV, respectively. In Figs. 3.25 and 3.26, the real and imaginary components of the dielectric permittivity (ϵ' and ϵ'') have been combined to display an extended frequency dependence. To accomplish this display, the inverse relation between the log of the frequency and the temperature defined for a thermally activated process was used. The curves drawn through the data emphasize the complex, but reproducible, frequency dependence observed for each set of measurements. The step in the capacitive component of the permittivity and the corresponding high-frequency peak in the imaginary component are the prominent features in the spectra and are characteristic of a polarization process. Other low-frequency fluctuations observed in the imaginary component of the permittivity are not understood.

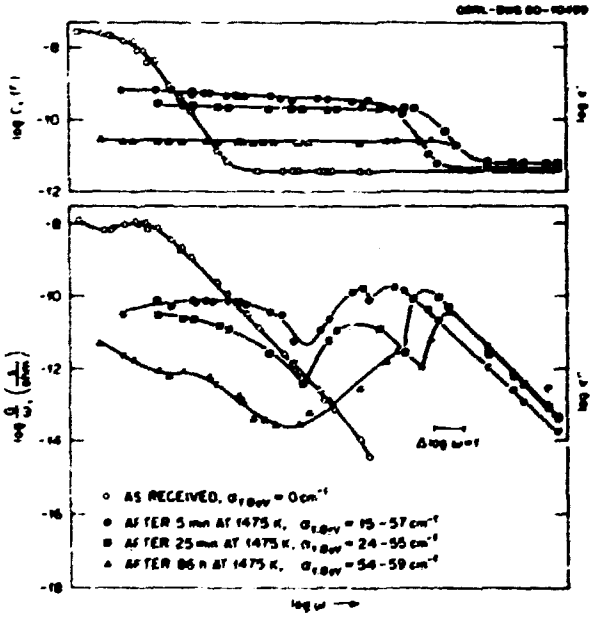

Fig. 3.25. The complex dielectric permittivity plotted as a function of frequency for a Li-doped MgO crystal before and after preparatory heat treatments for the specified time periods. Electrode area · sample thickness = 7.8 cm.

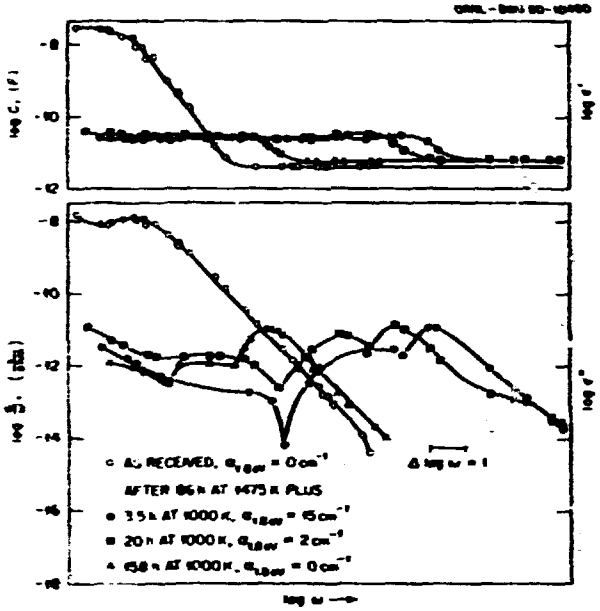

Fig. 3.26. The complex dielectric permittivity plotted as a function of frequency for a Li-doped MgO crystal after an 86-h preparatory heat treatment followed by anneals for the specified time periods.

Electrical and optical data (Fig. 3.25) were measured for the as-received sample and after periodic interruptions in the preparatory heat treatment. After only 5 min at 1475 K, the $[Li]^0$ centers were formed, and the most prominent features in the spectra of the real and imaginary components of the dielectric permittivity shifted to a much higher frequency. This shift means that the relaxation time for the polarization process has become shorter. The low-frequency capacitive component of the permittivity continued to decrease as the heat treatment was extended to a total of 86 h. After the initial heat treatment of 5 min, there was a large gradient of $[Li]^0$ centers in the plane of the sample. The absorption coefficient at 1.8 eV varied from 15 to 57 cm^{-1} (Fig. 3.25). Longer thermal treatments diminished the gradient significantly.

The $[Li]^0$ centers that are produced at 1475 K can be annealed at temperatures near 1000 K. This removal of $[Li]^0$ centers was accompanied by a progressive shift of the step and peak in the capacitive and resistive components of the permittivity to lower frequencies (Fig. 3.26). This shift approaches but does not reestablish the electrical properties of the untreated sample. The relaxation times for the polarization process in the as-received condition and after 158 h at 1000 K are identical, if a

local field correction is applied so that the ratio of the real and measured relaxation times is inversely proportional to the capacitive component of the permittivity at low frequencies. The rate at which the $[Li]^0$ centers anneal depends on the length of the preparatory heat treatment. For the conditions shown in Fig. 3.26, the rate was much slower than after a preparatory heat treatment of only 5 min at 1200 K.

From these results, the $[Li]^0$ coloration is directly related to a decrease of five orders of magnitude in the relaxation time for the polarization process. This large change most likely results from a change in the state of aggregation of the defects in the crystal rather than from the behavior of isolated dipoles. The nonreversible decrease in the capacitive component of the permittivity is believed to be due to a second process, which may be indirectly related to the stability of the $[Li]^0$ centers.

---

1. Eugene P. Wigner Fellow.
2. J. B. Lacy et al., *Phys. Rev. B* **18**, 4136 (1978).
3. D. J. Eisenberg et al., *Appl. Phys. Lett.* **33**, 479 (1978).
4. Y. Chen et al., *Solid State Commun.* **33**, 441 (1980).

4. Transport Properties of Solids

Investigations of transport properties are emphasized within the Division in research programs that study fast-ion conductors, superconductors, and the behavior of ceramic insulating materials in harsh environments. The fast-ion conduction program combines physical properties measurements with model calculations in attempts to establish the mechanisms of ionic conductivity and to determine the effects of intercalated water, impurity ions, and crystal composition on ion transport in the β- and β''-aluminas. Research in superconductivity is directed toward gaining an understanding of fluxoids, their interaction with crystalline defects, and the production of new metastable superconducting materials by the combined techniques of ion implantation and pulsed laser annealing. The high-temperature ceramics program seeks to understand mass and charge transport processes at elevated temperatures and the mechanisms by which defects, impurities, valence changes, and aggregation alter these properties.

Fast-ion conduction research during this reporting period emphasized examination of conductivity anomalies observed in mixed-ion (Li, Na) β-aluminas and the effects of water intercalation in the conducting plane of these systems. The conductivity anomalies can be understood on the basis of different site occupancy of mobile cations as a function of ionic radii, the formations of ion pairs, and a higher activation energy for escape of the larger ion from mixed-ion pairs. Also during this period, the research effort in β''-alumina systems was increased, and initial determinations of some of the properties of these materials are reported here.

Studies of FLL by SANS have continued to be emphasized in investigations of superconducting materials. An intrinsic hysteresis with applied magnetic field was measured in the FLL of superconducting Nb, and a plausible explanation of its origin was constructed. Related investigations of both metastable and equilibrium configurations of FLL in other materials were carried out, and the first direct observation of a FLL in a high-field material, V_3Si, was made. The variation in the superconducting transition temperature in alloys of Al and H, produced by low-temperature H ion implantation, was also investigated.

Studies of electrical conductivities at elevated temperatures of MgO single crystals doped with transition metal impurities have shown that the effect of doping is small compared with the variation in conductivity of nominally pure crystals. Moreover, these studies demonstrated that vacancies compensating for trivalent impurities were not the major current carrier at $T < 1850$ K. However, in Fe-doped $MgAl_2O_4$ it was determined that conductivity is enhanced when Fe is in the trivalent, rather than divalent, state; this result is consistent with ionic conduction due to cation vacancy motion.

FAST-ION CONDUCTORS

PROPERTIES OF SINGLE CRYSTAL β''-ALUMINAS[1]

J. B. Bates
G. M. Brown[2]
T. Kaneda[3]
W. E. Brundage
J. C. Wang
Herbert Engstrom

Sodium beta"-alumina ($Na\beta''$) is an important solid electrolyte material because of its high ionic conductivity. It is known that the conductivity of $Na\beta''$ is several times greater than that of $Na\beta$ over a large temperature range. However, in contrast with the case of the β-aluminas, many physical properties of the β''-aluminas remain unknown because of the lack of single crystals of sufficient size and quality required by various experimental techniques. Recently, we have been able to grow relatively large single crystals of $Na\beta''$. Studies of this material and of the Li, K, Rb, and Ag analogues using Raman scattering, ionic conductivity, neutron diffraction, and theoretical model calculations have been initiated.

Large single crystals of $Na\beta''$ were grown[4] by slow evaporation of Na_2O from a mixture of Na_2CO_3, MgO, and Al_2O_3 at temperatures from 1923 to 1973 K. Single crystals of Li, K, Rb, and $Ag\beta''$ were prepared by ion exchange in the appropriate molten nitrate.

The specimen of $Ag\beta''$-alumina used in our diffraction experiments was approximately a rectangular parallelepiped with 1.1 × 6.0 × 4.7 mm dimensions and a 114-mg weight. It was found by preliminary x-ray precession photography to be a single crystal of good quality having the symmetry of space group $R\bar{3}m$. The unit cell dimensions for the triply primitive hexagonal cell, determined by the method of least squares from the second moments of 2θ scans of 106 reflections in the 2θ range from 23° to 98° are given in Table 4.1. Standard procedures were used to collect and make a preliminary reduction of intensity data for 664 independent neutron reflections. The preliminary processing included the application of absorption corrections. In the refinement process it was found that the distribution of Ag^+ ions could be described using the 18*h* sites with 0.269 fractional occupancy just as in the Reidinger description of the $Na\beta''$ structure.[5] However, much less smearing out of the Ag^+ density in $Ag\beta''$ relative to that of Na^+ in $Na\beta''$ is implied by the detailed parameters of the $Ag\beta''$ model. The contrast between the two distributions is clearly shown by the comparison of the anisotropic thermal parameters U_{11}, U_{22}, and U_{33} for Na^+ and Ag^+ given in Table 4.1. These differences imply a much tighter binding of Ag^+ compared with Na^+ in β''-alumina, which is consistent with the result that $Na\beta''$ is a much better conductor than $Ag\beta''$.

Table 4.1. Structural data for $Ag\beta''$-alumina

Unit cell parameters[a]

$a_0 = 5.6263(6)$ Å
$c_0 = 33.4403(4)$ Å

Composition

$0.81Ag_2O{\cdot}0.68MgO{\cdot}5Al_2O_3$

$0.27Ag^+$ on 18h and $0.34Mg^{2+}$ on Al(2) sites

Anisotropic thermal parameters[b,c] (Å²)

	U_{11}	U_{22}	U_{33}
Ag^+	0.0559	0.0692	0.0106
Na^+	0.1245	0.3871	0.3042

[a] Parameters for triply primitive hexagonal unit cell.
[b] From the temperature factor expression, $\exp[-2\pi^2(h^2a^{*2}U_{11} + k^2b^{*2}U_{22} + l^2c^{*2}U_{33} + 2hka^*b^*U_{12} + 2hla^*c^*U_{13} + 2klb^*c^*U_{23})]$.
[c] Sodium parameters from ref. 5.

Raman scattering from β''-aluminas was investigated for the primary purpose of identifying the attempt frequency for ion transport.[6] The wave numbers of the Raman bands which can be ascribed to vibrations of the mobile cations are listed in Table 4.2. The assignment of the peaks to A' or A'' symmetry species of the C_s point group is based on the analysis of the normal modes of a defect cluster consisting of a vacant site surrounded by three cations (see below).

Table 4.2 Wave numbers (cm^{-1}) of the Raman bands assigned to vibrations of mobile cations in β''-aluminas[a]

^6Li	^7Li	Na	K	Ag
445(A')	437(A')	220(A')		
409(A')	397(A')	170(A')		
		142(A')	90(A")	90(A')
		93(A')	78(A')	50(A")
		85(A")	78(A")	31(A')
		33(A")		22(A')

[a] Values for $Na\beta''$, $K\beta''$, and $Ag\beta''$ were observed at 15 K. Values for $^6Li\beta''$ and $^7Li\beta''$ were observed at 300 K. Peaks are assigned to the A' or A'' species of the C_s point group.

We have made model calculations similar to those for the β-aluminas to understand the Raman scattering from the mobile cations and to study the conduction mechanism of the β''-aluminas. The potential energy model included Coulomb, short-range repulsive, and polarization energy terms. Starting from the ideal structure of Naβ'' with all 6c Na^+ sites occupied, a Na^+ ion was removed from the crystal and 13 Na^+ ions near the vacant site were allowed to relax so as to minimize the total potential energy of the system. The calculated minimum energy configuration of the ions is illustrated in Fig. 4.1. This figure shows the O^{2-} ions in the conducting layer; the calculated positions of the Na^+ ions, which are displaced alternately above and below the plane of the O^{2-} ions; and the vacant Na site. The three Na^+ ions surrounding a vacancy relax inward toward the vacancy, and the surrounding cations relax away from their ideal positions as shown in Fig. 4.1. This result explains why, from the neutron diffraction data,[5] all of the Na^+ ions were found to be located on the 18*h* positions near the 6c sites. The C_{3v} symmetry at a vacant site may or may not be preserved, depending on the vacancy-ion distance. Our calculations showed that the most stable configuration above 0 K has one vacancy-cation distance slightly larger than the other two. The symmetry about the vacancy in this case is C_s rather than C_{3v}.

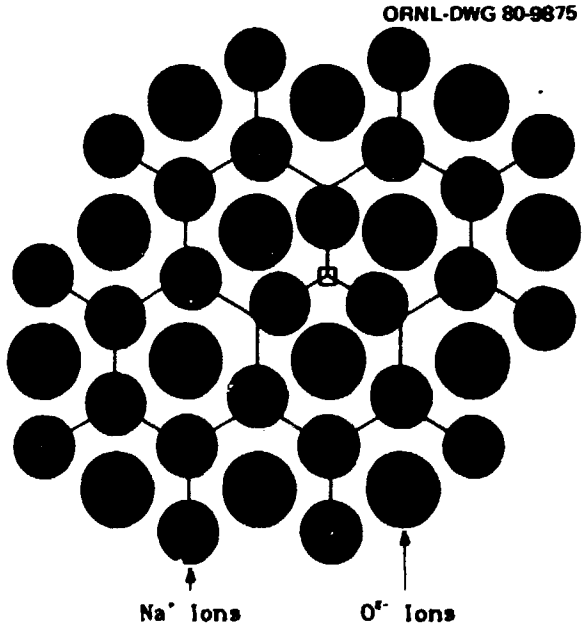

Fig. 4.1. Calculated positions of Na^+ ions near the plane defined by the O^{2-} ions in Naβ''-alumina. Open box denotes vacant cation site.

Ion transport in β''-alumina occurs by means of a vacancy mechanism, and we have made some preliminary model calculations of the details of this mechanism. Starting with the minimum energy configuration shown in Fig. 4.1, one of the three Na^+ ions neighboring a vacancy was moved in small steps toward the vacant site. To minimize the potential energy, nearby Na^+ ions were allowed to relax after each step. This process was continued until the ion and vacancy exchanged sites. The activation energy, taken to be the difference between the potential energy at the equilibrium configuration, was calculated to be about 0.02 eV. Although the calculated activation energy is much smaller than the experimental value of 0.18 eV, it is consistent with the low attempt frequency observed at 33 cm^{-1}. Not only is the calculated activation energy (0.02 eV) an order of magnitude smaller than the measured value, but the calculated pre-exponential factor is likewise nearly an order of magnitude smaller than the experimental result. The disagreement between experiment and theory can be resolved by assuming a temperature-dependent activation energy.

---

1. Summary of paper: p. 261 in *Fast Ion Transport in Solids, Electrodes and Electrolytes*, ed. by P. Vashishta, J. N. Mundy, and G. K. Shenoy, North Holland, New York, 1979.
2. Chemistry Division, ORNL.
3. Guest scientist from Fuji Photo Film Company, Tokyo, Japan.
4. W. E. Brundage and J. B. Bates, *Solid State Div. Prog. Rep. Sept. 30, 1978*, ORNL-5486, p. 194.
5. F. Feidinger, S. LaPlaca, and W. L. Roth, private communication on work in progress.
6. J. B. Bates et al., *Solid State Commun.* 32, 261 (1979).

ON THE NON-ARRHENIAN BEHAVIOR OF β''-ALUMINAS

J. C. Wang J. B. Bates

Conductivity measurements of β''-aluminas[1,2] show an interesting non-Arrhenian behavior that was not observed for the β-aluminas. The apparent activation energies defined by

$$E_{app} = -k \frac{d[\ln(\sigma T)]}{d(1/T)} \qquad (1)$$

are temperature dependent and show high values that are not consistent with the high ionic conductivities observed.

We have made potential energy calculations for Naβ''-alumina and obtained the activation energy

and attempt frequency for a vacancy conduction mechanism. The activation energy is much smaller than E_{app} from Eq. (1), and the calculated attempt frequency is quite low but seems to be consistent with an observed Raman band from the Na^+ ions in Naβ''-alumina.[3]

These discrepancies can be resolved by assuming that the true activation energy E is temperature dependent and is of the form

$$E = a + bT^{1/2} + cT , \tag{2}$$

where a, b, and c are constants. This expression, combined with the Arrhenius equation

$$\sigma T = \sigma_0 e^{-E/kT} , \tag{3}$$

can fit the conductivity results quite well. From Eqs. (1–3) it can be shown easily that

$$E_{app} = E - T\left(\frac{dE}{dT}\right) . \tag{4}$$

Therefore, the apparent activation energies may be much higher than the true activation energies.

A possible justification of the term $T^{1/2}$ in Eq. (2) is that the vacancies in β''-aluminas (about 1/6 of the number of conducting-ion sites) may have some long-range order at low temperatures, resulting in high activation energies for diffusion. As the temperature increases, thermal motion destroys the long-range order, causing the activation energy for vacancy diffusion to decrease. The oscillation amplitude of an ion at T is proportional to $(kT)^{1/2}$. If we treat an oscillating ion about its equilibrium position as a dipole, its interaction with a charged particle will be proportional to $T^{1/2}$.

The long-range order of vacancies may depend on cation concentration and the charge-compensating impurities. This may be the reason why the conductivities and Raman band intensities depend on sample preparation conditions and why the diffuse x-ray bandwidths change rapidly in some temperature range.

1. J. T. Kummer, *Progress in Solid State Chemistry*, vol. 7, p. 141, ed. by H. Reiss and J. O. Molaldin, Pergamon, New York, 1972.

2. G. C. Farrington and J. L. Briant, p. 395 in *Fast Ion Transport in Solids, Electrodes and Electrolytes*, ed. by P. Vashishta, J. N. Mundy, and G. K. Shenoy, North Holland, New York, 1979.

3. J. B. Bates et al., p. 261 in *Fast Ion Transport in Solids, Electrodes and Electrolytes*, ed. by P. Vashishta, J. N. Mundy, and G. K. Shenoy, North Holland, New York, 1979.

RAMAN SPECTROSCOPY OF β''-ALUMINA AND β''-GALLIA

N. J. Dudney[1] Roger Frech[2]
J. B. Bates W. E. Brundage

The β''-alumina structure consists of spinel-like layers separated by relatively open planes containing mobile alkali cations. Different cations can be substituted into the spinel layers during the crystal growth. A comparison of the Raman spectra for such substitutional compositions aids in identifying the vibrational modes within the spinel layer.

Polarized Raman spectra were measured for three compositions with the β''-alumina structure. Single crystals were grown from a mixture of Na_2CO_3 and the appropriate oxides.[3] The sample compositions and crystal growth temperatures were

$0.8Na_2O \cdot 0.6MgO \cdot 5Al_2O_3$ (1725°C),

$0.8Na_2O \cdot 0.6ZnO \cdot 5Al_2O_3$ (1640°C),

$Na_2O \cdot 6Ga_2O_3$ (1375°C).

The divalent cations are required to stabilize the β''-alumina structure but are not necessary for the gallate.

The tabulated phonon modes and examples of the spectra for the three crystals are shown in Table 4.3 and Fig. 4.2. The scattering geometry was defined by orthogonal axes where c is perpendicular to the conducting plane; β''-alumina belongs to the space group $R\bar{3}m$. For the ideal composition, $Na_2O \cdot 5Al_2O_3$, the selection rules for the D_{3d} point group predict the irreducible representations for the $k = 0$ optic modes of the atoms in the spinel block:[4] $\Gamma = 10A_{1g} + 3A_{2g} + 13E_g + 3A_{1u} + 10A_{2u} + 13E_u$. The Raman active modes and the polarizations in which they occur are A_{1g} $(a'a', cc)$ and E_g $(a'a', a'a, ca)$. The number of phonon peaks observed for each material agrees reasonably well with the predicted number of normal modes. Frequently the relative intensities for different polarizations did not clearly distinguish whether the mode had an A_{1g} or E_g symmetry. This unclarity may result from some disorder in the structure caused by the presence of the stabilizing divalent cations.

As shown in Table 4.3, several corresponding phonon modes were identified in both the aluminates and the gallate. At higher energies (>500 cm^{-1}) the vibrational modes must involve primarily the motion of the oxygen ions because the peak wave numbers are nearly equal. The wave-number ratios for the

Table 4.3. Phonon wave numbers and symmetry assignments from the Raman spectra of Mg- and Zn-stabilized Naβ″-alumina and selected phonon wave numbers from the Naβ″-gallate spectrum which help identify the vibrational modes

Wave numbers are measured in cm^{-1}

Naβ″-alumina, Mg stabilized		Naβ″-alumina, Zn stabilized		Naβ″-gallate
E_g modes	A_{1g} modes	E_g modes	A_{1g} modes	
111		111		68
	251		256	167
	280	285		
	309	305		
342		325		
	329		333	183
		348		
358		362		208
384		387		247
	422		415	
			426	
461		461		
544		543		
573		571		509
	585		581	
603		603		551
	651		647	582
	678		680	
690		686		
	746			
777		778		683
790		793		727
	895		894	

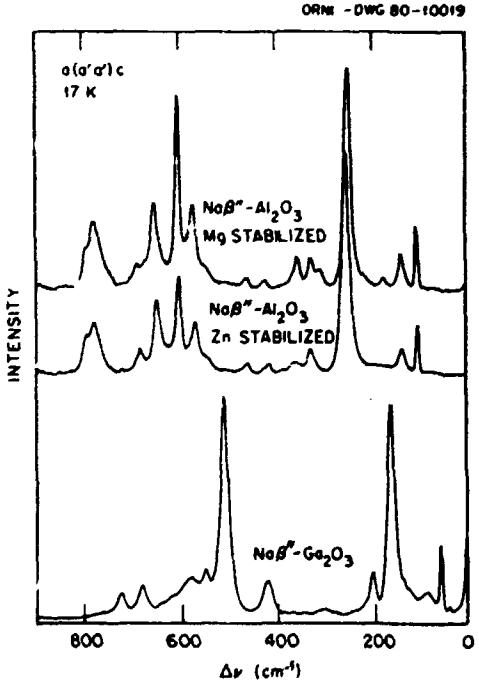

Fig. 4.2. Raman spectra of Naβ″-alumina, stabilized with Mg or Zn, and Naβ″-gallate measured at 17 K for $a(a'a')c$ scattering.

aluminate and gallate modes at lower energies are comparable to the square root of the cation mass ratio, $\sqrt{m_{Ga}/m_{Al}} = 1.6$. Therefore, these modes involve motion of Al(Ga) ions. The two intense phonon peaks at 111 and 251 cm^{-1} in the aluminates are believed to be associated with the motion of the Al ions on either side of the O^{2-} ions that form the spacer columns between the spinel blocks. Possible normal modes consistent with the symmetry assignments of these two peaks are a shearing motion of the Al ions parallel to the conduction plane and a symmetric breathing motion perpendicular to the conduction plane.

The spectra for the Mg- and Zn-stabilized aluminas display a number of differences. Phonon modes that are strongly associated with the motion of these stabilizing cations are expected to have a peak wave-number ratio near 1.6 because of the difference in the atomic masses. Modes of this type have not been identified unambiguously.

1. Eugene P. Wigner Fellow.
2. Oak Ridge Associated Universities research participant from the University of Oklahoma, Norman.

3. W. E. Brundage and J. B. Bates, "Growth of β''-Alumica and Sodium Gallate Single Crystals," this report.

4. J. B. Bates and Roger Frech, *Chem. Phys. Lett.* 60, 95 (1978).

CONDUCTING-ION CORRELATIONS IN β- AND β''-ALUMINA

B. C. Larson J. F. Barhorst

The ionic conductivity of β- and β''-alumina varies significantly with conducting-ion species (i.e., Na, K, Ag, Li) and with crystal growth parameters.[1] The identification of the microscopic phenomena affecting the ionic conductivity is important in determining the ion-ion and the ion-lattice interactions controlling ionic transport and, hence, in understanding the details of the conduction mechanism in these materials. In this work, x-ray diffuse scattering has been used to investigate conducting-ion correlations in β- and β''-aluminas through the study of the diffuse superlattice streaks resulting from diffraction from the ions in the conducting planes.

As reviewed by Allen et al.,[2] the width and structure of the superlattice streaks contain information on in-plane and inter-plane conducting-ion correlations. The rather weak inter-plane interactions lead to quasi-two-dimensional scattering characteristics in the form of modulated streaks normal to the conducting planes, and these modulations have been used in an attempt to establish short-range-order models.[3] The widths of these scattering intensity streaks give information on the coherence length (size, of two-dimensional ion clusters in the conducting planes from which the Scherrer formula can be used to estimate coherent cluster size.

In the present work, carried out in cooperation with the superionic conductivity program in the Solid State Division, we have used monochromatic CuKα x rays and a linear position-sensitive detector system to measure the widths of the (4/3, 1/3, *l*) streaks in Naβ-, Kβ-, and Agβ-aluminas and Naβ''- and Kβ''-aluminas. We have found cluster dimensions of 1.8, 2.0, and 2.5 nm for Naβ-, Agβ-, and Kβ-aluminas, respectively, and 8.3- and 5.6-nm sizes for Naβ''- and Kβ''-aluminas, respectively. As has been observed in other studies,[3] the conductivity varies qualitatively as the inverse of these cluster sizes within the β- and β''-alumina systems. In a comparison of the scattering from high-temperature-grown (1700°C) Naβ''-alumina with low-temperature-grown (1650°C) Naβ''-alumina, it was found that the low-temperature material had ~15% smaller cluster sizes than those in the high-temperature-grown material. This observation can be correlated with a higher conductivity observed[1] for low-temperature-grown Naβ''-alumina. Although a quantitative correlation of cluster sizes with ionic conductivity has not been attempted, there seems to be good evidence in both β- and β''-alumina that the formation of large ordered clusters is associated with lower conductivity material.

1. G. C. Farrington and J. L. Briant, p. 395 in *Fast Ion Transport in Solids, Electrodes and Electrolytes*, ed. by P. Vashishta, J. N. Mundy, and G. K. Shenoy, North Holland, New York, 1979.

2. S. J. Allen, Jr., et al., p. 279 in *Superionic Conductors*, ed. by G. D. Mahan and W. L. Roth, Plenum Press, New York, 1976.

3. D. B. McWhan et al., *Phys. Rev. B* 17, 4043 (1978).

INFRARED ABSORPTION AND RAMAN SCATTERING FROM H_2O IN $Na_{1-x}Li_x\beta$-ALUMINAS[1]

J. B. Bates Herbert Engstrom
Roger Frech[2] J. C. Wang
T. Kaneda[3]

The presence of water in β-alumina and its effect on the diffusion of mobile cations in this material have been noted in several studies. Klein, Story, and Roth[4] obtained evidence from NMR measurements that H_2O diffuses into the conducting plane of Naβ by observing a marked change in the ^{23}Na quadrupole coupling constant when finely divided powdered samples were exposed to air. We have observed[5] that small amounts of H_2O in Naβ-alumina cause a marked decrease in the ionic conductivity of single crystals, whereas after heating the crystals in vacuum at 400°C, the conductivity increases to its nominal dry-state value as the intensity of infrared absorption at 3200 cm^{-1} decreases to zero. Understanding the nature of these hydration states in Liβ and in the mixed-ion systems, $Na_{1-x}Li_x\beta$, is important in understanding the effect of H_2O on the conductivity and long-term behavior of these materials.

Samples of $Na_{1-x}Li_x\beta$-alumina with $x \leq 0.7$ were prepared by ion exchange of Naβ single crystals in molten $LiNO_3$ at 350°C, and those with higher Li^+ concentrations were prepared by ion exchange in molten $AgNO_3$ to form Agβ followed by treatment in molten $LiNO_3$ saturated with LiCl (30 mole %) at 350°C. The Li and Na compositions were determined from atomic absorption and emission measurements of dissolved samples and are believed to be accurate to 10%. Infrared transmission spectra were measured at 25°C using a Fourier transform spectrometer equipped with a 4× beam condenser. The infrared

light was incident along the [001] direction of the crystals. Raman scattering measurements were made at 25°C in the region of the H_2O stretching modes, using the 488.0-nm line of an Ar laser operating at 950 mW as the excitation source.

The infrared spectra of samples of different Na-Li compositions are shown in Fig. 4.3. The three major peaks observed for crystals containing high concentrations of Li^+ are labeled as A, B, and C. The pure Naβ sample was heated in H_2O vapor at 200°C for several days before the measurements were performed. The remaining samples of $Na_{1-x}Li_x\beta$ were measured as prepared, without additional treatment in water vapor. The infrared bands in Fig. 4.3 result from the symmetric (ν_1) and antisymmetric (ν_3) stretching modes of H_2O molecules in the crystals.

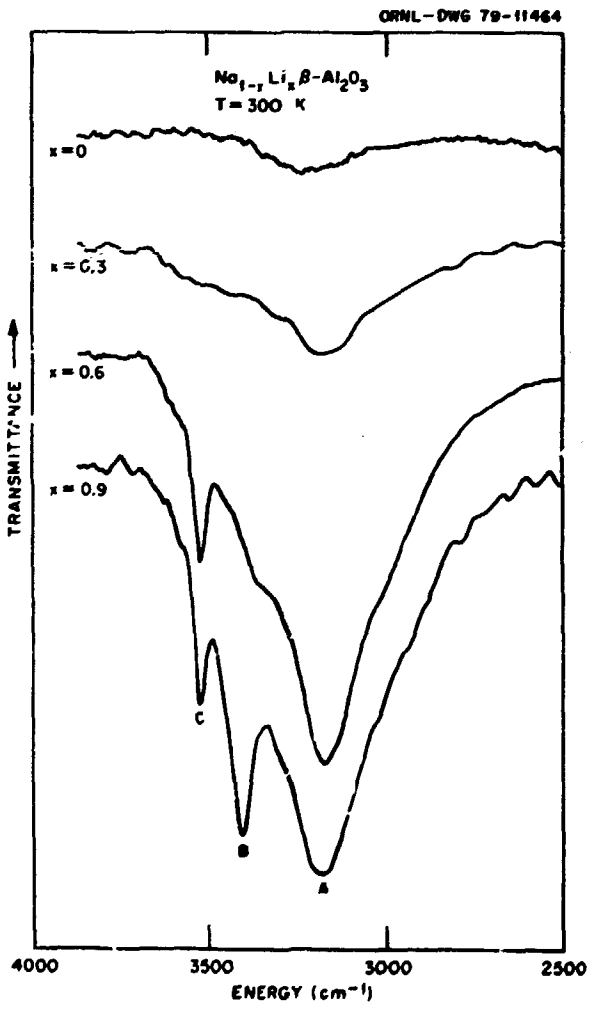

Fig. 4.3. Infrared transmission spectra at 25°C of $Na_{1-x}Li_x\beta$-Al_2O_3 single crystals. The pure Naβ crystal was treated in H_2O vapor at 200°C for several days prior to measurement. The remaining samples were measured after ion exchange.

These spectra show that the extent of hydration, as indicated by the decrease in transmission of these bands, increases with increasing Li^+ concentration.

The peak energies and values of $(1/d)\log(I_0/I)$, where d = sample thickness, for the bands near 3150 cm^{-1} and labeled A in Fig. 4.3 are listed in Table 4.4. Because $(1/d)\log(I_0/I) = \epsilon c$, where ϵ is the extinction coefficient and c is the concentration, the results in Table 4.4 show that the concentration of H_2O molecules giving rise to the A band increases by more than a factor of 30 as the Li^+ content increases to $x \geq 0.6$, assuming that ϵ does not change significantly with composition. We have found that the relative intensities of the A, B and C bands are quite sensitive to the Li^+ concentration.

Table 4.4. Peak wave numbers and reciprocal extinction lengths for the major infrared band centers of H_2O in $Na_{1-x}Li_x\beta$-aluminas

x	Wave No. (cm^{-1})			$(1/d)\log(I_0/I)$, Band A (cm^{-1})
	A	B	C	
0	3150			0.34
0.3	3180	3460[a]		3.49
0.6	3165	3350	3520	12.20
0.9	3175	3400	3520	9.67

[a]The band at 3460 cm^{-1} appears as a shoulder in some samples but as the major peak in others.

From the integrated intensities of the three peaks in the lower curve of Fig. 4.3 ($x = 0.9$), we estimate that the sample of $Na_{0.1}Li_{0.9}\beta$ contained on the order of 10^{20} water molecules per cubic centimeter, or about 0.1 molecules per unit cell. Recent studies[6] have shown, however, that Na-Li β-alumina samples are far from completely hydrated after ion exchange.

The results shown in Fig. 4.3 support the idea that hydration occurs during ion exchange from H_2O dissolved in the molten salt. This theory was verified in the following experiment: A Naβ crystal was exchanged in $LiNO_3$ that had been recrystallized several times in D_2O. In addition to the O-H stretching bands in the 3500 cm^{-1} region, the infrared spectrum of the exchanged crystal showed corresponding O-D peaks in the region near 2500 cm^{-1} caused by vibrations of HDO species.

Samples of hydrated $Na_{0.1}Li_{0.9}\beta$ were heated in vacuum at temperatures between 50 and 900°C for periods ranging from 30 min to 10 h. Some of the infrared spectra recorded after such treatment are shown in Fig. 4.4. No significant change in peak intensity was observed for temperatures below 400°C

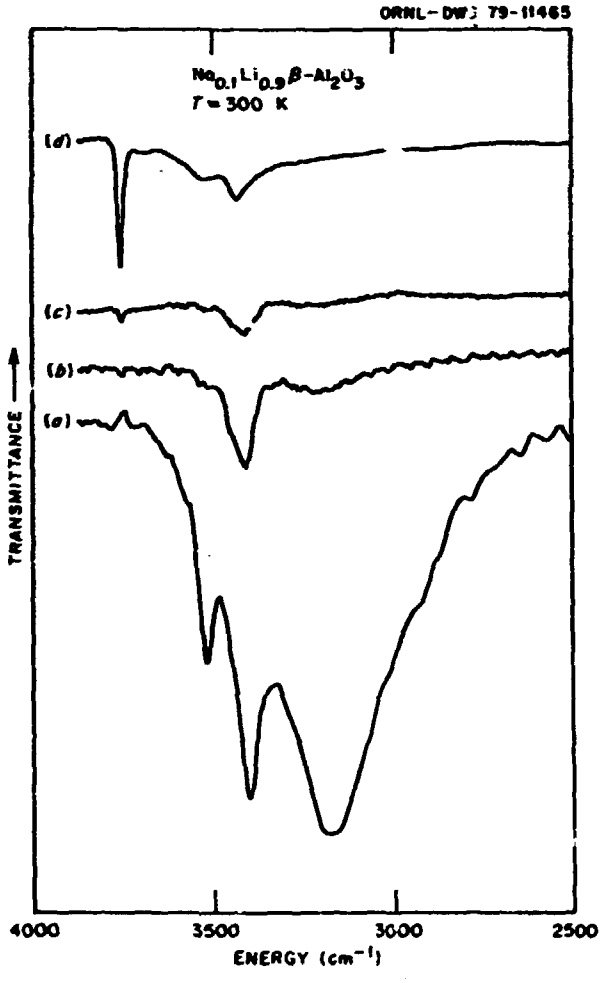

Fig. 4.4. Infrared spectra at 25°C of $Na_{0.1}Li_{0.9}\beta$-Al_2O_3. (*a*) As prepared, (*b*) after heating in vacuum for 1 h at 500°C, (*c*) after heating in vacuum for 1 h at 600°C, and (*d*) after heating in vacuum for 9 h at 600°C.

and for treatment times of 30 to 120 min. After heating at 400°C for 30 min, however, the value of $\log(I_0/I)$ at 3175 cm^{-1} decreased from 0.63 to 0.30, and it decreased further to 0.10 after an additional 60-min heating at 400°C. On heating a sample at 600°C or above, a new peak at 3750 cm^{-1} appeared and continued to grow in intensity with prolonged heat treatment.

The results in Fig. 4.3 and Table 4.4 show that the amount of H_2O which enters into β-alumina increases as the Li concentration increases. Only one absorption band of H_2O in $Na\beta$ can be identified in the spectrum measured at 25°C. As Li is introduced into the sample, more distinct peaks can be observed, and we believe that several distinct types of H_2O species may exist in crystals containing high concentrations of Li^+. The stability of the hydrates formed in $Na_{1-x}Li_x\beta$ also depends on the Li composition. The water in pure $Na\beta$ is completely removed by heating a sample in vacuum at 300–400°C. In $Na_{0.1}Li_{0.9}\beta$, however, no significant changes were observed to occur in the spectra until the crystal was heated to 400°C for 2 h or more. The new peak at 3750 cm^{-1}, which appears after heating at 600°C, is assigned to OH^-. Reaction of H_2O remaining in the sample could provide the protons for formation of OH^-, and the spectra could support a model in which these protons are bound to the columnar oxygen ions, with the O-H bond parallel to the conducting plane.

All of the experimental results support a mechanism in which water molecules diffuse into the conducting planes of β-alumina and become associated with the mobile cations. The two O^{2-}-ion layers above and below the conducting plane in β-alumina are closely packed (slightly distorted). The columnar O^{2-} ions may also be considered as forming a closely packed layer with three-fourths of the ions missing. The missing ions are those that would occupy the mO positions. Therefore, it is reasonable to place the O atom of H_2O molecules on those mO sites that are not occupied by mobile cations. If we assume that the 15% excess cations share BR sites in pairs such that each member of the pair occupies a mO position, then the maximum number of H_2O molecules per unit cell is 5.4.

The maximum hydration number requires most of the cations on a BR site to be surrounded by three H_2O molecules. However, the ionic radii of Na^+ and K^+ are sufficiently large that they cannot remain on a BR site if an H_2O molecule occupies a neighboring mO position. To accommodate a neighboring water molecule, the cation may move away from the center of the BR site toward an empty mO position, causing an increase in the total potential energy of the system. The larger the ionic radius, the greater the displacement required to accommodate an H_2O molecule and the larger the increase in potential energy. Therefore, we can expect that the number of H_2O molecules which can be placed around a BR site will decrease with increasing ionic radius. This is consistent with the trend we observed in which $Li\beta$ was found to contain much more water than $Na\beta$, and no water has been detected from infrared measurements of $K\beta$-alumina single crystals. Because the ionic radius of Li^+ is sufficiently small and because the Li^+ ions can deviate away from the BR site along the *c*-direction, it

's possible in Liβ to place three H_2O molecules on neighboring mO positions and thereby achieve the maximum predicted degree of hydration.

1. Summary of paper to be published.
2. Oak Ridge Associated Universities research participant from the University of Oklahoma, Norman.
3. Guest scientist from Fuji Photo Film Company, Tokyo, Japan.
4. D. Kline, H. Story, and W. L. Roth, *J. Chem. Phys.* 57, 5180 (1972).
5. T. Kaneda, J. B. Bates, and J. C. Wang, *Solid State Commun.*, 28, 469 (1978).
6. J. B. Bates et al., "Reaction on H_2O with $Na_{1-x}Li_x\beta$-Aluminas," this report.

REACTION OF H_2O WITH $Na_{1-x}Li_x\beta$-ALUMINAS

J. B. Bates Herbert Engstrom
N. J. Dudney[1] B. C. Larson
J. C. Wang

Recently we reported[2] that during ion exchange of Naβ-alumina single crystals in molten $LiNO_3$ or LiCl-$LiNO_3$, H_2O molecules dissolved in the melt diffuse into the conducting plane and become associated with the mobile cations. The concentration of H_2O and the stability of the hydrate formed during ion exchange were found to increase with increasing Li^+ ion concentration. Several experiments have been initiated to study the kinetics and mechanism, as well as to determine the equilibrium constants, for the reaction of H_2O with β-alumina.

Single crystals of Liβ- and $Na_{1-x}Li_x\beta$-alumina were prepared by ion exchange of Naβ-alumina as described elsewhere.[2] Crystals of Liβ, $Na_{0.3}Li_{0.7}\beta$, and Naβ were treated in H_2O vapor at 235°C for various lengths of time. Preliminary measurements of infrared absorption, weight loss as a function of time and temperature, ionic conductivity, *c*-lattice parameter change, and Raman scattering were made before and after treatment of these specimens.

Graphs of peak infrared absorbance (A) at 3175 cm^{-1} of $Na_{0.3}Li_{0.7}\beta$ measured at intervals from 0 to 24 h and of Naβ at 3160 cm^{-1} at intervals from 0 to 500 h are shown in Figs. 4.5*a* and 4.5*b*, respectively. The solid line in Fig. 4.5*a* is a fit of the data points to an exponential function, $A = a\exp(kt)$, where a and k are constants and t is the accumulated treatment time in H_2O. These results show that, up to 24 h, the rate of reaction of H_2O with $Na_{0.3}Li_{0.7}\beta$ accelerates with time. Measurements of peak absorbance at 3175 cm^{-1} beyond 24 h of treatment could not be made because the sample became nearly totally absorbing. Similar studies with Liβ show that the rate of reaction is even faster than the rate observed with the $Na_{0.3}Li_{0.7}\beta$ crystal. The solid line in Fig. 4.5*b* is a fit of the absorbance at 3160 cm^{-1} to a linear function, $A = a + kt$. Comparison of Figs. 4.5*a* and 4.5*b* shows that the rate of reaction of H_2O with Naβ is much slower than the reaction rate with $Na_{0.3}Li_{0.7}\beta$. Tentatively we conclude that not only does the concentration of H_2O in $Na_{1-x}Li_x\beta$-alumina increase with increasing Li^+ concentration, but the rate of reaction increases as well. Weight loss measurements of a Liβ crystal treated for 16 h gave the composition $1.24Li_2O \cdot 11Al_2O_3 \cdot 1.22H_2O$. When this sample was heated slowly in vacuum from 25°C, weight change occurred at 175°C. The graph of weight loss vs time at 175°C followed closely an exponential curve from the onset of weight loss to the point of essentially complete dehydration.

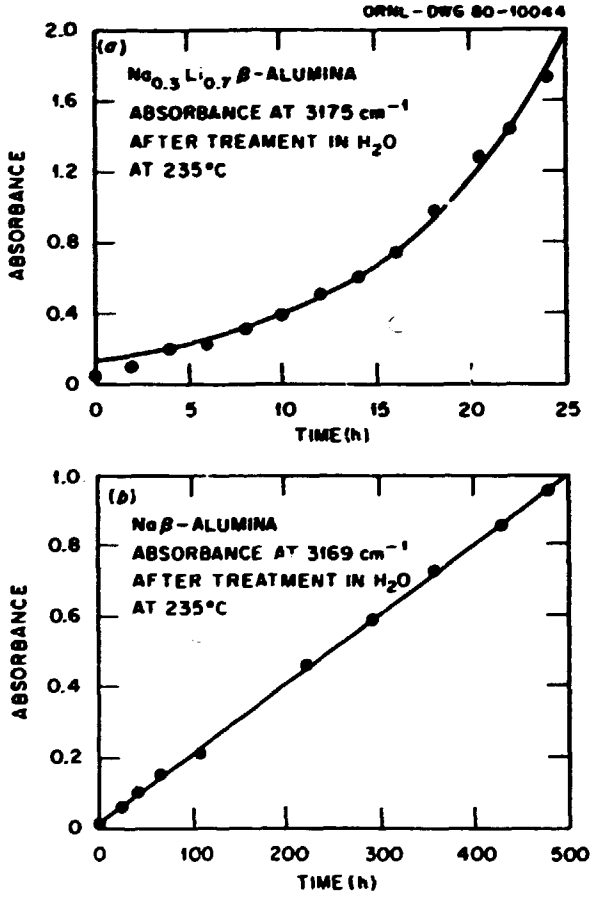

Fig. 4.5. Infrared absorption measured after heating in H_2O at 235°C for t hours. (*a*) Absorption at 3175 cm^{-1} in $Na_{0.3}Li_{0.7}\beta$-alumina, (*b*) absorption at 3160 cm^{-1} in Naβ-alumina.

X-ray measurements showed that the c-lattice constant of Naβ increased by about 0.06% after treatment for 480 h in H_2O, whereas the c-lattice constant of Liβ increased by about 0.5% after 64 h of treatment. From the latter result, we propose a possible mechanism accounting for the kinetic data in Fig. 4.5*a*: The diffusion of H_2O into the conducting plane of Liβ causes an expansion of the lattice along the c direction, lowering the activation energy for diffusion. The net result is that the rate of water diffusion into the conducting planes increases with increasing amounts of H_2O in the planes.

The ionic conductivities of the $Na_{1-x}Li_x\beta$ crystals showed marked decreases with increasing H_2O concentration. This further substantiates the claim[2,3] that H_2O molecules diffuse into the conducting planes and become coordinated to the mobile cations.

1. Eugene P. Wigner Fellow.
2. J. B. Bates et al., *Solid State Ionics* (in press); "Infrared Absorption and Raman Scattering from H_2O in $Na_{1-x}Li_x\beta$-Aluminas," this report.
3. T. Kaneda et al., *Mater. Res. Bull.* 14, 1053 (1979).

CHARACTERIZATION OF HEAT-TREATMENT-INDUCED CHANGES IN Li-Naβ-ALUMINA SINGLE CRYSTALS[1]

R. R. Dubin[2] J. B. Bates
J. S. Kasper[2] T. Kaneda[3]

Single crystals of Li-Naβ-alumina with 40 to 95% substitution of Li^+ for Na^+ were annealed in air and in vacuum at temperatures up to 1000°C. The specimens were examined before and after each heat treatment by pulsed NMR, Raman scattering, infrared absorption, and x-ray diffraction. After annealing at 600°C or above, the two original Raman bands caused by $^7Li^+$ vibrations merged into a single peak accompanied by a narrowing of spinel block phonon bands. The 1000°C annealing introduced a broad ^7Li NMR response and substantially reduced narrow-line ^7Li intensity. X-ray diffraction patterns showed that a second phase grows epitaxially with the β-alumina structure as a result of high-temperature heat treatment. The results of our experiments show that changes in the behavior of Li^+ ions occur when Li-Naβ-alumina is heated at temperatures of 600°C or above. These changes are not caused by the loss of H_2O, nor are they reversible by rehydration. The NMR data show that the mobility of the Li^+ ions and hence their contribution to the ionic conductivity are greatly reduced as a result of annealing above 700°C. Based on evidence from the x-ray diffraction studies, we suggest that the changes observed in the magnetic resonance and Raman spectra are caused by the growth of a new phase having a spinel-like structure. The extra reflections observed after heat treatment are consistent with the epitaxial formation of $LiAl_5O_8$ in the β-alumina structure.

We believe that this work provides the first experimental evidence that Li ion diffusion in β-alumina is not confined to the conducting plane. Our experimental results can be explained with the following model. The Li-Naβ-alumina structure formed by ion exchange at moderate temperatures is inherently unstable at elevated temperatures. Stabilization occurs by diffusion of Li^+ out of the conducting plane and into the interstices between the closely packed O layers of the spinel block. When complete, this Li^+ diffusion results in the formation of a spinel-like Li compound such as $LiAl_5O_8$. This formation of a second phase necessitates decomposition of the conducting plane, which must occur by Li^+ diffusion between neighboring unit cells.

The results discussed here help explain the observation[4] that high-temperature annealing decreases Li^+ conductivity in Li^+-substituted Naβ-alumina. Our present interpretation suggests that the high Li^+ conductivity reported[5] for Li-Naβ-alumina may be degraded at elevated temperature by eventual Li^+ trapping in the spinel block.

1. Summary of paper: p. 361 in *Fast Ion Transport in Solids, Electrodes and Electrolytes*, ed. by P. Vashishta, J. N. Mundy, and G. K. Shenoy, North Holland, New York, 1979.
2. General Electric Corporate Research and Development Center, Schenectady, N.Y.
3. Guest scientist from Fuji Photo Film Company, Tokyo, Japan.
4. M. S. Wittingham and R. A. Huggins, *Solid State Chemistry, Proceedings of 5th Materials Research Symposium*, NBS Special Publication 364 (July 1972).
5. W. L. Roth and G. C. Farrington, *Electrochim. Acta* 22, 767 (1977).

MODEL STUDIES OF MIXED-ION β-ALUMINAS[1]

J. C. Wang Herbert Engstrom
J. B. Bates D. F. Pickett, Jr.[3]
T. Kaneda[2] Sang-il Choi[4]

Conductivity anomalies observed in mixed-ion β-aluminas have been investigated by model calculations similar to the one used previously.[5] These

calculations include Coulombic, short-range repulsive, and polarization energy terms and show that

1. when large mobile cations are introduced into β-aluminas containing smaller cations, the large cations tend to occupy positions near BR sites alone;
2. small mobile cations introduced into a β-alumina containing larger mobile cations tend to form pairs either with themselves or with the larger cations; and
3. for a mixed-ion pair, the activation energy for escape of the larger ion from the shared potential well is much higher than that for the smaller ion.

When a K^+ ion is introduced into the ideal structure of Naβ-alumina, it may either occupy a position near a BR site alone or share a potential well to form a pair with a Na^+ ion, as is shown in Fig. 4.6. The calculated potential energy difference between the two situations is given by

$$V(\mathrm{Na—K, Na}) - V(\mathrm{Na—Na, K}) = 0.11\ \mathrm{eV}\ ,$$

where $V(X—Y, Z)$ represents the potential energy of the system when X and Y form a pair and Z occupies a neighboring BR site alone. The first term of the equation corresponds to the potential energy of the configuration shown in Fig. 4.6. Because $V(\mathrm{Na—Na, K}) < V(\mathrm{Na—K, Na})$, a K^+ ion in Naβ-alumina tends to occupy a position near a BR site alone.

On the other hand, when a Na^+ ion is introduced into the ideal structure of Kβ-alumina, it tends to form a pair with a K^+ ion:

$$V(\mathrm{K—K, Na}) - V(\mathrm{K—Na, K}) = 0.14\ \mathrm{eV}\ .$$

These and similar results calculated for other mixed crystals are summarized in Table 4.5. It is generally true that when larger mobile cations are introduced into a β-alumina containing smaller mobile cations, they tend to occupy positions near BR sites alone. In contrast, smaller mobile cations introduced into a β-alumina containing larger mobile cations tend to form pairs either among themselves or with the large cations.

Our calculations also show that when a doubly charged cation is introduced into the ideal structure of β-alumina, it will not form an ion pair with a singly charged cation. Rather, from charge neutrality considerations, the doubly charged cation will replace a mobile-ion pair.

ORNL-DWG 79-11983

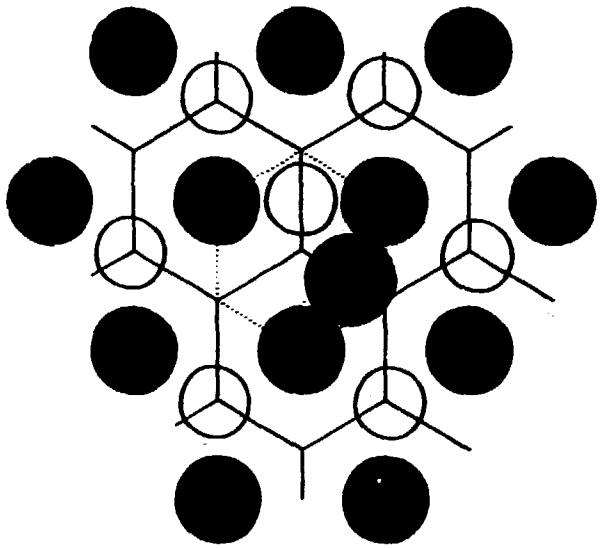

Fig. 4.6. Minimum potential energy configuration of a Na^+-K^+ pair in Naβ-alumina. The open circles are Na^+ ions, the large solid circle is the K^+ ion, and the smaller solid circles are O^{2-} ions. The dotted lines indicate the shared potential well.

Table 4.5. Calculated potential energies of various ion configurations in Li, Na, and Kβ-aluminas

Host material	Ion configuration[a]	Potential energy[b] (eV)
Liβ	(Li—Li, Na)	V1
	(Li—Na, Li)	V1 + 0.20
Na β	(Li—Li, Na)	V2
	(Li—Na, Li)	V2 + 0.29
	(Na—Li, Na)	V3
	(Na—Na, Li)	V3 + 0.65
	(Na—Na, K)	V4
	(Na—K, Na)	V4 + 0.11
	(K—Na, K)	V5
	(K—K, Na)	V5 + 0.15
Kβ	(Li—Li, K)	V6
	(Li—K, Li)	V6 + 0.39
	(K—Li, K)	V7
	(K—K, Li)	V7 + 0.84
	(Na—Na, K)	V8
	(Na—K, Na)	V8 + 0.12
	(K—Na, K)	V9
	(K—K, Na)	V9 + 0.14

[a] In the notation $(X—Y, Z)$, $X—Y$ denotes the paired ions and Z denotes the ion occupying a neighboring BR site alone.

[b] V1, V2, ..., V9 represent arbitrary reference potential energies.

The activation energy for the escape of one type of ion out of the potential well of a mixed-ion pair, as illustrated in Fig. 4.6, may be quite different from that of the other ion type. Because of the difference in ionic radii and polarizabilities, the two ions experience different potentials in the same potential well. As the ions attempt to escape from the region through correlative motion, the smaller ion receives more help from the larger ion than the larger ion can receive from the smaller one. The calculated activation energies for the escape of a cation from a mixed-cation pair in Liβ-, Naβ-, and Kβ-aluminas are given in Table 4.6. For example, the calculated activation energy for the escape of the K^+ ion in Fig. 4.6 out of the potential well that it shares with a Na^+ ion to form a new K^+-Na^+ pair in a neighboring potential well is

$$E(\mathrm{Na}-\mathrm{K}^*, \mathrm{Na}) = 0.30 \text{ eV} .$$

The activation energy for the Na^+ ion to escape from the shared potential well is much smaller:

$$E(\mathrm{K}-\mathrm{Na}^*, \mathrm{Na}) = 0.15 \text{ eV} .$$

In general, for a mixed-ion pair, the activation energy for escape of the larger ion from the shared potential well is higher than that of the smaller ion.

Table 4.6. Activation energies of diffusion in Li, Na, and Kβ-aluminas

Host material	Ion configuration	Activation energy (eV)	
		Calculated	Observed[a]
Liβ	(Li Li*, Li)[b]	0.38	0.378
	(Na Li*, Li)	0.24	
	(Li Na*, Li)	0.65	
Naβ	(Na Na*, Na)	0.20	0.165
	(Na Li*, Na)	0.24	
	(Li Na*, Na)	0.65	
	(Li Li*, Na)	0.43	
	(K Na*, Na)	0.15	
	(Na K*, Na)	0.30	
	(Na Na*, K)	0.24	
Kβ	(K K*, K)	0.27	0.233
	(Li Li*, K)	0.54	
	(Li K*, K)	0.84	
	(K Li*, K)	0.29	
	(Na K*, K)	0.37	
	(K Na*, K)	0.16	

[a] From ref. 6.

[b] In the notation $(X - Y^*, Z)$, Y^* denotes the ion escaping from the X-Y pair and Z denotes the ion with which Y forms a new pair in a neighboring potential well.

The results listed in Tables 4.5 and 4.6 can be applied to explain, at least qualitatively, the mixed-cation effects on conductivity observed in β-aluminas and to interpret the changes in relative intensities of the Raman or infrared bands from mixed conducting cations when the composition ratio varies.

---

1. Summary of paper: p. 379 in *Fast Ion Transport in Solids, Electrodes and Electrolytes*, ed. by P. Vashishta, J. N. Mundy, and G. K. Shenoy, North Holland, New York, 1979.
2. Guest scientist from Fuji Photo Film Company, Tokyo, Japan.
3. Hughes Aircraft Company, Los Angeles, Calif.
4. University of North Carolina, Chapel Hill.
5. J. C. Wang, M. Gaffari, and S. I. Choi, *J. Chem. Phys.* **63**, 772 (1975).
6. Y. F. Y. Yao and J. T. Kummer, *J. Inorg. Nucl. Chem.* **29**, 2453 (1967).

NON-DEBYE CAPACITANCE IN β-ALUMINA

Herbert Engstrom J. B. Bates J. C. Wang

The development of new solid electrolytes for use in batteries of high power densities requires a fundamental understanding of the mechanisms of ionic conduction in these materials. Accurate measurements of the electrical properties, particularly the conductivity, are very important in achieving such an understanding. We have employed a fully automated, computer-controlled network analyzer to obtain such data on the β-aluminas over a wide range of frequencies and temperatures.

Implicit in several recent conductivity studies[1-3] of the β-aluminas is the assumption that the impedance of these crystals may be represented by a capacitor C, which corresponds to the interfacial capacitance of the electrodes, in series with a resistor R, which corresponds to the bulk resistivity. The impedance of this circuit is given by

$$Z = R - i/\omega C . \tag{1}$$

Such a material resembles a Debye solid, because its equivalent dielectric constant may be expressed in the form of the usual Debye permittivity:

$$\epsilon(\omega) = \frac{\sigma}{i\omega} = \frac{C}{1 + i\omega\tau} \frac{l}{A} , \tag{2}$$

where σ is the complex conductivity, $\tau = RC$, and l is the length and A the surface area of the crystal.

A. K. Jonscher[4] has pointed out that the accepted model[5] of ionic conductivity in the β-aluminas implies that many-body effects may be important. According to Jonscher's analysis, rapid hopping of the conduction ions, together with a much slower motion of the screening ions, may lead to non-Debye behavior in which the permittivity is given by

$$\epsilon(\omega) = \epsilon_\infty[1 + a_n[1 - i\cot(\pi n/2)]\omega^{n-1}), \qquad (3)$$

where $n < 1$ and a_n is a real constant. For the β-aluminas at audio frequencies and above, $a_n\omega^{n-1}$ is much greater than 1, in which case it is possible to show that the functional dependence of the impedance may be expressed as

$$Z = R + \frac{D}{\omega^n \tan(\pi n/2)} - \frac{iD}{\omega^n}, \qquad (4)$$

where D is related to the permittivity.

Figure 4.7 shows the measured values (points) of the impedance Z of a Naβ-alumina crystal at room temperature. It is clearly evident that the real part of Z has a frequency dependence. The solid lines of Fig. 4.7 are graphs of $\mathrm{Re}(Z)$ and $-\mathrm{Im}(Z)$ from Eq. (4), using the best fit parameters. This equation was fit to data taken over the temperature range of 20° to 500°C. In agreement with the results of other workers,[1-3] the static conductivity was found to follow an Arrhenius dependence on temperature, as is illustrated in Fig. 4.8. Measurements on four Naβ-alumina samples cut from the same boule gave a mean activation energy of 0.1455 ± 0.0018 eV. The parameter a_n in Eq. (3) was also found to be strongly temperature dependent: its value increases from 3×10^8 at $T = 25$°C to $\sim 10^9$ at $T = 500$°C, where the values are given in the appropriate MKS units. At room temperature, $n \cong 0.80$ and remains at about this value until T reaches ~200°. At that temperature, n begins to decrease, reaching ~0.65 at $T = 500$°C. For a Debye crystal, $n = 0$; the departure from Debye behavior is quite large, even at ambient temperatures.

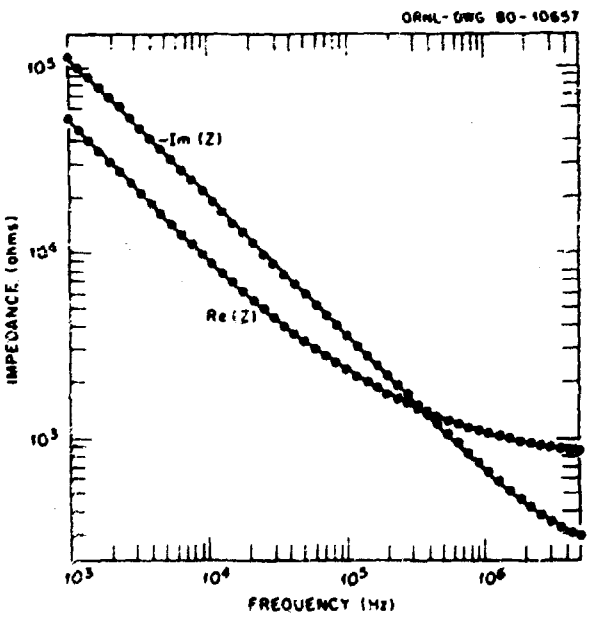

Fig. 4.7. Real and imaginary parts of the impedance Z of a Naβ-alumina crystal at room temperature. Points show experimentally measured values; lines show best fit parameters using Eq. (4).

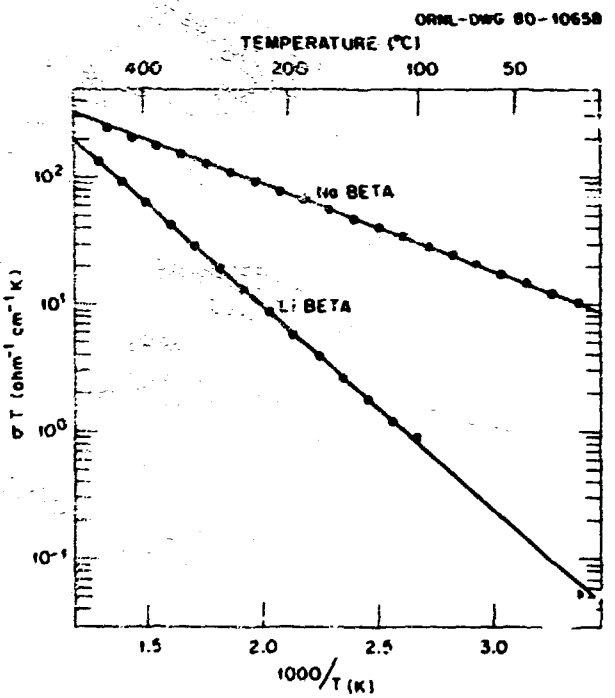

Fig. 4.8. Arrhenius dependence of the electrical conductivity, σ, for Naβ- and Liβ-alumina.

Also illustrated in Fig. 4.8 is the temperature dependence of the conductivity of a Liβ-alumina crystal. We found that its impedance was even less Debye-like than that of Naβ-alumina, having an n of about 0.67 for those temperatures shown. The data for this crystal gave an activation energy of 0.31777 ± 0.00014 eV.

Accurate measurements of the three parameters of Eq. (4) promise to provide much more information

about the microscopic processes that take place in fast-ion conductors than has previously been possible.

1. W. L. Fielder et al., *J. Electrochem. Soc.* 122, 528 (1975).
2. S. J. Allen, Jr., et al., *Phys. Rev. B* 17, 4031 (1978).
3. T. Kaneda et al., p. 371 in *Fast Ion Transport in Solids, Electrodes and Electrolytes*, ed. by P. Vashishta, J. N. Mundy, and G. K. Shenoy, North Holland, New York, 1979.
4. A. K. Jonscher, *J. Mater. Sci.* 13, 553 (1978).
5. J. C. Wang, M. Gaffari, and S. I. Choi, *J. Chem. Phys.* 63, 772 (1975).

RAMAN SCATTERING FROM NH_4^+ AND ND_4^+ IN β-ALUMINA[1]

J. B. Bates J. C. Wang
T. Kaneda[2] Herbert Engstrom

The β-aluminas are a class of nonstoichiometric aluminates with the composition $(1 + x)M_2O \cdot 11Al_2O_3$ ($x \cong 0.15$ to 0.30), where M is a monovalent cation. The alkali-metal and Agβ-aluminas are known for their high ionic conductivities. The structure of these materials consists of closely packed spinel blocks separated by loosely packed planes containing the mobile M^+ ions and bridging O^{2-} ions. Rapid diffusion of the M^+ cations is two-dimensional within the loosely packed planes. Because of the nonstoichiometry, the M^+ cation sublattice in β-alumina is disordered. This disorder and the resulting high mobility of the M^+ ions make β-alumina an interesting host material in which to study complex ions such as NH_4^+. Our primary aim in this study was to examine the effect of local symmetry and disorder on the internal modes of NH_4^+ and ND_4^+.

Single-crystal samples of ammonium-substituted β-alumina were prepared by heating single crystals of Naβ in molten NH_4NO_3 or ND_4NO_3 (98% D) at 453 K for times from a few hours to 400 h. For ND_4^+ substitution, the powdered nitrate and Naβ single crystals were sealed under vacuum in Pyrex tubes to prevent exchange of D with H in atmospheric water vapor. Depending on the ion exchange times, the crystals studied contained from 10 to 100% of Na^+ replaced by NH_4^+(ND_4^+).

The crystal structures of all the β-aluminas are isomorphic and belong to the space group D_{6h}^4. Analysis of x-ray diffraction data shows that most of the mobile cations occupy 6*h* (C_{3v}) sites very close to the 2*b* (D_{3h}) BR site.[3] In Naβ, the remaining Na^+ ions occupy 6*h* positions midway between the bridging O^{2-} ions. Because β-alumina contains from 2.3 to 2.6 mobile cations per unit cell (the exact number depends on the method of crystal growth and quantity of impurities present), the 6*h* sites are not filled, and the cation sublattice is therefore disordered.

The Raman spectra show that the internal modes of NH_4^+ and ND_4^+ are split into several components. In ordered structures, splittings of the internal modes of complex ions are caused by removal of degeneracy by the static field at a particular site (site-group splitting) and/or by coupling of the internal modes as a result of correlated motion of the ions on equivalent sites (factor-group splitting). Factor-group analysis requires the lattice to be ordered and furthermore assumes that there are long-range interactions of sufficient strength to cause interionic coupling of internal vibrations. Because the cation sublattice is disordered, neither a simple site-group nor factor-group analysis can be applied to the modes of NH_4^+ in $NH_4\beta$.

The Raman scattering from the internal modes of NH_4^+ ions in β-alumina can be understood, however, if the ions on nonequivalent sites are treated as independent scattering centers and if the disordered distribution of the ions on these sites is taken into account in calculating the forms of the scattering tensors. The analysis of the Raman data suggests that the ammonium ions occupy three sets of nonequivalent sites. Because some of the same components of the internal modes evidently appear in all polarizations, the effective local field symmetry of one set of ions must be either $C_s^\perp$ (σ perpendicular to the conducting plane) or C_1. The other two sets of sites could have either C_{2v} or $C_s^\parallel$ symmetry (σ parallel to the conducting plane). From potential energy calculations based on either an electrostatic model or a hydrogen-bonding model, the preferred orientation at the BR and mO sites has the C_2 axes of the ions parallel to the conducting plane, with two protons located in the plane and bound to the O(5) ions and two protons bound to O^{2-} ions in the layers above and below the conducting plane. These results are in agreement with the choice of either C_{2v} or $C_s^\parallel$ site symmetry. The calculations rule out $C_s^\perp$ as a possibility, but they provide no clues as to the possible origin of a local field of C_1 symmetry.

The internal and external mode spectra of ammonium ions in β-alumina are sensitive to changes in ion concentration and sample temperature. The pronounced line broadening of the internal modes with increasing temperature above about 75 K can be attributed to coupling with rapid reorientation of the ions. Librational modes of ND_4^+ and NH_4^+ evidently

occur in the region between 200 and 350 cm^{-1}, whereas the translational modes occur between 100 and 190 cm^{-1}.

1. Summary of paper to be published.
2. Guest scientist from Fuji Photo Film Company, Tokyo, Japan.
3. C. R. Peters et al., *Acta Crystallogr. Sect. B:* 27, 1826 (1971).

SUPERCONDUCTIVITY

INTRINSIC HYSTERESIS IN THE FLL OF SUPERCONDUCTING Nb

D. K. Christen H. R. Kerchner
S. T. Sekula

The high-resolution double-crystal neutron diffractometer has enabled measurements of a previously unrecognized property of the FLL in a type II superconductor possessing an attractive flux-line interaction. The phenomenon was observed in a nearly perfect, 13-mm-diam, single-crystal Nb sphere. The effect is described here briefly, along with a plausible explanation of its origin.

As the applied magnetic field is quasi-statically reduced from mixed-state values to IMS values, the microscopic field-dependent separation between the flux lines is observed to "overshoot" and then reattain that fixed separation that is characteristic of the flux-line density within the FLL domains of the IMS. From an experimental viewpoint, this effect is manifested as a dip in the highly resolved scattering angle 2θ from a given set of FLL planes and, correspondingly, in the average flux density per unit cell of the FLL, $b = \phi_0/A_c$, where ϕ_0 is the flux quantum and A_c is the area of the FLL unit cell. The phenomenon is repeatable, static, and absent when the field is increased.

Figure 4.9 illustrates this effect, where the FLL was formed either by reducing the applied field H_a from a value above the upper critical field H_{c2} or by increasing it from below the lower critical field H_{c1} (in the flux-free Meissner state). Here, b and H_a are plotted as (small) parameters reduced by the equilibrium flux density B_0, caused by the attractive flux-line interaction; H_a is referenced with respect to the theoretical macroscopic field boundary between the mixed state and the IMS. For a spherical sample, the IMS occupies the applied-field interval $^2/_3 H_{c1} \leq H_a \leq {}^2/_3 H_{c1} + {}^1/_3 B_0$ (i.e., on the scale of Fig. 4.9, $-1 \leq 3\Delta H_a/B_0 \leq 0$) and is characterized by domains of FLL in equilibrium with flux-free regions.

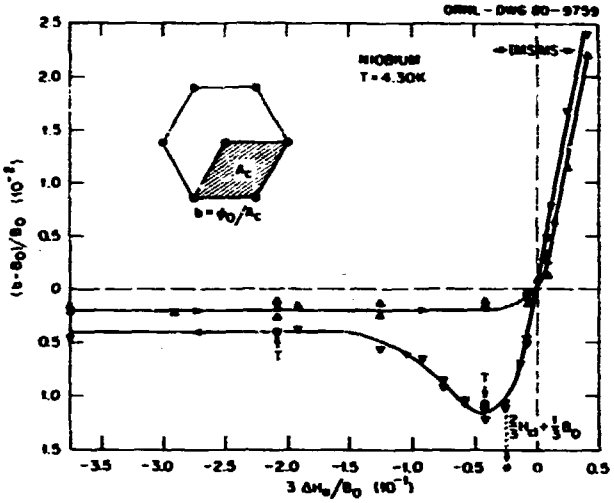

Fig. 4.9. The irreversibility in the flux density per FLL unit cell, b, for various histories of the applied field H_a. The points determining H_a are relative to the theoretical, macroscopic field boundary between the mixed state and IMS; those determining b are relative to the macroscopic flux density B_0 determined by the attractive flux-line interaction. The points labeled by T indicate that the history was such that the temperature of the sample was lowered from above T_c in the fixed applied field. The position on the abscissa designated by an asterisk is the observed applied field below which a subsequent increased field path would produce a hysteresis loop.

The existence of these domains provides motivation for attempting to understand the observed irreversibility in terms of an equilibrium or quasi-equilibrium thermodynamic analysis, especially in view of the essentially reversible bulk magnetic behavior of this sample in the mixed state, where there are no domain effects.[1] In fact, there are small energy contributions caused by the domains which can contribute nonnegligibly in a specimen of finite size. They arise because

1. the negative flux-line interaction energy results in flux lines on the surface of a (cylindrical) FLL domain being at a relatively higher energy than those in the bulk (surface tension) and
2. the magnetic-field energy external to the sample is higher than that of a material possessing the same macroscopic, but microscopically uniform, internal flux density.

In analogy to a type I superconductor in the intermediate state, it is the small energy trade-off between these two contributions that produces the

equilibrium domain structure in the IMS. There is yet another parameter to consider in the type II case, however—the energy variation associated with interflux-line spacings that differ from that given by B_0. It is possible to show by minimization of the free energy that, for an arbitrary domain structure, the mixed state is "super cooled" to an applied field and flux density given by

$$\Delta H_a^* = -\frac{B_0}{3C_L V} \times \left| \partial u/\partial\left(\frac{\Delta b}{B_0}\right) + (1 + 8\pi C_L/B_0^2)\,\partial u/\partial\zeta \right|$$

and

$$\Delta b(\Delta H_a^*) = 3\Delta H_a^*/(1 + 8\pi C_L/B_0^2)$$

at the point where the full FLL begins to break up. Here, u is the small energy resulting from the domain effects (1) and (2) above, ζ is the volume fraction of the sample devoid of FLL, and C_L is the elastic compressibility modulus of the FLL. That is, upon decreasing the applied field into the IMS, it is at first energetically more favorable to expand the FLL (lower $\Delta b/B_0$) than to open holes in it, down to the fields ΔH_a^* and $\Delta b(\Delta H_a^*)$.

Thus, the inclusion of domain-energy effects in the thermodynamic free energy can predict an apparent supercooling of the mixed state without resorting to nonequilibrium phenomena (in fact, consideration of nonequilibrium effects such as surface or bulk flux pinning leads to results that are contradictory to observation). However, other features of Fig. 4.9, such as the magnitude of supercooling, the recovery from the dip as the field is decreased further, and the observed irreversibility once $3\Delta H_a/B_0$ is below the dip, can only be explained semiquantitatively by consideration of particular models for domain structures. Two such structures that are reasonable for $\zeta \ll 1$ are (1) flux-free tube-like voids in the FLL and (2) FLL vacancies. A series of straightforward arguments leads to the following results for the domain energies:

$$\text{Voids:} \quad u \cong C_{VOID}\,\zeta\left(1 + \frac{\Delta b}{B_0} - \frac{15}{28}\zeta\right),$$

$$\text{Vacancies:} \quad u \cong C_{VAC}\,\zeta(1 + \Delta b/B_0).$$

The constants C_{VOID} and C_{VAC} depend on FLL parameters such as the binding energy between two flux lines (B_0 and ϕ_0) and geometric factors. An estimate of their magnitude yields $C_{VOID}/C_{VAC} \cong 0.03$. Then, flux-free voids are the more stable domain structure for the small-ζ IMS region. However, voids cannot be formed spontaneously upon coming from a history of a full FLL. Indeed, on decreasing-field history, individual flux-line vacancies must first nucleate at the sample surface, then quasi-statically cluster in order to achieve a void structure. On increasing-field history, this requirement is absent because the FLL is formed from the flux-free Meissner state, and the voids may be formed by the gradual coalescing of isolated FLL islands.

Within this picture, most of the features of Fig. 4.9 are explicable, and the relative sizes of the effects are in semiquantitative accord with those given by the estimated magnitudes of C_{VOID} and C_{VAC}. However, we have made no attempt to characterize the detailed mechanism by which the void structure evolves from flux-line vacancy clustering. We note in passing that an FLL history that involves application of a fixed field and subsequent lowering of the sample temperature from above the transition temperature T_c yields results (Fig. 4.9) similar to the decreased-field history. This observation is consistent with the formation of the IMS, its having arisen from a mixed-state history in both cases.

Thus, the history effect described above, present on the microscopic level of the interfluxoid spacing, is seen to be predicted by the net attractive flux-line interaction and its resultant influence on small energies associated with the domains in the IMS. Semiquantitative agreement with a thermodynamic description indicates that the phenomenon is a heretofore unrecognized, intrinsic irreversibility.

---

1. H. R. Kerchner, D. K. Christen, and S. T. Sekula, *Phys. Rev. B* 21, 86 (1980).

CORRELATIONS BETWEEN MULTIPLY ORIENTED FLUX-LINE DOMAINS AND ANISOTROPY EFFECTS

D. K. Christen S. T. Sekula

Additional information regarding correlations between the FLL and the crystal lattice has been obtained for pure Nb. Analysis of small-angle neutron-scattering data reveals that the tendency for a well-defined FLL orientation (e.g., nearest-neighbor direction) with respect to certain real crystal axes is significantly degraded when the applied

magnetic field is parallel to particular lattice directions. These directions correspond to those crystal axes where multiply oriented coexisting FLL domains were previously observed to form.[1] This phenomenon is shown in Fig. 4.10, manifested as the relative width of rocking-curve peaks of FLL diffracted neutrons, for the applied fields parallel to various crystal-lattice directions in the (100) and (1$\bar{1}$0) planes. For sample orientations lying between

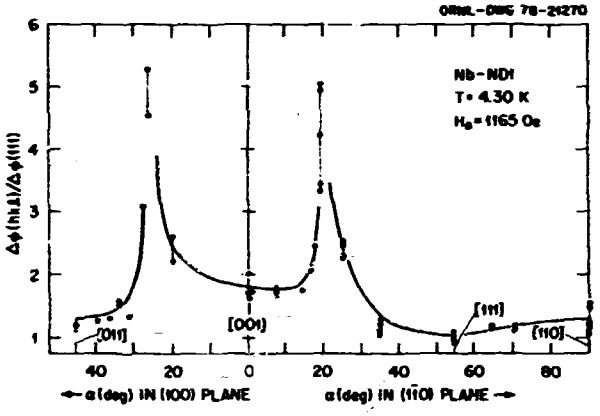

Fig. 4.10. Relative rocking-curve widths of the FLL in the IMS for a scattering geometry where $\Delta\phi$ measures the "mosaic" spread of the FLL. The applied field is parallel to crystal-lattice directions $[hkl]$ in the (100) and (1$\bar{1}$0) planes, measured by an angle α relative to the [001] axis. The data are normalized to the width $\Delta\phi(111)$, the case where H_a lies parallel to a (111) crystalline axis.

the two peaks in rocking-curve width, two coexisting FLL domains of different orientation (but the same symmetry) were observed to occupy the sample, whereas outside that orientation range, a single FLL existed. From a theoretical viewpoint, these widths are most likely related to the relative restoring force at the free-energy minimum with respect to FLL–crystal-lattice orientation shifts. Current theories of the FLL–crystal-lattice correlations fail to predict multiply oriented domains at all, so that a rigorous comparison must await improvements in the theory.

1. P. Thorel and D. K. Christen, *J. Appl. Crystallogr.* 1, 654 (1978).

THE CRITICAL FIELDS H_c AND H_{c2} OF SUPERCONDUCTING Nb[1]

H. R. Kerchner D. K. Christen
S. T. Sekula

Our measurements of the thermodynamic critical field H_c and the upper critical field H_{c2} of a Nb crystal have been compared with realistic microscopic theory. This comparison tests the current theoretical picture of the electronic properties of Nb. Specifically, H_c is sensitive to the strength of the electron-phonon interaction and to the density of electron states at the Fermi surface. Near the critical temperature T_c, H_{c2} is sensitive to the mean square Fermi velocity and to the electron-phonon interaction. At lower temperatures, $H_{c2}/T_c[dH_{c2}/dT]_{T_c}$ is enhanced by the variation of the Fermi velocity over the Fermi surface and its relative anisotropy depends on Fermi surface averages of the Fermi velocity. Qualitatively, these effects have been well known for some time, and several quantitative comparisons have appeared in the literature. However, recent theoretical results and our recent improvement in the precision of H_c measurements make a new comparison worthwhile.

The experimental technique[2] and a summary of the H_{c2} measurements[3] were described previously. Our results for H_{c2} are in excellent agreement with earlier measurements and with calculations based mainly on band theory.[4] We just note here that recent theoretical progress enables us to deduce a reliable value for the mean square (renormalized) Fermi velocity. Our value, 2.68×10^5 m/s, is in excellent agreement with the value deduced from de Haas–van Alphen and cyclotron resonance measurements.[5]

By using some thermodynamic relations, H_c was deduced from double integrals of the measured field derivative of the mixed-state magnetization.[2] The sample showed excellent magnetic reversibility in the mixed state, and the data obtained in the less reversible IMS were not used to determine H_c. In this way, the uncertainty in H_c caused by magnetic hysteresis was significantly reduced over previous measurements.

New theoretical calculations of H_c for Nb have recently become available,[6,7] in which several models of the phonon spectrum and the electron phonon interaction were used. In Fig. 4.11, our data are compared with calculations based on a theoretical model interaction[7] and models deduced from tunneling measurements by groups at Stanford and MIT. The shape of the deviation function plot

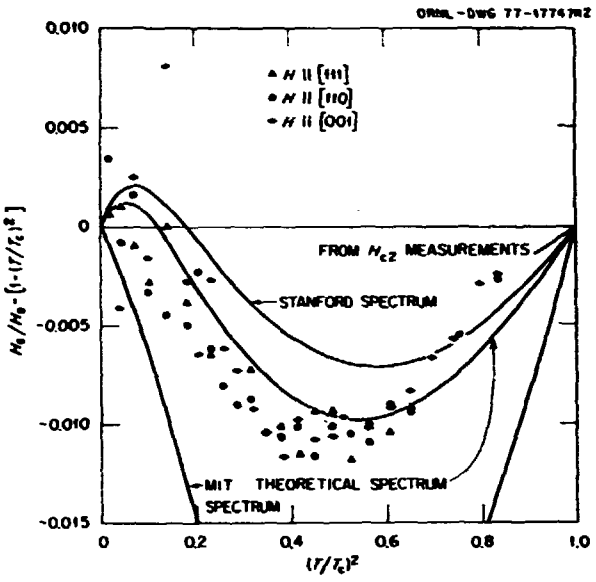

Fig. 4.11. The deviation function plot for H_c of Nb. Data are presented for three different orientations of the same sample in the applied field. As required thermodynemically, no orientation dependence is evident in the data.

(shown in the figure) depends primarily on the value of the electron-phonon coupling parameter λ. Curves corresponding to a low value of λ, such as the MIT model (λ = 0.3), lie below the data; curves corresponding to a high value, such as the Stanford model (λ = 1.0), lie above the data. Comparison of our data with such curves indicates that $\lambda = 0.9 \pm 0.1$.

Careful analysis of the H_c and H_{c2} measurements points up a curious discrepancy in the theory. The electron-phonon interaction is expected to reduce the band theory Fermi velocity by the factor $1 + \lambda = 1.9$. The corresponding ratio of the band velocity to the experimental Fermi velocity is 2.3. The same comment applies also to the density of electron states deduced either from the H_c measurements or from the low-temperature specific heat. (The two experiments give identical values.) Because an error of some 20% in the magnitude of the band theory velocity and density of states is difficult to reconcile with the impressive success of band theory in describing both the de Haas–van Alphen orbits and the anisotropy of H_{c2}, it appears likely that the difficulty is associated with the many-body renormalization factor $1 + \lambda$.

1. Summary of paper to be published.
2. H. R. Kerchner, D. K. Christen, and S. T. Sekula, *Solid State Div. Annu. Prog. Rep., April 30, 1977*, ORNL-5328, p. 125.
3. H. R. Kerchner, D. K. Christen, and S. T. Sekula, *Phys. Rev. B* 21, 86 (1980).
4. W. H. Butler, to be pulbished.
5. G. W. Crabtree et al., *Phys. Rev. Lett.* 42, 390 (1979).
6. J. M. Daams and J. P. Carbotte, p. 715 in *Transition Metals, 1977*, ed. by M. J. G. Lee and J. M. Perz, Institute of Physics Conference Series No. 39, London, 1978.
7. W. H. Butler, *Proceedings Third Conference on Superconductivity in d- and f-Band Metals*, Academic Press, New York, in press.

OBSERVATION OF AN FLL IN V_3Si BY SMALL-ANGLE NEUTRON DIFFRACTION

D. K. Christen F. M. Mueller[1]

The high-resolution, double-perfect-crystal, small-angle neutron diffractometer was used to obtain the first direct observations of an FLL in the high-field, type II, superconducting material V_3Si. The FLL was found to be essentially polycrystalline, although the sample was a large (1 cm^3) single crystal, having the *A*15 structure. There was high correlation in the interfluxoid spacing, as deduced by the diffraction peak widths. Arguments are presented below which describe the distinction of the observed polycrystalline flux-line structure from that of an amorphous, filamentary array.

The FLLs were grown by applying a fixed magnetic field parallel to the axis of the cylindrical crystal and subsequently lowering the sample temperature from above the transition temperature $T_c \cong 16.8$ K down to 4.2 K, where the experiments were performed. In this way the resulting flux density within the sample can never be larger than the applied field. Figure 4.12 shows the observed scattered intensities for two different applied fields and for different azimuthal orientations of the sample. The first-order (10) diffraction peaks are 15–18 arc-s in width, about four times that of the instrument resolution, and have a relative dispersion $\Delta 2\theta / 2\theta \cong 6\%$. The nearly azimuthally independent scattering pattern is shown in Fig. 4.13, where there is some indication that the FLL may be comprised of mosaic blocks distributed with a large, ~47° spread in relative orientation.

The observed diffraction-peak widths and rocking-curve intensities can be interpreted by one or a combination of the following phenomena:

1. The structure is comprised of large, perfect mosaic blocks of FLL having a nearly random relative orientation. The broadened diffraction peaks result from an instrumental property whereby beam defocusing arises from the large mosaic distribution.

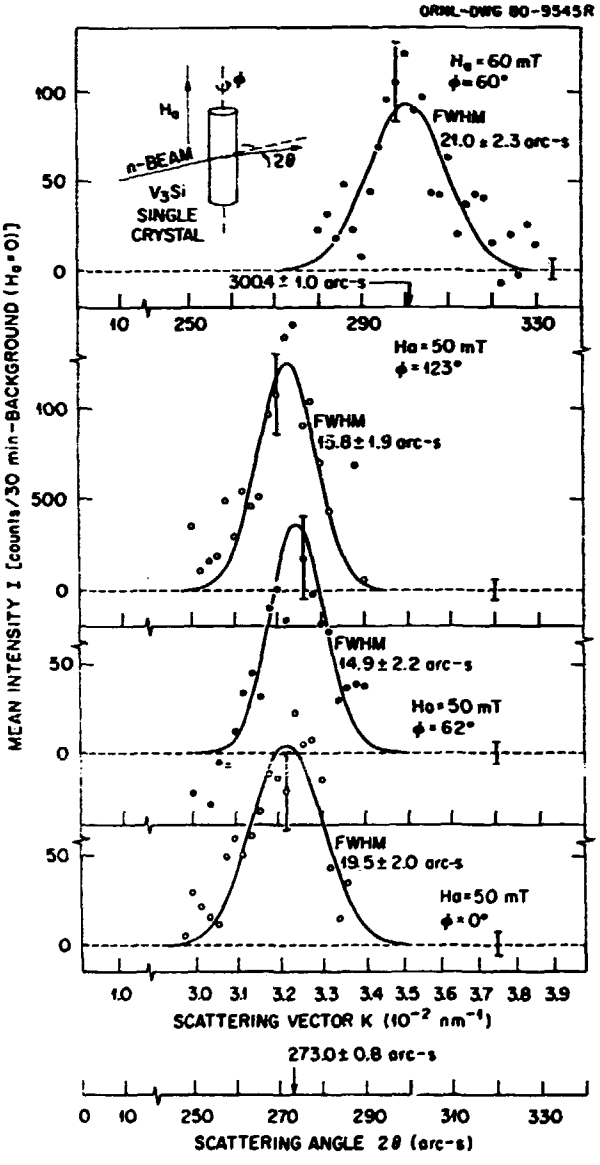

Fig. 4.12. Scattered neutron intensity as a function of the scattering angle 2θ or scattering vector K. The data are presented as the difference between averages of at least two separate runs each with the field applied and with it removed in order to subtract the background (dashed line). Total count rates per 30 min were about 1000. The inset shows the experimental geometry used, where ϕ is the azimuthal rotation angle of the sample about a vertical axis.

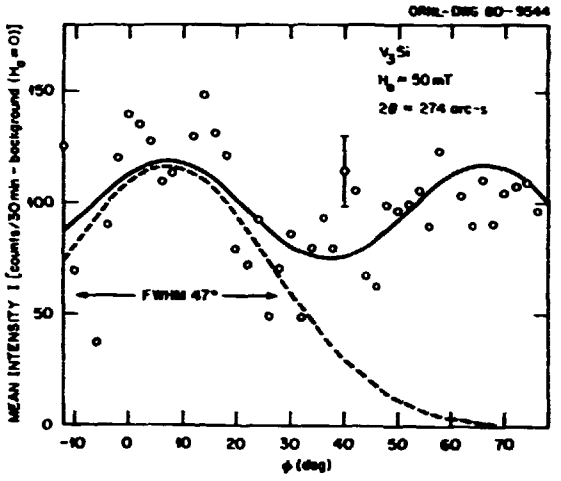

Fig. 4.13. Scattered neutron intensity as a function of the azimuthal orientation of the sample, for 2θ fixed at the position of a diffraction peak. The solid curve is the best fit of expected intensity from a Gaussian distribution of mosaic FLL blocks. The dashed curve represents that distribution function (in arbitrary units).

2. The structure is made up of very small, perfect mosaic FLL domains, and the observed peak widths are caused by block-size effects.

3. There is a *d*-spacing distribution within the mosaic blocks that, in possible combination with 1 and 2, gives rise to the observed broadening.

4. The FLL symmetry within the blocks is such that two separate Bragg reflections are superposed to broaden the diffraction peak of the "powder" pattern.

5. The structure is an amorphous array of flux lines.

Although it is difficult to separate out any combined effects of the above phenomena 1–4, it is reasonable to preclude the fifth possibility by arguing that 1 or 2 alone could reasonably explain the observed data. By assuming perfect, delta-function diffraction response at the double-perfect crystals (as an approximation to the observed intrinsic ~4 arc-s resolution), one can obtain a simple expression for the expected additional 2θ-peak broadening due to effect 1. In the limit of very large mosaic spread, the relative 2θ-peak width is given by

$$\Delta 2\theta/2\theta = \Delta\theta_h \cot\theta_B , \qquad (1)$$

where θ_B is the Bragg angle at the silicon crystals and $\Delta\theta_h$ is the horizontal angular collimation of the incident beam. Equation (1) yields the result $\Delta 2\theta/2\theta \cong 5\%$, very close to the observed dispersion, 6%.

Likewise, the second (block-size-broadening) effect alone could explain the observations, provided that the imagined cylindrical FLL mosaic blocks possess a mean diameter of ~3000 nm, resulting in a density of $\sim 1.5 \times 10^5$ mm^{-2}. This density is not unreasonable, because one expects the material to be

composed of about 2% second-phase precipitates that can act as pinning centers for the FLL domains.

Thus, phenomenon *1*, along with possible small effects arising from 2, 3, and 4, leads one to conclude that the flux-line structure in the present V_3Si sample is one of a highly mosaic lattice.

Some limits may be assigned to the allowed symmetry of the FLL within the mosaic domains by considering the flux density implied by the observed scattering angles. Because of flux quantization, the mean flux density in an FLL is given by

$$B = \phi_0 \left(\frac{2\theta_{10}}{\lambda_n}\right)^2 f(\alpha, \beta, \gamma) . \qquad (2)$$

Here, ϕ_0 is the flux quantum, λ_n the neutron wavelength, and $f(\alpha, \beta, \gamma)$ is a function of the three angles α, β, and γ, which determine the symmetry of the FLL triangular half-cell. For a hexagonal FLL, $f = \sqrt{3}/2$; for a square it is unity.

For both the applied-field intensities of Fig. 4.12, the square FLL symmetry can be eliminated, because it would result in a flux density greater than the applied field. As mentioned above, this result is impossible because of the technique used to grow the FLL. On the other hand, a hexagonal FLL symmetry yields $B = 46.8$ mT and $B = 56.1$ mT for $H_a = 50$ mT and $H_a = 60$ mT, respectively, values that are understandable in terms of the tendency for flux to be expelled from the specimen during cooldown.

It is possible to compare the observed diffracted intensity in the (10) peak to that calculated from fundamental superconducting parameters for V_3Si. The expected integrated intensity, I_{10}, normalized to the incident neutron flux, I_0, is given by

$$\frac{I_{10}}{I_0} = \left(\frac{\gamma}{4}\right)^2 \frac{\lambda_n^2 (B/\phi_0)^{3/2} (\sqrt{3}/2)^{1/2}}{(1 + 8\pi^2 \lambda^2 B/\sqrt{3}\phi_0)^2} . \qquad (3)$$

Here, γ is the gyromagnetic ratio for the neutron, and λ is the penetration depth for V_3Si at 4.2 K. From literature values[2,3] of critical-field measurements, we estimate $\lambda \cong 90$ nm. Equation (3) then yields the results $I_{10}/I_0 \cong 1.4 \times 10^{-4}$ cm^2, which compares very well with the observed normalized intensity 1.35×10^{-4} cm^2 obtained from the 2θ peaks of Fig. 4.12 and the observed direct-beam flux behind the sample.

These preliminary studies reveal that the FLL conformation is not well correlated with the real CL. We believe that this is caused by a lack of sufficient homogeneity in the V_3Si single crystal used here and the attendant effects of flux pinning by second-phase precipitates. In cooperation with the Crystal Growth and Characterization Group, efforts are being made to obtain well-characterized, homogeneous samples in order to answer the fundamentally important questions regarding FLL real crystal anisotropic interactions.

---

1. Consultant from Physics Laboratory and Research Institute for Materials, Nijmegen, The Netherlands.
2. S. Foner and E. S. McNiff, Jr., *Appl. Phys. Lett.* **32**, 122 (1978).
3. Y. Muto et al., *J. Low Temp. Phys.* **34**, 617 (1979).

SINGLE-CRYSTAL FLL IN TaN

D. K. Christen H. W. Weber[1]
Y. K. Chang

The TaN system is an interesting one from the standpoint of superconductivity. By addition of N into interstitial solution, Ta can be made to transform from an intrinsic type I superconductor to one of type II behavior below a certain temperature T^* (less than the transition temperature T_c), which depends on the particular N concentration. Moreover, in single-crystal materials for T near to T^*, it is possible to observe an anisotropy-induced conversion from type I to type II magnetic behavior as a function of the crystalline axis along which the applied field is directed.[2]

Preliminary studies have been conducted to observe FLLs in the type II regime of these materials by means of small-angle neutron diffraction. An 8.5-mm-diam, single-crystal sphere of Ta was loaded with N to two different concentrations ($C_N = 0.115$ at. % and $C_N = 0.19$ at. %) by heat treatment in a low-pressure N atmosphere.

At the larger concentration, the sample was type II at all temperatures up to T_c; at the lower concentration, the sample was transforming. We were able to observe a well-defined single-crystal FLL in the type II regime for both concentrations. The FLL perfection, defined in terms of the rocking-curve widths, was found to be systematically better by a few percent for the sample having the lower N content. For the case where the field was applied parallel to a (110) crystal axis, the observed isosceles triangular half-cells of the FLL possessed symmetries bracketing that which we had previously observed in pure Nb under comparable conditions.[3] These features may provide a test for the current theories of anisotropy and its relation to the FLL symmetry.

Attempts were made to observe the FLL at T^* for H // ⟨111⟩, an orientation of type II behavior. The preliminary results, however, were unsuccessful, most likely because of the very small FLL scattering-form factor and limitations posed by the instrument signal-to-noise.

1. 1979 summer research participant from Atominstitut der Österreischen Universitäten, Vienna, Austria.
2. H. W. Weber, J. F. Sporne, and E. Seidl, *Phys. Rev. Lett.* 41, 1502 (1978).
3. D. K. Christen et al., *Phys. Rev. B* 21, 102 (1980).

FLUX-LINE PINNING BY SMALL NITRIDE PRECIPITATES IN Nb[1]

H. R. Kerchner D. K. Christen
J. Narayan S. T. Sekula

The magnetic hysteresis of superconducting Nb single crystals containing ≤100-Å-diam nitride precipitates was investigated by ac- and dc-magnetization measurements. Introducing the precipitates into the samples produced only an insignificant change in the critical-current density J_c, except near the critical fields H_{c1} and H_{c2}. The samples trapped flux when the applied field was reduced to zero from above H_{c1}, and they exhibited dramatic peaks in J_c for applied fields within 3% of the upper critical field H_{c2}. Neither effect was present before the introduction of the precipitates.

The experimental method and preliminary results have been described previously.[2] During the present reporting period, the temperature dependence of the peak width was measured and a detailed comparison was made between the critical-state observations and theory. The comparison indicates that the conventional theory describes this system quite well. In particular, the appearance of the peaks near H_{c2} in the absence of significant change in J_c at slightly lower fields is clear evidence of a threshold effect.

From the images obtained by TEM under different diffraction conditions, the strain distribution was found to have the symmetry properties corresponding to those of a platelet, coherent precipitate. From the comparison of observed black-white images with the calculated contrast, the cumulative displacement of the crystal planes across the precipitate-matrix interface was estimated to be 7 Å. The size distribution was narrowly peaked at about 80 Å diam, with no precipitates observed having larger than 130 Å diam.

Of the elementary interactions that can be estimated between a flux line and a precipitate, the dominant one in our case is the second-order elastic interaction,[3] which arises from the spatial variation of the elastic moduli C_{ij} of the superconducting material in the mixed state. Because the strains associated with each precipitate fall off more rapidly than does the spatial variation of the moduli (i.e., the flux-line spacing), ΔC_{ij} may be removed from the integral expression for the interaction energy I. Then

$$I = \sum_{ij=1}^{6} \Delta C_{ij}\, \partial W / \partial C_{ij} ,$$

where W is the elastic energy associated with the precipitate. The TEM results indicated that the strains and hence W could be well approximated by those associated with a prismatic dislocation loop with a Burgers vector of 7 Å. For a dislocation loop, W is given by a closed expression,[4] which can easily be differentiated with respect to each modulus. The interaction energy I for either a small loop or a small coherent precipitate arises mainly from the spatial variation of the shear modulus C_{44}, and it is substantially larger than previous estimates of the first-order elastic interaction and of the second-order interaction, considering only the variation of the bulk modulus.[5]

In the conventional statistical summation theory, weakly interacting defects can contribute to J_c only in the field ranges near H_{c1} and H_{c2}, where they can produce an elastic instability in the FLL. Using our estimate of the elementary interaction I and Schmucker and Brandt's theoretical results[6] for the FLL deformation caused by a point force, we can estimate the field range ΔH near H_{c2}, where the precipitates should contribute to J_c. The observed peak width near H_{c2} is compared directly with this calculated field range ΔH in Fig. 4.14. There, measurements of $\Delta H / H_{c2}$ for one sample obtained at various temperatures are plotted as a function of H_{c2}. The data agree with the theory as accurately as can be expected from the quality of the theoretical estimates.

The statistical summation theory described elsewhere in this report[7] also predicts a peak near H_{c2}. However, the predicted peak width is less than that predicted by the conventional theory and has the opposite temperature dependence. At fields below the peak, the new theory predicts a lower J_c than the background J_c we observe in these samples with or without precipitates. The observations on this system

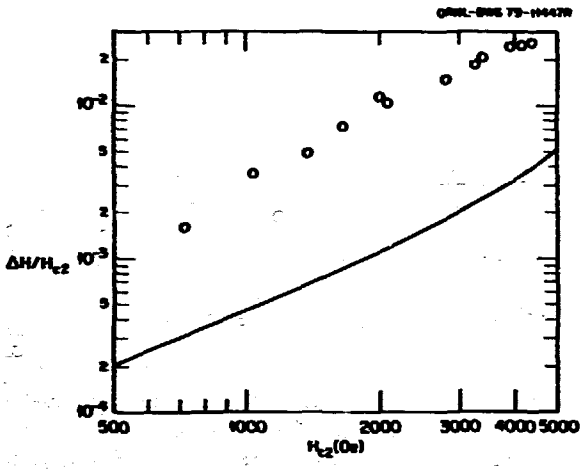

Fig. 4.14. Experimental and theoretical temperature dependence indicated by points and curve, respectively, of the reduced peak width $\Delta H/H_{c2}$.

do not contradict the new theory. Rather, this system provides a good example of a dilute array of point-like defects, to which the conventional theory applies.

1. Summary of paper: *Phys. Rev. Lett.* 44, 1146 (1980).
2. H. R. Kerchner et al., *Solid State Div. Prog. Rep., Sept. 30, 1978*, ORNL-5486, p. 141.
3. R. Labusch, *Phys. Rev.* 170, 470 (1968).
4. F. Kroupa, *Czech. J. Phys. B* 10, 284 (1960).
5. E. J. Kramer, *Philos. Mag.* 33, 331 (1976).
6. R. Schmucker and E. H. Brandt, *Phys. Status Solidi B* 79, 479 (1977).
7. H. R. Kerchner, "Theory of the Statistical Summation of Weak FL-Pinning Forces," this report.

THEORY OF THE STATISTICAL SUMMATION OF WEAK FLUX-LINE-PINNING FORCES

H. R. Kerchner

The universality of lossless current-carrying capacity of type II superconductors in the mixed state has remained a profound mystery because the conventional theory of the statistical summation of pinning forces predicts a threshold effect.[1] Many defects that interact only weakly with the FLL are not expected to contribute to the critical-current density. Although the threshold effect has recently been observed in a system of small nitride precipitates in Nb,[2] the existence of sizable critical-current densities in many other samples containing only weakly interacting defects remains unexplained. In an attempt to understand the universal observation of critical currents in type II superconductors, a theoretical investigation of the statistical summation of pinning forces has been initiated.

The threshold criterion in the conventional statistical summation theory requires the interaction between an individual defect and a flux line to be sufficiently strong to create an elastic instability in the FLL. When the interaction is not strong enough, the pinning forces caused by randomly arranged defects are of random directions and they are expected to cancel. However, the present investigation shows that a group of defects of sufficient number always produces an elastic instability in the FLL, even for vanishingly small individual flux-line-defect interactions. To see this result, one must observe that the force exerted by a group of random defects increases in proportion to the square root of their number and therefore in proportion to the square root of the volume containing them. In contrast, the effective spring constant describing the restoring force on the same FLL volume increases only in proportion to the cube root of the volume. The elastic instability occurs when the derivative of the total pinning force with respect to FLL displacement becomes larger than the spring constant.

Because any coherent FLL volume larger than some critical volume V is unstable, the lattice must break up into small volumes V (of coherent lattice) that are not coherent with each other. The magnitude of the pinning force on each coherent volume V is $(nV\langle f^2\rangle)^{1/2}$ for a system of defects of number density n and mean square pinning force $\langle f^2\rangle$. In the critical state, the volume pinning-force density F becomes $F = (n\langle f^2\rangle/V)^{1/2}$.

Calculations of the expected field dependence of F have been completed for a simple model interaction. The interaction energy between a single point-like defect and the FLL is assumed to be given by the perturbation theory expression

$$\Delta E = \mu_0 H_c^2 \alpha |\psi|^2 ,$$

where H_c is the thermodynamic critical field of the material, ψ is the (unperturbed) superconducting order parameter, and α is a measure of the interaction strength with the dimensions of volume.[3] The elastic response of the FLL is characterized by wave-vector-dependent elastic moduli in the isotropic approximation.[4] Figure 4.15 illustrates the predicted dependence of F on the reduced flux density $b = B/B_{c2}$ for two values of the Ginzburg-Landau parameter κ and for several values of the dimensionless ratio $n\alpha^2/\xi^3$,

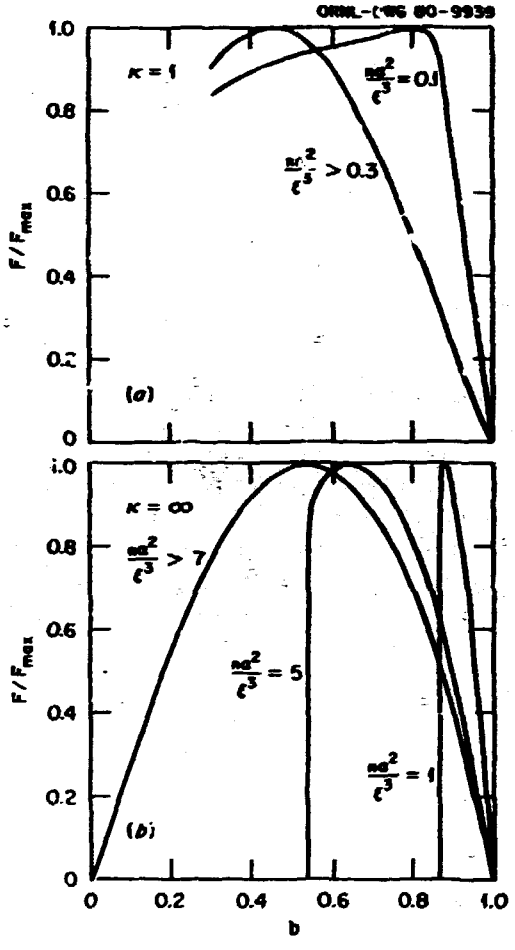

Fig. 4.15. The dependence of the pinning-force density $F = J_c B$ (reduced by its maximum value) on the reduced flux density $b = B/B_{c2}$ for several values of the parameter $n\alpha^2/\xi^3$. (*a*) Results for a superconductor with a small Ginzburg-Landau parameter κ. (*b*) Results for a superconductor with a large κ.

where ξ is the Ginzburg-Landau coherence length. When $n\alpha^2/\xi^3$ is small, F is small and nearly independent of b except near $b = 1$, where the volume V shrinks rapidly (creating a pronounced peak in F in high-κ materials) until the distortion is limited by the shear strength of the FLL. When $n\alpha^2/\xi^3$ is sufficiently large, the peak occupies the whole range of b. In that case, $F(b)$ is given by a dome-shaped curve whose shape is independent of $n\alpha^2/\xi^3$.

For many types of defects, $n\alpha^2/\xi^3$ is temperature dependent. The present theory predicts that the shape of the $F(b)$ curve should be temperature dependent when $n\alpha^2/\xi^3$ (and therefore F) is small but temperature independent when $n\alpha^2/\xi^3$ is large and $F(b)$ is large and dome shaped. Such a correlation between scaling-law behavior [i.e., temperature-independent $F(b)/F_{max}$] and a large, dome-shaped $F(b)$ is a feature of much of the experimental literature.

In principle, a number of other predictions of this theory can be compared with experimental observations. The lack of coherence between different FLL regions leads to line broadening of a diffracted neutron beam. The critical volume V may be identified with the activation volume in the theory of thermally activated flux creep.[5] The calculated distortion of the coherent FLL regions gives the "pinning penetration depth"[6] and the "depinning frequency."[7] Finally, if the theory is generalized to describe dynamic as well as static situations, one should be able to predict flux-flow noise spectra. A correct theory of the critical state should be capable of describing all of the above effects in a consistent way. At present, no other theoretical approach shows much promise of such a capability.

1. R. Labusch, *Cryst. Lattice Defects* 1, 1 (1969).
2. H. R. Kerchner et al., "Flux-Line Pinning by Small Nitride Precipitates in Nb," this report.
3. E. H. Brandt, *J. Low Temp. Phys.* 28, 263, (1977).
4. E. H. Brandt, *J. Low Temp. Phys.* 26, 709 (1977).
5. P. W. Anderson and Y. B. Kim, *Rev. Mod. Phys.* 36, 39 (1964).
6. A. M. Campbell, *J. Phys. C* 2, 1492 (1969).
7. J. I. Gittleman and B. Rosenblum, *Phys. Rev. Lett.* 16, 734 (1966).

LOW-TEMPERATURE H-ION IMPLANTATION IN Al

S. T. Sekula J. R. Thompson[1]

The occurrence of superconductivity in metastable alloys of Al and H produced by low-temperature ion implantation has been investigated. Films of Al were electron-beam evaporated onto room-temperature sapphire substrates at rates of 5–15 nm/s in bell jar pressures of $0.5–1.5 \times 10^{-4}$ Pa, using 5*N* source material. The films as prepared had residual resistance ratios, corrected for thickness effects, of ~30.

The films were mounted in a variable-temperature He cryostat[2] equipped for four-probe, electrical-resistivity measurements. By implanting H into the Al target at $T \lesssim 10$ K, AlH_x alloys could be prepared with the concentration x many orders of magnitude above the equilibrium solubility. In situ electrical measurements were used to follow the progression of sample resistance and superconducting transition temperature T_c. In work on a 300-nm film, H ions at 27 keV/amu were implanted in a layer of thickness

$2\Delta R_p \sim 120$ nm near the rear of the film (R_p, the projected range, was 240 nm). Superconducting transition temperatures were observed for ion fluences ϕ greater than 2×10^{21} ions/m^2. With increasing fluence, T_c displayed a saturating behavior that extrapolated to $T_c^{max} = 5.9$ K, as seen in Fig. 4.16. Values within 0.2 K of this were observed for a fluence of 6×10^{21} ions/m^2, corresponding to $AlH_{0.7}$. During this series of implantations, the composite sample resistivity ρ monotonically increased to $\sim 6 \times 10^{-8}$ Ω·m from an initial value of 0.2×10^{-8} Ω·m. It varied as a weak power of fluence ($\rho \sim \phi^{0.35}$) and showed no evidence of saturation.

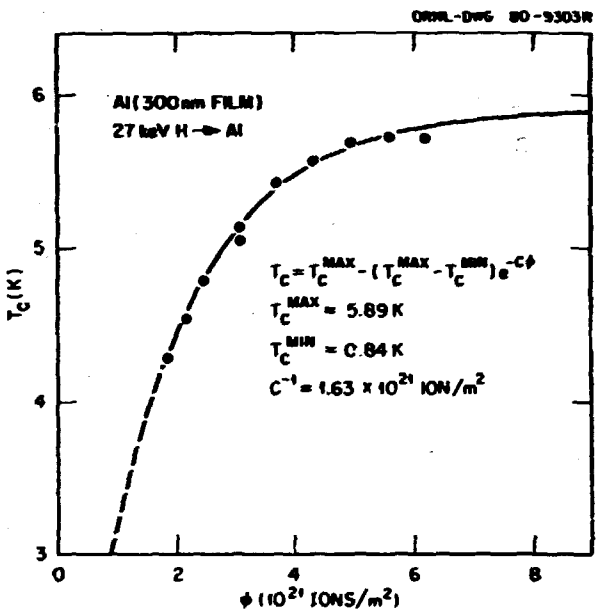

Fig. 4.16. Superconducting transition temperature T_c of Al vs H-ion fluence ϕ.

To improve the homogeneity of this 300-nm sample, a second, more shallow series of H implantations was made at 10 keV/amu. After an additional fluence of 4.0×10^{21} ions/m^2, ρ increased to 13×10^{-8} Ω·m; there was little or no change in T_c. This latter feature suggests that the superconducting coherence length in $AlH_{0.7}$ is considerably less than 120 nm, the width of the initial implantation. A final series of implantations at 10 and 27 keV/amu raised the average composition in much of the sample to AlH_2. The maximum transition temperature was unchanged, whereas ρ increased to 16.3×10^{-8} Ω·m. This resistivity is much greater than that obtained by neutron radiation damage in bulk samples or by Al ion irradiation in low-oxygen Al films.[3] It can be accounted for by the high concentration of H ions in the alloy, which provides a high density of scattering centers and may help to stabilize severe disorder in the lattice as well.

Isochronal annealing studies were performed on this as well as on a 160-nm film, for which the overall behavior was qualitatively similar. With increasing annealing temperature, both the residual resistivity and T_c decreased in a correlated manner. At first these properties were little changed, but subsequent annealing of the 300-nm film to 100 K reduced T_c to 4.4 K, whereas ρ decreased by 9%.

1. Adjunct research and development participant from the University of Tennessee, Knoxville.
2. S. T. Sekula and J. R. Thompson, "Low-Temperature Ion-Implantation Cryostat," this report.
3. P. Ziemann et al., *Z. Physik B* 35, 141 (1979).

LOW-TEMPERATURE ION IMPLANTATION CRYOSTAT

S. T. Sekula J. R. Thompson[1]

A versatile apparatus for studying materials prepared at low temperatures using ion beam techniques has been successfully interfaced with the Solid State Division ion accelerator. Features include (1) provision for variable-temperature operation from 3–300 K; (2) long, economical holding time for liquid He, with substantial refrigeration power; (3) ion beam accessibility to the material under study, with beam-defining apertures and electrodes; (4) electrical resistivity measurements; and (5) accurate positioning of the target with respect to implantation and analyzing ion beam directions.

Two major design considerations for the apparatus, reliability and cleanliness, were constraints arising from usage with the accelerator. Both requirements have been met. In operation the system has proved to be quite reliable, with six to ten experimental runs successfully completed. Also, considerable care in selecting construction materials and in assembly resulted in desired compatibility with the vacuum requirements of the accelerator system. This feature was important, because there is a single, common vacuum for the entire integrated system. With the cryostat at room temperature, overnight pumping of the substantial volume gave $P \sim 2.5 \times 10^{-5}$ Pa; cooling the cryostat to He temperature reduced the pressure by about one order

of magnitude, near or below the base pressure of the empty chamber.

The versatility of the apparatus is illustrated by the variety of studies for which it has been used. Experiments have included low-temperature ion implantations for production of metastable superconducting alloys,[2] thermal-annealing studies of the alloys produced, and ion-mixing investigations.[3] The provisions for sample elevation and rotation about the vertical axis, essential in this work, have functioned satisfactorily.

Several refinements have been incorporated into the cryostat design. One is a variable thermal coupling between the He bath and target block. This facilitates the variable-temperature operation as required in low-temperature annealing studies. A second improvement is a redesigned thermal radiation shield that also carries beam-defining electrodes and a solenoid-operated shutter. The latter device is to reduce further thermal radiation incident upon the sample and to allow high-precision measurements.

Overall, the ion implantation cryostat has proven to be a versatile and reliable apparatus for studies using ion beams at low temperatures and is considered fully operational.

---

1. Adjunct research and development participant from the University of Tennessee, Knoxville.
2. S. T. Sekula and J. R. Thompson, "Low-Temperature H-Ion Implantation in Al," this report.
3. B. R. Appleton et al., "Ion Beam Mixing and Pulsed Laser Annealing," this report.

HIGH TEMPERATURE CONDUCTIVITY OF INSULATING MATERIALS

ELECTRICAL PROPERTIES OF SPINEL

R. A. Weeks J. Woosley[1]
E. Sonder C. Wood[1]

Spinels have been suggested as liner materials for MHD channels because of the compatibility of $MgAl_2O_4$ spinel, which is a good insulator, with Fe-containing spinels, which can be tailored by varying the Fe content to have desirable electrical conductivities.[2] We have measured electrical properties of pure $MgAl_2O_4$ and material containing small amounts of Fe. Results include the following.

Electrical Conductivity of Pure and Fe-Doped $MgAl_2O_4$ Spinel[3]

The electrical conductivity of nominally pure and Fe-doped $MgAl_2O_4$ spinel has been measured over the temperature range 700–2000 K. The results for pure stoichiometric spinel can be fitted by exponential expressions with different activation-energy parameters in three temperature ranges. The conductivity of a sample containing 0.1% Fe is the same as that of pure samples when the Fe is in the Fe^{2+} form; the conductivity increases by approximately a factor of 2 when the Fe is in the Fe^{3+} form. The results are consistent with ionic conduction caused by motion of cation vacancies.

Photoelectric Effects in $MgAl_2O_4$ Spinel[4]

The electronic and transport properties of $MgAl_2O_4$ spinel have been investigated photoelectrically. Photoemission of holes and electrons into spinel from metal contacts (Pt, Au, Ta, Mo, and Cu) has been used to determine barrier heights. From this information as well as from vacuum UV photoconductivity data, we have obtained the following energy band parameters: the Fermi level lies ~3 eV below the bottom of the conduction band, which in turn is located ~2 eV below the vacuum level; the band gap is ~9 eV. Photoemission was not observed from graphite electrodes, which form ohmic contacts. Electron, neutron, or γ irradiation produced three photoconductivity bands of half widths of ~0.5 eV with peaks at 4.5, 5.0, and 5.5 eV. The three bands, equally spaced in energy, may be associated with the same center. In Fig. 4.17 the photoconductivity spectrum of one such sample is compared with the absorption spectrum of neutron- and electron-irradiated spinel samples. It is clear that the shape of the photoconductivity spectrum has no correspondence with the absorption at 5.4 eV, indicating that

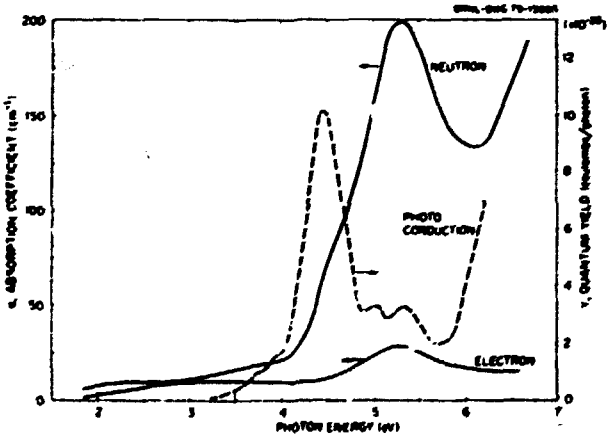

Fig. 4.17. Photoconductivity of nominally pure $MgAl_2O_4$ spinel as a function of the energy of incident light.

radiation-produced F centers are not an important source of current carriers.

Thermoelectric Power Measurements

A light-pulse technique has been developed for the measurement of Seebeck coefficients of high-resistivity materials. Measurements can be made on materials with resistivities up to 10^{12} Ω·cm and, with the present apparatus, at temperatures up to 1200°C. A primary advantage of this technique is in the elimination of spurious voltages. It has been applied to the measurement of the thermoelectric properties of single-crystal spinel, $MgAl_2O_4$. Between 500 and 1200°C the charge carriers are positive; the magnitude of the Seebeck coefficient ranges from 1.2 mV/°C at 500°C to 0.1 mV/°C at 1200°C.

1. Northern Illinois University, DeKalb.
2. T. O. Mason et al., p. 77 in *Proceedings of Sixth International Conference on Magneto-hydro-dynamic Electrical Power Generation*, vol. II, CONF-75061-P2, U.S. Department of Commerce, Washington, D.C., 1975.
3. R. A. Weeks and E. Sonder, *J. Am. Ceram. Soc.* 63, 75 (1980).
4. J. D. Woosley et al., *Phys. Rev. B* (in press).

ELECTRICAL BREAKDOWN AT HIGH TEMPERATURE

E. Sonder R. A. Weeks

As has been demonstrated, some insulating oxides such as MgO break down when subjected to moderate electric fields for lengthy periods of time at high temperature.[1] A calculation performed for MgO (ref. 2) predicts that thermal runaway will occur for normal values of thermal conductivity and electrical properties of MgO, if the temperature is raised to approximately 2000°C. The fact that we are able to observe instabilities at temperatures as low as 1200°C indicates that either a process other than thermal runaway produces breakdown or that large changes in the electrical and/or thermal properties of MgO are produced by moderate electric fields, so that thermal runaway can proceed.

It is conceivable that at 1200°C a sample might be heated far above the furnace temperature by the electric current flowing through it. The thermal conductivity of MgO is sufficiently high to prevent large gradients of temperature to be supported within the sample. To determine whether the whole sample could rise much above the furnace temperature, a thermocouple was embedded in a sample to measure the temperature difference between the sample and the furnace. It was found that the temperature rise of the sample was approximately 3 K/W, which corresponds to a rise of at most 50°C at currents at which thermal instabilities arise.

It is rather difficult to obtain information concerning the temperature or electric-field dependence of breakdown, because incubation times of 100 h are typical and samples can only be used once. We have found that at applied voltages too small for breakdown to occur, the initial current flow decreases monotonically, presumably because of polarization. At higher voltages the initial (polarization) decrease changes to an increase after approximately 1 min. On the assumption that this increase in current is a necessary condition for incubating and eventually producing breakdown, we have measured the temperature dependence of the voltage necessary to overcome this initial polarization. The upper curves of Fig. 4.18 indicate the temperature depen-

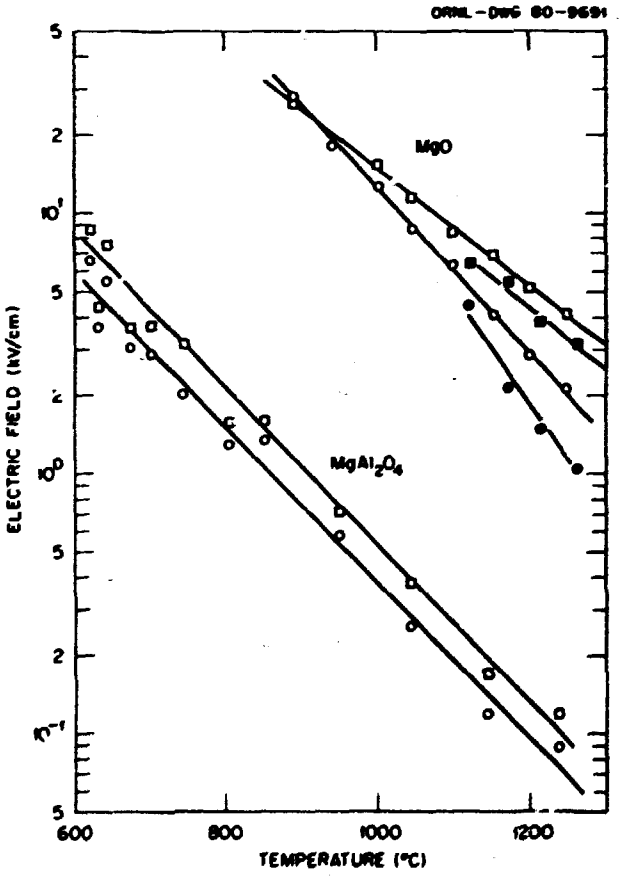

Fig. 4.18. Temperature dependence of the electric field necessary to overcome initial polarization in MgO and $MgAl_2O_4$.

dence of the electric field necessary to cause the current in an MgO sample to increase after 1 min. The data show that there is a large temperature dependence between 900 and 1300°C. Also, the data indicate that the sample is not symmetric for a reversal of the electric-field polarity. The open circles and squares indicate opposite polarities of applied field. Moreover, the filled squares and circles illustrate that, after many cycles of increasing the voltage in alternating polarities, the increase in current after 1 min occurs at lower values of the electric field. If the temperature dependence of the initial polarization reflects that of the actual breakdown, then it becomes apparent that a field an order of magnitude greater than that used at 1200°C is necessary to cause breakdown at temperatures below 900°C.

Figure 4.18 also includes similar data for $MgAl_2O_4$, which has been observed to break down at 1200°C with much lower electric fields and in a shorter time than MgO. As one might expect, the electric field necessary to overcome the initial polarization is less than that for MgO by more than an order of magnitude. The temperature dependence is similar, as is the behavior caused by changes in polarity, as indicated by the open circles and squares in Fig. 4.18 pertaining to $MgAl_2O_4$.

Nominally pure crystals of MgO and $MgAl_2O_4$ subjected to electric-field treatments at temperatures $\geq$1050°C develop dark streaks extending from the negative electrode toward the positive electrode. Electron-magnetic-resonance spectra of MgO with such dark streaks exhibit components produced by ferrimagnetic resonance. In MgO crystals that contained as little as 150 ppm Fe, the magnetic field at which these components are found is a function of the orientation of the crystal with respect to the applied laboratory field. This orientation dependence is shown in Fig. 4.19.

If it is assumed that these ferrimagnetic components are caused by magnetic particles in the form of platelets, then the direction of the magnetization of the platelets, $H_{particle}$, will lie in the plane of the platelets. When the applied laboratory field is parallel to the surface of the platelets, the field, H_{res}, required for resonance is

$$H_{res} = \frac{h\nu}{g\beta} - H_{particle} ,$$

where we assume that $g = 2$, and ν and β are the spectrometer frequency (35 GHz) and the Bohr magneton, respectively. The internal field of the particle $H_{particle} = 4\pi M_s$, where M_s is the saturation magnetization of the particle. As the applied field is rotated out of the plane of a particle, the condition for resonance will still be the sum of the component of the applied field in the plane of the platelet and its internal field. This is illustrated in the Fig. 4.19 inset. The curve shown in Fig. 4.19 is calculated

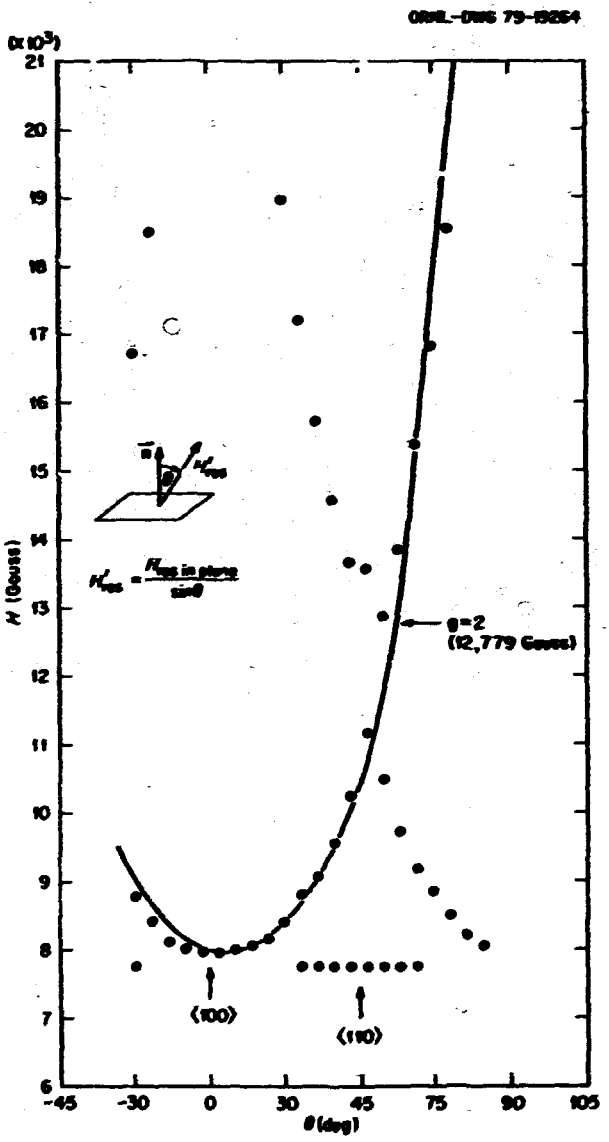

Fig. 4.19. Orientation dependence of the ferrimagnetic resonance spectra of electric-field-treated, nominally pure MgO crystals. The laboratory magnetic field was rotated about a ⟨100⟩ crystal direction. Two principal crystallographic directions are indicated by arrows at the bottom of the figure. The fields and angles at which spectral components were observed are denoted by dots. The curve is fitted to one of the spectral components at the minimum field at which it was observed.

on this basis. The fit between the observed fields for resonance and the curve is quite good, giving support to the assumption that ferrimagnetic particles are in the form of platelets. Because the field was rotated about a ⟨100⟩ crystal direction, the platelets that produce the spectrum from which these data are obtained are congruent with the crystal [100] planes. The spectral components of dark-streak material from crystals containing ~2000 ppm of Fe are not as well resolved as the components in the spectra of nominally pure crystals. There is a relatively intense component in the region of 1.27 T which exhibits only a slight orientation dependence. The components that have the orientation dependence shown in Fig. 4.19 are relatively much weaker and decrease in amplitude as they move to higher fields.

Electron microscopy of the dark-streak material from crystals containing ~2000 ppm Fe has shown the presence of particles of Fe metal, FeO, and $MgFe_2O_4$.[3] These particles have not been detected in the dark-streak material of the nominally pure crystals. On the basis of similar spectral components in the two types of dark-streak material, we assume that the components in the nominally pure material are caused by one of the precipitate types observed in the more heavily doped samples. From the difference between the field $H_0 = h\nu/g\beta$ and the minimum field at which resonance is observed, $H \approx 0.8$ T, we estimate that $H_{particle} \approx 0.4$ T. For Fe_{metal}, $4\pi M_s = 2.18$ T; for $MgFe_2O_4$, $4\pi M_s = 0.14$ T.[4] Thus, *it is not possible to determine whether spectral components of the particles are caused by Fe metal or* $MgFe_2O_4$ or by some other kind of magnetic compounds.

Spectral components of dark-streak material from a $MgAl_2O_4$ crystal containing 800 ppm Fe were also ferrimagnetic. However, the orientation dependence of these components was negligible as compared with those in the MgO material. These components were centered at a field of 1.27 T ($g = 2$) for $\nu \approx 35$ GHz. Because of this negligible orientation dependence, we tentatively attribute these components to particles with approximately spherical shapes.

1. E. Sonder et al., *J. Appl. Phys.* 49, 5971 (1978).
2. F. Modine, *Solid State Div. Prog. Rep., Sept. 30, 1978*, ORNL-5486, p. 125.
3. J. Narayan et al., *Solid State Div. Prog. Rep., Sept. 30, 1978*, ORNL-5486, p. 128.
4. *AIP Handbook*, pp. 5-208 and 5-211, McGraw-Hill, New York, 1957.

ELECTRICAL CONDUCTIVITIES AT ELEVATED TEMPERATURES OF MgO SINGLE CRYSTALS DOPED WITH Fe, Cr, Ni, AND Li[1]

R. A. Weeks E. Sonder

Electrical conductivities of MgO single crystals doped with Fe, Ni, Cr, and Li up to concentrations of ≤2500 μg/g have been measured over a 900–1850 K temperature range. The conductivities of the transition metal–doped samples fell slightly outside the range of values reported for nominally pure crystals (total impurity concentrations ≤500 μg/g); the conductivity of Li-doped MgO was approximately two orders of magnitude higher. Treatment of Fe- and Cr-doped samples at 1500–1850 K in CO gas caused the ratio of divalent to trivalent impurity to increase greatly for MgO:Fe and very little for MgO:Cr. The conductivity, on the other hand, changed little for MgO:Fe and increased by approximately a factor of 3 for MgO:Cr. It is concluded that the vacancies that charge compensate for the trivalent transition metal ions are not the predominant carriers of electric current in MgO below 1850 K.

1. Summary of paper: *Revue Internationale des Hautes Temperatures et des Refractaires* (in press).

EFFECTS OF ELECTRIC FIELDS ON THE CONDUCTIVITY OF Y_2O_3 SINGLE CRYSTALS

R. A. Weeks L. A. Boatner
E. Sonder M. M. Abraham

Moderate electric fields applied to single crystals of MgO and $MgAl_2O_4$ at temperatures ≥1000°C produce large increases in electrical conductivities. It has been suggested[1] that a fraction of the charge carriers in these materials is ionic and that the increases in conductivity may be related to ionic charge transport. If this suggestion has validity, then *in an oxide in which the charge carriers are electronic, moderate electric fields would not induce changes in* conductivity. One such oxide is Y_2O_3. Tallan and Vest[2] have found that at temperatures ≥1200°C the conductivity of Y_2O_3 is "pure electronic." We have measured the conductivity of a single crystal of Y_2O_3 as a function of electric-field treatments at ~1200°C to determine if the temperature dependence of the conductivity is altered by such treatments.

The crystals were grown by the arc-fusion technique. Rectangular 1 × 1 × 0.3 cm parallelepipeds were cut from a boule and prepared for measurements as described elsewhere.[1] Measurements of dc conductivity were made with a three-electrode system. The results of the measurements are shown in Fig. 4.20. The conductivity of the as-received sample showed only a slight temperature dependence between 500 and 1000°C. Above 1000°C, the rate of increase of conductivity with temperature was greater. After this initial measurement, a field of 450 V cm^{-1} was applied. After 40 h, a fourfold decrease in conductivity was measured and the low-temperature (<900°C) conductivity decreased by more than two orders of magnitude.

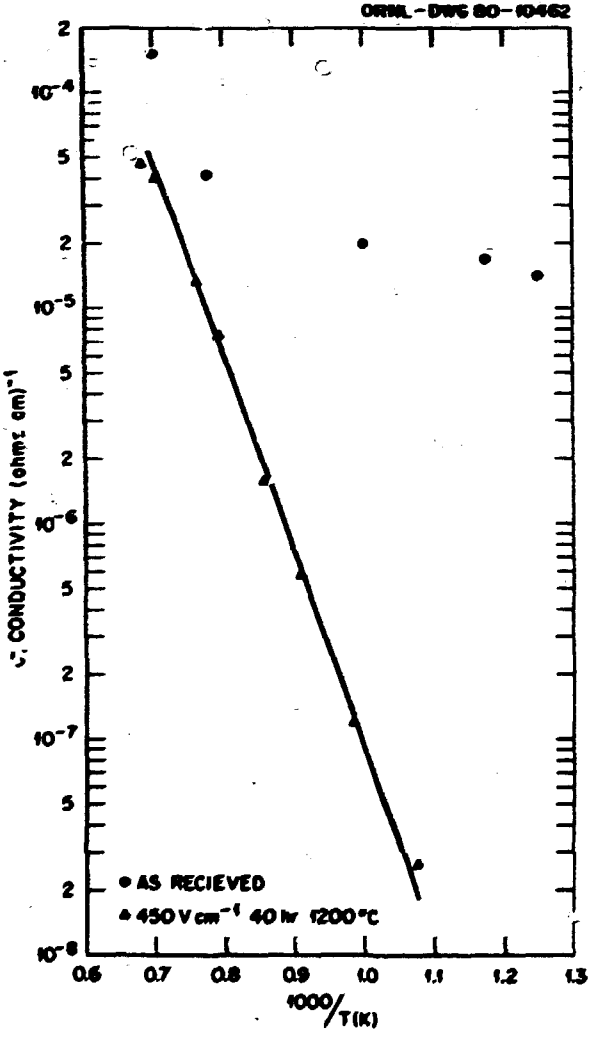

Fig. 4.20. Temperature dependence of electrical conductivity of an untreated Y_2O_3 crystal and one subjected to an electric field of 450 V/cm for 40 h at 1200°C.

As shown in Fig. 4.20, the conductivity data after the treatments agree with the function $\ln \sigma = a + b/kT$ over the range of temperature in which measurements were made. The slope of the curve is 1.8 eV, a value in reasonable agreement with that reported by Tallan and Vest[2] for the 1200–1600°C range.

The single crystals, as received, had a black coloration and were opaque at a thickness ≥0.1 cm. After the field treatment described above, the treated crystal was white, but still opaque.

The initial decrease in the conductivity of Y_2O_3 crystals with electric-field treatment is similar to that observed in MgO crystals. However, the subsequent changes in conductivity differ from those observed in MgO. Up to at least the total time of electric-field treatment (76 h), there was no indication of the thermal-electric breakdown that has been observed in MgO and $MgAl_2O_4$. The decoloration of the Y_2O_3 crystal also indicates that the changes produced by electric-field treatments differ from those observed in MgO and $MgAl_2O_4$. In those materials, the electric-field treatment produced a darkening of treated samples.

One of the significant effects of the electric-field treatment on the conductivity was the extension of the high-temperature (1200–1600°C) conductivity processes observed by Tallan and Vest[2] to lower temperatures. The treatment apparently removed from the sample charge carriers that provide a large low-temperature conductivity. These carriers may be responsible for the black coloration.

1. E. Sonder et al., *J. Appl. Phys.* **49**, 5971 (1978).
2. N. M. Tallan and R. W. Vest, *J. Am. Ceram. Soc.* **49**, 401 (1966).

CURRENT VOLTAGE CHARACTERISTICS OF Li-DOPED MgO OXIDIZED AT ELEVATED TEMPERATURES[1]

Y. Chen J. L. Boldú[2]
M. M. Abraham V. M. Orera[3]

During growth of Li-doped MgO crystals by the arc-fusion technique, the crystals are generally subjected to a reducing atmosphere under the electric arc of graphite rods. As a result, most of the Li coagulates into Li_2O precipitates.[4] Upon oxidation of these crystals at elevated temperatures, $[Li]^0$ centers (substitutional Li^+O^- complexes) are produced. The stability of these thermochemically generated $[Li]^0$

centers, as opposed to unstable ones induced by ionizing radiation at low temperatures, is attributed to hopping of holes in a region of high $[Li]^0$ concentration (called a microgalaxy), which is caused by the dissolution of Li from a Li_2O precipitate. Therefore, these regions should be *p*-type semiconducting; the greater the $[Li]^0$ concentration, the higher the conductivity.[5]

A characteristic feature exhibited by crystals containing $[Li]^0$ centers is that the current density as a function of electric field (*I-E*) is nonlinear but is symmetric for positive and negative bias. There are two regimes to a plot of the relationship. At small electric fields, the effective conductivity is small and the current density is caused primarily by polarization effects. At higher fields the curves become more linear, and the current is attributed to field-assisted sweeping (tunneling) of holes between neighboring microgalaxies. If these microgalaxies occur in the vicinity of dislocations, as polarization studies and $[Li]^0$ decoration along slip planes seem to suggest, then the internal electric fields can reach $\sim 10^5$ V cm^{-1} for external fields of 10^2–10^3 V cm^{-1}.

The measured *I-E* characteristics are different for different oxidation temperatures. Typical current-field dependence for three different temperatures is shown in Fig. 4.21. To elucidate the contrasting shape of the curves rather than the magnitude of the current density, the normalized current I/I_{2500}, where I_{2500} is the current at 2500 V/cm, is plotted. As the oxidation temperature increases, the slope begins to rise at lower fields. The linear portion of the 1250-, 1450-, and 1550-K curves extrapolates to zero current

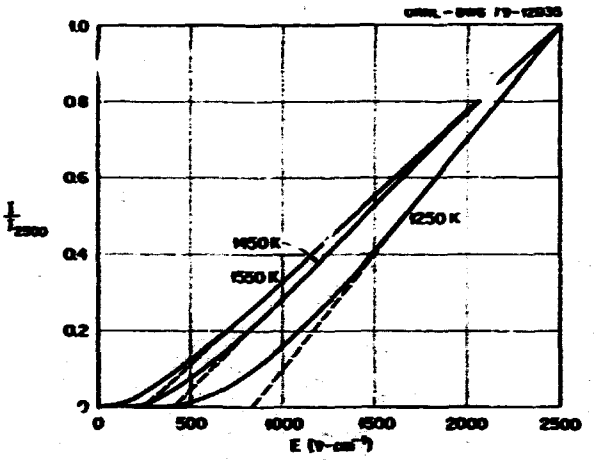

Fig. 4.21. Normalized current density vs electric field for samples heated in flowing O for 5 min.

at ~800, 400, and 300 V/cm, respectively. These observations suggest that for higher oxidation temperatures, hole tunneling proceeds at lower fields. We conclude that the effective dimensions of the dielectric medium between the semiconducting inclusions diminish with increasing temperatures.

---

1. Summary of paper: *Journal de Physique* (in press).
2. Guest scientist from Instituto de Fisica, U.N.A.M., Mexico, D.F.
3. Guest scientist from University of Zaragoza, Zaragoza, Spain.
4. J. Narayan et al., *Philos. Mag.* 38, 747 (1978).
5. Y. Chen et al., *Solid State Commun.* 33, 441 (1980).

5. Neutron Scattering

The objective of the Neutron Scattering Program continues to be the study of the structure and dynamics of condensed matter on a microscopic level. Much of the information obtained through neutron scattering is unique, in that it cannot be obtained through other experimental techniques, and it is important, in that it provides fundamental details of structures and of atomic interactions. Such information is essential for increasing our knowledge of the solid state and in providing insight to, and guidance for, the solution of our long-range energy-related materials problems.

We are in a period of expansion in terms of the total neutron scattering capability at ORNL and of diversity in terms of sponsors and users of the facilities. A major new facility is nearing completion at the HFIR. This is the 30-m SANS instrument, funded by NSF as part of the National Center for Small-Angle Scattering Research established at ORNL under a joint agreement between NSF and DOE. The three Ames Laboratory instruments are now in routine operation at the ORR. Through the efforts of DOE, we are engaged in preliminary negotiations with the government of Japan to establish a United States-Japan Cooperative Program on Neutron Scattering; this program would involve the construction of one or two new instruments at the HFIR, to be funded by the Japanese. Plans have been initiated to start a more formal users' program that will make our facilities more accessible to university and industrial scientists within the United States. Of course, until this program has been established, our informal programs for visitors will continue to be active. During the period of this report, the ORNL neutron scattering facilities have been used by about 35 scientists from other organizations, many of whom have paid several visits to the Laboratory.

In the SANS research, several very promising investigations have been initiated at the 5-m instrument at the ORR. A combined neutron and x-ray study is aimed at characterizing the pore size distribution in oil shales, both the total distribution of pores and the distribution of oil-bearing pores. In collaboration with members of the Chemistry Division, the small-angle scattering technique has been used to measure molecular weights of coal dissolved in pyridine. The SANS technique has also been used in such diverse studies as compatibility of polymer blends, irradiation-produced voids in metals, decomposition of metal alloys and magnetic clusters in spin glass materials. We anticipate that all these areas of research will flourish when the 30-m instrument at the HFIR is in operation.

Our traditional activity in the field of lattice dynamics continues, but perhaps the emphasis has shifted toward studies of anomalous behavior. An excellent example is the case of α-U. An earlier study of the phonon dispersion curves showed a pronounced dip in one of the branches. Studies of the temperature dependence of this branch have

demonstrated that a periodic lattice distortion results from the condensation of this soft phonon. Other examples of anomalous behavior that have been studied during this reporting period are soft phonons in Tc, the origin of the Verwey transition in magnetite, invar alloys of the 3d series, and the mixed-valence material CeSn$_3$.

In the area of magnetic scattering, there has been a resurgence of activity on magnetic structures, prompted by the desire to understand reentrant superconductors and by recent theoretical work on the complex magnetic structure of Nd. Initial work on the magnetic excitation spectra of Er in the sinusoidally modulated phase has been performed. Conventional spin-wave theory does not apply in this case, so there is a challenging task in understanding the unusual features of the observed spectra. The existence of spin waves above the Curie temperature and the nature of the paramagnetic state are questions that have been addressed by experiments on the magnetic excitations in Gd above T_c and by polarized beam experiments on magnons in Ni.

These neutron scattering efforts have been enhanced considerably by beneficial interactions with members of the Solid State Theory Program and the Crystal Growth and Characterization Program.

SMALL-ANGLE NEUTRON SCATTERING

THE NATIONAL CENTER FOR SMALL-ANGLE SCATTERING RESEARCH

W. C. Koehler
R. W. Hendricks[1]
H. R. Child
S. P. King
J. S. Lin
G. D. Wignall

Early in 1977, a research proposal entitled "Construction and Operation of a National User-Oriented Small-Angle Scattering Facility at the Oak Ridge National Laboratory" was prepared by Wallace C. Koehler and Robert W. Hendricks for submission to the NSF. With approval from ORNL and DOE, this proposal was amended and expanded to include part-time use of existing ORNL SAXS and SANS facilities, thereby creating an NCSASR at ORNL. After the necessary reviews and site visits, the expanded proposal was accepted by the NSF; and a grant of $1.4 million was made to ORNL for a three-year period beginning January 1, 1978.

The previous progress report[2] outlined plans for the construction of the NSF-funded 30-m SANS facility and for the operation of the center. This report reviews progress made toward the implementation of those plans.

The most visible sign of progress is the partial construction of the 30-m, SANS facility at the HFIR. All major pieces of hardware, with one exception to be mentioned later, have been built or purchased; and the assembly of the system is in its final stages.

Extensive testing and tuning of the monochromator systems have been done. Among the six pairs of graphite monochromators, some crystals exhibit higher mosaic spread (0.6–0.7° FWHM) than that desired and specified. However, these were kept because they were the best available at the time of purchase. As a result of the high mosaicity, the overall efficiency of the monochromator systems is reduced; nevertheless, a very usable beam has been produced. With a 1.9- by 1.9-cm^2 slit at the monochromator end of the presample flight path and a 1.2- by 1.2-cm^2 slit at a counter 10 m away, a counting rate of 3.4×10^4 neutrons/s of Be-filtered neutrons (≅4.75 Å) is obtained. Although this rate is about a factor of 2 less than the value originally calculated, we believe that we can approach a flux of 10^5 neutrons/cm^2-s on the sample under the standard-resolution conditions by replacing the poorer crystals with better-grade material. Final testing and tuning will be deferred until the position-sensitive detector has been calibrated.

The construction of the detector, a 64- by 64-cm^2, ^{3}He-filled, position-sensitive proportional counter of the Kopp-Borkowski type, has now been completed in the Instrumentation and Controls Division and has been installed at the HFIR, where it is undergoing final testing.

A data acquisition system, based on the Mod-Comp II minicomputer, is nearly operative. This system has been adapted from that developed several years ago for use with the 10-m SAXS camera. Considerable thought and effort have gone into modifying the original software package in order to accommodate the anticipated large numbers of users of the facility. One experimenter can now collect data and a second process data simultaneously. It is expected that the instrument will be available for routine user operation on July 1, 1980.

An unfinished component of the 30-m machine is flight path shielding, which was deferred until measurements could be made to determine how much shielding was really required. It has been found experimentally that 2 in. of wood shielding rather than the originally estimated 10 in. will suffice. This shielding is essential to provide the low background and good signal-to-noise ratio necessary for a successful SANS facility. It will also provide a means of eliminating thermal gradients from the top to the bottom of the tank and the concomitant flexing of it. Plans are to install this shield in May 1980. A schematic diagram of the instrument as it will appear in early 1980 is shown in Fig. 5.1.

1. Metals and Ceramics Division, ORNL.
2. W. C. Koehler and R. W. Hendricks, *Solid State Div. Prog. Rep., Sept. 30, 1978*, ORNL-5486, p. 149.

CHARACTERIZATION OF OIL-BEARING SHALES BY SAS TECHNIQUES

G. D. Wignall W. C. Koehler
H. R. Child R. W. Hendricks[1]

Oil shales represent a large untapped petroleum reserve. The hydrocarbon material is, however,

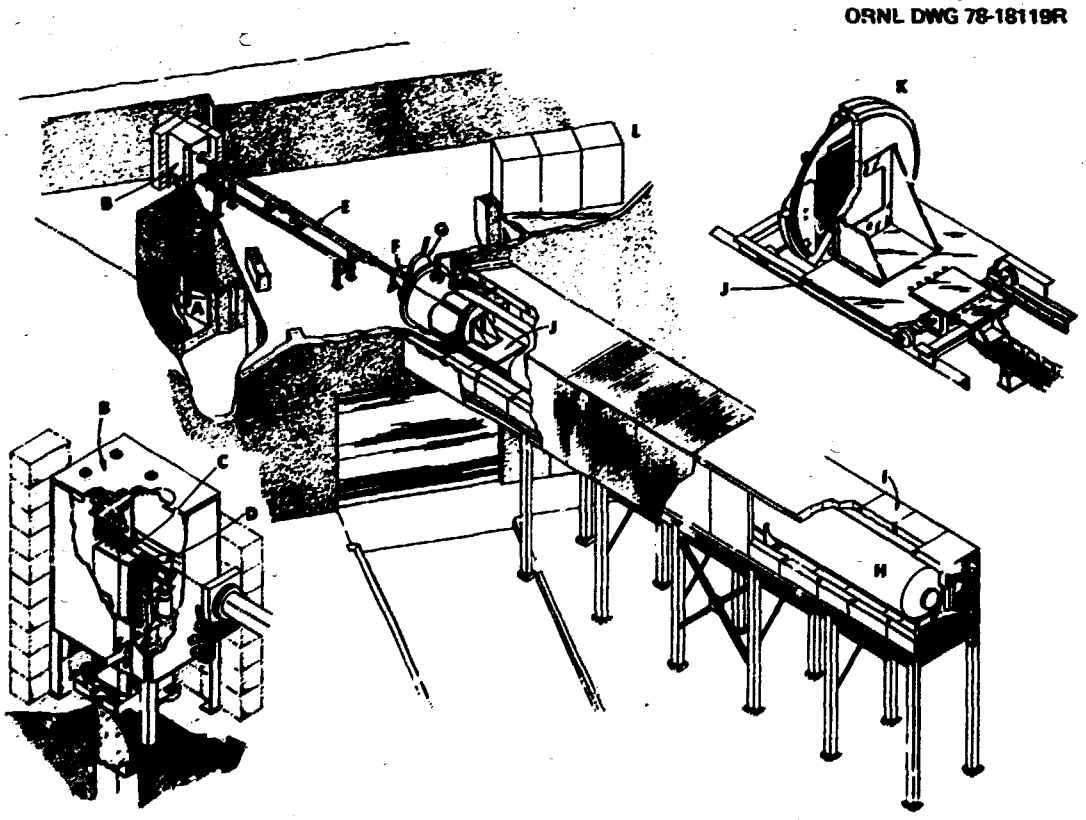

(A) LOWER MONOCHROMATOR HOUSING
(B) UPPER MONOCHROMATOR HOUSING
(C) GRAPHITE MONOCHROMATING CRYSTALS
(D) COLD BERYLLIUM FILTER
(E) COLLIMATOR AND NEUTRON BEAM GUIDE
(F) SAMPLE CHAMBER
(G) 30-cm GATE VALVE
(H) 30-cm × 182 cm dia VACUUM FLIGHT PATH
(I) 30-cm WOOD SHIELDING
(J) DETECTOR CARRIAGE
(K) 112-cm dia TWO-DIMENSIONAL POSITION-SENSITIVE DETECTOR 64 × 64 cm ACTIVE AREA)
(L) DATA ACQUISITION SYSTEM

Fig. 5.1. Thirty-meter SANS facility.

extremely difficult to recover because the dense, compact nature of the shale restricts the microporous pathways needed for migration of the organic material. In situ shale-oil recovery techniques center on a variety of methods for increasing the porosity and permeability of the shale formation. A detailed knowledge of the pore-size distribution is, therefore, fundamental to understanding and controlling the permeability of oil in these systems.

Very little information is currently available on the size of grains and pores in compact shales, which are believed to be in the range 5 to 2000 Å. As SAS techniques are well established for the characterization of porous materials in this size range,[2-4] a series of experiments aimed at developing these techniques for the study of oil-bearing shales has been undertaken on samples provided by a leading oil company.

In principle, SANS experiments can give the total pore distribution in a material, including empty pores and those filled with hydrocarbons (oil, kerogen, etc.). If the ratio of H to C is approximately 2:1, the coherent scattering from a filled pore is virtually zero due to the cancellation between the coherent scattering lengths of C ($b_C = 0.66 \times 10^{-12}$ cm) and hydrogen ($b_H = -0.37 \times 10^{-12}$ cm). Hence, hydrocarbon-filled pores scatter neutrons similarly to empty pores; therefore, SANS measurements should give information on the total pore distribution.

On the other hand, for x-ray scattering measurements, the increased electron density of hydrocarbon-filled pores can be expected to reduce their scattering, and one might expect to measure a pore distribution dominated by the empty pores. Subtraction of the distributions taken from SANS and SAXS measurements should, in principle, give information on the oil-bearing pores in the shale.

Initial experiments have demonstrated that shales formed in low-pressure geological formations have isotropic scattering patterns, indicating a random orientation of the pores. Shales formed in superpressure formations have anisotropic scattering patterns with an axis of cylindrical symmetry perpendicular to the bedding planes, indicating that the pores are anisotropic with the long axis preferentially oriented in these planes. Debye, Anderson, and Brumberger[5] developed a model for the scattered intensity $I(K)$ from a system of holes (pores) randomly dispersed in a matrix of uniform electron density, which predicts a linear variation of $I^{-1/2}(K)$ with K^2. Figure 5.2 shows that this prediction fits the measured scattering to a good approximation. The pore dimensions calculated using the Debye formulation are shown in Table 5.1.

The dimensions revealed by SANS and SAXS are clearly different, and the initial indications are that

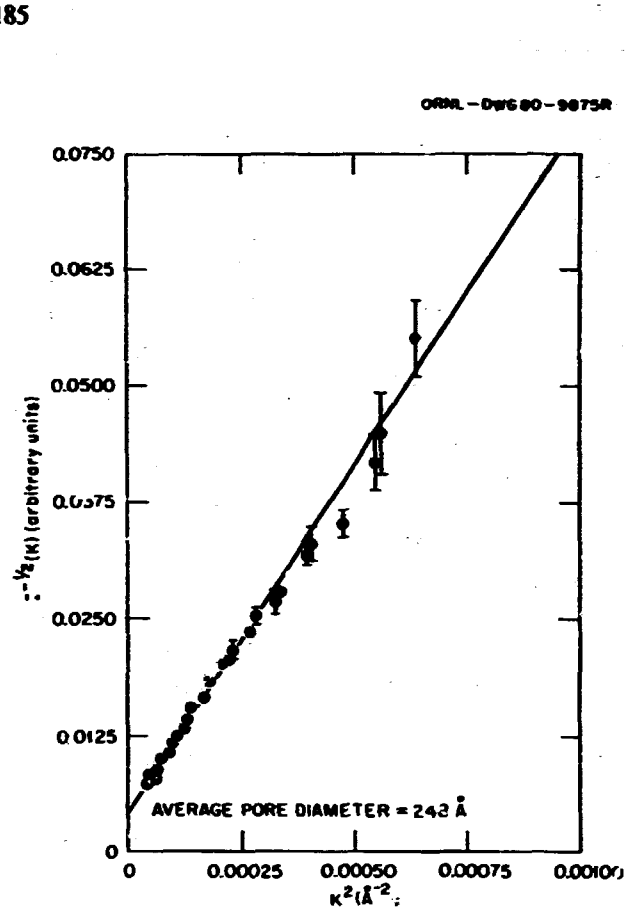

Fig. 5.2. Typical Debye plot [$I^{-1/2}(K)$ vs K^2] for superpressure oil shale. Average pore diameter equals

$$\frac{3}{2(1-\phi)}\sqrt{\frac{\text{slope}}{\text{intercept}}},$$

where ϕ = volume fraction of pores.

Table 5.1. Average pore diameters or axes obtained via SAXS and SANS for a series of oil-shale samples

Sample	Shale formation	Scattering pattern	Average pore diameter or axis (Å)	
			SAXS	SANS
1	Low-pressure	Isotropic	144	>600
2	High-pressure	Anisotropic	118 (long axis) 65 (short axis)	403 (average over both axes)
3	High-pressure	Anisotropic	135 (long axis) 86 (short axis)	248 (average over both axes)

the hydrocarbons in these samples are contained predominantly in the larger pores (>150 Å), thereby reducing their contribution to the SAXS patterns.

Further experiments are in progress to establish the relative contribution of voids and grains to the scattering and to assess the validity of the SAS

methods for examining samples from other important oil-bearing geological formations (e.g., diatomites, chalks, etc.).

1. Metals and Ceramics Division, ORNL.
2. G. W. Longman et al., *Colloid Polym. Sci.* 252, 298 (1974).
3. R. W. Hendricks, *Philos. Mag.* 30, 819 (1974).
4. J. S. Lin et al., *J. Appl. Crystallogr.* 11, 621 (1978).
5. P. Debye, H. R. Anderson, and H. Brumberger, *J. Appl. Phys.* 28, 679 (1957).

SANS FROM COAL SOLUTIONS

B. E. Maxwell[1] H. R. Child
A. H. Narten[1]

Coal chemists have used several methods to determine molecular weights of coal and coal derivatives which were originally developed for other systems. These methods include vapor pressure osmometry[2-4] and gel permeation chromatography.[4,5] However, the method believed to be the most reliable, although too expensive and time-consuming for routine work, is the measurement of the density gradient by optical means during ultracentrifugation.[4] This method has been coupled with ultrafiltration to separate the coal solutions by particle size. It is known that SAS of either x rays or neutrons can provide weight-averaged molecular weights $\bar{M}_w$.[6,7] We have conducted preliminary neutron scattering experiments on coal powders and solutions to investigate this method of determining $\bar{M}_w$. The powder samples, although yielding a large signal, were subject to uncertainties because of voids and pores that may be present in the sample.[7] To eliminate this complication and to study the possible presence of "molecules" of coal, we have examined solutions of Illinois No. 6 vitrinite in deuterated pyridine. The coal samples were treated by one of three methods: (1) toluene pyrolysis in 1:1 at 400°C for 4 min (designated run No. 596); (2) Na/K reduction in glyme/triglyme quenched with H_2O, after which the base soluble portion is collected following centrifugation, acidified, and dried (603); and (3) Na/K reduction in glyme/triglyme, H_2O-quenched, base-insoluble material collected after centrifugation and dried (602). A fourth sample was left untreated (No. 598). Each sample was continuously extracted with D_5-pyridine and ultracentrifuged at 20,000 rpm for 1 h.

We have used the word "molecules" in the previous description, but this concept is not proven and, in fact, a long-term purpose of these experiments is to determine if such a concept is valid. A terminology of microparticle or macromolecule might be applied with equal validity.

Neutron SAS data were collected at the ORR, using the new 5-m SANS facility at an incident wavelength of 4.82 Å. The $K = 4\pi \sin\theta/\lambda$ range was $6 \times 10^{-3} \leq K \leq 5 \times 10^{-3}$ Å^{-1}. The data were corrected for the sample transmission, background, and solvent/sample cell scattering and were converted to absolute macroscopic cross sections by measuring the incident beam intensity.

Our analysis of the data is based on the observation that the scattered intensity can be represented by the square of a Lorentzian function plus a constant. The solid lines in Fig. 5.3 are least squares fits to this functional form. Such a dependence has been predicted[8] for particles having an autocorrelation function $\gamma(r)$ expressed by

$$\gamma(r) = e^{-r/a}, \qquad (1)$$

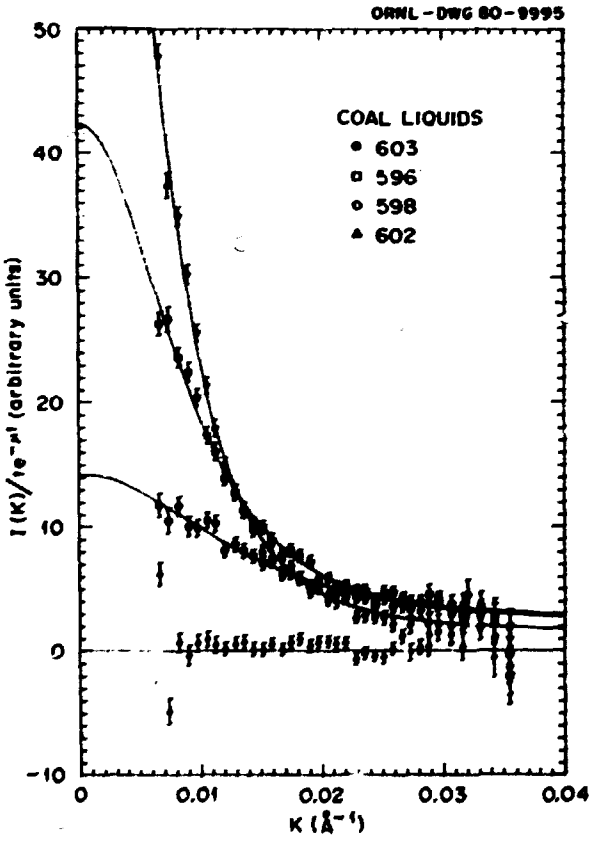

Fig. 5.3. SANS intensities from coal solutions vs K. The solid curves are least squares fits to the data of Eq. (2).

where a is correlation distance and is a measure of the size of the fluctuation. For this $\gamma(r)$ the intensity is given by

$$I(k) = I(0)[1 + k^2a^2]^{-2}, \quad (2)$$

which is the observed functional form. We obtain $I(0)$, a, and a constant background by least squares fits to the data. Particle size is often expressed in terms of the radius of gyration[9] R_g, which can be evaluated from $\gamma(r)$ analytically; in this case, $R_g^2 = 6a^2$. This R_g concept is well defined only for a low-density system of randomly oriented identical particles; and, if these conditions are not valid, R_g must be considered as an average over the size distribution. It can be shown that R_g is weighted more heavily toward the larger particles.

The weight-averaged molecular weights $\bar{M}_w$ are related to $I(0)$ by[5]

$$I(0) = Kte^{-xt}\frac{d\Sigma}{d\Omega}(0), \quad (3)$$

with

$$\frac{d\Sigma}{d\Omega}(0) = N_0\rho c(1-c)n(\bar{F}_A - \bar{F}_B)^2/\bar{w}, \quad (4)$$

where N_0 is Avogadro's number, $\bar{w}$ is average atomic weight per atom, ρ is density of solution, c is concentration of coal "molecules," n is number of average atoms per coal molecule, and $\bar{F}_A$ and $\bar{F}_B$ are the average scattering amplitudes per atom of the coal and the pyridine, respectively. For deuterated pyridine, $\bar{F}_B = 0.691 \times 10^{-12}$ cm and $\bar{F}_A$ can be calculated from the elemental analysis of each coal sample. The observed value of $\frac{d\Sigma}{d\Omega}(0)$ is divided by the known values in Eq. (4) to yield the number of average atoms per coal molecule n and then, $\bar{M}_w = n\bar{w}$.

Our results for n, shown in Table 5.2, are subject to rather large uncertainties, which are estimated to total about ±25% from the calibrations and the background correction procedure. It should be emphasized that because these data represent very small signals on a rather large background when compared to previous measurements at this facility, we are pushing the capabilities of the machine close to the limit. In addition, the interpretation of n is open to question on fundamental grounds because the coal solution might be expected to contain a range of sizes of molecules. A much wider range of K is beyond the capacity of this machine at present. Future experiments are planned on various solutions as a function of concentration to attempt to utilize and refine the experimental technique to its fullest extent.

1. Chemistry Division, ORNL.

2. B. S. Ignasiak, S. K. Chakabartty, and N. Berkowitz, *Fuel* 57, 507 (1978).
3. K. W. Chung, L. L. Anderson, and W. H. Wiser, *Fuel* 58, 847 (1979).
4. H. P. Hombach, Ph.D. dissertation, Westfalischen Wilhelms-Universitat zu Munster.
5. J. W. Larsen and P. Chondhurg, *J. Org. Chem.* 44, 2856 (1979).
6. J. S. Higgi . and R. S. Stein, *J. Appl. Crystallogr.* 11, 349 (1978).
7. J. S. Lin et al., *J. Appl. Crystallogr.* 11, 621 (1978).
8. P. Debye and A. M. Bueche, *J. Appl. Phys.* 20, 518 (1949).
9. A. Guinier and G. Fournet, *Small-Angle Scattering of X-rays*, John Wiley, New York, 1955.

SANS STUDIES OF A COMPATIBLE POLYMER BLEND, ATACTIC POLYSTYRENE–POLY(2,6 DIMETHYL PHENYLENE OXIDE)[1]

G. D. Wignall H. R. Child
F. Li-Aravena[2]

In recent years the SANS technique has been increasingly used for the study of chain configuration

Table 5.2. Comparison of coal solutions in deuterated pyridine

Sample run	Analysis per 100 C atoms	Concentration (%)	$\frac{d\Sigma}{d\Omega}(0)$ (cm^{-1})	R_g (Å)	n	$\bar{M}_w$ (g)
Illinois No. 6 vitrinite	$C_{100}H_{93.8}N_{1.8}S_{1.9}O_{10.8}$					
596 (PCS-II-4)	$C_{100}H_{86.9}N_{4.1}S_{0.7}O_{5.9}$	4.2	16.3	144	2.1×10^4	1.5×10^5
598 (CS-IV-6)	$C_{100}H_{86.1}N_{3.8}S_{0.4}O_{5.9}$	4.85	9.93	89.3	1.1×10^4	8.1×10^4
602 (NCS-I-B)	$C_{100}H_{103.4}N_{2.7}S_{0.8}O_{5.1}$		0			
603 (NCS-I-A)	$C_{100}H_{90.1}N_{3.7}S_{0.9}O_{7.3}$	1.69	25.4	226	6.5×10^4	4.6×10^5

in bulk amorphous[3] and crystalline polymers[4,5] in the melt and solid state. Samples analyzed by this technique are made up of a host polymer matrix in which a small number (~4%) of isotopically substituted (tagged) polymer molecules are dispersed. The difference in coherent scattering length b between D and H results in a marked contrast between hydrogenated and deuterated molecules.

The SANS methods were first used to investigate polymer compatibility by Kirste, Kruse, and Ibel[6] for both incompatible and compatible blends. The majority of chemically dissimilar polymer pairs are incompatible, and techniques (differential calorimetry, optical microscopy, etc., hitherto used to probe this phenomenon are sensitive to macroscopic fluctuations in composition, from which compatibility at the segmental level must be inferred. Furthermore, the techniques do not provide information on chain configuration in blends or whether the molecules are perturbed from their configuration in the homopolymer. The SANS technique is an extremely sensitive test of compatibility at the segmental level, and Ballard, Rayner, and Schelten[7] used this technique to demonstrate that polystyrene and poly-α-methyl styrene formed a truly compatible mixture. This communication reports the results of an investigation on a polymer blend, polystyrene-PPO (commercially marketed as Noryl), which demonstrates that this system is compatible on a segmental level and that the chain dimensions are similar to those in the homopolymer.

The neutron scattering samples were fabricated with a (hydrogenous) PPO matrix in which concentrations of 1.3, 4.2, and 6.1 wt % of DPS were dissolved. A PPO matrix was chosen to minimize the contrast due to any residual voids in the system by means of partial cancellation between the scattering lengths of C ($b_C = 0.6\times10^{-12}$ cm) and H ($b_H = -0.37\times10^{-12}$ cm). For each sample the background matrix scattering was subtracted by performing measurements on a blank sample containing no tagged molecules.

The SANS experiments were performed on the 5-m instrument in operation at the ORR.[8] The scattering patterns from the tagged blends and the blank were each measured over a 32×32 array for a period of ~16 h; after correction for background and sample thickness and transmission, the corresponding scattering from the polymer blank was subtracted. The resulting two-dimensional array of corrected data points was averaged over a ring of constant width as a function of radius from the center of the beam to obtain the intensity over a range of scattering vectors, 7×10^{-3} Å$^{-1} \leq K = (4\pi/\lambda)\sin\theta \leq 0.035$ Å^{-1}. These intensities were calibrated by comparison with scattering from water and by direct measurements of the incident beam and hence placed on an absolute scale.

Values of the radius of gyration R_g and molecular weight Σ_0 of the tagged molecules were obtained, respectively, from the slope and intercept of Guinier plots (I^{-1} vs K^2) of the scattering data (see Fig. 5.4 and Table 5.3). It is clear that the molecular weights measured by SANS and osmometry are equal within the experimental error (~20%). Schelten et al.[5] showed that deviations from a statistical distribution involving less than one monomer unit in 1000 would cause Σ_0 to exceed M_w by a factor of ~100. Thus the close agreement recorded above confirms that a statistical distribution of DPS in PPO has been achieved. This conclusion is similar to that resulting from extensive studies of compatibility made on this system by conventional techniques[9,10] and confirms that information on the compatibility of polymer blends on a segmental level can successfully be inferred from these techniques.

The dimensions of DPS in PPO are close to the dimensions of DPS in PSH,[3] although a small

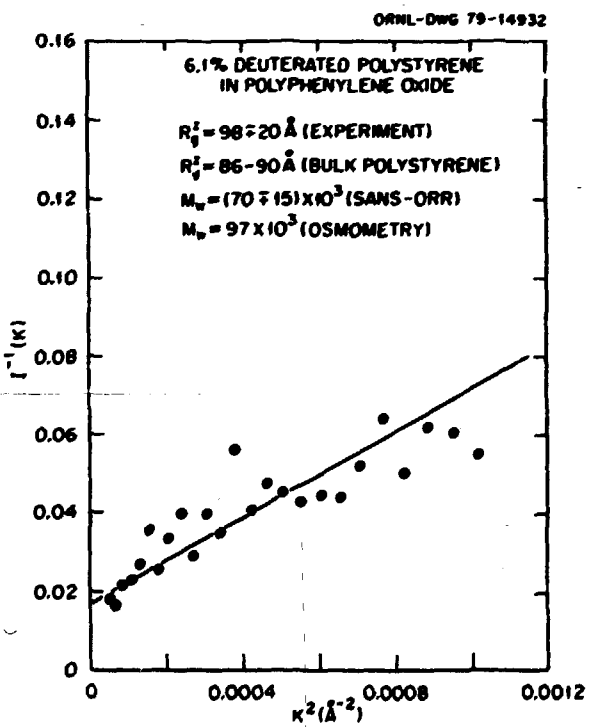

Fig. 5.4. Plot of I^{-1} vs K^2 for sample containing 6.1 wt % deuterated polystyrene in PPO.

Table 5.5. Measured values of Σ_0 and $R_g = \langle s^2 \rangle_w^{1/2}$ for DPS in PPO[a]

Sample (wt % DPS)	$R_g = \langle s^2 \rangle_w^{1/2}$ (Å)	Σ_0 (g)
6.1	98 ± 20	(70 ± 15) × 10^3
4.2	100 ± 20	(82 ± 20) × 10^3
2.3	100 ± 20	(90 ± 20) × 10^3

[a]Tagged molecules (DPS), $M_w = 97 \times 10^3$, $M_w/M_n = 1.1$; matrix (PPO) $M_w = 46.4 \times 10^3$, $M_w/M_n = 2.7$; and R_g of DPS in PSH is 85–90 Å.

expansion of the chain cannot be ruled out within the experimental error. The variation of Σ_0 with concentration indicates a positive second virial coefficient in the range $1 \times 10^{-5} \leq 2A_2 \leq 1.5 \times 10^{-4}$/mole $g^{-2}cm^{-3}$.

1. Summary of paper to be published.
2. Guest scientist from Comision de Energia Nuclear, Santiago, Chile.
3. G. D. Wignall, D. G. H. Ballard, and J. Schelten, *Eur. Polym. J.* 10, 861 (1974).
4. J. Schelten et al., *Polymer* 17, 751 (1976).
5. J. Schelten et al., *Polymer* 18, 111 (1977).
6. R. G. Kirste, W. A. Kruse, and K. Ibel, *Polymer* 16, 120 (1975).
7. D. G. H. Ballard, R. Rayner, and J. Schelten, *Polymer* 17, 349 (1976).
8. H. R. Child and S. Spooner, *Journal Applied Crystallography* (to be published).
9. W. J. MacKnight, J. Stoelting, and F. E. Karasz, *Adv. Chem. Ser.* 99, (29 (1977).
10. F. E. Karasz, W. J. MacKnight, and J. Stoelting, *J. Appl. Phys.* 41, 4357 (1970).

SANS INVESTIGATIONS OF IRRADIATION-PRODUCED VOIDS USING THE ORR SANS MACHINE[1]

S. Spooner[2] W. E. Reitz[3]
H. R. Child

The SANS technique can be used to advantage in the investigation of void structure produced by reactor irradiation because the method is essentially nondestructive and the interfering effects of gamma radioactivity can be distinguished from neutron scattering in measurements of hot samples. Two void structure investigations were undertaken on the ORR SANS machine under less than ideal conditions. First, the incident neutron flux in this prototype machine is low by comparison with other SANS machines in the United States or Europe. Second, sample dimensions were not optimized. Nevertheless, some useful results were gained from analysis of scattering.

Niobium and Nb-Zr alloys doped with He became available from the Metals and Ceramics Division in the form of microtensile specimens that had been irradiated at several temperatures and fluences in the HFIR. A shoulder section from each specimen (4 mm in diameter, 4 mm long) was used for scattering experiments. The scattering from voids could be measured in these specimens after correction for a gamma background scattering. This background was distinguished from neutron scattering by putting a Cd sheet in the incident beam, thus blocking neutron scattering from the voids. The void scattering was easily separated from gamma and instrumental background only at small angles. The apparent size of voids in these samples was such that it was not possible to establish clearly the Gaussian form of scattering in the small-angle range of data measured. It was found instead that the scattering curves conformed closely to a K^{-4} dependence. The data are plotted in Fig. 5.5 in which the straight lines show the K^{-4} behavior. Under these circumstances the structural information that could be obtained from these data was limited. An estimate of the Porod radius (square root of the second moment) was calculated from the ratio of the invariant $Q_0 [= \int_0^\infty K^2 I(K)\, dK]$

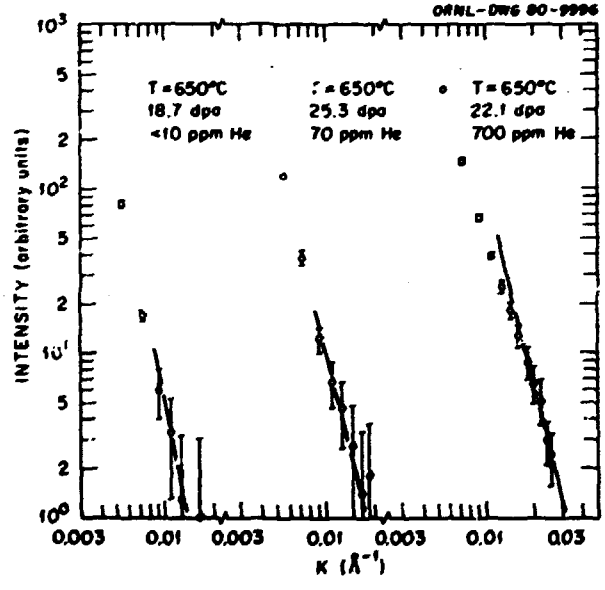

Fig. 5.5. Neutron scattering from voids in Nb–1% Zr samples that have been doped with 134 ppm He. The radiation dose of each sample is measured by the displacements per atom (dpa).

to the Porod constant P [$= K^4 I(K)$]. The void fractions were calculated from Q_0 after absolute calibration of the scattering intensity with the *incident beam intensity*. However, the values obtained are subject to large errors. It may be recorded that the trends of the void fraction follow fairly well the densometric determinations made elsewhere. At this point in the analysis, it can be said that trends and magnitudes of the void structure parameters have been established and that continuation of the work on the HFIR SANS machine is both feasible and promising of detailed results.

A 304 stainless steel specimen taken from an EBR-II control-rod thimble presented another kind of problem which may represent an important limitation in the study of irradiated stainless steel. The SANS study of this specimen has shown a large scattering and possible interference peak in the scattering distribution. It is known that various intermetallic phases including carbides appear in neutron-irradiated stainless steels and that there are several possible sources of scattering: (1) voids, (2) nonmagnetic precipitates, (3) magnetic carbides, and (4) multiple scattering.

In recent experiments on this specimen, a magnetic field was employed to determine the possibility of scattering from ferromagnetic phases. The principle of this experiment is that magnetic scattering vanishes for scattering vectors parallel to the magnetization so that the difference in scattering with and without field yields an estimate of the amount of ferromagnetic phases present. However, no response with applied field could be measured at a statistically significant level.

The scattering data were then examined in terms of void scattering. A most unlikely result was derived from the calculated scattering invariant Q_0. After calibration of the scattering, it was found that the apparent void fraction was many times higher than a physically reasonable value.

Our conclusion is that the observed intensity is not single scattering from voids nor is it from ferromagnetic precipitates. Nonmagnetic precipitates remain a possibility as the source of scattering, and the multiple scattering possibilities need to be evaluated. Multiple scattering from voids in stainless steel may be a particularly serious problem because of the high scattering amplitudes of the principal components of this alloy. The experimental approach to this problem calls for varying the sample dimensions, which would be expensive when dealing with irradiated specimens. A general computer program is needed to calculate the effects of multiple SAS. Although multiple scattering may have important effects on Q_0, it cannot explain the observed interference peak.

---

1. Summary of paper to be published.
2. Consultant from Georgia Institute of Technology, Atlanta.
3. Georgia Institute of Technology, Atlanta.

SANS ANALYSIS OF THE DECOMPOSITION OF Mn–40% Cu ALLOY

S. Spooner[1] E. R. Vance[2]
H. R. Child

The fcc solid solution structure of Mn-rich Mn-Cu alloys can be retained from the high-temperature, single-phase region into the low-temperature two-phase region by quenching. Upon annealing, eventual decomposition into a Cu-rich gamma phase and virtually pure Mn can be preceded by what appears to be a precipitation or clustering of Mn zones. These enriched zones have been shown to undergo a low-temperature transformation from cubic to tetragonal structure which is accompanied by a paramagnetic to antiferromagnetic transformation. To date, the precise form of the clustering or precipitation reactions in the solid solutions has not been elucidated. However, SANS experiments are particularly well suited to this study because of the strong scattering contrast between Cu and Mn. Some low-angle scattering investigations have been done but without sufficient angular resolution to give detailed structural information. In the present study samples of polycrystalline Mn–40% Cu alloys were annealed at 350, 450, and 550°C for 2 h for study on the ORR SANS machine. Data were collected with both short- and long-path configurations so that scattering over a wide range of scattering angle could be examined. The neutron counts were converted into absolute cross sections by use of the measured incident beam intensity and the instrumental geometry. The data are shown in Fig. 5.6.

A strong scattering appears at the smallest angles for the three samples. Alloys annealed at 450 and 550°C exhibit a peak or shoulder in the scattering which resembles scattering commonly seen in alloys undergoing precipitation. For 550°C annealing, the scattering at the smallest angles is strongly enhanced.

The scattering seen for 450 and 550°C annealing is interpreted qualitatively on a model of competing decomposition processes: (1) precipitation of a large zone (possibly pure Mn) and (2) precipitation of

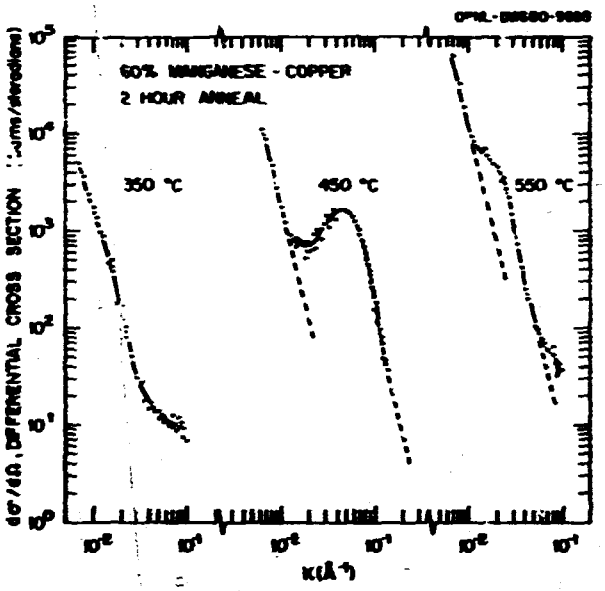

Fig. 5.6. Differential cross sections at small angles for Mn-40% Cu alloys quenched and then annealed for 2 h at 350, 450, and 550°C.

small Mn-rich zones in response to a metastable miscibility gap. The first process yielding large precipitates would only give rise to scattering seen at the smallest angles, and the scattering might take the form of K^{-4} dependence appropriate to the Porod limit of scattering. The scattering from precipitates coming from the second process would be seen at larger angles. The appearance of an intensity maximum is most likely due to a solute-depleted region surrounding the precipitate, and a size estimate could be made from the determination of the Porod radius.

A rough calculation of the integrated scattering Q_0 attributable to the small precipitates was made on the scattered intensity with corrections for the K^{-4} scattering appearing at small angles. The integrated scattering so obtained for the sample annealed at 450°C was much larger than the same quantity at 550°C. The Porod radius calculated for small precipitates is approximately 30 Å at 450°C and 60 Å at 550°C. The Porod radius is defined as Q_0/P, where $P = K^4 I(K)$, in the region where P is constant. Since the K^{-4} intensity is much larger at 550°C, the following interpretation is made. Alloy decomposition at 550°C proceeds primarily by the precipitation of large (probably pure Mn) precipitates, but precipitations of small metastable zones can occur to a lesser extent. At 450°C the principal mode of decomposition is precipitation of the small metastable zones. It appears that study of the decomposition process at 450°C and below in these alloys will yield information on the metastable miscibility gap with relatively little interference from the second precipitation process.

---

1. Consultant from Georgia Institute of Technology, Atlanta.
2. Pennsylvania State University, University Park.

MAGNETIC SANS FROM $Fe_{0.7}Al_{0.3}$

H. R. Child W. C. Koehler

The complex magnetic behavior of Fe-Al slightly off stoichiometry from the Fe_3Al phase has recently been investigated by neutron scattering.[1] An irregular piece of the sample was used for preliminary SANS experiments, which showed anomalous results. However, they could not be quantitatively analyzed because of the irregular shape. We have repeated the SANS experiments on a polycrystalline sample of similar but not quite identical heat treatment. The sample had the nominal composition of $Fe_{0.7}Al_{0.3}$ and was in the form of a flat disk. The intensity from this sample showed similar behavior and allowed quantitative cross-section measurements.

Figure 5.7 shows the intensity at constant $K = (4\pi \sin\theta)/\lambda$ values vs temperature. The $Fe_{0.7}Al_{0.3}$ has been found to be ferromagnetic below ~400 K, paramagnetic below ~170 K, and micromagnetic below ~90 K. It appears that this sample has its transition at 200 K instead of 170 K but otherwise seems to behave the same as the previous specimen. (We plan to characterize the sample more completely by wide-angle scattering and magnetization measurements.) We believe that the large asymmetric peak at 200 K is associated with the "inverse Curie temperature" proposed[2,3] for this material, at which temperature the ferromagnetic phase becomes paramagnetic. The sizes of the ferromagnetic clusters found by neutron scattering[1] apparently are altered dramatically at this temperature. The clusters seen in the SANS measurements are much larger than the ones seen in the previous wide-angle neutron study. The present data yield clusters of about 500-Å diameter containing ~5×10^6 atoms at 9 K and even larger ones near the peak at 200 K.

Another interesting point is that the temperature at which a maximum is observed is different for each value of K. This has also been observed for spin glass materials[4] and, in fact, appears to be characteristic of

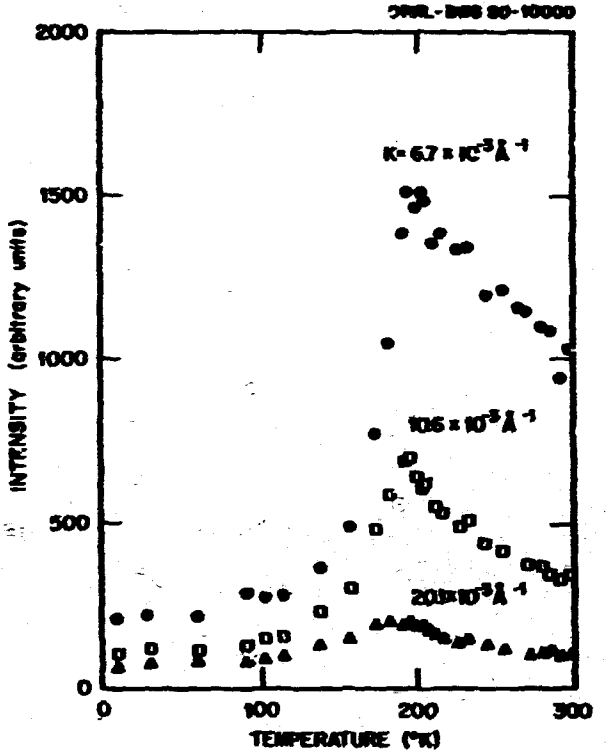

Fig. 5.7. Scattered intensity vs temperature at various K from an $Fe_{74}Al_{26}$ polycrystalline sample.

them. These maxima in the spin glasses are interpreted as the freezing temperature,[5] which have the property of a K-dependent ordering temperature. The intensity near the peak at 200 K does not seem to follow the Lorentzian form one expects for ferromagnetic disorder scattering,[1] and this behavior has also been seen for spin glass alloys. It probably indicates the presence of a distribution of sizes of the magnetic clusters. The application of a magnetic field of 0.4T was sufficient to eliminate almost all small-angle scattering in the observed region of K from 7×10^{-3} to 30×10^{-3} Å^{-1}. The sample was apparently converted to a simple-ordered ferromagnet in the presence of this field, and the cluster scattering went into the Bragg peaks. However, more field was required for the conversion at 9 K than at 200 K or above.

We conclude that there are probably two phenomena occurring in this material: (1) the inverse Curie temperature at which the ferromagnetic to paramagnetic phase change occurs and (2) the simultaneous presence of large clusters that freeze out at lower temperatures. Further study will be necessary to understand this complex magnetic material.

1. J. W. Cable, L. David, and R. Parra, *Phys. Rev. B* 16, 1132 (1977).

2. A. Arrott and H. Sato, *Phys. Rev.* 114, 1420 (1959).
3. R. D. Shull, H. Okamoto, and P. A. Beck, *Solid State Commun.* 20, 863 (1976).
4. H. P. Murani, *J. Appl. Phys.* 49, 1604 (1978).
5. S. F. Edwards and P. W. Anderson, *J. Phys. F* 5, 965 (1975).

INVESTIGATION OF THE EFFECTS OF APPLIED MAGNETIC FIELD ON SANS FROM DEFORMED STAINLESS STEEL

S. Spooner[1] H. R. Child

Austenitic stainless steel is normally paramagnetic but can be rendered partially ferromagnetic by mechanical deformation. Deformation in excess of 20% strain induces the formation of a ferromagnetic martensite-like phase, the amount of which increases with the deformation strain. The martensite phase formed is platelike, with the plate orientation dependent on the exact geometry of the deformation shear. The SANS has been found[2] to be very intense, with the scattering at a fixed angle proportional to the third power of the deformation strain. To learn more about the origin of this scattering and the behavior of the martensite phase, SANS studies were made with a magnetic field applied to stacks of rolled stainless steel sheets.

The rolled sheets were stacked together and placed in the neutron beam, with the rolling direction vertical and the sheet normal parallel to the incident beam. The magnetic field was applied in the horizontal direction and was also perpendicular to the incident beam. The magnetic scattering interaction is directional and depends on the angle between the diffraction vector and the magnetization vector. The scattering intensity at a fixed scattering angle is expected to exhibit a $\sin^2\alpha$ dependence, with α being the azimuthal angle measured on the two-dimensional area detector.

In Fig. 5.8*a* the radial scattering intensity averaged over the azimuthal angle at a fixed K shows a reduction in scattering upon application of the magnetic field. This observation is expected from the effect of the alignment of the sample magnetization. Figure 5.8*b* shows the variation of scattering intensity at a fixed K with azimuthal angle for zero field and $H = 2.0$ T. A $\sin^2\alpha$ dependence is shown in the field-on curve although the intensity does not go to zero at 0 and 180°. This may be caused by a spread in the direction of the diffraction vector due to finite resolution at small scattering angles or by nonmagnetic scattering sources. At zero applied field the scattering intensity is increased, but there remains a $\sin^2\alpha$ dependence of the same magnitude seen with the applied field.

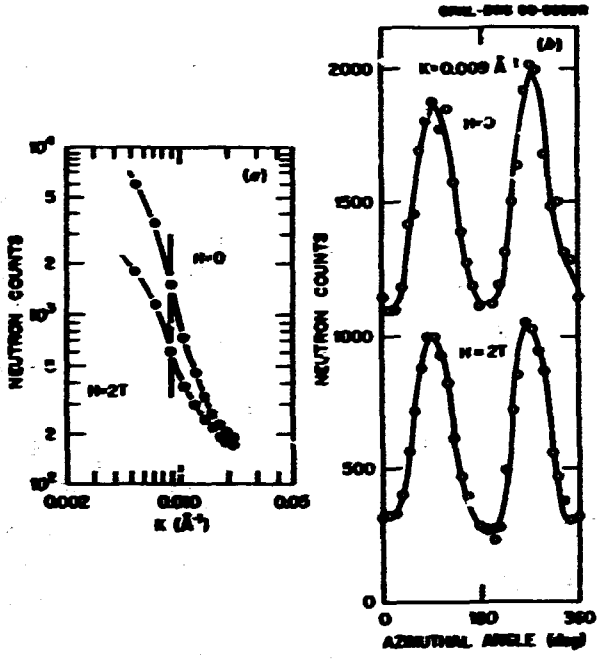

Fig. 5.8. (*a*) Radially averaged small-angle scattering from a sample of 304L stainless steel deformed 72% by rolling; (*b*) scattering intensity at $K = 0.009$ Å^{-1} as a function of azimuthal angle with 2.0T field (lower curve) and with no field (upper curve).

We believe that the angular variation is caused by scattering from ferromagnetic precipitates that retain their magnetization when the field is reduced to zero. We plan to repeat the experiment with the sample rotated 90° about the incident beam axis. We expect that the azimuthal variation will stay fixed relative to the applied field direction. If it rotates with the sample, the conclusion would be that the particles have very high magnetic anisotropy or that the scattering is coming from nonmagnetic precipitates with nonspherical shapes.

The strong increase in the angular independent scattering when the field is reduced to zero is thought to be caused by magnetic domains that are swept out at high fields. The probable source of the scattering is the domain walls. Multiple refraction of the incident beam in traversing many domains may also be responsible for this effect.

1. Consultant from Georgia Institute of Technology, Atlanta.
2. S. Spooner and H. R. Child, *Solid State Div. Prog. Rep., Sept. 30, 1978*, ORNL-5486, p. 154.

LATTICE DYNAMICS

OBSERVATION OF A CDW IN α-U AT LOW TEMPERATURE[1]

H. G. Smith — R. M. Nicklow
N. Wakabayashi — G. H. Lander[3]
W. P. Crummett[2] — E. S. Fisher[3]

Almost 20 years ago anomalies were first reported in the elastic constants of α-U metal at low temperature.[4] Since then, a great variety of experiments have been undertaken to elucidate the nature of low-temperature phase transition at ~43 K, but with little success, except to present a wealth of seemingly contradictory evidence.[5-7] We have performed neutron scattering experiments that show that a superlattice results from a condensation of a soft LO phonon near $\mathbf{q} = (1/2, 0, 0)$ at low temperature. We have tentatively associated this PLD as evidence of a CDW state, although we do not know the electronic origin of this distortion.

Interestingly, the wave vector of the CDW appears commensurate with a lattice slightly (0.4%) expanded with respect to the fundamental α-U lattice but coexisting with the α phase. We do not have a complete explanation of the nature of this coexistence; however, the problem is reminiscent of that found in the ω-phase precipitation in the Zr-Nb alloys,[8] and we have made some progress in understanding the position of the CDW peaks in α-U by using concepts recently advanced to understand the ω-phase alloys.[9,10]

Because the most dramatic anomalies occur in the elastic constants, specifically c_{11}, the present experimental program started with a neutron inelastic scattering investigation at ORNL of the phonon dispersion curves along the principal symmetry directions at room temperature.[11] The most interesting curves are those in the [100] direction reproduced in Fig. 5.9*a*. Here we see that the frequency of one of the Σ_4 branches is very low near $\mathbf{q} = [1/2, 0, 0]$. The eigenvector of this mode is $(u, v, 0; u, v, 0)$, that is, out-of-phase (optic) displacements in the x direction and in-phase (acoustic) displacements in the y direction. The observed neutron intensities near $\mathbf{q} = [1/2, 0, 0]$ indicate that, for this wave vector, the mode predominantly consists of optic-like x-direction displacements. Its temperature dependence is also shown.[12] A central peak begins to appear around 60 K and grows very rapidly below 40 K (see Fig. 5.9*b*). Under these conditions, it becomes very difficult to separate the elastic from the inelastic scattering without employing very good resolution,

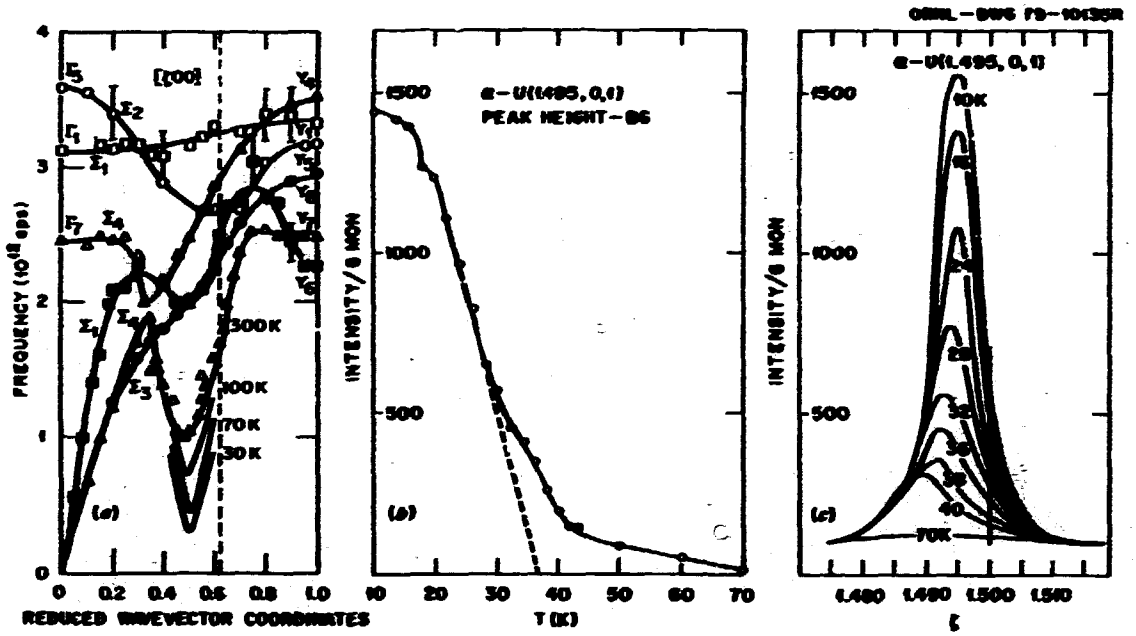

Fig. 5.9.(*a*) Dispersion curves of α-U in the [100] direction, (*b*) intensity of (1.495, 0, 1) reflection vs *T*; and (*c*) peak shape and position of the (1.495, 0, 1) reflection vs *T*.

which, in turn, reduces the intensity. Nevertheless, indications are that the dip in the Σ_4 LO branch does not collapse to zero energy but has a minimum at 0.4 THz (1.6 MeV). Measurements of other phonon modes, such as Σ_1 and Σ_3, revealed no anomalies near the zone center at low temperatures. Figure 5.9*c* shows high-resolution elastic scans near the (1.5, 0, 1) position as a function of temperature. All the superlattice reflections occur close to the positions $(h + 1/2, k, l)$ corresponding to the condensation of a phonon mode near $\mathbf{q} = [1/2, 0, 0]$. This corresponds to a simple sinusoidal modulation of the displacements in the *x* direction and requires a doubling of the unit cell in the same direction. The small deviations from a commensurate lattice are significant and are discussed below.

The appropriate crystallographic description in terms of the new unit cell is space group $D_{2h}^{13} - Pmnm$ (origin at center of symmetry), $Z = 8$, with atoms in 4(*f*): $\pm(\epsilon, y_1, 1/4)$; $\pm(1/2 - \epsilon, y_1, 1/4)$; 2(*a*): $\pm(1/4, y_2, 1/4)$; 2(*b*): $\pm(1/4, y_3, 3/4)$. The term $\epsilon \cong 0.001$ and, at this stage of the investigation, y_2 and y_3 are taken to be $1/2 + y_1$, and $1/2 - y_1$, respectively.

We now turn to the wave vector of the CDW. In Fig. 5.9*c* the peak position at low temperature is slightly less than (1.5, 0, 1), that is, at $(1.5 - {}^3/_2\delta, 0, 1)$. If the reflection corresponded to an incommensurate CDW, we should expect a peak at $(2.5 + {}^3/_2\delta, 0, 1)$ so that the two peaks are equidistant from the point (2, 0, 1). However, this is not found experimentally. Rather, we find the peak on the high side of (2, 0, 1) to be closer to $(2.5 - {}^5/_2\delta, 0, 1)$. A detailed analysis, which has considered resolution effects, of the positions of a large number of superlattice reflections $((h + 1/2)(1 - \delta), k, l)$ in both zones seems to show that the wave vector is commensurate, $\mathbf{q} = [1/2, 0, 0]$, with a lattice whose lattice constant a_s is slightly larger than twice the original lattice constant a_o. We find that

$$a_s/2a_o = 1 + \delta = 1.0037 \pm 0.0004 .$$

The exact positions of the above reflections are then (1.4945, 0, 1) and (2.4908, 0, 1) with respect to the α lattice at 11 K, a most unusual situation.

The shifts in the weak reflections may be due to discommensurations.[13,14] One such model was used by Horovitz, Murray, and Krumhansl[9] to explain the rather unusual diffuse scattering observed in some Zr-Nb alloys, in which a diffuse ω phase coexists with the bcc β phase, in terms of narrow "stacking solitons." The ω phase is thought to "feel" the perturbating potential of the β phase. We have applied these ideas to the problem of the wave vector in α-U with some success. Consequently, from our experimental data, it appears that the atoms want to

be displaced slightly from the crystallographic mirror planes at x = 0, causing a lattice expansion incommensurate with the α lattice. The results of our model calculations, based on the one-dimensional formalism of Horovitz, Murray, and Krumhansl,[9] are in semiquantitative agreement with the observed data. The weak superlattice reflections are shifted to lower q values, in quantitative agreement with the shift δ, and the fundamental peaks are shifted to higher q values, which are still below the α-phase peaks ($\Delta h = 0.005$ for the (2, 0, 0) reflection). The value of the parameter λ we used ($\lambda = 0.98$) is very different from that used in the ω-phase problem ($\lambda = 0.2$) and produces quite different effects. This large value of λ corresponds to wide "stacking solitons," and the phase shift varies slowly over many unit cells rather than over a narrow region as in the Zr-Nb system. The calculations omit any coherent relations between the α and α' regions and, therefore, predict two (2, 0, 0) peaks slightly separated, contrary to observation. This prediction may merely reflect the limitations of the one-dimensional model. An alternative explanation (unproven here) is that coherent relations exist between the α and α' regions such that they contribute coherently to the fundamental peaks. Such a model would probably involve a more complex arrangement of the discommensurations than has been proposed here. Additional diffuse scattering[12] at low temperatures also indicates that the structural distortion may be somewhat more complex than has been described above.

In conclusion, we believe that the present results represent a major step forward in understanding the properties of α-U at low temperature. This material is also a superconductor with $T_c \sim 0.1$ K, but T_c can be raised to ~2 K with modest pressure,[5] an elevation that also inhibits the α-α' transition at 43 K. We plan to study the soft mode and superlattice formation as a function of pressure in the near future. Although the formation of a superlattice in α-U is well established and is discussed in terms of a CDW, the exact relationship of the wave vector to the fundamental lattice is an intriguing, new problem.

1. Summary of paper to be published.
2. Baptist College of Charleston, Charleston, S.C.
3. Argonne National Laboratory, Argonne, Ill.
4. E. S. Fisher and H. G. McSkimin, *Phys. Rev.* **124**, 67 (1961); E. S. Fisher and D. Dever, *Phys. Rev.* **170**, 607 (1968).
5. For general reviews, see a number of chapters in *The Actinides: Electronic Structure and Related Properties*, ed. by A. J. Freeman and J. B. Darby, Academic, New York, 1974; T. F. Smith and E. S. Fisher, *J. Low Temp. Phys.* **12**, 631 (1973).
6. C. S. Barrett, M. H. Mueller, and R. L. Hitterman, *Phys. Rev.* **129**, 625 (1963).
7. G. H. Lander and M. H. Mueller, *Acta Crystallogr. B* **26**, 129 (1970).
8. W. Lin, H. Spak, and B. W. Batterman, *Phys. Rev. B* **13**, 5158 (1976).
9. B. Horovitz, J. L. Murray, and J. A. Krumhansl, *Phys. Rev. B* **18**, 3549 (1978).
10. R. Pynn, *J. Phys. F* **8**, 1 (1978).
11. W. P. Crummett et al., *Phys. Rev. B* **19**, 6028 (1979).
12. H. G. Smith et al., *Proceedings of Conference on Superconductivity in d and f Band Metals* (a table of observed and calculated intensities), Academic, New York (in press); *Proceedings of Conference on Modulated Structures – 1979* (in press); *AIP Conf. Proc.* **53**, 226 (1979).
13. W. McMillan, *Phys. Rev. B* **14**, 1496 (1976).
14. Per Bak and J. Timonen, *J. Phys. C* **11**, 4901 (1978).

NEUTRON DIFFUSE SCATTERING IN MAGNETITE DUE TO MOLECULAR POLARONS[1]

Y. Yamada[2] N. Wakabayashi
R. M. Nicklow

A detailed study on neutron diffuse scattering has been carried out to verify a model that describes the property of valence fluctuations in magnetite above the Verwey transition T_v. This model assumes the existence of a molecular polaron complex composed of two excess electrons and a local displacement mode of oxygens within the fcc primitive cell. It is assumed that at sufficiently high temperatures randomly distributed molecular polarons fluctuate independently by making hopping motions through the crystal or by dissociating into smaller polarons. The lifetime of each molecular polaron is assumed to be long enough to induce an instantaneous strain field around it. Based on this model, the neutron diffuse scattering cross section due to randomly distributed, dressed molecular polarons has been calculated. A precise measurement of the quasi-elastic scattering of neutrons has been carried out at 150 K. The observed results definitely show the characteristics predicted by the model calculation, thus providing evidence for the existence of the proposed molecular polarons. From this standpoint, the Verwey transition of magnetite may be viewed as the cooperative ordering process of dressed molecular polarons. Possible extensions of the model may describe the ordering and the dynamical behavior of the molecular polarons.

1. Summary of paper: *Physical Review* (in press).
2. Guest scientist from Osaka University, Osaka, Japan.

PHONONS IN TRANSITION METAL ALLOYS

N. Wakabayashi
H. G. Smith
F. Brotzen[1]
B. Higuera[2]
Y. Nakai[3]
Y. Noda[4]
Y. Endoh[5]

Phonon dispersion curves of various transition metal alloys have been measured by neutron scattering techniques, and the results are summarized here.

$Fe_{0.82}V_{0.18}$

The phonon dispersion curves of Fe have been studied quite extensively in the past,[6] while those for V could not be measured by neutron scattering techniques due to its extremely low coherent scattering cross section for neutrons. Therefore, the dispersion curves of V were determined indirectly by measuring the thermal diffuse scattering of x rays,[7] and they seem to show rather anomalous features not unlike those for Nb and Ta, in particular, rather low frequencies for the LA(110) mode. Because the atomic masses for V and Fe are similar, the differences in the phonon dispersion curves in these metals are due to the difference in the number of the valence electrons. In order to obtain more information about the role of the valence electrons in determining the phonon dispersion curves of these transition metals, the phonon dispersion curves of bcc $Fe_{0.82}V_{0.18}$ were measured, and some of the results are shown in Fig. 5.10. The changes in the dispersion curves from those for Fe are rather small in view of the fact that the addition of V reduces the number of the valence electrons per atom by nearly one. A similar change in electron number results in significant differences in the phonon spectra of V and Cr. This result may indicate that the electron-ion interactions are much weaker in Fe than in V and is also consistent with the shorter range of interatomic interaction in Fe compared with that in V, as deduced from the interatomic force constant analysis of the dispersion curves of these metals.

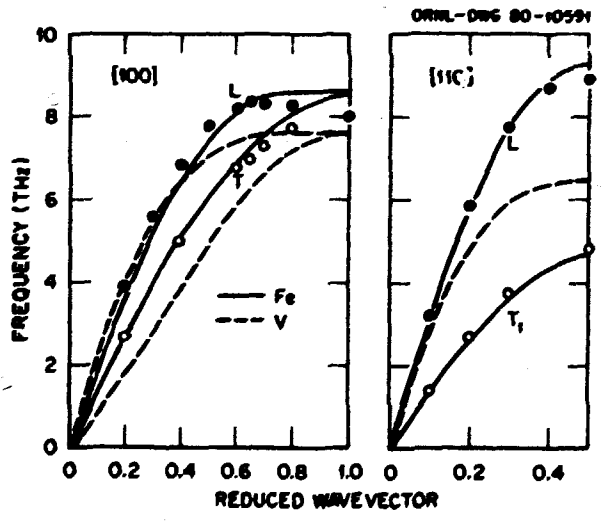

Fig. 5.10. Phonon dispersion curves for $Fe_{0.82}V_{0.18}$. Solid and dashed lines indicate dispersion curves for Fe and V, respectively. The curves for the T_1 mode in these metals are nearly indistinguishable.

$Fe_{0.65}Ni_{0.35}$

This invar alloy is known to exhibit a softening of the T_1 (110) mode as the temperature is lowered.[8] In addition, indications of a simultaneous increase in phonon widths were observed earlier. High-resolution experiments performed using the triple-axis spectrometer at the HFIR confirmed these interesting phenomena, which may be related closely to the invar properties, in particular, to the negative thermal expansion coefficient at low temperatures.

$Fe_{0.7}Mn_{0.3}$

Although the thermal expansion coefficient of this alloy does not become negative, it has an unusual temperature dependence below the Neel temperature. The dispersion curves do not exhibit very anomalous features, and a modified shell model involving interactions out to the second neighbor seems to reproduce the data satisfactorily.

$Ta_{1-x}W_x$

Significant advances made recently in constructing microscopic pictures of lattice dynamics for transition metals may soon make possible the calculation of phonon dispersion curves from the knowledge of the electronic structures of various transition metals and alloys. In fact, a recent attempt by Varma and Weber[9] has been rather successful in reproducing anomalous features of dispersion curves[10] for the system $Nb_{1-x}Mo_x$ ($x = 0$–1). In order to gain more confidence in this nearly first-principles calculation, one would like to perform a similar calculation on a slightly different system and compare the result with experimental data. As an example of such a system, a 5-*d* transition metal alloy system, $Ta_{1-x}W_x$, was chosen, and the phonon dispersion curves have been measured for $x = 0.23, 0.50, 0.67$. Some of the results are summarized in Fig. 5.11. As the W concentration is increased, the anomalous features in the Ta dispersion curves gradually disappear, and the frequencies of all the modes increase constantly. These results are very similar to those obtained for the Nb-Mo system and should shed further light on

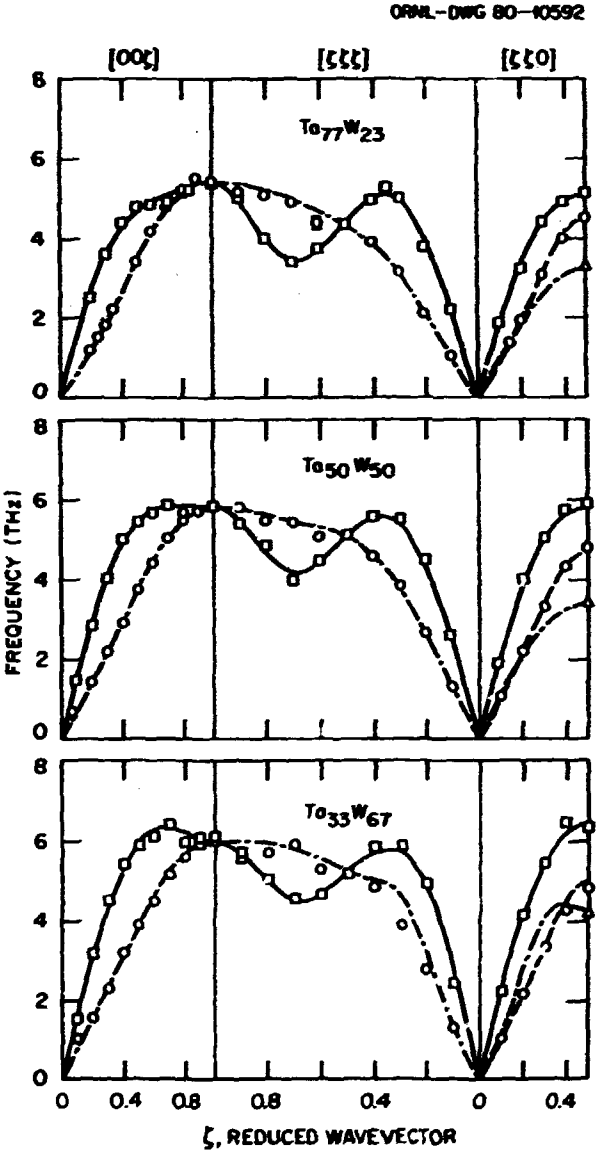

Fig. 5.11. Phonon dispersion curves for Tc-W alloys. The lines represent results of seven-neighbor Born-von-Kármán model fits.

the microscopic origin of the phonon anomalies in transition metals.

1. Rice University, Houston, Tex.
2. 1979 summer research participant from Rice University, Houston, Tex.
3. Guest scientist from Osaka University, Osaka, Japan.
4. Guest scientist from Sendai Radio Technical College, Sendai, Japan.
5. Tohoku University, Sendai, Japan.
6. B. N. Brockhouse, H. E. Abou-Helal, and E. D. Hallman, *Solid State Commun.* 5, 211 (1967); V. J. Minkiewicz, G. Shirane, and R. Nathans, *Phys. Rev.* 162, 528 (1967); C. van Dijk and J. Bergsma, p. 223 in *Neutron Inelastic Scattering*, IAEA, Vienna, 1968.
7. R. Colella and B. W. Batterman, *Phys. Rev. B* 1, 3913 (1970).
8. For a review of the lattice dynamics in invar alloys, see Y. Endoh, *J. Magn. Magn. Mater.* 10, 177 (1979).
9. C. M. Varma and W. Weber, *Phys. Rev. B* 19, 6142 (1979).
10. B. M. Powell, P. Martel, and A. D. B. Woods, *Phys. Rev.* 171, 727 (1968).

SOFT PHONONS IN hcp Tc

H. G. Smith N. Wakabayashi

Earlier measurements of the phonon dispersion curves of hcp Tc (a superconductor with $T_c = 7$ K) revealed the existence of anomalously low frequency optic modes having polarization vectors parallel to the c-axis. To obtain further information about the nature of these soft modes, the temperature dependencies of the dispersion curves have been investigated. The results for the phonons in the (001) direction are summarized in Fig. 5.12. The LO mode frequency at the Γ-point is nearly degenerate with the TO mode at room temperature. As the temperature is lowered, the LO mode softens dramatically while the TO mode remains virtually unaffected. Although no phase transition is known to occur below room temperature, this soft mode may be an indication of an incipient lattice instability associated with the superconductivity of this metal. This dispersion curve of this longitudinal mode has been interpreted on the basis of a dipolar fluctuation model involving only nearest-neighbor couplings. The frequency can be written within this phenomenological model as

$$4\pi^2 M\nu^2 = A(1 - \cos \pi\zeta) - \frac{B^2(1 - \cos \pi\zeta)^2}{1 + C(1 - \cos \pi\zeta)},$$

where M is atomic mass and A, B, and C represent the nearest-neighbor ion-ion interaction, ion-dipolar modulation coupling, and the dipolar-dipolar coupling, respectively. As one can see from the solid lines in the figure, the temperature dependence can be reproduced very well by varying the C parameter a few percent. Thus, the soft mode may be a manifestation of the lattice instability caused by the coupling between dipolar modulations. Interestingly, the anomalous longitudinal dispersion curve for Ru can be reproduced satisfactorily only by a model that includes the degree of freedom associated with the monopolar fluctuation, if the range of coupling is limited to the nearest-neighbor only (dashed line in Fig. 5.12).

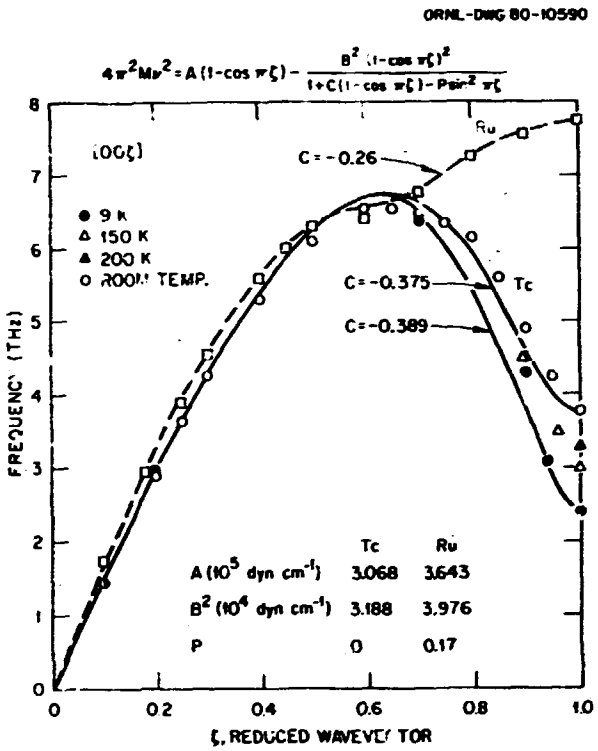

Fig. 5.12. Temperature dependence of the longitudinal mode in the [001] direction for Tc. The softening near $\zeta = 1.0$ can be reproduced by a nearest-neighbor dipolar fluctuation model (solid lines). The phonon dispersion curve for Ru at room temperature can be reproduced only by including the monopolar fluctuation term represented by the parameter P.

LATTICE DYNAMICS OF THE MIXED-VALENT $CeSn_3$

C. Stassis[1] G. D. McMasters[1]
C.-K. Loong[1] R. M. Nicklow

In recent years considerable theoretical and experimental interest has focused on the unstable valence behavior observed in rare earth and actinide alloys and intermetallic compounds. A consistent theoretical explanation of the fascinating properties of these systems will substantially further our understanding on a fundamental level of the electronic properties and the electron-phonon interactions in solids. Also, from a practical point of view, it is hoped that the study of these systems can contribute to our understanding of catalysis (which involves a valence change of one of the components involved in the process) as well as of high T_c superconductivity.

Although neutron scattering is an ideal experimental tool for the investigation of mixed-valence behavior in solids, few experiments have been performed because of the difficulty of growing single crystals of these systems. Two years ago single crystals of $CeSn_3$ of sufficient size for neutron experiments were grown at the Ames Laboratory, and we started a systematic neutron scattering investigation of the magnetic and lattice dynamical properties of this compound.

Because polarized neutron experiments[2] provided direct evidence for the mixed-valent character of $CeSn_3$, a systematic study of the dispersion curves of this compound along the [100], [110], and [111] symmetry directions was initiated. The most spectacular feature of the dispersion curves of $CeSn_3$ is the anomalous behavior observed along the [111] symmetry direction (Fig. 5.13). The longitudinal-like

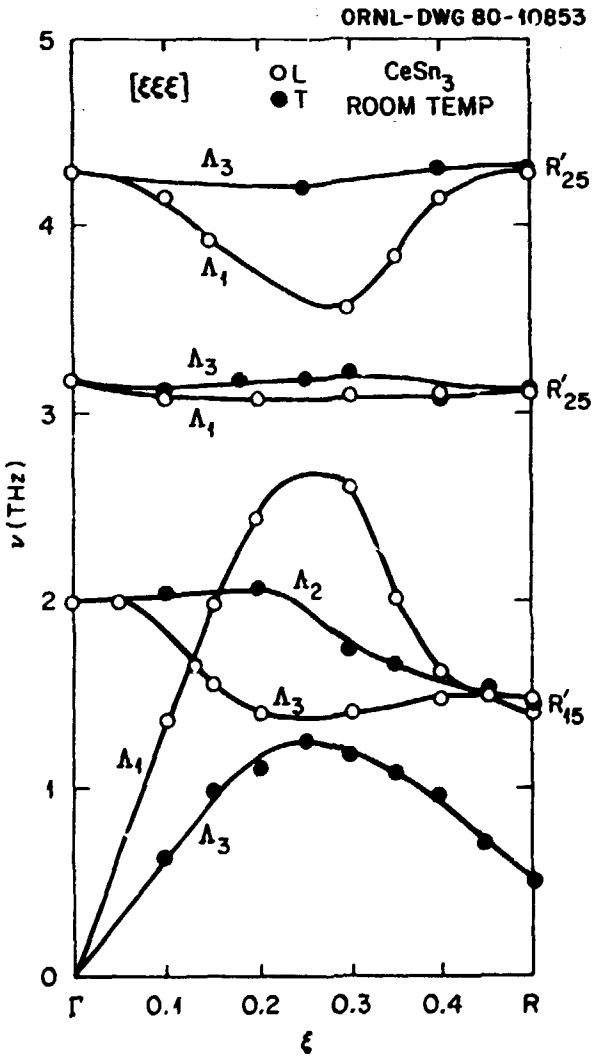

Fig. 5.13. The phonon dispersion relation for the [111] direction of $CeSn_3$ at room temperature.

optical branches are unusually soft and actually lie below the corresponding transverse branches;[3] also noticeable is the very low frequency (~2 MeV) of the TA[111] zone boundary mode. Thus, the phonon coupling to the valence fluctuation is significant even at room temperature. Although the detailed experimental results cannot be explained quantitatively in simple terms, the effect of the electron-phonon coupling on the frequencies can be easily visualized. Because only phonon modes that involve a volume change are expected to be strongly affected by the valence fluctuations. In fact, an examination of the phonon modes of $CeSn_3$ shows that the valence fluctuation effects should be more pronounced in the [111] direction, a finding which is in agreement with the experimental results. A quantitative analysis of the experimental results in terms of present-day theories[4] of mixed-valence systems is presently in progress.

1. Ames Laboratory and Iowa State University, Ames.
2. C. Stassis et al., *J. Appl. Phys.* **50**, 7567 (1979).
3. Similar results were obtained in the study of the mixed-valent $Sm_{.75}Y_{.25}S$: H. A. Mook and R. M. Nicklow, *Phys. Rev. B* **20**, 1656 (1979).
4. P. Entel et al., *Phys. Rev. Lett.* **43**, 2002 (1979); H. Bilz et al., *Phys. Rev. Lett.* **43**, 1998 (1979).

LATTICE DYNAMICS OF Ni_3Al

C. Stassis[1] C.-K. Loong[1]
F. Kayser[1] R. M. Nicklow

The properties of Ni_3Al are of considerable technological importance because the high-temperature strength of many Ni-base superalloys is due to the temperature dependence of the yield-stress behavior of Ni_3Al. In fact, the yield stress of Ni_3Al increases[2] dramatically upon raising the temperature from 77 to 900 K, and this effect was found to depend strongly on the orientation of the single-crystal specimens. Because it has been suggested[3] that these properties are related to lattice effects, we initiated a study of the lattice dynamics of Ni_3Al on stoichiometric single-crystal specimens.

The dispersion curves of Ni_3Al were measured at room temperature along the [100], [110], and [111] symmetry directions. We observed no unusual features in the room-temperature dispersion curves of this compound. In fact, a two-nearest-neighbor Born–von-Kármán model (10 independent force constants) provides a satisfactory fit to the experimental results, and the lattice specific heat added to the calculated electronic contribution is in quite good agreement with the measured total specific heat of Ni_3Al. Thus, the room-temperature results indicate that the temperature and orientation dependence of the yield strength of Ni_3Al is not directly related to the lattice dynamical properties of the compound. Therefore, it seems more likely that the temperature and orientation dependence of the yield stress is due to thermally activated cross slip of dislocations from the [111] onto [100] planes.

1. Ames Laboratory and Iowa State University, Ames.
2. C. Lall, S. Chin and D. P. Pope, *Metall. Trans.* **10A**, 1323 (1979).
3. R. G. Davies and N. S. Stoloff, *Trans. Metall. Soc. AIME* **233**, 714 (1965).

NEUTRON SCATTERING STUDY OF H DIFFUSION IN Th

W. A. Kamitakahara[1] D. T. Peterson[1]
D. Khatamian[1] H. A. Mook

The temperature dependence of the quasi-elastic scattering from a single crystal of $ThH_{0.12}$ has been measured to determine the geometry of the diffusion paths for H in Th metal. The measurements require high-resolution neutron scattering techniques and were made on the magnetically pulsed time-of-flight spectrometer using the correlation technique to obtain as high a signal-to-noise ratio as possible. The data have been compared with several models, and the most obvious model, in which protons diffuse by jumps from tetrahedral sites to nearest-neighbor tetrahedral sites, is in clear disagreement with the data. Other models in better accord with experiment are being considered.

1. Ames Laboratory and Iowa State University, Ames.

MAGNETIC PROPERTIES

MAGNETIC PROPERTIES OF Nd[1]

R. M. Moon C. Stassis[3]
W. C. Koehler G. R. Kline[3]
B. Lebech[2] S. K. Sinha[4]

In the first neutron diffraction study of Nd, Moon, Cable, and Koehler[5] discovered a complex diffraction pattern indicating modulated moment behavior

and at least two magnetic phases. They proposed approximate models to account for the major features of the diffraction patterns but acknowledged that the models were inadequate to explain all the features. In particular, small satellites found at the reciprocal lattice positions $(h \pm q, 0, 0)$ in the high-temperature phase (7.5–19.9 K) were not explained by their model. Recently, Bak and Lebech[6] have proposed a much more complicated model for the high-temperature phase based on Landau symmetry arguments and renormalization-group theory. By combining the experimental observation that the high-temperature transition is of second order with their theoretical considerations, they reached the interesting conclusion that the stable phase must have a triple-q structure.

However, the more complex magnetic model of Bak and Lebech still does not account for the troublesome peaks at $(h \pm q, 0, 0)$. They proposed a strong spin-lattice coupling that would produce a periodic modulation of the nuclear positions and result in nuclear satellites at $(h \pm q, 0, 0)$. This proposition has now been shown to be false, both by neutron polarization analysis experiments[1] and by x-ray diffraction.[7] The polarization analysis experiments clearly showed that the $(1 - q, 0, 0)$ satellite is caused by a modulated magnetic moment component in the basal plane and perpendicular to $\mathbf{b}_i$. None of the proposed magnetic models contained such a feature. Furthermore, the satellites have been shown to be slightly split in a direction parallel to this new magnetic component. That is, if $\hat{a}_i$ is a unit vector in the basal plane perpendicular to one of the six equivalent reciprocal lattice basis vectors $\mathbf{b}_i$, the propagation vectors of the modulated moment are

$$\mathbf{q}_i = q_{\parallel}\,\mathbf{b}_i \pm q_{\perp}|b_i|\hat{a}_i\ .$$

We find that $q_{\parallel}$ varies from 0.125 at 7.5 K to 0.145 at 19.9 K, while $q_{\perp}$ is 0.003 at 7.5 K, reaches a maximum of 0.006 at 15 K, and then falls to zero at 18.5 K. Polarization analysis experiments also show that the direction of the modulated moment is continuously variable in this temperature range. It is clear that the magnetic structure is more complex than hitherto imagined. The question of single-q or triple-q is still open.

We have now collected a fairly complete set of polarization analysis data on $(h \pm q, 0, l)$ peaks at 10 K. When combined with existing unpolarized beam data obtained by B. Lebech at Risø, these data will allow separate determinations of the structures associated with moment components parallel and perpendicular to the $\hat{a}_i$ directions. Preliminary results indicate that a good fit will be obtained with an extension of the Bak-Lebech model which includes moment components parallel to $\hat{a}_i$.

In another series of experiments using the conventional polarized beam technique, we have measured the temperature dependence of the magnetic susceptibility at the two crystallographic sites over the range 1.7 to 100 K. This measurement was done by inducing a ferromagnetic component through application of a magnetic field, measuring polarization ratios on several Bragg peaks, and then deducing the moment on the cubic and hexagonal sites. A calculated atomic $4f$ form factor in the dipole approximation was used in obtaining the atomic moments. Our results are displayed in Fig. 5.14. The applied field was 0.243 T for temperatures up to 31.6 K and then was increased to 0.486 T. Note that above 40 K, the two sites have the same susceptibility, indicating that crystal field and exchange effects are

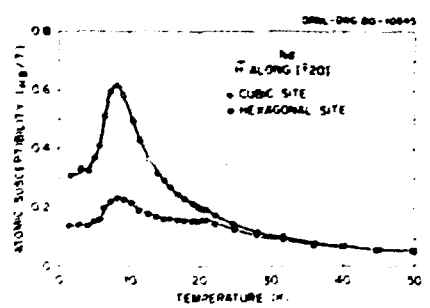

Fig. 5.14. Atomic susceptibility of Nd for both crystal sites as determined by polarized neutron diffraction.

small compared to this temperature. There is a slight cusp in both curves near the Néel point of 19.9 K indicating that both sites are partially ordered below the Néel point as in the Bak-Lebech model. It is probable that these cusps occur at a slightly higher temperature because of the applied field. In the temperature range 7.5 to 19.5 K, the largest ordered component is on the hexagonal site, so it is reasonable that the cubic site would have the larger susceptibility. Below 7.5 K the magnetic structure changes, with the major quantitative change being a much larger ordered component on the cubic sites, which is consistent with the rapid decrease in the cubic site susceptibility.

The crystal used in these experiments was grown by O. D. McMasters of the Ames Laboratory.

1. Summary of papers: R. M. Moon et al., *Phys. Rev. Lett.* **43**, 62 (1979); R. M. Moon and W. C. Koehler, *Journal of Magnetism and Magnetic Materials* (in press).

2. Guest scientist from Riso National Laboratory, Roskilde, Denmark.
3. Ames Laboratory and Iowa State University, Ames.
4. Argonne National Laboratory, Argonne, Ill.
5. R. M. Moon, J. W Cable, and W. C. Koehler, *J. Appl. Phys.* 35, 1041 (1964).
6. Per Bak and Bente Lebech, *Phys. Rev. Lett.* 40, 800 (1978).
7. B. Lebech, J. Als-Nielsen, and K. A. McEwen, *Phys. Rev. Lett.* 43, 65 (1979).

MAGNETIC FIELD DEPENDENCE OF THE NEUTRON SCATTERING FROM THE REENTRANT SUPERCONDUCTOR $ErRh_4B_4$

H. A. Mook Z. Fisk[1]
M. B. Maple D. C. Johnston[1]

Because of its unusual magnetic and superconducting properties, the ternary compound $ErRh_4B_4$ has stimulated considerable interest. We have made powder diffraction measurements on $ErRh_4B_4$ placed in a magnetic field. The sample was held at a constant temperature of 1.79 K, and measurements of the long-range magnetic order were made by examining the strength of the (101) magnetic diffraction peak. At magnetic fields higher than 80 mT, the superconductivity is destroyed and long-range magnetic order is observed. The (101) peak intensity increases with increasing field, the ordered moment values corresponding to $5.06 \pm 0.5\,\mu_B$ at 1 T and $6.9 \pm 0.5\,\mu_B$ at 2 T. The ordering is found to be ferromagnetic, with the moment oriented in the tetragonal basal plane. The peaks are resolution limited, showing long-range magnetic order of at least 150 Å.

Figure 5.15 shows the field dependence of the (101) intensity for low field values. We see that there is no magnetic intensity until the applied field is greater than 80 mT, at which point long-range magnetic order develops suddenly. The ordered moment increases with increasing fields up to 140 mT, at which point the field was lowered in value. The ordered moment gets smaller with reduced fields but follows a line back toward the origin giving a large hysteresis. At small fields the ordered moment departs from this line and there is a small ordered moment even at zero field. This behavior is consistent with a suggestion by Freeman and Jarlburg[2] that, in lowering an external field from a value higher than the critical field, it may be possible to form a mixed state in which normal and ferromagnetic regions of the compound coexist with superconductivity.

1. University of California, San Diego.
2. A. J. Freeman and T. J. Jarlburg, *J. Appl. Phys.* 50, 1876 (1979).

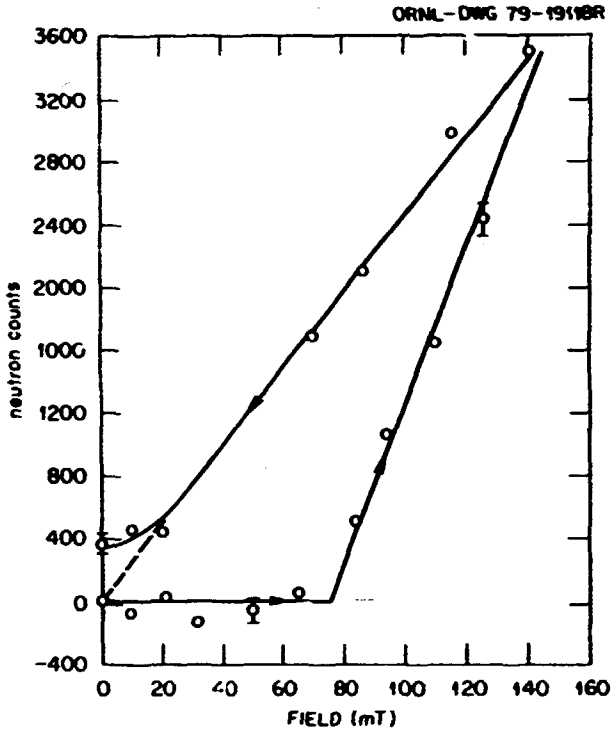

Fig. 5.15. Magnetic intensity of the (101) reflection from $ErRh_4B_4$ as a function of an applied magnetic field. Arrows indicate the direction of change of magnetic field.

NEUTRON SCATTERING STUDY OF REENTRANT SUPERCONDUCTIVITY IN $Ho_{0.6}Fr_{0.4}Rh_4B_4$

H. A. Mook M. B. Maple[1]
W. C. Koehler Z. Fisk[1]
D. C. Johnston[1]

Since the discovery of reentrant superconductivity in $ErRh_4B_4$[2] and $Ho_{1.2}Mo_6S_8$,[3] there has been a great deal of interest in the nature of the superconducting-magnetic transition at the lower critical temperature T_{c2}. The pseudoternary system $(Er_{1-x}Ho_x)Rh_4B_4$ is a particularly good testing ground for the experimental and theoretical studies of reentrant superconducting behavior. $HoRh_4B_4$ becomes a ferromagnet at low temperatures, ordering directly from the paramagnetic normal state. The material orders along the *c* axis with nearly the full free ion Ho moment. The transition is found to be second order, with considerable magnetic precursor or critical scattering observed above the ordering temperature.[4] $ErRh_4B_4$ is a reentrant superconductor with an upper and lower transition temperature of about 8.7 and 1.0 K. It orders ferromagnetically at the lower transition temperature in the basal plane with a moment of $5.6\,\mu_B$, and considerable precursor scattering is again found above the ordering temperature.[5]

Our measurements on the superconducting-magnetic transition in $Ho_{0.6}Er_{0.4}Rh_4B_4$ show that the material orders in a very different manner from either $ErRh_4B_4$ or $HoRh_4B_4$. Figure 5.16 shows the magnetization as measured from the strength of the (101) magnetic peak plotted vs temperature. We see little, if any, critical or precursor scattering above the ordering temperature of 3.60 K. Instead, there is a sudden jump in the magnetization at 3.60 K; and since the magnetic scattering intensity is proportional to the square of the magnetic moment, we find that the system develops almost one-half of its saturated moment in a temperature interval of 0.05 K. Little hysteresis was found in the transition temperature, but hysteresis was found in the magnetization developed at a given temperature. The transition appears to be first order, which is the expected behavior when superconductivity is destroyed by a macroscopic magnetic field. The magnetic ordering was found to be ferromagnetic with the moment along the c axis. The moment value is about $5.0 \pm 0.5\mu_B$ at 1.6 K, a value considerably below the free ion moment for Ho or Er, but is consistent with a model in which only the Ho atoms order with their full moment value. Additional measurements are planned for the $(Er_{1-x}Ho_x)Rh_4B_4$ system to further elucidate the nature of the superconducting to magnetic transition.

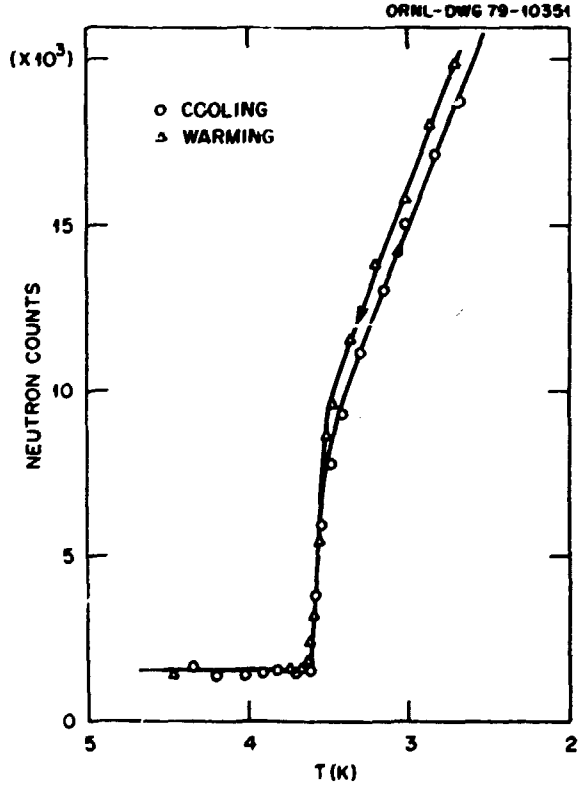

Fig. 5.16. Temperature dependence of magnetization at the superconducting-magnetic transition in $Ho_{0.6}Er_{0.4}Rh_4B_4$ as determined from the (101) peak intensity.

1. University of California, San Diego.
2. W. A. Fertig et al., *Phys. Rev. Lett.* 38, 987 (1977).
3. M. Ishikawa and O. Fisher, *Solid State Commun.* 23, 37 (1977).
4. G. H. Lander, S. K. Sinha and F. Y Fradin, *J. Appl. Phys.* 50, 1990 (1979).
5. D. E. Moncton, et al., *Phys. Rev. Lett.* 39, 1164 (1979).

MAGNETIC STRUCTURES OF HoB_4

W. C. Koehler Z. Fisk[1]
H. A. Mook M. B. Maple[1]

The rare earth tetraborides, except for PrB_4, have macroscopic magnetic properties characteristic of antiferromagnets. The Néel temperatures of the heavy rare earth tetraborides fall off monotonically from 42 K for GdB_4 to 10 K at YbB_4 for that of HoB_4, which is anomalously low at 7 K.[2] These compounds are interesting in themselves, they are, furthermore, starting materials in the preparation of the reentrant superconductors RRh_4B_4, where R is a rare earth atom.

Neutron diffraction measurements have been made on polycrystalline specimens of ErB_4 and DyB_4.[3] From the data a simple colinear antiferromagnetic structure has been proposed. The moments, which are parallel to the c axis of the crystallographic tetragonal unit cell, are arranged in sheets of parallel spins that alternate in sign along a direction in the plane normal to the c axis. The intensity-vs-temperature variation of the magnetic peak intensities is typical of a second-order phase transition.

Recently, we have initiated a study of the magnetic properties of HoB_4. The sample, originally in the form of tiny crystals, was crushed to a fine powder and loaded into a thin-walled Al capsule. A portion of the sample was checked by x-ray diffraction by Burl Cavin, Metals and Ceramics Division, who reported lattice constants $a = 7.087$ Å and $c = 4.007$ Å at room temperature. No lines other than those expected for the tetragonal HoB_4 structure were observed.

Neutron diffraction patterns were taken at room temperature and at various lower temperatures down

to 1.8 K. From these data, in agreement with recent measurements of the specific heat,[4] we conclude that there are two magnetic phases in HoB_4. The phase at higher temperatures, which has T_c at about 7.5 K, is characterized by a series of magnetic reflections that cannot be indexed on any simple multiple of the chemical cell lattice parameters. At about 5.7 K, these reflections abruptly disappear and magnetic intensity appears at the positions characteristic of the ErB_4 magnetic structure. Several additional weak magnetic reflections exist as well. The transition to the lower temperature structure appears to be a first-order transition, while a second-order transition occurs at the higher temperature. The lower phase transition is illustrated by the data of Fig. 5.17.

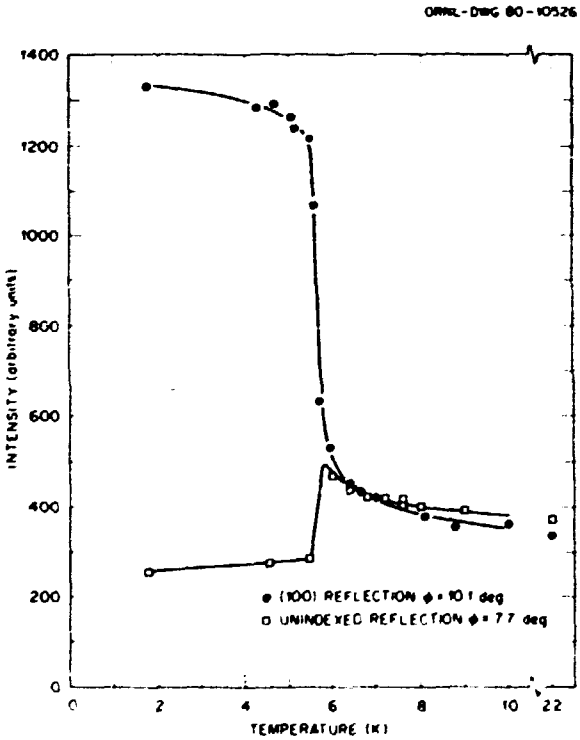

Fig. 5.17. Temperature dependence of the intensity of two magnetic reflections in HoB_4. Circles: (100) at a scattering angle $\phi = 10.1°$. Squares: unindexed reflection at $\phi = 7.7°$. The intensities shown are uncorrected for background and reflect the changes in paramagnetic scattering with temperature.

As yet, the magnetic structure of the high-temperature phase is unknown. The low-temperature phase has a uniaxial component with moments along the c axis. In addition, there is most probably a component normal to the c axis that is oscillatory or helical. Single-crystal structure studies are in progress.

---

1. University of California, San Diego.
2. K. H. J. Buschow and J. H. N. Creyghton, *J. Chem. Phys.* 57, 3910 (1972).
3. W. Schafer, G. Will, and K. H. J. Buschow, *J. Chem. Phys.* 64, 1994 (1976).
4. M. B. Maple, private communication.

MAGNETIC MOMENT DISTRIBUTION IN Ni-Pt ALLOYS[1]

R. E. Parra[2] J. W. Cable

The magnetic behavior of disordered Ni-Pt alloys near the critical concentration (c_0) for the onset of ferromagnetism has been interpreted in terms of the Stoner-Edwards-Wohlfarth model of weak itinerant ferromagnetism. This interpretation implies a spatially homogeneous moment distribution in sharp contrast to the behavior of other Ni-base systems such as Ni-Cu and Ni-Rh, which exhibit distinctly inhomogeneous moment distributions in the form of ferromagnetic clusters near c_0. The neutron results on Ni-Cu and Ni-Rh have been interpreted in terms of a local environment model that leads to ferromagnetic clusters near c_0 and that should probably also apply to Ni-Pt. To help resolve this question, we decided to determine the moment distribution in Ni-Pt alloys by neutron diffuse scattering methods.

The neutron cross sections give directly the nuclear, $S(\mathbf{K})$, and the nuclear-magnetic, $M(\mathbf{K})$, correlations. In the absence of lattice distortions, these are given by

$$S(\mathbf{K}) = \sum_{\mathbf{R}} e^{i\mathbf{K}\cdot\mathbf{R}} \langle (p_{\mathbf{n}+\mathbf{R}} - c)(p_{\mathbf{n}} - c) \rangle \; c(1-c) \qquad (1)$$

and

$$M(\mathbf{K}) = \sum_{\mathbf{R}} e^{i\mathbf{K}\cdot\mathbf{R}} \langle (p_{\mathbf{n}+\mathbf{R}} - c)\mu_{\mathbf{n}} \rangle \; c(1-c) \, , \qquad (2)$$

where $\langle\,\rangle$ denotes a configurational average, $p_{\mathbf{n}}$ is the number of impurity atoms at lattice site $\mathbf{n}$, $S(\mathbf{K})$ describes the positional SRO, and $M(\mathbf{K})$ describes the moment response to a site occupation fluctuation.

Nuclear scattering functions were obtained from both the polarized and unpolarized neutron data. These functions show very pronounced structure corresponding to a large amount of SRO and were least squares fitted to the function

$$S(K) = \sum_i Z_i \alpha_i \frac{\sin KR_i}{KR_i} + \sum_i Z_i \beta_i \left(\frac{\sin KR_i}{KR_i} - \cos KR_i \right), \quad (3)$$

where Z_i is the coordination number of the shell of radius R_i and α_i and β_i are SRO and lattice distortion parameters. Fitted parameters for all the alloys are given in Table 5.4.

The observed $M(K)$ functions, shown in Fig. 5.18, exhibit less pronounced structure. The solid curves were fitted to the expression

$$M(K) = \bar{\mu}_{Pt} f_{Pt}(K) - \bar{\mu}_{Ni} f_{Ni}(K) + \sum_i Z_i m_i \frac{\sin KR_i}{KR_i} \quad (4)$$

to obtain the average moments. Here we neglect the small lattice distortion terms and use $f_{Ni} = \exp(-0.044\ K^2)$ and $f_{Pt} = \exp(-0.105\ K^2)$, which closely approximate the experimental form factors over this limited K region. The difference between the Ni and Pt form factors allows a direct determination of $\bar{\mu}_{Ni}$ and $\bar{\mu}_{Pt}$ as fitting parameters. The moments obtained are given in Table 5.5, where the quoted errors are the statistical errors from the fitting. The average moment per alloy atom as calculated from these fitted values is compared with our bulk magnetization data in the last two columns of Table 5.5. The agreement is quite satisfactory.

The effects of SRO on the moment distribution can be removed by simply dividing $M(K)$ by $S(K)$. The moment disturbance functions $M(K)$ obtained in this way are shown in Fig. 5.19. These show the same general behavior as the $M(K)$ functions for Ni-Cu and Ni-Rh alloys, that is, there are peaks in the forward direction which become sharper with increasing impurity content. This behavior corresponds to moment disturbance effects that become

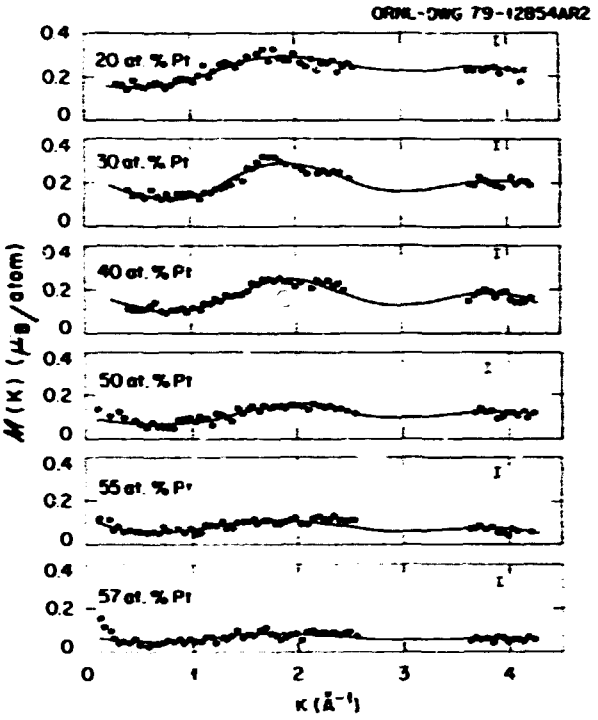

Fig. 5.18. Nuclear-magnetic correlation functions of Ni-Pt.

Table 5.5. Moment disturbance parameters of Ni-Pt alloys

x	$\bar{\mu}_{Ni}$	$\bar{\mu}_{Pt}$	δ	ϕ_1	$\bar{\mu}_{moment}$	$\bar{\mu}_{magn}$
0.2	0.515(20)	0.27(3)	0.81(15)	0.28(3)	0.465(23)	0.482(24)
0.3	0.44(22)	0.22(2)	0.83(17)	0.25(5)	0.381(17)	0.381(19)
0.4	0.37(19)	0.19(2)	0.34(14)	0.25(6)	0.301(15)	0.285(14)
0.5	0.79(18)	0.17(2)	0.20(3)	0.01(2)	0.226(14)	0.185(9)
0.55	0.15(18)	0.057(22)	0.16(3)	0.01(3)	0.149(15)	0.163(5)
0.57	0.145(18)	0.079(22)	0.10(2)	0.005(1)	0.147(15)	0.078(4)

Table 5.4. SRO and lattice distortion parameters

x	α_1	α_2	α_3	α_4	α_5	β_1	χ^2/ν
0.2	0.116(5)	0.098(20)	0.061	0.073	0.050	0.013(4)	0.96
0.3	0.160(5)	0.191(19)	0.017	0.042	0.092	0.043(4)	1.59
0.4	0.150(5)	0.215(19)	0.056	0.096	0.107	0.050(4)	1.68
0.5	0.135(5)	0.226(18)	0.063	0.075	0.059	0.057(4)	1.37
0.55	0.167(5)	0.294(21)	0.069	0.138	0.117	0.071(5)	1.37
0.57	0.122(5)	0.176(20)	0.041	0.095	0.025	0.067(4)	1.98

increasingly longer ranged with increasing Pt content. The solid curves here were fitted to the expression

$$M(K) = \Delta\mu(K) + \sum_i Z_i \phi_i \frac{\sin KR_i}{KR_i} + \sum_i Z_i \gamma_i \left(\frac{\sin KR_i}{KR_i} - \cos KR_i \right) / S(K), \quad (5)$$

where ϕ_i and γ_i are the moment disturbance and lattice distortion parameters. We assume a Yukawa form for ϕ_i, that is,

$$\phi_i = \frac{R_1}{R_i} \phi_1 \exp[-k(R_i - R_1)], \quad (6)$$

and fit to the parameters ϕ_1, k, and γ_1. The magnetic parameters are given in Table 5.5.

The $M(K)$ functions displayed in Fig. 5.19 correspond to inhomogeneous moment distributions that may be described as ferromagnetic clusters in the critical concentration region. Nevertheless, the bulk measurements give evidence of clusters for Ni-Cu and Ni-Rh but not for Ni-Pt in this region. We believe the reason for this is the difference in SRO of these systems and not in the underlying mechanism for the onset of ferromagnetism. Ni-Rh forms truly random alloys, Ni-Cu exhibits clustering, and Ni-Pt shows a strong preference for unlike nearest neighbors. Note that $M(K)$ describes the moment response to a site occupation fluctuation in the actual SRO state. This response is unaffected by SRO in Ni-Rh, enhanced by SRO in Ni-Cu, and damped out by SRO in Ni-Pt.

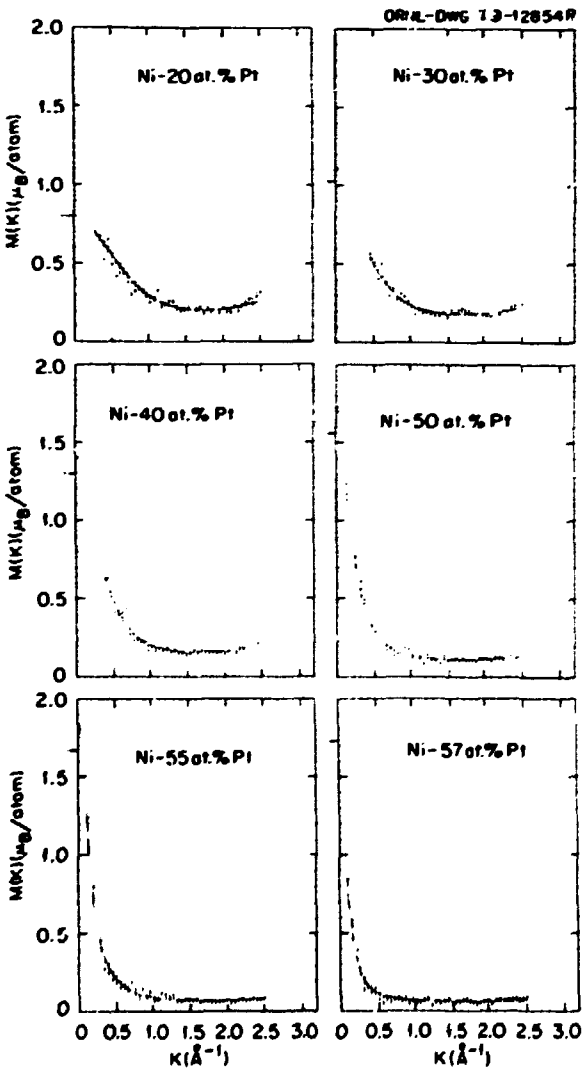

Fig. 5.19. Moment disturbance functions of Ni-Pt.

1. Summary of paper: *J. Appl. Phys.* **50**, 7522 (1979).

2. IVIC graduate laboratory participant from Georgia Institute of Technology, Atlanta; present address: Instituto Venezolano de Investigaciones Cientificas, Caracas, Venezuela.

DETERMINATION OF THE Pd-Gd EXCHANGE CONSTANT BY NEUTRON DIFFUSE SCATTERING AND THE Pd POLARIZATION IN PdGd ALLOYS[1]

J. W. Cable R. E. Parra[2]

Magnetization data[3] for ferromagnetic Pd-Gd alloys in low magnetic fields give saturation moments smaller than the expected 7 μ_B/Gd. This finding has been interpreted as evidence for a negative Pd d-band polarization. However, from a semiempirical fit of high-field magnetization data for more dilute paramagnetic alloys, Guertin et al.[4] conclude that the Gd moment does not saturate, even at 4.2 K and 20 T, and that no evidence exists for a negative Pd polarization. We have determined th · field and temperature dependence of the Gd moment in the ternary alloy $Pd_{0.98}Fe_{0.01}Gd_{0.01}$ from neutron diffuse scattering measurements. An effective Pd-Gd exchange constant is derived and used in a simple molecular field model to reexamine the magnetization data for the binary Pd-Gd alloys.

Polarized-neutron diffuse-scattering measurements were made on polycrystalline samples of $Pd_{0.99}Fe_{0.01}$, $Pd_{0.99}Gd_{0.01}$, and $Pd_{0.98}Fe_{0.01}Gd_{0.01}$ prepared with the low-absorbing isotope ^{160}Gd. At these concentrations, the ternary alloy cross section is just the sum of the binary alloy cross sections. Furthermore, since the Pd-Fe subsystem is much more strongly coupled ($T_c \cong 50$ K) than the Pd-Gd subsystem ($T_c \cong 2$ K), the dramatic H and T dependencies of the ternary cross sections shown in Fig. 5.20 may be attributed to reorientation of the Gd moment relative to the Pd-Fe moments. Thus, in Fig. 5.20, the 4.2 K, 0.2 T data correspond to Pd-Fe moments aligned parallel to the applied field, while the Gd moments are aligned antiparallel. This is illustrated by the solid curve, which represents the difference between the two binary alloy cross sections. This opposite Gd moment alignment can be destroyed by increasing the field to 4 T, where the ternary cross section becomes nearly the same as that of Pd-Fe.

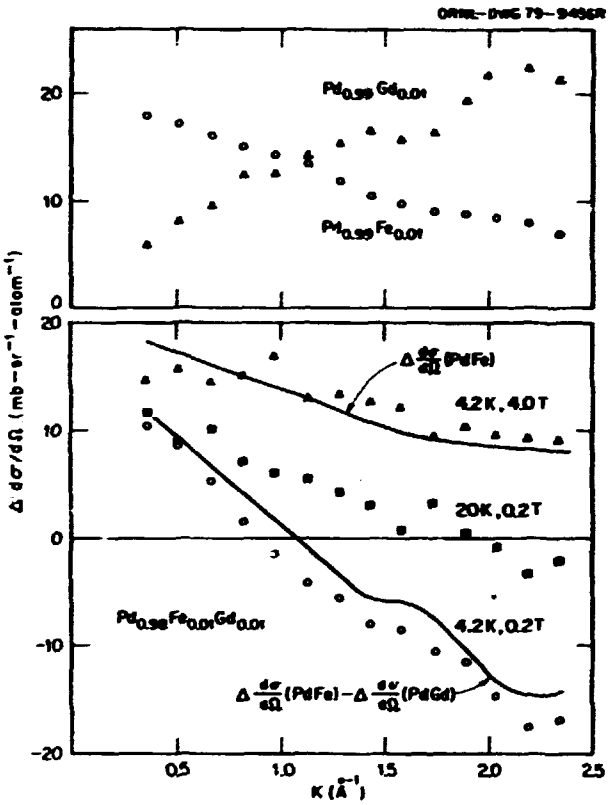

Fig. 5.20. Polarized-neutron difference cross sections for $Pd_{0.99}Fe_{0.01}$, $Pd_{0.99}Gd_{0.01}$, and $Pd_{0.98}Fe_{0.01}Gd_{0.01}$.

These results suggest a molecular field model in which the applied field just cancels the effective field at the Gd sites near 4 T, and, indeed, the observed behavior is consistent with a spin 7/2 Brillouin function and an effective field of −3.9 T. The alloy $Pd_{0.99}Fe_{0.01}$ has a giant moment of 8 μ_B with 3 μ_B localized on the Fe atom so that the average Pd moment is 0.05 μ_B. We assume that this also occurs in the ternary alloy; if so, the effective field of −3.9 T corresponds to a Pd-Gd exchange constant of $J = -0.018 \pm 0.001$ eV. Within experimental error, this is the same as was determined[5,6] from g-shift data for paramagnetic alloys in the 500-ppm concentration region. A constant J over such a large concentration range implies that the effective field at a Gd site arises from a linear superposition of long-range interactions. In that event, a mean field treatment of the effective fields at both the Gd and the Pd sites should be a good approximation. We now examine the magnetization of the binary Pd-Gd alloys in terms of such a model.

Within a simple molecular field model, the magnetization of dilute Pd-Gd alloys is

$$\sigma = \sigma_{Gd} + \sigma_{Pd} = 7\,\mu_B\, c B_{7/2}(x) + \chi H_{Pd}\,, \qquad (1)$$

where

$$x = g\,\mu_B\, S H_{Gd}/kT\,,$$

and with

$$H_{Gd} = H_0 + J\,\sigma_{Pd}/g^2\,\mu_B^2\,. \qquad (2)$$

and

$$H_{Pd} = H_0 + J\,\sigma_{Gd}/g^2\,\mu_B^2\,. \qquad (3)$$

Here, σ_{Gd} saturates for $H_0 \geq 15$ T and σ_{Pd} can then be extracted from the parameterized data of ref. 4. Extrapolation of the high-field σ_{Pd}-vs-H_0 data to $\sigma_{Pd} = 0$ gives the effective field at the Pd sites while the slope gives χ. The J values obtained by this procedure are in reasonable agreement with the neutron and g-shift results, and the χ values show the same kind of concentration dependence as was observed[4] for PdY and PdLu alloys. This agreement supports the model, which we, therefore, extend into the low-field region.

The calculated magnetizations are compared with experiment in Fig. 5.21. Here, the solid curves represent the data, and the dashed curves are calculated by iteration using Eqs. (1), (2), and (3). In this calculation J is taken from the neutron data and χ from the high-field slope of σ_{Pd} vs H_0. The overall

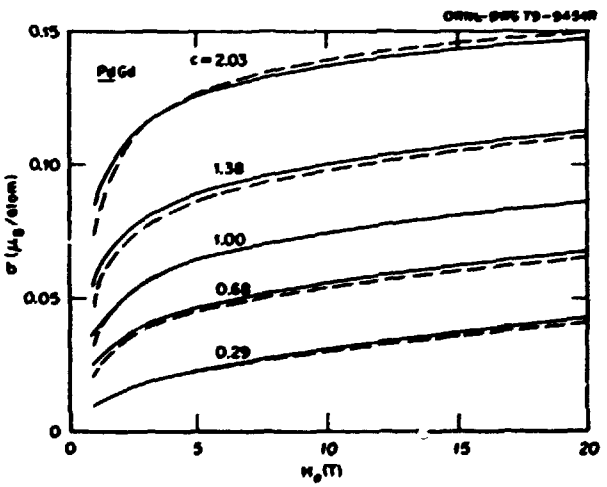

Fig. 5.21. Comparison of the calculated and observed PdGd magnetizations. Solid curves are the parameterized data of ref. 4, and the dashed curves are calculated from the molecular field model. Concentrations are in at. % Gd.

agreement is very good, especially in view of the fact that no fitting is involved.

The calculated Pd magnetizations are negative at low fields. We suggest that this situation carries over into the ferromagnetic region, where the spontaneous Pd polarization per Gd ion is $7\chi J/g^2\,\mu_B$. At 2% Gd, where $\chi = 5.1 \times 10^{-4}$ emu/mole, this gives $\sigma_{Pd}/c = -0.5\,\mu_B$ to be compared with Crangle's results,[3] which vary from about $-1.0\,\mu_B$ at 2% Gd down to $-0.5\,\mu_B$ at 10% Gd. We conclude that the spontaneous Pd polarization is opposite to the Gd moment but that it can be reversed in high magnetic fields.

---

1. Summary of paper: *Phys. Rev. B* 20, 2765 (1979).
2. IVIC graduate laboratory participant from the Georgia Institute of Technology, Atlanta; present address: Instituto Venezolano de Investigaciones Cientificas, Caracas, Venezuela.
3. J. Crangle, *Phys. Rev. Lett.* 13, 569 (1964).
4. R. P. Guertin et al., *Phys. Rev. B* 7, 274 (1973).
5. R. A. Devine et al., *Solid State Commun.* 11, 525 (1972).
6. R. H. Taylor and B. R. Coles, *J. Phys. F* 4, 303 (1974).

MAGNETIC EXCITATIONS IN Er

R. M. Nicklow N. Wakabayashi

While all the heavy rare earth metals (Tb-Tm) possess quite unusual and complex long-range magnetic ordering, the phase diagram of Er is perhaps the most unusual. Below about 18 K, the magnetic structure of Er (which has the hcp crystal structure) is the so-called ferromagnetic spiral or conical structure. In this structure, the direction of the atomic moments is a superposition of a ferromagnetic component parallel to the c axis and a basal plane component that rotates from plane to plane, forming a spiral with a wave vector that is incommensurate with the lattice. Between 84 K (the Néel temperature) and 52 K, the basal plane moment is not ordered and the c-axis moment is modulated nearly sinusoidally, again with a period that is not commensurate with the lattice. As the temperature is lowered, the basal plane component begins to order at 52 K, and between 52 K and 18 K, the magnetic order gradually changes from the longitudinally modulated structure to the conical structure.

In the conical structure, because the total moment on each atom participates in the long-range order, a theoretical description of the magnetic excitations in terms of spin waves is possible. Previous neutron scattering measurements at ORNL of the spin-wave dispersion relation shed considerable light both on the form of the dispersion relation and on the magnetic exchange and anisotropy interactions.[1]

In the longitudinally modulated structure, only a portion (which varies from atom to atom) of the total atomic moment participates in the long-range order. The types of magnetic excitations to be expected in such a structure and their relationship to the interatomic magnetic interactions are not yet clear from a theoretical point of view. However, the possible existence of new types of excitations related to time-dependent changes in the phase and amplitude of an incommensurate structure have been proposed for charge density waves. Consequently, we have undertaken a program to characterize experimentally the magnetic excitation spectrum for Er, which possesses one of the few longitudinally modulated spin-density wave structures in nature.

The major portion of the recent experimental work has been carried out at 60 K. At this temperature the modulation wave vector $\mathbf{q}_0$ for the magnetic structure is approximately $\mathbf{q}_0 = (0, 0, 0.29)2\pi/c$. Preliminary results obtained in exploratory measurements can be broadly categorized into two groups. In one group energy scans for constant Q with Q between (002) and (003) and between (100) and (101), in reduced reciprocal lattice units, show rather broad energy distributions having some structure that depends on Q. Some typical results are shown in Fig. 5.22. Significant intensity extends to energies above that (0.95 THz) corresponding to the maximum spin-wave energy observed previously[1] in the conical phase at 5 K or in this experiment at 10 K (see Fig. 5.22).

The second group of results was obtained in Q-scans with the energy transfer held constant at various values between 0.1 and 0.5 THz. In these measurements Q was scanned through values that included the positions of satellites, $\tau \pm \mathbf{q}_0$, where τ is a reciprocal lattice vector that corresponds to the Bragg diffraction peaks of the incommensurate structure. Results obtained for Q near $(0, 0, 2 - q_0)$ are shown in Fig. 5.23. In this figure Q is plotted relative to the satellite position so that data for different temperatures can be compared, because q_0 is temperature-dependent. At 10 K two peaks that correspond to the spin wa[illegible] at $\pm\mathbf{q}$ as measured previously[1] are observed. [illegible] this temperature the conical structure produces intense satellite diffraction peaks due to the ordering of the basal plane moment. Consequently, the peaks observed in Fig. 5.23 at 10 K correspond to acoustic spin waves. As the temperature is raised above 50 K, the basal plane moment is no longer ordered and the satellite intensity at $(0, 0, 2 - q_0)$ essentially vanishes. Nevertheless, strong inelastic scattering remains,

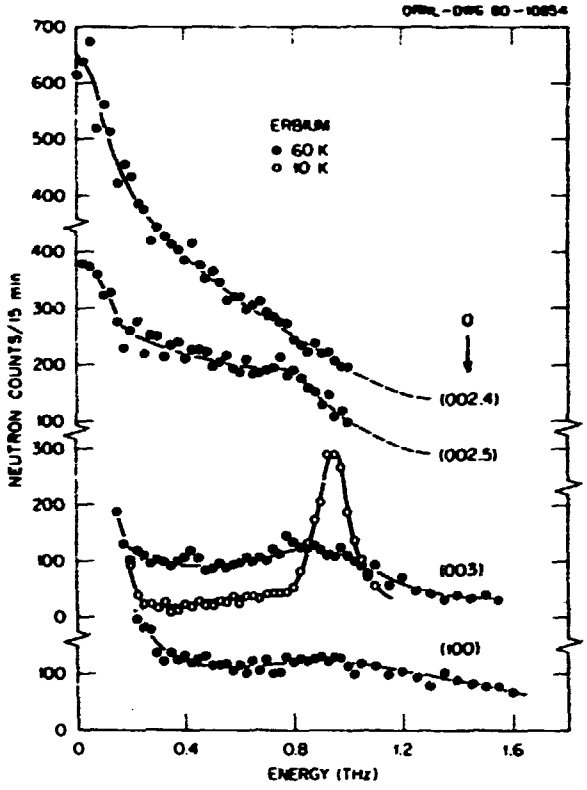

Fig. 5.22. Constant-Q measurements of the energy distribution of neutrons scattered by Er at 60 and 10 K.

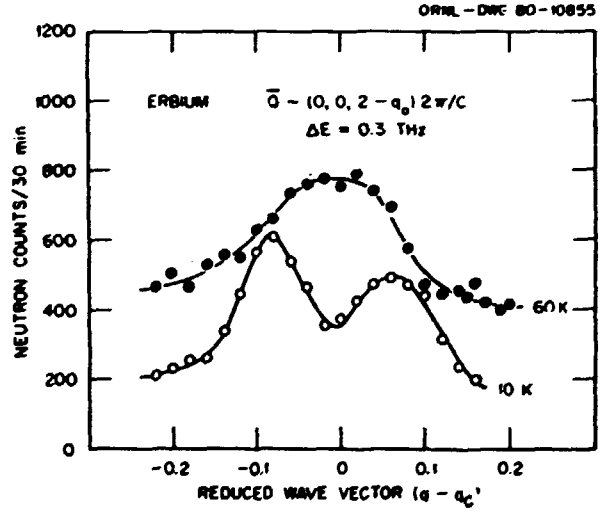

Fig. 5.23. Constant-E measurements of the neutron scattering near $Q = (0, 0, 2\text{-}q_0)$ at two temperatures.

although it is not possible with the q- resolution used for the measurements shown in Fig. 5.23 to resolve any structure that might indicate the existence of well-defined spin waves at this temperature. However, a small increase in the q-width of the scattering with increasing energy is observed which may be indicative of a very steep dispersion relation. Inelastic scattering with similar intensity is also observed in the vicinity of $(0, 0, 2 + q_0)$, $(1, 0, q_0)$ and $(1, 0, 1 + q_0)$ even though the elastic intensities at these various satellite positions differ by several orders of magnitude.

---

1. R. M. Nicklow et al., *Phys. Rev. Lett.* 27, 334 (1971).

TEMPERATURE DEPENDENCE OF THE MAGNETIC EXCITATIONS IN Gd

J. W. Cable N. Wakabayashi R. M. Nicklow

We have measured the magnetic excitations above and below the Curie temperature in Gd by inelastic neutron scattering. Gadolinium is particularly appealing for this type of study for several reasons. It has the least complicated magnetic ordering of all the rare earth metals, being a simple ferromagnet below $T_c = 293$ K. Furthermore, the $4f$ shell of the Gd ion is half filled, so that there are no complications associated with orbital moments or crystal field effects. Therefore, the spin dynamics are determined only by isotropic Heisenberg exchange interactions. Experimentally, the system is favorable because of readily accessible energy transfers and because of the large moment per atom, which gives high neutron scattering intensities.

The constant-Q neutron measurements were made out to the Brillouin zone boundaries in the [001] and [100] directions and covered the temperature range $0.3 \leqslant T/T_c \leqslant 2.0$. The observed magnetic excitation spectra are illustrated in Fig. 5.24, which shows the thermal evolution of spin waves propagating along the [001] direction. The left panel shows the typical behavior of small q spin waves. Here, the spin-wave peak observed at low temperature shifts rapidly down in energy with increasing temperature and near T_c collapses into a Lorentzian-shaped line centered at zero energy transfer. There is little, if any, broadening of the peak width. The typical large q behavior is shown in the right panel, where, there is a relatively slow decrease in the peak position with increasing temperature. In contrast to the small q behavior, there is appreciable line broadening due to lifetime effects caused by magnon-magnon interactions. The spin-wave peak is no longer observed at 295 K, which is just above T_c, but a shoulder remains on the excitation spectrum and persists up to about 1.2 T_c.

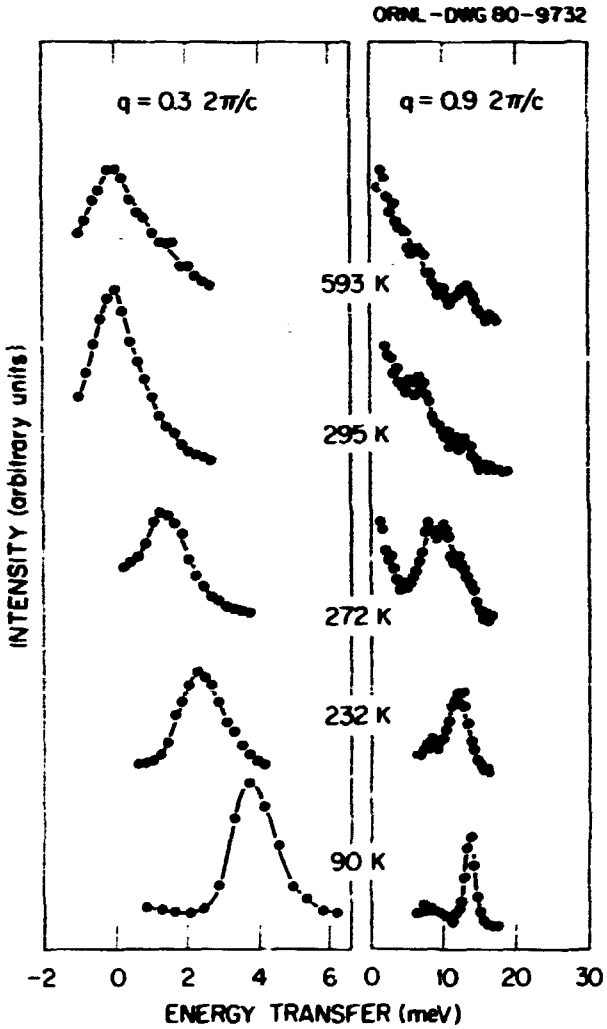

Fig. 5.24. Temperature evolution of the magnetic excitation spectra of Gd.

Most theoretical treatments of magnetic excitations deal with the $T = 0$ and $T \gg T_c$ limits at general q values or with the small q limit at general temperatures. Very little work has been done in the large q-intermediate temperature regions covered by these measurements. There is a recent numerical calculation by Hubbard[1] which qualitatively reproduces some of the observed features. However, these calculations were for a simple cubic structure with nearest-neighbor interactions, and it is not clear how these would be altered for the present case of an hcp structure with long-range interactions. At this stage we can only conclude that the observed shoulder in the magnetic excitation spectrum shows that there are characteristic frequencies associated with the spin correlations in Gd above T_c. Further measurements and analyses are in progress.

1. J. Hubbard, *J. Phys. C* 4, 53 (1971).

FORBIDDEN MAGNON SCATTERING IN $Ni_{0.99}Mo_{0.01}$

C. H. Perry[1] R. M. Moon
R. D. Lowde[2] J. B. Sokoloff[3]
B. Pagonis[3]

The observation of neutron scattering from magnons in Ni above T_c by Mook, Lynn, and Nicklow[4] has prompted a number of theoretical papers. The basic physical concept in these theories is that there must exist strong short-range magnetic order above T_c. That is, the local magnetization varies slowly throughout space so that its average value is zero but there exist regions sufficiently large to sustain spin-wave excitations in which the local magnetization is nearly constant and nonzero. Sokoloff[5] has pointed out an interesting consequence of this behavior on the polarization dependence of the neutron cross section, and this polarization effect has been demonstrated experimentally by Sokoloff et al.[6]

Consider first the polarization dependence of the magnon cross section in a saturated ferromagnet, first derived by Sáenz.[7]

$$\frac{d^2\sigma}{d\Omega dE'} \sim [1 + (\hat{Q}\cdot\hat{M})^2 + 2(\hat{Q}\cdot\hat{M})(\hat{Q}\cdot\hat{P})] ,$$

where $\hat{Q}$ is the unit scattering vector, $\hat{M}$ is the unit magnetization vector, and $\hat{P}$ is the unit neutron polarization vector. This factor enters the cross section for magnon creation (neutron energy loss); for magnon annihilation, the sign of the third term is reversed. For the case when $\hat{Q}$, $\hat{M}$, and $\hat{P}$ are all parallel, this factor goes from 4 to 0 when the neutron polarization is reversed; that is, the cross section for one of the incident neutron spin states is forbidden.

Now imagine that the sample is made up of small regions, or droplets, in which the magnetization is constant but the direction of the magnetization changes from one droplet to another. We apply a weak field along Q to control the direction of the average magnetization and assume that the neutron polarization is aligned along the field direction. There may be a distribution of droplet sizes, but at least some of them should be large enough to sustain

magnon excitations. Under these conditions the magnon cross section becomes

$$\frac{d^2\sigma^{\pm}}{d\Omega dE'} \sim [1 + \langle\cos^2\theta\rangle \pm 2\langle\cos\theta\rangle] .$$

where $\pm$ refers to the initial neutron polarization, θ is the angle between the local magnetization and the scattering vector, and the averages go over those droplets large enough to sustain magnons. The appearance of the forbidden (−) magnon scattering is thus associated with droplets of nonzero θ, that is, with regions in which the local magnetization deviates in direction from the average magnetization.

We have begun a systematic study of this effect by measuring the (±) magnon intensities from a single crystal of ^{60}Ni with 1 at. % Mo as an impurity. We expect that the droplet distribution will be a function of temperature and applied field and that the fraction of droplets in which magnons can be excited will depend on the magnon wavelength. Accordingly, parameters in our experiments have been temperature (322 K < T < 637 K), applied field (0.34, 0.54, 0.84 T), and energy transfer (8, 12, 16, 20 MeV). The basic experiment consisted of a constant ΔE scan from Q = (1.5, 0, 0) to (2.5, 0, 0) on the triple-axis polarized-beam spectrometer at the HFIR. The (110) reflection from a ^{57}Fe(Si) crystal was used as a polarizing monochromator, and the (002) reflection from pyrolytic graphite was used as an analyzer. We believe that the primary effect of the Mo impurity is to lower the Curie point from 631 K for pure Ni to 584 K for our sample as determined by observing the critical scattering.

The analysis of these data is incomplete, but some of the results for an energy transfer of 8 MeV and an applied field of 0.84 T are shown in Fig. 5.25. Here we show the ratio of the forbidden (−) magnon intensity to the total of allowed (+) plus forbidden intensities. As expected, this plot starts at zero at low temperature when $\langle\cos\theta\rangle = 1$ and approaches $\frac{1}{2}$ in the paramagnetic region where $\langle\cos\theta\rangle = 0$. This plot suggests that droplet formation begins between 500 and 550 K. The complete analysis will produce such plots as a function of applied field and energy transfer. In addition, we will isolate the $\langle\cos\theta\rangle$ term by calculating $(\Gamma^{+} - \Gamma^{-})$ and test its relationship to the bulk magnetization, which is proportional to $\langle\cos\theta\rangle$ averaged over the entire sample.

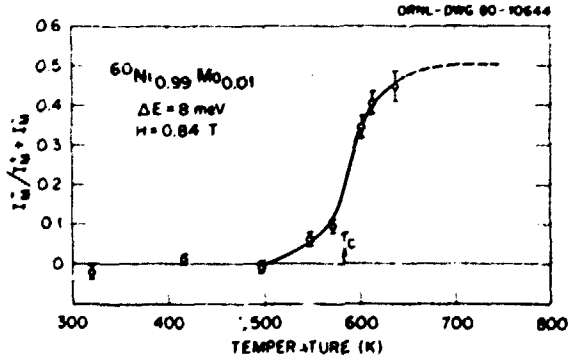

Fig. 5.25. Growth of forbidden magnon intensity as a function of temperature.

1. Consultant from Northeastern University, Boston, Mass., with partial support by the NSF.
2. Consultant from AERE, Harwell, England.
3. Northeastern University, Boston, Mass., with partial support by the NSF.
4. H. A. Mook, J. W. Lynn, and R. M. Nicklow, *Phys. Rev. Lett.* **30**, 556 (1973).
5. J. B. Sokoloff, *J. Phys. F* **5**, 1946 (1975).
6. J. B. Sokoloff et al., *J. Appl. Phys.* **50**, 1961 (1979).
7. A. W. Sáenz, *Phys. Rev.* **119**, 1542 (1960).

INDUCED MAGNETIC FORM FACTOR OF $Sm_{0.76}Y_{0.24}S$

R. M. Moon

Earlier work[1] had shown that the induced magnetic form factor of $^{154}Sm_{0.76}Y_{0.24}S$, a mixed-valence material, is approximately equal to that expected for the Sm^{2+} ion. The crystal used in this earlier study was large enough (52 mm^3) so that extinction was a definite problem. To minimize the extinction correction, only the weak peaks (*hkl* odd) were measured. To produce a more complete set of data and to make our earlier conclusion more quantitative, we have remeasured this material using a smaller crystal (13 mm^3). Both the strong and weak peaks were measured at 78 K in a field of 4.25 T, using the standard polarized-neutron technique. To eliminate extinction effects, measurements were performed at three different neutron wavelengths and the results were extrapolated to zero wavelength.

The observed polarization ratios were converted to susceptibilities and are displayed in Fig. 5.26. The solid curve is the calculated Sm^{2+} form factor normalized to the bulk susceptibility measured on the same sample. To an excellent approximation, the neutron results are given by the calculated curve minus a small constant, a most peculiar result. While many experimental factors could lead to uncertainties in the vertical scale factor, I can think of nothing that could lead to an apparent shift of the zero position on the vertical scale. The tentative conclusion is

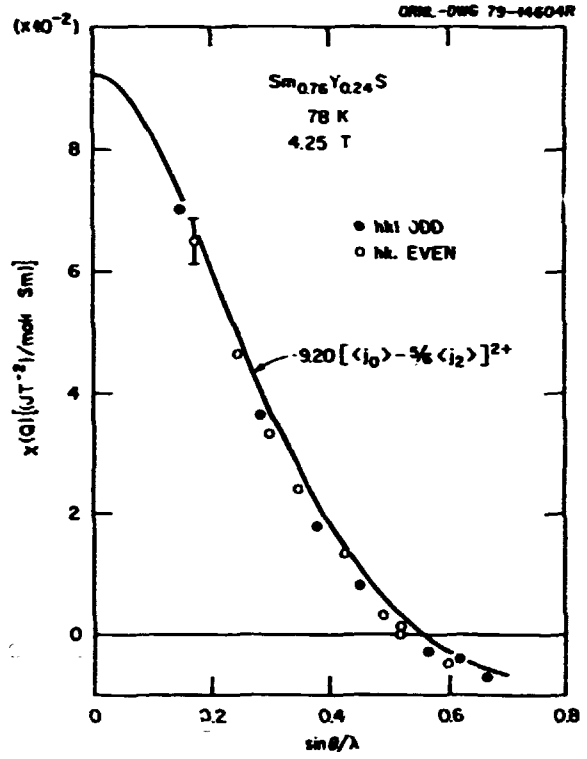

Fig. 5.26. Comparison of observed and calculated susceptibilities. The calculated curve is normalized to the measured bulk susceptibility. Except for the second reflection, experimental errors are about the size of the data points.

that these data show that the *4f* electron distribution is slightly different than it is in Sm^{2+}.

From lattice constant measurements the apparent valence at 78 K is +2.3. We plan to repeat these measurements at about 300 K, where the apparent valence is about +2.6. In addition, we hope to acquire a suitable crystal of ^{154}SmS, which should show pure Sm^{2+} behavior at atmospheric pressure. The goal is to obtain a quantitative measure of the apparently small changes in the *4f* electron distribution in going to the mixed-valence state.

---

1. R. M. Moon et al., *J. Appl. Phys.* **43**, 2107 (1978).

6. Crystal Growth and Characterization

Improvements in efficiencies of present-day energy technologies and the development of advanced energy systems will require solutions to a variety of materials problems. The primary purposes of the Crystal Growth and Characterization Program are to identify materials problems that relate to DOE research objectives; to prepare and to characterize research specimens of high quality for use in research programs in the Solid State Division, in other ORNL divisions, and in other laboratories; and to perform collaborative work with various groups engaged in energy-related research. During the period covered by this report, the growth and characterization of superconducting materials with the A15 structure were continued; growth of large, optical-quality single crystals of Naβ'' Al_2O_3 was achieved; refractory metals and alloys were prepared for investigations of fluxoid pinning in superconductors, phonon spectra, fracture, H absorption, and many other phenomena; also, the preparation and characterization of ferroelectric materials were continued. Table 6.1 in this section of the report shows representative examples of research specimens prepared during this period, their utilization, and the various organizations benefiting from this activity.

A new program investigating the suitability of the lanthanide orthophosphates for primary containment of alpha-active nuclear waste was initiated as a joint effort with ORNL research staff members in the Chemistry and the Metals and Ceramics divisions. Single crystals of the lanthanide orthophosphates with both the monazite and zircon structures were successfully grown, and it was demonstrated that monazite powders, produced by precipitation from molten urea, could be hot pressed and compacted to 97% of theoretical density.

The maintenance of a current data base on crystal growth, purification, characterization, and availability of research specimens by RMIC continued to provide valuable service to the research community. In cooperation with Plenum Press, a two-volume directory on crystal growth methods was published. A compilation of refractive index data for solids was initiated, and it is anticipated that this bibliography will be published during 1980.

CRYSTAL GROWTH AND CHARACTERIZATION PROGRAM

L. A. Boatner Y. K. Chang
M. M. Abraham H. E. Harmon
W. E. Brundage J. O. Ramey
M. Rappaz[1]

The various activities of the crystal growth and characterization group result in the production of a wide variety of research-quality samples whose properties are of interest not only to researchers within the Solid State Division but to scientists in other ORNL divisions, other DOE-supported laboratories, and other research organizations in general. Extensive sample characterization is required throughout the preparation of these materials, and the corresponding characterization techniques include a wide variety of standard and some newly developed methods.

To realize the maximum utilization of these often unique specimens, a continuing policy of loaning samples to cooperating research groups for supplementary physical property measurements is maintained. Measurements made on these samples often complement the research efforts of Solid State Division members and, in particular, investigations made by workers in foreign research institutions serve as a means of enhancing exchanges of technical information. Representative examples of some of the research specimens and their utilization are provided in Table 6.1.

1. Swiss National Fund for Scientific Research Fellow from École Polytechnique Institut, Lausanne, Switzerland.

Table 6.1. Loan of samples for research outside the Research Materials Program

Material	Type of study	To whom sent	Organization
Nb	Thermal conductivity	K. Krasst	Cornell University
Ni	He implantation	K. Farrell	ORNL
Ni	Fracture	S. Ohr	ORNL
Ni	Evaporation	S. Sekula	ORNL
Ta	Oxygen diffusion	R. Carpenter	ORNL
Ta	Photoemission	T. Sham	BNL
Ti	Ion bombardment	K. Farrell	ORNL
V	O diffusion	R. Carpenter	ORNL
V	Electron microscopy	E. Kenik	ORNL
W	Positron annihilation	L. Hulett	ORNL
Nb-Ta	Superconductivity	H. Kerchner	ORNL
W-Re	Neutron scattering	N. Wakabayashi	ORNL
Nb + 18 at. % Ge	Superconductivity	S. Sekula	ORNL
Nb + 18 at. % Ge	Neutron scattering	H. Smith	ORNL
V_3Ge	Ion channeling	O. Meyer	ORNL
V_3Ge	Ion channeling	B. Stritzker	ORNL
V_3Ge	Neutron scattering	H. Smith	ORNL
V_3Si	Ion channeling	O. Meyer	ORNL
V_3Si	Ion channeling	B. Appleton	ORNL
V_3Si	Ion channeling	B. Stritzker	ORNL
V_3Si	Ultrasonic attenuation	K. Kojima	Yokohama City University, Japan
MgO	Optical spectroscopy	V. Orera	University of Zaragoza, Spain
MgO	Optical spectroscopy	R. Williams	Naval Research Laboratory
MgO	Photoconductivity	G. Summers	Oklahama State University
MgO	Characterization	D. Readey	Ohio State University
MgO	Laser fabrication	A. Mooradian	Lincoln Laboratory, MIT
MgO	Radiation damage	J. Alvarez-Rivas	Junta de Energia Nuclear, Madrid, Spain
MgO	Radiation damage	E. Pells	AERE, Harwell, England
MgO	Raman	F. Lüty	University of Utah
CaO	Grain boundary and bulk transport	L. DeJonghe	LBL
CaO	Characterization	D. Readey	Ohio State University
MgO:Li	EPR	J. Boldú	National University of Mexico, Mexico, D.F.

Table 6.1 (continued)

Material	Type of study	To whom sent	Organization
MgO:Li	Thermal conductivity	H. Weinstock	Illinois Institute of Technology
MgO:Li	Optical spectroscopy	V. Orera	University of Zaragoza, Spain
MgO:Li	Thermal conductivity	D. Hasselman	Virginia Polytechnic Institute and State University
MgO:Li	Effect of O partial pressure	W. Gourdin	LLL
MgO:Li	Electrical conductivity	D. Eisenberg	University of North Carolina
MgO:Li	Internal friction	A. Nowick	Columbia University
MgO:Li	Light scattering	W. Unruh	University of Kansas
MgO:Li	Raman	F. Lüty	University of Utah
MgO:Li	Radiation damage	J. Alvarez-Rivas	Junta de Energia Nuclear, Madrid, Spain
MgO:Li	Positron annihilation	P. Cheng	National University of Taiwan, Taiwan
MgO:Li	Conductivity	W. Kingery	MIT
MgO:Li	Optical studies	N. Edelstein	LBL
MgO:K	Light scattering	W. Unruh	University of Kansas
MgO:Mg	EPR	H. Stapleton	University of Illinois
MgO:Fe	EPR	W. Kingery	Massachusetts Institute of Technology
MgO:Fe	Radiation damage	J. Alvarez-Rivas	Junta de Energia Nuclear, Madrid, Spain
MgO:Ni	Luminescence	W. Sibley	Oklahoma State University
MgO:Ni	Laser fabrication	A. Mooradian	Lincoln Laboratory, MIT
MgO:Ni	Light scattering	W. Unruh	University of Kansas
MgO:Ni	Radiation damage	J. Alvarez-Rivas	Junta de Energia Nuclear, Madrid, Spain
MgO:Ni	Luminescence	N. Edelstein	LBL
MgO:Co	Luminescence	W. Sibley	Oklahoma State University
MgO:Cu	Light scattering	W. Unruh	University of Kansas
CaO:Li	Relaxation times	H. Stapleton	University of Illinois
CaO:Na	Relaxation times	H. Stapleton	University of Illinois
CaO:Ca	ODMR	J. Spaeth	Gesamthochschule, Paderborn, Germany
CaO:Ca	Relaxation times	H. Stapleton	University of Illinois
CaO:Ca	Optical studies	N. Edelstein	Lawrence Berkeley Laboratory
SrO:Sr	ENDOR	J. Spaeth	Gesamthochschule, Paderborn, Germany
CeO_2	Diffusion	A. Franklin	NBS
$HfSiO_4$:Er	Optical studies	N. Edelstein	LBL
$ThSiO_4$:Er	Optical studies	N. Edelstein	LBL

THE CRYSTAL STRUCTURE OF $CePO_4$[1]

G. W. Beall[2] D. F. Mullica[3]
L. A. Boatner W. O. Milligan[3]

Cerium orthophosphate is a synthetic analog of the naturally occurring mineral monazite. The lack of precise current structural data for materials of this type has prompted the study of pure $CePO_4$. Knowledge of the structural base of this material is critical to future studies of radiation-damage effects in the actinide-doped lanthanide orthophosphate single crystals that have been grown in the Solid State Division at ORNL. Single crystals of $CePO_4$ were grown in covered Pt crucibles from a $Pb_2P_2O_7$ melt by gradual cooling from 1360°C at a rate of 1°C/h. The surrounding lead pyrophosphate matrix was then leached from the crystals with hot nitric acid.

A single crystal of $CePO_4$ ground to a sphere (450 μm diam) was selected for three-dimensional data collection on an Enraf-Nonius CAD-4 automated x-ray diffractometer using Mo K_α radiation (λ = 0.71073 Å). The position of the Ce atom was obtained from a Patterson map. This metal position was used to phase a difference Fourier map in order to obtain

the positions of the P and O atoms. These positions were refined using a full-matrix least squares program, and convergence was obtained after several cycles. The unit cell is monoclinic (space group $P2_1/n$) with $a = 6.777(3)$, $b = 6.993(3)$, $c = 6.445(3)$ Å, and $\beta = 103.54(4)°$. The structure was found to be made up of Ce atoms irregularly coordinated with nine oxygens and linked together by distorted tetrahedral phosphate groups. The local coordination of the trivalent Ce ion in $CePO_4$ is illustrated in Fig. 6.1. The accurate bond distances and angles determined in this investigation are expected to be

ORNL-DWG 80-10587

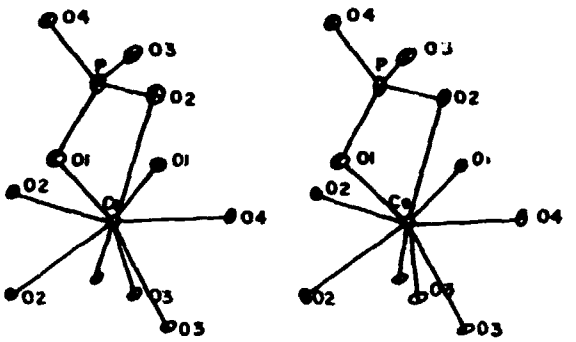

Fig. 6.1. Stereo view of the local coodination of Ce^{3+} in $CePO_4$.

very valuable in future studies of radiation damage in analogs of monazite synthesized with significant amounts of actinide impurities from nuclear waste material.

---

1. Summary of paper to be published.
2. Chemistry Division, ORNL; present address: Radian Corporation, Austin, Texas.
3. Baylor University, Waco, Texas.

MONAZITE AND OTHER LANTHANIDE ORTHOPHOSPHATES AS ALTERNATE ACTINIDE WASTE FORMS[1]

L. A. Boatner C. B. Finch[2]
M. M. Abraham G. W. Beall[2]
J. O. Ramey P. Huray[4]
M. Rappaz[5]

The selection of a suitable material for the primary containment of radioactive nuclear wastes is currently a significant unresolved problem. Because of the long half-lives ($\sim 10^3$ to 10^6 years) of some actinide isotopes formed during reactor operation, the requirements for safe isolation of such primary waste forms are very restrictive. In particular, the isolation material must be chemically and physically stable during long periods of exposure to the various conditions in a given geological repository. For storage in deep geological formations, hydrothermal conditions can be encountered, and this eventually presents an unusually hostile set of environmental conditions. Additional criteria that must be satisfied by a primary waste form include chemical and physical stability in the presence of high levels of α-particle radiation and the ability to retain actinide ions at the elevated temperatures appropriate to practical concentrations of nuclear waste.

Because borosilicate (and other) glasses are relatively inexpensive and can be produced on a large industrial scale, they have received considerable attention as possible nuclear waste containment media. As shown by several authors, however, many glasses readily devitrify and are unstable when exposed to hydrothermal conditions or α-particle radiation damage. For these reasons their suitability as a stable nuclear waste form has recently been called into question, and crystalline materials are now being considered as an alternate approach to the radioactive waste isolation problem.

Mineralogical studies have shown that a few minerals are capable of preserving their structure during long-term exposure to relatively high α-particle fluxes. One such mineral is a mixed orthophosphate, (La, Ce, Nd, Y ...)PO_4, known as monazite. Monazite ores are the principal source of the world's supply of Th, and some monazites also contain up to 16 wt % UO_2. Investigations of both Th- and U-bearing monazites have shown that these minerals are not characterized by extensive metamictization. Additionally, the overall long-term chemical and physical stability of monazite has been established from the dating of 2×10^9-year-old deposits found in Brazil. The diffusion rates of U in monazite have been found to be low as compared with those in other minerals; and, finally, acid solubility studies have shown that the lanthanide orthophosphates are characterized by a negative temperature coefficient of solubility (i.e., these substances exhibit the relatively unusual property of becoming less soluble as the solvent temperature increases). This almost unique set of chemical and physical properties led to the idea that synthetically produced analogs of monazite could represent an optimum primary actinide waste form.

Single crystals of the lanthanide orthophosphates were grown in order to perform x-ray, EPR, Mössbauer, radiation-damage, and chemical-stability studies. Orthophosphate crystals of every member of the lanthanide transition series (except $PmPO_4$) were grown using flux techniques. Crystals of YPO_4, $ScPO_4$, and $LuPO_4$ (zircon structure) were also grown.

Figure 6.2 shows several crystals of $LaPO_4$ doped with 0.5 wt % ^{241}Am oxide. These crystals are shown inside the growth crucible and are still entrained by the solidified $Pb_2P_2O_7$ flux, which is removed by boiling in nitric acid. Natural monazite ores are known to contain relatively high concentrations of U (i.e., up to 15 wt % UO_2), and it was possible to grow single crystals with similar U concentrations. Additionally, Pu-doped $LaPO_4$ crystals were grown from a starting composition of 90 wt % La_2O_3 and 10 wt % $^{242}PuO_2$.

ORNL-PHOTO 3596-79

Fig. 6.2. Flux-grown single crystals of $LaPO_4$ doped with 0.5 wt % $^{241}Am_2O_3$. The crystals are still in the flux, which has solidified and has not yet been removed by boiling in nitric acid.

The visible spectra for $LaPO_4$ single crystals doped with various actinides are shown in Fig. 6.3. Because it is totally transparent in the region studied, $LaPO_4$ was selected as the host orthophosphate. The ^{238}U-doped crystals, whose absorption spectrum is shown at the top of Fig. 6.3, contain 10 wt % UO_2 and have a deep green color indicative of tetravalent U. When the spectrum was examined in detail, the 4+ state was confirmed. Crystals of $CePO_4$ and (45 at. % Sm, 45 at. % Ce) (PO_4) have also been grown with a 10 at. % U dopant. In both of these crystals the ^{238}U tetravalent state was also confirmed. (The Ce in these crystals appears to be a mixture of Ce^{4+} and Ce^{3+}, with

ORNL-DWG 80-10343

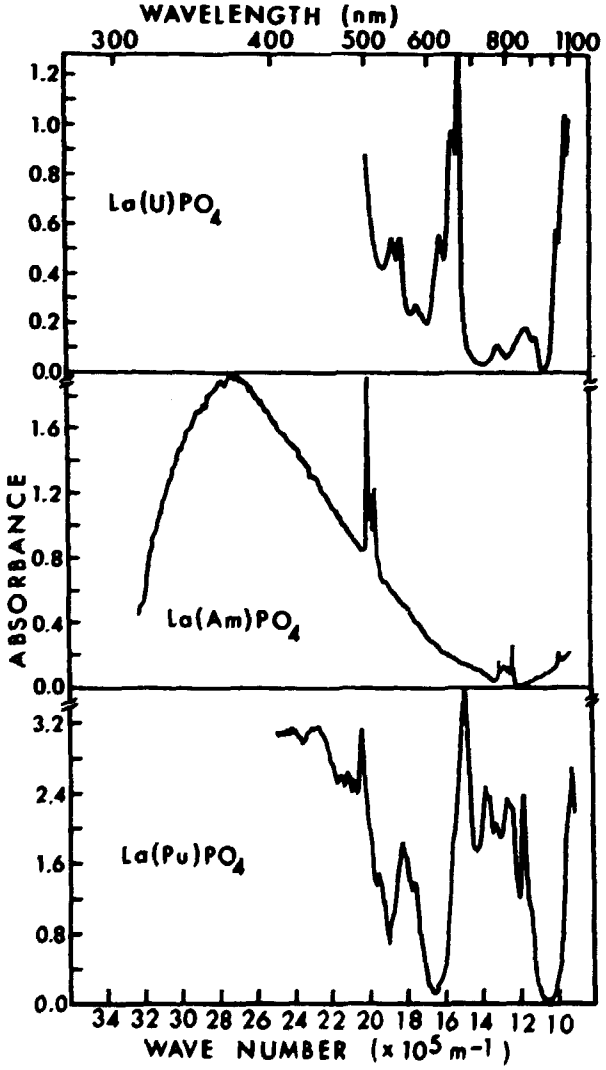

Fig. 6.3. Optical absorption spectra of doped $LaPO_4$ single crystals. Top: grown with 10 wt % UO_2. Middle: doped with 0.5 wt % Am_2O_3. Bottom: grown with 10 wt % $^{242}PuO_2$.

Ce^{3+} the predominant species.) These results are in agreement with observations of tetravalent U in natural monazite. The middle spectrum in Fig. 6.3 was obtained for $LaPO_4$ containing 0.5 wt % $^{241}Am_2O_3$. This spectrum shows that the Am is in the trivalent state, an observation that is consistent with the known redox chemistry of Am. These crystals have a pronounced amber color after cooling from the growth process and darken to a deep brown after several days at room temperature. This deepening color appears to be associated with radiation damage due to alpha decay and atom recoil from the ^{241}Am. The color can be annealed out at approximately 500°C to produce perfectly clear material, but the color returns in less than 24 h at room temperature. The spectrum shown at the bottom of Fig. 6.3 was obtained for $LaPO_4$ containing 10 wt % $^{242}PuO_2$.

Mössbauer-effect studies were performed using $La(Am)PO_4$ as a source and NpO_2 as an absorber at 4.2 K. The observed Mössbauer spectrum showed that an absorption with a small splitting occurred with an isomer shift in the neighborhood of +17 mm/s and that a second absorption with a larger splitting occurred with an isomer shift in the neighborhood of −35 mm/s. The observed splitting is believed to result from a small electric field gradient for the absorption of 17 mm/s (consistent with Np^{5+}) and a larger electric field gradient for the absorption at −35 mm/s (consistent with Np^{3+}). The absorption at −35 mm/s is probably a result of the recoiling ^{237}Np having found a normal $NpPO_4$ site prior to its recoilless deexcitation. The large 5+ Mössbauer absorption is somewhat surprising because the parent Am is trivalent.

The leachability of a waste form is one of the most important factors in determining its suitability for use in a nuclear waste repository. Leach tests of orthophosphate crystals resulted in IAEA leach indices that were smaller than those reported for grouts or borosilicate glasses by a factor of 16 for $CePO_4$ in 4 *M* NaCl at 200°C and 1724 kPa (250 psi) and a factor of 295 for $La(Am)PO_4$ in distilled water at 200°C and 1724 kPa (250 psi). These results are even more striking since the leaching studies on the glasses and grouts were conducted at room temperature and atmospheric pressure.

---

1. Summary of paper: *Scientific Basis for Nuclear Waste Management*, vol. II, ed. by C. J. Northrup, Plenum Press, New York (in press).
2. Metals and Ceramics Division, ORNL.
3. Chemistry Division, ORNL; present address: Radian Corporation, Austin, Texas.
4. The University of Tennessee, Knoxville.
5. Swiss National Fund for Scientific Research Fellow from Ecole Polytechnique Institut, Lausanne, Switzerland.

PREPARATION AND COMPACTION OF SYNTHETIC MONAZITE POWDERS[1]

M. M. Abraham T. C. Quinby
L. A. Boatner D. K. Thomas
M. Rappaz[2]

Analogs of the mineral monazite, a mixed lanthanide orthophosphate ($LnPO_4$), are potentially important primary containment forms for the isolation of actinide nuclear wastes.

The viability of a radioactive-waste isolation system utilizing lanthanide orthophosphates as the primary containment mechanism is, of course, dependent on the ease with which such wastes can be converted into the phosphate form and processed to produce dense bodies presenting relatively small surface areas to attack by leachants. A molten urea precipitation process, similar to that employed by Aaron et al.[3] in producing their "cermet" waste form, was used to convert lanthanide oxides into the orthophosphate form. The size of the resulting particulates could be controlled to the point where high-density bodies (~97% of theoretical density) were produced by hot-pressing at 28,000 kPa (4000 psi) and at temperatures significantly below those required to form the multiphase "Synroc" crystalline waste form. Variations in the orthophosphate particle size and shape caused by the use of varying amounts of urea are illustrated in Fig. 6.4. The urea precipitation process was applied to every naturally occurring lanthanide element in the transition element series from La to Gd. A systematic study of precipitation conditions vs particle size and hot-pressing conditions vs solid-body density was carried out for $CePO_4$ and $LaPO_4$. These particular compounds were selected because they can be considered as structural prototypes of the mineral monazite. Examples of the high-density pellets produced by hot-pressing $CePO_4$ powders are shown in Fig. 6.5.

The EPR technique was employed in comparing the properties of urea-precipitated $CePO_4$ powders and flux-grown single crystals. Powders and single crystals of $CePO_4$ (and the other lanthanide orthophosphates in the first half of the transition series) were prepared with a trace impurity of Gd^{3+}. The electronic properties of the $^8S_{7/2}$ ground state of trivalent Gd are extremely sensitive to the local

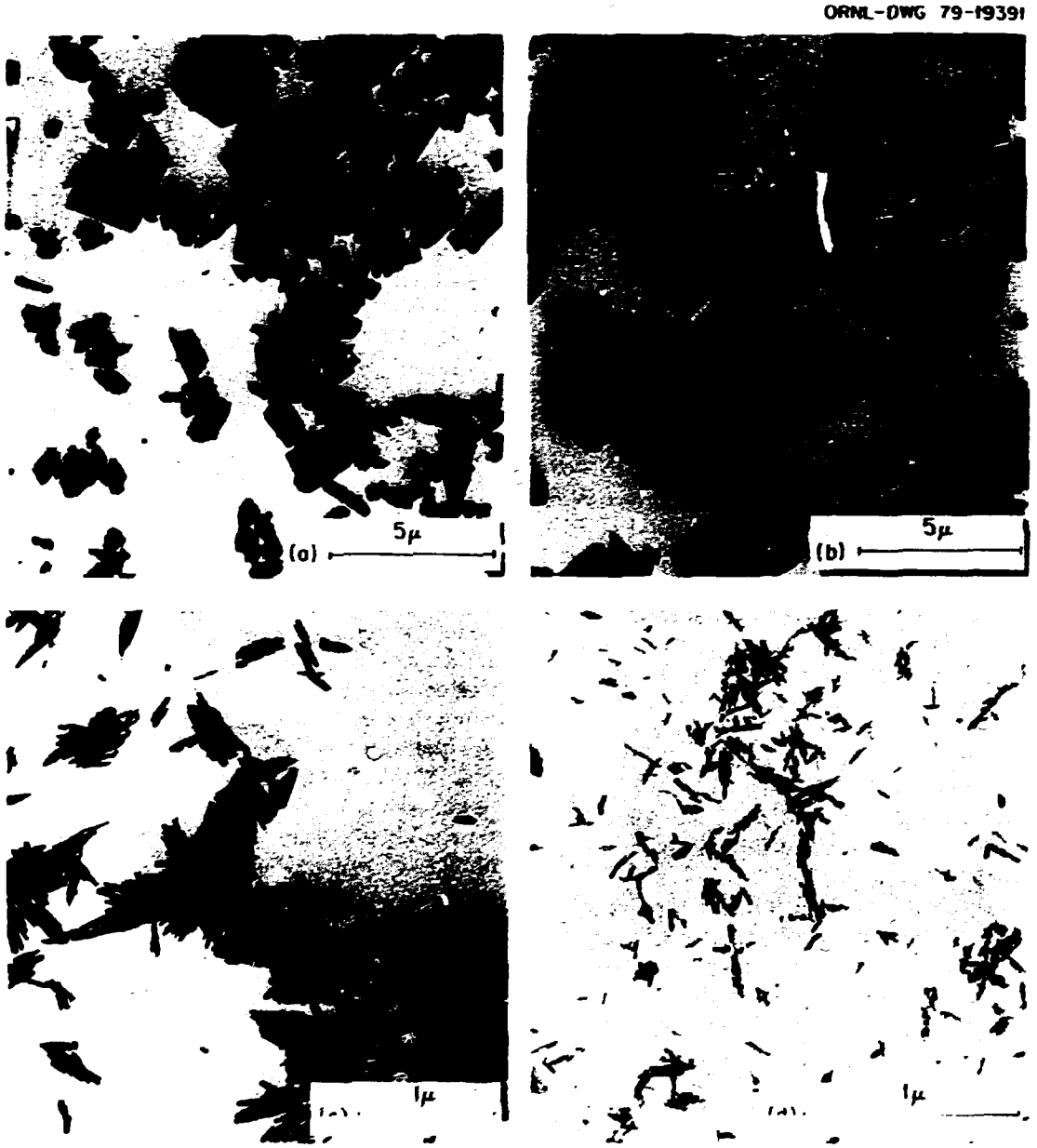

Fig. 6.4. Transmission electron micrographs comparing $CePO_4$ particles in powders precipitated with and without urea and particles obtained from mechanically grinding single crystals. The effect on particle size of varying urea concentrations is clearly evident: (*a*) mechanically ground single crystals; (*b*) precipitated powder without urea; (*c*) precipitated powder with a urea:$CePO_4$ mole ratio of 90:1; (*d*) precipitated powder with a urea:$CePO_4$ mole ratio of 720:1.

ORNL-PHOTO 3458-79

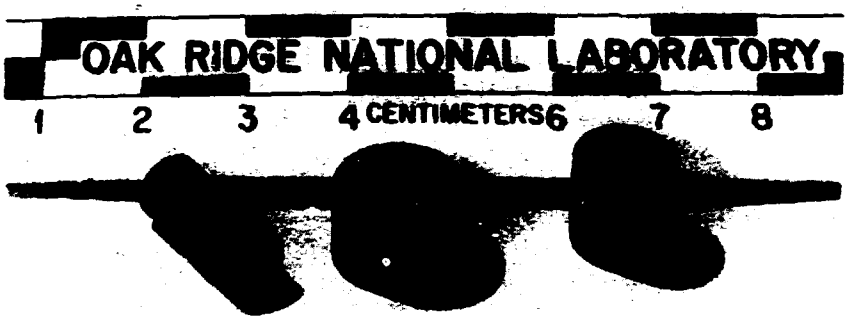

Fig. 6.5. Hot-pressed pellets of $CePO_4$ formed from precipitated powders.

environment of the surrounding crystalline electric field, and the associated EPR spectra can be used to detect small variations in the local crystal structure. A comparison of the "powder" spectrum of Gd^{3+} in $CePO_4$ powder precipitated in molten urea with the spectra obtained from doped single crystals showed that the Gd^{3+} impurity occupies the identical type of substitutional site in both the precipitated powders and the flux-grown single crystals. Trivalent Cm is the actinide analog of Gd^{3+} and is expected to occupy the same type of substitutional site in an orthophosphate waste form.

These studies show that both lanthanide oxides and lanthanide nitrates can be readily converted into an orthophosphate form whose particle size may be controlled to a sustantial degree and that the location, within the host crystal structure, of other lanthanide impurities is not affected by the processing sequence. The ability to synthesize bodies by hot-pressing of urea-precipitated powders with an appropriate grain size was demonstrated, and these findings have an important bearing on the ability to utilize highly stable lanthanide orthophosphates as a primary containment form for the hazardous α-active wastes generated by nuclear reactors.

1. Summary of paper to be published.
2. Swiss National Fund for Scientific Research Fellow from École Polytechnique Institut, Lausanne, Switzerland.
3. W. S. Aaron, T. C. Quinby, and E. H. Kobisk, *Cermet High Level Waste Forms*, ORNL TM-6404 (June 1978).

EPR INVESTIGATIONS OF Gd^{3+} IN SINGLE CRYSTALS AND POWDERS OF THE ZIRCON-STRUCTURE ORTHOPHOSPHATES YPO_4, $ScPO_4$, AND $LuPO_4$[1]

M. Rappaz[2] J. O. Ramey
M. M. Abraham L. A. Boatner

The tetragonal xenotime (YPO_4) and monoclinic monazite ($CePO_4$) orthophosphates are known to be chemically and physically stable in geological environments and are also radiation resistant. For these reasons, materials of this type are current candidates for the primary containment of radioactive actinide solid wastes.

The lanthanide (and related) orthophosphates may be divided into two classes: those of the first half of the series ($LaPO_4$ through $GdPO_4$) that have the monoclinic "monazite" structure and those of the second half of the lanthanide series ($TbPO_4$ through $LuPO_4$) plus $ScPO_4$ and YPO_4 that have the tetragonal zircon structure. The EPR spectra of paramagnetic impurities in diamagnetic hosts such as the lanthanide orthophosphates provide information regarding the valence states and crystalline site symmetries occupied by these impurities. This type of information is relevant to investigations of the solid state electronic properties of mixed lanthanide-actinide orthophosphates on a microscopic basis and of the effects of such properties on the characteristics of a related primary waste form. An obvious paramagnetic ion-probe for the lanthanide orthophosphates is Gd^{3+} because its electronic configuration ($[Xe]4f^7 - {}^8S_{7/2}$, which is chemically similar to the $[Rn]5f^7 - {}^8S_{7/2}$ configuration of the actinide ion Cm^{3+}) and relaxation behavior permit its magnetic resonance to be observed at room temperature, and its

spectrum gives a clear indication of the local symmetry at an impurity site.

In obtaining EPR results for Gd^{3+} in the tetragonal-symmetry orthophosphates $ScPO_4$, YPO_4, and $LuPO_4$, both single-crystal samples and precipitated powders of all three hosts were investigated, and a full determination of the spin-Hamiltonian parameters was made.

Single crystals of YPO_4, $ScPO_4$, and $LuPO_4$ doped with Gd^{3+} were grown by means of a flux technique. A mixture consisting of 3.5 g of the corresponding lanthanide oxide, 0.1 mol % Gd_2O_3 and 60 g of $PbHPO_4$ was placed in a 50-cm^3 Pt crucible, which was covered with a tight-fitting Pt lid to reduce flux evaporation. (Decomposition of $PbHPO_4$ at high temperature results in the formation of $Pb_2P_2O_7$, which serves as the flux.) The Pt crucible was placed in a furnace; the temperature was raised to 1360°C, held at this level for 16 h, and then slowly lowered to 900°C at a rate of 1°C/h. At this point the furnace was allowed to cool to room temperature, and the orthophosphate crystals were removed by dissolving the flux in boiling nitric acid. A large crystal of $LuPO_4$ grown by this technique is shown in Fig. 6.6.

ORNL-PHOTO 1181-80

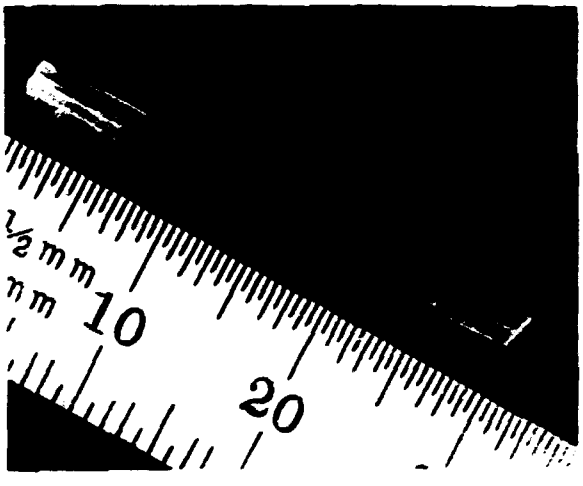

Fig. 6.6. A large flux-grown single crystal of $LuPO_4$ doped with Gd^{3+}.

Although all three crystals have the same type of tetragonal structure, the crystal habit of $ScPO_4$ (platelet-like shape) is different from that of $LuPO_4$ and YPO_4, both of which grow in the form of long, thin bars.

Because single crystals are both difficult and expensive to produce, they should not be considered as a practical means of containing radioactive nuclear wastes on a large industrial scale. A realistic process will entail the conversion of waste material into the form of orthophosphate powders, which would then be compacted into as dense a body as possible. For this reason the investigation was extended to include EPR studies of Gd-doped YPO_4, $ScPO_4$, and $LuPO_4$ powders produced by a precipitation-calcination technique. Briefly, this technique consisted of dissolving the lanthanide oxide-Gd_2O_3 mixture in a nitric acid solution and then adding a stoichiometric amount of $(NH_4)_2HPO_4$ to produce a phosphate-nitrate metathesis. Variable amounts of $(NH_2)_2CO$ added during the ensuing precipitation controlled the size of the orthophosphate particles that ultimately formed the powder. Calcination at 800°C removed the urea, and very fine powders (grain size smaller than 0.1 μm) were obtained.

The EPR powder spectrum obtained for Gd^{3+} in YPO_4 is shown in Fig. 6.7, together with the corresponding EPR spectra observed for the single-crystal host. These measurements were performed at K_a-band (i.e., ~35 GHz) and room temperature. As shown in Fig. 6.7, the EPR transitions in the single-crystal spectra for the orientations $\mathbf{H} \| c$ and $\mathbf{H} \| a$ are at exactly the same magnetic-field positions as the shoulders and divergences, respectively, in the corresponding EPR powder spectra. Therefore, the form of the spin-Hamiltonian and the associated b_n^m parameters are the same for the flux-grown YPO_4 single crystals and the analogous precipitated powders. This indicates that in the three tetragonal-symmetry orthophosphate hosts $ScPO_4$, YPO_4, and $LuPO_4$, the Gd^{3+} impurities occupy the same type of site in the single crystal and in the powder, even though the preparation techniques were very different. Moreover, because this site is unique, it is the lanthanide substitutional site. The ability to verify that lanthanide or actinide impurities will still occupy a given crystallographic site following a multistep chemical- (or physical-) processing sequence and that they have not become complexed with possible point defects or converted to the occupation of some interstitial position during such a sequence represents an important capability for assuring predictable solid state chemical properties.

Crystalline systems other than the lanthanide orthophosphates are currently being considered as primary radioactive waste forms, and this technique can also be applied to single crystals or powders of such multiphase systems to compare the local environments of pertinent impurities and to study the effects resulting from the process used to form a given waste-host complex.

1. Summary of paper to be published.

2. Swiss National Fund for Scientific Research Fellow from École Polytechnique Institut, Lausanne, Switzerland.

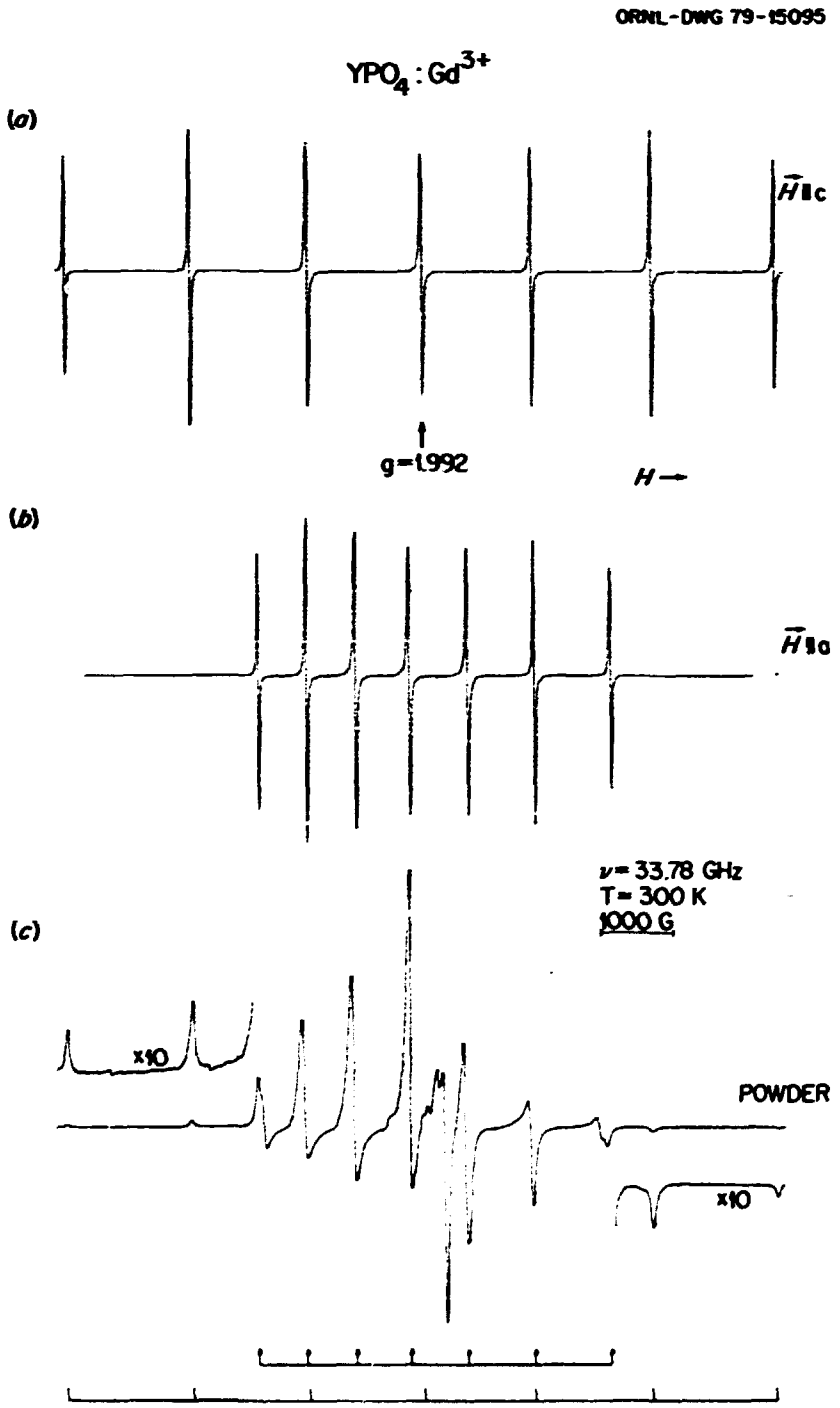

Fig. 6.7. EPR spectrum of Gd^{3+} in YPO_4. (*a*) Single crystal with $\mathbf{H} \| c$; (*b*) single crystal with $\mathbf{H} \| a$; (*c*) powder.

CRYSTAL GROWTH OF *A15* INTERMETALLIC COMPOUNDS

Y. K. Chang H. E. Harmon

Superconducting materials with high-superconducting to normal-state transition temperatures (T_c) have potentially important applications in the areas of electric power generation and transmission. More than half of the approximately 80 intermetallic compounds now known to form in the so-called *A15* (or *β-W*) phase are superconductors, and, most significantly, some of the materials characterized by the highest known superconducting transition temperatures are found within this family of substances. Accordingly, high-quality single crystals of *A15* compounds are of interest for use in numerous experimental programs, including studies of phonon spectra by inelastic neutron scattering or by ultrasonic attenuation, general superconducting properties (such as fluxoid pinning or the anisotropy of T_c), lattice disorder (because of ion damage) by ion-channeling studies, and the Fermi surface by the de Haas van Alphen effect. These studies depend on the availability of large high-quality single crystals.

Stoichiometric mixtures of either Ti_3Au, Ti_3Pt, V_3Si, or V_3Ge and nonstoichiometric mixtures of Nb_3Ge_{1+x} were prepared by casting in a high-purity He arc melter. Each mixture was then crushed and remelted four to five times by induction heating in a water-cooled gold-plated boat to achieve a high degree of homogeneity and to form rods for the subsequent crystal growth. Crystals of all the indicated materials were grown from the melt. Three different methods were employed in the growth processes. Single crystals of the *A15* compound Ti_3Au can be successfully prepared by means of the EBFZ method. The EBFZ system operates only under vacuum, however, and its application to the growth of other *A15* compounds is restricted because of the high vapor pressures of many of these compounds at their melting temperatures. Therefore, two new crystal-growth systems were placed in operation to produce single crystals of the *A15* compounds by means of alternate techniques. First, a medium-pressure IFZ system, which can be operated up to a pressure of 2 MPa, was installed; second, a tri-arc furnace, in which the crystal is pulled from a water-cooled hearth, was placed in operation. The tri-arc commercial unit was modified so that the arcs generated from the three electrodes were stabilized for slow crystal pulling. Growth rates for these methods were varied from 5 to 10 mm/h. The results for single crystals prepared by these methods are outlined in Table 6.2, together with some of the growth parameters and the range of crystal diameters produced by each method. Four single crystals of V_3Si and one single crystal of V_3Ge produced in the IFZ system are shown in Figs. 6.8 and 6.9. Annealing of the V_3Ge crystals at about 1400°C for 4 h following the growth process was found to improve the overall crystal quality.

CHARACTERIZATION OF *A15* INTERMETALLIC COMPOUNDS

Y. K. Chang H. R. Kerchner

A number of the more important physical properties, such as superconducting transition temperature (T_c), resistivity, and martensitic transformation temperature (T_m), have been measured for some of the *A15* single crystals prepared in this

Table 6.2. Summary of crystal growth of *A15* compounds

	Tri-arc	EBFZ	IFZ
Atmosphere, Pa	2.7×10^4 Ar	10^{-6}–10^{-7}	7×10^4–2×10^5 Ar
Growth speed, mm/h	4–12	5–10	5–10
Rod diam, mm	2–5	5–9	6–9
Overall success of crystal growth[a]			
V_3Si	Good	Fair	High
V_3Ge			High
Nb_3Ge_{1+x}	Good		Fair
Ti_3Pt	Fair	Fair	Fair
Ti_3Au		High	

[a]Success includes length of crystal: fair = a few mm; good = 10–15 mm; high = >15 mm.

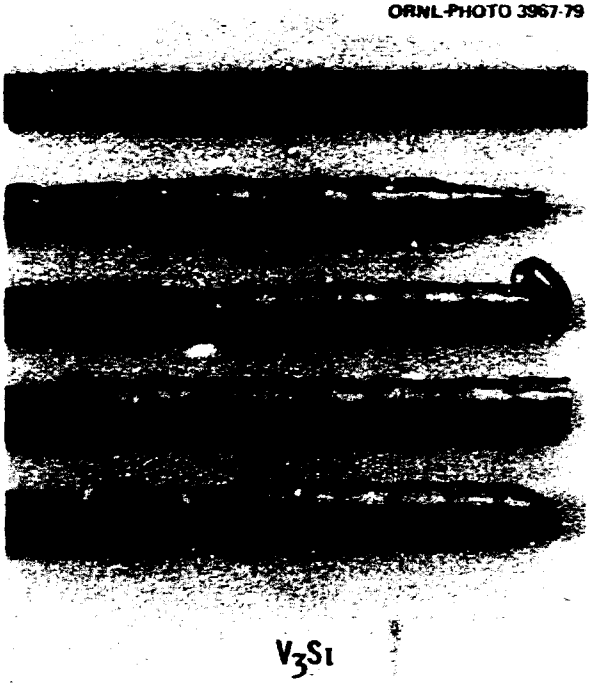

Fig. 6.8. Four V_3Si crystals prepared in the medium-pressure IFZ system.

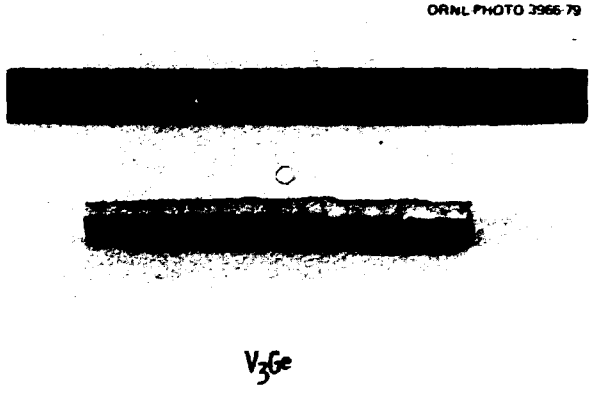

Fig. 6.9. One of the V_3Ge crystals prepared in the medium-pressure IFZ system.

laboratory. These measurements were performed using a four-probe resistance technique on rectangular prisms (about 7 mm long and 1 mm^2 in cross section) that had been cut from *A15* single-crystal rods and then chemically etched. The current leads were In-soldered to the ends of each specimen, and voltages were measured between two spring-loaded contacts. The specimens were cooled by a continuous-flow liquid-He cryostat, and temperatures were measured using a calibrated Si diode. A direct current of 50 mA was employed to obtain accurate values of the specimen resistance just above T_c and at room temperature. Observations of the discontinuity in the resistance at T_c and in the temperature dependence of the resistance near T_m were made by using a much smaller ac excitation current to eliminate possible errors associated with self-heating.

The experimental results obtained for five different V_3Si crystals are given in Table 6.3. Here A denotes a sample cut from that portion of the crystal that grew first and B from that portion of the crystal formed at the termination of the growth process. Crystal T1 was prepared in the tri-arc furnace, and crystals MP1 to MP4 were prepared in the IFZ system. Crystal MP4 had been contaminated during preparation, and it is not surprising that the lowest resistivity ratios were found for this crystal. The uniformity of the resistivity ratio from one end to the other of each crystal (MP1 to MP4) indicated the absence of gross variation of composition in spite of the tendency of Si to evaporate from the melt during the zone pass. On the other hand, the small differences in T_c observed and the presence of broad and multiple transitions in many samples indicated some degree of inhomogeneity. The highest temperatures at which there was evidence of superconductivity (T_c onset) were nearly identical in all samples cut from crystals T1, MP1, and MP3, indicating the presence of at least some accurately stoichiometric V_3Si in each sample. As expected, high transition temperature correlated well with high resistivity ratios. We found evidence of a martensitic transformation near 21 K in both the lowest-resistivity and highest-resistivity samples. The reasons for the occurrence of this low-temperature structural transformation remain unclear at the present time; although some researchers have found its occurrence to be correlated with high resistivity ratios, we have not.

Table 6.4 summarizes the results obtained for single crystals of V_3Ge. Crystals MP1 and MP3 were produced in the IFZ system. Crystal MP3 was annealed for 4 h at 1400°C in 0.13 MPa Ar gas, however. This annealing treatment resulted in a higher T_c and a higher resistivity ratio, most likely because of an improvement in the long-range order. The relatively large ΔT_c's indicate that this material can be improved further, possibly by optimizing the annealing treatment.

Table 6.3. Results of resistivity ratios, superconducting transition temperatures (T_c), and martensitic transformation temperature (T_m) measured on V_3Si single crystals

Specimen	$\rho(295)$ $\rho(T_c)$	T_c onset (K)	T_c (K)	ΔT_c (K)	T_m (K)
T1		16.93[a]	16.8[illegible][a]	0.17[a]	q
MP3-A	30	16.88	16.85	0.03	
-B1	30	16.84	16.79	0.05	
-B2		16.88[a]	16.70[a]	0.04[a]	21 + 0.5[b]
MP1-A	15	16.92	16.85	0.08	
			16.55	0.04	
-B	14	16.75	16.70	0.11	
MP2-A	12	16.75	16.72	0.11	
			16.26	0.11	
-B	12		16.29	0.02	
MP4-A	10		16.20	0.57	
			16.02	0.04	21.8
-B	10	16.70	16.57	0.14	
			16.13	0.08	21.9

[a]From inductive measurement.
[b]From x-ray diffraction.

Table 6.4. Results of resistivity ratios and superconducting transition temperatures (T_c) of V_3Ge single crystals

Specimen	$\rho(295)$ $\rho(T_c)$	T_c onset (K)	T_c (K)	ΔT_c (K)
MP1		6.30	6.16	0.09
MP3-A	3.4	6.57	6.44	0.10
-B	7.1	7.10	6.90	0.13

GROWTH OF β''-ALUMINA AND SODIUM GALLATE SINGLE CRYSTALS

W. E. Brundage J. B. Bates

The properties of β-alumina and the β''-alumina family of materials are currently being studied by a variety of techniques. These materials are a potentially important class of solid electrolytes, and single crystals with varying compositions are required in the current series of investigations.

Crystals of β''-alumina were grown at a constant temperature in covered cylindrical Pt crucibles from melts containing an Na_2O excess. These melts were held at temperatures ranging from 1640 to 1700°C for times in excess of 200 h. The upper surface of the original melt is usually converted into a clear crystalline layer, which may be one single crystal. This situation is illustrated in Fig. 6.10. A void is found below this layer, and additional crystals and solidified feed material are found at the bottom of the crucible. Crystals with good optical quality can be recovered, and one such specimen is shown in Fig. 6.11.

Fig. 6.10. Top view of a β''-alumina-filled crucible after 250 h at 1700°C.

Bettman and Peters[1] have stated that the β''-alumina phase can be stabilized when either MgO or Li_2O is present. The crystals grown from the liquid phase in the present experiments had the β'' form when MgO was present, but only the β form was found when Li_2O was used. Lithium was present in the β-alumina only as a substitute for a portion of the

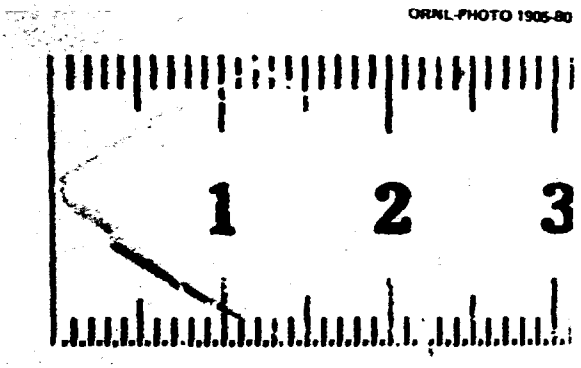

Fig. 6.11. Crystals of β''-alumina removed from crucible (centimeter scale).

Na. Good quality β'' crystals were also grown when ZnO was added for stabilization. The characterization of these Zn-stabilized crystals using a variety of techniques is currently in progress.

Sodium gallate crystals can be grown that are isomorphous with β''-alumina, and such crystals are of interest for comparison purposes. Although β''-alumina must also have Mg, Li, or Zn incorporated into the spinel block in order to stabilize the β''-phase, in the gallate this phase is stable at room temperature with no additional stabilizer. Gallate crystals several millimeters in diameter were grown by isothermal evaporation of a Na_2O flux. The β''-phase crystals were produced by placing a mixture of either Na_2CO_3:$3Ga_2O_3$ or Na_2CO_3:$2Ga_2O_3$ powders in a Pt tray and maintaining the temperature at 1375°C for about 250 h.

1. M. Bettman and C. R. Peters, *J. Phys. Chem.* **73**, 1774 (1969).

PREPARATION OF REFRACTORY-METAL AND ALLOY SINGLE CRYSTALS

Y. K. Chang H. E. Harmon
W. E. Brundage

The EBFZ technique has been used to prepare single-crystal research specimens of a number of refractory metals and alloys including: Mo, Nb, Pd, Ta, Ti, V, W, Nb-Ta, and W-Re. Additional treatments such as vacuum annealing, gas doping, quenching, orienting, cutting, etching, and polishing were frequently given to these specimens, which were employed in investigations involving fluxoid pinning in superconductors, phonon spectra, photoemission, fracture, positron annihilation, and H absorption.

A spherical Ta specimen was cut from a single crystal and treated at 2200°C under O_2 partial pressure of 6.5×10^{-5} torr for 5 h. The sample was then outgassed under a vacuum of 1×10^{-9} torr at the same temperature to reduce the C content. Precipitates were introduced in the crystal by treating the specimen under a N partial pressure of 3.85×10^{-5} torr at 2130°C for 20 h. A treatment of this duration allowed the N to reach its equilibrium concentration. A He gas quench ensured the trapping of N in the bulk of the sample.

Because of its large positive work function, W is believed to be an excellent candidate material for application as a positron-beam modulator. To evaluate a modulator of this type, four (110) slices with 7 × 15 mm surfaces were wire-cut from a [100] cylindrical W single crystal. A square beam channel was then formed by holding the slices on a 6 × 6 mm mandrel and fixing them in place with a W wire. This assembly was suspended in an induction furnace and annealed at about 2400°C under a vacuum of 1×10^{-9} torr for 3 d to anneal out the strain damage produced by cutting and to sinter the W slices together. The assembly was then cooled to room temperature over a 2-d period to avoid vacancy trapping. The resulting W beam modulator resulted in an increase in the positron intensity by a factor of 2.

An alloy crystal formed from a mixture of 5% Fe in Pd was prepared for use in neutron diffraction experiments. Several attempts were made to grow the crystal by the seeded Czochralski method, but each resulted in a multigrain sample. A satisfactory crystal was grown, however, by employing the Bridgman technique with a conical alumina crucible.

A Ni-18% Pt crystal was grown by the Czochralski method using self-nucleation on a Pt wire, and this specimen was also the subject of a study using neutron diffraction techniques.

GROWTH HABIT OF Ni SINGLE CRYSTALS

Y. K. Chang H. E. Harmon

A series of experiments was performed using the EBFZ technique to study the influence of impurities, strain, and temperature fluctuations on the growth direction of single-crystal Ni. The most favorable growth orientation was determined to be the [111] direction when very pure (5*N*) Ni was used as the starting material. The [100] direction was most favorable, however, when less pure (3*N*) Ni was

employed. Crystals produced from starting rods (3*N*) that had been strained by swaging had a strong tendency to grow along the [111] direction. Crystals produced from four quadrant sectors cut from a 1.3-cm-diam rod did not exhibit a preferential growth direction, however. A simulated temperature fluctuation was applied to the crystal during the growth process by superimposing a square wave whose amplitude was as large as 5% of the total power and whose period was 10 s. No correlation was found between the growth direction and these temperature fluctuations.

CRYSTAL GROWTH OF $LaNi_5$

Y. K. Chang H. E. Harmon

Hydrogen is a potentially important fuel whose proper use could contribute significantly to the solution of existing energy problems; accordingly, a number of materials for the efficient storage and release of H are currently being investigated. The present experimental evidence indicates that the substance $LaNi_5$ is characterized by excellent H absorption and desorption properties, and studies of well-characterized single crystals of this material are, therefore, of considerable practical interest. Starting stoichiometric mixtures of $LaNi_5$ were prepared by melting in an arc melter filled with purified Ar gas. The mixtures were then crushed and remelted four to five times in a Ag boat by induction heating to ensure homogeneity. The final melt was used to shape the mixture into the form of a rod for crystal growth in the EBFZ system. Two float-zone passes were made on the specimen under a vacuum of at least 1×10^{-6} torr at a zone speed of 2.9 cm/h. Grains of about 1 cm in size were identified by the x-ray Laue back-reflection method. A $LaNi_5$ crystal grown by this technique is shown in Fig. 6.12.

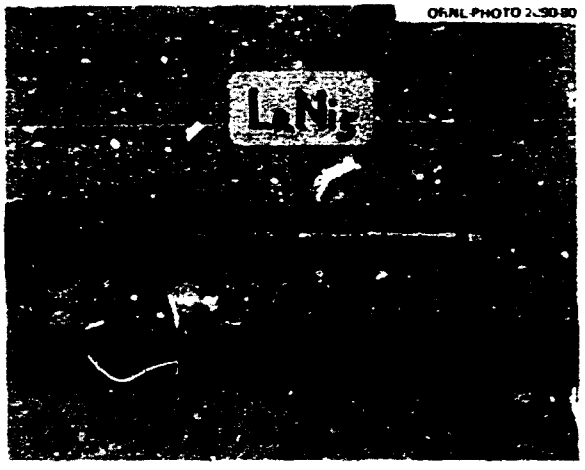

Fig. 6.12. A $LaNi_5$ crystal grown by the EBFZ method.

QUANTUM FERROELECTRICITY IN $K_{1-x}Na_xTaO_3$ AND $KTa_{1-y}Nb_yO_3$[1]

U. T. Höchli[2] L. A. Boatner

The effect known as ferroelectricity arises when forces between polarizable ions in a solid produce a spontaneous displacement of these ions which results in a lattice polarization below some characteristic (Curie) temperature. Fluctuations in this polarization may be thermally induced, as in the case of classical ferroelectrics, or, if the Curie temperature is near 0 K, the fluctuations can be due to quantum-mechanical zero-point motion. The term "quantum ferroelectric" is applied to those systems where fluctuations in the polarization result from the zero-point motion. Quantum-mechanical effects in ferroelectricity have been observed previously by Sawaguchi et al.,[3] who found that at low temperature the dielectric constant of $SrTiO_3$ did not obey the Curie-Weiss law but rather that it could be described by the following expression:

$$\epsilon - \epsilon_{T=\infty} = C\,[\tfrac{1}{2}T_1\coth(T_1/2T) - T_0]^{-1}, \qquad (1)$$

where T_1 represents the dividing temperature between the quantum-mechanical and classical regions. This equation had been derived earlier by Barrett,[4] using a model based on a quantum-statistical ensemble of oscillators. More recently, Eq. (1) has been used to fit measurements of the dielectric constants of $KTaO_3$ under atmospheric, as well as applied, isotropic pressure. In spite of its apparent ability to provide a reasonable fit to this dielectric-constant data, Eq. (1) is in contradiction with the limiting behavior of $\epsilon(T \to 0)$ as predicted by the more recent quantum theoretical treatments of incipient ferroelectrics with $T_c = 0$, as well as with the behavior predicted by the acoustic-optic mode-coupling model that is applicable for low, but nonzero, critical temperatures. The variation of ϵ with temperature predicted in the more recent theoretical works is given by

$$\epsilon - \epsilon_{T=\infty} = B(T - T_c)^{-\gamma}, \qquad (2)$$

where $\gamma = 2$ (quantum theory) for $T_c = 0$ and $\gamma \approx 1.4 \pm 0.2$ (mode-coupling model) for temperatures to ~100 K.

Experimental determinations of variations in the dielectric constant, spontaneous polarization, and elastic compliance as a function of temperature and impurity concentration were made for $K_{1-x}Na_xTaO_3$ and $KTa_{1-y}Nb_yO_3$, and these results show that the physical properties of quantum ferroelectrics differ from those of classical ferroelectrics in the following ways: First, for a quantum ferroelectric, transition temperature depends on impurity concentration (i.e., on an effective order parameter) as $T_c \propto (x - x_c)^{1/2}$, as opposed to $T_c \propto (x - x_c)$ for the classical case. Here the critical impurity concentration is denoted by x_c. Second, the inverse dielectric constant varies with temperature as $\epsilon^{-1} \propto T^2$ for the quantum-mechanical case, instead of $\epsilon^{-1} \propto T$. Finally, the distribution of transition temperatures in a given macroscopic sample with a Gaussian impurity concentration distribution is $p(T_c) \propto T_c \exp(-\alpha T_c)$ for the quantum ferroelectric, as opposed to a Gaussian for the classical situation. The term $p(T_c)$ represents the probability of finding a region with a transition temperature T_c. These results are in agreement with previous theoretical predictions of some of the distinguishing characteristics of quantum ferroelectricity.

---

1. Summary of paper: *Phys. Rev. B* 20, 266 (1979).
2. IBM Zurich Research Laboratory, Switzerland.
3. E. Sawaguchi, A. Kikuchi, and Y. Kodera, *J. Phys. Soc. Jpn.* 17, 1666 (1962).
4. J. H. Barrett, *Phys. Rev.* 86, 118 (1952).

KTN AS A HOLOGRAPHIC STORAGE MATERIAL[1]

L. A. Boatner E. Krätzig
R. Orlowski[2]

Because the Curie point of $KTa_{1-x}Nb_xO_3$ (or KTN) can be controlled by varying the Nb content, it is possible to tailor or optimize the electro-optic properties for a given application. Accordingly, solid-solution KTN crystals are of particular interest for the holographic storage of information via the photorefractive effect. It is possible to use the linear electro-optic effect for the storage of volume phase holograms when the material is in the ferroelectric phase, and quadratic electro-optic effects can be used for the nonferroelectric cubic phase. KTN single crystals exhibit the best storage sensitivities measured for electro-optic crystals thus far, but the storage times reported previously for this material have been limited to only 10 h.

Electrical-transport investigations employing incoherent light have been carried out for KTN crystals of varying composition. The mean displacement of the optically excited charge carriers was determined for various transport mechanisms in the cubic and ferroelectric phases, and measurements of the dark conductivity and electro-optic coefficients were made. The results of these measurements were used to determine the associated holographic storage properties (i.e., the photorefractive sensitivity and the storage time).

The KTN single crystals used in this work were grown by a variation of the flux technique, and the Curie temperature (T_c) of each sample was determined from measurements of the temperature dependence of the static dielectric constant. The composition of the $KTa_{1-x}Nb_xO_3$ crystals could be determined by using the results of Triebwasser[3] and the measured values of T_c. Values of T_c were found in the range from −273 to +75°C, corresponding to values of x (i.e., Nb content) between 0 and 0.5. Poling of the ferroelectric samples was accomplished by heating the crystals above the Curie point, applying an electric field of about 3 kV/cm, and then cooling down to room temperature. After several poling cycles, no deviation from single-domain behavior could be detected.

Electrical-transport measurements employing incoherent light were performed in the spectral region between 1.5 and 4.0 eV. The crystals were uniformly illuminated, and the electric fields were applied to the samples by means of edge electrodes fabricated with a Ag paste. The photoconductivity arising from the drift of optically excited charge carriers in an external electric field was found to depend linearly on both the field strength and the light intensity up to the highest intensities used in the present measurements (several mW/cm^2). The electro-optic coefficients were determined from ac-field-induced refractive index changes, and the results of these measurements are in good agreement with those of earlier investigations. The light-energy density necessary to record an elementary volume phase grating with a 1% read-out efficiency was found to be of the order of 100 $\mu J/cm^2$ for KTN in either the ferroelectric or the nonferroelectric phase. These results compare favorably with those reported for other electro-optic materials. Dark storage times

of up to one year were found for the most sensitive KTN crystals.

1. Summary of paper: *Ferroelectrics* 27/28, 247 (1980).
2. Philips GmbH Forschungslaboratorium, Hamburg, Germany.
3. S. Triebwasser, *Phys. Rev.* 101, 993 (1956).

EXTRINSIC PEAK IN THE SUSCEPTIBILITY OF INCIPIENT FERROELECTRIC $KTaO_3$:Li[1]

U. T. Höchli[2] H. E. Weibel[2]
L. A. Boatner

Displacive-type ferroelectrics are particularly simple systems whose response function, as represented by the dielectric constant, allows a peak centered at $\omega = 0$ to be resolved with an accuracy of $\Delta\omega = 1$ Hz. From numerous possible examples of such systems, $KTaO_3$:Li was selected because Li was previously identified in this host and its position in the lattice was determined as being "off center." The Li impurity is in a substitutional site for K and couples linearly to the order parameter, which, in this case, is represented by the polarization. Since the Li ion is off center, it may occupy any one of several equivalent positions and can hop between these positions with an Arrhenius frequency of $\nu = \nu_0 x \exp(-\Delta/kT)$, where Δ represents the potential barrier height separating equivalent positions. Depending on whether the hopping frequency ν is above or below the frequency of observation, the Li would represent a "relaxing" or "frozen" defect. These conditions are exactly those required by the current theoretical explanation of the dynamic susceptibility of impurities near a phase transition.

To investigate the dynamics of the Li impurity, its complex dielectric response was measured as a function of observation frequency, sample temperature, and Li concentration. From determinations of the dielectric response for samples with varying concentrations of Li, it was possible to show that the dielectric dispersion is proportional to the Li concentration below 1.2%. Additionally, a polarization can be frozen in by cooling the sample from above 30 K to 4 K with a dc bias of about 2×10^5 V/m. The polarization is a continuous function of the Li concentration and is about twice as large for E||⟨100⟩ as for E||⟨111⟩. The cumulative results show that the Li impurity is responsible for the observed dielectric dispersion and is consistent with a ⟨100⟩ off-center direction. Additionally, these results show that Li is an impurity that, when incorporated in the $KTaO_3$ host at concentrations below ~1%, is responsible for an extremely narrow (1 kHz) central peak. Its dynamic properties are correctly described by the mean-field dynamics of a static impurity in a ferroelectric host. At higher concentrations the central peak is broadened, and above ~25 K the transition between static and dynamic behavior occurs. As long as the Li concentration is less than 24%, $KTaO_3$:Li does not become ferroelectric at any temperature, and the observed dielectric dispersion cannot be identified with a ferroelectric soft mode.

1. Summary of paper: *Phys. Rev. Lett.* 41, 1410 (1978).
2. IBM Zurich Research Laboratory, Switzerland.

STABILIZATION OF POLARIZED CLUSTERS IN $KTaO_3$ BY Li DEFECTS: FORMATION OF A POLAR GLASS [1]

U. T. Höchli[2] H. E. Weibel[2]
L. A. Boatner

Ferroelectric order may be present in a paraelectric lattice over a limited distance, termed the "coherence length." In these reasonably well defined regions of coherent polarization (or "clusters"), the polarization may be switched with a time delay that increases with increasing "cluster" size. This time delay leads to well-known dielectric dispersion and nuclear magnetic relaxation effects. Such clusters have been found to be mobile and to exhibit characteristics in agreement with those of some general models that predict the local behavior of the order parameter near the instability of the generating (here, paraelectric) phase.

If the polarization couples to a dipolar defect (for example, an impurity), then the region of coherent polarization or "cluster" tends to form around the defect and become localized. Additionally, if the intrinsic lifetime of the defect is large, then it determines the lifetime of the cluster. The size of the clusters formed in this way represents a measure of the coherence length. Dielectric relaxation and electret polarization effects in $KTaO_3$:Li were investigated as a function of Li concentration. The results have shown that doping an incipient ferroelectric such as $KTaO_3$ with dipolar impurities gives rise to a remanent polarization similar to that found in an electret and that this effect can be controlled by varying the amount of doping. Valuable information concerning the ferroelectric coherence length (about three to four lattice spaces in Li-doped $KTaO_3$) was

obtained from both static and dynamic measurements. When the Li concentration is low (i.e., below about 2%) and the clusters do not interact, the net polarization in regions that contain only a few tens of Li ions is believed to be zero, and the system represents a state that may be termed a "polar glass" by analogy with the magnetic system corresponding to a "spin glass."

1. Summary of paper: *J. Phys. C. Lett.* 12, L563 (1979).
2. IBM Zurich Research Laboratory, Switzerland.

LOW-TEMPERATURE THERMAL CONDUCTIVITY OF $KTaO_3$ AND KTN SINGLE CRYSTALS[1]

A. M. de Goër[2] B. Salce
L. A. Boatner

Mixed crystals of the type $KTa_{1-x}Nb_xO_3$ (KTN) are ferroelectrics with a transition temperature (T_c) that depends on the Nb content, x. The phase diagram for small x, established by dielectric and elastic measurements, shows that crystals with $x < 0.8\%$ remain paraelectric at all temperatures. The thermal conductivity (K) of several crystals with x varying from 0 to 3% was measured from 1.3 to 200 K; two samples were measured down to $T = 80$ mK. A standard stationary-heat-flow method was used, and the error in K is less than 7%. The single crystals were grown by means of a flux technique, using a high-temperature (1700 K) reaction of Ta_2O_5, Nb_2O_5, and an excess of K_2CO_3. The material, which was contained in a Pt crucible, was held at the maximum temperature for approximately 12 h and then slowly cooled (1 to 3 K/h) from 1700 to 1220 K. Self-nucleation usually resulted in the production of 1 to 4 large grains. Cooling from 1220 K to room temperature was accomplished in 8 to 10 h, and hot H_2O was then used to remove the flux and free the crystals. The samples were cut, using a wire saw, as parallelepipeds with cross sections of about 2×2 mm^2 and length 8 to 16 mm along the (100) axis. Typical compositional inhomogeneities can be estimated to be about 0.3%.

Three $KTaO_3$ crystals ($x = 0$) containing different impurities have been measured, and the results are shown in Fig. 6.13*a*. The "pure" sample contains some Ti as residual impurity. The introduction of Cu or Ag does not noticeably affect the thermal conductivity, and the existence of a minimum near 6 K appears to be an intrinsic feature. A Cu-doped sample was measured down to 80 mK (insert of Fig. 6.13*a*), and it is seen that K/T^3 reaches the Casimir limit

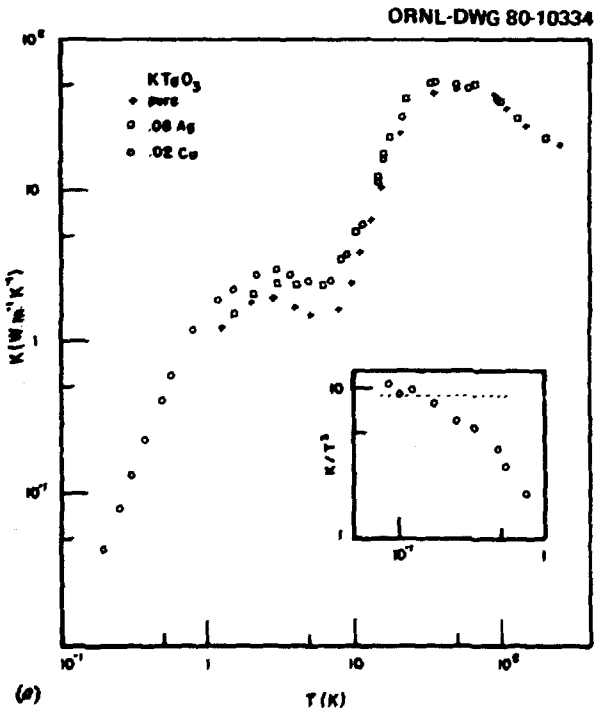

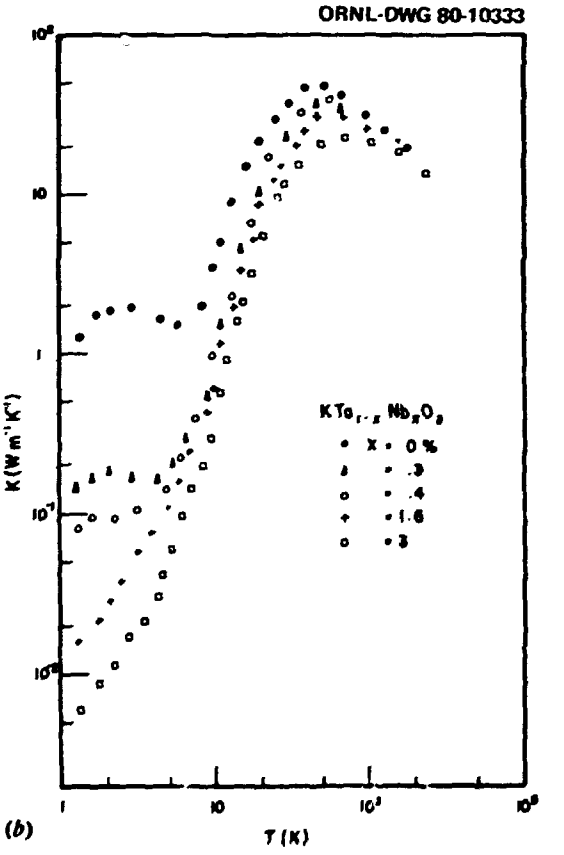

Fig. 6.13. Thermal conductivity of (*a*) $KTaO_3$ and (*b*) $KTa_{1-x}Nb_xO_3$ as a function of temperature.

at the lowest temperatures. Several KTN crystals were investigated, and the results are shown in Fig. 6.13*b*. The thermal conductivity decreases with increasing x, even for the nonferroelectric crystals with $x < 0.8\%$. There is no specific anomaly in K at T_c in the ferroelectric crystals ($T_c = 23$ K for $x = 1.6\%$ and 37 K for $x = 3\%$). One sample with $x = 1.6\%$ was measured down to 80 mK, and K is less than the Casimir limit by a factor $\cong 50$ at the lowest temperature. A feature observed in all KTN samples is that the temperature dependence of K is stronger than T^3 in the range 8–17 K.

1. Summary of paper: *Proceedings of the Third International Conference on Phonon Scattering in Condensed Matter*, ed. by H. J. Maris, Plenum Press, New York (in press).

2. Centre d'Etudes Nucléaires, Grenoble, France.

RESEARCH MATERIALS INFORMATION CENTER

T. F. Connolly G. C. Battle, Jr.

The RMIC has continued to collect, organize, and index the literature and to answer inquiries regarding the properties, characterization, preparation, and availability of ultrapure solid state research materials.

Mutual efforts with editors of Plenum Press and the Landolt-Bornstein data compilations are continuing. The main body of the material for a computer-indexed bibliography on Groups IV-V-VI transition-metal binary carbides, borides, nitrides, and oxides has been mailed to Plenum Press, where the keypunching for indexing and phototypesetting is being done. This bibliography will be a basic reference collection for research on high-temperature materials, which are becoming an important part of the coverage of RMIC.

An SDI system has been set up within the Solid State Division to provide literature searches and periodic updating of information for a variety of research projects and individuals. Search patterns, or "profiles," are designed after detailed discussions with Division members and stored on-line in a commercial computer to be activated automatically at each updating of the data base. Copies of the new references and abstracts are mailed to RMIC and distributed after being checked.

Possibly because of the introduction of the SDI service, there has been a noticeable increase in the number of requests for information, on a wide variety of subjects, from Division members.

The publications listed below and illustrated in Fig. 6.14 have, since Vol. 1 of the series Solid State Physics Literature Guides in 1970, reflected, in part, the subject areas covered by the Center. Each was produced when an increase in numbers of inquiries or the number of papers appearing in the literature indicated the need. There were two exceptions: Vols. 7 and 8 (on neutron scattering and microwave optics) were included in the series at the request of the compilers and as ready-made collections useful to the RMIC. The bibliographies also served the purpose of reducing the number of microfilm searches required to answer inquiries: callers could be referred to organized collections of references that answered the specific questions and often also supplied useful peripheral information.

ORNL-PHOTO 2048-80

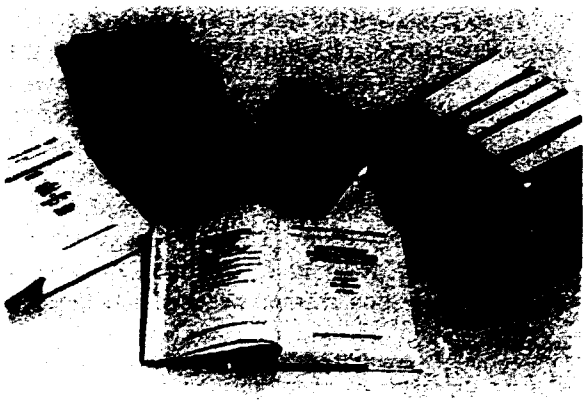

Fig. 6.14. Solid State Physics Literature Guides prepared by RMIC.

Volume 1, *Ferroelectric Materials and Ferroelectricity* (1970), was compiled with the assistance of Bell Telephone Laboratories computer processing and indexing after several individuals and groups had pointed out the need for a master reference covering the rapidly burgeoning literature in the field. The fact that the most interesting of the electro-optical materials were also ferroelectric added to the demand.

Volume 2, *Semiconductors—Preparation, Crystal Growth, and Selected Properties* (1972), was published largely in direct response to the numerous inquiries on preparation methods. The "properties" references pertain to the then newer compound semiconductors.

Volume 3, *Groups IV-V-VI Transition Metals and Compounds* (1972), represents the continuous interest in these materials but does not reflect the now

increased interest in their high-temperature properties, which appear in Volume 11 (in press).

Volume 4, *Electrical Properties of Solids—Surface Preparation and Methods of Measurement* (1972), represents an attempt to collect under one cover the details of measurements scattered throughout the literature. Dealing mainly with semiconductors but including other solids, the bibliography is arranged according to the property studied and materials examined.

Volume 5, *Bibliography of Magnetic Materials and Tabulation of Magnetic Transition Temperatures* (1972), is an example of a compilation created in response to many inquiries for specific data or for materials with specified magnetic properties. It is still widely used, but it needs updating.

Volume 6, *Ferroelectrics Literature Index* (1974), is an updating of Volume 1.

Volumes 7 and 8, *Scattering of Thermal Neutrons* (1974), and *Bibliography of Microwave Optical Technology* (1976), are dealt with above.

Volume 9, *Laser Window and Mirror Materials* (1977), deals with the physical and optical properties of laser auxiliary materials. Although most of the referenced work was sponsored by the Department of Defense and reflects a special interest in the highest-energy laser effects on these substances, it is of value to those using lasers for a wide variety of purposes. The theoretical references are of interest to those concerned with laser-irradiation damage.

Volume 10, *Crystal Growth Bibliography* (1977), the largest single collection of crystal-growth references, is actually two volumes—one the references and the other the author and permuted-title indexes. The permuted-title indexes permit searches not only by material but also by growth method. They also make possible the selection of references to either reviews or theory papers.

The new *Directory of Crystal Growth and Solid State Materials Production and Research* has been published, and a list of books that will be the core of the proposed ORNL High-Temperature Materials Laboratory library has been prepared.

7. Isotope Research Materials

The preparation of special chemical and physical forms of separated, high-purity isotopes is the task of the IRML. Research samples using nearly all stable isotopes and many radioisotopes (especially the actinide elements) are made to customer specifications in support of research programs throughout the United States and in foreign countries. In addition to satisfying isotope research material requirements for DOE programs, IRML provides an international service of sample preparation supplying samples unavailable from commercial sources to over 100 universities and commercial firms in more than 30 countries. During the reporting period approximately 4000 samples were prepared for the international scientific community. Support for this work comes directly from sales of materials and services; therefore, IRML has an integral sales function with associated inventory and revenue-accounting operations. Research and development activities in IRML are funded by DOE through the Office of Basic Energy Sciences and Office of Nuclear Waste Management.

Technical functions of IRML can be categorized generally into materials research and development, separation systems for tritium, inorganic chemical conversions, preparation of special physical material forms, fixation of high-level radioactive wastes in cermet form, radioisotope source preparations, purifications, single-crystal and epitaxial growth studies, and development of analytical techniques (usually nondestructive methods) that are compatible with characterization of thin film and other types of samples. From its inception, IRML has prepared particle accelerator targets; technologies of physical vapor deposition, chemical vapor deposition, mechanical rolling of metals, distillation of metals, metal reductions, arc melting, levitation melting, sintering, and other metallurgical and chemical processes were used to produce unique isotope-containing samples. Because of present-day interests in high-energy physics research, new technologies have been required to transform large (multigram) quantities of separated isotopes into thick, large-area target samples. In all operations, specific efforts to improve purity and conserve isotope resources are of vital importance, because the monetary value of isotopes consumed during a sample preparation may be many times the cost of assigned manpower and ancillary expense.

Procedures developed for handling stable isotope materials usually are equally applicable to radioisotope sample and source preparations. Adaption of preparative methods to radioisotopes generally implies modification for remote operations (hot-cell enclosure of processing equipment) or at least glove-box operations required for personnel protection. Almost all of the above noted operations have been adapted for radioisotope processing.

As a result of the technical capabilities developed for isotope sample preparations, a research and development program on ceramic and cermet waste forms is being carried out in IRML. Considerable progress has been made in translation of the laboratory-scale batch processing to continuous processing of simulated high-level reprocessing wastes into cermet solid storage forms. In addition, Thorex waste from NFS, New York, and sludge waste and untreated acid waste from the Savannah River Plant have been processed into cermet waste forms.

ELECTROCHEMICAL SEPARATION OF T FROM AQUEOUS EFFLUENT SYSTEMS

D. W. Ramey R. Taylor
M. Petek J. Ramey

As reported earlier,[1] bipolar electrolytic separation of H isotopes can offer significant advantages in power conservation, ease of operation, and cost of containment (when T is involved). In addition, large electrolytic isotope separation factors are achievable so that relatively few stages are required to achieve desired separation. The separation cell consists of bipolar electrodes placed between two terminal electrodes. Each bipolar electrode is permeable to elemental H and represents a separation stage, because the lighter isotope reacts and is transmitted through the electrode more rapidly than is the heavier isotope. Oxygen and hydrogen are evolved only at the terminal electrodes. For continuous separation, electrolyte solution is fed to the system continuously and is circulated countercurrent to the H mass flow. This scheme results in a cascaded system from which effluent streams enriched and depleted in the heavier isotope are withdrawn from opposite ends of the cell.

Some important features of the bipolar electrode, which are essential for the T separation process, have been studied using a single bipolar cell with a bipolar electrode of Pd-25% Ag alloy ($2.5\text{-}7.6 \times 10^{-2}$ mm thick). Values for α_{DT} and α_{HT} were measured at various temperatures at 0.15-, 0.21-, and 0.5-A/cm^2 current densities in 3-6 *N* NaOH [NaOD] electrolyte. Within these experimental conditions the separation factors at a single bipolar electrode are large (see Table 7.1) and practically unaffected by current density and NaOH concentration. A slight decline in the D-T separation factor was observed with increasing temperature; experimental data for the H-T separation factor as a function of temperature was not sufficiently accurate to detect any dependence.

Table 7.1. Hydrogen isotope separation factors on a single bipolar electrode

Temperature (°C)	α_{DT}	α_{HT}
30		11.7 ± 1.0
35	2.13 ± 0.05	
55	2.09 ± 0.03	10.8 ± 0.7
90	2.02 ± 0.03	11.4 ± 0.5

Maximum current densities, which can be applied to Pd-25% Ag bipolar electrodes without formation of gaseous H, were calculated using data from the literature (solubilities and diffusion coefficients for H and D in Pd-25% Ag at various temperatures). The agreement realized between calculated values and experimental results indicates that high H throughput can be achieved in the process. The voltage drop across the bipolar electrodes was measured as a function of current density, temperature, and the electrode thickness in the H_2O-NaOH and the D_2O-NaOD system. Typical data are shown in Fig. 7.1. Higher voltages at low temperatures and with thicker electrodes are associated with H and O gas formation at the bipolar electrode, that is, less than 100% H permeability.

A multibipolar cell is inherently a square cascade; that is, the mass flow (as defined by the constant current flow) is the same throughout the whole system. A mathematical model was derived specifically to describe multibipolar electrolysis.[2] Several laboratory experiments were performed using small multibipolar cells, and data from these experiments were used to verify the mathematical model. Figure 7.2 illustrates the agreement between the experimentally obtained T concentrations for the individual stages and those predicted by the mathematical model. In two protium-T experiments, the separation factors per stage were found to be 6.3 and 6.8, respectively. This protium-T separation

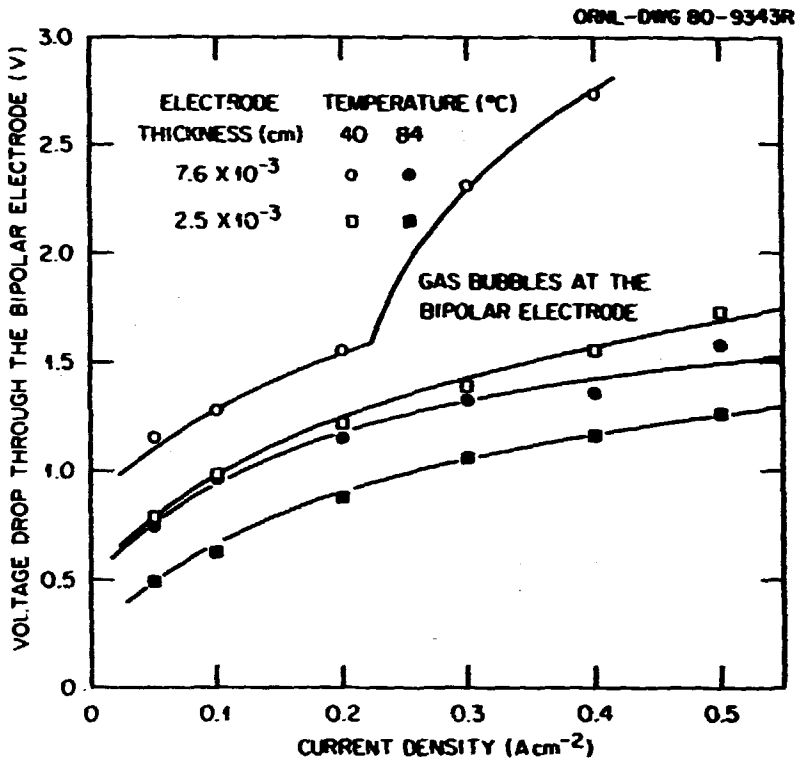

Fig. 7.1. Effect of current density on the voltage drop through a Pd-25% Ag bipolar electrode at two thicknesses and temperatures. Gas (H_2) bubbles appear at the electrode surfaces at current densities >0.2 A cm^{-2} at 40°C. Electrolyte is 6 N NaOH in H_2O.

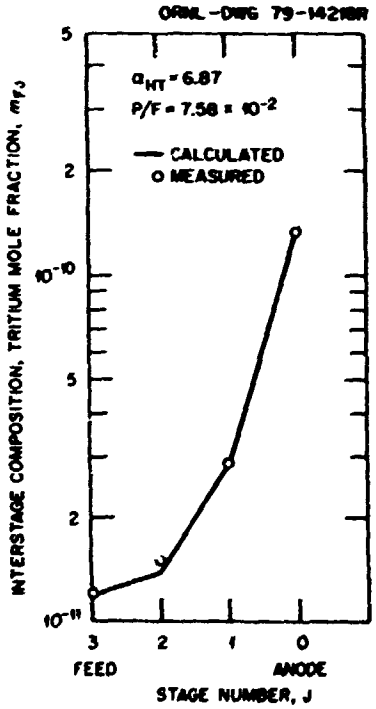

Fig. 7.2. Measured interstage compositions in the multibipolar experiments show excellent agreement with the calculated concentration profile.

factor was considerably smaller than that determined using a single bipolar cell (6.3 and 6.8 as compared to 11). Such a decrease in the interstage separation factor is believed not to be an intrinsic characteristic of the multibipolar cell concept but rather to be caused by intermixing of the electrolyte from adjacent cell compartments in these experiments.

Calculated mass transfer, as determined with a squared-off cascade model, as a function of electrical power consumption suggests that about 21% less power will be required for bipolar electrolytic separation as compared with normal electrolysis. This estimate represents only the present level of development; the savings could be as much as 30%. An even greater reduction in the voltage drop through the bipolar electrode may be possible with porous electrodes. The simplicity and efficiency of a multibipolar cell has great potential for use in designing a very compact separation facility.

---

1. D. W. Ramey et al., *Solid State Div. Prog. Rep. Sept. 30, 1978*, ORNL-5486, p. 199.
2. D. W. Ramey, *Tritium Separation from Light and Heavy Water by Bipolar Electrolysis*, ORNL-5581 (October 1979).

CERMETS FOR HIGH-LEVEL RADIOACTIVE WASTE CONTAINMENT

W. S. Aaron T. C. Quinby
D. W. Ramey D. K. Thomas

Continuing research and development efforts to form high-level reprocessing wastes into an inert cermet body have resulted in a totally modified flow sheet amenable to engineering scale-up. Schematic representation of the envisioned continuous process is shown in Fig. 7.3. Waste material, nitric acid, urea, and other metal and ceramic phase-forming materials are intimately mixed by dissolution at the head end of the process. Subsequent heating results in evaporation of water, and the resultant concentrated urea solution is sprayed into the vertical calcining furnace. A special ultrasonic spray nozzle was developed to be compatible with the viscous urea solution and to be capable of handling slurried materials of small particle size as well.

Use of spray calcination not only makes the process continuous but also permits decreased concentrations of urea to be used: 1:1 mole ratio of urea-to-nitrate ion vs 5:1 ratios (or more) used in bench-scale experiments. The cost is decreased, and the exothermic reaction resulting in the calciner at lower urea concentrations permits centerline temperatures of >1000 K to be maintained while the furnace wall temperature is approximately at the same level. Cyclone collection of calcined powder is used. Because of the Fe-Ni base-alloy composition of the cermet, the calcined material is magnetic. At present, magnetic collection of fine-particle-size calcine is being investigated. This process would significantly reduce the metal-filter clogging experienced in other spray calcination processes.

As seen in Fig. 7.3, calcined powder is subsequently extruded continuously into rods and then sintered to a high-density, low-porosity form. Sintering experiments have yielded significant results in that simple sintering of reduced calcine powder has been found to be of insufficient density, approximately 85% of that achieved by hot-pressing. However, by modifying the time-temperature kinetic scheme used in the reduction-sintering process, near theoretical density has been achieved on a laboratory scale. Figure 7.4 illustrates differences in the processes. Basically, liquid-phase sintering results in the mixed-oxide reduction process, which mostly eliminates void structure and enhances ceramic-phase compound formation and growth of particle size.

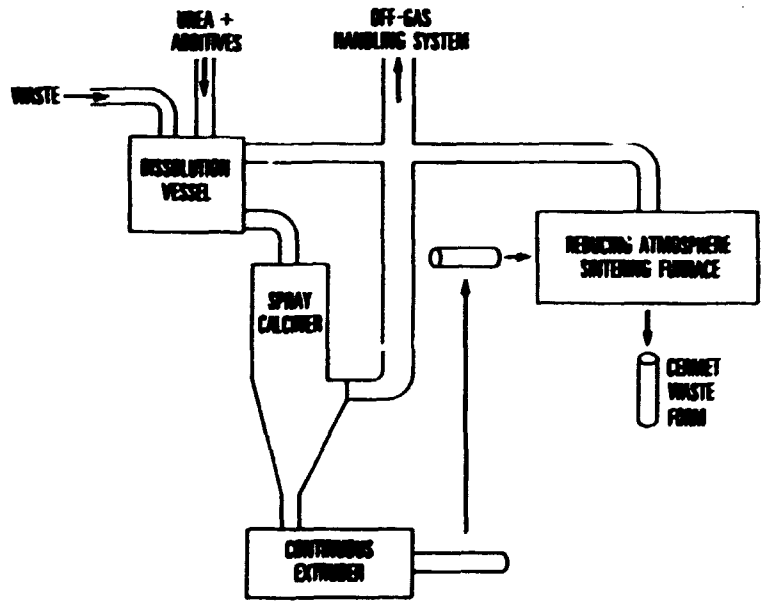

Fig. 7.3. Schematic representation of flow sheet for cermet preparation of reprocessing wastes illustrates engineering amenability.

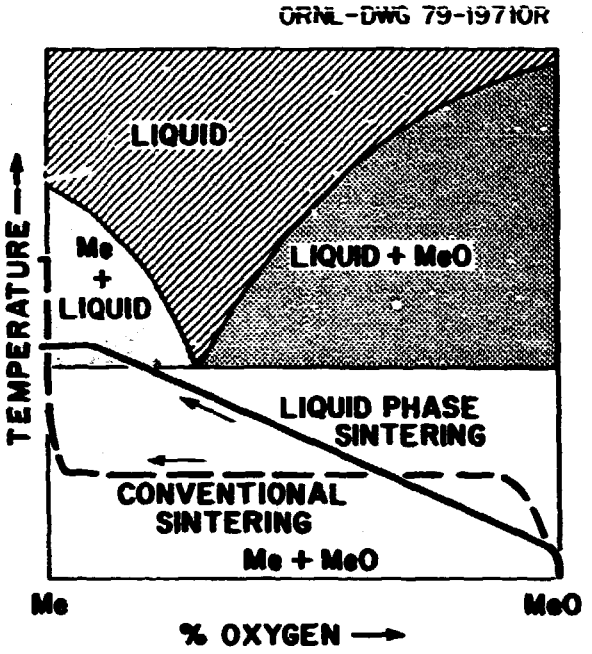

Fig. 7.4. Liquid-phase sintering results from temperature-time-phase manipulation.

Leach testing at PNL of cermets of simulated wastes containing radiotracers of Cs, Sr, and Ru prepared by hot-pressing has shown these materials to be comparable or superior to the best vitreous waste forms, depending on the leach conditions. One sample, subjected to a temperature of 630 K and a 10.7-MPa saturated brine solution for 7 d, lost relatively few contained fission products as compared to other waste forms and completely maintained its physical integrity.

Continuing research and development efforts have also resulted in improvements in the cermet product. The cermet waste form consists of particles of a variety of inert ceramic phases uniformly dispersed in and microencapsulated by a tailored metal matrix. While most of the fission and activation waste products are isolated in the ceramic phases, reducible radioactive species are incorporated in the alloy matrix. The cermet approach to waste management has been applied to both commercial and defense radioactive wastes, including SRP sludge and acid wastes, NFS acid Thorex waste, Idaho zirconia and alumina waste calcines, and one of the proposed commercial reprocessing waste formulations, PW-4b. Samples of actual SRP dried sludge and fresh acid wastes and NFS acid Thorex waste have been converted successfully to the cermet form in hot cells and subsequently characterized. In addition to the application of the cermet waste form to a variety of wastes, various disposal options are also being considered. Geological isolation of the solid waste form is the reference disposal option; however, currently, the cermet waste form is also being considered as an option for the outer space disposal of high-level radioactive wastes. Physical and chemical properties of synthetic and real waste cermets are summarized in Tables 7.2 and 7.3.

Table 7.2. Processing-related cermet characteristics

Waste loading	2–75 wt %
Waste-volume reduction	1:1–100:1
Ceramic-phase loading	20–50 wt %
Metal-phase loading	50–80 wt %
Metal-phase composition	70% Fe, 20% Ni, 5% Cu, 5% miscellaneous

Table 7.3. Typical cermet property ranges

Density	6.0–8.2 g cm^{-3}
Thermal conductivity	3–20 W m^{-1}°C^{-1}
Decay-heat loading	0.02–0.2 W cm^{-3}
Oxidation	
8 h 500°C air	~2-μm-thick oxide layer
2 h 800°C air	~5–7-μm-thick oxide layer
Thermal shock (2-cm-diam cylinders)	
Three cycles: 900°C to water quench	No damage detected metallographically
Leach rate	
Soxhlet test (72 h)	7.1×10^{-6} g cm^{-2} d^{-1}, 0.02% Cs loss

CERAMIC TARGETS AND SOURCES

T. C. Quinby D. K. Thomas

Compatibility of materials used experimentally in reactors becomes problematic at high temperatures. Generally, even metal-encapsulated, high-melting-point metals are unusable because of diffusive interactions with adjacent cladding material. In reactor temperature regimes of 1000 to 1400 K, only ceramic materials are useful because of their relatively inert properties. Because a wide variety of actinide nuclides are used to determine nuclear cross sections, it is desirable to prepare high-purity, well-characterized samples of these materials in a small encapsulated form.

With the technology developed to produce dosimeter "wires" of pure and diluted oxides,[1] easily sinterable oxide powders have been prepared by precipitation from molten urea. Cold compaction

and subsequent sintering produced high-density cylindrical pellets of the processed oxide. Alternatively, high-density, hot-pressed rods of oxide powder were also formed. In both cases, subsequent slicing of wafers by abrasive sawing provided thin, durable samples suitable for encapsulation. In most cases, 10- to 15-mm-diam wafers 0.4–0.6 mm thick were required; minimum thickness achieved by this technique was 0.2 mm.

When only small quantities of material were available, because of rarity or cost, individual ceramic disks were formed by hot-pressing. Unfortunately, minimum thickness achievable by this technique was 0.5 mm because of the difficulty in achieving uniformity with less material. All hot-pressing operations were performed using ATJ graphite dies at approximately 35 MPa and temperatures up to 1800 K.

All samples inserted into reactor cores must be encapsulated. Heat-pressure bonding of Cu or Al shells around the ceramic wafers was performed, as shown in Fig. 7.5. Using a tungsten carbide die set, dimensional tolerances could be maintained even after pressing many hundreds of such samples. Double encapsulation is achieved by pressure bonding a primary capsule around the first (see Fig. 7.5). In the case shown, the total outside diam of the second capsule was 19.1 mm ± 0.1 mm. In this manner samples of ^{235}U, ^{238}U, ^{237}Np, and ^{239}Pu as oxides have been prepared for FFTF, HFIR, and ORR reactor experiments.

---

1. H. L. Adair et al., *Solid State Div. Prog. Rep. Sept. 30, 1978*. ORNL-5486, p. 202.

STABLE ISOTOPE TARGET PREPARATION

W. B. Grisham K. B. Campbell
L. Zevenbergen

Preparation of accelerator targets and nuclear chemistry samples was a continuing effort in this reporting period. In most cases, the metallic form of the specific isotopes was required, and to this end

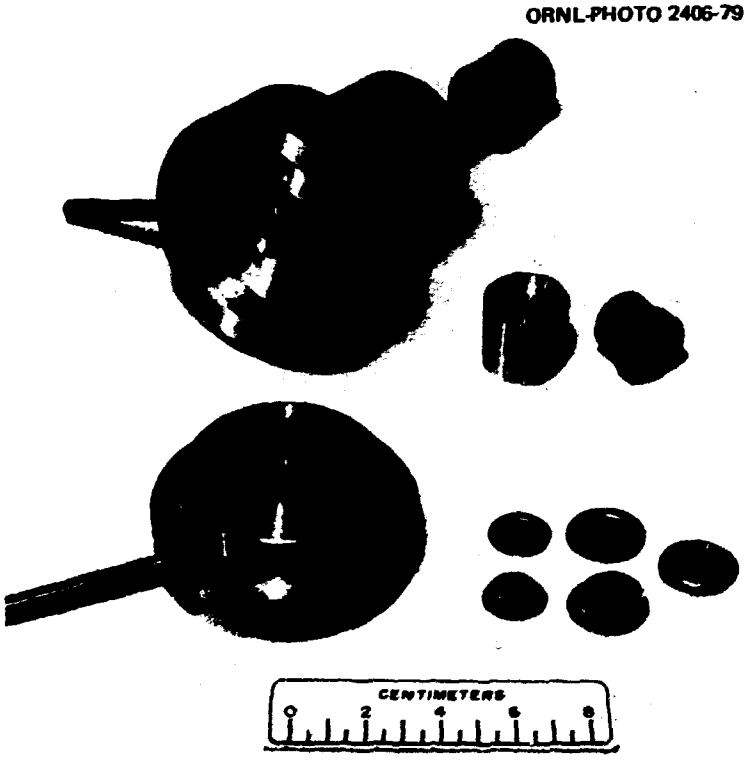

Fig. 7.5. Press, copper capsule components, typical actinide oxide disk, and completed doubly encapsulated sample (No. 41) illustrate pressure-bonding methodology.

39 metal preparations by simultaneous reduction-distillation using La or Th as the reductant were performed. Many of these metal preparations involved rather large quantities of material: 70 g of ^{145}Nd (91% conversion yield), 20 g of ^{87}Sr (87%), and 55g of ^{154}Sm (84%). Improved metal-fluoride reduction methods applicable to Gd, Nd, and Lu isotopes provided conversion yields greater than 90% in all cases. Considerable effort was expended to achieve high-efficiency reduction of <200-mg quantities of ^{176}Lu for LLL; this reduction could only be performed using Th as the reductant on lutetium oxide, with subsequent distillation of Lu metal at about 2500 K. Multiple distillations of the product were required to remove coevaporated Th metal. A sample of about 50 mg of 99.9% ^{176}Lu will be prepared by this technique; this enrichment is being achieved by electromagnetic separation at LLL, and the product material will have a value of about $150,000.

Thin film targets of many elements (isotopes) were prepared for accelerator experiments for international and domestic uses. Generally, samples of the more refractory elements offer the greatest difficulty and consume the greatest development effort. Especially in the thickness range of 200–1000 $\mu g/cm^2$, such films are difficult to prepare and maintain. Accelerator-source-material forms and ion filters were prepared in support of research at UNISOR. About 1300 cm^2 of 1 mg cm^2 Ta foil were produced in pinhole-free condition for this purpose. Special high-temperature purification of starting materials and intermediate annealing treatments were developed to produce this ultrathin, leak-tight material. Similarly, for the first time, W foil of 800 to 1000 $\mu g/cm^2$ thickness and in a maximum size of 6 cm^2 was prepared by mechanical rolling. Again complex heat-treatment and rolling schedules were developed to achieve this ultrathin sample.

RADIOISOTOPE TARGET PREPARATION

H. L. Adair B. L. Byrum J. M. Dailey

Hundreds of radioisotope-containing target samples have been prepared for accelerator applications or for use as radiation sources for instrument calibration and other purposes. Vapor deposition of most radionuclide species remains the most effective preparative method, especially for actinide oxide thin films. Mirror-like deposits of 38-mm-diam $^{233}UO_2$, $^{235}UO_2$, and $^{239}PuO_2$ on 0.013-mm-thick stainless steel, Ti, and Ni substrates were prepared by vapor deposition; these targets were used for total neutron cross-section experiments.

Continued experimentation with high-temperature fractionation of Am, Pu, and Cm has produced small samples of adequate chemical and nuclidic purity. Decontamination factors of $1–6 \times 10^6$ have been achieved between these nuclides in one or two distillations. Yttria crucibles must be used as the container material for mixtures of molten actinides during vaporization (and subsequent collection of distilled products in quartz receivers) so that intergranular attack of the container material can be avoided at temperatures of 1600 to 2000 K. In cooperation with LASL, slip casting and sintering of reaction-distillation crucibles of yttria were developed; although still being perfected, very satisfactory crucibles have been prepared. Currently being investigated are methods of preparing smaller particle size slips by use of the urea precipitation process to achieve "green" material suitable for forming very thin-wall, high-density sintered forms from yttria, zirconia, and thoria. Commercially available materials of this type generally have too low a density and too great a wall thickness; destructive cracking induced by thermal shock during heating or cooling can be reduced with thinner-wall bodies.

^{231}Pa FISSION-CHAMBER TARGETS

P. R. Kuehn H. L. Adair

During the past several years, IRML has prepared hundreds of fission-chamber deposits of actinide oxide for accurate neutron cross-section determinations. Most of these deposits were prepared in a vacuum environment by vapor deposition using electron bombardment heating. Normally, this technique requires gram quantities of actinide materials. When such large quantities of actinide materials are not available, alternative preparative methods, such as electroplating, spraying, or painting, must be considered.

During this review period a request was received from the Engineering Physics Division for six fission-chamber plates coated with $^{231}Pa_2O_5$. The target samples were to be used for the measurement of the fission cross section of ^{231}Pa for neutron energies from 0.4 to 12 MeV. Because less than 1 g of purified ^{231}Pa was available, the vacuum evaporation process was precluded.

An adaptation of a previously developed procedure[1] was used to prepare the required $^{231}Pa_2O_5$

deposits. After dissolution of the Pa_2O_5 in 8 *M* nitric acid and subsequent evaporation to dryness, the residue was dissolved in methyl alcohol to achieve a concentration of 2.68 mg/ml. A "lacquer" was prepared by adding 10 ml of the methanol solution to 10 ml of 3 wt % cellulose nitrate in amyl acetate. A total of six 88.36-cm^2 Ti substrates were painted on both sides with the ^{231}Pa-containing lacquer. The areal density of ^{231}Pa on each coated surface was 300 $\mu g/cm^2$. After the Ti substrates were painted, each substrate was heated for 3 h at approximately 450°C to vaporize or thermally decompose the organic material. The resulting deposits were found to be very adherent, and the experiments performed with these samples were notably successful.

1. J. W. Behrens, *Preparation of Fission Foils for Fission Ionization Chambers Using a Painting Technique*, UCRL-51476 (1973).

REACTOR DOSIMETRY MATERIALS

J. A. Setaro J. M. Dailey J. Lovegrove

In this reporting period, 2082 neutron dosimeters were prepared for domestic users and 380 samples for West Germany and Belgium reactors. This effort represents revenues totaling $228,000. As in past years, the majority of IRML-prepared dosimetry specimens are used in fast reactors, for example, the FFTF at Hanford, Washington. However, interest has grown recently in monitoring neutron spectral characteristics in commercial reactors and in sources for fusion energy experimental purposes; for these purposes neutron dosimeters similar to those used in FFTF will be used. If this application continues to grow, doubling of specimen preparation within IRML can be anticipated in the next period. New "wire" materials were prepared for use in neutron dosimeters (V encapsulated). About 10 m of pure ^{233}U- and $^{240}PuO_2$-extruded ceramic wire were produced and characterized; 10 m of 5 wt % Au-V and 5 wt % ^{238}U-V alloy wires were also prepared. The ceramic wire material was formed by the urea precipitation-extrusion-sintering method developed earlier. Metal-alloy wire was prepared by arc melting and drop casting with subsequent rotary swaging of the cast material to 0.5 mm diam. Alloy compositional uniformity was maintained at 99.7% over the entire length of the samples.

U.S./U.K. HIGHER ACTINIDE IRRADIATION TEST

H. L. Adair S. Raman[1] J. M. Dailey

A cooperative program between the United States and the United Kingdom was designed to verify the neutronic and irradiation performance of americium and curium oxides in a fast reactor, that is, the U.K. Prototype Fast Reactor at Dounreay, Scotland. The IRML has been charged with preparing both the sets of "fuel" specimens of Am_2O_3 and Cm_2O_3 and sets of dosimetry materials for monitoring neutron flux and energy spectra at the points of actinide irradiations. In three fuel pins, samples of hot-pressed $^{241}Am_2O_3$, $^{244}Cm_2O_3$, and $(^{241}Am_4{}^{244}Cm\overline{La}_7)_2O_3$ will be loaded; the latter compound contains a mixture ($\overline{La}$) of La, Ce, Nd, Sm in the mass ratio 1:2:3:1. All three materials will be prepared by precipitation of the dissolved cationic nuclides from molten urea—a process which most likely will form the required compound(s) and provide uniform particle size for subsequent compaction. Considerable care will be taken to ensure that the americium and curium sesquioxides are maintained in this easily oxidizable state, because high reactor temperatures would cause loss of O to occur if the dioxides were present. Each fuel sample will be 25.4 mm long and consist of stacked pellets having a length-to-diameter ratio of one or less. Loading of 1 to 20 mg of actinide oxides in V capsules will begin next month. Considerable quality assurance on all samples is required, especially with respect to void volume, phase identification, and verification of compound compositions.

1. Engineering Physics Division, ORNL.

CHEMICAL COMPATIBILITY OF THORIUM CARBIDES WITH Cr-Fe-Ni ALLOYS

E. C. Beahm[1] C. A. Culpepper W. S. Aaron

Fundamental studies associated with advanced fast breeder reactor fuels are being conducted in a cooperative effort with the Chemical Technology Division. Thermodynamic calculations and experimental phase studies are being used to determine the phases present in the interface, or reaction zone, between carbide fuel and the cladding alloy.

Thermodynamic calculations have been made at temperatures of 973 K and 1273 K for reactions at the

fuel-clad interface of uranium carbides with seven Cr-Fe-Ni alloys: type 316 stainless steel, type 330 stainless steel, A286, M813, PE-16, Inconel 706, and Inconel 718. The following species were considered to be possible reaction products (brackets denote solid solution): [Cr, Fe, Ni]; [$UNiC_2$, $UFeC_2$]; [UFe_2, UNi_2, UCr_2]; [$Cr_{23}C_6$, $Fe_{23}C_6$]; [Cr_7C_3, Fe_7C_3]; UNi_5; UC; $UCrC_2$; Cr_3C_2; $UNi_{3.67}$; $UNi_{3.33}$; U_2C_3; U_2NiC_3; U; and C. This list includes all known binary and ternary equilibrium compounds in the U-C-Cr-Fe-Ni system.

Type 316 stainless steel was significantly less reactive than any of the other alloys being considered. At temperatures where the complex carbides do not form, there is very little reaction between uranium monocarbide and the Cr-Fe-Ni content of type 316 stainless steel. This is because of its relatively high Fe content as compared to that in the other alloys. Nickel forms complex carbides and intermetallic compounds with large, negative free energies of formation, and Cr forms carbides with large, negative free energies of formation. Iron can take part in the formation of these compounds, but the contribution to the free energy of formation by Ni and by Cr is much more significant. Inconel 718, which contains the largest proportion of Ni of any of these potential cladding alloys, also produced the greatest amount of reaction product in the interface.

Liquidus temperatures for carbide fuel-clad compositions are being determined by use of a differential thermal analyzer. In these studies the effect of alloy Ni content on the temperature for liquid formation is being evaluated. This information is potentially of great importance in the safety of an operating carbide fuel reactor.

Experimental-phase diagram studies are being carried out on the U-Pu-Ni system in the range $2 \leqslant Ni/U + Pu \leqslant 5$. Annealed specimens are examined by use of x-ray-diffraction and SEM techniques. Phase information generated in these studies is needed for evaluating U, Pu carbide fuel-clad interactions.

1. Chemical Technology Division, ORNL.

CHEMICAL THERMODYNAMICS AND PHASE EQUILIBRIA IN ACTINIDE-CARBON-OXYGEN-CONTAINING SYSTEMS

T. M. Besmann[1] C. A. Culpepper

High-temperature chemical studies of actinide-carbide-oxide systems associated with the preparation and use of advanced fast breeder reactor fuels are being conducted in a cooperative effort with personnel of the Chemical Technology Division. Thermodynamic calculations and experimental measurements are used to determine phase equilibria and chemical thermodynamic properties of actinide carbides and oxycarbides.

Measurements have been made of the equilibrium CO pressure as a function of temperature for the ThO_2-ThC_2-C and $PuO_{1.5}$-$PuC_{1.5}$-C systems; this information, together with earlier experimental data, has allowed determinations of the heats of formation and entropies of the respective carbides. These data are some of the most accurate available. Such thermodynamic information is valuable in predicting optimum fuel-preparation conditions and in predicting and understanding in-reactor chemical behavior.

1. Chemical Technology Division, ORNL.

Publications and Papers

JOURNAL ARTICLES

M. M. Abraham, Y. Chen, W. C. Peters, J. Rubio O., and W. P. Unruh, "ENDOR of F^+ Centers in SrO," *J. Chem. Phys.* **71**, 3658 (1979).

H. L. Adair, "Preparation and Characterization of Radioactive Samples for Various Areas of Research," *Nucl. Instrum. Methods* **167**, 45 (1979).

B. R. Appleton, R. H. Ritchie, J. A. Biggerstaff, T. S. Noggle, S. Datz, C. D. Moak, H. Verbeek, and V. N. Neelavathi, "Radiative Electron Capture by Oxygen Ions in Single-Crystal Channels: Experiment and Theory," *Phys. Rev. B* **19**, 4347 (1979).

John H. Barrett, "Potential and Stopping Power Information from Planar Channeling Oscillations," *Phys. Rev. B* **20**, 3535 (1979).

J. B. Bates and Roger Frech, "Selection Rules for the Spinel Block Modes of β- and β''-Alumina Type Structures," *Chem. Phys. Lett.* **60**, 95 (1978).

J. B. Bates, T. Kaneda, W. E. Brundage, J. C. Wang, and H. Engstrom, "Raman Scattering from Mobile Cations in Sodium, Potassium, and Silver Beta"-Aluminas," *Solid State Commun.* **32**, 261 (1979).

J. B. Bates, J. C. Wang, and R. A. Perkins, "Mechanism for Hydrogen Diffusion in TiO_2," *Phys. Rev. B* **19**, 4130 (1979).

R. Behrisch, G. Maderlechner, B. [illegible] Scherzer, and M. T. Robinson, "The Sputtering Mechanism for Low Energy Light Ions," *Appl. [illegible]*, **18**, 391 (1979).

L. A. Boatner, E. Kratzig, and R. [illegible]rlowski, "KTN as a Holographic Storage Material," *Ferroelectrics* **27/28**, 247 (1980).

J. L. Boldú, M. M. Abraham, and Y. Chen, "Valence Compensation of Thermally Generated $[Li]^0$ in MgO," *Phys. Rev. B* **19**, 4421 (1979).

J. W. Cable and R. E. Parra, "Determination of the Pd-Gd Exchange Constant by Neutron Diffuse Scattering and the Pd Polarization in *Pd*Gd Alloys," *Phys. Rev. B* **20**, 2765 (1979).

J. V. Cathcart, R. A. Perkins, J. B. Bates, and L. C. Manley, "Tritium Diffusion in Rutile (TiO_2)," *J. Appl. Phys.* **50**, 4110 (1979).

C.-M. Chan, K. L. Luke, M. A. Van Hove, W. H. Weinberg, and S. P. Withrow, "The Structure of the C(2×2) Oxygen Overlayer on the Unreconstructed (110) Surface of Iridium," *Surf. Sci.* **7**, 386 (1978).

C.-M. Chan, S. C. Cunningham, K. L. Luke, W. H. Weinberg, and S. P. Withrow, "Determination of the Atomic Arrangement of the Unreconstructed Ir(110) Surface by Low Energy Electron Diffraction," *Surf. Sci.* **78**, 15 (1978).

Y. Chen, R. H. Kernohan, J. L. Boldú, M. M. Abraham, D. J. Eisenberg, and J. H. Crawford, "Enhancement of Electrical Conductivity in MgO Due to Lithium Impurities," *Solid State Commun.* **33**, 441 (1980).

H. R. Child, "Magnetic Short-Range Order in Gd," *Phys. Rev. B* **18**, 1247 (1978).

D. K. Christen, R. R. Kerchner, S. T. Sekula, and P. Thorel, "Equilibrium Properties of the Fluxoid Lattice in Single-Crystal Niobium. II. Small-Angle Neutron Diffraction Measurements," *Phys. Rev. B* **21**, 102 (1980).

D. K. Christen and P. Thorel, "Direct Observation of the Equilibrium Misalignment Between Fluxoids and an Applied Magnetic Field Due to Anisotropy Effects in a Type-II Superconductor," *Phys. Rev. Lett.* **42**, 191 (1979).

T. F. Connolly, "The Research Materials Information Center," *SSIE Science Newsletter* **9**, 1B (1979).

J. F. Cooke, "Band Theoretic Interpretation of Neutron Scattering Experiments in Metallic Ferromagnets," *J. Magn. Magn. Mater.* **14**, 112 (1979).

J. F. Cooke, "Itinerant Electron Magnetism in 3d-Transition Metals," *J. Appl. Phys.* **50**, 7439 (1979).

J. F. Cooke, "Role of Electron-Electron Interactions in the RKKY Theory of Magnetism," *J. Appl. Phys.* **50**, 1782 (1979).

M. J. Cready, J. M. Schultz, J. S. Lin, and R. W. Hendricks, "Effect of Crystallization Time on the Properties of Melt-Crystallized Linear Polyethylene," *J. Polymer Sci.* **17**, 725 (1979).

W. P. Crummett, H. G. Smith, R. M. Nicklow, and N. Wakabayashi, "Lattice Dynamics of Alpha-Uranium," *Phys. Rev. B* **19**, 6028 (1979).

H. L. Davis, J. R. Noonan, and L. H. Jenkins, "Determination of a Cu(110) Surface Contraction by LEED Intensity Analysis," *Surf. Sci.* **83**, 559 (1979).

H. W. Diehl, P. L. Leath, and Theodore Kaplan, "Traveling Pseudo-Fermion Approximation for Phonon Frequency Spectra of Binary Mixed Crystals," *Phys. Rev. B* **19**, 5044 (1979).

P. Ehrhart, H. D. Carstanjen, A. M. Fattah, and J. B. Roberto, "Diffuse Scattering Study of Vacancies in Gold," *Philos. Mag. A* **40**, 843 (1979).

H. Engstrom and J. B. Bates, "Raman Scattering from Boron-Implanted Laser-Annealed Silicon," *J. Appl. Phys.* **50**, 2921 (1979).

Herbert Engstrom, Roger Frech, and J. B. Bates, "Mode Coupling and ^{79}Br-^{81}Br Isotope Effects in the Raman Spectra of $NaClO_3$-$NaBrO_3$ Mixed Crystals," *J. Chem. Phys.* **69**, 5088 (1978).

G. P. Felcher, R. Maglic, and J. W. Cable, "Separation of the Spin and Orbital Magnetic Densities in Nickel," *J. Appl. Phys.* **50**, 1969 (1979).

R. Frech and J. B. Bates, "Raman, Infrared Reflection, and Emission Spectra of Sodium Beta-Alumina," *Spectrochim. Acta* **35A**, 685 (1979).

E. J. Friebele, D. L. Griscom, M. Staplebroek, and R. A. Weeks, "Fundamental Defect Centers in Glass: The Peroxy Radical in Irradiated High-Purity Fused Silica," *Phys. Rev. Lett.* **42**, 1346 (1979).

L. E. Halliburton, B. D. Perlson, R. A. Weeks, J. A. Weil, and M. C. Wintersgill, "EPR Study of the E_1' Center in Alpha Quartz," *Solid State Commun.* **30**, 515 (1979).

R. P. Hemenger, Theodore Kaplan, and L. J. Gray, "Theoretical Optical Spectra for Large Aggregates of Chromophores," *J. Chem. Phys.* **70**, 3324 (1979).

U. T. Höchli and L. A. Boatner, "Quantum Ferroelectricity in $K_{1-x}Na_xTaO_3$ and $KTa_{1-y}Nb_yO_3$," *Phys. Rev. B* **20**, 266 (1979).

U. T. Höchli, H. E. Weibel, and L. A. Boatner, "Extrinsic Peak in the Susceptibility of the Incipient Ferroelectric $KTaO_3$:Li," *Phys. Rev. Lett.* **41**, 1410 (1978).

U. T. Höchli, H. E. Weibel, and L. A. Boatner, "Stabilization of Polarized Clusters in $KTaO_3$ by Li Defects: The Formation of a Polar Glass," *J. Phys. C* **12**, L563 (1979).

T. J. Hoffman, M. T. Robinson, and H. L. Dodds, Jr., "Range Calculations Using Multigroup Transport Methods," *J. Nucl. Mater.* **85/86**, 597 (1979).

M. Hou and M. T. Robinson, "Computer Simulation of Low Energy Sputtering in the Binary Collision Approximation," *Appl. Phys.* **18**, 381 (1979).

M. Hou and M. T. Robinson, "The Conditions for Total Reflection of Low-Energy Atoms from Crystal Surfaces," *Appl. Phys.* **17**, 371 (1978).

M. Hou and M. T. Robinson, "Mechanisms for the Reflection of Light Atoms from Crystal Surfaces at Kilovolt Energies," *Appl. Phys.* **17**, 295 (1978).

W. Husinsky and A. R. Bruckmüller, "Energy Spectra of Sputtered Na Atoms from Bombardment of NaCl with 20 keV Gas Ions," *Surf. Sci.* **80**, 637 (1979).

D. P. Jackson and J. H. Barrett, "The Effects of Correlated Lattice Vibrations on Surface Backscattering Yields," *Phys. Lett.* **71A**, 35 (1979).

B. Jeffries, J. Feldott, G. P. Summers, and Y. Chen, "Temperature Dependence of Fluorescence Yield and Lifetime of F^+ Centers in SrO," *Phys. Rev. B* **21**, 1537 (1980).

G. E. Jellison, Jr., "N.M.R. Studies of Amorphous Phosphorus," *Solid State Commun.* **30**, 481 (1979).

G. E. Jellison, Jr., and S. G. Bishop, "Nuclear Spin-Lattice Relaxation in Thallium-Containing Chalcogenide Glasses," *Phys. Rev. B* **19**, 6418 (1979).

G. E. Jellison, Jr., G. L. Petersen, and P. C. Taylor, "Tunnelling Modes and Local Structural Order in Amorphous Arsenic," *Phys. Rev. Lett.* **42**, 1413 (1979).

G. E. Jellison, Jr., and P. C. Taylor, "Nuclear Quadrupole Spin-Lattice Relaxation in Rhombohedral Arsenic," *Solid State Commun.* **27**, 1025 (1978).

T. Kaneda, J. B. Bates, J. C. Wang, and H. Engstrom, "Effect of H_2O on the Ionic Conductivity of Sodium Beta-Alumina," *Mater. Res. Bull.* **14**, 1053 (1979).

T. Kaneda, J. B. Bates, and J. C. Wang, "Raman Scattering from $^6Li^+$ and $^7Li^+$ Ions in Lithium Beta-Alumina," *Solid State Commun.* **28**, 469 (1978).

Theodore Kaplan and L. J. Gray, "A Comment on Disordered Systems," *J. Phys. C* **12**, L721 (1979).

P. H. Karr, P. K. Predecki, R. W. Hendricks, and J. S. Lin, "Melting Temperature and Lamellar Thickening During Isothermal Crystallization of Bulk Polyoxymethylene," *Polym. Prepr. Am. Chem. Soc. Div. Polym. Chem.* **19**, 572 (1978).

H. R. Kerchner, D. K. Christen, and S. T. Sekula, "Equilibrium Properties of the Fluxoid Lattice in Single-Crystal Niobium. I. Magnetization Measurements," *Phys. Rev. B* **21**, 86 (1980).

R. H. Kernohan, C. J. Long, and R. R. Coltman, Jr., "Cryogenic Radiation Effects on Electric Insulators," *J. Nucl. Mater.* **85/86**, 379 (1979).

C. E. Klabunde, R. R. Coltman, Jr., and J. M. Williams, "The Effects of Irradiation on the Normal Metal of a Composite Superconductor: A Comparison of Copper and Aluminum," *J. Nucl. Mater.* **85/86**, 385 (1979).

W. C. Koehler and R. W. Hendricks, "The United States National Small-Angle Neutron Scattering Facility," *J. Appl. Phys.* **50**, 1951 (1979).

W. C. Koehler, R. M. Moon, and F. Holtzberg, "Magnetic Ordering Phenomena in TmS," *J. Appl. Phys.* **50**, 1975 (1979).

J. B. Lacy, M. M. Abraham, J. L. Boldú O., Y. Chen, J. Narayan, and H. T. Tohver, "Oxidation and Reduction of Lithium-Containing MgO at High Temperature," *Phys. Rev. B* **18**, 4136 (1978).

Uzi Landman, Ross N. Hill, and Mark Mostoller, "Lattice Relaxation at Metal Surfaces: An Electrostatic Model," *Phys. Rev. B* **21**, 448 (1980).

J. S. Lin, R. W. Hendricks, L. A. Harris, and C. S. Yust, "Microporosity and Micromineralogy of Vitrinite in a Bituminous Coal," *J. Appl. Crystallogr.* **11**, 621 (1978).

S. Liu, J. Moteff, R. W. Hendricks, and J. S. Lin, "Small-Angle X-ray Scattering Studies of Voids in Neutron-Irradiated Molybdenum," *J. Appl. Crystallogr.* **11**, 597 (1978).

G. W. Longman, G. D. Wignall, and R. P. Sheldon, "Investigation of Short Range Ordering in Polymers, Part 3: Molten Polyethylene and the Lower Alkanes," *Polymer* **20**, 1063 (1979).

D. V. McCaughan, R. A. Kushner, D. L. Simms, and C. W. White, "Effects of Bombardment by Low-Energy Neutral Particles on Silicon Dioxide," *J. Appl. Phys.* **51**, 299 (1980).

D. V. McCaughan, C. W. White, R. A. Kushner, and D. L. Simms, "Differences in Sodium Transport in SiO_2 Films Caused by Ions and Neutral-Particle Bombardment," *Appl. Phys. Lett.* **35**, 405 (1979).

D. B. McWhan, S. M. Shapiro, J. Eckert, H. A. Mook, and R. J. Birgeneau, "Pressure Dependence of Magnetic Excitations in SmS," *Phys. Rev. B* **18**, 3623 (1978).

F. A. Modine, "Circuit for Maintaining Constant Phototube Current in Polarization Modulation Spectroscopy," *Rev. Sci. Instrum.* **50**, 386 (1979).

F. A. Modine, "Stress-Induced Optical Dichroism of V Centers in MgO," *J. Phys. Chem. Solids* **40**, 305 (1979).

F. A. Modine, "The Seed Money Program," *ORNL Review* **12**, 27 (1979).

H. A. Mook and R. M. Nicklow, "Neutron Scattering Investigation of the Phonons in Intermediate Valence $Sm_{0.75}Y_{0.25}S$," *Phys. Rev. B* **20**, 1656 (1979).

H. A. Mook, T. Penney, F. Holtzberg, and M. W. Shafer, "Magnetic Excitations in the Intermediate Valence System $Sm_{0.75}Y_{0.25}S$," *J. Phys. C Paris* **6**, 837 (1978).

H. A. Mook and D. Tocchetti, "Neutron Scattering Measurements of the Generalized Susceptibility $\chi(q, E)$ for Ni," *Phys. Rev. Lett.* **43**, 2029 (1979).

R. M. Moon, "Polarized Neutron Diffraction in High Magnetic Fields," *J. Magn. Magn. Mater.* **11**, 253 (1979).

R. M. Moon, "Polarized Neutron Studies of Mixed-Valence Materials," *Nukleonika* **24**, 787 (1979).

R. M. Moon and W. C. Koehler, "Induced Magnetic Form Factor of $Ce_{0.736}Th_{0.264}$," *J. Appl. Phys.* **50**, 2089 (1979).

R. M. Moon and W. C. Koehler, "Magnetic Properties of SmN," *J. Magn. Magn. Mater.* **14**, 265 (1979).

R. M. Moon, W. C. Koehler, S. K. Sinha, C. Stassis, and G. R. Kline, "Does the 'Triple-q' Magnetic Structure Exist in Neodymium?" *Phys. Rev. Lett.* **43**, 62 (1979).

Mark Mostoller and Theodore Kaplan, "Coherent Locator Approach to Lattice Vibrations in Alloys with Diagonal and Geometrically Scaled Off-Diagonal Disorder," *Phys. Rev. B* **19**, 3938 (1979).

Mark Mostoller and Theodore Kaplan, "Elementary Excitations in the Surface Region of a Semi-Infinite Solid," *Phys. Rev. B* **19**, 552 (1979).

Mark Mostoller and Uzi Landman, "High Frequency Vibrational Modes at Stepped Pt(111) Surfaces," *Phys. Rev. B* **20**, 1755 (1979).

J. Narayan, "Depth of Melting Produced by Pulsed-Laser Irradiation," *Appl. Phys. Lett.* **34**, 312 (1979).

J. Narayan, "Formation of Dislocation Networks in Arsenic Implanted Thermally Annealed Silicon," *J. Electrochem. Soc.* **79-2**, 1289 (1979).

J. Narayan, "Laser and Electron Beam Processing of Semiconductors," *J. Electrochem. Soc.* **79-2**, 1247 (1979).

J. Narayan, "Laser and Electron Beam Processing of Silicon and Gallium Arsenide," *J. Electrochem. Soc.* **80**, 294 (1980).

J. Narayan and S. M. Ohr, "The Nature of High Energy Neutron Damage in Copper and Gold," *J. Nucl. Mater.* **85/86**, 515 (1979).

J. Narayan, R. A. Weeks, and E. Sonder, "Aggregation of Defects and Thermal-Electric Breakdown in MgO," *J. Appl. Phys.* **49**, 5977 (1978).

J. Narayan and F. W. Young, Jr., "Growth of Dislocations During Laser Melting and Solidification," *Appl. Phys. Lett.* **35**, 330 (1979).

R. M. Nicklow, W. P. Crummett, and J. M. Williams, "Neutron-Scattering Measurements of Phonon Perturbations in Irradiated Copper," *Phys. Rev. B* **20**, 5034 (1979).

J. R. Noonan and H. L. Davis, "LEED Analysis of the Reconstructed Au(110) Surface," *J. Vac. Sci. Technol.* **16**, 587 (1979).

S. M. Ohr, "Black-White Contrast of Dislocation Loops in Anisotropic Cubic Crystals," *Phys. Status Solidi A* **56**, 527 (1979).

S. M. Ohr and J. Narayan, "Electron Microscope Observation of Shear Cracks in Stainless Steel Single Crystals," *Philos. Mag. A* **41**, 81 (1980).

D. N. Olson, V. M. Orera, Y. Chen, and M. M. Abraham, "Thermally Generated $[Li]^{\circ}$ Centers in CaO," *Phys. Rev. B* **21**, 1258 (1980).

R. E. Parra and J. W. Cable, "Magnetic Moment Distribution in Ni-Pt Alloys," *J. Appl. Phys.* **50**, 7522 (1979).

D. B. Poker, G. G. Setser, A. V. Granato, and H. L. Birnbaum, "Low Temperature Anelastic Behavior of Niobium Containing Hydrogen," *Z. Phys. Chem. Neue Folge* **116**, 39 (1979).

P. P. Pronko, B. R. Appleton, O. W. Holland, and S. R. Wilson, "Anomalous Yield Enhancement for Highly Collimated 180° Scattering of He^{+} in Amorphous and Polycrystalline Materials," *Phys. Rev. Lett.* **43**, 779 (1979).

M. Rappaz, C. Solliard, A. Chatelâin, and L. A. Boatner, "Size Effects in the Crystal Field of Small Dielectric Particles," *Phys. Rev. B* **21**, 906 (1980).

M. Rasolt and H. L. Davis, "Anisotropic Contributions to the Optical Potential Employed in Theoretical Treatments of Electron Spectroscopies," *Phys. Rev. B* **20**, 5059 (1979).

M. Rasolt and D. J. W. Geldart, "Role of Gradient Corrections in Interpolation Formulae for Surface Energies," *Phys. Lett.* **73A**, 401 (1979).

M. Rasolt, G. Malmstrom, and D. J. W. Geldart, "Exchange Contribution to the Surface Energy of an Arbitrary Fermion System Within the Infinite Barrier," *Solid State Commun.* **31**, 335 (1979).

M. Rasolt, G. Malmstrom, and D. J. W. Geldart, "Wave Vector Analysis of Metallic Surface Energy," *Phys. Rev. B* **20**, 3012 (1979).

J. B. Roberto, R. A. Zuhr, J. L. Moore, and G. D. Alton, "Low-Energy Hydrogen Sputtering of Au, Ni, and Stainless Steel," *J. Nucl. Mater.* **85/86**, 1073 (1979).

J. Rubio O., E. Munoz P., J. Boldú O., Y. Chen, and M. M. Abraham, "EPR Powder Pattern Analysis for Mn^{2+} in Cubic Crystalline Fields," *J. Chem. Phys.* **70**, 633 (1979).

D. Rytz, L. A. Boatner, A. Chatelain, U. T. Höchli, and K. A. Muller, "Potential Octaedrique dans $KTa_{1-x}Nb_xO_3$ Pour un Ion $^6S_{5/2}:Fe^{3+}$," *Helv. Phys. Acta.* **51**, 430 (1978).

J. M. Schultz, J. S. Lin, and R. W. Hendricks, "A Dynamic Study of the Crystallization of Polyethylene from the Melt," *J. Appl. Crystallogr.* **11**, 551 (1978).

E. Sonder, K. F. Kelton, J. C. Pigg, and R. A. Weeks, "The Effect of Electric Current on the Conductivity of MgO Single Crystals at Temperatures Above 1300 K," *J. Appl. Phys.* **49**, 5971 (1978).

E. Sonder, T. G. Stratton, and R. A. Weeks, "Kinetics of Fe^{2+} Oxidation and Fe^{3+} Reduction in MgO," *J. Chem. Phys.* **70**, 4603 (1979).

C. Stassis, D. Arch, B. N. Harmon, and N. Wakabayashi, "Lattice Dynamics of hcp Ti," *Phys. Rev. B* **19**, 181 (1979).

C. Stassis, T. Gould, O. D. McMasters, K. A. Gschneidner, Jr., and R. M. Nicklow, "Lattice and Spin Dynamics of Gamma-Ce," *Phys. Rev. B* **19**, 5746 (1979).

C. Stassis, G. Kline, B. N. Harmon, R. M. Moon, and W. C. Koehler, "Field Induced Magnetic Form Factor of Zr," *J. Magn. Magn. Mater.* **14**, 303 (1979).

C. Stassis, C.-K. Loong, B. N. Harmon, S. H. Liu, and R. M. Moon, "Polarized Neutron Study of $CeSn_3$," *J. Appl. Phys.* **50**, 7567 (1979).

C. Stassis, C.-K. Loong, O. D. McMasters, and R. M. Moon, "Temperature Dependence of the Field Induced Magnetic Form Factor of $CeSn_3$," *J. Appl. Phys.* **50**, 2091 (1979).

C. Stassis, J. Zaretsky, and N. Wakabayashi, "Lattice Dynamics of bcc Zirconium," *Phys. Rev. Lett.* **41**, 1726 (1978).

Y. Tsunoda, N. Kunitomi, N. Wakabayashi, R. M. Nicklow, and H. G. Smith, "Phonon Dispersion Relations in the Disordered $Ni_{1-x}Pt_x$ System," *Phys. Rev. B* **19**, 2876 (1979).

N. Wakabayashi, H. G. Smith, K. C. Woo, and F. C. Brown, "Phonons and Charge Density Waves in 1T-$TiSe_2$," *Solid State Commun.* **28**, 923 (1978).

R. A. Weeks and E. Sonder, "Electrical Conductivity of Pure and Fe-Doped Magnesium Aluminum Spinel," *J. Am. Ceram. Soc.* **63**, 92 (1980).

J. F. Wendelken and M. V. K. Ulehla, "An ELS Vibrational Study of Carbon Monoxide Adsorbed on the Cu(110) Surface," *J. Vac. Sci. Technol.* **16**, 441 (1979).

J. F. Wendelken, S. P. Withrow, and P. S. Herrell, "Retractable, Rear-Viewing Low Energy Electron Diffraction Auger Spectroscopy System," *Rev. Sci. Instrum.* **51**, 255 (1980).

C. W. White, J. Narayan, B. R. Appleton, and S. R. Wilson, "Impurity Segregation by Pulsed-Laser Irradiation," *J. Appl. Phys.* **50**, 2967 (1979).

C. W. White, J. Narayan, and R. T. Young, "Laser Annealing of Ion-Implanted Semiconductors," *Science* **204**, 461 (1979).

C. W. White, P. P. Pronko, S. R. Wilson, B. R. Appleton, J. Narayan, and R. T. Young, "Effects of Pulsed Ruby-Laser Annealing on As and Sb Implanted Silicon," *J. Appl. Phys.* **50**, 3261 (1979).

C. W. White, S. R. Wilson, B. R. Appleton, and F. W. Young, Jr., "Supersaturated Substitutional Alloys Formed by Ion Implantation and Pulsed-Laser Annealing of Group-III and Group-V Dopants in Silicon," *J. Appl. Phys.* **51**, 738 (1980).

G. D. Wignall, H. R. Child, and F. Li-Aravena, "Small-Angle Neutron Scattering Studies of a Compatible Polymer Blend, Polystyrene-Polyphenylene Oxide," *Polymer* **21**, 131 (1980).

M. K. Wilkinson, "Crystallographic Contributions to the Energy Problem," *Phys. Today* **32**, 32 (1979).

J. M. Williams, C. E. Klabunde, J. K. Redman, R. R. Coltman, Jr., and R. L. Chaplin, "The Effects of Irradiation on the Copper Normal Metal of a Composite Superconductor," *IEEE Trans. Magn.* **15**, 731 (1979).

R. T. Young, J. Narayan, and R. F. Wood, "Electrical and Structural Characteristics of Laser-Induced Epitaxial Layers in Silicon," *Appl. Phys. Lett.* **35**, 447 (1979).

D. M. Zehner and H. H. Madden, "High Resolution *LMM* Auger Spectra from Argon Implanted in Be and Si," *J. Vac. Sci. Technol.* **16**, 562 (1979).

D. M. Zehner, C. W. White, and G. W. Ownby, "Preparation of Atomically Clean Silicon Surfaces by Pulsed-Laser Irradiation," *Appl. Phys. Lett.* **36**, 56 (1980).

D. M. Zehner, C. W. White, and G. W. Ownby, "Silicon Surface Structures After Pulsed-Laser Annealing," *Surf. Sci.* **92**, L67 (1980).

P. A. Zhdan, G. K. Boreskov, A. I. Boronin, A. P. Schepelin, S. P. Withrow, and W. H. Weinberg, "An XPS Investigation of CO Titration of Oxygen from an Ir(111) Surface," *Appl. of Surf. Sci.* **3**, 145 (1979).

R. A. Zuhr, R. E. Clausing, L. C. Emerson, and L. Heatherly, "Time Resolved Measurements of Impurity Deposition in ISX," *J. Nucl. Mater.* **85/86**, 979 (1979).

BOOKS AND PROCEEDINGS

W. S. Aaron, E. H. Kobisk, and T. C. Quinby, "Cermets for High Level Waste Containment," p. 191 in *Scientific Basis for Nuclear Waste Management*, vol. 1, Plenum Press, New York, 1979.

W. S. Aaron, E. H. Kobisk, and T. C. Quinby, "Development of Cermets for High Level Radioactive Waste Fixation," p. 164 in *Ceramics in Nuclear Waste Management*, Department of Energy CONF-790402, Washington, D.C., 1979.

D. L. Allara and C. W. White, "Microscopic Mechanisms of Oxidative Degradation and Its Inhibition at a Copper-Polyethylene Interface," p. 273 in *Stabilization and Degradation of Polymers (Advances in Chemistry Series)*, No. 169, ed. by D. L. Allara and W. L. Hawkins, American Chemical Society, Washington, D.C., 1978.

B. R. Appleton, "Use of Nuclear Reactions and Ion Channeling Techniques for Depth Profiling Hydrogen Isotopes in Solids," p. 64 in *The Analysis of Hydrogen in Solids*, DOE ER-0026, ed. by R. L. Schowebel and J. L. Warren, Washington, D.C., 1979.

B. R. Appleton, B. C. Larson, C. W. White, J. Narayan, S. R. Wilson, and P. P. Pronko, "New Materials Properties Achievable by Ion Implantation Doping and Laser Processing," p. 291 in *Laser Solid Interactions and Laser Processing—1978*, AIP Conference Proceedings No. 50, ed. by S. D. Ferris, H. J. Leamy, and J. M. Poate, New York, 1979.

B. R. Appleton, C. W. White, B. C. Larson, S. R. Wilson, and J. Narayan, "Laser Processing of Ion-Implanted Silicon," p. 1686 in *Proceedings of 1978 Conference on the Application of Small Accelerators in Research and Industry*, IEEE Transactions on Nuclear Sciences, vol. NS-26, ed. by J. L. Duggan, I. L. Morgan, and J. A. Martin, 1979.

J. B. Bates, "Structural, Dynamical, and Transport Properties of Hydrogen in Insulating Materials," p. 7 in *The Analysis of Hydrogen in Solids*, DOE ER-0026, ed. by R. L. Schowebel and J. L. Warren, Washington, D.C., 1979.

J. B. Bates, G. M. Brown, T. Kaneda, W. E. Brundage, J. C. Wang, and H. Engstrom, "Properties of Single Crystal Beta"-Aluminas," p. 261 in *Fast Ion Transport in Solids, Electrodes, and Electrolytes*, ed. by P. Vashishta, J. N. Mundy, and G. K. Shenoy, North Holland, New York, 1979.

K. Bōning, G. S. Bauer, H. J. Fenzl, R. Scherm, and R. M. Nicklow, "Neutron Inelastic Scattering Measurements of Phonon Dispersion Curves in Aluminum Reactor-Irradiated at 4.6 K," p. 386 in *Proceedings of the International Conference on Lattice Dynamics*, ed. by M. Balkanski, Flammarion Sciences, Paris, 1978.

W. H. Christie, R. J. Warmack, C. W. White, and J. Narayan, "Laser-Induced Redistribution of Ion-Implanted and Surface Deposited B in Silicon: A SIMS Study," p. 100 in *Secondary Ion Mass Spectrometry*, SIMS-II, ed. by A. Beeninghoven, C. A. Evans, R. A. Powell, R. Shimizu, and H. A. Storms, Springer-Verlag, New York, 1979.

W. H. Christie, C. W. White, and J. C. Wang, "The Effect of Laser Annealing on the Redistribution of Boron in Ion-Implanted Silicon," p. 155 in *Proceedings of the Conference on SIMS-Fundamentals and Applications*, Takarazuka, Japan, 1978.

J. W. Cleland, P. H. Fleming, R. D. Westbrook, R. F. Wood, and R. T. Young, "Electrical Property Studies of Neutron-Transmutation-Doped Silicon," p. 261 in *Neutron Transmutation Doping in Semiconductors*, ed. by J. M. Meese, Plenum Press, New York, 1979.

R. R. Dubin, J. S. Kasper, J. B. Bates, and T. Kaneda, "Characterization of Heat Treatment Induced Changes in Li-Na Beta-Alumina Single Crystals," p. 361 in *Fast Ion Transport in Solids, Electrodes, and Electrolytes*, ed. by P. Vashishta, J. N. Mundy, and G. K. Shenoy, North Holland, New York, 1979.

H. Engstrom, J. B. Bates, R. T. Young, J. R. Noonan, and C. W. White, "Infrared and Raman Spectra of Boron-Implanted, Laser-Annealed Silicon," p. 405 in *Laser Solid Interactions and Laser Processing—1978*, AIP Conference Proceedings No. 50, ed. by S. D. Ferris, H. J. Leamy, and J. M. Poate, New York, 1979.

T. Kaneda, J. B. Bates, J. C. Wang, and H. Engstrom, "Ionic Conductivity and Raman Spectra of Na-Li, K-Li, and K-Sn β-Al_2O_3," p. 711 in *Fast Ion Transport in Solids, Electrodes, and Electrolytes*, ed. by P. Vashishta, J. N. Mundy and G. K. Shenoy, North Holland, New York, 1979.

A. M. Keesee, T. F. Connolly, and G. C. Battle, Jr., "Crystal Growth Bibliography," vols. 10A and 10B of *Solid State Physics Literature Guides*, ed. by T. F. Connolly, Plenum Press, New York, 1979.

S. Kobayashi and S. M. Ohr, "In Situ Studies of Crack Propagation in bcc Metals," p. 424 in *Proceedings of Thirty-Seventh Annual Meeting of Electron Microscopy Society of America*, ed. by G. W. Bailey, Claitor's Press, Baton Rouge, 1979.

B. C. Larson, R. T. Young, and J. Narayan, "Defect Annealing Studies in Neutron Transmutation Doped Silicon," p. 281 in *Neutron Transmutation Doping in Semiconductors*, ed. by J. M. Meese, Plenum Press, New York, 1979.

C. J. Long, R. H. Kernohan, and R. R. Coltman, Jr., "Radiation Effects on Insulators for Superconducting Magnets," p. 141 in *Proceedings of the International Cryogenic Materials Conference: Special Seminar on Non-Metallic Materials and Composites at Low Temperatures*, Plenum Press, New York, 1979.

J. Narayan, B. C. Larson, and W. H. Christie, "Effect of Thermal Annealing in Boron-Implanted, Laser-Annealed Silicon," p. 440 in *Laser-Solid Interactions and Laser Processing—1978*, AIP Conference Proceedings No. 50, ed. by S. D. Ferris, H. J. Leamy, and J. M. Poate, New York, 1979.

J. Narayan and C. W. White, "Extent of Annealed or Melted Regions as a Function of Energy of Pulsed-Laser Irradiation," p. 446 in *Laser-Solid Interactions and Laser Processing—1978*, AIP Conference Proceedings No. 50, ed. by S. D. Ferris, H. J. Leamy, and J. M. Poate, New York, 1979.

J. Narayan, C. W. White, and R. T. Young, "Transmission Electron Microscope Study of Laser Annealing of Ion Damage in Silicon and Gallium Arsenide," p. 819 in *Proceedings of the International Conference on Ion Beam Modification of Materials*, vol. II, ed. by J. Gyulai, T. Lohner, and E. Pasztor, Central Research Institute for Physics, Budapest, 1979.

J. Narayan, R. T. Young, and C. W. White, "Characteristics of Laser-Annealed Ion-Implanted Solar Cells," p. 213 in *Proceedings of Laser Effects in Ion Implanted Semiconductors*, ed. by E. Rimini, University of Catania, Italy, 1978.

J. Narayan, R. T. Young, R. F. Wood, C. W. White, and W. H. Christie, "*p-n* Junction Formation by Laser-Induced Diffusion," p. 209 in *Proceedings of Laser Effects in Ion Implanted Semiconductors*, ed. by E. Rimini, University of Catania, Italy, 1978.

R. M. Nicklow, "Phonons and Defects," p. 191 in *Treatise on Materials Science and Technology (Neutron Scattering)*, vol. 15, ed. by G. Kostorz, Academic Press, New York, 1979.

O. S. Oen, "Penetration and Reflection of Low-keV Light Ions (H, D, He) Incident upon Solid Surfaces," p. 191 in *Proceedings of the Workshop on the Penetration of Low-Energy Particles*, ed. by S. Stern, New York University, 1979.

O. S. Oen and M. T. Robinson, "Computer Simulation of the Reflection of Hydrogen and Tritium from Solid Surfaces," p. 39 in *Proceedings of Symposium on Atomic Surface Physics (SASP)*, ed. by W. Lindinger, F. Howorka, and F. Egger, Institut für Atomphysik, Tirol, Italy, 1978.

J. B. Roberto and C. W. White, "Laser Fluorescence Techniques for In Situ Impurity Studies," chap. 19 in *Proceedings of the Workshop on New Diagnostics Related to Impurity Release*, Department of Energy, CONF-790585, ed. by C. R. Finfgeld and S. A. Cohen, Washington, D.C., 1979.

Mark T. Robinson, "Hydrogen Reflection Calculations," chap. 13 in *Proceedings of the Workshop on Hydrogen Recycling*, Department of Energy CONF-791057, Washington, D.C., 1980.

H. G. Smith, N. Wakabayashi, W. P. Crummett, R. M. Nicklow, G. H. Lander, and E. S. Fisher, "Observation of Superstructure in Alpha-U Near 43 K," p. 226 in *Modulated Structures*, ed. by J. M. Cowley, J. B. Cohen, M. B. Salamon, and B. J. Wuensch, American Institute of Physics, New York, 1979.

N. Wakabayashi and R. M. Nicklow, "Neutron Scattering and Lattice Dynamics of Materials with Layered Structures," p. 409 in *Electrons and Phonons in Layered Crystal Structures*, ed. by T. J. Wieting and M. Schluter, D. Reidel Publishing Company, Dordrecht, Holland, 1979.

J. C. Wang, J. B. Bates, T. Kaneda, H. Engstrom, D. F. Pickett, Jr., and Sang-il Choi, "Model Studies of Mixed-Ion Beta-Aluminas," p. 379 in *Fast Ion Transport in Solids, Electrodes, and Electrolytes*, ed. by P. Vashishta, J. N. Mundy, and G. K. Shenoy, North Holland, New York, 1979.

J. C. Wang, R. F. Wood, C. W. White, B. R. Appleton, P. P. Pronko, S. R. Wilson, and W. H. Christie, "Dopant Profile Changes Induced by Laser Irradiation of Silicon: Comparison of Theory and Experiment," p. 123 in *Laser-Solid Interactions and Laser Processing—1978*, AIP Conference Proceedings No. 50, ed. by S. D. Ferris, H. J. Leamy, and J. M. Poate, New York, 1979.

C. W. White, W. H. Christie, P. P. Pronko, B. R. Appleton, S. R. Wilson, R. T. Young, J. C. Wang, R. F. Wood, J. Narayan, and C. W. Magee, "Dopant Profile Changes Induced by Pulsed-Laser Annealing," p. 839 in *Proceedings of the International Conference on Ion Beam Modification of Materials*, vol. II, ed. by J. Gyulai, T. Lohner, and E. Pasztor, Central Research Institute for Physics, Budapest, 1979.

C. W. White, J. Narayan, B. R. Appleton, P. P. Pronko, S. R. Wilson, B. C. Larson, and R. T. Young, "Laser Annealing of Ion-Implanted Silicon," p. 41 in *Proceedings of Laser Effects in Ion-Implanted Semiconductors*, ed. by E. Rimini, University of Catania, Italy, 1978.

C. W. White, J. Narayan, and R. T. Young, "Laser Annealing of Ion-Implanted Silicon," p. 275 in *Laser-Solid Interactions and Laser Processing—1978*, AIP Conference Proceedings No. 50, ed. by S. D. Ferris, H. J. Leamy, and J. M. Poate, New York, 1979.

C. W. White, P. P. Pronko, B. R. Appleton, S. R. Wilson, and J. Narayan, "Lattice Location of Implanted As and Sb in Silicon After Pulsed-Laser Annealing," p. 809 in *Proceedings of the International Conference on Ion Beam Modification of Materials*, vol. II, ed. by J. Gyulai, T. Lohner, and E. Pasztor, Central Research Institute for Physics, Budapest, 1979.

C. W. White, W. H. Christie, P. P. Pronko, B. R. Appleton, S. R. Wilson, J. C. Wang, R. F. Wood, and C. W. Magee, "Pulsed-Laser Annealing Dopant Profile Changes," p. 133 in *Proceedings of Laser Effects in Ion-Implanted Semiconductors*, ed. by E. Rimini, University of Catania, Italy, 1978.

S. R. Wilson, B. R. Appleton, C. W. White, J. Narayan, and A. C. Greenwald, "Comparison of Pulsed Electron Beam Annealed with Pulsed Ruby Laser Annealed Ion-Implanted Silicon," p. 1697 in *Proceedings of 1978 Conference on the Applications of Small Accelerators in Research and Industry*, IEEE Transactions on Nuclear Science, vol. NS-26, No. 1, ed. by J. L. Duggan, I. L. Morgan, and J. A. Martin, 1979.

S. R. Wilson, B. R. Appleton, C. W. White, and J. Narayan, "Comparison of Effects of Pulsed Ruby Laser and Pulsed Electron Beam Annealing of $^{75}As^{+}$ Implanted Silicon," p. 481 in *Laser-Solid Interactions and Laser Processing—1978*, AIP Conference Proceedings No. 50, ed. by S. D. Ferris, H. J. Leamy, and J. M. Poate, New York, 1979.

S. R. Wilson, C. W. White, P. P. Pronko, R. T. Young, and B. R. Appleton, "Lattice Location of As and Sb Implanted in Silicon After Annealing with a Pulsed Ruby Laser," p. 351 in *Laser-Solid Interactions and Laser Processing—1978*, AIP Conference Proceedings No. 50, ed. by S. D. Ferris, H. J. Leamy, and J. M. Poate, New York, 1979.

R. F. Wood, "Laser Annealing," chap. 10 in *Microstructure Science, Engineering, and Technology*, National Academy of Sciences, Washington, D.C., 1979.

R. F. Wood, G. E. Giles, and J. R. Kirkpatrick, "Theoretical Analysis of Thermal and Mass Transport During Laser Annealing," p. 2 in *Laser Applications in Materials Processing*, vol. 198, ed. by J. F. Ready, Society of Photo-Optical Instrumentation Engineers, Bellingham, Washington, 1980.

R. T. Young, J. Narayan, R. D. Westbrook, and R. F. Wood, "Transmission Electron Microscopy and Electrical Properties Measurements of Laser-Doped Silicon and GaAs," p. 579 in *Laser-Solid Interactions and Laser Processing—1978*, AIP Conference Proceedings No. 50, ed. by S. D. Ferris, H. J. Leamy, and J. M. Poate, New York, 1979.

R. T. Young, J. Narayan, C. W. White, R. F. Wood, J. W. Cleland, R. D. Westbrook, and P. M. Mooney, "Electrical Characteristics of Ion-Implanted Laser-Annealed Silicon," p. 831 in *Proceedings of the International Conference on Ion Beam Modification of Materials*, vol. II, ed. by J. Gyulai, T. Lohner, and E. Pasztor, Central Research Institute for Physics, Budapest, 1979.

R. T. Young, R. F. Wood, J. Narayan, and W. H. Christie, "Laser Techniques in Photovoltaic Applications," p. 36 in *Laser Applications in Materials Processing*, vol. 198, ed. by J. F. Ready, Society of Photo-Optical Instrumentation Engineers, Bellingham, Washington, 1980.

R. A. Zuhr, B. R. Appleton, J. B. Roberto, and S. P. Withrow, "Ion Backscattering/Channeling and Nuclear Reaction Analysis of Tokamak-Exposed Samples," chap. 4 in *Proceedings of the Workshop on New Diagnostics Related to Impurity Release*, Department of Energy CONF-790585, Washington, D.C., 1979.

R. A. Zuhr, S. P. Withrow, J. B. Roberto, and B. R. Appleton, "In Situ Measurements of the Plasma Boundary Region in ISX," chap. 9 in *Proceedings of the DOE Workshop on Hydrogen Recyling*, Department of Energy CONF-791057, Washington, D.C., 1980.

REPORTS ISSUED

W. S. Aaron, T. C. Quinby, E. H. Kobisk, and D. K. Thomas, "Study of Ceramic and Cermet Waste Forms," p. 32 in *High Level Waste Program Progress Report for October 1, 1978, through March 31, 1979*, ORNL/TM-5866 (May 1979).

W. S. Aaron, T. C. Quinby, E. H. Kobisk, and D. K. Thomas, "Study of Ceramic and Cermet Waste Forms," p. 21 in *High Level Waste Program Progress Report for April 1, 1979, through June 30, 1979*, ORNL/TM-7013 (August 1979).

W. S. Aaron, T. C. Quinby, E. H. Kobisk, and D. K. Thomas, "Study of Ceramic and Cermet Waste Forms," p. 17 in *High Level Waste Program Progress Report for July 1, 1979, through September 30, 1979*, ORNL/TM-7118 (November 1979).

R. R. Coltman, Jr., C. E. Klabunde, R. H. Kernohan, and C. J. Long, *Radiation Effects on Organic Insulators for Superconducting Magnets*, ORNL/TM-7077 (November 1979).

T. F. Connolly, G. C. Battle, and Anne M. Keesee, *Directory of Crystal Growth and Solid State Materials Production and Research*, ORNL/RMIC-14 (March 1979).

W. Harrison and R. A. Weeks, "Preliminary Results from an Electron Paramagnetic Resonance Investigation of the Site Occupancy of Gd^{3+} in Pyrope Garnet," p. 568 in *Annual Report of the Director, Geophysical Laboratory, Carnegie Institution*, 1978–1979.

R. H. Kernohan, R. R. Coltman, Jr., and C. J. Long, *Radiation Effects on Organic Insulators for Superconducting Magnets*, ORNL/TM-6708 (May 1979).

D. W. Ramey, M. Petek, R. D. Taylor, E. H. Kobisk, J. Ramey, and C. A. Sampson, *Tritium Separation from Light and Heavy Water by Bipolar Electrolysis*, ORNL-5581 (October 1979).

T. P. Russell, R. S. Stein, M. K. Kopp, R. E. Zedler, R. W. Hendricks, and J. S. Lin, *The Application of a One-Dimensional Position-Sensitive Detector to a Kratky Small-Angle X-ray Camera*, ORNL/TM-6678 (November 1978).

P. Thorel and D. K. Christen, "Misalignment of Fluxoids and the Magnetic Field in Superconducting Niobium," *Bulletin du Department de la Recherche Fondementale 13, Grenoble, France* (Fall 1978).

THESES

R. E. Parra, "Neutron Study of Magnetic Moment Distribution in Ni-Pt Alloys," thesis submitted to the Graduate Council of the Georgia Institute of Technology in partial fulfillment of the requirements for the Ph.D. degree, September 1979.

D. B. Poker, "A Low Temperature Ultrasonic Study of Hydrogen in Niobium," thesis submitted to the Graduate Council of the University of Illinois in partial fulfillment of the requirements for the Ph.D. degree, January 1979.

R. D. Taylor, "An Investigation of the Effects of Trace Additions of Hydrogen Sulfide on the High-Temperature Reactions of Metals in CO at Ambient and Elevated Pressures," thesis submitted to the Graduate Council of the Georgia Institute of Technology in partial fulfillment of the requirements for the M.S. degree, August 1979.

S. R. Wilson, "Formation of Supersaturated Alloys by Ion Implantation and Pulsed-Laser Annealing," thesis submitted to the Graduate Council of North Texas State University in partial fulfillment of the requirements for the Ph.D. degree, August 1979.

PATENTS GRANTED

J. W. Cleland, R. D. Westbrook, R. F. Wood, and R. T. Young, *Polycrystalline Silicon Semiconducting Material by Nuclear Transmutation Doping*, U.S. patent No. 4,129,463 (December 12, 1978).

J. Narayan, C. W. White, and R. T. Young, *Method for Making Defect-Free Zone by Laser Annealing of Doped Silicon*, U.S. patent No. 4,181,538 (January 1, 1980).

J. Narayan and R. T. Young, *Method for Forming p-n Junctions and Solar Cells by Laser-Beam Processing*, U.S. patent No. 4,147,563 (April 3, 1979).

PAPERS PRESENTED AT TECHNICAL MEETINGS

Fall Meeting of the Swiss Physical Society, Brique, Switzerland, October 5–6, 1978:

U. T. Höchli, H. E. Weibel, and L. A. Boatner, "Dielectric Susceptibility and Local Freeze-Out of Li in $KTaO_3$"

Midwest Solid State Conference, Argonne, Illinois, October 6–7, 1978:

J. D. Woosley, C. Wood, R. A. Weeks, and E. Sonder, "Photoelectric Effect in Spinel"

Twenty-second Conference on Analytical Chemistry in Energy Technology, Gatlinburg, Tennessee, October 10–12, 1978:

C. W. White, "Characterization of Ion-Implanted, Laser-Annealed Silicon for Solar Cell Applications" (invited paper)

Nuclear Radiation Effects Meeting, Fort Monmouth, New Jersey, October 16–17, 1978:

R. A. Weeks, "Irradiation Effects on Color Centers in Glass" (invited paper)

Conference on SIMS-Fundamentals and Applications, Takarazuka, Japan, October 23–27, 1978:

W. H. Christie, C. W. White, and J. C. Wang, "The Effect of Laser Annealing on the Redistribution of Boron in Ion-Implanted Silicon"

Southeastern Section Meeting, American Physical Society, Blacksburg, Virginia, October 26–28, 1978:

R. H. Kernohan, R. R. Coltman, Jr., and C. J. Long, "Low-Temperature Irradiation Effects on Organic Insulators" [*Bull. Am. Phys. Soc.* **24**, 99 (1979)]

V. M. Orera, Y. Chen, and M. M. Abraham, "Influence of Lithium Impurities on the Hardening of Crystalline MgO" [*Bull. Am. Phys. Soc.* **24**, 99 (1979)]

J. C. Wang, "A Conduction Mechanism for the β-Alumina Family of Fast Ion Conductors" [*Bull. Am. Phys. Soc.* **24**, 106 (1979)] (invited paper)

C. W. White, "Properties of Ion-Implanted, Laser-Annealed Semiconductors" [*Bull. Am. Phys. Soc.* **24**, 106 (1979)] (invited paper)

Fall Meeting of the Society of Industrial and Applied Mathematics, Knoxville, Tennessee, October 30–November 3, 1978:

L. J. Gray and Theodore Kaplan, "Spectral Functions of Disordered Alloys"

American Physical Society Meeting, Colorado Springs, Colorado, October 30–November 3, 1978:

R. A. Langley, R. E. Clausing, R. J. Colchin, L. C. Emerson, L. Heatherly, J. E. Simpkins, R. A. Zuhr, and Y. Gomay, "Summary of Surface Studies in ISX-A" [*Bull. Am. Phys. Soc.* **23**, 855 (1978)]

R. A. Zuhr, B. R. Appleton, J. L. Moore, O. E. Schow III, J. B. Roberto, C. W. White, and S. P. Withrow, "Plasma Edge Particle Transport in ISX" [*Bull. Am. Phys. Soc.* **23**, 791 (1978)]

FACSS Meeting, Boston, Massachusetts, October 30–November 3, 1978:

C. W. White, "The Use of Ion Beams for Surface and Depth Profile Analysis" (invited paper)

Workshop on Solute Segregation and Phase Stability During Irradiation, Gatlinburg, Tennessee, November 1–3, 1978:

J. Narayan, B. C. Larson, and O. S. Oen, "Depth Distribution of Damage in Copper Irradiated with MeV Cu and Ni Ions"

Fifth Conference on the Use of Small Accelerators for Research and Industry, Denton, Texas, November 6–8, 1978:

B. R. Appleton, C. W. White, B. C. Larson, S. R. Wilson, and J. Narayan, "Laser Processing of Ion-Implanted Silicon" [*Bull. Am. Phys. Soc.* **23**, 1032 (1978)] (invited paper)

S. R. Wilson, B. R. Appleton, C. W. White, J. Narayan, and A. C. Greenwald, "Comparison of Pulsed Electron Beam Annealed with Pulsed Ruby Laser Annealed Ion-Implanted Silicon"

American Nuclear Society Winter Meeting, Washington, D.C., November 12–17, 1978:

W. S. Aaron, E. H. Kobisk, and T. C. Quinby, "Formation of Cermet High Level Waste Forms for Repository Storage" [*Trans. Am. Nucl. Soc.* **30**, 284 (1978)]

U.S. Department of Energy Program Review Meeting on Hydrogen in Metals, Germantown, Maryland, November 13, 1978:

S. M. Ohr, "Electron Microscope Studies of Fracture in Solids" (invited paper)

Twenty-fourth Annual Conference on Magnetism and Magnetic Materials, Cleveland, Ohio, November 14–17, 1978:

J. F. Cooke, "Role of Electron-Electron Interactions in the RKKY Theory of Magnetism"

W. C. Koehler and R. W. Hendricks, "The United States National Small-Angle Neutron Scattering Facility" (invited paper)

W. C. Koehler, R. M. Moon, and F. Holtzberg, "Magnetic Ordering Phenomena in TmS"

R. M. Moon and W. C. Koehler, "Induced Magnetic Form Factor of $Ce_{0.736}Th_{0.264}$"

C. Stassis, C.-K. Loong, and R. M. Moon, "Temperature Dependence of the Field-Induced Magnetic Form Factor of $CeSn_3$"

Workshop on Ion-Induced Displacement Cascades in Metals, Bad Honnef, Germany, November 22–24, 1978:

M. T. Robinson, "Computer Simulation of Displacement Cascades in Metals" (invited paper)

Twenty-fifth National Symposium of the American Vacuum Society, San Francisco, California, November 28–December 1, 1978:

J. R. Noonan and H. L. Davis, "A LEED Analysis of the Reconstructed Au(110) Surface"

J. F. Wendelken and M. V. K. Ulehla, "An ELS Vibrational Study of Carbon Monoxide Adsorbed on the Cu(110) Surface"

D. M. Zehner and H. H. Madden, "High Resolution *LMM* Auger Spectra from Argon Implanted in Be and Si"

Materials Research Society Symposium on Laser-Solid Interactions and Laser Processing, Boston, Massachusetts, November 28–December 1, 1978:

B. R. Appleton, B. C. Larson, C. W. White, J. Narayan, S. R. Wilson, and P. P. Pronko, "New Materials Properties Achievable by Ion Implantation Doping and Laser Processing"

H. Engstrom, J. B. Bates, R. T. Young, J. R. Noonan, and C. W. White, "Infrared and Raman Spectra of Boron-Implanted, Laser-Annealed Silicon"

J. Narayan, B. C. Larson, and W. H. Christie, "Effect of Thermal Annealing in Boron-Implanted, Laser-Annealed Silicon"

J. Narayan and C. W. White, "Extent of Annealed or Melted Regions as a Function of Energy of Pulsed-Laser Irradiation"

J. C. Wang, R. F. Wood, C. W. White, B. R. Appleton, P. P. Pronko, S. R. Wilson, and W. H. Christie, "Dopant Profile Changes Induced by Laser Irradiation of Silicon: Comparison of Theory and Experiment"

C. W. White, J. Narayan, and R. T. Young, "Laser Annealing of Ion-Implanted Silicon" (invited paper)

S. R. Wilson, B. R. Appleton, C. W. White, and J. Narayan, "Comparison of Effects of Pulsed Ruby Laser and Pulsed Electron Beam Annealing of $^{75}As^{+}$-Implanted Silicon"

S. R. Wilson, C. W. White, P. P. Pronko, R. T. Young, and B. R. Appleton, "Lattice Location of As and Sb Implanted in Silicon After Annealing with a Pulsed Ruby Laser"

R. T. Young, J. Narayan, R. D. Westbrook, and R. F. Wood, "Transmission Electron Microscopy and Electrical Properties Measurements of Laser-Doped Silicon and GaAs"

Materials Research Society Symposium on Scientific Basis for Nuclear Waste Management, Boston, Massachusetts, November 29–December 1, 1978:

W. S. Aaron, E. H. Kobisk, and T. C. Quinby, "Cermets for High-Level Waste Containment"

Workshop on Penetration of Low-Energy Particles, New York, New York, January 4–5, 1979:

O. S. Oen, "Penetration and Reflection of Low-keV Light Ions (H, D, He) Incident Upon Solid Surfaces"

Gordon Research Conference on Crystal Growth, Santa Barbara, California, January 15–19, 1979:

F. W. Young, Jr., "Crystal Growth Aspects of Laser Annealing" (invited paper)

ORLS/DOE Workshop on Analysis of Hydrogen in Solids, Albuquerque, New Mexico, January 23–25, 1979:

B. R. Appleton, "Use of Nuclear Reactions and Ion-Channeling Techniques for Depth Profiling Hydrogen Isotopes in Solids" (invited paper)

J. B. Bates, "Structural, Dynamical, and Transport Properties of Hydrogen in Insulating Materials" (invited paper)

First Topical Meeting on Fusion Reactor Materials, Miami Beach, Florida, January 29-31, 1979:

T. J. Hoffman, H. L. Dodds, Jr., and M. T. Robinson, "Range Calculations Using Multigroup Transport Methods"

R. H. Kernohan, C. J. Long, and R. R. Coltman, Jr., "Cryogenic Radiation Effects on Electric Insulators"

C. E. Klabunde, R. R. Coltman, Jr., and J. M. Williams, "The Effects of Irradiation on the Normal Metal of a Composite Superconductor: A Comparison of Copper and Aluminum"

J. Narayan and S. M. Ohr, "The Nature of High-Energy Neutron Damage in Copper and Gold"

T. S. Noggle, J. M. Williams, B. R. Appleton, and T. Iwata, "Damage Production Rates of Ni Ions in Ni"

J. B. Roberto, R. A. Zuhr, J. L. Moore, and G. D. Alton, "Low-Energy Hydrogen Sputtering of Au, Ni, and Stainless Steel"

R. A. Zuhr, R. E. Clausing, and L. C. Emerson, "Time-Resolved Measurements of Impurity Deposition in ISX"

Annual AIME Meeting, New Orleans, Louisiana, February 18–20, 1979:

S. M. Ohr and S. Kobayashi, "Distribution of Dislocations in the Plastic Zone of Shear Cracks"

Frühjahrstagung der Deutschen Physikalischen Gesellschaft, Münster, Germany, March 12–16, 1979:

W. Husinsky, R. Bruckmüller, and P. Blum, "Thermische Effekte beim Sputtern von Na-Targets"

American Physical Society Meeting, Chicago, Illinois, March 19–23, 1979:

M. M. Abraham, L. A. Boatner, and F. A. Modine, "Paramagnetic Resonance Spectra Associated with Electrolytically Colored MgO" [*Bull. Am. Phys. Soc.* **24**, 413 (1979)]

D. Arch, E. N. Harmon, C. Stassis, and N. Wakabayashi, "Lattice Dynamics of hcp Ti" [*Bull. Am. Phys. Soc.* **24**, 487 (1979)]

J. B. Bates, T. Kaneda, W. E. Brundage, J. C. Wang, G. M. Brown, and H. Engstrom, "Properties of Beta"-Alumina" [*Bull. Am. Phys. Soc.* **24**, 398 (1979)]

L. A. Boatner, M. Linvill, and F. A. Modine, "$KTaO_3$ Photoelectrochemical Cells" [*Bull. Am. Phys. Soc.* **24**, 274 (1979)]

L. A. Boatner, F. A. Modine, M. M. Abraham, W. H. Christie, and T. Negas, "Electrolytic Coloration of MgO at High Temperatures" [*Bull. Am. Phys. Soc.* **24**, 413 (1979)]

J. L. Boldú, E. F. Montesa, Y. Chen, and M. M. Abraham, "Neutron Irradiations in Li-Doped MgO Oxidized at Elevated Temperatures" [*Bull. Am. Phys. Soc.* **24**, 414 (1979)]

Y. Chen, R. H. Kernohan, J. L. Boldú, and M. M. Abraham, "Electrical Conductivity of MgO due to Lithium Impurity" [*Bull. Am. Phys. Soc.* **24**, 412 (1979)]

D. K. Christen, S. T. Sekula, and P. Thorel, "History Dependence of the Flux-Line Lattice in a Defect-Free Niobium Sphere" [*Bull. Am. Phys. Soc.* **24**, 484 (1979)]

J. F. Cooke "First-Principles Phonon Calculations in Molybdenum and Niobium" [*Bull. Am. Phys. Soc.* **24**, 457 (1979)]

H. L. Davis and D. M. Zehner, "Preliminary LEED Analysis of the Clean Re(0001) Surface" [*Bull. Am. Phys. Soc.* **24**, 468 (1979)]

H. W. Diehl, P. L. Leath, and T. Kaplan, "Spectra Density of Binary Mixed Crystals with Off-Diagonal Disorder" [*Bull. Am. Phys. Soc.* **24**, 394 (1979)]

G. E. Jellison, Jr., G. L. Petersen, and P. C. Taylor, "Pulsed Nuclear Quadrupole Resonance (NQR) in Amorphous and Orthorhombic Arsenic" [*Bull. Am. Phys. Soc.* **24**, 307 (1979)]

W. A. Kamitakahara and N. Wakabayashi, "Lattice Dynamics of Cadmium" [*Bull. Am. Phys. Soc.* **24**, 486 (1979)]

T. Kaneda, J. B. Bates, J. C. Wang, and H. Engstrom, "Raman and Infrared Spectra, and Ionic Conductivity of Mixed Na-Li Beta-Alumina" [*Bull. Am. Phys. Soc.* **24**, 398 (1979)]

H. R. Kerchner, Y. K. Chang, D. K. Christen, and J. Narayan, "Fluxoid Pinning by Small Nitride Precipitates in Niobium" [*Bull. Am. Phys. Soc.* **24**, 485 (1979)]

S. Kobayashi and S. M. Ohr, "Electron Microscope Observation of Crack Propagation in bcc Metals" [*Bull. Am. Phys. Soc.* **24**, 253 (1979)]

W. C. Koehler and R. W. Hendricks, "The U.S. National Small-Angle Neutron Scattering Facility—A Progress Report" [*Bull. Am. Phys. Soc.* **24**, 256 (1979)] (invited paper)

B. C. Larson and J. F. Barhorst, "X-ray Scattering from Loops in Neutron-Irradiated Copper" [*Bull. Am. Phys. Soc.* **24**, 241 (1979)]

F. A. Modine, L. A. Boatner, M. M. Abraham, W. P. Unruh, and R. Bunch, "Optical Studies of Electrolytically Colored MgO" [*Bull. Am. Phys. Soc.* **24**, 413 (1979)]

H. A. Mook, R. C. Larson, and B. Van Bodegom, "Neutron and X-ray Scattering Study of the 18 K Transition in MEM(TCNQ)$_2$" [*Bull. Am. Phys. Soc.* **24**, 355 (1979)]

J. Narayan, R. A. Weeks, and E. Sonder, "Electron Microscope Study of Defect Substructures Resulting from Thermal-Electric Breakdown" [*Bull. Am. Phys. Soc.* **24**, 413 (1979)]

J. Narayan and R. F. Wood, "Melt-Front Penetration Produced by Pulsed-Laser Irradiation" [*Bull. Am. Phys. Soc.* **24**, 401 (1979)]

R. M. Nicklow, W. P. Crummett, R. F. Wood, and M. Mostoller, "Phonon-Defect Mode Hybridization in $KCl_{1-x}(KCN)_x$ Studies by Neutron Scattering" [*Bull. Am. Phys. Soc.* **24**, 487 (1979)]

R. M. Nicklow, M. Pomerantz, and A. Segmuller, "Neutron Scattering from Mn-Stearate Films of Few Molecular Layers" [*Bull. Am. Phys. Soc.* **24**, 488 (1979)]

S. M. Ohr and S. Kobayashi, "Dislocation Model of Shear Crack Propagation" [*Bull. Am. Phys. Soc.* **24**, 252 (1979)]

D. N. Olson, M. M. Abraham, Y. Chen, V. M. Orera, R. F. Wood, and T. M. Wilson, "Electron Defects in Non-Stoichiometric CaO:Li" [*Bull. Am. Phys. Soc.* **24**, 412 (1979)]

V. M. Orera, Y. Chen, and M. M. Abraham, "Imprinting of Dislocation Bands in Mechanically Deformed MgO Using [Li]^0 Defects" [*Bull. Am. Phys. Soc.* **24**, 412 (1979)]

D. B. Poker, G. G. Setser, A. V. Granato, and H. K. Birnbaum, "Evidence for Tunneling of Hydrogen in Niobium from Ultrasonic Measurements" [*Bull. Am. Phys. Soc.* **24**, 491 (1979)]

R. L. Prater, L. L. Chase, and L. A. Boatner, "Raman Studies of Impurity-Induced Ferroelectricity in $KTaO_3$" [*Bull. Am. Phys. Soc.* **24**, 508 (1979)]

Mark Rasolt, G. Malmstrom, and D. J. W. Geldart, "Wave Vector Analysis of Metallic Surface Energy" [*Bull. Am. Phys. Soc.* **24**, 438 (1979)]

C. Stassis, J. Zaretsky, and N. Wakabayashi, "Lattice Dynamics of bcc Zr" [*Bull. Am. Phys. Soc.* **24**, 487 (1979)]

Martin Úlehla, "Systematic Approach to the Problem of Disordered Systems" [*Bull. Am. Phys. Soc.* **24**, 394 (1979)]

N. Wakabayashi, "Phonons in Transition Metals: Neutron Scattering and Model Studies" [*Bull. Am. Phys. Soc.* **24**, 421 (1979)] (invited paper)

J. C. Wang, J. B. Bates, T. Kaneda, and H. Engstrom, "On the Ionic Conduction Mechanisms of β''-Aluminas" [*Bull. Am. Phys. Soc.* **24**, 433 (1979)]

R. F. Wood, J. C. Wang, G. E. Giles, and J. R. Kirkpatrick, "Calculations of Dopant Redistribution in Arsenic-Implanted Laser-Annealed Silicon" [*Bull. Am. Phys. Soc.* **24**, 314 (1979)]

J. D. Woosley, C. Wood, E. Sonder, and R. A. Weeks, "Photoelectric Effects in Spinel" [*Bull. Am. Phys. Soc.* **24**, 449 (1979)]

R. T. Young, J. Narayan, R. D. Westbrook, and R. F. Wood, "Formation of Epitaxial *p-n* Junctions by Pulsed-Laser Radiation" [*Bull. Am. Phys. Soc.* **24**, 314 (1979)]

International Conference on Modulated Structures, Kailua-Kona, Hawaii, March 22–25, 1979:

H. G. Smith, W. P. Crummett, R. M. Nicklow, N. Wakabayashi, G. H. Lander, and E. S. Fisher, "Observation of Superstructure in Alpha-U near 43 K"

New Mexico Chapter of the American Vacuum Society Meeting, Albuquerque, New Mexico, April 24–26, 1979:

C. W. White, "Laser Annealing of Semiconductor Materials" (invited paper)

American Ceramic Society Meeting, Cincinnati, Ohio, April 29–May 2, 1979:

W. S. Aaron, E. H. Kobisk, and T. C. Quinby, "Development of Cermets for High-Level Radioactive Waste Fixation" [*Am. Ceram. Soc. Bull.* **58**, 322 (1979)]

Y. Chen, R. H. Kernohan, M. M. Abraham, and J. L. Boldú, "Enhanced Electrical Conductivity in MgO due to Lithium Impurity" [*Am. Ceram. Soc. Bull.* **58**, 368 (1979)]

Y. Chen, V. M. Orera, and M. M. Abraham, "Lithium Decoration of Slip Planes in MgO by Oxidation and Reduction at High Temperatures" [*Am. Ceram. Soc. Bull.* **58**, 349 (1979)]

E. J. Friebele, D. L. Griscom, M. Staplebroek, and R. A. Weeks, "The Peroxy Radical: A Fundamental Defect Center in Fused SiO_2," [*Am. Ceram. Soc. Bull.* **58**, 381 (1979)]

E. Sonder, T. G. Stratton, and R. A. Weeks, "Kinetics of Fe^{2+} Oxidation and Fe^{3+} Reduction in MgO Single Crystals" [*Am. Ceram. Soc. Bull.* **58**, 350 (1979)]

H. T. Tohver, M. M. Abraham, Y. Chen, R. F. Wood, W. A. Sibley, and T. M. Wilson, "Luminescence in Nonstoichiometric MgO" [*Am. Ceram. Soc. Bull.* **58**, 370 (1979)]

Information Meeting on Sputtering, San Diego, California, April 30–May 1, 1979:

J. B. Roberto, "Status of Light-Ion Sputtering" (invited paper)

ORNL Bimonthly Colloquium, Oak Ridge, Tennessee, May 3, 1979:

W. S. Aaron, "A Novel High-Level Waste Form" (invited paper)

International Conference on Fast-Ion Transport in Solids, Lake Geneva, Wisconsin, May 21–25, 1979:

J. B. Bates, G. M. Brown, T. Kaneda, W. E. Brundage, J. C. Wang, and H. Engstrom, "Properties of Single-Crystal Beta"-Aluminas" (invited paper)

R. R. Dubin, J. S. Kasper, J. B. Bates, and T. Kaneda, "Characterization of Heat-Treatment-Induced Changes in Li-Na Beta-Alumina Single Crystals"

T. Kaneda, J. B. Bates, J. C. Wang, and H. Engstrom, "Ionic Conductivity and Raman Spectra of Na-Li, K-Li, and K-Sn β-Al_2O_3"

J. C. Wang, J. B. Bates, T. Kaneda, H. Engstrom, D. F. Pickett, Jr., and Sang-il Choi, "Model Studies of Mixed-Ion Beta-Aluminas"

Workshop on New Diagnostic Techniques Relating to Impurity Release, Germantown, Maryland, May 31–June 1, 1979:

J. B. Roberto and C. W. White, "Laser Fluorescence Techniques for In Situ Impurity Studies"

R. A. Zuhr, B. R. Appleton, J. B. Roberto, and S. P. Withrow, "Ion Backscattering/Channeling and Nuclear Reaction Analysis of Tokamak-Exposed Samples"

Photovoltaic Materials and Device Measurements Workshop, Arlington, Virginia, June 11–13, 1979:

R. F. Wood, R. T. Young, R. D. Westbrook, J. Narayan, W. H. Christie, and J. W. Cleland, "New Techniques for the Study and Control of Grain Boundary Effects"

R. T. Young, C. W. White, J. Narayan, and W. H. Christie, "Characterization of Laser-Annealed, Ion-Implanted Polycrystalline Si"

Third High Efficiency and Radiation Damage Solar Cell Meeting, Cleveland, Ohio, June 13–14, 1979:

R. T. Young, R. F. Wood, R. D. Westbrook, J. Narayan, and C. W. White, "Laser Techniques in Photovoltaic Research"

IEEE International Symposium on Applications of Ferroelectrics (ISAF), Minneapolis, Minnesota, June 13–15, 1979:

L. A. Boatner, E. Krätzig, and R. Orlowski, "KTN as a Holographic Storage Material"

NATO Advanced Study Institute on Physics and Chemistry of Refractory Oxides, Aleria, Corsica, June 17–July 1, 1979:

E. Sonder and T. F. Connolly, "Characterization and Bulk Properties of Oxides"

E. Sonder and R. A. Weeks, "Ion Motion in Refractory Oxides"

Thirty-ninth Annual Conference on Physical Electronics, College Park, Maryland, June 18–20, 1979:

M. Rasolt and H. L. Davis, "Anisotropic Contributions to the Optical Potential Employed in Theoretical Treatments of Electron Spectroscopies"

Third Conference on Superconductivity in d- and f-Band Metals, San Diego, California, June 21–23, 1979:

H. R. Kerchner, D. K. Christen, S. T. Sekula, and P. Thorel, "Equilibrium Properties of the Fluxoid Lattice in Single-Crystal Niobium"

H. A. Mook, W. C. Koehler, M. B. Maple, Z. Fisk, and D. C. Johnston, "Neutron-Scattering Study of the Superconducting-Magnetic Transition in $Ho_{0.6}Er_{0.4}Rh_4B_4$"

H. G. Smith, W. P. Crummett, N. Wakabayashi, R. M. Nicklow, G. H. Lander, and E. S. Fisher, "Soft Phonons and Lattice Instabilities in Alpha-Uranium"

H. G. Smith, N. Wakabayashi, G. W. Webb, Z. Fisk, F. M. Mueller, A. Arko, and D. Lowndes, "Phonon Spectra in *A*-15 Superconducting Compounds"

Ninth Conference on Surface Studies and Fourth SUBWOG-12B Technical Exchange, Golden, Colorado, June 26–29, 1979:

H. H. Madden and D. M. Zehner, "Electron Spectroscopic Investigations of the Oxidation of Beryllium"

Workshop on Sputtering Caused by Plasma (Neutral Beam)-Surface Interaction, Argonne, Illinois, July 8–10, 1979:

J. B. Roberto, "Light-Ion Sputtering Yields"

Materials Research Council Review Meeting on Rapidly Solidified Materials, La Jolla, California, July 16–17, 1979:

C. W. White, "Solubility Enhancement in Silicon by Ion Implantation and Pulsed-Laser Annealing" (invited paper)

International Colloquium on Materials for High-Temperature Energy Sources, Toronto, Canada, July 16–19, 1979:

R. A. Weeks and E. Sonder, "Charge and Mass Transport in MgO"

Second Joint INTERMAG-Magnetism and Magnetic Materials Conference, New York, July 17–20, 1979:

J. F. Cooke, "Itinerant Electron Magnetism in 3d-Transition Metals" (invited paper)

R. E. Parra and J. W. Cable, "Magnetic Moment Distribution in NiPt Alloys"

Symposium on the Physics of Surfaces and Optical Properties of Solids, Mexico City, Mexico, July 17–20, 1979:

Y. Chen, "Semiconducting Properties of Li-Doped MgO" (invited paper)

International Symposium II on Solar Energy Fundamentals and Applications, Izmir, Turkey, August 6–8, 1979:

E. Benes, M. Bruck, F. P. Viehböck, P. Blum, L. Wimmer, W. Husinsky, and K. C. Harms, "Standardized Data Acquisition Package for the Analysis of Multicomponent Heating Systems"

American Crystallographic Association Meeting, Boston, Massachusetts, August 12–17, 1979:

J. E. Epperson, J. Faber, R. W. Hendricks, and J. S. Lin, "Small Angle Scattering Observations of a Decomposing Ni-Al Alloy"

J. M. Schultz, J. S. Lin, R. W. Hendricks, and R. G. Kepler, "Temperature-Dependent Small-Angle X-ray Scattering from Poly(vinylidene Fluoride)"

J. M. Schultz, J. S. Lin, R. W. Hendricks, J. Petermann, and R. M. Gohil, "Annealing Behavior of Polypropylene Films Crystallized from a Highly Extended Melt"

G. D. Wignall, "Small-Angle Neutron Scattering Studies of Semicrystalline Polymers"

Eighth International Conference on Atomic Collisions in Solids, Hamilton, Ontario, Canada, August 13–17, 1979:

M. J. Alguard, R. L. Swent, R. H. Pantell, S. Datz, J. H. Barrett, B. L. Berman, and S. D. Bloom, "Radiation from Channeled Leptons"

J. H. Barrett and D. P. Jackson, "Role of Correlations of Lattice Vibrations in Channeling"

W. Husinsky, "Velocity Measurements of Sputtered Atoms by the Laser-Doppler Method" (invited paper)

W. Husinsky, R. Bruckmüller, and P. Blum, "Investigation of Thermal and Collisional Contributions to the Sputtering of Sodium, Sodium Halides, and Samarium Targets"

O. S. Oen, "Redefined Scattering Cross Section in Monatomic Solids"

P. P. Pronko, B. R. Appleton, O. W. Holland, and S. R. Wilson, "Near-Surface Yield Enhancement in Narrow Acceptance 180° Elastic Scattering for He Ion and Non-Crystalline and Poly-Crystalline Solids"

Thirty-seventh Annual Meeting of the Electron Microscope Society of America, San Antonio, Texas, August 13–17, 1979:

S. Kobayashi and S. M. Ohr, "In Situ Studies of Crack Propagation in bcc Metals"

Annual Meeting of the Society of Photo-Optical Instrumentation Engineers, Symposium on Laser Applications in Materials Processing, San Diego, California, August 27–30, 1979:

R. F. Wood, G. E. Giles, and J. R. Kirkpatrick, "Theoretical Analysis of Thermal and Mass Transport During Laser Annealing" (invited paper)

R. T. Young, R. F. Wood, J. Narayan, and W. H. Christie, "Laser Techniques in Photovoltaic Applications" (invited paper)

Conference on Phonon Scattering in Condensed Matter, Providence, Rhode Island, August 28–31, 1979:

A. M. de Göer, B. Salce, and L. A. Boatner, "Low-Temperature Thermal Conductivity of $KTaO_3$ and KTN"

International Conference on Neutron Scattering and Magnetism, Jülich, Germany, August 29–31, 1979:

J. F. Cooke, "Band Theoretic Interpretation of Neutron-Scattering Experiments in Metallic Ferromagnets" (invited paper)

R. M. Moon and W. C. Koehler, "Magnetic Properties of SmN"

Eleventh International Conference on Physics of Electronic and Atomic Physics, Kyoto, Japan, August 29–September 4, 1979:

S. Datz, J. H. Barrett, M. J. Alguard, R. L. Swent, R. H. Pantell, B. L. Berman, and S. D. Bloom, "Coherent Radiation from Correlated Collisions of Positrons with Si"

International Conference on Magnetism, Munich, Germany, September 3–7, 1979:

J. W. Cable and R. E. Parra, "Determination of the Pd-Gd Exchange Constant by Neutron Diffuse Scattering and the Pd Polarization in PdGd Alloys"

R. M. Moon, W. C. Koehler, C. Stassis, and G. R. Kline, "New Evidence on the Magnetic Structure of Nd"

International Conference on Polarized Neutrons in Condensed Matter Research, Zaborów, Poland, September 10–12, 1979:

R. M. Moon, "Polarized Neutron Studies of Mixed-Valence Materials" (invited paper)

Consultant Symposium on Rare Gases in Metals and Ionic Solids, Harwell, England, September 10–14, 1979:

V. Philipps, K. Sonnenberg, and J. M. Williams, "Helium Diffusion in Nickel at High Temperatures"

Fifth International Symposium of Nuclear Quadrupole Resonance Spectroscopy, Toulouse, France, September 10–15, 1979:

Gary L. Petersen, G. E. Jellison, Jr., and P. C. Taylor, "Pulsed NQR in Amorphous, Orthorhombic, and Rhombohedral Arsenic"

TMS-AIME Conference, Milwaukee, Wisconsin, September 16–20, 1979:

Y. K. Chang and H. E. Harmon, "Crystal Growth of *A*-15 Compounds"

S. Kobayashi and S. M. Ohr, "Dislocation Model of In Situ Fracture Experiments"

Third Europhysics Conference on Lattice Defects in Ionic Crystals, Canterbury, England, September 17–21, 1979:

Y. Chen, M. M. Abraham, J. L. Boldú, and V. M. Orera, "Current-Voltage Characteristics of Li-Doped MgO Oxidized at Elevated Temperatures"

V. M. Orera and F. A. Modine, "Magneto-Optical Properties of Metallic Colloids in Insulators"

J. Narayan, "Properties of *a* (100) Dislocations in Magnesium Oxide"

R. M. Nicklow, W. P. Crummett, R. F. Wood, and Mark Mostoller, "Neutron-Scattering Study of Coupled Defect-Phonon Modes in $KCl_{1-x}(KCN)_x$"

Spanish Royal Society of Physics and Chemistry, Jaca, Spain, September 24–27, 1979:

Y. Chen, "Semiconducting Properties of Li-Doped MgO" (invited paper)

International Symposium of Ionic Crystals, Russe, Bulgaria, September 25–30, 1979:

J. L. Boldú, V. M. Orera, Y. Chen, and M. M. Abraham, "Semiconducting Properties of Lithium-Doped MgO"

Third ASTM-EURATOM Symposium on Reactor Dosimetry, Ispra, Italy, October 1–5, 1979:

H. L. Adair, E. H. Kobisk, J. A. Setaro, T. C. Quinby, J. A. Carter, J. F. Emery, R. Walker, and J. Cooper, "Neutron Dosimeter Materials Development and Characterization"

Twenty-sixth National American Vacuum Society Symposium, New York, New York, October 2–5, 1979:

H. L. Davis and D. M. Zehner, "Structure of the Clean Re($10\bar{1}0$) Surface"

J. R. Noonan and H. L. Davis, "A 1979 LEED Analysis of Cu(100)"

D. M. Zehner, C. W. White, and G. W. Ownby, "A LEED, AES, and RBS Investigation of Si(100) Implanted with As"

Conference on Laser-Induced Crystallization in Solids, Mons, Belgium, October 4–6, 1979:

C. W. White, S. R. Wilson, F. W. Young, Jr., B. R. Appleton, and J. Narayan, "Nonequilibrium Solubility and Segregation in Ion-Implanted, Laser-Annealed Silicon" (invited paper)

Symposium on Northeastern Accelerator Personnel, Philadelphia, Pennsylvania, October 8–9, 1979:

O. E. Schow III, "SNEAP 1979 Laboratory Reports"

Electrochemical Society Symposium on Laser and Electron Beam Processing of Electronic Materials, Los Angeles, California, October 14–19, 1979:

J. Narayan, "A Comparative Study of Laser and Electron Beam Processing of Semiconductors" (invited paper)

J. Narayan, "Generation of Self-Interstitials During Thermal Treatments of Silicon"

J. Narayan, "Formation of Dislocation Networks in Arsenic-Implanted and Thermally Annealed Silicon"

U.S. Department of Energy Workshop on Hydrogen Recycling, Dublin, California, October 16–22, 1979:

M. T. Robinson, "Hydrogen Reflection Calculations" (invited paper)

R. A. Zuhr, S. P. Withrow, J. B. Roberto, and B. R. Appleton, "In Situ Measurements of the Plasma Boundary Region in ISX" (invited paper)

Symposium on Microcomputers and Microcomputer Application, Budapest, Hungary, October 17–19, 1979:

E. Benes, M. Bruck, F. P. Viehböck, P. Blum, L. Wimmer, W. Husinsky, and K. C. Harms, "Microprocessor-Controlled Data Acquisition System for Solar Heating Systems"

Symposium on Separation Science and Technology for Energy Applications, Gatlinburg, Tennessee, October 30–November 2, 1979:

D. W. Ramey, M. Petek, R. D. Taylor, P. W. Fischer, E. H. Kobisk, J. O. Ramey, and C. A. Sampson, "Hydrogen Isotope Separation by Bipolar Electrolysis with Countercurrent Electrolyte Flow"

Sixteenth International Thermal Conductivity Conference, Chicago, Illinois, November 7–9, 1979:

C. L. Tsai, A. R. Moodenbaugh, H. Weinstock, and Y. Chen, "Thermal Conductivity of Damaged MgO"

Southeastern Section Meeting, American Physical Society, Chattanooga, Tennessee, November 8–10, 1979:

M. D. Kellam, D. J. Eisenberg, J. H. Crawford, Jr., and Y. Chen, "The Effects of Annealing Parameters on MgO:Li Containing [Li]° Centers" [*Bull. Am. Phys. Soc.* **25**, 129 (1980)]

M. Rappaz, L. A. Boatner, and M. M. Abraham, "Characterization of Tetragonal Phosphate Crystals and Powders Doped with Rare-Earth Impurities" [*Bull. Am. Phys. Soc.* **25**, 127 (1980)]

American Nuclear Society Winter Meeting, San Francisco, California, November 11–16, 1979:

W. S. Aaron, E. H. Kobisk, T. C. Quinby, and D. K. Thomas, "Progress on the Cermet Approach to Nuclear Waste Management" [*Trans. Am Nucl. Soc.* **33**, 412 (1979)]

C. W. White, "Characterization of Ion-Implanted, Laser-Annealed Silicon for Solar Cell Applications" [*Trans. Am. Nucl. Soc.* **33**, 246 (1979)] (invited paper)

American Physical Society Meeting, Boston, Massachusetts, November 12–16, 1979:

J. B. Roberto, R. E. Clausing, L. C. Emerson, L. Heatherly, R. A. Langley, J. E. Simpkins, S. P. Withrow, and R. A. Zuhr, "Summary of Surface Studies in ISX-B" [*Bull. Am. Phys. Soc.* **24**, 1035 (1979)]

S. P. Withrow, R. A. Zuhr, and J. B. Roberto, "Deuterium Profiling in the Plasma Edge of ISX-B" [*Bull. Am. Phys. Soc.* **24**, 938 (1979)]

R. A. Zuhr, S. P. Withrow, and J. B. Roberto, "Heavy Impurity Transport in the Plasma Edge of ISX-B" [*Bull. Am. Phys. Soc.* **24**, 938 (1979)]

First Users' Group Workshop for National Center for Small-Angle Scattering Research, Oak Ridge, Tennessee, November 13–14, 1979:

D. K. Christen, "Very High Resolution Studies (500-6000 Å) on the Double Crystal Diffractometer" (invited paper)

J. S. Lin, "Chemical Applications of Small-Angle Scattering" (invited paper)

G. D. Wignall, "Small-Angle Scattering from Polymers" (invited paper)

Eighth Symposium on Engineering Problems of Fusion Research, San Francisco, California, November 13–16, 1979:

R. R. Coltman, Jr., C. E. Klabunde, and R. H. Kernohan, "Effects of Radiation at 5 K on Organic Insulators for Superconducting Magnets"

Materials Research Society Symposium on Scientific Basis for Nuclear Waste Management, Cambridge, Massachusetts, November 26–30, 1979:

W. S. Aaron, T. C. Quinby, and E. H. Kobisk, "Development and Characterization of Cermet Forms for Radioactive Waste"

L. A. Boatner, G. W. Beall, M. M. Abraham, C. B. Finch, P. G. Huray, and M. Rappaz, "Monazite and Other Lanthanide Orthophosphates as Alternate Actinide Waste Forms"

Materials Research Society Symposium on Laser and Electron Beam Processing of Materials, Cambridge, Massachusetts, November 27–30, 1979:

B. R. Appleton, C. W. White, B. Stritzker, O. Meyer, J. R. Gavaler, A. I. Braginski, and M. Ashkin, "Ion Implantation and Laser Annealing of High T_c Superconducting Materials"

H. Engstrom, "Infrared Reflectivity and Transmissivity of Boron-Implanted, Laser-Annealed Silicon"

F. H. Hsu and C. W. White, "Positron Annihilation in Ion-Implanted, Laser-Annealed Silicon"

J. Narayan, "Structural Defects in Laser- and Electron-Beam-Annealed Silicon" (invited paper)

J. Narayan and C. W. White, "Melting by Pulsed-Laser Irradiation"

C. W. White, S. R. Wilson, B. R. Appleton, and J. Narayan, "Surface Segregation in Laser Annealing of Ion-Implanted Silicon"

C. W. White, S. R. Wilson, B. R. Appleton, F. W. Young, Jr., and J. Narayan, "Supersaturated Substitutional Alloys in Silicon Formed by Ion Implantation and Laser Annealing"

R. F. Wood, J. C. Wang, G. E. Giles, and J. R. Kirkpatrick, "Macroscopic Theory of Pulsed-Laser Annealing" (invited paper)

R. T. Young, R. F. Wood, J. Narayan, and C. W. White, "Laser Processing of Polycrystalline Silicon Solar Cells"

D. M. Zehner, C. W. White, G. W. Ownby, and W. H Christie, "Silicon Surface Structure and Surface Impurities after Pulsed-Laser Annealing"

Materials Research Society Symposium on Surface Modification of Materials by Ion Implantation, Cambridge, Massachusetts, November 27–30, 1979:

N. G. Thompson, B. D. Lichter, B. R. Appleton, E. J. Kelly, and C. W. White, "Electrochemical Behavior of Titanium Implanted with Platinum"

Solar Energy Research Institute, Photovoltaic Program Office's Semiannual Polycrystalline Silicon Program Review Meeting, Pasadena, California, December 3–5, 1979:

R. F. Wood, "Laser Annealing in Photovoltaic Research" (invited paper)

Forty-second Statistical Mechanics Meeting, New Brunswick, New Jersey, December 13–14, 1979:

Martin Ulehla, "Gauge Fields and Order in Crystals and Glasses"

Fourteenth IEEE Photovoltaic Specialists Conference, San Diego, California, January 7–10, 1980:

G. E. Jellison, Jr., J. W. Cleland, and N. Fukuoka, "A Radiation-Resistant Substrate for a p^+-n-n^+ Solar Cell"

R. F. Wood, R. T. Young, J. Narayan, R. D. Westbrook, C. W. White, and W. H. Christie, "Laser Processing for High-Efficiency Solar Cells" (invited paper)

R. T. Young, R. F. Wood, J. Narayan, R. D. Westbrook, and W. H. Christie, "Laser Techniques for the Fabrication and Study of Polycrystalline Solar Cells"

Gordon Conference on Orientational Disorder in Crystals, Santa Barbara, California, January 14–18, 1980:

R. M. Nicklow, "Neutron Scattering from Coupled Phonon-Impurity Modes in $KCl_{1-x}(KCN)_x$"

AIME Annual Meeting, Las Vegas, Nevada, February 24–28, 1980:

S.-J. Chang and S. M. Ohr, "Thickness Dependence of the BCS Solution for Elastoplastic Cracks" [*J. Met.* 31, 142 (1979)]

Y. K. Chang and H. R. Kerchner, "Growth and Characterization of A-15 Intermetallic Compounds" [*J. Met.* 31, 123 (1979)]

S. Kobayashi and S. M. Ohr, "In Situ Electron Microscope Fracture Studies in Nickel" [*J. Met.* 31, 142 (1979)]

S. Kobayashi and S. M. Ohr, "Studies of Crack Propagation in Amorphous Niobium Oxide" [*J. Met.* 31, 141 (1979)]

B. C. Larson, "Crystal Defect Studies Using X-ray Diffuse Scattering" [*J. Met.* 31, 82 (1979)] (invited paper)

J. S. Lin, R. W. Hendricks, J. Bentley, and F. W. Wiffen, "Small-Angle X-ray Scattering Study on Neutron-Irradiation Effects in Molybdenum and Molybdenum Alloys" [*J. Met.* 31, 82 (1979)]

J. Narayan and S. M. Ohr, "Electron Microscope Study of Fracture in Doped-Silicon" [*J. Met.* 31, 141 (1979)]

S. M. Ohr, "Contrast Analysis of Dislocation Loops" [*J. Met.* 31, 119 (1979)] (invited paper)

S. M. Ohr and S. Kobayashi, "In Situ Studies of Crack Propagation in Solids" [*J. Met.* 31, (1979)]

Seminars

SOLID STATE DIVISION SEMINARS AT ORNL

D. M. Zehner served as Seminar Chairman during the period covered by this report. The following seminars were held:

"Application of Hohenberg-Kohn-Sham Theory to Chemical Bonding: 3*d*-Dimers,"[1] J. Harris, Kernforschungsanlage, Jülich, Germany

"Surface States on Metals,"[1] P. Sover, University of Pennsylvania, Philadelphia, Pennsylvania

"Non-Local Effects on the Fermi Surface of Metals,"[1] M. Rasolt, Solid State Division, ORNL

"Electron Lifetime Effects on Properties of *A*15 Compounds,"[1] L. Mattheiss, Bell Laboratories, Murray Hill, New Jersey

"Investigation of Atomic and Molecular Binding by Nuclear Resonance Scattering,"[2] O. Shahal, Nuclear Research Centre, Negev, Israel

"Excitons in the Sphalerite Structure," H. C. Schweinler, Health and Safety Research Division, ORNL

"Proton Conduction in the Solid Electrolytes β- and β''-Alumina," G. C. Farrington, General Electric Research and Development Corporation, Schenectady, New York

"High Resolution Neutron Spectrometry," F. Mezei, Institut Laue-Langevin, Grenoble, France

"CuCl—A High Temperature Superconductor?" C. W. Chu, University of Houston, Houston, Texas

"NSLS—The Synchrotron in our Future,"[3] B. C. Larson, Solid State Division, ORNL

"ORNL-NSF National Center for Small-Angle Scattering Research," W. C. Koehler, Solid State Division, ORNL

"New Stories About Mixed Dumbbell Interstitials," K. H. Robrock, Kernforschungsanlage, Jülich, Germany

"Cluster Nucleation at Undersized and Oversized Solutes in Copper," H. Wollenberger, Hahn-Meitner-Institut, Berlin, Germany

"Status of Neutron Scattering at WNR—Application to Materials Science," P. A. Seeger, Los Alamos Scientific Laboratory, Los Alamos, New Mexico

"Electron Scattering from Simple Adsorbed Molecules," M.V.K. Ulehla, Solid State Division, ORNL

"Small-Angle Neutron Scattering of Polymers—Methods and Results," R. Ullman, Ford Motor Company, Detroit, Michigan

"Magnetic Properties of $CeAl_2$," B. Barbara, C.E.N., Grenoble, France

"Electron Microscope Studies of Fracture in Solids,"[3] S. M. Ohr, Solid State Division, ORNL

"Plasma-Wall Interaction Studies on ISX,"[3] R. A. Zuhr, Solid State Division, ORNL

"Electron Microscope Studies of Clustering of Atomic Defects in Ion and Electron Irradiated FCC Metals," W. Jager, Max-Planck-Institut für Metallforschung, Stuttgart, Germany

"Electron Spin Polarization in Double Scattering LEED," J. Kirschner, Kernforschungsanlage, Jülich, Germany

"Melting and Solidification of the Surface Layer," S.-C. Hsu, University of Illinois, Urbana, Illinois

"The Recursion Method,"[3] M. Mostoller, Solid State Division, ORNL

"Electron Energy Loss Spectroscopy Vibrational Study of CO and O Adsorbed on Cu(110),"[3] J. F. Wendelken, Solid State Division, ORNL

"Metal Cluster Models: Applications to Chemisorption, Interstitial Hydrogen, and Magnetic Impurities,"[1] D. E. Ellis, Northwestern University, Evanston, Illinois

"Transport Phenomena in Magnetic Semiconductors,"[1] V. A. Kapustin, A. F. Ioffe Institute, Leningrad, USSR

"Local Density Approach to Bulk and Surface States,"[1] A. J. Freeman, Northwestern University, Evanston, Illinois

"Why Do Metals Form Alloys?"[1] C. H. Hodges, Daresbury Laboratory, Warrington, England

"Simple Theory of Transition Metals,"[1] W. A. Harrison, Stanford University, Palo Alto, California

"Phase Transitions and Symmetry," P. Bak, IBM Corporation, Yorktown Heights, New York

"Localization, Diffusion, and Trapping of Positive Muons in Copper, Niobium, and Aluminum," D. Richter, Kernforschungsanlage, Jülich, Germany

"Transient Capacitance Spectroscopy: A Study of Deep Levels in Semiconductors," P. M. Mooney, Vassar College, Poughkeepsie, New York

"Composition Modulated Alloys," J. B. Ketterson, Northwestern University, Evanston, Illinois

"A LEED/Auger/Loss Study of Oxygen Chemisorption on Bi(0001)," T. N. Taylor, Los Alamos Scientific Laboratory, Los Alamos, New Mexico

"Diffuse Scattering from Dislocation Loops—Comparison Between Analytical Approximations and Numerical Calculations," H. Trinkaus, Kernforschungsanlage, Jülich, Germany

"Raman Studies of Impurity Induced Ferroelectricity in Potassium Tantalate," L. L. Chase, Indiana University, Bloomington, Indiana

"Cermet Waste Forms,"[3] E. H. Kobisk, Solid State Division, ORNL

"Research Materials Information Center,"[3] T. F. Connolly, Solid State Division, ORNL

"Synchrotron Radiation: Instrumentation and Applications to X-ray Spectroscopy of Lα Edges in the 4 A Region,"[4] V. O. Kostroun, Cornell University, Ithaca, New York

"Conceptual Foundations of Flux Pinning in Type-II Superconductors,"[3] H. R. Kerchner, Solid State Division, ORNL

"Soft Modes and Lattice Instabilities in Alpha-Uranium,"[3] H. G. Smith, Solid State Division, ORNL

"Cancer, Energy, and the Environment," J. R. Totter, Institute for Energy Analysis, Oak Ridge, Tennessee

"Observation of Field-Dependent Impurity Scattering of Both Electrons and Holes in Magnetic Fields Near the Quantum Limit," D. H. Lowndes, University of Oregon, Eugene, Oregon

"Plans for a Spallation Source in West Germany," G. Bauer, Kernforschungsanlage, Jülich, Germany

"Oxidation Behavior of Thorium and Uranium Studied by Gravimetric and Surface Analysis Techniques," C. Colmenares, Lawrence Livermore Laboratory, Livermore, California

"Electrical and Optical Properties of Heavily Irradiated Gallium Arsenide," E.W.J. Mitchell, The Clarendon Laboratory, Oxford, England

"Electron Microscope Study of Defects in Silicon and Gallium Arsenide," D. K. Sadana, Lawrence Berkeley Laboratory, Berkeley, California

"Critical Fields in Multi-Layered Films," T. W. Haywood, University of North Carolina, Wilmington, North Carolina

"Stopping Power and Range Distribution of Light Ions in Solids," J. Biersack, Hahn-Meitner-Institut, Berlin, Germany

"Calculation of Transport Properties of Transition Metals," F. Pinski, State University of New York, Stony Brook, New York

"Monte-Carlo Renormalization Group," R. Swendsen, Brookhaven National Laboratory, Upton, New York

"Recent Developments in Strong-Coupling Superconductors," J. Carbotte, McMaster University, Hamilton, Ontario, Canada

"X-ray Spectra of Metals," G. D. Mahan, Indiana University, Bloomington, Indiana

"Recent Progress in Calculating T_c and H_{c_2} for Transition Metal Superconductors," W. H. Butler, Metals and Ceramics Division, ORNL

"Formation of Metastable Alloys by Ion Implantation and Laser Annealing," J. Poate, Bell Laboratories, Murray Hill, New Jersey

"Formation of Non-Equilibrium Alloys by Ion Implantation and Pulsed Laser Annealing," S. R. Wilson, Solid State Division, ORNL

"Particle Recycling Calculations for Tokamak First Wall Applications," O. S. Oen, Solid State Division, ORNL

"Anomalous Enhancement of Neutron Diffraction Intensities of Alpha-$LiIO_3$ Single Crystals with the Application of a DC Field," Z. Yang, Institute of Atomic Energy, Academy of Sciences, Peking, China, and Y. Li, Institute of Physics, Academy of Sciences, Peking, China

"Transport Mechanisms in Several Superionic Conductors as Determined by Neutron Diffraction and Temperature, Composition and Pressure Dependent Conductivity Measurements," R. J. Cava, National Bureau of Standards, Washington, D.C.

"Kinetics of Motion of Crystal-Melt Interface," D. Turnbull, Harvard University, Cambridge, Massachusetts

"Defect Production Processes in Irradiated Metals," W. F. Schilling, Kernforschungsanlage, Jülich, Germany

"New Evidence on the Magnetic Structure of Nd," R. M. Moon, Solid State Division, ORNL

"X-ray Study of Lattice Strain in Ion-Implanted Laser-Annealed Silicon," B. C. Larson, Solid State Division, ORNL

"Properties of Mixed-Ion Beta-Aluminas," T. Kaneda, Fuji Photo Film Company, Tokyo, Japan

"Photoemission in the Alkali Halides," G. D. Mahan, Indiana University, Bloomington, Indiana

"Atomic Geometry of Semiconductor Surfaces," C. B. Duke, Xerox Corporation, Webster New York

"Charge Transfer and Photorefractive Effects," E. Kratzig, Philips Research Laboratory, Hamburg, Germany

"Small-Angle Scattering in Polymer Science,"[5] (six lectures), W. C. Koehler and G. D. Wignall, Solid State Division, ORNL

"Contact Reactions Between Metal and Silicon," K. N. Tu, IBM Corporation, Yorktown Heights, New York

"Onset of 3*d* Magnetism in Rare-Earth Transition Metal Alloys," D. Givord, C.N.R.S., Grenoble, France

"Spin Dynamics of Magnetic Moments in Metals," M. Loewenhaupt, Kernforschungsanlage, Jülich, Germany

"The Modeling of Evolving Microstructure in Irradiated Materials,"[4] R. Bullough, Atomic Energy Research Establishment, Harwell, England

"Laser Annealing of Magnetic Bubble Materials," L. Schultz, University of Gottingen, Gottingen, Germany

"Polarized Neutron Magnetic Diffuse Scattering from Dilute Iron-Based Alloys," G. Parette, C.E.N., Saclay, France

"Magnetic Excitations in Stressed Pr and Pr Alloys," K. A. McEwen, University of Salford, Salford, England

"Investigation of Hydrodynamic Instability by Neutron Scattering," T. Riste, Institut of Atomenergie, Kjeller, Norway

"On the Martensitic Transformation in Manganese Alloys," R. D. Lowde, Atomic Energy Research Establishment, Harwell, England

"Energy, Angular, and Charge State Distributions of Hydrogen and Helium Backscattered from Metals with Energies Below 20 keV," H. Verbeek, Max-Planck-Institut für Plasmaphysik, Garching, Germany

"The Possibility of Superconductivity in Palladium Silver Alloys,"[1] B. Gyorffy, University of Bristol, Bristol, England

"Orbital Magnetization and Covalency in 3*d*-Transition Metal Salts: Some Problems in the Interpretation of Polarized Neutron Data," P. J. Brown, Institut Laue-Langevin, Grenoble, France

"Diffusion in Glasses and Glass Melts," G. Frischat, Technische Universitat Clausthal, Clausthal, Germany

"X-ray Standing Waves at Crystal Surfaces--A New Surface Structure Probe,"[4] P. L. Cowan, Bell Laboratories, Murray Hill, New Jersey

"Small-Angle Neutron Scattering Studies of Amorphous Polymers and Blends," G. D. Wignall, Solid State Division, ORNL

"Surface Structure Determination by Medium Energy Ion Scattering," M. F. van der Veen, Physical Sciences Laboratory, Stoughton, Wisconsin

"Low-Energy Light-Ion Sputtering," J. Bohdansky, Max-Planck-Institut für Plasmaphysik, Garching, Germany

"The Electron-Phonon Interaction and Electromagnetic Absorption in Metals,"[1] J. C. Swihart, Indiana University, Bloomington, Indiana

"Thermoelastic Effect, Grüneisen Parameter, and Thermal Conductivity," G. Cagliotti, CESNEF, Milano, Italy

"Silicon Surface Structure and Surface Impurities After Pulsed Laser Annealing,"[3] D. M. Zehner, Solid State Division, ORNL

"Monazite and Other Lanthanide Orthophosphates as Alternative Actinide Waste Forms,"[3] L. A. Boatner, Solid State Division, ORNL

"Velocity Measurements of Sputtered Atoms by the Laser Doppler Method," W. Husinsky, Solid State Division, ORNL

"Charge Exchange Processes Between Ions and Surfaces," W. Heiland, Max-Planck-Institut für Plasmaphysik, Garching, Germany

"Laser Annealing of Ion Implanted Silicon and Metal-Silicon Systems Studied by Rutherford Backscattering and Transmission Electron Microscopy," G. J. Eggermont, Philips Research Laboratories, Amsterdam, Netherlands

"How Well Does a Band Calculation Describe a Fermi Surface?—Case Studies from the Group VA and Platinum Group Metals,"[1] D. Koelling, Argonne National Laboratory, Argonne, Illinois

"Gravity and Inertia in Quantum Mechanics," S. A. Werner, University of Missouri, Columbia, Missouri

"Positron Annihilation Studies of Defects in Lead Alloys," G. R. Gruzalski, Harvard University, Cambridge, Massachusetts

"Vibrational Modes in Disordered Solids," F. Galeener, Xerox Research Center, Palo Alto, California

"Instrument Development at the ILL," T. Springer, Institut Laue-Langevin, Grenoble, France

"Laser-Induced Nuclear Polarization (LINUP)," C. Bemis, Jr., Physics Division, ORNL

"Infrared Reflectivity and Transmissivity of Boron-Implanted, Laser-Annealed Silicon,"[3] H. L. Ergstrom, Solid State Division, ORNL

"Surface Crystallography via LEED,"[3] H. L. Davis, Solid State Division, ORNL

"Superconducting Fluctuations $(SN)_x$,"[1] E. Z. deSilva, Bristol University, Bristol, England

"Theory of Magnetism for Rare Earths and Rare Earth-Transition Metal Compounds," P. A. Lindgard, Risø National Laboratory, Roskilde, Denmark

"Dense Plasma Dynamics During Pulsed Laser Annealing," E. Yoffa, IBM Corporation, Yorktown Heights, New York

"Kinetics of Phase Separations,"[1] J. S. Langer, Carnegie-Mellon University, Pittsburgh, Pennsylvania

"Is Pulsed Laser Annealed Silicon Hot?" J. A. Van Vechten, IBM Corporation, Yorktown Heights, New York

"Instabilities and Defects in High T_c Superconductors," L. R. Testardi, Bell Laboratories, Murray Hill, New Jersey

"Neutron Inelastic Scattering from Isolated Clusters of Magnetic Ions," A. Furrer, Institut für Reaktortechnik, Wurenlingen, Switzerland

"Organization and Activity of the Institute of Low Temperature and Structure Research, Polish Academy of Sciences, at Wroclaw," W. Suski, Polish Academy of Sciences, Wroclaw, Poland

"Fabrication of Solar Cells from Ion-Implanted, Pulsed Annealed Silicon," R. Galloni, Laboratorio LAMEL, Bologna, Italy

"Investigations of TiO_2 for Electrochemical Cell Applications," F. Viehbock, Institute für Allgemeine Physik, Technical University, Vienna, Austria

"A Universal Model for the Surface Energy of Solids,"[1] W. Kohn, Institute for Theoretical Physics, Santa Barbara, California

"Radiation Damage in *A15* Superconductors," O. Meyer, Nuclear Research Center, Karlsruhe, Germany

"Critical and Multicritical Phenomena in Adsorbed Monolayers,"[1] D. P. Landau, University of Georgia, Athens, Georgia

"Density Functional Theory Applied to Calculations of Phonon Spectra of Solids,"[1] S. K. Sinha, Argonne National Laboratory, Argonne, Illinois

"Relativistic Density Functional Theory and Some Applications,"[1] A. K. Rajagopal, Louisiana State University, Baton Rouge, Louisiana

"Effect of Paramagnetic Impurities in Itinerant Ferromagnets," M. Antonoff, University of Massachusetts, Boston, Massachusetts

"Tuneable Near-Infrared Lasers and Other Optical Devices," W. A. Sibley, Oklahoma State University, Stillwater, Oklahoma

"HVEM SANS Examination of Grain Boundary Cavitation," R. A. Page, Northwestern University, Evanston, Illinois

"Chemical Bonding at Semiconductor Surfaces for Photoemission Spectroscopy," J. Rowe, Bell Laboratories, Murray Hill, New Jersey

"The Determination of the Plasma Density of Sputtered Ions by Means of Pulsed Dye Laser Excited Fluorescence," H. B. Schweer, Kernforschungsanlage, Jülich, Germany

"Parameter Free Equation of State Calculations for Ionic Materials,"[1] L. I. Boyer, Naval Research Laboratory, Washington, D.C.

"Surface Magnetization of Ferromagnetic Ni(110): A Polarized Low Energy Electron Diffraction Experiment," G.-C. Wang, National Bureau of Standards, Washington, D.C.

"Cyclic Deformation of a Spinodal Copper Nickel Pin Alloy," M. Quin, Northwestern University, Evanston, Illinois

"Pencil Slip in Beta-Pin Single Crystal," S.N.G. Chu, University of Rochester, Rochester, New York

"The Magnetic Structure of Neodymium—A Hard Case to Solve," B. Lebech, Risø National Laboratory, Roskilde, Denmark

"An Astrophysical Model of Double Radio Sources,"[6] M. Burns, Cornell University, Ithaca, New York

"Electrochemical Behavior of Titanium Implanted with Platinum,"[7] N. G. Thompson, Vanderbilt University, Nashville, Tennessee

"State Dependence of the Chemical Bond in Nitrogen by Diffraction Methods," P. A. Egelstaff, University of Guelph, Guelph, Ontario, Canada

"Atomic Hydrogen in Ionic Crystals," J. M. Spaeth, Gesamthochschule Paderborn, Paderborn, Germany

"Melting by Pulsed Laser Annealing,"[3] J. Narayan, Solid State Division, ORNL

"Transient Capacitance Spectroscopy: A Brief Overview,"[3] G. E. Jellison, Jr., Solid State Division, ORNL

---

[1] Metals and Ceramics Division and Solid State Division joint theoretical seminar.
[2] Sponsored jointly by Physics Division and Solid State Division.
[3] Solid State Division Research in Progress Seminar Series.
[4] Sponsored jointly by Metals and Ceramics Division and Solid State Division.
[5] Series of six lectures sponsored by National Center for Small-Angle Scattering Research.
[6] Sponsored jointly by Fusion Energy Division and Solid State Division.
[7] Sponsored jointly by Chemistry Division and Solid State Division.

LECTURES AND SEMINARS

Lectures and seminars presented by Division members during the period covered by this report included the following:

M. M. Abraham—Massachusetts Institute of Technology, Cambridge, Massachusetts, "Introduction to Magnetic Resonance" and "Trapped Hole Centers in the Alkaline Earth Oxides"; Transuranium Research Laboratory, ORNL, "Synthetic Monazite (Orthophosphates as Alternate Waste Forms)" and "Introduction to Magnetic Resonance—Part I"

J. B. Bates—College of William and Mary, Williamsburg, Virginia, "Fast Ionic Transport in the Beta- and Beta"-Aluminas"

L. A. Boatner—IBM Zurich Research Laboratory, Zurich, Switzerland, École Polytechnique Fédérale, Lausanne, Switzerland, and Centre d'Etude Nucléaires, Grenoble, France, "Examples of Energy-Related Materials Problems"; Sam Houston State University, Huntsville, Texas, and Oklahoma State University, Stillwater, Oklahoma, "The Growth of Single Crystals and their Applications in Solid State Physics"; Indiana University, Bloomington, Indiana, "Lanthanide Orthophosphates as Alternate Actinide Waste Forms"; McGill University, Montreal, Canada, "Energy-Related Materials Problems"

J. W. Cable—Laboratoire Leon Brillouin, Saclay, France, "Neutron Diffuse Scattering Studies of NiPt Alloys"

Y. Chen—National Taiwan University, Taipei, Taiwan, "Electrical Conductivity of Lithium-Doped MgO"; University of Zaragoza, Zaragoza, Spain, "Electrical and Mechanical Properties of MgO:Li Crystals Oxidized at High Temperatures"; Northern Illinois University, Dekalb, Illinois, "The Effects of Oxidation and Reduction of Lithium-Doped MgO"; University of Alabama, Birmingham, Alabama, and Alabama A and M University, Huntsville, Alabama, "Semiconducting Properties of Lithium-Doped MgO"

J. F. Cooke—Kernforschungzentrum, Karlsruhe, Germany, "Lattice Dynamics of Transition Metal Superconductors"; Kernforschungsanlage, Jülich, Germany, "First Principles Phonon Calculations in Transition Metal Superconductors"; University of Maryland, College Park, Maryland, "First Principles Susceptibility Calculations in Itinerant Electron Ferromagnets"

H. L. Davis—Daresbury Laboratory, Warrington, England, "Some Current Surface Research at Oak Ridge National Laboratory"; University of Warwick, Coventry, England, "Aspects of Angular Resolved Auger Spectroscopy"

W. R. Husinsky—University of Salford, Salford, England, "Investigation of Thermal and Collisional Contributions to the Sputtering of Sodium, Sodium Halides, and Samarium Targets"

G. E. Jellison, Jr.—University of Maine, Orono, Maine, "NMR and NQR Studies of Amorphous Semiconductors"

W. C. Koehler—Chalk River Nuclear Laboratories, Ontario, Canada, and Laboratory Louis Néel, C.N.R.S., Grenoble, France, "Magnetic Scattering Studies at ORNL"; Centre d'Études Nucléaires, Saclay, France, "Les Structures Magnetiques du Neodym"; Institut Laue-Langevin, Grenoble, France, "The Magnetic Structures of Neodymium"; Laboratory of Crystallography, C.N.R.S., Grenoble, France, "The United States National Small-Angle Scattering Facility"

H. A. Mook—Rice University, Houston, Texas, "Magnetic Excitations in Itinerant Electron Transition Metals"; University of Illinois at Chicago Circle, Chicago, Illinois, "Magnetic Excitations in Crystalline and Amorphous Transition Metals"

R. M. Moon—Institut Laue-Langevin, Grenoble, France, "The Magnetic Structure of Neodymium—A Progress Report"; Institutt for Atomenergi, Kjeller, Norway, "Recent Polarized Neutron Research at ORNL"

J. Narayan—IBM Corporation, Yorktown Heights, New York, "Melting Phenomenon and Properties of Dislocations Associated with Laser Irradiation"

R. M. Nicklow—Naval Research Laboratory, Washington, D.C., "Hybridization of Phonons and the Internal Modes of Complex Impurities"

J. R. Noonan—University of Arkansas, Fayetteville, Arkansas, "Low Energy Electron Diffraction Analysis of Relaxed and Reconstructed Surfaces: The Copper and Gold (110) Surfaces"

O. S. Oen—University of Cincinnati, Cincinnati, Ohio, "The First Wall and Particle Recycling in Magnetic Fusion Reactors"

S. M. Ohr—National Bureau of Standards, Washington, D.C., "In Situ Electron Microscope Studies of Fracture in Solids"

M. Rasolt—University of Virginia, Charlottesville, Virginia, "Heat of Solution of Hydrogen in Aluminum"; Georgia Institute of Technology, Atlanta, Georgia, "Exchange and Correlation in a Homogeneous Electron Gas" and "Surface Energy Contribution in Simple Metals"

J. B. Roberto—Fusion Energy Division, ORNL, "Plasma-Surface Interaction Research in the Solid State Division"

M. T. Robinson—Max-Planck-Institut für Plasmaphysik, Garching, Germany, "Computer Simulation of Displacement Cascades and Sputtering"

S. T. Sekula—University of Wisconsin, Madison, Wisconsin, "Flux-Line Lattices in Superconducting Niobium"

H. G. Smith—University of Texas, Arlington, Texas, and Texas Christian University, Fort Worth, Texas, "Applications of Neutron Scattering to Problems in Solid State and Chemical Physics"; Clemson University, Clemson, South Carolina, Rice University, Houston, Texas, University of Houston, Houston, Texas, and University of Cincinnati, Cincinnati, Ohio, "Phonon Spectra, Lattice Instabilities, and Superconductivity"

E. Sonder—Washington University, St. Louis, Missouri, "Reactions in Ceramics Used at High Temperature"; Michigan State University, East Lansing, Michigan, "Defects in Alkali Halides"; Universidad Autónoma de Madrid, Madrid, Spain, and Junta de Energía Nuclear, Madrid, Spain, "Transport Properties in Refractory Oxides: Work at ORNL"; Chemical Physics Seminar, ORNL, "Kinetics of Fe Redox Reactions in MgO"; Clemson University, Clemson, South Carolina, "Ion Transport in Refractory Oxides"

M.V.K. Ülehla—University of Houston, Houston, Texas, and Health and Safety Research Division, ORNL, "Gauge Fields and Character of Order in Solids"

J. C. Wang—Chemical Physics Seminar, ORNL, "A Conduction Mechanism for the Beta-Alumina Family of Fast Ion Conductors"

R. A. Weeks—Case Western Reserve University, Cleveland, Ohio, and Wake Forest University, Winston-Salem, North Carolina, "Effect of Electric Fields on the Conductivity of MgO, $MgAl_2O_4$, and Al_2O_3 Crystals"

C. W. White—National Bureau of Standards, Washington, D.C., "Laser Annealing of Ion Implanted Materials"; Phillips Research Laboratories, Amsterdam, the Netherlands, "Laser Annealing of Ion Implanted Silicon"

G. D. Wignall—Florida State University, Tallahassee, Florida, "Small-Angle Scattering Studies of Semicrystalline Polyethylene and Polypropylene"; E. I. du Pont de Nemours and Company, Wilmington, Delaware, and General Electric Company, Schenectady, New York, "Chain Configuration in Amorphous and Crystalline Polymers by Small-Angle Scattering Techniques"; University of Massachusetts, Amherst, Massachusetts, "Recent Small-Angle Neutron Scattering Studies of Amorphous Polymers and Blends"; Sandia Laboratories, Albuquerque, New Mexico, "Small-Angle Scattering from Polymers"

J. M. Williams—Kernforschungsanlage, Jülich, Germany, Centre d'Étude Nucléaires, Fontenay-aux-Roses, France, Max-Planck-Institut für Metallforschung, Stuttgart, Germany, and EURATOM, Ispra, Italy, "Ion Radiation Damage versus Depth in Al Using Thin Film Techniques"

R. F. Wood—Clemson University, Clemson, South Carolina, University of Alabama, Tuscaloosa, Alabama and Auburn University, Auburn, Alabama, "Laser Annealing and Photovoltaic Program at ORNL"; Aarhus University, Aarhus, Denmark, and Kernforschungsanlage, Jülich, Germany, "Laser Annealing of Semiconductors"; Oak Ridge Associated Universities, Oak Ridge, Tennessee, "Photovoltaic Conversion of Solar Energy"

F. W. Young, Jr.—Johns Hopkins University, Baltimore, Maryland, "Processing of Materials by Ion Implantation and Laser Annealing"; Harvard University, Cambridge, Massachusetts, "Crystal Growth Studies Utilizing Laser Annealing"

R. T. Young—Southern Illinois University, Edwardsville, Illinois, "Laser Annealing of Ion-Implanted Semiconductors"

Scientific Professional Activities

M. M. Abraham	Member, Editorial Board, KTNAM, Revista de Fisica Member, Thesis Examining Committee, Massachusetts Institute of Technology, Cambridge, Massachusetts Member, Thesis Examining Committee, National University of Australia, Canberra, Australia
B. R. Appleton	Member, Editorial Board, *Nuclear Science Applications* Chairman, Particle Solid Interactions Gordon Conference (to be held in 1980) Adjunct Professor, Department of Physics, North Texas State University, Denton, Texas Member, Graduate School Doctoral Committee, Department of Materials Sciences, Vanderbilt University, Nashville, Tennessee Member, Organizing Committee, Sixth Conference on Use of Small Accelerators (to be held in 1980) Member, Fusion Program Committee, ORNL Chairman, Study Committee on Surface Modification, ORNL Participant, OBES/DOE Workshop on Analysis of Hydrogen in Solids, Albuquerque, New Mexico, 1979 Recipient, American Physical Society Fellowship, 1979
J. H. Barrett	Adjunct Professor, Department of Physics, North Texas State University, Denton, Texas Member, Ph.D. Thesis Committee, Department of Physics, North Texas State University, Denton, Texas
J. B. Bates	Member, Program Advisory Committee, International Conference on Fast Ion Transport in Solids, Electrolytes and Electrodes, Lake Geneva, Wisconsin, 1979 Member, Working Group, OBES/DOE Research Assistance Task Force Meeting on Materials Aspects of Solid Electrolyte Batteries, Germantown, Maryland, 1979 Co-Chairman, International Conference on Fast Ionic Transport in Solid Electrolytes (to be held in 1981) Associate Editor, *Solid State Ionics*
L. A. Boatner	Lecturer, ORAU Traveling Lecture Program, 1979-1980 Member, High Temperature Materials Laboratory Committee, ORNL Chairman, Workshop on Alternate Nuclear Waste Forms and Interactions in Geologic Media (to be held in 1980)
J. W. Cable	Member, Ph.D. Thesis Committee, School of Physics, Georgia Institute of Technology, Atlanta, Georgia
Y. Chen	Member, Program Committee, Conference on the Chemistry and Physics of Coal Utilization (to be held in 1980) Member, Program Committee, Symposium on Coal, American Physical Society Meeting (to be held in 1980)

H. R. Child	Lecturer, ORAU Traveling Lecture Program, 1979-1980
J. W. Cleland	Recipient, American Nuclear Society 1979 Radiation Industry Award, 1979
J. F. Cooke	Guest Scientist, Kernforschungsanlage, Jülich, Germany, June-September 1979
C. A. Culpepper	Recipient, American Nuclear Society Award, 1979
H. L. Davis	Member, Organizing and Program Committee, Conference on Determination of Surface Structure by LEED, Yorktown Heights, New York (to be held in 1980) Member, Executive Committee, Tennessee Valley Chapter, American Vacuum Society Co-Chairman, 1st Annual Symposium, Tennessee Valley Chapter, American Vacuum Society (to be held in 1980) Session Chairman, 7th Midwest Solid State Theory Symposium (in honor of J. Korringa), Columbus, Ohio, 1979
N. J. Dudney	Recipient, Eugene P. Wigner Fellowship, 1979
W. R. Husinsky	Organizing Committee, Symposium on Sputtering (to be held in 1980)
L. H. Jenkins	Member, General Committee, Physical Electronics Conferences Member, Wigner Fellowship Committee, ORNL Member, Exploratory Studies Review Committee, ORNL Member, Ph.D. Recruiting Steering Committee, ORNL Member, ORNL-ORAU Graduate Selection Panel
H. R. Kerchner	Lecturer, ORAU Traveling Lecture Program, 1978-1979
E. H. Kobisk	President, International Nuclear Target Development Society Chairman, World Conference of the International Nuclear Target Development Society
W. C. Koehler	Director, National Center for Small-Angle Scattering Research Member, Editorial Advisory Board, *Journal of Magnetism and Magnetic Materials* Member, Editorial Advisory Board, *Magnetism Letters* Editor, *Magnetic Form Factor Data Sheets*, International Union of Crystallography Member, Ph.D Thesis Committee, School of Physics, Georgia Institute of Technology, Atlanta, Georgia Member, International Advisory Committee, Conference on Neutron Scattering and Magnetism, Jülich, Germany, 1979 Participant, Ad Hoc Committee for Regional Instrumentation Facilities, National Science Foundation Recipient, Docteur Honoris Causa, University of Grenoble, Grenoble, France, 1979 Recipient, Union Carbide Corporation Fellowship, 1979
F. A. Modine	Coordinator, ORNL Seed Money Program Member, Exploratory Studies Review Committee, ORNL Secretary, Research Committee, ORNL
H. A. Mook	Member, Program Committee, Joint Intermag-Magnetism and Magnetic Materials Conference, New York, New York, 1979 Member, Program Advisory Committee, International Conference on Ternary Superconductors (to be held in 1980) Member, Review Committee, Intense Pulsed Neutron Source-I, Argonne National Laboratory Member, ZING Prototype Advisory Committee, Argonne National Laboratory Recipient, American Physical Society Fellowship, 1979

R. M. Moon	Member, Commission on Electron Charge, Spin, and Momentum Densities, International Union of Crystallography Member, Evaluation Panel for the Center for Materials Science, National Bureau of Standards
J. Narayan	Recipient, IR-100 Award for the Development of Low-Cost Laser-Diffused Solar Cells, 1979 Symposium Chairman, Materials Research Society Symposium on Defects in Semiconductors (to be held in 1980)
T. S. Noggle	Lecturer, ORAU Traveling Lecture Program, 1978–1979
J. R. Noonan	Vice Chairman and Program Chairman, Tennessee Valley Chapter, American Vacuum Society
O. S. Oen	Lecturer, ORAU Traveling Lecture Program, 1979–1980 Session Chairman, Workshop on Penetration of Low-Energy Particles, New York, New York, 1978
S. M. Ohr	Member, Chemistry and Physics of Metals Committee, the Metallurgical Society of AIME Member, Nuclear Metallurgy Committee, the Metallurgical Society of AIME Member, Nuclear Metallurgy Committee, Materials Science Division, American Society for Metals Participant, DOE Program Review Meeting on Hydrogen in Metals, Washington, D.C., 1978
J. B. Roberto	Member, OFE/DOE Subtask Group on Sputtering and Wall Effects Coordinator, OFE/DOE Information Meeting on Sputtering, San Diego, California, 1979 Coordinator, OFE/DOE Workshop on Sputtering Caused by Plasma (Neutral Beam) -Surface Interaction, Argonne, Illinois, 1979 Participant, OFE/DOE Workshop on New Diagnostics Related to Impurity Release, Germantown, Maryland, 1979 Member, Seed Money Proposal Review Committee, ORNL Member, Ph.D. Recruiting Program, ORNL
M. T. Robinson	Member, Editorial Advisory Board, *Journal of Nuclear Materials* Member, OFE/DOE Subtask Group A: Dosimetry and Damage Parameters
H. G. Smith	Lecturer, ORAU Traveling Lecture Program, 1978–1979
E. Sonder	Member, Advisory Board, *Diffusion and Defect Data (Nonmetals)*
R. A. Weeks	Member, Editorial Board, *Egyptian Journal of Solid State Physics* Member, Editorial Committee, *Journal of the American Ceramic Society* Consultant, Department of the Army, Research and Development Command, Fort Monmouth, New Jersey Adjunct Professor, Department of Mechanical Engineering and Materials Science, Vanderbilt University, Nashville, Tennessee Adjunct Professor, Department of Geology, University of Pennsylvania, Philadelphia, Pennsylvania Lecturer, ORAU Traveling Lecture Program, 1979–1980
J. F. Wendelken	Member, Ph.D. Recruiting Program, ORNL Guest Scientist, Kernforschungsanlage, Jülich, Germany, 1979–1980
R. D. Westbrook	Member, ASTM Committee F-1 Chairman, ASTM Symposium on Lifetime in Silicon, San Diego, California, 1979 Member, Technical Evaluation Committee, Solar Energy Research Institute

C. W. White	Member, Program Committee, Materials Research Society Symposium on Laser-Solid Interactions and Laser Processing, Boston, Massachusetts, 1978 Co-Chairman, Materials Research Society Symposium on Laser and Electron Beam Processing of Materials, Cambridge, Massachusetts, 1979 Co-editor, *Laser and Electron Beam Processing of Materials*, Academic Press, New York, 1980 Member, Program Committee, Materials Research Society Meeting (to be held in 1981) Lecturer, ORAU Traveling Lecture Program, 1978–1979
G. D. Wignall	Program Chairman and Organizer, Users' Group Workshop for National Center for Small-Angle Scattering Research, Oak Ridge, Tennessee, 1979
M. K. Wilkinson	Member, Advisory Panel for the Solid State Sciences Committee of the National Research Council Member, Executive Committee, Division of Condensed Matter Physics, American Physical Society Member, Advisory Committee, Division of Materials Research, National Science Foundation Member, Instrumentation Panel, Condensed Matter Sciences Advisory Subcommittee, National Science Foundation Member, Committee on Quality in Research, ORNL Member, Executive Committee, Southeastern Section of American Physical Society Adjunct Professor, School of Physics, Georgia Institute of Technology, Atlanta, Georgia Member, Organizing Committee, international Conference on Magnetism (to be held in 1985) Member, Program Advisory Committee, National Synchrotron Light Source, Brookhaven National Laboratory Member, Evaluation Panel for the Center for Materials Science, National Bureau of Standards Member, International Advisory Panel, Conference on the Neutron and its Application (to be held in 1982)
J. M. Williams	Guest Scientist, Kernforschungsanlage, Jülich, Germany 1978–1979
S. P. Withrow	Member, Ph.D. Recruiting Committee, ORNL Recipient, American Vacuum Society Shop Note Award, 1978
R. F. Wood	Chairman, Interim Steering Committee, International Conference on Defects in Insulating Crystals (to be held in 1981) Vice-Chairman, International Organizing Committee, International Conference on Defects in Insulating Crystals (to be held in 1981) Member, International Advisory Committee, Third Europhysics Topical Conference on Lattice Defects in Ionic Crystals, Canterbury, England, 1979 Editor, Solid State Physics, *Computer Physics Communications*, North-Holland Publishing Company Technical Consultant, National Research Council Ad Hoc Committee on Microstructure Fabrication Member, Professional Education Resource Committee, ORNL Symposium Co-Chairman, Electrochemical Society Symposium on Annealing of Semiconductors (to be held in 1980) Lecturer, ORAU Traveling Lecture Program, 1978–1979 Member, Program Review Panel, Solar Energy Research Institute Photovoltaic Program Office Participant, Photovoltaics Advanced Materials Review Meeting, Vail, Colorado, 1978 Recipient, IR-100 Award for the Development of Low-Cost Laser-Diffused Solar Cells, 1979

F. W. Young, Jr.	Member, Executive Committee, American Association of Crystal Growth Member, Editorial Board, *Topics in Crystal Growth* Member, Editorial Board, *Journal of Applied Physics* Member, Editorial Board, *Applied Physics Letters* Member, Review Committee, Intense Pulsed Neutron Source-I, Argonne National Laboratory Member, Visiting Committee, Materials Science Center, Cornell University
R. T. Young	Recipient, IR-100 Award for the Development of Low-Cost Laser-Diffused Solar Cells, 1979
D. M. Zehner	Member, ASTM E-42 Committee on Surface Analysis
R. A. Zuhr	Participant, OFE/DOE Workshop on New Diagnostics Related to Impurity Release, Germantown, Maryland, 1979 Participant, DOE Workshop on Hydrogen Recycling, Dublin, California, 1979

Personnel Changes

New Staff Members (Scientific Staff)

N. J. Dudney, Massachusetts Institute of Technology, Cambridge, Massachusetts
W. R. Husinsky, Technical University of Vienna, Vienna, Austria
J. S. Lin, transfer from Metals and Ceramics Division, ORNL
M. L. Linvill, University of California, Berkeley, California
D. H. Lowndes, University of Oregon, Eugene, Oregon
D. B. Poker, University of Illinois, Urbana, Illinois
T. C. Quinby, promotion from Solid State Division technical staff
J. R. Thompson, University of Tennessee Adjunct R&D Participant
G. D. Wignall, Imperial Chemical Industries Europa Ltd., Everberg, Belgium

Staff Transfers and Terminations

B. F. Early, Research Staff Member (retirement)
L. W. Hinton, Secretary (voluntary resignation)
O. W. Holland, Research Staff Member (completion of temporary assignment)
M. L. Linvill, Research Staff Member (completion of temporary assignment)
F. A. Modine, Research Staff Member (transfer to Program Planning and Analysis, Central Management Offices; temporary assignment)
J. K. Redman, Research Staff Member (retirement)
C. A. Sampson, Jr., Laboratory Technician (voluntary resignation)
A. F. Zulliger, Laboratory Technician (voluntary resignation)

Guest Assignments

A. Scientific Staff
F. L. Aravena, Comision Chilena de Energia Nuclear, Santiago, Chile
D. K. Arch, Iowa State University/Ames Laboratory, Ames, Iowa
N. Fukuoka, Osaka University, Osaka, Japan
T. Kaneda, Fuji Photo Film Company, Tokyo, Japan
D. Khatamian, Iowa State University/Ames Laboratory, Ames, Iowa
D. L. Kinser, Vanderbilt University, Nashville, Tennessee
B. Lebech, Risø National Laboratory, Roskilde, Denmark
C.-K. Loong, Iowa State University/Ames Laboratory, Ames, Iowa
O. A. Meyer, Nuclear Research Center, Karlsruhe, Germany
M.-K. Nacke, Kernforschungsanlage, Jülich, Germany
Y. Noda, Sendai Radio Technical College, Sendai, Japan
V. M. Orera, University of Zaragoza, Zaragoza, Spain
M. Rappaz, École Polytechnique Fédérale, Lausanne, Switzerland
H.-B. Schweer, Kernforschungsanlage, Jülich, Germany
J. L. Staudenmann, Iowa State University/Ames Laboratory, Ames, Iowa
B. W. Stritzker, Kernforschungsanlage, Jülich, Germany
Y. Yamada, Osaka University, Osaka, Japan
J. L. Zaretsky, Iowa State University/Ames Laboratory, Ames, Iowa

B. Graduate Students
- O. W. Holland, North Texas State University, Denton, Texas
- R. E. Parra, Georgia Institute of Technology, Atlanta, Georgia
- S. R. Wilson, North Texas State University, Denton, Texas

C. Great Lakes College Association Science Program
- J. E. Gastineau, Lawrence University, Appleton, Wisconsin
- D. N. Olson, St. Olaf College, Northfield, Minnesota

Summer Assignments

A. Scientific Staff
- R. L. Bullough, Atomic Energy Research Establishment, Harwell, England
- B. J. Higuera, Rice University, Houston, Texas
- R. D. Lowde, Atomic Energy Research Establishment, Harwell, England
- C. H. Perry, Northeastern University, Boston, Massachusetts
- H. W. Weber, Atominstitut der Osterreichischen, Universitaten, Vienna, Austria

B. Clerical Staff
- D. L. Coldts, Roane State Community College, Rockwood, Tennessee
- L. M. Smalley, University of Tennessee, Knoxville, Tennessee

C. ORAU—University Faculty
- M. D. Sherrill, Clemson University

D. ORAU—Undergraduate Research Trainees
- C. R. Allen, Jarvis Christian College, Hawkins, Texas
- R. W. Johnson, University of Southwestern Louisiana, Lafayette, Louisiana
- C. T. Parks, Jr., Stetson University, Deland, Florida

SOLID STATE DIVISION
PROGRAMMATIC MANPOWER DISTRIBUTION
FY 1979

Programs	Staff (person-years)	Guests (person-years)	Total (person-years)
AK 01 02 Basic Energy Sciences (Materials Science)	68.0	5.0	73.0
AF 02 30 Fusion (Magnetic Fusion)	5.0	0	5.0
AG 30 20 Commercial Waste Management (Solid Waste R&D)	1.0	0.5	1.5
JM 05 02 Defense Waste Management (Airborne Waste R&D)	3.5	0	3.5
Work for others	12.5	3.0	15.5
Total	90.0	8.5	98.5

SOLID STATE DIVISION

MARCH 1, 1988

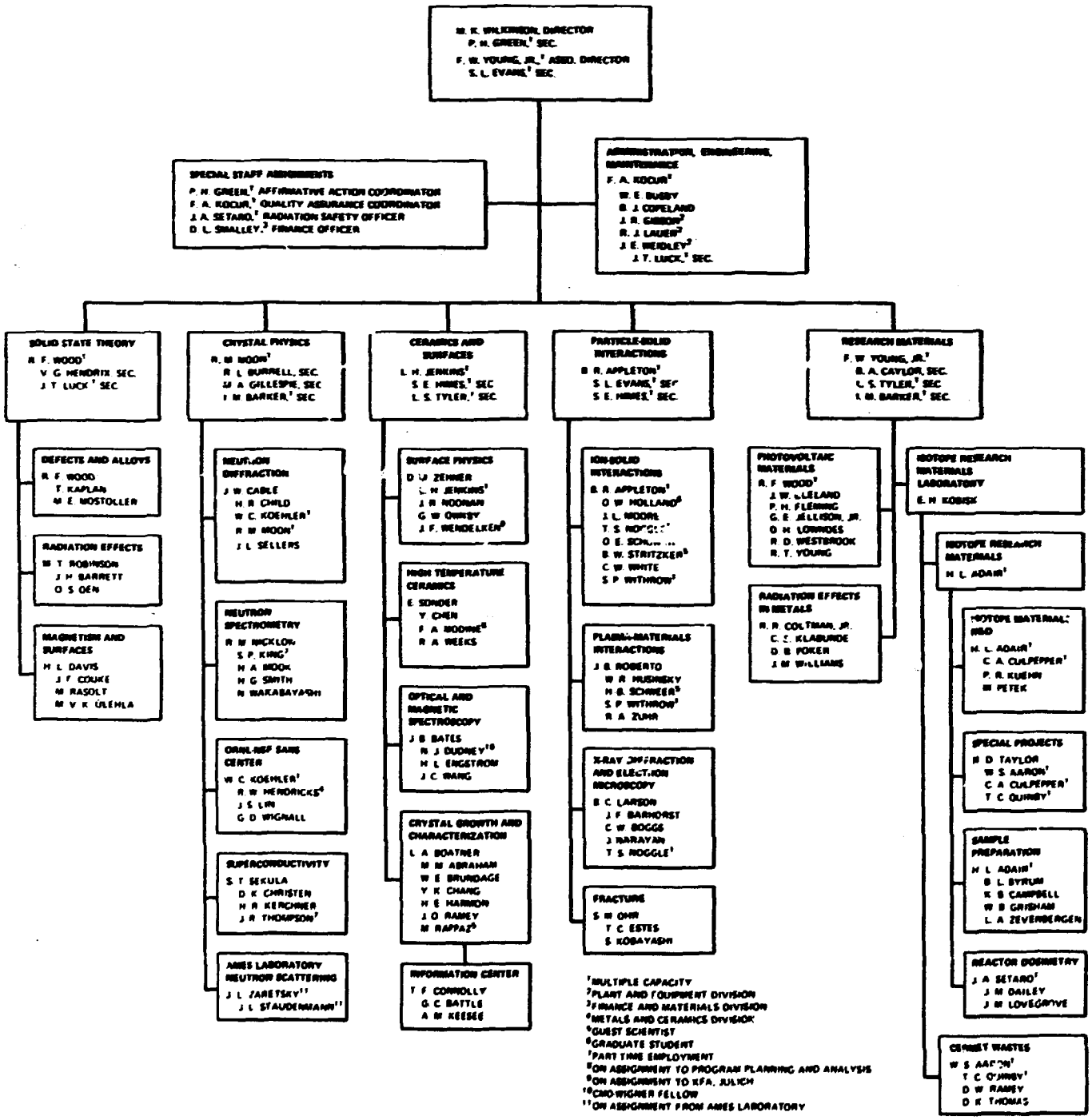

[1] MULTIPLE CAPACITY
[2] PLANT AND EQUIPMENT DIVISION
[3] FINANCE AND MATERIALS DIVISION
[4] METALS AND CERAMICS DIVISION
[5] GUEST SCIENTIST
[6] GRADUATE STUDENT
[7] PART TIME EMPLOYMENT
[8] ON ASSIGNMENT TO PROGRAM PLANNING AND ANALYSIS
[9] ON ASSIGNMENT TO KFA, JULICH
[10] ORO-WIGNER FELLOW
[11] ON ASSIGNMENT FROM AMES LABORATORY

INTERNAL DISTRIBUTION

1. W. S. Aaron
2. M. M. Abraham
3. H. L. Adair
4. E. D. Aebischer
5. B. R. Appleton
6. J. C. Ashley
7. S. I. Auerbach
8. J. A. Auxier
9. J. F. Barhorst
10. I. M. Barker
11. J. H. Barrett
12. J. B. Bates
13. G. C. Battle
14. L. A. Berry
15. J. A. Blackman
16. E. E. Bloom
17. L. A. Boatner
18. C. W. Boggs
19. W. E. Brundage
20. R. L. Burrell
21. W. E. Busby
22. W. H. Butler
23. B. L. Byrum
24. J. W. Cable
25. K. B. Campbell
26. B. A. Caylor
27. Y. K. Chang
28. Y. Chen
29. H. R. Child
30. D. K. Christen
31. G. W. Clark
32. J. W. Cleland
33. R. R. Coltman, Jr.
34. J. F. Cooke
35. B. J. Copeland
36. K. E. Cowser
37. J. A. Cox
38. C. A. Culpepper
39. J. M. Dailey
40. L. S. Darken
41. S. Datz
42. H. L. Davis
43. N. J. Dudney
44. S. L. Evans
45. H. L. Engstrom
46. T. C. Estes
47. D. E. Ferguson
48. P. H. Fleming
49. J. Fletcher
50. W. E. Fulkerson
51. M. A. Gillespie
52. P. H. Green
53. W. R. Grimes
54. W. B. Grisham
55. G. R. Gruzalski
56. H. E. Harmon
57. V. G. Hendrix
58. R. F. Hibbs
59. H. N. Hill
60. S. E. Himes
61. O. W. Holland
62. C. C. Hopkins
63. J. A. Horton
64. W. R. Husinsky
65. D. W. Jared
66. G. E. Jellison, Jr.
67. L. H. Jenkins
68. T. Kaplan
69. P. R. Kasten
70. S. V. Kaye
71. A. M. Keesee
72. O. L. Keller
73. H. R. Kerchner
74. S. P. King
75. C. E. Klabunde
76. E. H. Kobisk
77. F. A. Kocur
78. W. C. Koehler
79. P. R. Kuehn
80. B. C. Larson
81. J. S. Lin
82. R. S. Livingston
83. A. L. Lotts
84. J. M. Lovegrove
85. D. H. Lowndes
86. J. T. Luck
87. B. K. Lyon
88. F. C. Maienschein
89. L. K. Mansur
90. C. J. McHargue
91. L. E. McNeese
92. C. D. Moak
93. F. A. Modine
94. H. A. Mook
95. R. M. Moon
96. J. L. Moore

97. O. B. Morgan, Jr.
98. M. E. Mostoller
99. J. Narayan
100. R. M. Nicklow
101. T. S. Noggle
102. J. R. Noonan
103. F. E. Obenshain, Jr.
104. O. S. Oen
105. S. M. Ohr
106. G. W. Oliphant
107. G. W. Ownby
108. M. Petek
109. J. J. Pinajian
110. D. B. Poker
111. H. Postma
112. T. C. Quinby
113. D. W. Ramey
114. J. O. Ramey
115. M. E. Ramsey
116. M. Rappaz
117. M. Rasolt
118. C. R. Richmond
119. J. B. Roberto
120. M. T. Robinson
121. M. W. Rosenthal
122. O. E. Schow III
123. S. T. Sekula
124. J. L. Sellers
125. J. A. Setaro
126. W. D. Shults
127. M. J. Skinner
128. G. P. Smith
129. H. G. Smith
130. E. Sonder
131. P. H. Stelson
132. J. O. Stiegler
133. R. D. Taylor
134. D. K. Thomas
135. J. R. Thompson
136. D. B. Trauger
137. L. S. Tyler
138. M. V. K. Ulehla
139. N. Wakabayashi
140. G.-C. Wang
141. J. C. Wang
142. R. A. Weeks
143. J. R. Weir
144. J. F. Wendelken
145. R. D. Westbrook
146. C. W. White
147. G. D. Wignall
148-222. M. K. Wilkinson
223. J. M. Williams
224. S. P. Withrow
225. R. F. Wood
226. F. W. Young, Jr.
227. R. T. Young
228. D. M. Zehner
229. L. A. Zevenbergen
230. A. Zucker
231. R. A. Zuhr
232. Biology Library
233-234. Central Research Library
235. ORNL-Y-12 Technical Library Document Reference Section
236-237. Laboratory Records Department
238. Laboratory Records, ORNL R.C.

EXTERNAL DISTRIBUTION

239. Dr. S. Amelinckx, SCK/CEN 92460, Mol, Belgium
240. Dr. M. Antonini, Physics Div. Building 44, Joint Research Centre, EURATOM, 21020 Ispra (Varese), Italy
241. Dr. R. T. Arnold, Department of Physics, University of Mississippi, University, MS 38677
242. Dr. K. J. Bachmann, Bell Laboratories, 600 Mountain Avenue, Murray Hill, NJ 07974
243. Dr. T. Baldwin, Department of Physics, Southern Illinois University, Edwardsville, IL 62026
244. Dr. R. W. Balluffi, Department of Materials Science and Engineering, Massachusetts Institute of Technology, 77 Massachusetts Avenue, Cambridge, MA 02139
245. Dr. G. W. Beall, Radian Corporation, 8500 Shoal Creek Boulevard, Austin, TX 78766
246. Dr. H. Behrens, Zentralstelle für Atomkernergie-Dokumentation, 7514 Eggnestein-Leopoldshafen, Kernforschungszentrum, Germany
247. Dr. Rainer Behrisch, Max-Planck-Institut für Plasmaphysik, 8046 Garching/München, Germany
248. Bibliotheque, Institute Max von Laue-Paul Langevin, 156X Centre de Tri, 38042 Grenoble, Cedex, France
249. Dr. D. S. Billington, 35 Outer Drive, Oak Ridge, TN 37830

250. Dr. T. H. Blewitt, Materials Science Division, Argonne National Laboratory, 9700 South Cass Avenue, Argonne, IL 60439
251. Dr. J. L. Boldú, Instituto de Fisica, Universidad Nacional Autónoma de Mexico, Apartado Postal 20-364, Mexico 20, D.F.
252. Dr. William F. Brinkman, Bell Laboratories, 600 Mountain Avenue, Murray Hill, NJ 07974
253. Dr. F. Brown, Solid State Science Branch, Chemistry and Materials Division, Chalk River Nuclear Laboratories, Chalk River, Ontario, Canada
254. Dr. F. C. Brown, Department of Physics, University of Illinois, Urbana, IL 61801
255. Dr. Walter Brown, Room 1E452, Bell Laboratories, 600 Mountain Avenue, Murray Hill, NJ 07974
256. Dr. John Burnett, Division of Chemical Sciences, Office of Basic Energy Sciences, Office of Energy Research, U.S. Department of Energy, Washington, DC 20545
257. Dr. W. J. L. Buyers, Atomic Energy of Canada, Ltd., Chalk River, Ontario, Canada
258. Dr. N. Cabrera, Departmento de Fisica Fundamental, Facultad de Ciencias, Universidad Autónoma de Madrid, Canto Blanco, Madrid, Spain
259. Prof. Guiseppe Cagliotti, Instituto di Ingegneria Nuclear, Centro Studi Nucleari Enrico Fermi-CESNEF, Via Ponzio 34/3, 20133, Milano, Italy
260. Dr. R. L. Chaplin, Department of Physics, Clemson University, Clemson, SC 29631
261. Dr. L. L. Chase, Physics Department, 112 Swain Hall-West, Indiana University, Bloomington, IN 47401
262. Dr. Andre Châtelain, Lab. Phys. Exp., Federal Institute of Technology, 33 Av. Cour, 1007 Lausanne, Switzerland
263. Dr. Mui Fatt Chung, Physics Department, University of Singapore, Bukit Timah Road, Singapore 10
264. Dr. C. B. Clark, Department of Physics, University of North Carolina, Greensboro NC 27412
265. Dr. G. J. Clark, Mineral Physics Division, Commonwealth Scientific and Industrial Research Organization, P.O. Box 136, North Ryde, N.S.W. 2113, Australia
266. Dr. W. Dale Compton, Vice-President Research, Ford Motor Company, P.O. Box 1603, Dearborn, MI 48121
267. Dr. J. H. Crawford, Jr., Department of Physics and Astronomy, University of North Carolina, Chapel Hill, NC 27514
268. Dr. W. L. Crummett, Department of Physics, Montana State University, Bozeman, MT 59715
269. Dr. J. C. Crump III, 2... 6 Essex Road, Richmond, VA 23228
270. Mr. Floyd L. Culler, Jr., Electric Power Research Institute, 3412 Hillview Avenue, Palo Alto, CA 94303
271. Dr. G. Czjzek, Kernforschungszentrum Karlsruhe, Institut für Angewandte Kernphysik, Postfach 3640, D-7500 Karlsruhe, Germany
272. Dr. Lubomir David, Director, Centre de Fisica, Instituto Venezolano de Investigaciones Cientificas-Apartado 1827, Caracas 101, Venezuela
273. Prof. Dr. P. H. Dederichs, Institut für Festkorperforschung der Kernforschungsanlage Jülich GmbH, 5170 Jülich, Postfach 1913, Germany
274. Dr. J. Diehl, Max-Planck-Institut für Metallforschung, Institut für Werkstoffwissenschaften, D-7000 Stuttgart 1, Sestrasse 92BRD, Germany
275. Dr. J. Dienes, Department of Physics, Brookhaven National Laboratory, Upton, L.I., NY 11973
276. Prof. H.-D. Dietze, Institut für Theoretische Physik C, RWTH Aachen, 51 Aachen, Germany
277. Dr. G. Dolling, Atomic Energy of Canada, Ltd., Chalk River, Ontario, Canada
278. Dr. D. G. Doran, Hanford Engineering Development Laboratory, P.O. Box 1970, Richland, WA 99352
279. Dr. B. Dreyfus, Chef du DRF-G, Centre d'Etudes Nucléaires de Grenoble, 85X, 38041 Grenoble, Cedex, France

280. Dr. Norman Edelstein, Building 70-A, Room 1149, Lawrence Berkeley Laboratory, Berkeley, CA 94720
281. Dr. H. Ehrenreich, Division of Engineering and Applied Physics, Harvard University, Cambridge, MA 02138
282. Dr. P. Ehrhart, Institut für Festkorperforschung der Kernforschungsanlage Jülich GmbH, 5170 Jülich, Postfach 1913, Germany
283. Prof. T. L. Estle, Physics Department, Rice University, Houston, TX 77001
284. Prof. H. Y. Fan, Department of Physics, Purdue University, West Lafayette, IN 47907
285. Prof. Dr. W. Frank, Max-Planck-Institut für Metallforschung, Institut für Physik, 7 Stuttgart 80, Büsnacer Strasse 171, Germany
286. Prof. Arthur Freeman, Physics Department, Northwestern University, Evanston, IL 60201
287. Dr. J. Friedel, Physique des Solides, Université Paris Sud, 91405 Orsay, France
288. Dr. A. T. Fromhold, Department of Physics, Auburn University, Auburn, AL 36830
289. Dr. C. Peter Flynn, Director, Materials Research Laboratory, University of Illinois, Urbana-Champaign, IL 61801
290. Dr. N. Fukuoka, Department of Physics, College of General Education, Osaka University, Toyonaka, Osaka 560, Japan
291. Dr. B. N. Ganguly, Systems Analysis Area/W-147, Xerox Corporation, Webster, NY 14580
292. Dr. G. F. Garlick, 267 S. Benoit Avenue, Los Angeles, CA 90049
293. Dr. W. B. Gauster, Physical Research Division 8347, Sandia Laboratories, Livermore, CA 94550
294. Dr. H. A. Gersch, School of Physics, Georgia Institute of Technology, Atlanta, GA 30332
295. Dr. A.-M. de Goer, Centre d'Etudes Nucléaires de Grenoble, Service des Basses Températures, 85X, 38041 Grenoble, Cedex, France
296. Dr. A. N. Goland, Physics Department, 510-B, Brookhaven National Laboratory, Upton, L.I., NY 11973
297. Dr. M. Guinan, Lawrence Livermore Laboratory, P.O. Box 808, Livermore, CA 94550
298. Dr. B. Henderson, Department of Pure and Applied Physics, Physical Laboratory, Trinity College, Dublin 2, Ireland
299. Dr. T. J. Hicks, Department of Physics, Monash University, Clayton, Victoria, Australia 3168
300. Dr. J. W. Hodby, University of Oxford, Clarendon Laboratory, Oxford OX1 3PU, England
301. Dr. David K. Holmes, Physics Discipline, College of Arts, Sciences, and Letters, University of Michigan, 4901 Evergreen Road, Dearborn, MI 48128
302. Dr. H. H. Hopkins, Jr., Rockwell International, Atomics International Division, Rockwell-Hanford Operations, P.O. Box 800, Richland WA 99352
303. Dr. J. C. G. Houmann, Risø National Laboratory, DK4000, Roskilde, Denmark
304. Dr. Marc Hou, Physique des Surfaces, Faculté des Sciences, Université Libre de Bruxelles, Campus de la Plaine (C.P. 234), Boulevard de Triomphe, B-1050 Bruxelles, Belgium
305. Mr. J. T. Howe, 106 Columbia Drive, Oak Ridge, TN 37830
306. Dr. A. E. Hughes, Materials Development Division B552, Atomic Energy Research Establishment, Harwell, Didcot, Oxon. OX11 ORA, England
307. Dr. Tadao Iwata, Division of Physics, Japan Atomic Energy Research Institute, Tokai-mura, Ibaraki-Ken 319-11, Japan
308. Dr. P. K. Iyengar, Director, Physics and Metallurgy Groups, Bhabha Atomic Research Centre, Trombay, Bombay 400 085, India
309. Dr. W. A. Kamitakahara, Department of Physics, Iowa State University, Ames, IA 50010
310. Dr. D. W. Kammer, Department of Physics, Albion College, Albion, MI 49224
311. Dr. J. S. Kane, Associate Director for Basic Energy Sciences, Office of Energy Research, U.S. Department of Energy, Washington, DC 20545
312. Dr. T. Kaneda, Research Laboratories Tokyo, Fuji Photo Film Company, Ltd., Asakashi, Saitamaken, 351 Japan
313. Dr. Fred Keller, Department of Physics, Clemson University, Clemson, SC 29631

314. Dr. R. H. Kernohan, 10. Euclid Place, Oak Ridge, TN 37830
315. Dr. Q. H. Khan, N.P.D., PINSTECH, P.O Nilore, Rawalpindi, Pakistan
316. Dr. D. L. Kinser, Department of Materials Science, Vanderbilt University, Nashville, TN 37235
317. Dr. J. S. Koehler, Physics Department, University of Illinois, Urbana, IL 61801
318. Dr. Eckhard Krätzig, Physics Department, University of Osnabrück, 45 Osnabrück, Postfach 4469, Germany
319. Dr. R. Kropschot, Deputy Director, Office of Basic Energy Sciences, Office of Energy Research, U.S. Department of Energy, Washington, DC 20545
320. Dr. Ad Lagendijk, Universitaire Instelling Antwerpen, Department Natuurkunde, Universiteitsplein 1, 2610 Wilrijk, Belgium
321. Dr. C. Lehmann, Institut für Festkorperforschung der Kernforschungsanlage Jülich GmbH, 5170 Jülich, Postfach 1913, Germany
322. Dr. H. P. Leighly, Department of Metallurgical and Nuclear Engineering, University of Missouri-Rolla, Rolla, MO 65401
323. Dr. F. Li Aravena, Comision Chilena de Energia Nuclear, Los Jesuitas 645, Casilla 188D, Santiago, Chile
324. Librarian, Building 465, Atomic Energy Research Establishment, Harwell, Didcot, Oxon., OX11 ORA, England
325. The Librarian, Department of Physics, University of Islamabad, P.O. Box 1090, Islamabad, Pakistan
326. Dr. A. B. Lidiard, Theoretical Physics Division, Building 8.9, Atomic Energy Research Establishment, Harwell, Didcot, Oxon., OX11 ORA, England
327. Dr. W. M. Lomer, Research Director (Environment), Atomic Energy Research Establishment, Harwell, Didcot, Oxon., OX11 ORA, England
328. Dr. Stephen Lovesey, Rutherford Laboratory, Chilton, Didcot, Oxon., OX11 OQX, England
329. Prof. Dr. H.-O. Lutz, Fakultat für Physik, Universität Bielefeld, P.O. Box 8640, D-4800 Bielefeld 1, Germany
330. Dr. J. W. Lynn, Department of Physics, University of Maryland, College Park, MD 20742
331. Dr. R. W. Major, Department of Physics, University of Richmond, Richmond, VA 23173
332. Dr. W. C. Mallard, Physics Department, Georgia State University, Atlanta, GA 30303
333. Dr. R. Medina, Centro de Fisica, Instituto Venezolano de Investigaciones Cientificas, Apartado 1827, Caracas 101, Venezuela
334. Dr. A. Merlini, Physics Division, C.C.R. EURATOM, 21020 Ispra (Varese), Italy
335. Dr. J. W. Mitchell, Department of Physics, University of Virginia, Charlottesville, VA 22901
336. Dr. E. Munoz P, Instituto de Fisica, Universidad Nacional Autonoma de Mexico, Apartado Postal 20-364, Mexico 20, D. F.
337. Dr. R. B. Murray, Physics Department, University of Delaware, Newark, DE 19711
338. Dr. Taki Negas, Solid State Chemistry, Ceramic, Glass, and Solid State Science Division, Building 223, Room B-220, National Bureau of Standards, Washington, DC 20234
339. Dr. L. H. Nosanow, Head, Condensed Matter Materials Section, Division of Materials Research, National Science Foundation, Washington, DC 20550
340. Dr. A. S. Nowick, Columbia University, 1146 S. W. Mudd Building, New York, NY 10027
341. Oak Ridge Associated Universities, MERT Division Library, P.O. Box 117, Oak Ridge, TN 37830
342. Office of Assistant Manager for Energy Research and Development, U.S. Department of Energy, Oak Ridge Operations Office, Oak Ridge, TN 37830
343. Dr. D. N. Olson, Department of Physics, St. Olaf College, Northfield, MN 55057
344. Dr. V. M. Orera, Departamento de Fisica Fundamental, Facultad de Ciencias, Universidad de Zaragoza, Zaragoza-6, Spain
345. Dr. A. W. Overhauser, Department of Physics, Purdue University, West Lafayette, IN 47907
346. Dr. Arthur Pepe, Centre de Recherches Nucléaire, 67037 Strasbourg Cedex, France

347. Dr. Robert L. Park, Director, Center of Materials Research, University of Maryland, College Park, MD 20742
348. Dr. R. E. Parra, Centro de Física, Instituto Venezolano de Investigaciones Científicas Apartado 1827, Caracas 101, Venezuela
349. Dr. Hans Peisl, Sektion Physik, Universität München, Geschwister-Scholl-Platz 1, 8000 München, 22/Germany
350. Physics/Optics/Astronomy Library, 374 Bausch and Lomb Building, University of Rochester, Rochester, NY 14627
351. Dr. Elliott Pierce, Director, Division of Chemical Sciences, Office of Basic Energy Sciences, Office of Energy Research, U.S. Department of Energy, Washington, DC 20545
352. Dr. T. Pinkston, Department of Physics and Astronomy, Vanderbilt University, Nashville, TN 37240
353. Dr. David Long Price, Solid State Science Division, Argonne National Laboratory, 9700 South Cass Avenue, Argonne, IL 60439
354. Dr. W. Reichardt, Kernforschungszentrum Karlsruhe GmbH, Institut für Angewandte Kernphysik 1, Postfach 3640, D-7500 Karlsruhe, Germany
355. Dr. R. W. Reynolds, General Research Corporation, 307 Winn Drive, Huntsville, AL 35807
356. Dr. James R. Rice, Division of Engineering, Brown University, Providence, RI 02912
357. Dr. T. Riste, Institutt for Atomenergi, P.O. Box 40, 2007 Kjeller, Norway
358. Dr. J. E. Rives, Department of Physics, University of Georgia, Athens, GA 30602
359. Dr. C. A Rotter, Department of Physics, West Virginia University, Morgantown, WV 26506
360. Dr. J. M. Rowe, Reactor Radiation Division, National Bureau of Standards, Washington, DC 20234
361. Dr. J. Rubio O., Instituto de Física, Universidad Nacional Autonoma de Mexico, Apartado Postal 20-364, Mexico 20, D.F.
362. Dr. Haruo Saito, College of General Education, Osaka University, 1-1, Machikaneyama-cho, Toyonaka-shi, Osaka 560, Japan
363. Dr. William R. Savage, Department of Physics and Astronomy, University of Iowa, Iowa City, IA 52242
364. Dr. Kurt Scharnberg, Institut für Angewandte, Universität Hamburg, Jungiusstrasse 11, D-2000 Hamburg 36, Germany
365. Dr. R. Scherm, PT B, Abt 7.3, Postfach 3345, 33 Braunschweig, Germany
366. Dr. W. Schilling, Institut für Festkorperförschung der Kernforschungsanlage der Jülich GmbH, 5170 Jülich, Postfach 1913, Germany
367. Prof. Dr. W. Schmatz, Kernforschungszentrum Karlsruhe GmbH, Institut für Angewandte Kernphysik 1, Postfach 3640, D-7500 Karlsruhe, Germany
368. Dr. W. Schnepple, EG&G, Energy Measurements Group, Santa Barbara Operations, 130 Robin Hill Road, Goleta, CA 93017
369. Prof. R. Schuttler, I.N.S.A. Service Informatique, Avenue de Rangueil, F-31077 Toulouse, Cedex, France
370. Dr.H. B. Schweer, Institut für Festkorperförschung der Kernforschungsanlage Jülich GmbH, 5170 Jülich, Postfach 1913, Germany
371. Prof. Dr. A. Seeger, Max-Planck-Institut für Metallforschung, Institut für Physik, Heisenbergstrasse 1, Postfach 800665, D-7000 Stuttgart 80, Germany
372. Dr. David N. Seidman, Department of Materials Science and Engineering, Bard Hall, Cornell University, Ithaca, NY 14850
373. Dr. C. G. Shull, Department of Physics, Massachusetts Institute of Technology, Cambridge, MA 02139
374. Dr. W. A. Sibley, Assistant Vice President for Research, 101 Whitehurst, Oklahoma State University, Stillwater, OK 74074
375. Dr. R. H. Silsbee, Clark Hall, Physics Department, Cornell University, Ithaca, NY 14853
376. Dr. K. Sonnenberg, Institut für Festkorperförschung der Kernforschungsanlage Jülich GmbH, 5170 Jülich, Postfach 1913, Germany

377. Prof. Dr. T. Springer, Directeur, Institute Max von Laue-Paul Langevin, Avenue des Martyrs, 38042 Grenoble, Cedex, France
378. Dr. Stephen Spooner, Department of Chemical Engineering, Georgia Institute of Technology, Atlanta, GA 30332
379. Dr. R. L. Sproull, President, University of Rochester, Rochester, NY 14627
380. Dr. D. K. Stevens, Director, Division of Materials Sciences, Office of Basic Energy Sciences, Office of Energy Research, U.S. Department of Energy, Mail Station J-309, Washington, DC 20545
381. Dr. J. R. Stevenson, Acting Vice President for Academic Affairs, Georgia Institute of Technology, Atlanta, GA 30332
382. Prof. R. Street, Vice-Chancellor, The University of Western Australia, Nedlands, Australia 6009
383. Dr. B. G. Streetman, Department of Electrical Engineering, University of Illinois, Urbana, Il 61801
384. Dr. B. W. Stritzker, Institut für Festkorperforschung der Kernforschungsanlage Jülich GmbH, 5170 Jülich, Postfach 1913, Germany
385. Dr. M. L. Swanson, Chalk River Nuclear Laboratories, Chalk River, Ontario, Canada KOJ 1JO
386. Dr. F. J. E. Tasset, Institute Max von Laue-Paul Langevin, 156X Centre de Tri, 38042 Grenoble, Cedex, France
387. Dr. J. D. Tewhey, L-209, Lawrence Livermore Laboratory, University of California, P.O. Box 808, Livermore, CA 94550
388. Dr. D. O. Thompson, Ames Laboratory, Iowa State University, Ames, IA 50010
389. Dr. M. W. Thompson, School of Mathematical and Physical Sciences, University of Sussex, Brighton, BN1 9QH, Sussex, England
390. Dr. J. O. Thomson, Department of Physics, The University of Tennessee, Knoxville, TN 37917
391. Dr. H. T. Tohver, Department of Physics, University of Alabama, Birmingham, AL 35233
392. Dr. G. T. Trammell, Department of Physics, Rice University, Houston, TX 77001
393. Dr. J. G. Traylor, Buena Vista College, Storm Lake, IA 50588
394. Dr. James B. Trice, Program Manager, General Electric AEP, Room 7246,C7, P.O. Box 8661, Philadelphia, PA 19101
395. Dr. Werner Uelhoff, Institut für Festkorperforschung der Kernforschungsanlage Jülich GmbH, 5170 Jülich, Postfach 1913, Germany
396. Universidade Federal de Minas Gerais, ICEX-Depto de Fisica, Servico de Documentacão, 30.000—Belo Horizonte—MG—Brazil
397. Dr. W. P. Unruh, Department of Physics, University of Kansas, Lawrence KS 66044
398. Dr. W. E. Vehse, Department of Physics, University of West Virginia, Morgantown, WV 26506
399. Dr. H. Verbeek, Max-Planck-Institut für Plasmaphysik, D-8046 Garching, Germany
400. Dr. P. R. Vijayaraghavan, Nuclear Physics Division, Bhabha Atomic Research Centre, Trombay, Bombay 400 085, India
401. Dr. G. Vogl, Hahn-Meitner Institut für Kernforschung, D-1 Berlin 39, Glienicker Strasse 100, Germany
402. Dr. F. L. Vook, Solid State Sciences, Org. 5100, Sandia Laboratories, Albuquerque, NM 87115
403. Prof. David Walsh, Department of Physics, Ernest Rutherford Physics Building, McGill University, 3600 University Street, Montreal PQ, H3A 2TB, Canada
404. Prof. George D. Watkins, Sherman Fairchild Laboratory 161, Lehigh University, Bethlehem, PA 18015
405. Dr. M. S. Webster, Department of Physics and Astronomy, Vanderbilt University, Nashville, TN 37203
406. Dr. M. S. Wechsler, Department of Metallurgy, Iowa State University, Ames, IA 50010

407. Dr. A. M. Weinberg, Director, Institute for Energy Analysis, Oak Ridge Associated Universities, Oak Ridge, TN 37830
408. Dr. H. F. Wenzl, Institut für Festkorperförschung der Kernforschungsanlage Jülich GmbH, 5170 Jülich, Postfach 1913, Germany
409. Dr. C. W. Wert, Head, Department of Metallurgy and Mining Engineering, University of Illinois, Urbana, IL 61801
410. Dr. E. P. Wigner, 8 Ober Road, Princeton, NJ 08540
411. Dr. W. Williams, Materials Research Laboratory, University of Illinois, Urbana-Champaign, IL 61801
412. Dr. S. R. Wilson, Semiconductor Group, Motorola, Incorporated, 5006 East McDowell, Mail Drop B-132, Phoenix, AZ 85008
413. Dr. T. M. Wilson, Department of Physics, Oklahoma State University, Stillwater, OK 74074
414–421. Dr. R. R. Winters, Director, Oak Ridge Science Semester, GLCA, Denison University, Main Street, Granville, OH 43023
422. Dr. Mark C. Wittels, Division of Materials Sciences, Office of Basic Energy Sciences, Office of Energy Research, U.S. Department of Energy, Mail Station J-309, Washington, DC 20545
423. Dr. E. O. Wollan, Cedars of Edina, Apartment 113-B, 7340 Gallagher Drive, Edina, MN 55435
424. Prof. Dr. H. Wollenberger, Hahn-Meitner Institut für Kernforschung Berlin, Glienicker Strasse 100, 1000 Berlin 39, Germany
425. Dr. R. A. Young, School of Physics, Georgia Institute of Technology, Atlanta, GA 30332
426. Dr. Solomon Zwerdling, Northeast Solar Energy Center, 70 Memorial Drive, Cambridge, MA 02142
427. Dr. K. Zwilsky, Chief, Materials and Radiation Effects Branch, Office of Fusion Energy (ETM), Office of Energy Research, U.S. Department of Energy, Washington, DC 20545
428–454. Technical Information Center, U.S. Department of Energy, Oak Ridge, TN 37830

☆ U.S. GOVERNMENT PRINTING OFFICE 1980-640-245/253